An Investigation of The Effect of Low Impact Shock Processes on Breakdown of Sandstone at Meteor Crater

Ankit Kumar Verma

A thesis Submitted in partial fulfilment of the requirement of the degree of Doctor of Philosophy in Geography

2019



Trinity College Dublin
Coláiste na Tríonóide, Baile Átha Cliath
The University of Dublin

Ad astra per aspera

Declaration

I declare that this thesis has not been submitted as an exercise for a degree at this or any other university and it is entirely my own work.

I agree to deposit this thesis in the University's open access institutional repository or allow the library to do so on my behalf, subject to Irish Copyright Legislation and Trinity College Library conditions of use and acknowledgement.

Ankit K. Verma

An Investigation of The Effect of Low Impact Shock Processes on Breakdown of Sandstone at Meteor Crater

Ankit K. Verma

Abstract

Impact cratering is one of the most common geologic processes shaping all the terrestrial planetary bodies and moons in our solar system. The widespread presence of craters on terrestrial planets and moon in the inner solar system shows that impact cratering was a dominant process during the early history of the solar system. Asteroid and comet impacts can influence the geologic and climatic history of terrestrial planets and impact processes can also play a significant role in subsequent rock breakdown on planetary bodies. The formation of impact craters has a catastrophic effect on target lithology, producing a range of heterogeneities and deformation features in rocks. Recognising how these heterogeneities and deformation features affect the mechanisms and kinetics of rock weathering provides a framework for understanding impact inheritance in rock breakdown.

Research within the past few decades has revealed extensive shock related features and deformations in rocks in the impact craters. In recent years, stress history and rock control are recognised important in controlling the rate and nature of breakdown. This thesis is the first detailed and comprehensive investigation of the effect of impact metamorphism processes on subsequent rock breakdown.

The focus of this thesis is to understand how the inheritance from low impact shock (<10 GPa) deformations and heterogeneities affects subsequent rock breakdown. This is achieved through a combined field and laboratory approaches that examined rock breakdown on impacted, and non-impacted rocks of the same lithology that are exposed at Meteor Crater site, Arizona. Rock hardness data and topographic data using a Structure from Motion (SfM) photogrammetry-based method developed in this thesis was used to compare rock breakdown between impacted and non-impacted sandstone outcrops at Meteor Crater site. The topographic data collected in the field was analysed using a range of roughness and morphometric parameters. The rock samples collected from the Meteor Crater and additional small number of impactite samples from West Clearwater Impact

Structure (Canada) and Ries Crater (Germany) were characterised and assigned a shock level in the laboratory using different analytical techniques (petrographic microscopy, powder X-ray diffraction, scanning electron microscopy, X-ray computed tomography). Further, these samples were used in a physical weathering simulation in semi-arid conditions. The rock samples were analysed before and after the experiments to identify and quantify changes. This research advanced the field of rock breakdown by providing insight into the influence of impact processes on subsequent rock breakdown processes.

This thesis has revealed the following new insights: (1) The low impact shocked sedimentary rocks show a decrease in porosity. (2) Macrofracturing and microfracturing caused by low impact shock occur in all types of impactites. Macrofracturs of 0.1-0.2 mm and microfractures 0.1-5 μm in aperture are observed in all types of impactites. (3) The rock breakdown experiment results showed that impactites exhibit an accelerated decline in strength compared to non-impacted control samples. (4) Rock type and impact deformation history are important in controlling the rate of deterioration. (5) Close-range Structure from Motion (SfM) photogrammetry can be used to collect sub-mm resolution topographic data on rock surfaces in the field. (6) Rock hardness, rock surface roughness and morphometric analysis revealed no substantial difference in terms of nature of breakdown between low shocked and ushocked Moenkopi Sandstone at Meteor Crater site. (7) Aspect related microclimate within Meteor Crater affects the nature of rock breakdown on different crater sidewalls.

This thesis has improved the understanding of low shock deformed sandstones in impact craters and provided an insight into the role of low shock inheritance on subsequent rock breakdown. This research also advances the data collection methods on rock breakdown in field and laboratory settings by developing and applying novel SfM photogrammetry and X-ray computed tomography (CT) techniques.

Acknowledgements

The four-year journey to complete my PhD thesis has been both miserable and magical. I have been blessed to have known and met many wonderful, kind and generous people along this journey and without their help and support this thesis could not be completed. I am grateful for their help, inspiration, friendship and support. I would like to thank and acknowledge their help and support sincerely.

I owe an enormous debt of gratitude to my PhD supervisor Dr Mary Bourke for great opportunity to work with her in Ireland. It was tough moving away from family and friends and settling in a new country for this PhD. Mary has been the source of my inspiration for my passion of studying planetary sciences. I cannot thank her enough for her advice, encouragement, optimism, trust, motivation, insight, support, and belief in my 'rock breaking and impact making' capabilities throughout my PhD. I will always remain indebted for her moral support during difficult times when I felt lost and down. She gave me complete freedom to investigate new ideas and granted me the independence to lead my PhD project. She initiated and allowed me to pursue collaborations within and outside Ireland. I have learned a great deal of research-life lessons from her. I enjoyed working with Mary and will undoubtedly continue to collaborate with her in future. Her mentorship was instrumental to my evolution into a more confident scientist. I would also like to thank Dr Juan Diego Rodriguez-Blanco, Prof Heather Viles, and Prof Gordon Osinski for further research expertise and guidance. Heather offered me the opportunity to work with her in Oxford Rock Breakdown Laboratory. She made sure that I felt welcomed and had all the facilities require to conduct my experiment in Oxford. I would also like to extend my sincere thanks to my confirmation panel members: Dr Gayle McGlynn and Dr Robin Edwards.

I want to thank Mr Neil Kearny and Mr Noel McGinley for their help in Geology labs. Mr Frances Hendron is thanked for preparing thin sections for me. I was benefited from the discussion on geology with Dr Gavin Kenny, Dr Catherine Rose, Dr Teresa Ubide, Dr Balz Kamber, Dr Robbie Goodhue and Dr Quentin Crowley during the beginning of my PhD.

Mr Colin Reid, Ms Leona O'Connor, Dr Paul Guyett are thanked for their help using Scanning Electron Microscope at Centre for Microscopy and Analysis.

A big thanks to Dr Elaine Treacy, Dr James Canavan and Mr Terrence Dunne at the Geography department for their assistance in preparations for field and lab work.

All the technical staff at Oxford Rock Breakdown Laboratory Dr Mona Edwards, Dr Hong Zhang, and Mr Ayush Srivastava are thanked for their warm hospitality and help in conducting the Physical weathering experiment.

A myriad thanks must go to Dr Farah Ahmed, Dr Jens Najorka, Dr Amin Garbout, and Dr Tobias Salge for hosting me at Natural History Museum in London and training me to collect data using X-ray diffraction and X-ray computed tomography (CT).

Many thanks to Dr Justin Hagerty, Dr Tenielle Gaither, Dr Ryan Anderson, and Dr Lauren Edgar for providing useful advice and assistance during my visit at United States Geological Survey Astrogeology Centre.

Dr David Kring has proven an ever-generous field guide during my visits to Meteor Crater and offered greater insight about the impact cratering process in the field.

Prof David Whiteman and METCRAX team are thanked for providing data from METCRAX I and METCRAX II experiments.

I am grateful to the following organisations, societies and institutions for providing funding to cover research, travel and laboratory work for the research included in this thesis: Irish Geomorphology Group Travel Award, American Geophysical Union Fall Meeting General Travel Grant, Trinity Trust Travel Grant, Geography Postgraduate Travel Grant, Trinity College Dublin, Trinity Association and Trust Travel Grant, Geological Remote Sensing Group Student Travel Bursary, Trinity Trust Travel Grant, Europlanet 2020 Research Infrastructure Access Grant (Europlanet 2020 RI has received funding from the European Union's Horizon 2020 research and innovation programme under grant agreement No 654208), International Association of Sedimentologists Postgraduate Grant, British Society for Geomorphology Postgraduate Research Grant, Barringer Family Fund for Meteorite Impact Research, The J.N. Tata Gift Scholarship, The Sir Dorabji Tata Trust Travel Grant, The J.N. Tata Endowment Scholarship for the higher education of Indians, Faculty of Engineering, Mathematics and Science, India (PhD) Scholarship, Trinity College Dublin, Trinity Postgraduate Research Studentship Award, Natural History Museum, London, Oxford Rock Breakdown Laboratory, University of Oxford, Centre for Microscopy and Analysis, Trinity College Dublin. A

huge thanks to Meteor Crater Enterprises, Barringer family, Bar T Bar ranch for permitting me to work at Meteor Crater site.

My fellow PhD student have been an invaluable support network during my PhD. Niamh has always motivated and cheered me up and helped in the field and lab when I needed. The comradeship of Chris, Jane Feeney, Jane Maher, Lauren, Maxime, Maria Teresa, Nivelton has always provided support and distraction from work.

Finally, special gratitude to all my friends outside the college, especially Prabhjot, Abhishek, Vignesh, Yonglin, Rajat, Shikhar, Deepak.

Thanks to Ian and Patsy for providing a home away from home for four years.

Most of all, I wish to thank my parents and family for financial and emotional support. Without their unwavering support throughout my career, I would not have achieved everything that I have so far.

Dedicated to

My mum

&

Dad

Table of contents

1. INTRODUCTION 1

1.1. ROCK BREAKDOWN AND LANDSCAPE EVOLUTION 1

1.2. SCALE ISSUES IN ROCK WEATHERING 5

1.3. IMPACT CRATERING 9

1.3.1. Stages of crater formation 9

1.3.1.1. Contact and compression 9

1.3.1.2. Excavation 10

1.3.1.3. Modification 10

1.3.2. Types of craters 13

1.3.2.1. Simple craters 13

1.3.2.2. Complex craters 13

1.3.2.3. Multiring structures 14

1.4. IMPACT CRATERING AND ROCK BREAKDOWN ON MARS 14

1.5. EFFECT OF IMPACT INHERITANCE ON ROCK BREAKDOWN 17

1.6. THEMES OF THE THESIS AND OUTLINE 24

1.7. AUTHOR CONTRIBUTIONS 27

REFERENCES 29

2. PETROGRAPHIC PROPERTIES OF IMPACTITES 45

ABSTRACT 45

2.1. IMPACTITES 45

2.2. SHOCK METAMORPHISM 46

2.3. EFFECT OF SHOCK ON POROSITY AND PERMEABILITY OF SEDIMENTARY AND CRYSTALLINE ROCKS 48

2.4. MATERIALS AND METHODS 49

2.4.1. Samples 49

2.4.1.1. Meteor Crater Samples: Sedimentary impacted rocks 51

2.4.1.2. West Clearwater Impact Structure samples: Crystalline impacted rocks, impact melt rocks, and impact breccias 52

2.4.1.3. Ries Crater samples: Impact melt-bearing breccia or suevite 53

2.4.2. Sample preparation 53

2.4.3. Characterisation of samples 53

2.4.3.1. Quantitative X-ray diffraction (XRD) for identification of mineral phases in rock samples 54
2.4.3.2. Petrographic examination using Scanning Electron Microscope (SEM) and Petrographic Microscope 55
2.4.3.3. X-ray Computed Tomography (CT) 56
2.5. RESULTS AND DISCUSSION **56**
2.5.1. Sedimentary impactites 56
2.5.1.1. Coconino Sandstone (CS) 57
2.5.1.2. Moenkopi Sandstone (MS) 61
2.5.2. Crystalline impactites 64
2.5.3. Impact melt rocks and impact breccias 66
2.5.3.1. Clast rich fine-grained impact-melt rock 66
2.5.3.2. Clast-poor fine-grained impact melt rock 67
2.5.3.3. Clast-free impact melt rock 70
2.5.3.4. Lithic impact breccia (without melt particles) 72
2.5.3.5. Impact melt-bearing breccia or suevitic breccia (with melt particles) 74
2.6. CONCLUSIONS **76**
REFERENCES **77**
3. THE EFFECT OF IMPACT-GENERATED HETEROGENEITIES AND DISCONTINUITIES ON THE SUBSEQUENT WEATHERING OF IMPACTITES: INSIGHTS FROM LABORATORY EXPERIMENTS **85**
ABSTRACT **85**
3.1. INTRODUCTION **86**
3.1.1. Previous work 87
3.2. MATERIALS AND METHODS **89**
3.2.1. Sample source 89
3.2.1.1. Meteor Crater Samples: Sedimentary impacted rocks 89
3.2.1.2. West Clearwater Impact Structure samples: Crystalline impacted rocks, impact melt rocks, and impact breccias 89
3.2.1.3. Ries Crater samples: Impact melt-bearing breccia or suevite 90
3.2.2. Sample preparation 90
3.2.3. Characterisation of samples 90

3.2.3.1. Quantitative X-ray diffraction (XRD) for identification of mineral phases in rock samples 91
3.2.3.2. Petrographic examination using scanning electron microscope (SEM) and petrographic microscope 91
3.2.3.3. X-ray computed tomography (CT) 92
3.2.4. Laboratory weathering experiment 93
3.2.4.1. Weathering experiment design 93
3.2.4.2. Change metrics 95
3.2.4.3. Desalination experiment 96
3.3. RESULTS **97**
3.3.1. Characterisation of rock samples 97
3.3.2. Experimental results 100
3.3.2.1. Sedimentary impactites 101
3.3.2.1.2. Coconino Sandstone (CS) 101
3.3.2.1.2. Moenkopi Sandstone (MS) 103
3.3.2.2. Crystalline Impactites 105
3.3.2.3. Impact melt rocks and impact breccias 107
3.3.2.3.1. Clast rich fine-grained impact-melt rock 108
3.3.2.3.2. Clast poor fine-grained impact-melt rock 108
3.3.2.3.3. Clast free impact melt rock 109
3.3.2.3.4. Lithic breccia 109
3.3.2.3.5. Impact melt-bearing breccia or suevite 109
3.4. DISCUSSION AND INTERPRETATION **111**
3.4.1. Role of simulated semi-arid environmental conditions 111
3.4.2. Size and shape of the blocks 112
3.4.3. Severity and mode of deterioration 113
3.4.4. Fracture propagation 114
3.4.5. Lithology 114
3.5. CONCLUSION **119**
REFERENCES **120**

4. A STRUCTURE FROM MOTION PHOTOGRAMMETRY-BASED METHOD TO GENERATE SUB-MILLIMETRE RESOLUTION DIGITAL

ELEVATION MODELS FOR INVESTIGATING ROCK BREAKDOWN FEATURES 129

ABSTRACT 129

4.1. INTRODUCTION 129

4.1.1. Structure from Motion (SfM) 132

4.2. METHODOLOGY 134

4.2.1. Equipment 135

4.2.2. Control target and local coordinate system 135

4.2.3. Data processing 136

4.2.4. DEM generation workflow in Photoscan 137

4.2.5. Error evaluation experiments 138

4.2.5.1. Experiment design 138

4.2.5.2. Estimating errors 141

4.3. EXPERIMENT RESULTS 142

4.3.1. Distribution of horizontal and vertical errors 142

4.3.2. Role of image variables in DEM error 144

4.3.3. Repeatability 146

4.5. FIELD APPLICATION OF SFM FOR DEM GENERATION 147

4.5.1. Data collection 147

4.5.2. Field Results 150

4.5.2.1. DEMs of Moenkopi outcrops in the field 150

4.6. DISCUSSION 154

4.6.1. High-resolution DEMs with low errors 155

4.6.2. DEM resolution 156

4.6.3. DEM errors 156

4.6.4. Portable and affordable 157

4.6.5. Importance of microtopographic data in the rock breakdown 158

4.7. CONCLUSION 160

REFERENCES 161

5. THE EFFECT OF LOW IMPACT SHOCK DEFORMATION ON THE SUBSEQUENT BREAKDOWN OF SANDSTONE IN A SEMI-ARID ENVIRONMENT 174

ABSTRACT 174

5.1. INTRODUCTION 174
5.1.1. Sandstone weathering 177
5.2. STUDY SITE 179
5.2.1. Meteor Crater 179
5.2.1.1. Introduction 179
5.2.1.2. Geologic setting 182
5.2.1.3. Target rocks 184
5.2.1.4. Age of the crater 186
5.2.1.5. Distribution of Ejecta 187
5.2.1.6. Past and present environment 188
5.2.1.7. Erosion and crater degradation 189
5.2.2. Control sites 191
5.3. METHODOLOGY 192
5.3.1. Contemporary microclimate at the study site 193
5.3.1.1. Microclimatic sensor installation in the field 193
5.3.1.2. The Meteor Crater Experiment - METCRAX I and METCRAX II data 196
5.3.1.3. Solar insolation modelling 196
5.3.2. Rock breakdown features documentation at Meteor Crater and the control sites 196
5.3.3. Petrophysical characterisation of Moenkopi Sandstone 197
5.3.4. Rock hardness measurements 197
5.3.5. Structure from Motion: Digital Elevation Model generation 198
5.3.6. Analysis of boulder DEMs to quantify breakdown features 199
5.3.6.1. Areal Surface Roughness Parameters 200
5.3.6.1.1. Standard deviation of height (Sq) 200
5.3.6.1.2. Standard deviation of slope (Sdq) 201
5.3.6.1.3. Maximum height (Sz) 201
5.3.6.1.4. Vector Ruggedness Measure (VRM) 202
5.3.6.2. Morphometric classification of geomorphic features 202
5.3.7. Statistical analysis of the data 202
5.4. RESULTS 203
5.4.1. Microclimate at the study site 203
5.4.1.1. Microclimatic data retrieved from iButtion sensors 203

5.4.1.2. Microclimatic data from METCRAX I and METCRAX II 205
5.4.2. Photo documentation of breakdown features 212
5.4.3. Petrographic properties of unshocked and shocked Moenkopi Sandstone 216
5.4.4. Rock Hardness 218
5.4.5. Areal surface roughness analysis 219
5.4.5.1. Standard Deviation of height (Sq) 220
5.4.5.2. Standard Deviation of slope (Sdq) 224
5.4.5.3. Maximum height (Sz) 227
5.4.5.4. Vector Ruggedness Measure (VRM) 230
5.4.6. Morphometric feature classification 233
5.4.7. Effects of crater wall aspect on weathering 237
5.5. DISCUSSION **239**
5.5.1. Rock hardness, roughness and morphometric features 239
5.5.2. Recommendation of roughness parameters for breakdown feature analysis 241
5.5.3. Effect of low shock on the breakdown of Moenkopi Sandstone 245
5.5.4. Effect of aspect on the breakdown of Moenkopi Sandstone 248
5.6. CONCLUSION **250**
REFERENCES **252**
6 SYNTHESIS **272**
6.1. OVERVIEW **272**
6.2. CONTRIBUTION AND BROADER IMPLICATION OF THIS RESEARCH **272**
6.3. IMPLICATION OF LABORATORY EXPERIMENTS ON WEATHERING AT METEOR CRATER **275**
6.4. THE IMPLICATION FOR ROCK BREAKDOWN ON EARLY MARS **276**
6.5. SUGGESTED FUTURE WORK **279**
6.5.1. Photogrammetry and roughness analysis 279
6.5.2. Physical weathering experiments 280
6.5.3. Chemical Weathering experiments 280
6.5.4. Field studies 282
REFERENCES **283**

APPENDIX 1. A COMPARISON OF STRUCTURE FROM MOTION PHOTOGRAMMETRY AND THE TRAVERSING MICRO EROSION METER FOR MEASURING EROSION ON ROCK SHORE PLATFORMS.....291

ABSTRACT 291

A.1.1. INTRODUCTION 291

A.1.1.1. The Micro Erosion Meter and the Traversing Micro Erosion Meter 292

A.1.1.2. Structure from Motion Photogrammetry.....294

A.1.2. METHODS 296

A.1.2.1. A manufactured Coordinate Reference System for SfM-MVS.....296

A.1.2.2. The experiments.....296

A.1.2.3. Data collection.....299

A.1.2.4. Repeatability 299

A.1.2.5. Data processing.....300

A.1.2.5.1. Digital Elevation Models 300

A.1.2.5.2. DEMs of Difference.....300

A.1.2.5.3. Rugosity.....300

A.1.2.5.4. DEM accuracy and error propagation 301

A.1.3. RESULTS 302

A.1.3.1. Accuracy and error propagation.....302

6.4.6. A1.3.2. Repeatability.....303

6.4.7. A.1.3.3. Rugosity.....304

6.4.7.1. A.1.3.3.1. Very low rugosity platform: B1 305

A.1.3.3.2. Moderate rugosity platform (B2).....308

A.1.3.3.3. Relatively high rugosity platform (B3).....310

A.1.3.4. Comparison of the T/MEM and SfM-MVS for measuring erosion on shore platforms 312

A.1.3.4.1. Installation 312

A.1.3.4.2. Data collection 313

A.1.3.4.2. Data processing.....314

A.1.3.4.3. Hardware costs.....314

A.1.3.4.4. Software costs 314

A.1.3.4.5. Resolution and Error.....314

A.1.4. DISCUSSION 315
A.1.5. CONCLUSIONS 318
REFERENCES 318
APPENDIX 2. SUPPLEMENTARY MATERIAL FOR CHAPTER 2 325
APPENDIX 3. SUPPLEMENTARY MATERIAL FOR CHAPTER 3 345
APPENDIX 4. SUPPLEMENTARY MATERIAL FOR CHAPTER 4 353
APPENDIX 5. SUPPLEMENTARY MATERIAL FOR CHAPTER 6 363

Chapter 1

1. Introduction

Impact cratering is a ubiquitous and one of the most catastrophic geologic processes that has played a crucial role in the evolution and modification of the crust on all planetary bodies with solid surfaces (e.g. terrestrial planets, moons and asteroids) (Gillet and Goresy, 2013). Impact cratering occurs when a projectile travelling with hypervelocity strikes and excavates the surface of the planetary body. Impacting projectiles can be asteroids, comets, accretional remnants, impact disrupted satellites, and tidally disrupted planetesimals from the inner or outer solar system (Strom and Woronow, 1982; Melosh, 1989). During the early history of the solar system (4 - 3.5 Ga), after the accretion of the terrestrial planets, the rate of impact bombardment was very high due to the anomalous influx of projectiles, such that craters were widespread on early Earth (Fig 1.3) (Marchi et al., 2014). This period is commonly known as Late Heavy Bombardment (LHB). Since the end of the LHB, the rate of impact of larger asteroids or comets (> 1 km) has decreased significantly, and smaller impacts (< 1 km) are relatively more frequent (Malin et al., 2006; Byrne et al., 2009; Daubar et al., 2011).

The effect of impacts on subsequent rock breakdown has not yet received sufficient attention in geomorphology. Several studies have investigated the geology, morphology, structure, erosion and degradation of crater landforms (Grant and Schultz, 1993a; Grant and Schultz, 1993b; Osinski and Pierazzo, 2012; Golombek et al., 2014; Kenkmann et al., 2014) and references therein), and relatively few have examined the inherited effects of impacts on subsequent weathering (Boslough et al., 1986; Boslough and Cygan, 1988; Cygan et al., 1989; Leroux, 2005; Bell, 2015; Bell, 2017). It is necessary to assess the role of impact inheritance on the subsequent style and rate of rock breakdown. The focus of this thesis is to understand how the inheritance from the impact process affects the subsequent breakdown of impacted rocks at impact sites.

1.1. Rock breakdown and landscape evolution

Rock breakdown describes a range of geomorphic processes (weathering and erosion) that transforms rock masses into soil or regolith and unconsolidated rock materials. Rock breakdown processes are a function of surface material, the availability of the abrasive agent, climate, and tectonic setting (Laity, 2009a). Weathering refers to the adjustment of the chemical, mineralogical and physical properties of rocks in response to surface environmental conditions (Heslop, 2003; Summerfield, 2014). Conventionally, all the weathering processes and mechanisms can be broadly classified into physical, chemical and

biological (Smith, 2009; Warke, 2013). A detailed discussion of these processes is provided by Bland and Rolls (1998b), (Heslop, 2003), (Smith, 2009), (Warke, 2013), and (Summerfield, 2014). Erosion refers to the removal of land surface by wind, water, gravity, or ice (Allaby, 2013). Most forms of erosion, sediment transport, and denudation depend upon the in-situ weathering of geologic material by physical, chemical, and biological processes (Turkington et al., 2005; Viles, 2011). Thus, it can be said that rock breakdown is necessary for all denudation (Turkington et al., 2005).

Rock weathering is undoubtedly one of the most critical and fundamental phenomena in landscape evolution and landform development (Heslop, 2003; Turkington et al., 2005). In comparison with other terrestrial surface processes, weathering is often slow and difficult to recognise (Viles, 2011; Viles, 2013b). At the small scale, weathering processes produce many peculiar landforms in rock outcrops (e.g., alveoli, pits), sediment bodies (e.g., grus), and soil or regolith (Turkington et al., 2005; Bourke and Viles, 2007). Weathering plays a significant role in the development of soil, regolith, and weathering profiles (Turkington et al., 2005).

Weathering influences landscape evolution through the production of small to medium scale individual landforms and the generation of sediment and topographic development (Viles, 2011). The exogenic component of the rock cycle is described by the debris cascade concept which consists of three stages: debris source, transport path, and depositional processes (Heslop, 2003; Benn and Evans, 2014). This cycle may go through several iterations to produce the denudation of the Earth's surface (Heslop, 2003). There are some landforms (e.g., karst, etchplains) where weathering is the primary agent of landform modification (Turkington et al., 2005). Such landforms are formed due to denudational mechanisms (e.g., solution) that are directly weathering-dependent (Turkington et al., 2005; Smith, 2009).

Early landscape evolution research dismissed the role of weathering processes in landscape evolution as it was believed that structural and erosional controls play a major role in landscape development (Ollier, 1960; Mabbutt, 1961; Thomas, 1966) and deep weathering was distinctive to the humid tropics (Turkington et al., 2005). During 20th century, geomorphologists viewed landscapes as erosion-controlled (Davis and Johnson, 1909), and did not believed weathering to be a significant control on landscape development (Gregory, 1911) as it was considered a static process, rather than a mobile agent of change (Foye, 1921; Turkington et al., 2005). Traditionally, weathering has been perceived as time-dependent

rather than distance-dependent (de Boer, 1992; Turkington et al., 2005). Geomorphologists often use knowledge of weathering mechanisms, processes, rates, forms, and their relationship to various rock and environmental controls (e.g., climate, biota, and exposure time) to understand landscape histories and environmental change (Turkington et al., 2005; Goudie, 2016). Residual weathering features have played a significant role in interpreting both environmental change and relative ages of exposed surfaces, paleosurfaces, and sediments (Turkington et al., 2005).

Traditionally, regolith has been treated as a function of weathering minus erosion by landscape evolution models (Turkington et al., 2005). Deepening at the weathering front is not only a product of physio-chemical processes but also is closely linked to biodynamic deepening (Turkington et al., 2005). Twidale et al. (2005) suggested that denudation can be a factor in shore platform development, where residual weathering has dominant control on coastal landform evolution rather than contemporary wave-dominated erosion processes. Twidale et al. (2005) highlight the significance of weathering processes and products, even in environments commonly seen as dominated by other geomorphic agents.

Geomorphologists determine relative ages of the landscape by estimating the amount weathering in rock clasts in regolith and transported sediment along with additional geomorphological parameters (Turkington et al., 2005). Weathering of clasts may be viewed as a 'chronofunction' (White et al., 1998); nonetheless the parameter and techniques that can be used to determine the age depend on individual site (Turkington et al., 2005). The depth of weathering rind has been considered more reliable in determining the relative ages than the clast roughness, hardness, size, or roundness (Sumner et al., 2002; Sak et al., 2004). The relationship between weathering and time is perhaps non-linear and complex (Viles, 2001). Relative age dating techniques have been valuable in understanding of modus operandi of landscape evolution, for example, the relative areal coverage of surfaces of varying ages, rate of surface incision, and forecasting the hillslope stability (Mills, 2005; Turkington et al., 2005).

Concepts of landscape denudation and the knowledge of nature and rate of chemical denudation are continually advanced in newer studies (e.g., Campbell et al. (2002), Beylich et al. (2004)). Simms (2004) found that denudation of limestone landscapes progresses by dissolution at a rate directly proportional to runoff. Chemical weathering in cold regions has been getting more attention (Hall et al., 2002) and the belief that mechanical erosion

processes are primarily responsible for removal of silicate minerals is being challenged (Turkington et al., 2005). Studies conducted by Dixon and Thorn (2005) in Alpine and Arctic areas showed that chemical weathering is a significant agent of mass removal in cold regions. Weathering and denudation are directly related by solution and solute transport in these geomorphic systems. Dixon and Thorn (2005) identified strong self-reinforcing feedback between solution and solute transport, for example, glacial erosion renews the exposure of the geomorphic surfaces that leads to sustaining higher weathering rates. Glacial erosion continues to expose the fresh mineral surface to weathering on a short term basis; Anderson (2005) exhibited a direct relationship between physical erosion rates and rates of chemical denudation.

Hall et al. (2002) demonstrated that the freeze-thaw is not the only mechanism responsible for weathering in high mountain area rather thermal stress and biochemical processes also play an important role in weathering. In this study, Hall et al. (2002) found that the distribution of lichen seems to be affected by microclimatic factors, this can be linked to experimental work by Carter and Viles (2003) where they showed that lichen distribution, in turn, ameliorates rock surface temperature and moisture conditions (Turkington et al., 2005). A vital contribution to the rock weathering research was made by Viles (2005) in interpreting the relationship between rock response and microclimate to weathering in a hot desert.

Lithology, rock structure, and the environmental conditions near the rock surface are fundamental in controlling rock weathering (Goudie, 2016). Geology and tectonic process a major role in controlling landscape evolution but of late the role of small-scale rock heterogeneities and the effect of microclimatic has been getting recognised. Weathering experiments have shown the importance of physical rock properties (Rodriguez-Navarro and Doehne, 1999) and mineralogical differences (Cardell et al., 2003), and microclimatic conditions (Pope et al., 2002; Viles, 2005) in controlling rock response to weathering processes. Aspect exerts a key control on the rate of weathering (Williams and Robinson, 2000; Hall et al., 2002).

Weathering research has traditionally been, to some extent bimodal, with microscale and landscape-scale investigations being conducted simultaneously, but not successfully linked (Viles, 2001; Turkington et al., 2005). Phillips (2005) finally addressed the everlasting issue of scale linkage by establishing the prevalence of dynamical instability in weathering

systems across a range of scales (Turkington et al., 2005). Phillips (2005) proposed stability/instability regimes that are directly linked to spatial and temporal scales by considering stability conditions for weathering and related processes at four hierarchical levels.

1.2.Scale issues in rock weathering

Rock surfaces of various sizes exposed in arid environment evolve from outcrops (m-km) to rock fragments (mm-cm) mantling the desert surface (Heslop, 2003). Ultimately, these rock bodies are broken down to their constituent mineral grains and are thought to be source of desert loess (Goudie and Day, 1980). Weathering take place over a very wide range of timescales, from instantaneous granular detachment from rock surface, to the millions of years of dissolution to produce karst landscape (Viles, 2013b). Weathering processes rarely operate in isolation from one another, and the weathering processes occur in synergy with other geomorphological processes at a variety of levels (Smith, 2009; Viles, 2013b). It is necessary to integrate the detailed understanding of weathering at the nano- and microscales to their role in the evolution of complex landforms and landscapes (Smith, 2009).

Laboratory experiments and analytical techniques have been used to study individual weathering processes at the microscale in recent investigations (Viles and Moses, 1998; Edwards et al., 2002; Naylor and Viles, 2002; Moses et al., 2014). Weathering studies have found it challenging to successfully link the mineral scale weathering to weathering at the landscape scale, and there is apparent disparity in the scales of enquiry in weathering studies (Turkington et al., 2005). Warke (1996b) and Smith (2009) demonstrate the importance of spatial and temporal scale in our understanding of the role of weathering processes in landform development and landscape evolution. Smith (2009) bring into the attention that investigations in weathering studies tend to be process-oriented and reductionist in nature. Firstly, the majority of in situ weathering studies are limited to the short-term duration and small spatial extent. This is problematic because long term significance of weathering where a small number of areas have been mapped in detail, and where knowledge of the medium to long term climate variability is limited. Secondly, process studies have tended to focus on weathering features that show measurable change within a few years. Thirdly, inclination

towards reductionist nature has encouraged the examination of specific weathering mechanisms in isolation.

Heslop (2003) suggested that in order to link process and form in weathering studies, the whole should be considered greater than the sum of its constituent parts. Smith (2009) recommended that in order to understand the landscape in which weathering takes place, weathering mechanisms must be established within wide temporal and spatial contexts. Many researchers have made a valuable contribution towards, stressing on the importance of inheritance effects on rock breakdown (Warke, 1996a; Warke, 1996b; Warke, 2007; Viles et al., 2010; Viles et al., 2018). The concept of temporal inheritance stresses on the importance of context to interpretations of rock breakdown. This notion is widened in the doctoral thesis of Heslop (2003), which stresses the significance of both spatial and temporal frameworks to explain the breakdown of clasts in the Atacama desert.

The key to understand the behaviour of weathering systems in present requires the knowledge of inheritance effects from geomorphic processes in the past (Viles, 2013b). The inheritance is defined as the stress history that individual rock bodies experience during their path through the debris cascade (Warke, 1996b; Heslop, 2003). Exposure of rocks to weathering and other geomorphic processes in the past typically effects how they breakdown today, exhibiting the importance of initial conditions to such self-organizing systems (Viles, 2013b). Such inheritance effects can occur over many different timescales, from decades to millennia at least (Viles, 2013b). Warke (1996b) stresses the importance of a temporal perspective via the concept of inheritance. Warke (1996b) suggested that inheritance effects are not largely related to contemporary conditions. She recommended that the concept of inheritance should be extended to comprise stress effects produced through every iteration of the breakdown cycle. Heslop (2003) highlights that the concept of inheritance underpins the notion that the rock breakdown and the production of weathering forms are historical events. Their description includes the understanding of contemporary processes and how these function and interact within a historical context defined by the specific spatial and temporal conditions (Heslop, 2003).

Heslop (2003) recommended that the investigations of weathering processes and forms should be seen as the product of a series of spatially and temporally integrated mechanisms. A review of spatiotemporal scale issues in weathering studies by Viles (2001) emphasises a number of problems in upscaling our understanding of weathering processes to the landscape

scale. Many of the potential methods to the crossing of scale boundaries are deep-rooted in the interpretation of geomorphic phenomenon as non-linear dynamical systems (Viles, 2001; Viles, 2013b). Viles (2001) concludes that weathering systems are complex, self-organising systems and that at larger scales, multiple controlling factors come into play of which some may not operate at the microscopic scale.

Viles (2001) explored the issue of scale linkage in weathering studies. She raised four points:

1. Are there characteristic spatio-temporal scales of weathering landform and processes?
2. Are the scales of process observation the same as process operation?
3. How can scale linkage in process-form observations across different spatio-temporal scales be achieved?
4. How do different scales of processes and forms interact to produce weathering and associated landforms?

Viles (2001) suggested several approaches to tackle these issues. Rock breakdown in arid environment contributes to both landscape and landform development at a variety of scales (Fig 1.1). Nevertheless, weathering research has focussed on micro- to mesoscale forms because it is more difficult to assess the role of rock breakdown in landscape change compared to small scale rock breakdown features and forms (Goudie and Viles, 1997). Following Viles (2001), Heslop (2003) produced a Stommel diagram to show the perceived spatio-temporal distribution of features and landforms commonly linked with rock breakdown in the arid environment. Fig 1.1 links the spatio-temporal distribution of landforms and features to the rock surface continuum (Heslop, 2003). These two ideas can be linked to accentuate that the small features developing on rock surfaces are the result of the processes of weathering and erosion driving the debris cascade and moving rock bodies through the debris continuum (Heslop, 2003). Ultimately, debris is produced by the reduction of rock bodies (Heslop, 2003). This contributes to the production of landforms comprising debris accumulation, which include slope equiplanation and desert pavements (Heslop, 2003).

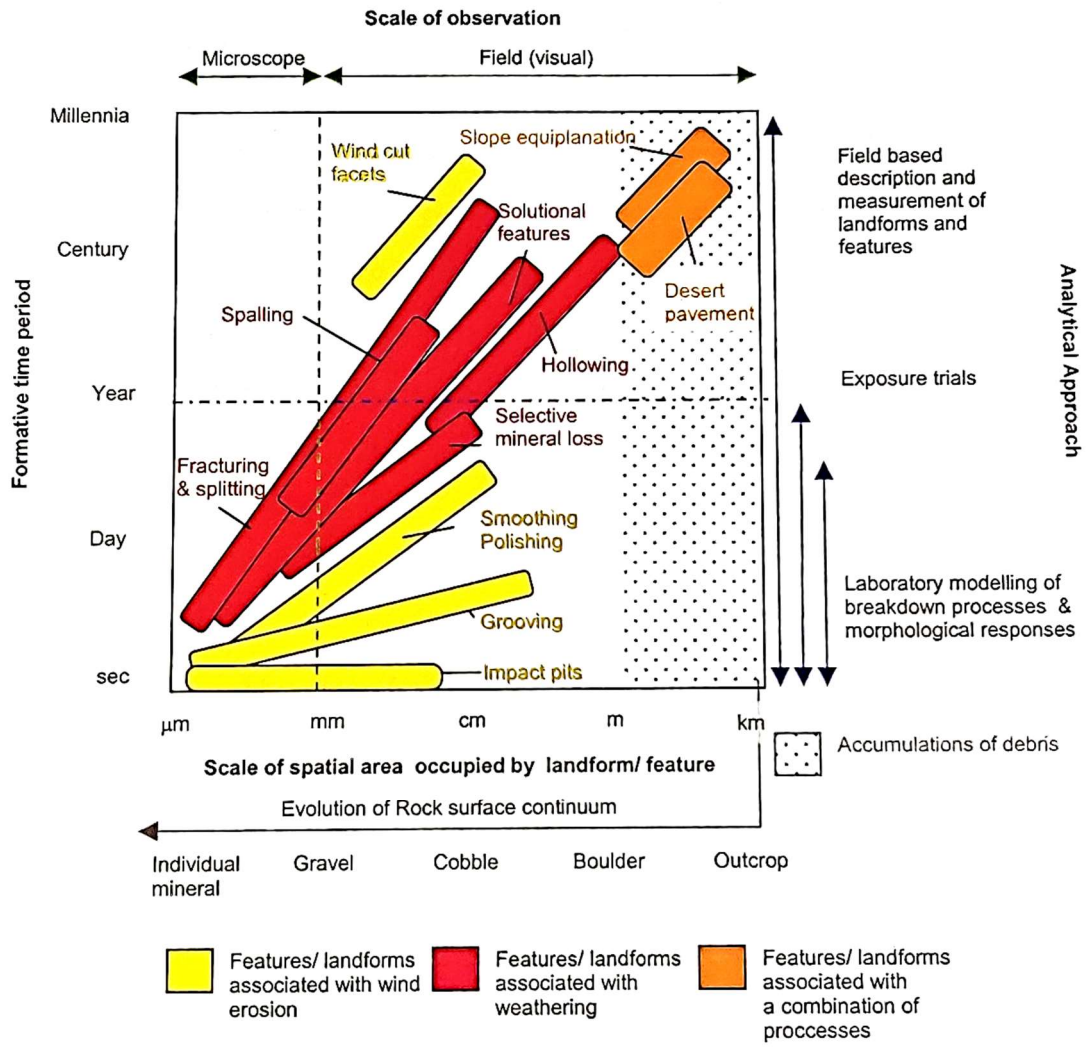


Fig 1.1. Stommel diagram showing the spatio-temporal distribution of landforms and features associated with rock breakdown in deserts. This diagram uses colour to link landforms and features with processes commonly associated with their formation. This is done tentatively acknowledging that form is not indicative of process and that some forms may be equifinal in nature. As such, the genetic associations suggested by this diagram reflect the prevailing view expressed by researchers from the literature. This diagram also illustrates the scales of observation and analytical approaches suitably adapted for the investigation of these landforms and features over appropriate spatial and temporal scales. From Heslop (2003).

1.3.Impact Cratering

Impact craters are formed when the surface of a planetary body is excavated by the impact of a projectile that is travelling with hypervelocity (a speed tens of kilometres per second) (Strom and Woronow, 1982; Melosh, 1989). Impact craters provide fundamental information about planetary evolution and composition through the excavation of large amounts of sub-surface material on inaccessible planetary bodies which can only be observed by satellites and telescopes. On planetary bodies with no tectonic activities impact processes provide an external source of energy and heat (Melosh, 1989).

1.3.1. Stages of crater formation

The process of impact cratering is a continuous process; however, the crater formation event is divided into three stages to reflect the dominant mechanism acting at each stage: 1) Contact and compression; 2) excavation; and 3) modification. All three stages affect geology and target rock properties which largely depend on qualitative and quantitative parameters associated with the incoming projectile and lithology (Melosh, 1989; Simpson, 2015).

1.3.1.1.Contact and compression

The first stage of impact cratering process, contact and compression, commences at the instant when the leading edge of the moving projectile strikes the target rock surface (Fig 1.2). This initiates passage of series of shockwaves through target rocks (Fig 1.2). At the immediate moment of contact, the first wave originates from the projectile-target interface and propagates through the target rock. The second wave, rarefaction wave, is produced after the first shockwave reaches the trailing end of the projectile, it gets reflected forward into the projectile (French, 1998; Pickersgill, 2014; Simpson, 2015).

The point of impact is surrounded by a series of concentric, quasi-hemispherical shock zones; each zone has characteristics range of peak shock pressure (Pierazzo and Melosh, 2000). The peak shock pressure decreases exponentially with the distance from the point of impact (Melosh, 1989; Pierazzo and Melosh, 2000). The target rocks at the contact point get strongly compressed leading to peak shock pressure exceeding 100 GPa (French, 1998; Rosa, 2012). The shock wave generated at the point of impact propagate outward over distances of many kilometres into the target rock. As the passage of shock wave increases the magnitude of the strength of the target rocks, results in melting, vaporisation, and shock

metamorphism of target rocks in the immediate proximity of the point of impact (Melosh, 1989).

As the rarefaction wave passes from back to the front end of the projectile, acting as an unloading mechanism to the projectile. The immense shock pressures and the associated high temperatures from impact are released that can result in complete melting and vaporisation of the projectile (French, 1998; Simpson, 2015). The end of contact and compression stage is marked by complete unloading of the projectile and transfer of rarefaction wave into target rocks. (Osinski and Pierazzo, 2012; Pickersgill, 2014; Simpson, 2015). The entire contact and compression stage usually lasts for 10^{-3} to 10^{-1} seconds for most of the impact events (French, 1998). This depends on projectile's composition, size and initial velocity (Melosh, 1989).

1.3.1.2.Excavation

Excavation stage begins at the immediate end of the contact and compression stage. During the excavation stage, a quasi-hemispherical shock wave radiates in all directions from the point of impact and propagates through target rocks (Fig 1.2) (French, 1998; Osinski and Pierazzo, 2012). The passage of the shock and rarefaction waves through target rocks cause loosening and mobilisation of rock material (Osinski and Pierazzo, 2012). An initial transient cavity with a diameter of several times compared to that of the projectile is excavated during this process (Melosh, 1989). This transient cavity is lined with melt and shocked rocks produced during impact (French, 1998). During this stage, vaporised rock material expands outward in a plume; some melted and fractured material is either ejected or displaced out of the crater, deforming the adjacent rocks, uplifting the surface near the crater rim and infiltrating the rocks located beneath the crater (Rosa, 2012). The ballistically ejected rocks beyond the transient crater rim during excavation forms the continuous ejecta blanket (Osinski and Pierazzo, 2012). The excavation stage lasts seconds to minutes depending on the size and type of the crater (Osinski and Pierazzo, 2012). As the energy of shock wave dissipates to the point when they no longer have enough energy to displace target rocks, marks the end of excavation stage (Melosh, 1989).

1.3.1.3.Modification

The modification stage is the last stage in impact cratering process. It consists of all processes that affect the impact structure after the excavation stage. After the transient crater has been completely excavated, the modification stage begins (Fig 1.2). During this stage, the

transient crater is modified by gravitational forces (French, 1998). The modification due to gravitational forces is mainly dependent on the size of the transient cavity, the properties of the target rock, and the gravity of the impacted body (Melosh, 1989; Osinski and Pierazzo, 2012). In small craters on Earth (<2-4 km), this results in slumping of debris from the crater wall and filling the bottom of the crater floor (Melosh, 1989). In larger craters, rebound of the transient crater floor results in the formation of a central uplift, while the steep walls of the transient cavity undergo gravitational collapse forming slump terraces on the walls (Melosh, 1989). Modification continues for several years and has no marked end. The gravitational processes which govern the modification of the crater slowly merge into endogenic surficial processes such as erosion and deposition (French, 1998; Osinski and Pierazzo, 2012).

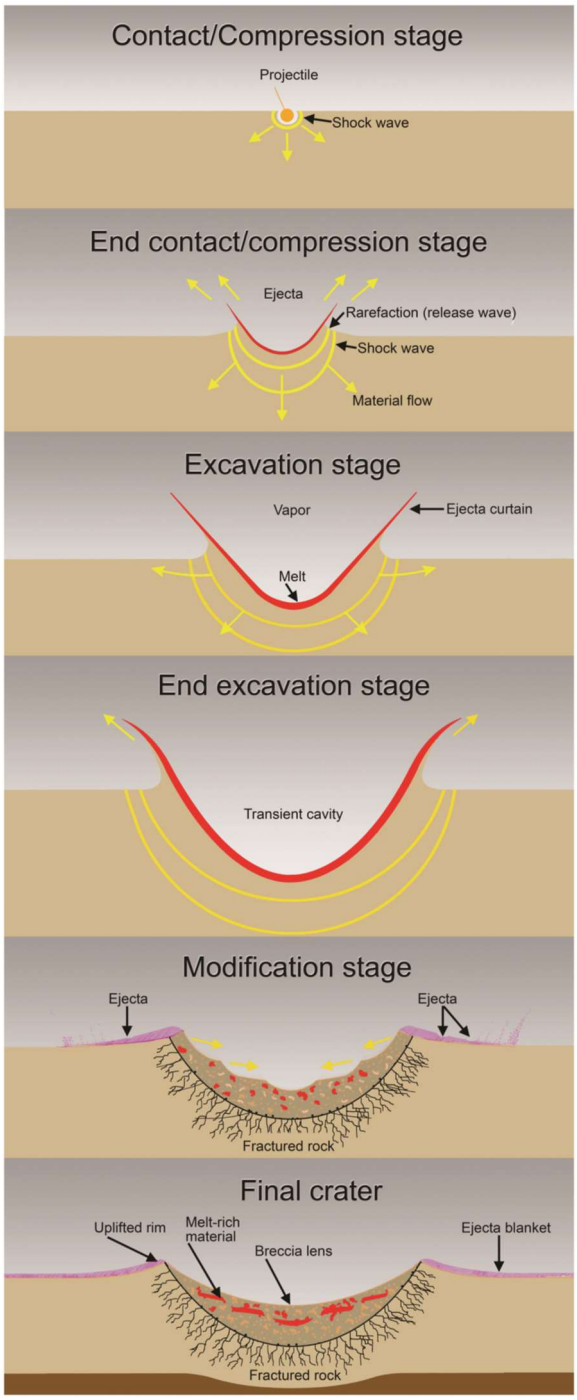


Fig 1.2. Six views of simple crater formation (generic and schematic). Projectile penetrates the surface and generates a shock wave. A transient crater begins to grow as excavation begins. The transient crater reaches its maximum depth before reaching its maximum radius. When excavation is complete, any remaining debris on the crater walls slump inward to form a breccia lens. Melt will be distributed in the ejecta and any material that falls back on top of the breccia lens. If the crater-forming event is energetic enough, then melt will also be

incorporated into the breccia lens. (Illustration from an educational poster, Geological Effects of Impact Cratering, David A. Kring, NASA Univ. Arizona Space Imagery Center, 2006).

1.3.2. Types of craters

Impact craters are categorized into three types based on size and morphology: (1) Simple Craters; (2) Complex Craters; (3) Multiring basins. The size and morphology of the crater formed during an impact event depend on the amount of energy released due to impact which is related to the size and composition of the projectile, and gravity of the planetary body on which impact event takes place (Melosh, 1989; French, 1998). The lower the gravity, the larger the size transition from simple to complex crater. On the Moon, the transition from simple to the complex crater is at ~20 km (diameter) compared to 4-5 km on Earth (French, 1998). The structural and geological characteristics of impact crater and kind of impactites produced mainly depends on target rock properties (Simpson, 2015).

1.3.2.1.Simple craters

Simple Craters are bowl-shaped depressions with a diameter of less than a few kilometres; they tend to have the shape and dimensions of the original transient cavity. On Earth, simple craters range from 1-4 km in diameter (French, 1998; Osinski and Pierazzo, 2012). These types of craters lack central uplifts and rings. Simple craters are slightly modified after a transient crater is formed by minor collapse of upper crater walls in the crater cavity and by infill of ejected rocks in the crater (French, 1998; Osinski and Pierazzo, 2012). During modification stage, the simple crater gets filled with the allochthonous impactites which consist of a thin breccia lens of both shocked and unshocked material, and a mixture of shock-melted rocks and fallback ejecta and debris slumped from the crater walls and rim (French, 1998; Osinski and Pierazzo, 2012). The target rocks beneath the crater floor get fractured and brecciated but are usually not displaced during impact (French, 1998; Grieve and Therriault, 2013; Kenkmann et al., 2014). Meteor Crater in Arizona is the most famous example of a simple crater on Earth.

1.3.2.2.Complex craters

Complex Craters on Earth have diameter >4 km and generally characterised by a central uplift, flat floor, and extensive inward collapse around the rim. (French, 1998; Osinski and Pierazzo, 2012). With the increase in the size of the complex crater, the central uplift region

becomes a series of concentric alternating rings and basins (French, 1998). During the formation of central peaks, the rim of the structure may experience collapse along concentric faults (French, 1998; Osinski and Pierazzo, 2012). This creates a ring graben. The final shape of complex crater consists of a central uplift, an annular trough and an outer rim (French, 1998; Osinski and Pierazzo, 2012; Rosa, 2012).

The crater is infilled with both shocked and unshocked target rocks; fallback ejected rocks, non-continuous melt bodies, and continuous melt sheets (French, 1998; Osinski and Pierazzo, 2012). The rocks beneath the crater floor are fractured and brecciated and may contain intrusions or dykes of allochthonous material from crater wall or frictional melt material known as pseudotachylite (French, 1998; Osinski and Pierazzo, 2012). The amount of impact melt produced and distributed in complex craters depends on the target rock composition, fluid saturation, and impact projectile parameters (French, 1998; Osinski and Pierazzo, 2012).

1.3.2.3.Multiring structures

Multi-ring impact structures can reach up to 1000 km in diameter and are uncommon on Earth. These impact structures are characterised by alternating uplifted rings and low-lying and faulted basins (French, 1998; Osinski and Pierazzo, 2012). Multi-ring basins are found on the surface of other terrestrial planets and the moon where these structures are preserved due to the lack of tectonic activities and erosion (Osinski and Pierazzo, 2012).

1.4. Impact cratering and rock breakdown on Mars

During the early history of Earth and Mars, the rate of impact was very high (Wetherill, 1975). More than 350,000 impact craters with a diameter ≥1 km have been documented on Mars (Robbins and Hynek, 2012). A range of impacted rocks or impactites are expected to be present in craters on Mars. Osinski and Melosh (2004) suggested that a diverse range of impactites should also be expected on Mars, given the role of volatiles in the generation and deposition of ejecta (Weiss and Head, 2014). During the last two decades, unmanned missions roving the surface of Mars as well as orbiters have confirmed the detection of impactites such as impact breccia (Hayes et al., 2011), lithic impact breccia (Squyres et al., 2012), impact melt breccia (Squyres et al., 2012; Arvidson et al., 2014), impact spherules

and tektites (Newsom et al., 2014; Kah, 2015), impact melts and glasses (Schultz and Mustard, 2004) as well as fractured target rocks.

The surface of Mars is dominated by rocks of basaltic to andesitic composition (Chevrier and Mathé, 2007; Carr and Head, 2010). Sedimentary outcrops of evaporitic and basaltic composition have been found at the Opportunity and Curiosity rover landing sites (Grotzinger et al., 2005; Grotzinger et al., 2014). Float rocks ranging in size from cobble to boulder have been observed on Mars (Sharp and Malin, 1984; Ward et al., 1999; Sullivan et al., 2007; Smith et al., 2009; Clarke, 2011; Williams et al., 2013).

It is possible that Earth and Mars undergo similar breakdown processes (Burns, 1993; Thomas et al., 2005), but in conditions clearly different (Catling and Leovy, 2006). Frost weathering (Matsuoka and Murton, 2008), thermoclasty (McFadden et al., 2005), haloclasty (Doehne, 2002), wetting and drying (Hall and Hall, 1996), and diverse aeolian and fluvial processes (Bourke and Viles, 2007) are identified as chief physical breakdown processes on Earth. Many of these processes may be acting on Mars as well.

The long-term evolution of Martian water cycle (Bibring et al., 2006; Clarke, 2011) has led to a secular change in rock breakdown processes on Mars throughout its geologic history (Chevrier and Mathé, 2007). The earliest epochs in Martian geologic history are characterised by neutral to alkaline water dominated erosion and weathering (Bibring et al., 2006). As water became scarcer and its activity transient, the environment was subject to more acidic sulfate-dominated (McLennan and Grotzinger, 2008) chemical and physical weathering. In the most recent time a very slow physical processes in cold and bone dry conditions, assisted by aeolian activity (Chevrier and Mathé, 2007), solar insolation (Eppes et al., 2015), and moisture-driven processes such as frost-thaw and/or acid fog dominate (Chevrier and Mathé, 2007; Clarke, 2011).

There is considerable evidence suggesting that some types of weathering process may be currently taking place (Burns and Fisher, 1993; Bridges et al., 2004; Thomas et al., 2005) on Mars. Physical weathering is the major, non-tectonic mechanism for the rock breakdown on Mars (Jagoutz, 2006; Eppes et al., 2015). Most of the rock surfaces observed at various landing sites appear to have been abraded mechanically rather than broken down by chemical weathering. Noachian (~4.1-3.7 Gyr) Martian surfaces have undergone chemical weathering (Carr and Head, 2010; Ehlmann and Edwards, 2014) which may not be very efficient on present day Mars. There has been active aeolian processes, in addition to dune forms (Bourke

et al., 2010; Hobbs et al., 2010), resulting in rock abrasion features such as ventifacts and other small scale feature.

During the Noachian period (approx. 4.1 to 3.7 billion years ago), Mars possessed an atmosphere about as dense as Earth's, but most of it was lost to space due to solar wind and ultraviolet rays. The early climate of Mars was suitable to support chemical weathering (Zolotov and Mironenko, 2016). Spectroscopic data from orbiters and in-situ analysis by landers and rovers have detected secondary alteration minerals of rocks on Mars (Ehlmann and Edwards, 2014; Table 1). Bibring et al. (2006) use data from the OMEGA Visible and Infrared Mineralogical Mapping Spectrometer on board the Mars Express identified secondary alteration minerals such as phyllosilicates, sulfates, carbonates and oxides. Ehlmann and Edwards (2014) found evidence of hydrated silicates such as clay minerals are widespread in the Noachian crust of Mars or in locations where Noachian crust is exposed due to impact event. The Martian history has been characterised by three dominant process: a non-acidic aqueous alteration responsible for producing clay-bearing phyllosilicates in Noachian (~4.1-3.7 Gyr); the Hesperian (~3.7-3.1 Gyr) was dominated by an acidic aqueous alteration, producing sulfate minerals such as Jarosite, anhydrite, gypsum, and kieserite; from the end of this period to the present an atmospheric aqueous alteration producing iron oxides (Bibring et al., 2006).

A question currently under discussion for Mars is whether the aqueous alteration processes occurred episodically or were sustained over periods sufficiently long to sustain habitable environment on Mars (Des Marais et al., 2008). Understanding the nature and rate of weathering can help answer this question and constrain the past climate on Mars and perhaps contribute to the early “warm and wet” (Carter et al., 2015) versus “cold and icy” (Fairén, 2010) climate debate (Palumbo and Head, 2017; Ming et al., 2008). Viles et al. (2010) ran Mars weathering simulations for 12 days on basalt and found that rocks with stress history will deteriorate due to thermal cycling in present-day Mars conditions. They report no change in rock strength for rocks that were not pre-stressed.

Noachian craters are widespread on Mars. Cratering events during Noachian would have produced an enormous amount of impactites consisting of shocked crystalline minerals and impact glasses (Boslough, 1991; Schultz and Mustard, 2004). Our understanding of impact-induced modification and activation processes on subsequent weathering is limited on Mars. Most of the cratering of terrestrial and Martian surface occurred during the period of early

bombardment in the solar system, and therefore, these rocks have been exposed for billions of years to the weathering environment on Mars. Several studies have reported that most of the hydrous alteration minerals (i.e. phyllosilicates) on Mars are associated with impact craters and old cratered terrain (Tornabene et al., 2013; Ehlmann and Edwards, 2014; Loizeau et al., 2015; Carter et al., 2015). This suggests that the crater landforms housed lacustrine environments, where enhanced hydrological processes would have been in operation. These impact shock processes and the impact gardening of surface material on Mars have been the dominant process that contributed to the evolution of chemical, mineralogical, and physical properties of the Martian regolith (Boslough, 1991; Knauth et al., 2005)

1.5. Effect of impact inheritance on rock breakdown

There are 190 confirmed impact structures on Earth (Fig 1.4) (Earth Impact database). Terrestrial impact structures are usually poorly preserved and continually erased from rock records due to progressive erosion, volcanic resurfacing and dynamic plate tectonic activity (Grieve and Pesonen, 1992; Grieve and Robertson, 1979; Goudie and Viles, 2012; Grant and Schultz, 1993a; Grant and Schultz, 1993b; Hergarten and Kenkmann, 2015). However, on other planetary surfaces (e.g., Moon and Mars), where erosion and tectonic activity is currently limited or absent, abundant and well-preserved craters and impact basins are widespread (Werner, 2008; Robbins and Hynek, 2012). Impact craters are very common on Mars (Fig 1.5); in fact, more than 350,000 impact craters with diameter ≥1 km have been documented on Mars (Robbins and Hynek, 2012).

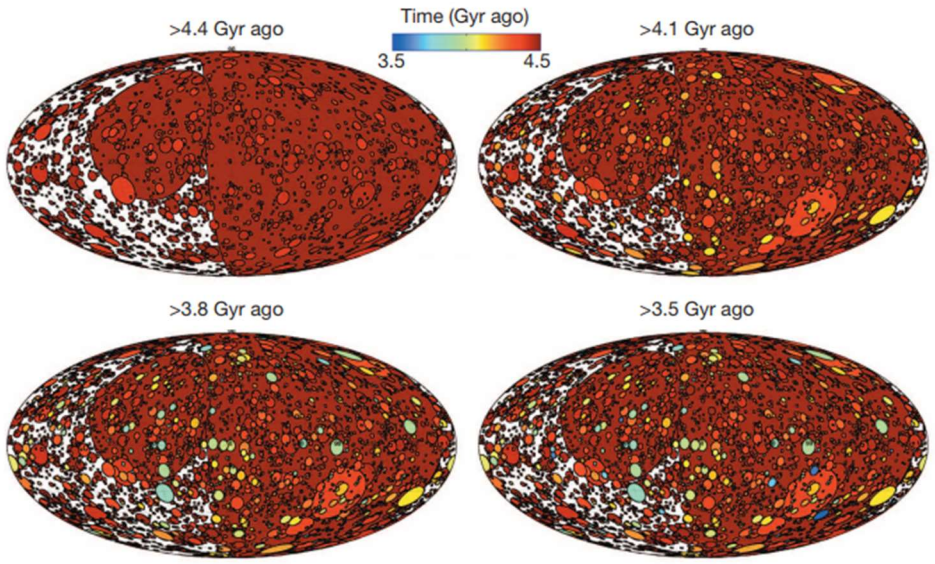


Fig 1.3. Spatial distribution and sizes of craters formed on the early Earth, from (Marchi et al., 2014). Mollweide projections of the cumulative record of craters at four different times. Each circle indicates the final crater size estimated from the transient cavity size from (Marchi et al., 2014) simulation and a conservative estimate for the transient-to-final crater size scaling. The colour coding indicates the time of impact. The smallest projectiles considered have a diameter of 15 km and an estimated impact velocity of ~16 and ~25 km/s before and after 4.15 Ga, respectively, and a most likely impact angle of 45°.

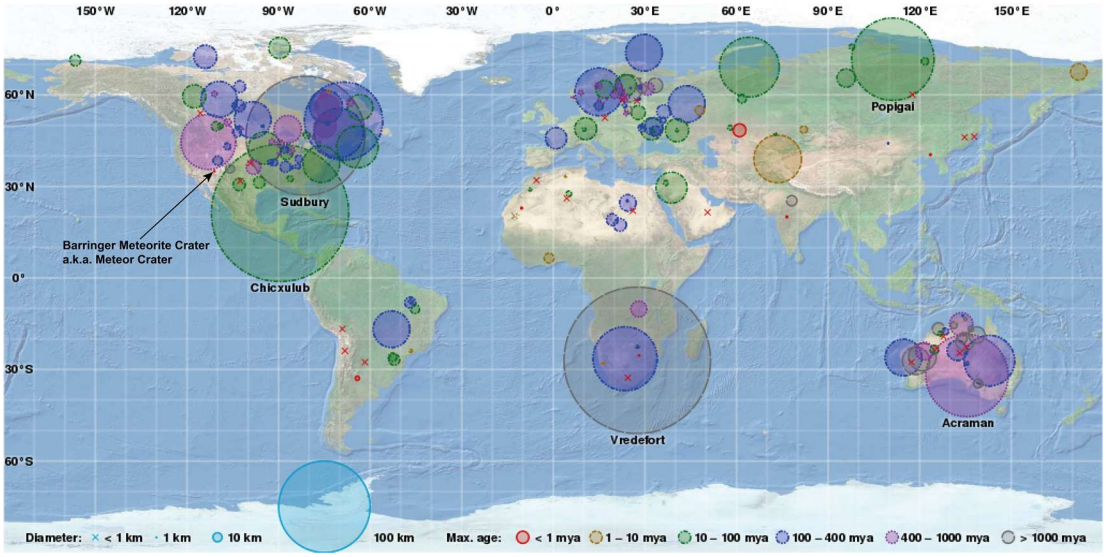


Fig 1.4. Location of confirmed impact craters on the Earth (Earth Impact Database). The size of the circle represents the diameter of the crater and colour of the circle shows the age.

The world map is in equirectangular projection. This map is a modified version of the map produced by Lee (2018).

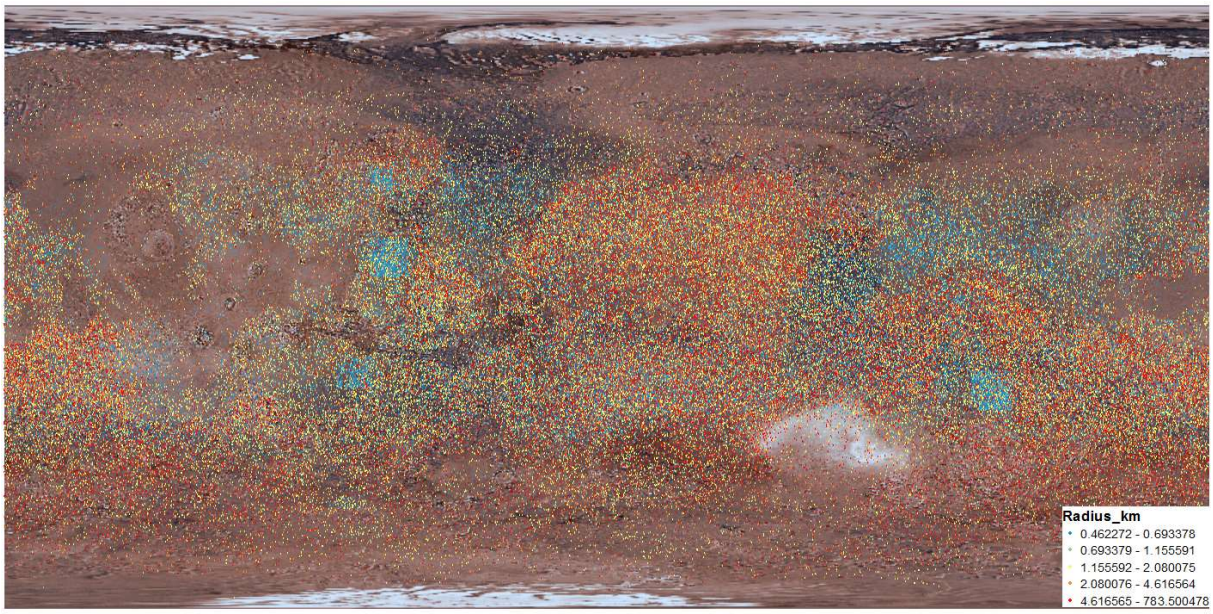


Figure 1.5. The distribution of impact craters on present-day Mars. Salamunićcar et al. (2012) catalogued 132, 843 Martian impact craters manually and using crater detection algorithms. These crater range in diameter from 0.46 to 783.5 Km.

The formation of impact craters is an instantaneous event that has a catastrophic effect on the geology at regional and sometimes global scales because the energy released during the process is much higher than any endogenic geological processes such as volcanic explosions, earthquakes, or the slow movements of plate tectonics (French, 1998; Kenkmann et al., 2014). During an impact cratering event, a tremendous amount of target rocks are excavated due to impact fragmentation and spallation (Melosh, 1989; Senthil Kumar et al., 2014), creating freshly exposed surfaces as ejecta and crater rim uplift deposits (Osinski et al., 2011). In addition, larger impact events generate an enormous amount of igneous rocks in the form of impact melt rocks and impact breccias (Caudill et al., 2018; Osinski et al., 2018). Once emplaced, weathering and erosional processes gradually rework impactites (Stöffler et al., 2007), breaking down larger debris and reducing vertical relief (Chapman, 2007). Similar to other subaerial rocks, impact rocks and ejecta are affected by mechanical, chemical and biological breakdown processes (Thomas et al., 2005). On a heavily impacted planetary

surface, impactites (or impact rocks) may undergo a different style and rate of weathering compared to non-impacted rocks when exposed to weathering environment (Tornabene et al., 2013; Boslough, 1991). Thus, the study of the subsequent breakdown of impactites is critically important for our understanding of rock breakdown processes on Early Earth and Mars – when the climate was different, and impact rate was much higher than today – and present-day Earth and Mars.

Rock breakdown is responsible for regolith/soil production and plays a vital role in climate control via atmosphere-lithosphere interaction, biogeochemical cycling and landform evolution on a planetary scale (Goudie and Viles, 2012; Viles, 2013b). A considerable amount of literature is available on weathering (Moses et al., 2014; Bland and Rolls, 1998b) and references therein) and many studies have been conducted to understand the efficacy of weathering in desertic environments (Smith et al., 2005; Warke, 2007; Heslop, 2003; Viles et al., 2018; Viles et al., 2010; Viles and Goudie, 2007; Viles, 2005; Goudie et al., 2002; Laity and Bridges, 2009; Laity et al., 2001). Rock weathering is a slow process in deserts and depends on several factors such as lithology and rock properties, environment and microclimate, presence of salt, and stress history (Cooke et al., 2006; Viles, 2011; Sharma, 2010; Bland and Rolls, 1998b; Heslop, 2003; Warke, 2007; Viles et al., 2018). In recent years a few researchers have emphasised on the effect of stress history (inherited weakness from an extended period of past weathering) on subsequent weathering (Warke, 2007; Viles et al., 2010; Viles et al., 2018). These studies used simulated pre-stressed rocks (sedimentary and crystalline) with different weathering histories and subjected rocks to experimental weathering or field exposure trials in arid conditions. They found that pre-stressed rocks deteriorate faster than un-stressed rocks. Moreover, the nature of pre-stressing has a significant effect on the rate of breakdown (Warke, 2007; Viles et al., 2010; Viles et al., 2018). However, no attempts to study the effect of heterogeneities and deformation caused by the impact process on subsequent weathering have been made to date.

The impact metamorphism processes and their effects differ in non-porous crystalline target rocks in comparison to porous sedimentary rocks (Kieffer, 1971b; Cockell and Osinski, 2007; Osinski, 2007; Singleton et al., 2011; Stöffler et al., 2018). In particular, no detailed study has been undertaken to explore the role of impact metamorphism on subsequent style and rate of rock breakdown.

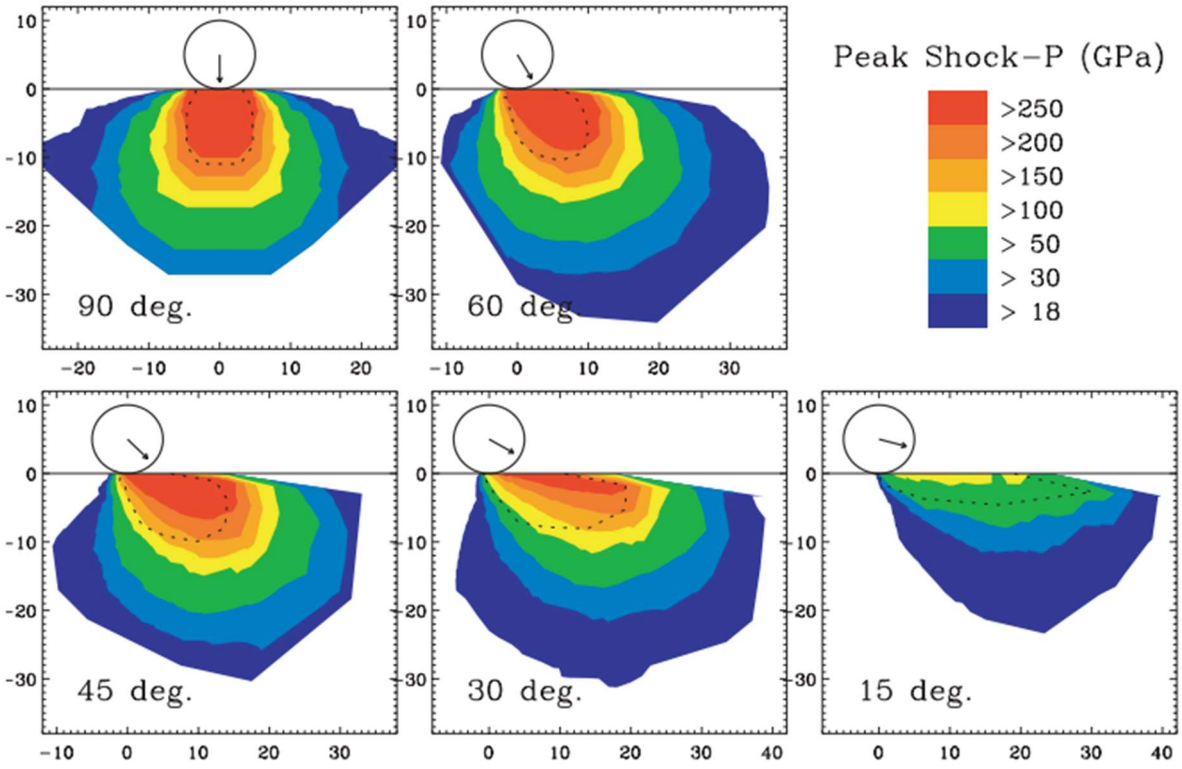


Fig 1.6. Peak shock pressure contours in the plane of impact (i.e., the plane perpendicular to the target surface that includes the projectile's line of flight) for a series of three-dimensional hydrocode simulation, at various impact angles. The dashed black line represents the isobaric core. The projectile, 10 km in diameter, is shown for scale. Vectors illustrate the direction of impact. From Pierazzo and Melosh (2000).

During an impact event, a quasi-hemispherical shock wave travels radially in all directions through the target rocks at supersonic velocities (French, 1998; Pierazzo and Melosh, 2000; Stöffler et al., 2018). The amplitude of the shock decays exponentially with the radial distance from the point of impact due to the consumption of energy in causing deformations (Fig 1.6) (French, 1998; Pierazzo and Melosh, 2000; Kenkmann et al., 2014). This is translated into more intense shock-related deformation and melting of target rocks extensively beneath and around the impact crater compared to those located at a far distance (Pierazzo and Melosh, 2000; Kenkmann et al., 2014). In the case of porous rocks like sandstone, this effect is more pronounced (Kieffer, 1971b; Kieffer et al., 1976b). The resultant rock characteristics are influenced by a complex set of processes that involve shock wave, temperature, pressure and original target rock properties (Gillet and Goresy, 2013). Impact cratering generates transient strain rates due to the passage of shock wave through

the target rocks may reach 10^4-10^6 s^{-1}, well outside the magnitude of standard geological processes by order of 10^7-10^{12} (French, 1998). Shock pressure of several gigapascals can exceed the effective strength of target lithology by three to four orders of magnitude leading to melting, vaporisation, shock metamorphism, fracturing and fragmentation of rocks as well as deformation and high-pressure mineral phase transformations (Melosh, 1989; Grieve and Therriault, 2013; Kenkmann et al., 2014). There is also a large volume of rocks in impact craters that show no sign of shock metamorphism and plastic deformation but are deformed at the sub-shock level by brittle fracturing mechanisms (Kieffer, 1971a; Madden et al., 2006; Kenkmann et al., 2014; Rae et al., 2017). The brecciation and fracturing due to impact results in a decrease in density of target rocks at the impact site and surrounding ejecta blanket, causing a gravity anomaly (French, 1998; French and Koeberl, 2010). Impact processes induce a wide range of fracture systems such as radial, concentric and conical fractures and decompression cracks (Kumar, 2005; Kumar and Kring, 2008; Newsom et al., 2013; Wright, 2013). These fractures and microcracks will increase secondary porosity and affect total porosity and permeability of the rocks. The role of micro-fracturing as a control on the moisture flux in rocks is held to be important in subsequent rates of rock breakdown (Sousa et al., 2005; Anders et al., 2014). However, this is not well understood in any environment.

Naturally occurring distinct diagnostic mineral deformation features related to impact shock waves such as planer fractures, planar deformation features, feather features, toasting, mosaicism, kink bands, high-pressure mineral phase transformations and impact shock melting at various shock pressures are well documented in the literature (French and Koeberl, 2010; Ferrière and Osinski, 2013; Stöffler et al., 2018), and assigned shock pressure levels by calibrated laboratory experiments (Kieffer, 1971b; Shipman et al., 1971; Kieffer et al., 1976a). What has not been investigated is the role of these features on subsequent weathering of rocks.

During impact, porosity, permeability and density can dramatically change depending on the energy released during impact and target lithology as well as the location of the rock from the point of impact (Kieffer, 1971b; Cockell and Osinski, 2007; Singleton et al., 2011). For crystalline rocks, a nonlinear but clear correlation can be found between decreasing density and increase shock pressure caused due to fracturing, vesiculation and differential mineral melting (Singleton et al., 2011). In case of porous sedimentary rocks density increases due to pore collapse at low shock pressure levels (<10 GPa) and decreases as shock pressure increases (25 > P > 10 GPa) due to vesiculation and formation of glasses (Kieffer, 1971a;

Kieffer, 1971b). At lower shock pressure (<10 GPa) sandstones are weakly lithified due to comminution and fracturing of grains but become strongly lithified or cohesive due to the formation of glasses and melts that weld mineral grains at higher shock pressure (>10 GPa) (Kieffer, 1975).

Low shock pressures (<10 GPa) cause pore collapse in sandstone whereas high shock pressures (25 > P > 10 GPa) can produce vesiculation (Kieffer, 1971a; Kieffer, 1971b; Cockell and Osinski, 2007). At even higher shock pressures (>30 GPa) the porosity is reduced as minerals recrystallise from the melt (Cockell and Osinski, 2007). If impact rocks are subject to longer-term heating and annealing during crater cooling, the porosity and permeability will be affected further. For highly porous substrates (such as sandstones), more of the impact energy is taken up in pore collapse resulting in lesser solid state transformations and higher post-shock temperatures than a similar impact into non-porous crystalline target lithology (Kieffer, 1971b; Madden et al., 2006). In crystalline rocks, porosity increases with an increase in shock pressure levels (Singleton et al., 2011). This is caused due to fracturing and differential mineral melting during the passage of the shock and subsequent rarefaction wave (Singleton et al., 2011).

In addition to shocked target rocks in crater wall and ejecta blanket, complex impact processes produce produces a range of impact melt rocks and impact breccias. Complex flow and ejection processes mix rocks belonging to different shock levels to produce breccias (French, 1998; Grieve and Therriault, 2013; Kring, 2017). At higher shock pressures (>50 GPa) during hypervelocity impact, protolith target rocks are consumed by melting processes. These melt rock materials solidify to form impact melt rocks (Osinski et al., 2018). These materials are distributed within and around the crater. A range of impactites such as shocked target rocks, impact melt rocks, impact breccias, impact melt-bearing breccias, and tektites are usually found at impact sites. Impactites are classified into autochthonous, parautochthonous and allochthonous based on origin and current location at the impact site. Allochthonous impactites are further classified into proximal and distal based on distance from the impact site. A detailed classification of impactites can be found in Stöffler et al. (2007) and Grieve and Therriault (2013).

Over the past few decades, a number of studies have proposed different classification system to assign different levels to shocked rocks with different stages of shock metamorphism (Kieffer, 1971b; Kieffer et al., 1976a; Osinski, 2007; Singleton et al., 2011). These

classifications are based on presence or absence of diagnostic shock effects in rocks and minerals. Since the behaviour of shock waves varies in porous sedimentary rocks and non-porous crystalline rocks, different classification schemes are used (Stöffler et al., 2018). A detailed and updated shock classification of silicate rock can be found in Stöffler et al. (2018).

Newsom et al. (2013) and Wright (2013) reported a unique style of rock breakdown associated with decompression cracks in impacted basalt at Lonar Crater, India. Natural silicate glass is susceptible to accelerated dissolution than their crystalline counterparts (Wolff-Boenisch et al., 2006). Since, impact generated glasses have a different texture, density and structure (French and Koeberl, 2010), they may weather/alter differently. The structural defects, deformations and change in surface area of minerals makes shocked rocks more susceptible to chemical weathering than unshocked rocks (Boslough and Cygan, 1988; Bell, 2017). Moreover, microstructures and defects in minerals generated during impact shock (e.g. Planar Fractures, Planar Deformation Features, mosaicism, microfractures) can provide permeable pathways for fluid circulation leading to chemical weathering (Leroux, 2005; Furukawa et al., 2011). Increasing shock pressures also cause devolatilization in minerals (Madden et al., 2006), which may affect the response of rocks to thermal weathering (Farquharson et al., 2017). Environmental conditions and heterogeneities in rock properties exert an important control in rock breakdown. Earlier studies have demonstrated that pore geometry affects rock susceptibility to weathering and controls the intensity of weathering (Tuğrul, 2004).

In this thesis, I explore the effect of low shock deformation and heterogeneities produced due to melting and brecciation on the subsequent breakdown of impactites. To investigate this, I conducted a physical weathering experiment in simulated semi-arid conditions on impactites and performed a field survey at Meteor Crater in Arizona. This thesis advances the field of rock breakdown by providing insight into the influence of impact processes on subsequent rock breakdown processes. This work also provides insight into the fundamental mechanisms affecting the degradation of impact craters on planetary bodies.

1.6. Themes of the thesis and outline

This thesis contains 6 chapters. Chapter 1, this chapter, is an introduction to the thesis. Chapter 2 and 5 contains laboratory analysis and literature review of relevant topics. Three

of these chapters consist of one published paper (Chapter 4) and two manuscripts prepared (Chapter 3 and 5) for submission to peer-reviewed journals. Because these chapters were prepared as individual manuscripts, they each contain variably comprehensive introductions as well as self-contained conclusions. Chapter 6 contains a synthesis of the principal findings from Chapter 2-5 placed in the broader context of the aims of this thesis. The thesis concludes with a number of suggestions for further work in the field.

In this thesis, I explore the effect of impact processes on rock breakdown in terrestrial semi-arid conditions. Specifically, this thesis investigates subsequent breakdown of low impact shocked sandstone. Also, a small number of low-shocked crystalline rocks, impact melt rocks and impact breccias were studied to compare the difference in lithology of impactites on rock breakdown. To address these questions, I undertook a laboratory and field-based approach to study the breakdown of impactites. This thesis has five central aims:

1. To characterise petrographic properties of impactites (Chapter 2).
2. To explore the effect of impact-generated heterogeneities and discontinuities on the subsequent weathering of impactites (Chapter 3).
3. To develop a method to generate sub-mm resolution topographic data of rock surfaces at Meteor Crater site for investigation of rock breakdown features (Chapter 4).
4. To investigate the effect of low-impact shock on nature of breakdown of Sandstone (Chapter 5).

Chapter 2 provides a summary of the impact cratering process. The chapter focuses on the mechanism of crater formation, the morphology of crater, impactites and its classification, and shock metamorphism. This chapter also contains petrographic analysis and description of samples used in this research. I presented the petrographic analysis of low shocked Moenkopi and Coconino Sandstone from Meteor Crater (Arizona), low shocked crystalline rocks, impact melt rocks and impact breccias from West Clearwater impact structure (Canada), and suevite or impact melt-bearing breccia from Ries Crater (Germany) in this chapter. These samples were analysed using optical petrographic microscopy, scanning electron microscopy, and powder X-ray diffraction techniques.

Chapter 3 presents the first physical weathering experiment conducted on impactites. This chapter explores the effect of impact-generated heterogeneities and discontinuities on the subsequent weathering of impactites. In order to better understand the role of low-shock

inheritance on rock breakdown, a rock breakdown experiment was conducted in a simulated environmental cabinet under conditions similar to terrestrial semi-arid conditions. I cycled temperature (-2 to 35 °C) and relative humidity (13-45%) lasting 8 hours for 13 days. Impactite samples included low shocked sedimentary and crystalline rocks, impact melt rocks and impact breccias. The detailed petrographic properties of these samples are described in chapter 2. A combination of techniques (petrographic microscopy, XRD, SEM, X-ray computed tomography, Equotip, photographic monitoring, and weighing) was used to characterise the rock samples relative to unshocked rocks, and to assess the shock related changes before and after the experiments. The low shocked sedimentary rocks show a decrease in porosity by 38% (Coconino sandstone) and 88% (Moenkopi sandstone) compared to unshocked counterparts. Macrofractures of 0.1-0.2 mm and microfractures 0.1-5 μm in aperture are observed in all types of impactites. The experiment results show that impactites exhibit an accelerated decline in strength compared to non-impacted control samples. However, rock type and impact deformation history are important in controlling the rate of deterioration.

In contrast to previous chapters, Chapter 4 presents a new method to generate sub-millimetre resolution digital elevation models (DEMs) of weathered rock surfaces using SfM photogrammetry technique in the field. I apply a close-range structure from motion (SfM) photogrammetry-based method in the field and use it to generate high-resolution topographic data for weathered boulders and bedrock. The method was pilot tested on extensively weathered Triassic Moenkopi sandstone outcrops near Meteor Crater in Arizona. Images were taken in the field using a consumer grade DSLR camera and were processed in commercially available software Agisoft Photoscan to build dense point cloud. Dense point clouds were registered to a local 3D coordinate system (x, y, z) which was developed using a specially designed triangle coded control target and then exported as digital elevation models (DEMs). The accuracy of the DEMs was validated under controlled experimental conditions. A number of checkpoints were used to calculate errors. I also evaluated the effects of image and camera parameters on the accuracy of our DEMs. I report a horizontal error of 0.5 mm and vertical error of 0.3 mm in our experiments. My approach provides a low-cost method, for obtaining very high-resolution topographic data on weathered rock surfaces (area < 10 m^2). The method developed in this chapter is applied in the field to collect topographic data for Moenkopi sandstone at Meteor Crater for chapter 5.

In chapter 5, I investigated the effects of low impact shock on subsequent nature of breakdown of Moenkopi Sandstone by undertaking a comparative field study between low shocked Moenkopi Sandstone crater wall rock and ejecta on the rim and unshocked boulders and bedrocks present at the control sites. I used the Schmidt Hammer to collect rock hardness data and SfM method developed in chapter 4 to generate high-resolution DEMs of Moenkopi sandstone at Meteor Crater and Control sites. The DEMs generated was analysed using a range of areal surface roughness parameters and morphometric geomorphic feature classification. I found no statistical significant difference in terms of rock hardness, roughness and morphometric geomorphic features between low-shocked and unshocked Moenkopi Sandstone. However, a statistical significant difference in terms of rock hardness, roughness and morphometric features at multiple scales between N and S-SW facing crater wall slopes for Moenkopi Sandstone at Meteor Crater was found. This indicates that low-shocked generated deformation combined with aspect related microclimatic variations are responsible for weathering of Moenkopi sandstone at Meteor Crater.

Chapter 6 is a synthesis of the findings from the research presented in the chapters 2-6 of this thesis and the wider implications of the new findings to the field of rock breakdown in the arid environment. The broader implication of this research on early Earth and Mars is also discussed. Finally, some suggestions for future work stemming from the findings presented and challenges faced in the research are discussed.

1.7. Author Contributions

The four core chapters of this thesis consist of one published manuscript (chapter 4) and two manuscripts prepared for submission (chapter 3 and 5) to peer-reviewed journals. Additionally, there is one thesis chapter (Chapter 2). Also, a published manuscript on the application of method developed in chapter 4 is included in Appendix 1. I am the lead author of all these manuscripts in this thesis and second author of the manuscript in the appendix 1. I solely conducted field, laboratory and experimental work in this thesis. Dr Mary C. Bourke provided supervision, financial support and contributed through guidance, discussion and editing of all chapters of this thesis. All the manuscripts in this thesis are multi-authored and details of author contribution are expanded on below.

The publication status and a list of co-authors is presented at the outset of each chapter. The contribution from the co-authors is expanded below.

Chapter 2: Petrographic properties of Impactites

Author: Ankit K. Verma

Status: Thesis chapter

Contribution: A.K.V. conducted all the analytical analysis in this chapter. Juan Diego Rodriguez-Blanco advised A.K.V. on X-ray Diffraction analysis methods. A.K.V. collected samples from Meteor Crater (Arizona). Gordon R. Osinski provided West Clearwater Impact structure (Canada) samples. Mary C. Bourke provided samples from Ries Crater (Germany). A.K.V. wrote this chapter with editorial feedback provided by J.D.R.B. and editing by MCB.

Chapter 3: The effect of impact-generated heterogeneities and discontinuities on the subsequent weathering of impactites: insights from laboratory experiments

Authors: Ankit K. Verma, Mary C. Bourke, Heather A. Viles, Gordon R. Osinski, Juan Diego Rodriguez-Blanco

Status: Manuscript prepared for submission in a peer-reviewed journal

Contribution: A.K.V. developed the idea of weathering experiments on impactites and designed the experiment with input from M.C.B. and H.A.V. H.A.V. suggested the desalination experiment. A.K.V. designed the desalination experiment. A.K.V. conducted the weathering and desalination experiments. A.K.V. and M.C.B. collected samples from Meteor Crater (Arizona), G.R.O. provided samples from West Clearwater Impact structure (Canada), M.C.B. provided samples from Ries Crater (Germany) A.K.V. performed the petrographic analysis on all the samples with advice from J.D.R.B. A.K.V. wrote the manuscript with guidance, discussion and editing from M.C.B and editorial feedback from J.D.R.B and H.A.V.

Chapter 4: A Structure from Motion photogrammetry-based method to generate sub-millimetre resolution Digital Elevation Models for investigating rock breakdown features

Authors: Ankit K. Verma and Mary C. Bourke

Status: Published in Earth Surface Dynamics

Contribution: A.K.V. developed the control target and designed the SfM experiment with input from M.C.B. A.K.V. collected, processed and analysed field and experimental data. A.K.V. wrote the manuscript with guidance, discussion and editing from M.C.B.

Chapter 5: The effect of low-shock impact deformation on the subsequent breakdown of Moenkopi Sandstone at Meteor Crater, Arizona in a semi-arid environment

Authors: Ankit K. Verma, Mary C. Bourke and David A. Kring

Status: Manuscript prepared for submission in a peer-reviewed journal

Contribution: A.K.V. planned the fieldwork with input from M.C.B. A.K.V. conducted fieldwork with assistance from D.A.K. and M.C.B. A.K.V. collected, processed and analysed all the data from the field. A.K.V. wrote the manuscript with guidance, discussion and editing from M.C.B

Appendix I: A comparison of Structure from Motion Photogrammetry and the Traversing Micro Erosion Meter for measuring erosion on rock shore platforms

Authors: Niamh D. Cullen, Ankit K. Verma and Mary C. Bourke

Status: Published in Earth Surface Dynamics

Contribution: N.D.C. prepared and wrote the main body of the manuscript with discussion and contributions from A.K.V. and M.C.B. N.D.C. designed the experiment with input from A.K.V. and M.C.B. A.K.V. designed the original coordinate reference system, and N.D.C designed the field adapted version with input from A.K.V and M.C.B. N.D.C and A.K.V carried out the experiments. A.K.V. processed images and generated the digital elevation models. N.D.C. carried out data analysis. A.K.V. and M.C.B reviewed and edited the final manuscript.

References

Allaby M. (2013) *A dictionary of geology and earth sciences*: Oxford University Press.

Anders MH, Laubach SE and Scholz CH. (2014) Microfractures: A review. *Journal of Structural Geology* 69: 377-394.

Anderson SP. (2005) Glaciers show direct linkage between erosion rate and chemical weathering fluxes. *Geomorphology* 67: 147-157.

Arvidson R, Squyres S, Bell J, et al. (2014) Ancient aqueous environments at Endeavour crater, Mars. *Science* 343: 1248097.

Bell M. (2015) Experimentally Shocked and Altered Basalt: Laboratory Analogs for Calibration of Mars Remote Sensing and In Situ Data.

Bell M. (2017) Experimentally Shocked and Altered Basalt: VNIR Spectra of Mars Analog Materials.

Benn D and Evans DJ. (2014) *Glaciers and glaciation*: Routledge.

Beylich AA, Kolstrup E, Thyrsted T, et al. (2004) Chemical denudation in arctic-alpine Latnjavagge (Swedish Lapland) in relation to regolith as assessed by radio magnetotelluric-geophysical profiles. *Geomorphology* 57: 303-319.

Bibring J-P, Langevin Y, Mustard JF, et al. (2006) Global mineralogical and aqueous Mars history derived from OMEGA/Mars Express data. *Science* 312: 400-404.

Bland W and Rolls D. (1998) *Weathering: an introduction to the scientific principles*: Arnold, Hodder Headline, PLC.

Boslough M. (1991) Shock modification and chemistry and planetary geologic processes. *Annual review of Earth and planetary sciences* 19: 101-130.

Boslough M, Venturini E, Morosin B, et al. (1986) Physical properties of shocked and thermally altered nontronite: Implications for the Martian surface. *Journal of Geophysical Research: Solid Earth* 91.

Boslough MB and Cygan RT. (1988) Shock-enhanced dissolution of silicate minerals and chemical weathering on planetary surfaces. *Lunar and Planetary Science Conference Proceedings.* 443-453.

Bourke MC, Lancaster N, Fenton LK, et al. (2010) Extraterrestrial dunes: An introduction to the special issue on planetary dune systems. *Geomorphology* 121: 1-14.

Bourke MC and Viles HA. (2007) *A photographic atlas of rock breakdown features in geomorphic environments*.

Bridges N, Cooper G, Eddlemon E, et al. (2004) Aeolian Abrasion, a Dominant Erosion Agent in the Martian Environment. *AGU Fall Meeting Abstracts.* 07.

Burns RG. (1993) Rates and mechanisms of chemical weathering of ferromagnesian silicate minerals on Mars. *Geochimica et Cosmochimica Acta* 57: 4555-4574.

Burns RG and Fisher DS. (1993) Rates of oxidative weathering on the surface of Mars. *Journal of Geophysical Research: Planets (1991–2012)* 98: 3365-3372.

Byrne S, Dundas CM, Kennedy MR, et al. (2009) Distribution of mid-latitude ground ice on Mars from new impact craters. 325: 1674-1676.

Campbell SW, Dixon JC, Thorn CE, et al. (2002) Chemical denudation rates in Kärkevagge, Swedish Lapland. *Geografiska Annaler: Series A, Physical Geography* 84: 179-185.

Cardell C, Rivas T, Mosquera M, et al. (2003) Patterns of damage in igneous and sedimentary rocks under conditions simulating sea-salt weathering. *Earth Surface Processes and Landforms: The Journal of the British Geomorphological Research Group* 28: 1-14.

Carr MH and Head JW. (2010) Geologic history of Mars. *Earth and Planetary Science Letters* 294: 185-203.

Carter J, Loizeau D, Mangold N, et al. (2015) Widespread surface weathering on early Mars: A case for a warmer and wetter climate. *Icarus* 248: 373-382.

Carter N and Viles H. (2003) Experimental investigations into the interactions between moisture, rock surface temperatures and an epilithic lichen cover in the bioprotection of limestone. *Building and Environment* 38: 1225-1234.

Catling DC and Leovy C. (2006) Mars Atmosphere History and Surface Interactions. *Encyclopedia of the solar system*.

Caudill C, Osinski G and Tornabene L. (2018) Ejecta Deposits of Bakhuysen Crater, Mars. *Icarus*.

Chapman M. (2007) *The geology of Mars: evidence from earth-based analogs*: Cambridge University Press.

Chevrier V and Mathé P. (2007) Mineralogy and evolution of the surface of Mars: a review. *Planetary and Space Science* 55: 289-314.

Clarke J. (2011) Extraterrestrial arid surface processes. In: Thomas DS (ed) *Arid Zone Geomorphology.* Third ed.: John Wiley & Sons, Ltd., 61-82.

Cockell CS and Osinski GR. (2007) Impact-induced impoverishment and transformation of a sandstone habitat for lithophytic microorganisms. *Meteoritics & Planetary Science* 42: 1985-1993.

Cooke RU, Warren A and Goudie AS. (2006) *Desert geomorphology*: CRC Press.

Cygan RT, Casey WH, Boslough MB, et al. (1989) Dissolution kinetics of experimentally shocked silicate minerals. *Chemical geology* 78: 229-244.

Daubar I, McEwen A, Byrne S, et al. (2011) New craters on Mars and the Moon. *Lunar and Planetary Science Conference.* 2232.

Davis WM and Johnson DW. (1909) *Geographical essays*: Ginn.

de Boer DH. (1992) Hierarchies and spatial scale in process geomorphology: a review. *Geomorphology* 4: 303-318.

Des Marais D, Jakosky BM and Hynek BM. (2008) Astrobiological implications of Mars' surface composition and properties. *The Martian Surface-Composition, Mineralogy, and Physical Properties* 1: 599.

Dixon JC and Thorn CE. (2005) Chemical weathering and landscape development in mid-latitude alpine environments. *Geomorphology* 67: 127-145.

Doehne E. (2002) Salt weathering: a selective review. *Geological society, London, special publications* 205: 51-64.

Edwards HG, Holder JM, Seaward MR, et al. (2002) Raman spectroscopic study of lichen-assisted weathering of sandstone outcrops in the High Atlas Mountains, Morocco. *Journal of Raman Spectroscopy* 33: 449-454.

Ehlmann BL and Edwards CS. (2014) Mineralogy of the Martian surface. *Annual review of Earth and planetary sciences* 42: 291-315.

Eppes M-C, Willis A, Molaro J, et al. (2015) Cracks in Martian boulders exhibit preferred orientations that point to solar-induced thermal stress. *Nature communications* 6.

Fairén AG. (2010) A cold and wet Mars. *Icarus* 208: 165-175.

Farquharson J, Griffiths L, Baud P, et al. (2017) Compressive strength evolution of thermally-stressed Saint Maximin limestone. *AGU Fall Meeting Abstracts.*

Ferrière L and Osinski GR. (2013) Shock metamorphism. In: Osinski GR and Pierazzo E (eds) *Impact Cratering: Processes and Products.* John Wiley & Sons, 106-124.

Foye WG. (1921) "Denudation", "erosion", "corrosion", and "corrasion". *Science* 54: 130-131.

French BM. (1998) Traces of catastrophe: A handbook of shock-metamorphic effects in terrestrial meteorite impact structures. *Technical Report, LPI-Contrib-954*.

French BM and Koeberl C. (2010) The convincing identification of terrestrial meteorite impact structures: What works, what doesn't, and why. *Earth-Science Reviews* 98: 123-170.

Furukawa Y, Sekine T, Kakegawa T, et al. (2011) Impact-induced phyllosilicate formation from olivine and water. *Geochimica et Cosmochimica Acta* 75: 6461-6472.

Gillet P and Goresy AE. (2013) Shock events in the solar system: the message from minerals in terrestrial planets and asteroids. *Annual review of Earth and planetary sciences* 41: 257-285.

Golombek M, Warner N, Ganti V, et al. (2014) Small crater modification on Meridiani Planum and implications for erosion rates and climate change on Mars. *Journal of Geophysical Research: Planets* 119: 2522-2547.

Goudie A and Viles H. (1997) Salt Weathering Hazards. John.

Goudie AS and Day MJ. (1980) Disintegration of fan sediments in Death Valley, California, by salt weathering. *Physical Geography* 1: 126-137.

Goudie AS and Viles HA. (2012) Weathering and the global carbon cycle: geomorphological perspectives. *Earth-Science Reviews* 113: 59-71.

Goudie AS, Wright E and Viles HA. (2002) The roles of salt (sodium nitrate) and fog in weathering: a laboratory simulation of conditions in the northern Atacama Desert, Chile. *Catena* 48: 255-266.

Goudie ASJE-sr. (2016) Quantification of rock control in geomorphology. 159: 374-387.

Grant JA and Schultz PH. (1993a) Degradation of selected terrestrial and Martian impact craters. *Journal of Geophysical Research: Planets (1991–2012)* 98: 11025-11042.

Grant JA and Schultz PH. (1993b) Erosion of ejecta at Meteor Crater, Arizona. *Journal of Geophysical Research: Planets (1991–2012)* 98: 15033-15047.

Gregory J. (1911) The Terms" Denudation,"" Erosion,"" Corrosion," and" Corrasion". *The Geographical Journal* 37: 189-195.

Grieve R and Pesonen L. (1992) The terrestrial impact cratering record. *Tectonophysics* 216: 1-30.

Grieve R and Robertson P. (1979) The terrestrial cratering record: I. Current status of observations. *Icarus* 38: 212-229.

Grieve RA and Therriault AM. (2013) Impactites: Their characteristics and spatial distribution. *Impact Cratering: Processes and Products*: 90-105.

Grotzinger JP, Arvidson R, Bell J, et al. (2005) Stratigraphy and sedimentology of a dry to wet eolian depositional system, Burns formation, Meridiani Planum, Mars. *Earth and Planetary Science Letters* 240: 11-72.

Grotzinger JP, Sumner D, Kah L, et al. (2014) A habitable fluvio-lacustrine environment at Yellowknife Bay, Gale Crater, Mars. *Science* 343: 1242777.

Hall K and Hall A. (1996) Weathering by wetting and drying: some experimental results. *Earth Surface Processes and Landforms* 21: 365-376.

Hall K, Thorn CE, Matsuoka N, et al. (2002) Weathering in cold regions: some thoughts and perspectives. *Progress in Physical Geography* 26: 577-603.

Hayes A, Grotzinger J, Edgar L, et al. (2011) Reconstruction of eolian bed forms and paleocurrents from cross-bedded strata at Victoria Crater, Meridiani Planum, Mars. *Journal of Geophysical Research: Planets* 116.

Hergarten S and Kenkmann T. (2015) The number of impact craters on Earth: Any room for further discoveries? *Earth and Planetary Science Letters* 425: 187-192.

Heslop EEM. (2003) Clast breakdown in the Atacama Desert, Chile :An intergrated field and laboratory approach. University of Oxford.

Hobbs SW, Paull DJ and Bourke MC. (2010) Aeolian processes and dune morphology in Gale Crater. *Icarus* 210: 102-115.

Jagoutz E. (2006) Salt-induced rock fragmentation on Mars: The role of salt in the weathering of Martian rocks. *Advances in Space Research* 38: 696-700.

Kah LC. (2015) Images from Curiosity: A New Look at Mars. *Elements* 11: 27-32.

Kenkmann T, Poelchau MH and Wulf G. (2014) Structural geology of impact craters. *Journal of Structural Geology* 62: 156-182.

Kieffer S, Schaal R, Gibbons R, et al. (1976a) Shocked basalt from Lonar impact crater, India, and experimental analogues. *Lunar and Planetary Science Conference Proceedings.* 1391-1412.

Kieffer SW. (1971a) I. Shock metamorphism of the Coconino sandstone at Meteor Crater, Arizona. II. The specific heat of solids of geophysical interest. California Institute of Technology.

Kieffer SW. (1971b) Shock Metamorphism of the Coconino Sandstone. *Journal of Geophysical Research*.

Kieffer SW. (1975) From regolith to rock by shock. *The Moon* 13: 301-320.

Kieffer SW, Phakey PP and Christie JM. (1976b) Shock processes in porous quartzite: Transmission electron microscope observations and theory. *Contributions to Mineralogy and Petrology* 59: 41-93.

Knauth LP, Burt DM and Wohletz KH. (2005) Impact origin of sediments at the Opportunity landing site on Mars. *Nature* 438: 1123-1128.

Kring DA. (2017) Guidebook to the geology of Barringer Meteorite Crater, Arizona (aka Meteor Crater): for the 80th Annual Meeting of the Meteoritical Society July 2017. Lunar and Planetary Institute.

Kumar PS. (2005) Structural effects of meteorite impact on basalt: Evidence from Lonar crater, India. *Journal of Geophysical Research: Solid Earth* 110.

Kumar PS and Kring DA. (2008) Impact fracturing and structural modification of sedimentary rocks at Meteor Crater, Arizona. *Journal of Geophysical Research: Planets (1991–2012)* 113.

Laity J, Bridges N and Boyle T. (2001) Ventifact Formation in the Mojave Desert: Field Analogs for Martian Processes. *Field Trip and Workshop on the Martian Highlands and Mojave Desert Analogs.* 4004.

Laity JE. (2009) Landforms, landscapes, and processes of aeolian erosion. *Geomorphology of Desert Environments.* Springer, 597-627.

Laity JE and Bridges NT. (2009) Ventifacts on Earth and Mars: Analytical, field, and laboratory studies supporting sand abrasion and windward feature development. *Geomorphology* 105: 202-217.

Lee CMG. (2018) Earth Impact Database world map. Wikipedia.

Leroux H. (2005) Weathering features in shocked quartz from the Ries impact crater, Germany. *Meteoritics & Planetary Science* 40: 1347-1352.

Loizeau D, Carter J, Mangold N, et al. (2015) Widespread Surface Weathering on Early Mars: possible implication on the Past Climate. *EGU General Assembly Conference Abstracts.*

Mabbutt JA. (1961) A stripped land surface in Western Australia. *Transactions and Papers (Institute of British Geographers)*: 101-114.

Madden MEE, Kring DA and Bodnar RJ. (2006) Shock reequilibration of fluid inclusions in Coconino sandstone from Meteor Crater, Arizona. *Earth and Planetary Science Letters* 241: 32-46.

Malin MC, Edgett KS, Posiolova LV, et al. (2006) Present-day impact cratering rate and contemporary gully activity on Mars. 314: 1573-1577.

Marchi S, Bottke W, Elkins-Tanton L, et al. (2014) Widespread mixing and burial of Earth's Hadean crust by asteroid impacts. *Nature* 511: 578.

Matsuoka N and Murton J. (2008) Frost weathering: recent advances and future directions. *Permafrost and Periglacial Processes* 19: 195-210.

McFadden L, Eppes M, Gillespie A, et al. (2005) Physical weathering in arid landscapes due to diurnal variation in the direction of solar heating. *Geological Society of America Bulletin* 117: 161-173.

McLennan S and Grotzinger J. (2008) The sedimentary rock cycle of Mars. *The Martian Surface-Composition, Mineralogy, and Physical Properties* 1: 541.

Melosh HJ. (1989) Impact cratering: A geologic process. *Research supported by NASA. New York, Oxford University Press (Oxford Monographs on Geology and Geophysics, No. 11), 1989, 253 p.* 1.

Mills HH. (2005) Relative-age dating of transported regolith and application to study of landform evolution in the Appalachians. *Geomorphology* 67: 63-96.

Ming DW, Morris RV and Clark BC. (2008) Aqueous alteration on Mars. *The Martian Surface—Composition, Mineralogy, and Physical Properties*: 519.

Moses C, Robinson D and Barlow J. (2014) Methods for measuring rock surface weathering and erosion: a critical review. *Earth-Science Reviews* 135: 141-161.

Naylor LA and Viles HA. (2002) A new technique for evaluating short-term rates of coastal bioerosion and bioprotection. *Geomorphology* 47: 31-44.

Newsom HE, Mangold N, Kah LC, et al. (2014) Gale crater and impact processes–Curiosity's first 364 Sols on Mars. *Icarus*.

Newsom HE, Wright SP, Misra S, et al. (2013) Comparison of simple impact craters: A case study of Meteor and Lonar Craters. *Impact Cratering: Processes and Products*: 271-289.

Ollier C. (1960) The inselbergs of Uganda. *Zeitschrift fur Geomorphologie* 4: 43-52.

Osinski G and Melosh H. (2004) Impactites on Mars: What Should We Expect and What is the Role of Volatiles? *Second Conference on Early Mars: Geologic, Hydrologic, and Climatic Evolution and the Implications for Life.*

Osinski GR. (2007) Impact metamorphism of CaCO3-bearing sandstones at the Haughton structure, Canada. *Meteoritics & Planetary Science* 42: 1945-1960.

Osinski GR, Grieve RA, Bleacher JE, et al. (2018) Igneous rocks formed by hypervelocity impact. *Journal of Volcanology and Geothermal Research*.

Osinski GR and Pierazzo E. (2012) *Impact cratering: Processes and products*: John Wiley & Sons.

Osinski GR, Tornabene LL and Grieve RA. (2011) Impact ejecta emplacement on terrestrial planets. *Earth and Planetary Science Letters* 310: 167-181.

Palumbo A and Head J. (2017) Impact cratering as the cause of climate change, atmospheric alteration, and late Noachian valley network formation on Mars: An assessment. *6th Mars Atmosphere Modeling and Observations Workshop.* 17-20.

Phillips JD. (2005) Weathering instability and landscape evolution. *Geomorphology* 67: 255-272.

Pickersgill AE. (2014) Shock metamorphic effects in lunar and terrestrial plagioclase feldspar investigated by optical petrography and micro-X-ray diffraction.

Pierazzo E and Melosh H. (2000) Melt production in oblique impacts. *Icarus* 145: 252-261.

Pope GA, Meierding TC and Paradise TR. (2002) Geomorphology's role in the study of weathering of cultural stone. *Geomorphology* 47: 211-225.

Rae A, Collins G, Grieve R, et al. (2017) Complex crater formation: Insights from combining observations of shock pressure distribution with numerical models at the West Clearwater Lake impact structure. *Meteoritics & Planetary Science* 52: 1330-1350.

Robbins SJ and Hynek BM. (2012) A new global database of Mars impact craters≥ 1 km: 2. Global crater properties and regional variations of the simple-to-complex transition diameter. *Journal of Geophysical Research: Planets* 117.

Rodriguez-Navarro C and Doehne E. (1999) Salt weathering: influence of evaporation rate, supersaturation and crystallization pattern. *Earth Surface Processes and Landforms: The Journal of the British Geomorphological Research Group* 24: 191-209.

Rosa DF. (2012) *The sheet of impact melt at West Clearwater Lake, Northern Quebec*: McGill University (Canada).

Sak PB, Fisher DM, Gardner TW, et al. (2004) Rates of weathering rind formation on Costa Rican basalt. *Geochimica et Cosmochimica Acta* 68: 1453-1472.

Salamunićcar G, Lončarić S, Mazarico EJP, et al. (2012) LU60645GT and MA132843GT catalogues of Lunar and Martian impact craters developed using a Crater Shape-based interpolation crater detection algorithm for topography data. 60: 236-247.

Schultz PH and Mustard JF. (2004) Impact melts and glasses on Mars. *Journal of Geophysical Research: Planets* 109.

Senthil Kumar P, Prasanna Lakshmi K, Krishna N, et al. (2014) Impact fragmentation of Lonar Crater, India: Implications for impact cratering processes in basalt. *Journal of Geophysical Research: Planets* 119: 2029-2059.

Sharma VK. (2010) *Introduction to process geomorphology*: CRC Press.

Sharp RP and Malin MC. (1984) Surface geology from Viking landers on Mars: A second look. *Geological Society of America Bulletin* 95: 1398-1412.

Shipman F, Gregson V and Jones A. (1971) *A shock wave study of Coconino Sandstone*: National Aeronautics and Space Administration.

Simms MJ. (2004) Tortoises and hares: Dissolution, erosion and isostasy in landscape evolution. *Earth Surface Processes and Landforms* 29: 477-494.

Simpson SL. (2015) Geochemical and mineralogical studies of meteorite impact-generated hydrothermal systems on Earth and tracing sources of water: observations from the Rochechouart impact structure, France. University of Glasgow.

Singleton AC, Osinski GR, McCAUSLAND PJ, et al. (2011) Shock-induced changes in density and porosity in shock-metamorphosed crystalline rocks, Haughton impact structure, Canada. *Meteoritics & Planetary Science* 46: 1774-1786.

Smith B. (2009) Weathering processes and forms. *Geomorphology of desert environments.* Springer, 69-100.

Smith B, Warke P, McGreevy J, et al. (2005) Salt-weathering simulations under hot desert conditions: agents of enlightenment or perpetuators of preconceptions? *Geomorphology* 67: 211-227.

Smith P, Tamppari L, Arvidson R, et al. (2009) H2O at the Phoenix landing site. *Science* 325: 58-61.

Sousa LM, del Río LMS, Calleja L, et al. (2005) Influence of microfractures and porosity on the physico-mechanical properties and weathering of ornamental granites. *Engineering Geology* 77: 153-168.

Squyres SW, Arvidson RE, Bell J, et al. (2012) Ancient impact and aqueous processes at Endeavour Crater, Mars. *Science* 336: 570-576.

Stöffler D, Grieve R, Fettes D, et al. (2007) Impactites. *Metamorphic rocks: A classification and glossary of terms, recommendations of the International Union of Geological Sciences*: 82-92.

Stöffler D, Hamann C and Metzler K. (2018) Shock metamorphism of planetary silicate rocks and sediments: Proposal for an updated classification system. *Meteoritics & Planetary Science* 53: 5-49.

Strom R and Woronow A. (1982) Solar System cratering populations. *Lunar and Planetary Science Conference.* 782-783.

Sullivan R, Arvidson R, Grotzinger J, et al. (2007) Aeolian geomorphology with MER Opportunity at Meridiani Planum, Mars. *Lunar Planet. Sci., XXXVIII* 2048.

Summerfield MA. (2014) *Global geomorphology*: Routledge.

Sumner P, Nel W, Holness S, et al. (2002) Rock weathering characteristics as relative-age indicators for glacial and post-glacial landforms on Marion Island. *South African Geographical Journal* 84: 153-157.

Thomas M, Clarke J and Pain C. (2005) Weathering, erosion and landscape processes on Mars identified from recent rover imagery, and possible Earth analogues. *Aust. J. Earth Sci.* 52: 365-378.

Thomas MF. (1966) Some geomorphological implications of deep weathering patterns in crystalline rocks in Nigeria. *Transactions of the Institute of British Geographers*: 173-193.

Tornabene LL, Osinski GR, McEwen AS, et al. (2013) An impact origin for hydrated silicates on Mars: A synthesis. *Journal of Geophysical Research: Planets* 118: 994-1012.

Tuğrul A. (2004) The effect of weathering on pore geometry and compressive strength of selected rock types from Turkey. *Engineering Geology* 75: 215-227.

Turkington AV, Phillips JD and Campbell SW. (2005) Weathering and landscape evolution. *Geomorphology* 67: 1-6.

Twidale C, Bourne J and Romani JV. (2005) Beach etching and shore platforms. *Geomorphology* 67: 47-61.

Viles H. (2011) Weathering systems. In: Thomas DS (ed) *Arid Zone Geomorphology: Process, Form and Change in Drylands.* III ed.: John Wiley & Sons, 85-101.

Viles H, Ehlmann B, Wilson CF, et al. (2010) Simulating weathering of basalt on Mars and Earth by thermal cycling. *Geophys. Res. Lett.* 37: L18201.

Viles H and Goudie A. (2007) Rapid salt weathering in the coastal Namib desert: implications for landscape development. *Geomorphology* 85: 49-62.

Viles H, Messenzehl K, Mayaud J, et al. (2018) Stress histories control rock-breakdown trajectories in arid environments. *Geology* 46: 419-422.

Viles H and Moses C. (1998) Experimental production of weathering nanomorphologies on carbonate stone. *Quarterly Journal of Engineering Geology and Hydrogeology* 31: 347-357.

Viles HA. (2001) Scale issues in weathering studies. *Geomorphology* 41: 63-72.

Viles HA. (2005) Microclimate and weathering in the central Namib Desert, Namibia. *Geomorphology* 67: 189-209.

Viles HA. (2013) Synergistic Weathering Processes In: Shroder JF (ed) *Treatise on Geomorphology.* San Diego: Academic Press, 12-26.

Ward A, Gaddis L, Kirk R, et al. (1999) General geology and geomorphology of the Mars Pathfinder landing site. *Journal of Geophysical Research: Planets (1991–2012)* 104: 8555-8571.

Warke P. (2007) Complex weathering in drylands: implications of 'stress' history for rock debris breakdown and sediment release. *Geomorphology* 85: 30-48.

Warke P. (2013) 4.12 Weathering in Arid Regions.

Warke PA. (1996a) Inheritance effects in building stone decay. *Processes of urban stone decay. Donhead, London* 32: 43.

Warke PA. (1996b) Inheritance effects in the weathering of debris under hot arid conditions.

Weiss DK and Head JW. (2014) Ejecta mobility of layered ejecta craters on Mars: Assessing the influence of snow and ice deposits. *Icarus* 233: 131-146.

Werner S. (2008) The early martian evolution—Constraints from basin formation ages. *Icarus* 195: 45-60.

Wetherill G. (1975) Late heavy bombardment of the moon and terrestrial planets. *Lunar and Planetary Science Conference Proceedings.* 1539-1561.

White K, Bryant R and Drake N. (1998) Techniques for measuring rock weathering: application to a dated fan segment sequence in southern Tunisia. *Earth Surface Processes and Landforms* 23: 1031-1043.

Williams R, Dietrich W, Grotzinger J, et al. (2013) Curiosity's Mastcam images reveal conglomerate outcrops with water-transported pebbles. *Lunar and Planetary Science Conference.* 1617.

Williams R and Robinson D. (2000) Effects of aspect on weathering: anomalous behaviour of sandstone gravestones in southeast England. *Earth Surface Processes and Landforms: The Journal of the British Geomorphological Research Group* 25: 135-144.

Wolff-Boenisch D, Gislason SR and Oelkers EH. (2006) The effect of crystallinity on dissolution rates and CO2 consumption capacity of silicates. *Geochimica et Cosmochimica Acta* 70: 858-870.

Wright S. (2013) Decompression Cracks in Altered Basalt Under Solid-State Shock Pressures: A New Macroscopic Shock Texture. *LPI Contributions* 1737: 3049.

Zolotov MY and Mironenko MV. (2016) Chemical models for martian weathering profiles: Insights into formation of layered phyllosilicate and sulfate deposits. *Icarus* 275: 203-220.

Chapter 2

2. Petrographic properties of impactites

Abstract

Impact cratering is a ubiquitous process in the solar system and has been a crucial process in shaping all terrestrial planets. The impact is an instantaneous process that occurs when a projectile travelling with hypervelocity strikes a planetary surface. During an impact event, a tremendous amount of energy is transferred to the target rocks through shock pressure resulting in shock-related deformation, melting, fracturing and brecciation. Target rock properties (e.g. porosity and density) are changed. The rocks produced as a result of an impact are collectively known as impactites. In this chapter the petrographic analysis of low shocked Moenkopi and Coconino Sandstone from Meteor Crater (Arizona), low shocked crystalline rocks, impact melt rocks and impact breccias from West Clearwater Impact Structure (Canada), and suevite or impact melt-bearing breccia from Ries Crater (Germany) is presented. These samples were analysed using petrographic microscopy, Scanning Electron Microscopy, and powder X-ray Diffraction.

2.1. Impactites

Impactite is the term used to collectively refer all the products formed or affected by impact metamorphism processes. The classification of impact rocks is based on their abundance of melt and lithic (non-melted) material, and relative location within the structure (Stöffler et al., 2007; French and Koeberl, 2010; Simpson, 2015).

In addition to shocked target rocks in crater wall and ejecta blanket, complex impact processes produce a range of impact melt rocks and impact breccias. Complex flow and ejection processes mix rocks belonging to different shock levels to produce breccias (French, 1998; Grieve and Therriault, 2013; Kring, 2017). At higher shock pressures (>50 GPa) during hypervelocity impact, protolith target rocks are consumed by melting processes. These melt rock materials solidify to form impact melt rocks (Osinski et al., 2018). These materials are distributed within and around the crater. A range of impactites such as shocked target rocks, impact melt rocks, impact breccias, impact melt-bearing breccias, and tektites are usually found at impact sites. Impactites are classified into three main categories based on their origin and current location at the impact site: autochthonous, those found in their original pre-impact location; parautochthonous which have been moved or brecciated but

appear to be in their original place; and allochthonous which originate from beyond their current location. Allochthonous impactites are further classified into proximal and distal (those within and nearby crater and those further away from the crater, respectively) based on distance from the impact site. A detailed classification of impactites can be found in Stöffler et al. (2007) and Grieve and Therriault (2013).

2.2. Shock metamorphism

The passage of shock waves through target rocks during impact results in shock metamorphism in rocks (Ferrière and Osinski, 2013). The shock metamorphism produces distinctive and diagnostic shock features in minerals and rocks, which can be used to estimate the amount of shock pressure and temperature experienced by the target rocks (French, 1998; Stöffler et al., 2007; French and Koeberl, 2010; Osinski and Pierazzo, 2012; Stöffler et al., 2018).

Planar deformation features (PDFs) are sets of straight, closed parallel planar lamellae along which glass is typically found. PDFs are often less than 2 μm thick and typically spaced 2 to 10 μm apart (French and Koeberl, 2010; Ferrière and Osinski, 2013). They are formed most commonly in quartz and more rarely in feldspars (French, 1998; French and Koeberl, 2010). PDFs form as a result of mechanical shock deformation at a range of pressures, from 5 to 35 GPa and may contain small decoration by fluid inclusions, sometimes with minerals such as hematite, resulting from post-impact aqueous alteration and annealing (French and Koeberl, 2010). PDFs differ from planar fractures (PFs), which are open planar cracks, often >3 μm wide and spaced ~15-20 μm apart, also following crystallographic planes (French, 1998; French and Koeberl, 2010; Osinski and Pierazzo, 2012).

Diaplectic glass also known as thetomorphic glasses, forms by solid-state transformation of framework silicate minerals such as quartz and feldspar (French and Koeberl, 2010). These glasses are amorphous, optically isotropic, retaining the chemical composition, morphology, and texture of the original mineral grain (French and Koeberl, 2010). Diaplectic glasses do not show flow textures or vesiculation and are known to preserve grain boundaries, cleavage, and twin lamellae of their original mineral grain (French and Koeberl, 2010). Diaplectic glasses retain a significant degree of short-range structural order compared to melt glasses that have lost their internal ordered atomic arrangements (French and Koeberl, 2010). In crystalline rocks, these glasses start forming at 28 GPa for An-plagioclase and 35 GPa for quartz compared to more porous sedimentary rocks in which diaplectic glasses begins

forming at as low as 5 GPa for quartz (French, 1998; French and Koeberl, 2010; Osinski and Pierazzo, 2012).

Toasted quartz is a post-shock thermal feature. It appears distinct brown-yellow, dirty, "toasted" in transmitted light due to the high density of inclusions (Ferrière and Osinski, 2013). Toasted quartz grains have a high albedo and appear opaque bright white grain in hand sample (Simpson, 2015).

Kink bands in micas are formed during impact and occur at high angles to the direction of cleavage (French and Koeberl, 2010; Ferrière and Osinski, 2013). Mosaicism is another shock feature that typically occurs in quartz. Mosaicism is an irregular extinction pattern patterns seen crystals comprising of several subdomains with different optic axis under transmitted light (French and Koeberl, 2010; Ferrière and Osinski, 2013). However, kink bands and mosaicism are not diagnostic of impact and are also formed by other geological processes (French and Koeberl, 2010).

Ballen quartz is spherical to the hemispherical texture that is developed in quartz due to post-shock recrystallisation of higher temperature polymorphs (e.g. α-quartz, α-cristobalite) and glasses (French and Koeberl, 2010; Ferrière and Osinski, 2013). Ballen quartz is believed to form at ≥ 35 GPa of shock pressure (Ferrière and Osinski, 2013).

Shatter cones are macroscopic shock feature that only forms at pressures between 2 and 10 GPa during impact (French, 1998; French and Koeberl, 2010; Osinski and Pierazzo, 2012). Shatter cones are conical, radiating striations forming on fracture surfaces of fine-grained sedimentary and fine-crystalline igneous target rocks (French, 1998; French and Koeberl, 2010).

Metastable high-pressure polymorphs of quartz are formed due to shock metamorphism. Coesite forms at 30-60 GPa and stishovite at 12-45 GPa in crystalline rocks whereas in sedimentary rocks they can form between 10-60 GPa (French and Koeberl, 2010; Stöffler et al., 2018). They usually occur as inclusions in diaplectic glasses or PDFs (French and Koeberl, 2010). Stishovite is the only high-pressure polymorph of quartz that only forms during impact (French, 1998; Osinski and Pierazzo, 2012).

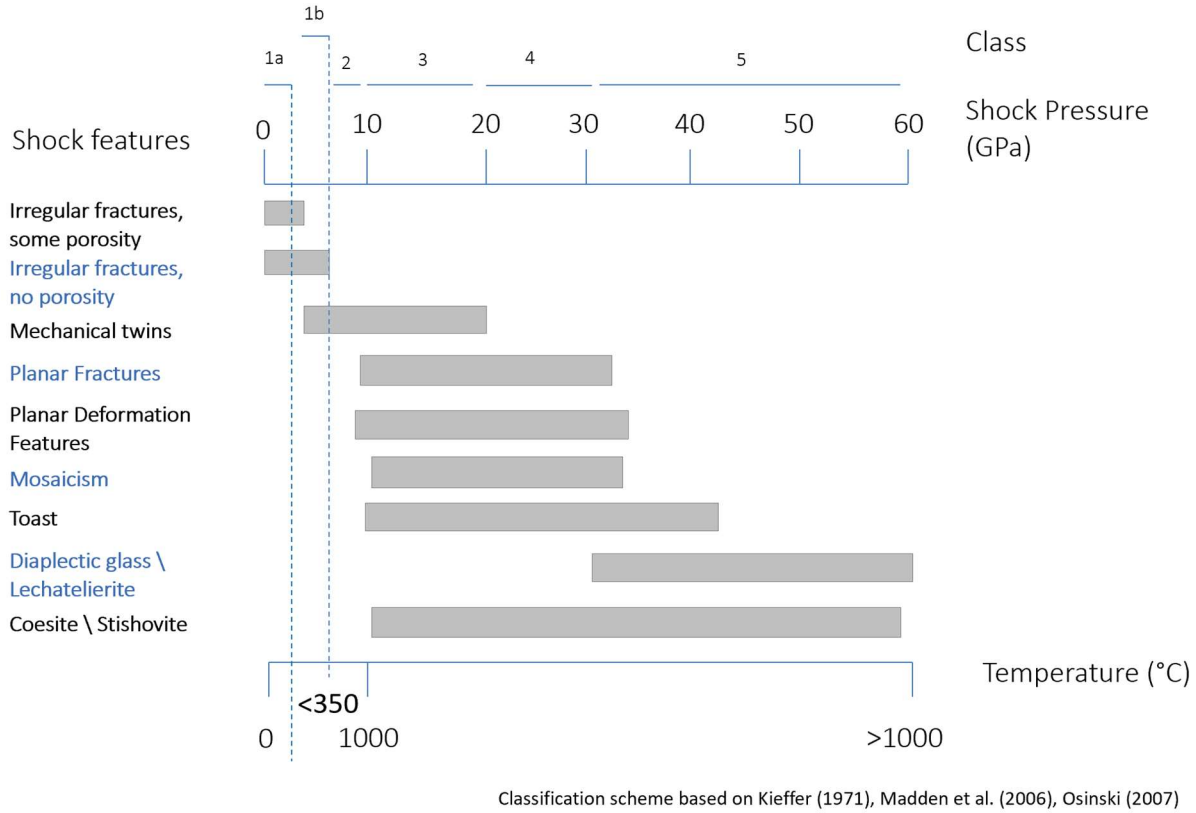


Fig 2.1. Shock metamorphism in Sandstone.

2.3. Effect of shock on porosity and permeability of sedimentary and crystalline rocks

During impact, porosity, permeability and density can dramatically change depending on the energy released during impact and target lithology as well as the location of the rock from the point of impact (Kieffer, 1971b; Cockell and Osinski, 2007; Singleton et al., 2011). For crystalline rocks, a nonlinear but clear correlation can be found between decreasing density and increase shock pressure caused due to fracturing, vesiculation and differential mineral melting (Singleton et al., 2011). In case of porous sedimentary rocks density increases due to pore collapse at low shock pressure levels (<10 GPa) and decreases as shock pressure increases (>10 GPa, <25 GPa) due to vesiculation and formation of glasses (Kieffer, 1971a; Kieffer, 1971b). At lower shock pressure (<10 GPa) sandstones are weakly lithified due to comminution and fracturing of grains but becomes strongly lithified or cohesive due to formation glasses and melts that weld mineral grains at higher shock pressure (>10 GPa) (Fig 2.1) (Kieffer, 1975).

Low shock pressures (<10 GPa) causes pore collapse in sandstone whereas high shock pressures (>10, <25 GPa) can cause vesiculation (Fig 2.1) (Kieffer, 1971a; Kieffer, 1971b; Cockell and Osinski, 2007). At even higher shock pressures (>30 GPa) the porosity is reduced as minerals recrystallise from the melt (Cockell and Osinski, 2007). If impact rocks are subject to longer-term heating and annealing during crater cooling, the porosity and permeability will be affected further. For highly porous substrates (such as sandstones), more of the impact energy is taken up in pore collapse resulting in lesser solid-state transformations and higher post-shock temperatures than a similar impact into non-porous crystalline target lithology (Madden et al., 2006; Kieffer, 1971b). In crystalline rocks, porosity increases with an increase in shock pressure levels (Singleton et al., 2011). This is caused due to fracturing and differential mineral melting during the passage of the shock and subsequent rarefaction wave (Singleton et al., 2011).

2.4. Materials and Methods

2.4.1. Samples

Various types of impactites were selected for this study because of their different impact history. Thirty-four samples of impactites and non-impacted rocks were selected for the analysis (Table 2.1). These rock samples are sourced from Meteor Crater (USA), West Clear Water impact structure (Canada), and Ries crater (Germany) (Fig 2.2). These rock samples include low-shocked sedimentary and crystalline rocks, impact melt rocks, and impact breccias.

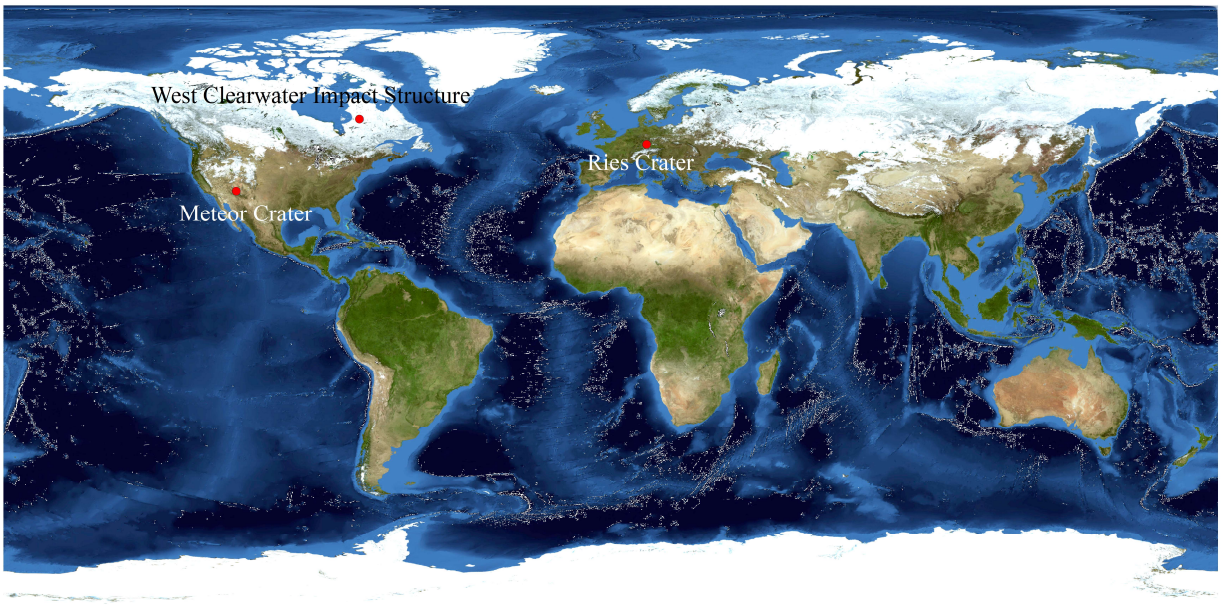


Fig 2.2. The map showing the location of three impact craters from where rock samples are collected. Image source: Blue Marble: Next Generation collected by NASA Terra Moderate Resolution Imaging Spectroradiometer (MODIS).

Table 2.1. Summary of the samples analysed in this study.

Impact site/control site	Location	Type of impactite/rock	No. of samples	Unshocked control sample	Note
Meteor Crater	Arizona, USA	Coconino Sandstone (CS)	8	2	Unshocked CS samples were collected from Clear Creek Reservoir
		Moenkopi Sandstone (MS)	9	2	Unshocked MS samples were collected along Meteor Crater road.
West Clearwater Impact Structure	Quebec, Canada	Crystalline impacted rock	3	none	These samples were collected during NASA FINESSE mission
		Impact melt rock	6	none	
		Impact breccia	3	none	
Ries Crater	Bavaria, Germany	Impact melt-bearing breccia or suevite	1	none	

2.4.1.1.Meteor Crater Samples: Sedimentary impacted rocks

Meteor Crater aka Barringer Meteorite Crater is in a relatively low-relief portion of the southern part of the Colorado Plateau approximately 55 km east of Flagstaff near the town of Winslow in north-central Arizona. Two types of sedimentary rock samples were included in this study. These are Permian Coconino sandstone and Triassic Moenkopi sandstone from the 50,000 years old 1.2 km diameter Meteor Crater in Arizona (Shoemaker and Kieffer, 1979; Kieffer, 1971a). Eight impacted Coconino sandstone and nine impacted Moenkopi sandstone samples were collected from NW, NE, SE and S crater walls and ejecta blanket on the south side of the crater during a field campaign in 2015 and 2017 (Fig 2.3). Non-impacted varieties of Coconino and Moenkopi sandstone samples were included as control samples. Two non-impacted Moenkopi sandstone samples were collected from two sites along Meteor Crater road, 5 and 9 km from the Meteor Crater visitor centre in 2016 (Fig 5.5). Two non-impacted Coconino sandstone samples were collected from Clear Creek Reservoir 50 km from Meteor Crater visitor centre in 2016. Freshly broken samples from outcrops and float samples were collected wherever possible. Care was taken while removing the samples from outcrops; use of hammer was avoided as it can produce fractures in the rocks. Impacted samples were named according to Barringer Crater reference collection naming convention, so these sample names are used throughout this study.

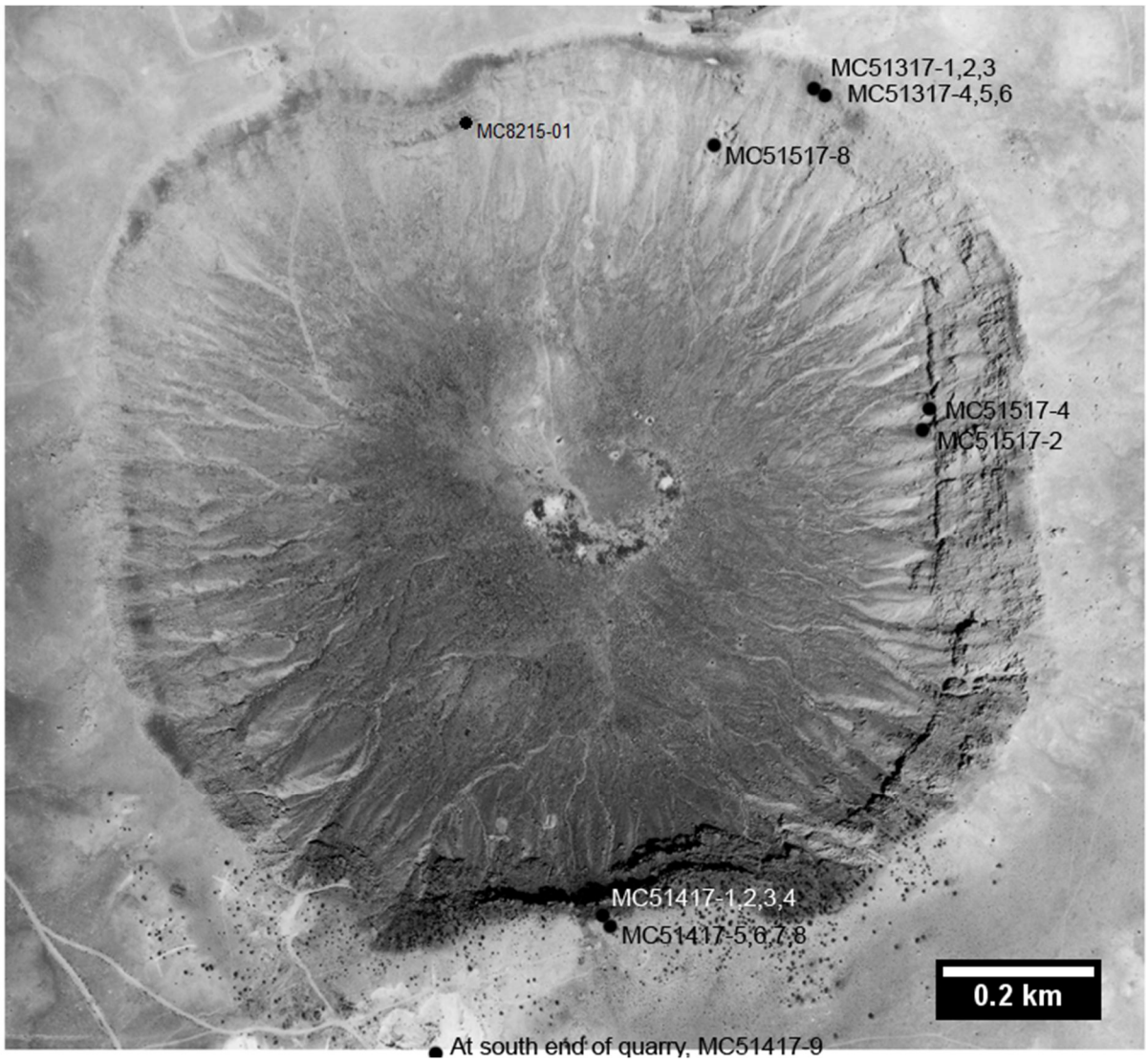


Fig 2.3. Sampling location at Meteor Crater. Image source: USGS.

2.4.1.2. West Clearwater Impact Structure samples: Crystalline impacted rocks, impact melt rocks, and impact breccias

The ~36 km diameter West Clearwater Impact Structure (WCIS) is about 125 km east of Hudson Bay in Quebec, Canada (Simonds et al., 1978). WCIS is ~286 Ma old and is relatively well preserved with a large ring of islands in the ~30 km diameter lake (Schmieder et al., 2015; Osinski and Grieve, 2017). The samples from this crater were collected during NASA FINESSE (Field Investigation to Enable Solar System Science and Exploration) expedition in 2014 by one of the co-authors. Target lithologies comprise of granitic gneiss, granite, tonalite, granodiorite, quartz monzodiorite with later diabase dykes (Simonds et al., 1978; Phinney et al., 1978; Rosa, 2012; Osinski and Grieve, 2017; Rae et al., 2017). Osinski and Grieve (2017) proposed a general stratigraphy of impactites from the bottom to top in

the sequence: Fractured basement > Lithic impact breccia > impact melt-bearing breccia or suevite > clast rich impact melt rock > clast poor impact melt rock > clast free impact melt rock.

Impacted granite and tonalite samples were collected from around the rim and impact melt rocks and impact breccias were collected from ring islands. Samples were named according to NASA FINESSE WCIS campaign naming convention, and these sample names are used throughout this study.

2.4.1.3.Ries Crater samples: Impact melt-bearing breccia or suevite

The ~26 km diameter Ries Crater in western Bavaria, Germany is one of the best-preserved terrestrial mid-sized complex impact structures (Pohl et al., 1977). Ries crater was formed ~15 million years ago in the flat-lying sequence of Mesozoic sedimentary rocks that unconformably overlie Hercynian crystalline basement (Pohl et al., 1977; Osinski, 2003; Rocholl et al., 2018; Schmieder et al., 2018). Suevite samples from this crater are used in this study. The sample came from the repository collection of one of the co-authors, so its location in the field is not known.

2.4.2. Sample preparation

Polished thin section of 30 μm thickness was prepared for petrographic examination in sample preparation laboratory at Department of Geology in Trinity College Dublin. Powdered samples were prepared in a mortar and pestle for powder X-ray Diffraction analysis.

2.4.3. Characterisation of samples

Several Laboratory analysis techniques were used to characterise petrographical properties in rock samples. Characterisation of samples was necessary to describe the deformation and changes in rock samples due to impact. Samples were assessed to determine compositional and textural properties using a combination of qualitative and quantitative techniques such as SEM, XRD, petrographical microscopy, X-ray CT. In order to classify each sample into a shock pressure class, the shock deformation state of quartz was determined in polished thin section under a petrographic microscope. These features are then matched to the published classification, and the shock pressure class was assigned to the samples (Kieffer, 1971b; Stöffler et al., 2018). These shock levels were assigned based on the presence and absence of specific shock features (e.g. PF, PDFs) in quartz and decreasing quartz content in the samples due to conversion into high-pressure polymorphs and glass. Quantitative X-ray

diffraction was used to determine the high-pressure polymorphs in the samples. The shock progression seen in the quartz is similar to other studies (Kieffer, 1971b; Rosa, 2012; Rae et al., 2017; Engelhardt, 1997).

These laboratory analysis methods are described in the following sections.

2.4.3.1. Quantitative X-ray diffraction (XRD) for identification of mineral phases in rock samples

Quantitative powder X-ray diffraction (XRD) analysis was performed on rock samples to identify and measure minerals and their high-pressure polymorphs formed during impact. This was necessary to classify rock samples into various shock pressure classes. In addition, XRD was used to identify salt species present in the field.

The Bruker D5000 in Trinity College Dublin has a 2.2 kW Cu long fine focus (0.4 x 12mm filament), with the following optical configuration: 2.5° primary soller, 1 mm aperture diaphragm, 1 mm scattered radiation diaphragm, no secondary soller, 0.2 mm detector diaphragm and a secondary curved graphite monochromator ahead of the scintillation counter. A scan of the sample was made from 5 to 70° 2θ at a speed of 2 seconds / 0.02° step at 40 kV and 40 mA. Sample rotation was used. This technique was used to determine the mineral composition and identify high-pressure polymorphs of quartz in the Moenkopi Sandstone. These data allowed us to assign shock pressure class to these samples based on abundances of higher-pressure mineral polymorphs. Rietveld refinement was used to determine the weight percentage of various mineral phases in the samples.

The Panalytical X'Pert Pro XRD at Natural History Museum, London was used to analyse Coconino sandstone, crystalline impactites, melt rocks and breccia samples. It has a primary monochromator and para-focussing optics for high-resolution measurements of Cu radiation, with divergence slit 0.25, soller slits 0.02 rad, and an X'celerator solid-state detector. It used Bragg Brentano geometry. Data was collected from 3-120° 2θ with a step size of 0.017°, per step 100 s at 45 kV and 40 mA.

Identification of crystalline phases was carried out with the Philips X'pert HighScore software in combination with the Powder Data File (PDF-2, The International Centre for Diffraction Data (ICDD)). The criteria used for identified minerals are – quartz (Levien et al., 1980; Glinnemann et al., 1992), kaolinite (Gruner, 1932; Bish and Von Dreele, 1989), muscovite (Brigatti et al., 1998), rutile (Swope et al., 1995), albite (Downs et al., 1994), microcline (Bailey, 1969), hornblende (Phillips et al., 1989), prehnite (Žunić et al., 1990),

clinochlore (Nelson and Guggenheim, 1993), andesine (Fitz Gerald et al., 1986), montmorillonite (Viani et al., 2002), hematite (Maslen et al., 1994), orthoclase (Colville and Ribbe, 1968), anorthoclase (Harlow, 1982), sanidine (Phillips and Ribbe, 1973), biotite (Brigatti and Davoli, 1990), gypsum (Boeyens and Ichharam, 2002), illite (Drits et al., 2010), calcite (Sitepu et al., 2005), and dolomite (Althoff, 1977) . Pattern-matching refinement and quantification of percentage of crystalline phases in rock samples were carried out with the Rietveld refinement software TOPAS (Bruker and Topas, 2003).

2.4.3.2. Petrographic examination using Scanning Electron Microscope (SEM) and Petrographic Microscope

A petrographic microscope and SEM were used to analyse and identify the composition and impact associated deformation features (e.g., PF, PDFs, microfractures) of the rock. Polished thin sections were examined under Nikon Eclipse LV100 petrographic microscope. Grain size and sorting analysis for sedimentary rocks were carried out by using the DSG-master Matlab tool developed by Buscombe (2013). A Zeiss Axio Imager 2 microscope was used to obtain mosaics of thin sections in order to understand the composition and clast-matrix relationship of the rocks.

A Tescan Mira XMU field emission scanning electron microscope (SEM) at the Centre for Microscopy and Analysis (CMA) in Trinity College Dublin was used to obtain backscattered electron (BSE) images of thin sections of rocks. The SEM was equipped with a KE Developments Centaurus system. Thin sections were carbon coated to a thickness of 10 nm to allow conductivity. BSE images were obtained at a working distance of 18 mm. Beam operating conditions were 20 kV of accelerating voltage and probe current of 10 pA.

SEM BSE mosaics of size ~50 mm^2 were obtained for porosity determination of impacted and non-impacted samples (Buhl et al., 2013b). SEM BSE mosaics (~50 mm^2) represents a significant subsection of the entire thinsection. The area for BSE mosaic was selected manually by locating subsection of thinsection that roughly represented the whole thinsection. Macrofractures were avoided in the field of view BSE mosaic for estimating primary porosity of rock sample in order to avoid any bias in the result. Porosity in rock samples was estimated by quantitative BSE image analysis in freely available software Image J following the method used by (Buckman et al., 2017). BSE images have high contrast, which enables discrimination between grains and the lowest intensity (or darkest) epoxy-filled pore spaces. Images were scaled manually using the pixel scale information in

image J. Grey-Scale intensity thresholding was visually applied at the default setting by manually adjusting the intensity in order to capture the maximum degree of observed porosity in image J. The percentage area of thresholded pore space was measured for porosity percentage determination in image J. The grey to black regions in image represents pores and white regions in image represents rock substrate (Fig 2.4). Image J calculates the percentage of the thresholded area (pore space – grey to back region) by dividing the area of grey to black regions by total area of the image. BSE images were also used to quantify the microfractures in rock samples. The width and length of the fractures were measured from scaled BSE images in image J. Automatic fracture density, and intensity quantification from SEM-BSE images is challenging due to the complexity of grey-scale textures of pores, grains and cement in comparison to fractures (Gomez and Laubach, 2006; Healy et al., 2017). In addition, obtaining cm^2 areas of the SEM-BSE mosaic is a time-consuming and expensive process. The aperture and length of the fractures were manually measured from BSE images. However, quantification of the microfractures intensity and density in impacted samples are beyond the scope of this paper.

2.4.3.3.X-ray Computed Tomography (CT)

X-ray CT was used to visualise and quantify macro-fractures present in the sample blocks. Nikon Metrology HMX ST 225 X-ray CT at Natural History Museum was used to characterise the samples. X-ray CT images were acquired at 200 kV and 200 µA using 0.5 mm copper filter and ultra-focus x-ray head. Approximately 3142 projections were acquired at 2 frames per projection by 0.2 mm detector pixel size. X-ray CT scan 2 hours for each sample at 0.046 mm voxel size. The scan was reconstructed into 16-bit unsigned raw file format, and it took 1.5 hours for each sample. The resolution of 0.046 mm per voxel is the best that could be achieved for 5 cm cube rock block with our setup.

2.5. Results and discussion

In this study, sedimentary and crystalline impactites samples were classified into shock pressure classes using XRD, SEM-BSE, and petrographic microscopy observation following classification by (Kieffer, 1971b; Kieffer, 1971a; Madden et al., 2006; Stöffler et al., 2018).

2.5.1. Sedimentary impactites

2.5.1.1.Coconino Sandstone (CS)

Unshocked Coconino sandstone: The unshocked CS is pale buff, white, fine-grained, saccharoidal, cross-bedded aeolian Sandstone of average porosity ~20% (Kieffer, 1971a). Detrital quartz grains in the sandstone are generally well rounded, well-sorted, and, have an average grain size ranging 0.09-0.16 mm (Table 2.2 and Fig A.2.1 in Appendix 2). The grain diameters in CS range from 0.01 – 0.37 mm (Fig A.2.1 in Appendix 2). CS contains 94-99 % quartz 0.4-5% kaolinite, minor feldspar, heavy minerals (rutile, zircon), and calcite and hematite as secondary minerals can occur in trace quantity. The percentage composition of minerals present in Coconino Sandstone was determined by Rietveld refinement method (section 2.2.3.1). A number of quartz grains have been observed to contain fluid inclusions (Madden et al., 2006). The quartz grains do not show wavy extinction when seen under crossed polars with a petrographic microscope. CS is weakly to moderately well cemented with silica, in the form of recrystallised quartz overgrowth on the grains (Kieffer, 1971a). In hand specimen, the CS may be either: (1) massive sandstone, in which laminations if they exist, are several centimetres thick, and (2) laminated sandstone, containing parallel laminations which are 0.5 to 2.0 mm thick (Appendix 3). The most extensive variations of mineralogy, porosity and grain size are associated with the laminations. Many hand specimens part easily along the laminations (Kieffer, 1971a). Subparallel laminae 5.0 to 17.5 mm thick are separated by thin laminae 0.5 mm thick containing more than average amount of silt and clay-sized grains (Kieffer, 1971a). The pores are heterogeneously distributed in Coconino sandstone (Kieffer, 1971a). The bulk density of CS found to be between 1.98 (Shipman et al., 1971) and 2.08 (Ai and Ahrens, 2004) g/cm^3. The grain density of Coconino sandstone is 2.67 g/cm^3 (Shipman et al., 1971). The dry and wet (water-saturated) crushing strength of Coconino sandstone is 31.4 and 36.4 MPa (Shipman et al., 1971). Ai and Ahrens (2004) measured tensile strength of CS 17 MPa for 2.4×10^{-6} s strain rate and 20 MPa for 1.4×10^{-6} s strain rate. They also reported the tensile strength of 30 MPa for the onset of radial cracks and 40 MPa for complete fragmentation. For a more detailed petrographic study on Coconino sandstone, readers are referred to (Whitmore et al., 2014; Kieffer, 1971a).

Table 2.2. Description of properties of Coconino Sandstone samples. Same sample names with Roman numerals in brackets indicate blocks cut from the same sample.

Coconino Sandstone	Sample Size (cm)	Type of rock	Porosity (%)	Grain size (mm)	Sorting	Lamination	Visible macro-fracture in hand sample	CT Scan
MC51517-8 (II)	~5×5×5	Crater wall rock	13.69	0.16	0.09	One band of ~1 mm thick lamination, massive	No	Yes
MC51417-5 (II)	~5×5×5	Ejecta	5.81	0.12	0.08	5 sets parallel lamination bands, width of band is 1 mm	No	No
MC51417-9	~7×7×3	Ejecta from quarry	10.98	0.1	0.07	no but friable sample	No	No
MC51417-8	~5×4×4	Ejecta	12.27	0.09	0.06	No, massive	No, crumbled corner	No
MC51517-4	~5×5×5	Crater wall rock	13.69	0.12	0.08	No, massive	One set of fracture 4 cm in length and 0.2 mm width only visible on two adjacent surfaces	Yes
MC51417-7	~5×5×5	Ejecta	18.5	0.14	0.09	8 bands of width 1 mm parallel, closely spaced 0.5 cm	No	No
MC51417-6	~5×5×5	Ejecta	14.42	0.09	0.07	No, massive	No	No
MC51517-8 (I)	~5×5×5	Crater wall rock	13.69	0.16	0.09	No, massive	One set of fracture,5.5 cm in length, 0.2 mm wide, visible only on two adjacent surfaces of the block	Yes
MC51417-5 (I)	~5×5×5	Ejecta	5.81	0.12	0.08	5 sets parallel lamination bands, width of band is 1 mm	No	Yes
MC51517-2	~5×5×3	Crater wall rock	12.72	0.11	0.07	Four bands of lamination with 1 mm width, closely spaced 0.5 cm	One set of fracture 3 cm in length and 0.2 cm in width only visible on two adjacent surfaces, broke along a fracture or lamination during sample preparation	No
CLR-1	~5×5×5	Control	20.44	0.09	0.07	No, massive	1.5 cm long fracture, visible on two adjacent surfaces only.	Yes
CLR-2	~5×5×5	Control	20.93	0.09	0.04	No, massive	No	Yes

Shocked Coconino Sandstone: We only describe samples belonging to shock pressure class 1a and 1b in detail here, as only these samples are used in this study. The shock metamorphism features observed with increasing shock pressure in CS have been described in detail previously. Kieffer (1971b) has classified CS into six shock pressure classes based on petrographic observation, along with quantitative XRD measurements of quartz and its polymorphs. A detailed study of shock features in CS under transmission electron microscopy is reported in Kieffer et al. (1976b). For a detailed description of shock pressure class 2-5 (5-60 GPa) of CS readers are referred to elsewhere (Kieffer, 1971b; Kieffer, 1971a;

Kieffer, 1975; Kieffer et al., 1976b; Madden et al., 2006). Even though shock metamorphism in Coconino Sandstone has been studied in detail previously, it was necessary to understand the shock deformation in samples that we have collected to understand their behaviour in the weathering experiment conducted in chapter 3.

Class 1a (<5GPa): Class 1a CS may have experienced <5 GPa of shock pressure during impact. In general, specimens of class 1a shocked CS do not differ in macroscopic appearance from unshocked Coconino sandstone (Appendix 3). The mean grain size ranges 0.09 – 0.16 mm (Table 2.2) and grains are weakly to moderately cemented. In thin section, these rocks have less porosity than massive unshocked Coconino sandstone. Porosity has been reduced in these samples due to compaction caused by slight translation and rotation of individual grains or small group of grains during the passage of shock waves (Fig 2.4 and Table 2.2). However, remnant porosity is still visible under a petrographic microscope (Fig 2.4). The apparent porosity in thin section measured from SEM-BSE images of Coconino Sandstone ranges between 5-18% (Table 2.2). Less than 5% of quartz grains show wavy extinction under crossed polars. Class 1a samples retain their original grain size as in found in unshocked samples and 37-65% quartz grains displayed irregular microfractures (Fig 2.4) (Madden et al., 2006).

Class 1b (~5 GPa): Class 1b CS have experienced approximately 5 GPa shock pressure during impact. Class 1b rock is fragile and friable, fine-grained, powdery in texture. The rock is snow-white in hand sample and can be broken by gentle hand pressure (Appendix 3). The size of the grains is reduced by fracturing (Fig 2.4h). The fracturing of grains occurs irregularly throughout the rock, only a fraction of the grains preserves the original grain size (Fig 2.4h). These isolated grains are surrounded by much smaller, highly fractured quartz particles. In class 1b CS ~98% of grains contain irregular fractures (Madden et al., 2006). No high-pressure phases are detectable by powder X-ray method.

The aperture/width of intragranular microfracture in the quartz grains in low shocked Coconino sandstone ranged from 0.1-5 μm.

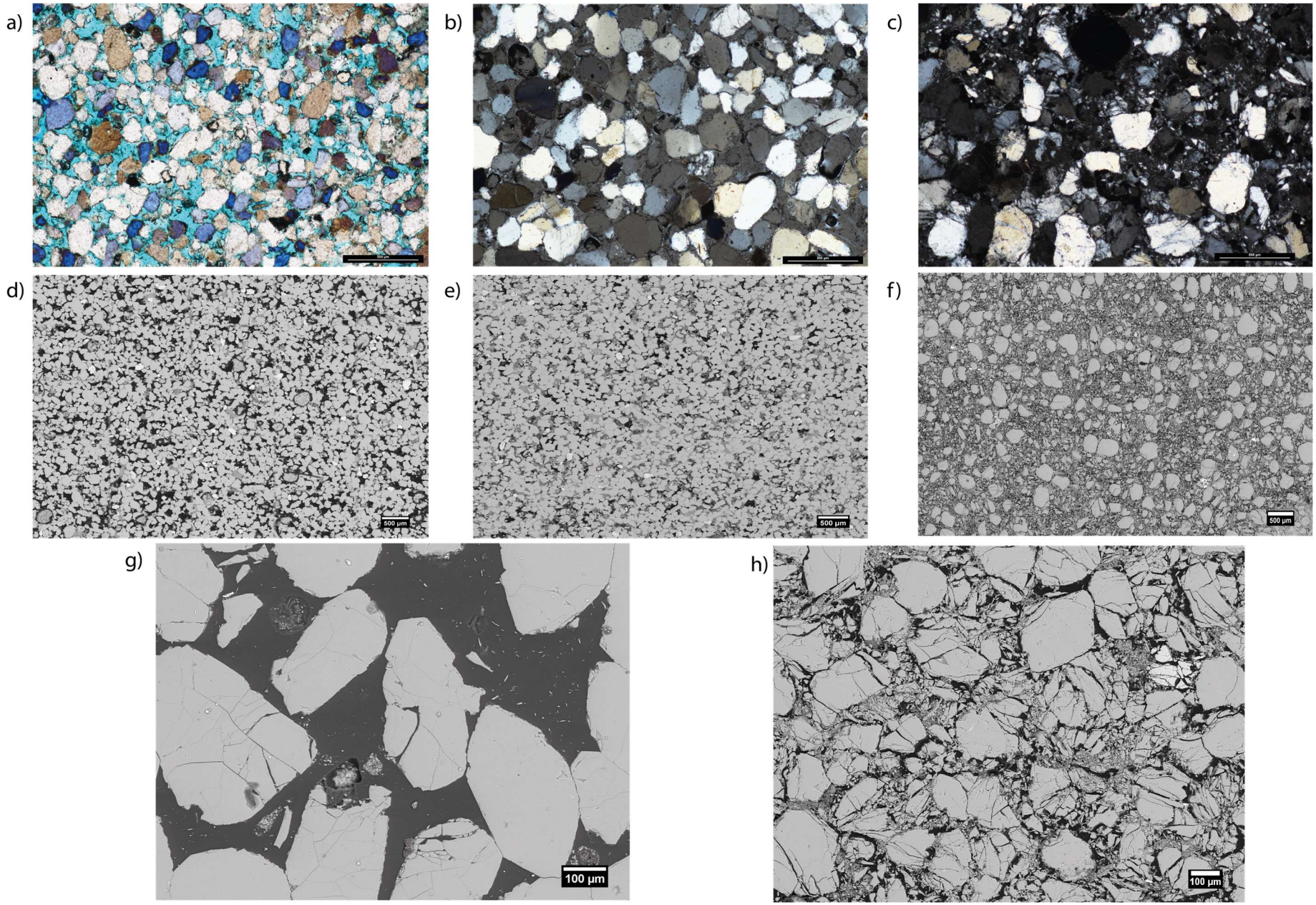

a)
b)
c)
d)
e)
f)
g)
h)
500 µm
100 µm

Fig 2.4. Coconino sandstone (CS). (a) Photomicrograph of unshocked CS with visible porosity in crossed polars. Blue epoxy represents pore space. Scale bar is 500 µm. (b) Photomicrograph of Class 1a CS showing a collapse in pore space Scale bar is 500 µm. (c) Photomicrograph of Class 1b CS with apparent primary porosity in crossed polars. Scale bar is 500 µm. (d) BSE image of unshocked CS showing pore spaces. Black substrate represents pores. Scale bar is 500 µm. (e) BSE image of class 1a CS showing a reduction in porosity. Scale bar is 500 µm. (f) BSE image of class 1b CS showing collapsed primary pores and extensive fracturing in quartz grains. Scale bar is 500 µm. (g) BSE image showing intragranular fractures in quartz grain in class 1 a CS. Scale bar is 100 µm. (h) BSE image displaying pervasive grain fracturing in quartz grains in class 1b CS. Scale bar is 100 µm.

2.5.1.2. Moenkopi Sandstone (MS)

Table 2.3. Description of properties of Moenkopi sandstone samples. Same sample names with Roman numerals in brackets indicate blocks cut from the same sample.

Moenkopi Sandstone	Sample Size (cm)	Type of rock	Porosity (%)	Grain size (mm)	Sorting	Lamination	Visible microfracture in Hand sample	CT scan
MC51317-5	~5×5×5	Ejecta	0.74	0.09	0.07	Four set of sub-parallel cross lamination	No	No
MC51317-1	~5×5×5	Crater wall rock	0.58	0.09	0.06	Three sets of sub-parallel cross-laminations	No	No
MC51317-4 (I)	~5×5×5	Crater wall rock	1.09	0.1	0.07	Three sets of sub-parallel cross laminations	One big 5 cm long and 0.2 mm wide orthogonal fracture visible on all facets. Smaller fractures are ranging from 1-2 cm long 0.1 mm wide visible on multiple facets.	Yes
MC51317-03	~5×5×5	Crater wall rock	0.50	0.1	0.06	No, massive	No	No
MC51417-1 (I)	~5×5×5	Crater wall rock	0.96	0.09	0.05	Three set of sub-parallel cross lamination	No	No
MC8215-01	~5×5×3	Crater wall rock	0.7	0.09	0.06	No, massive	Two sets of fractures passing through two facets, the first one is 2 cm in length and second is 6 cm long. The aperture of the fractures is 0.1 mm	Yes
MC51317-2	~5×5×5	Crater wall rock	0.78	0.09	0.06	Three sets of sub-parallel cross-lamination	Six set of fracture along cross-lamination on different facets. the length of fracture ranges	No

							from 1-2 cm and aperture 0.1 mm	
MC51417-1 (II)	~5×5×4.5	Crater wall rock	0.96	0.09	0.05	One set of visible cross lamination	Two sets of small fractures on two adjacent faces, ranging in length from 1-2.5 cm and aperture 0.1 mm	No
MC51417-2 (II)	~5×5×5	Ejecta	0.71	0.07	0.05	One set of cross-lamination	No	No
MC51317-6	~5×4×5	Ejecta	0.83	0.09	0.07	No, massive	One set of 4 cm long fracture visible on two adjacent facets. the aperture of the fracture is 0.1 mm	No
MC51417-2 (I)	~5×5×5	Ejecta	0.71	0.07	0.05	Three sets of sub-parallel cross-laminations	No	No
MC51317-4 (II)	~5×5×3	Crater wall rock	1.09	0.1	0.07	Two sets of sub-parallel cross-laminations	Three sets of fracture ranging from 1.5-5 cm and aperture 0.1-0.2 mm visible on three facets	No
MC51417-2 (III)	~5×5×2.5	Crater wall rock	0.71	0.07	0.05	Three sets of sub-parallel cross-laminations	No	No
CS16-01	~5×5×5	Control	8.39	0.1	0.06	No, massive	No	Yes
CS16-02	~5×5×5	Control	5.23	0.08	0.06	Four set of sub-parallel cross lamination	No	No

Unshocked Moenkopi sandstone is very fine-grained sandstone which is cemented by carbonates. Moenkopi contains 50-80 % quartz, microcline, muscovite, hematite and kaolinite in minor amounts and remainder being composed of carbonate minerals (calcite and dolomite). The percentage composition of minerals present in Moenkopi Sandstone was determined by Rietveld refinement method (see section 2.2.3.1). Quartz is subrounded, equant, and well-sorted and has subhedral grain boundary (See Appendix 2). The matrix is very-fine grained and iron-rich. The mean grain size ranges from 0.07-0.1 mm. The grain size ranges from 0.009-0.12 mm (Table 2.3). The texture of the rock is grain-supported. The porosity in unshocked Moenkopi Sandstone ranges 5-8.5% (Table 2.3). Some of the Moenkopi Samples contain cross laminations in hand samples.

Class 1a (<5GPa): Class 1a MS may have experiences <5 GPa of shock pressure during impact. In hand specimen, there is no visible difference between class 1a and unshocked MS (Appendix 3). No high-pressure polymorphs were identified in XRD analysis and no change in mineralogy was observed in class 1a MS compared to unshocked MS. Macroscopic fractures are present in some of the class 1a MS samples (Fig 2.5f). Due to low shock, this

porosity is reduced in class 1a MS (Fig 2.5). The porosity in low shocked Moenkopi is 0.5-1% (Fig 2.5 and Table 2.3). No irregular grain fracturing due to impact can be seen in class 1a MS (Fig 2.5). A small amount of the quartz grains show wavy extinction.

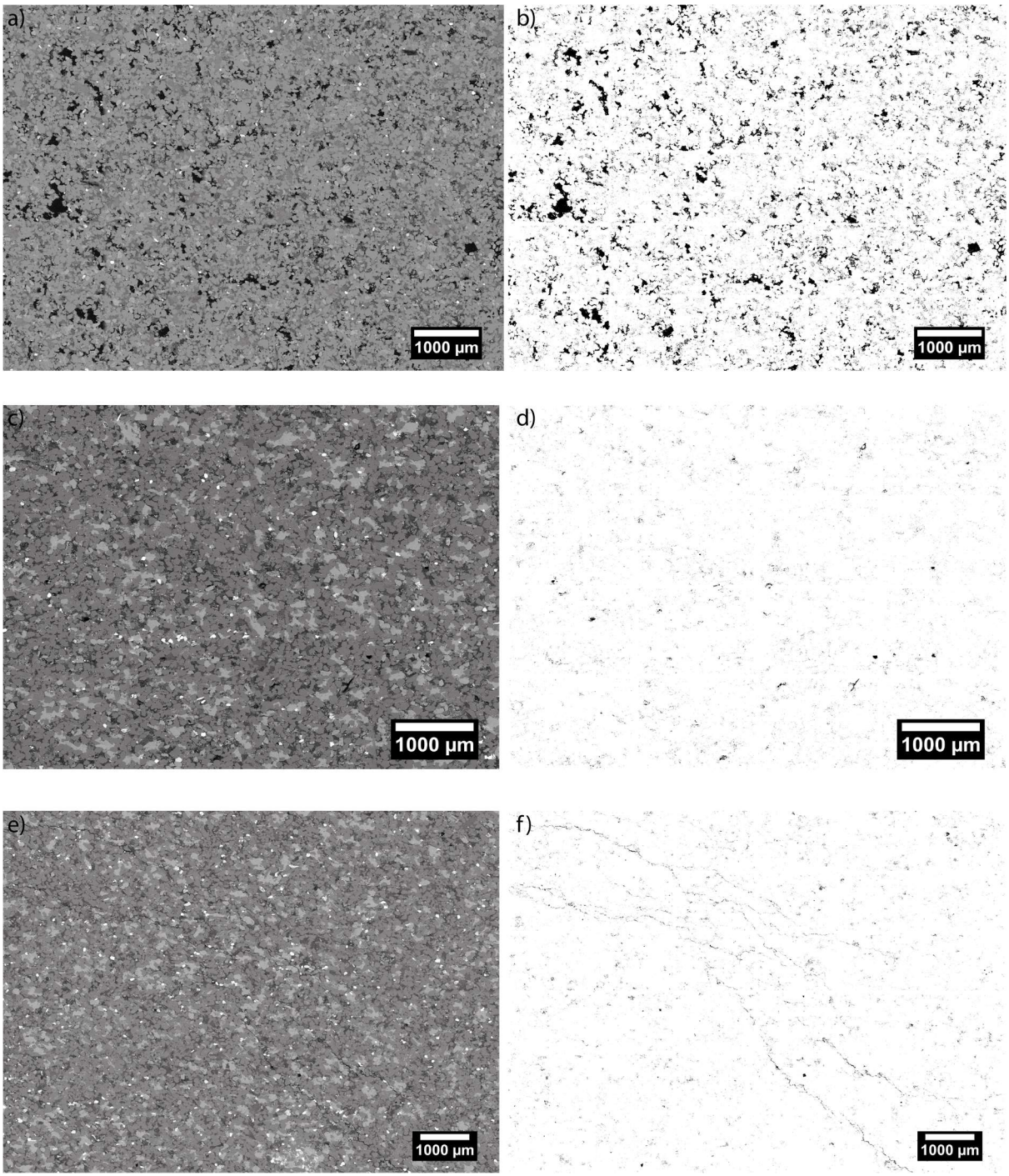


Fig 2.5. Moenkopi sandstone. (a) BSE image of unshocked MS showing pores. Black substrate represents pore spaces. (b) thresholded image-(a) showing pores in black colour. (c) BSE image of class 1a MS showing reduced porosity. (d) thresholded image-(c)

displaying reduced pore spaces in black. (e) BSE image of class 1a MS with macro-fractures. (f) thresholded image-(e) showing macro-fractures as faint black linear features.

2.5.2. Crystalline impactites

Two low shocked granite and one low shocked tonalite sample were used in the weathering experiment. We did not have any unshocked equivalent of crystalline impactites.

Table 2.4. Description of properties of crystalline impactite samples.

WCIS target rocks	Sample Size (cm)	Type of rock	Porosity (%)	Visible microfracture in Hand sample	CT scan
WCIS-14 MK-004	~5×5×5	Target rock from around rim (granite)	0.07	Multiple macro-fractures on all surfaces ranging in length from 2-5 cm and 0.1 mm in aperture	Yes
WCIS-14 MK-001a	~3.5×3.5×3	Target rock from around rim (granite)	negligible	One set of fracture 4 cm in length and 0.1 mm width only visible on two adjacent surfaces	No
WCIS-14 Oz-015	~4×3×3	Target rock from around rim (Tonalite)	0.26	No	No

Class 1a granite (<10 GPa): Class 1a granite samples may have experienced <10 GPa shock pressure during impact. The granite sample has pinkish-grey hue in hand sample (Appendix 3). Class 1a granite is medium-grained hypidiomorphic, equigranular, with average grain-sizes varying from ~1 up to ~3 mm (Appendix 2). The granite samples contain quartz, albite, microcline and in minor amounts muscovite and clinochlore (Appendix 2). Feldspar grains are subhedral to anhedral and make up the dominant mineralogy of the sample (Appendix 2). Chemical alteration can be observed in feldspar crystals. Albite is more strongly altered than microcline. Intragranular and intergranular fracturing is pervasive in the sample (Fig 2.6). Planar fracture is present in quartz grains (Fig 2.6). The primary porosity in granite is ≤0.07% (Table 2.4).

Class 1a tonalite (<10 GPa): Class 1a tonalite have undergone low shock (<10 GPa) deformation during impact. The sample looks greenish in hand sample (Appendix 3). Class 1a tonalite is medium grained hypidiomorphic, equigranular, with average grain-sizes varying from ~ 1mm to up to ~3 mm (Appendix 2). Class 1a tonalite contains quartz, albite, biotite, hornblende and in minor amounts calcite and clinochlore (Appendix 2). Albite grains are subhedral to anhedral and are the dominant mineral present in the sample. Intragranular fracturing is pervasive in the sample (Fig 2.6). Kink bands can be observed in biotite (Fig 2.6). Planar Fractures in quartz is present (Fig 2.6). The primary porosity in the tonalite sample is 0.26% (Table 2.4).

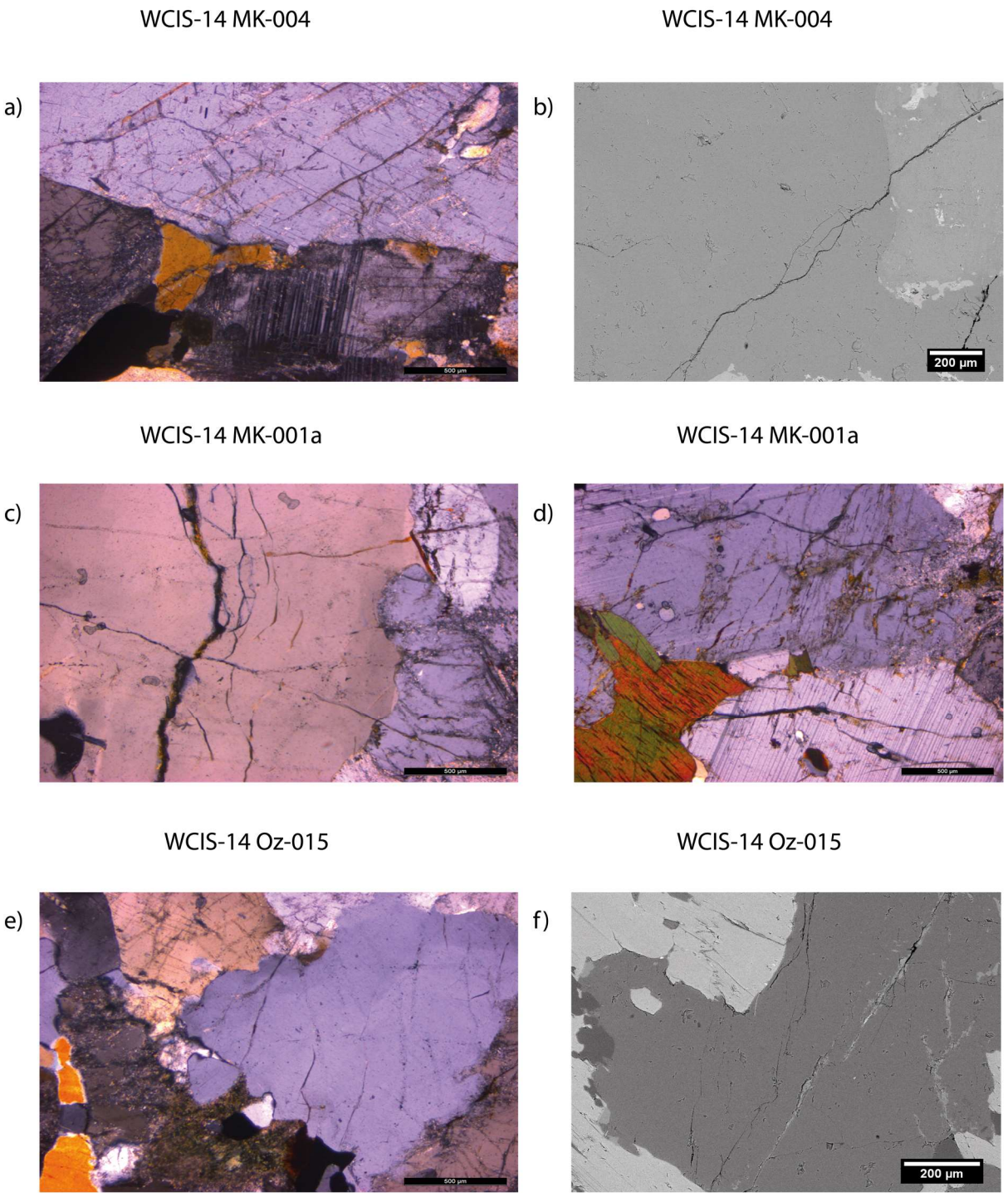


Fig 2.6. Crystalline impactites. (a), (c), and (d) Photomicrographs of class 1a granite samples showing extensive fracturing grains in crossed polars (XPL). In (a) Planar Fractures (PFs) in quartz can be seen. (b) BSE image showing intergranular fractures in class 1 a granite. (e) Photomicrograph of class 1a tonalite showing microfractures in quartz grains in crossed polars (XPL). In the bottom left of this image kink bands in biotite is visible. (f) BSE image of class 1a tonalite showing intragranular fractures in a grain. Scale bar in photomicrographs (a), (c), (d), and (e) is 500µm.

2.5.3. Impact melt rocks and impact breccias

Table 2.5. Description of properties of impact melt rock and impact breccia samples.

Impactites	Sample Size (cm)	Type of rock	Porosity (%)	Visible microfracture in Hand sample	CT scan
WCIS-14 RW-019	~3.5×3.5×3.5	Clast rich fine-grained impact melt rock	2.91	No	No
WCIS-14 MK-082	~5×5×3	Clast poor fine-grained impact-melt rock	0.15	Multiple macro-fractures on all surfaces ranging in length from 1-5 cm and 0.1 mm in aperture	No
WCIS-14 MK-015	~5×5×3	Clast poor fine-grained impact melt rock	0.28	Multiple macro-fractures are ranging from 3-5 cm and 0.1 mm in aperture visible on multiple facets/ surfaces. Two vugs of diameter 0.5 and 1 cm are visible on two facets.	Yes
WCIS-14 MK-087	~3×3×3	Clast poor fine-grained impact-melt rock	0.61	A few fractures ranging in length 1-2 cm with aperture less than 0.1 mm seen on three facets.	No
WCIS-14 MK-60	~4×4×4	Clast free impact melt rock	1.51	One fracture 3 cm in length and 0.1 mm visible on one surface only	No
WCIS-14 MK-077	~5×4×3	Clast free impact melt rock	0.21	No	No
WCIS-14 MK-058B	~5×5×3	Lithic breccia	2.07	No	No
WCIS-14 058C	~4×4×4	Lithic breccia	2.57	One set of fracture 4 cm in length and 0.1 mm in aperture visible on only one facet	Yes
WCIS-14 Oz-005	~5×5×3	Impact melt-bearing breccia or suevite	3.46	Multiple small fractures of length 1.5 cm and aperture 0.1mm visible three facets	No
Suevite (I)	~5×5×5	Impact melt-bearing breccia or suevite	10.39	Multiple macro-fractures on all surfaces ranging in length from 1-5 cm and 0.1-0.2 mm in aperture on all facets of the rocks.	Yes
Suevite (II)	~5×5×5	Impact melt-bearing breccia or suevite	10.39	Multiple macro-fractures on all surfaces ranging in length from 1-5 cm and 0.1-0.2 mm in the aperture. In hand sample observation, this sample contains more fractures and vitreous phases compared to Suevite (I)	Yes

2.5.3.1. Clast rich fine-grained impact-melt rock

WCIS-14 RW-019 is a clast rich melt rock. This sample is massive and appears reddish-purple colour in hand sample due to oxidation of matrix (Appendix 3). Clast rich melt rocks contain up to 25% fragments coarser than 1 mm (Rosa, 2012). The subhedral morphology of feldspar in the rock indicates that the matrix is crystallised from a melt (Phinney et al., 1978). Clast rich impact melt rock contain quartz, andesine, sanidine, and minor muscovite, hematite and montmorillonite. Clast rich impact melt rock is more coherent than lithic breccia and impact melt-bearing breccias, the melted material in the sample weld the clasts together. Porosity in this sample was 2.9% (Table 2.5). Clasts usually compose 40-60%, and matrix occupies 60-40% of most of the samples (Rosa, 2012). Under the petrographic microscope in clast rich impact melt rock, the matrix appears dark brown, nearly extinct under crossed polars, and very fine-grained (<10 μm) (Fig 2.7 b). The matrix is composed of microlites made of iron oxide and plagioclase (<10 μm) (Fig 2.7 b and c). The matrix has

reacted with embedded clasts in clast rich impact melt rock (Fig 2.7). Clasts in the sample have micro-fractures (Fig 2.7).

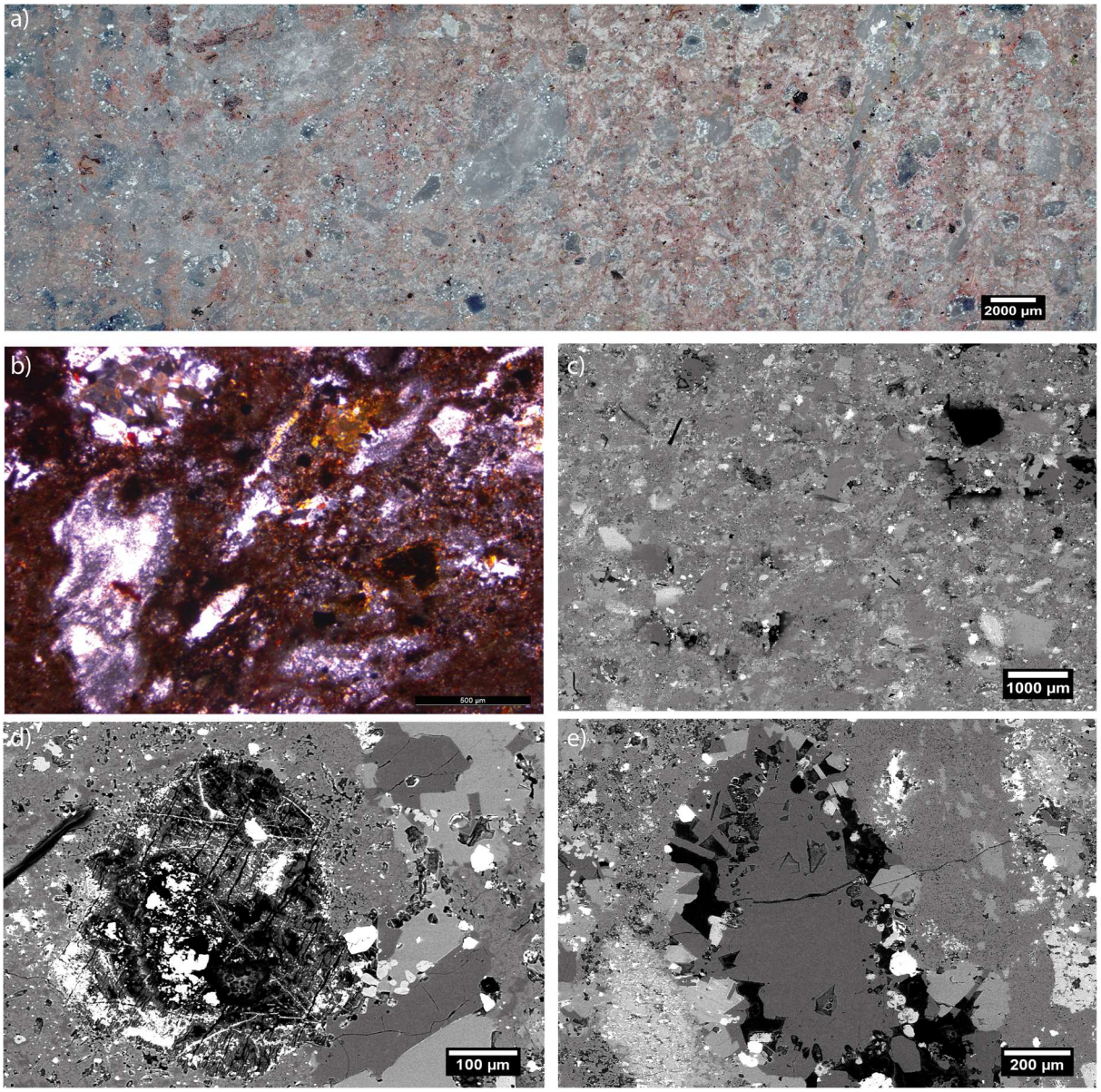


Fig 2.7. Clast-rich fine-grained impact melt rock, WCIS-14 RW-019. (a) Photomicrograph in PPL showing the distribution of clasts in the melt matrix. (b) Photomicrograph in XPL showing the dark brown matrix and clasts. Scale bar is 500 µm. (c) SEM BSE mosaic showing the distribution of clasts in the melt matrix. (d) and (e) show the clasts that have altered due to reaction with melt matrix.

2.5.3.2. Clast-poor fine-grained impact melt rock

WCIS-14 MK-015, WCIS-14 MK-087 and WCIS-14 MK-082 are clast-poor fine-grained melt rock. The clast-poor impact melt rocks WCIS-14 MK-015, and WCIS-14 MK-087 appears red to purple in hand sample (Appendix 3). Whereas, WCIS-14 MK-082 looks

yellowish-brown in hand sample (Appendix 3). Clast poor impact melt rock contains less than 15% clasts larger than 1 mm across (Simonds et al., 1978; Rosa, 2012). Clast poor impact melt rocks WCIS-14 MK-015, and WCIS-14 MK-087 contain microcline, muscovite, andesine, and montmorillonite in minor quantity (Appendix 2). Clast-poor impact melt rock WCIS-14 MK-082 consist of quartz, anorthite, albite, sanidine and minor amounts of montmorillonite (Appendix 2). In thin section, WCIS-14 MK-082 appears very different than WCIS-14 MK-015 and WCIS-14 MK-087 (Fig 2.8-2.9). The melt matrix (size <50 µm) in WCIS-14 MK-082 displays interlocking texture (Fig 2.8), whereas in WCIS-14 MK-015 and WCIS-14 MK-087 matrix displays fine-grained microlites (<10 µm) feldspar (Fig 2.9). Clasts in all clast-poor impact melt rocks are fractured and reacted with surrounding melt matrix (Fig 2.8-2.9). The matrix is oxidised in the samples. WCIS-14 MK-082 appears to be extensively chemically weathered/altered (Fig 2.8). WCIS-14 MK-015 may have been affected by hydrothermal alteration as it contains quartz vugs (Fig 2.9 a). Porosity in clast-poor impact melt rock is very low (0.15-0.6%) (Table 2.5).

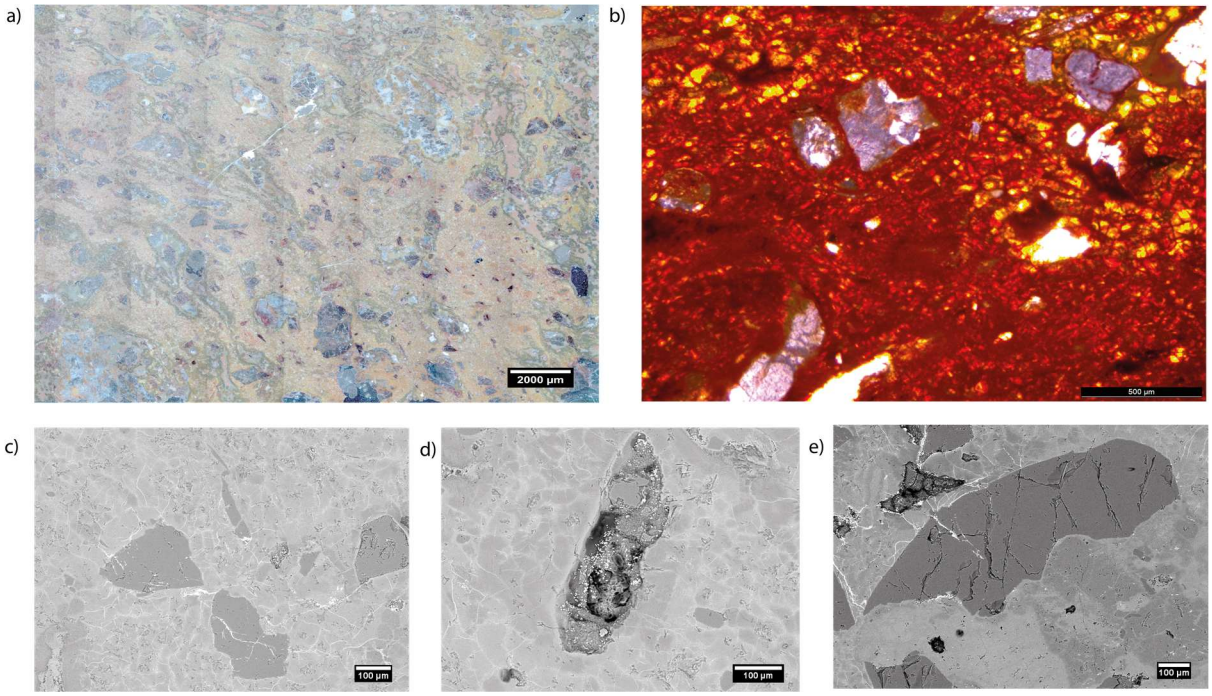
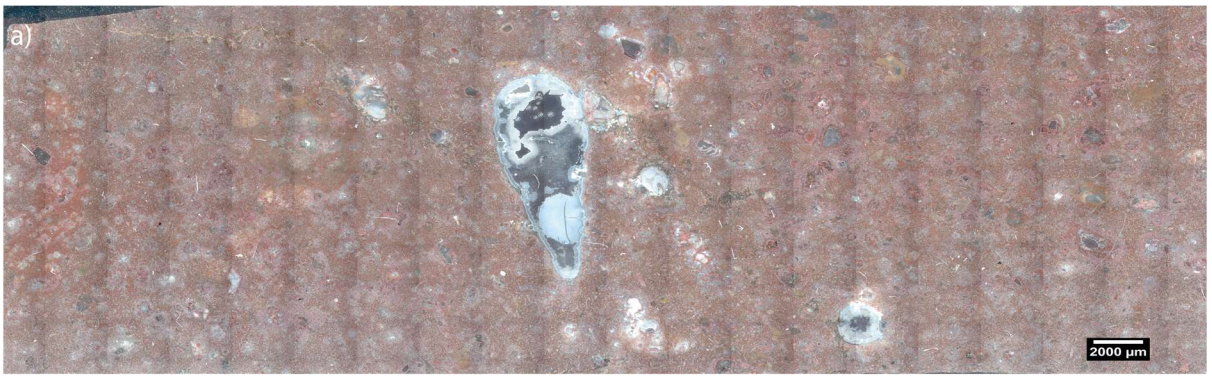
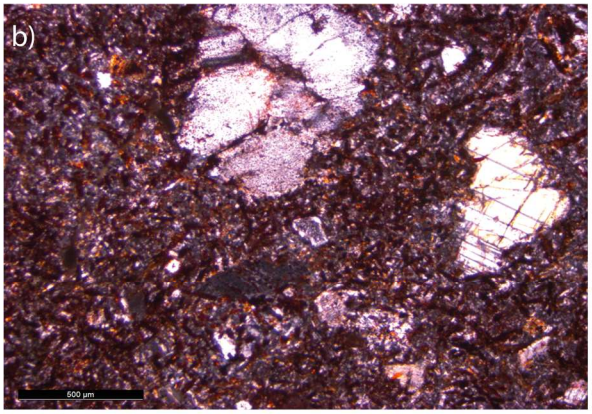
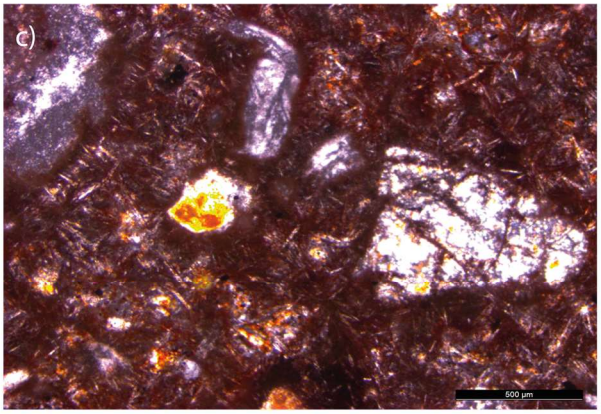
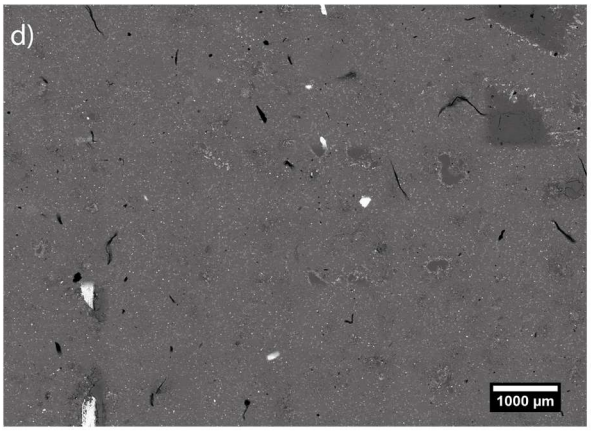


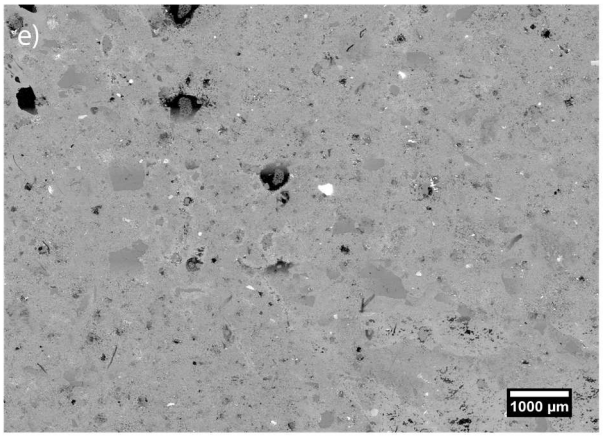
Fig 2.8. Clast poor fine-grained impact melt rock, WCIS-14 MK-082. (a) Optical microscopy mosaic in PPL showing the distribution of clasts in melt matrix. Melt flow patterns can be seen in the bottom left of the image. Scale bar is 2000 µm. (b) Photomicrograph in XPL clasts surrounded by melt matrix. The melt seems to be oxidised. Scale bar is 500 µm. (c), (d), and (e) show the clasts that seem to have reacted with melt. Scale bar is 100 µm.

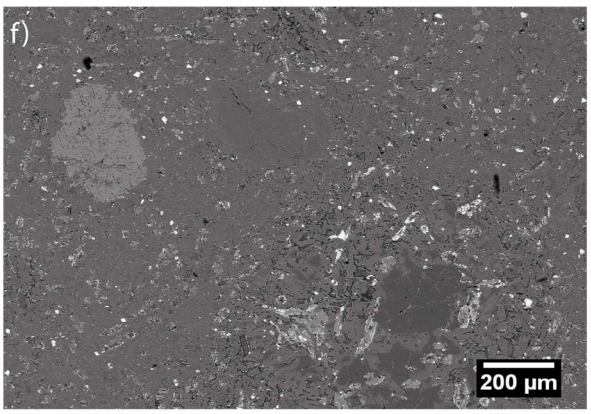

a)
2000 µm


b)
500 µm


c)
500 µm


d)
1000 µm


e)
1000 µm


f)
200 µm

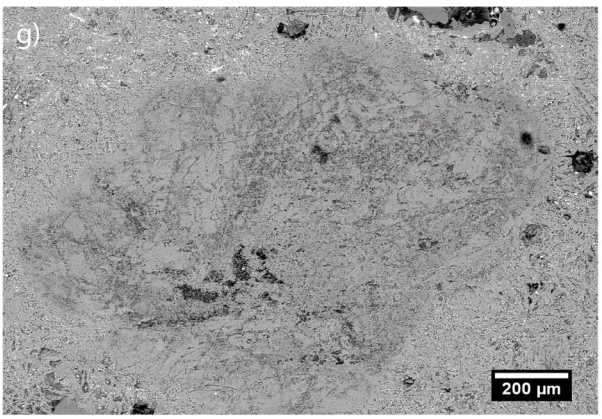

g)
200 µm

Fig 2.9. Clast-poor fine-grained impact melt rock. (a) Optical microscopy mosaic of the sample WCIS-14 MK-015 showing the distribution of the clasts in melt matrix. In the centre of the thinsection, a tear-shaped vein is present. Scale bar is 2000 µm. (b) Photomicrograph of the sample WCIS-14 MK-015 in XPL showing the clasts embedded in needle-shaped crystallite melt matrix. Scale bar is 500 µm. (c) Photomicrograph of the sample WCIS-14 MK-087 in XPL showing the clasts embedded in needle-shaped crystallite melt matrix. Scale bar is 500 µm. (d) SEM BSE mosaic of sample WCIS-14 MK-015 showing the distribution of the clast in melt matrix. (e) SEM BSE mosaic of sample WCIS-14 MK-087 showing the distribution of the clast in melt matrix. (f) SEM BSE image of sample WCIS-14 MK-015 showing clast embedded in melt matrix. (g) SEM BSE image of sample WCIS-14 MK-087 showing a clast that has reacted with melt matrix.

2.5.3.3.Clast-free impact melt rock

WCIS-14 MK-060 and WCIS-14 MK-077 are clast-free impact melt rock. These samples contain no clast up to the size of 1 mm. These samples appear reddish-brown in hand sample (Appendix 3). They appear to be more coherent than clast-rich, and clast-poor impact melt rocks. These samples contain quartz, anorthite, albite, muscovite, hornblende and minor montmorillonite (Appendix 2). The matrix is oxidised and consist of devitrified glass (Fig 2.10 b and c). At high magnification, plagioclase laths (<10 µm) in matrix show interstitial texture (Fig 2.10). Some of the small plagioclase clasts appears to be resorbed (Fig 2.10). Clasts are fractured and have reacted to melt matrix (Fig 2.10). Porosity in clast free impact melt rock ranges between 0.2-1.5% (Table 2.5).

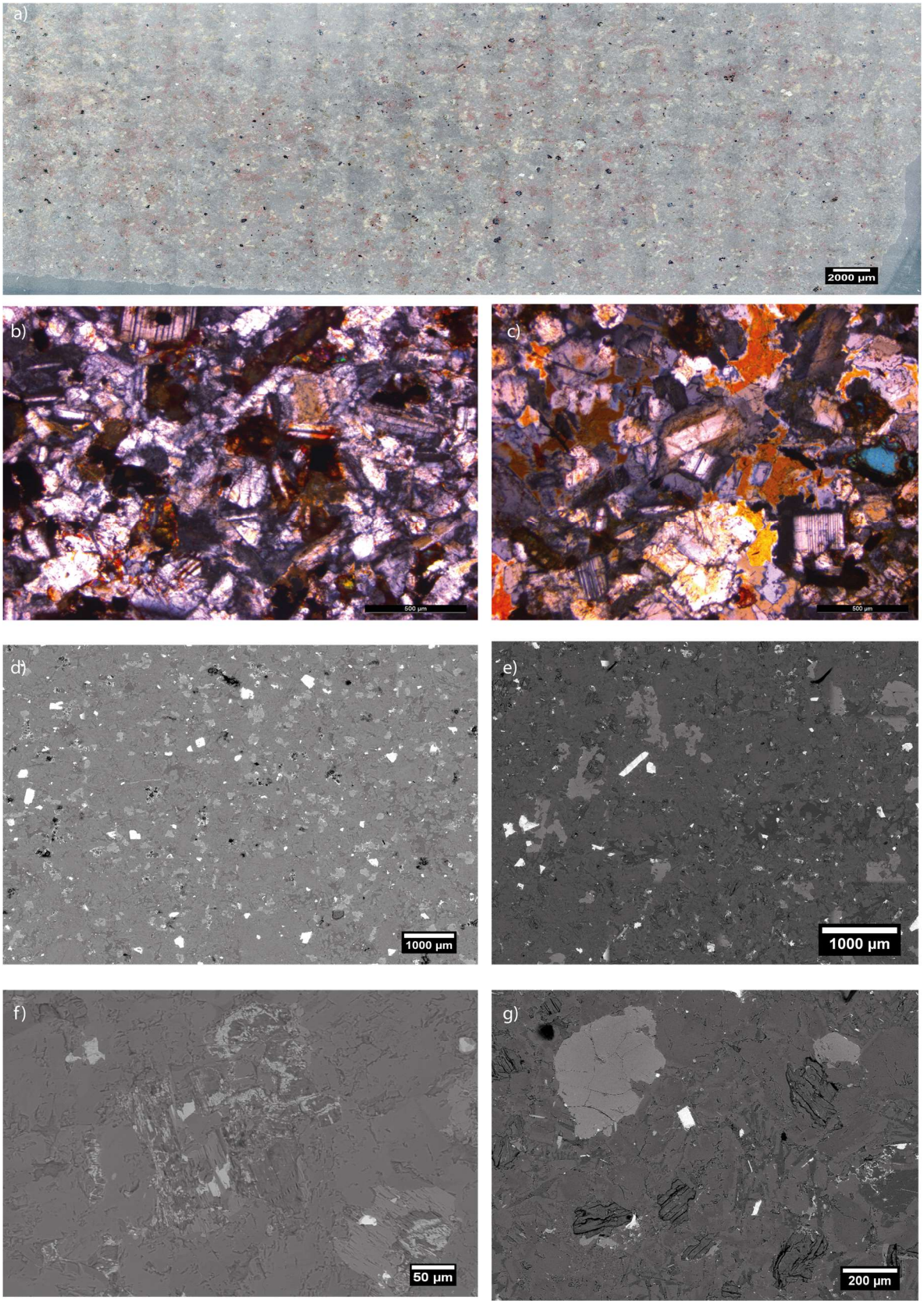


Fig 2.10. Clast-free impact melt rock. (a) Optical microscopy mosaic of sample WCIS-14 MK-60 in PPL show the distribution of minerals in melt matrix. Scale bar is 2000 µm. (b) Photomicrograph of sample WCIS-14 MK-60 in XPL showing the small mineral crystals

embedded in melt matrix. Scale bar is 500 µm. (c) Photomicrograph of sample WCIS-14 MK-077 in XPL showing the small mineral crystals embedded in melt matrix. Scale bar is 500 µm. (d) SEM BSE mosaic of sample WCIS-14 MK-60 showing the distribution of the clast in melt matrix. (e) SEM BSE mosaic of sample WCIS-14 MK-077 showing the distribution of the clast in melt matrix. (f) SEM BSE image of sample WCIS-14 MK-60 showing a clast that has reacted with melt matrix. (g) SEM BSE image of sample WCIS-14 MK-077 showing a clast that has reacted with melt matrix.

2.5.3.4. Lithic impact breccia (without melt particles)

WCIS-14 MK-058B and WCIS-14 058C are polymict lithic impact breccia that does not contain melt. Lithic breccia appears red in hand sample (Appendix 3). These samples contain larger clast (≥1 mm) embedded in the clastic matrix (Fig 2.11). The breccia samples consist of quartz, albite, orthoclase, muscovite, montmorillonite and minor hematite (Appendix 2). The clasts are fractured and contain shock features (Fig 2.11). Toasted quartz and PDFs and PFs was observed in quartz and feldspar. In the thin section, matrix appears reddish-brown due to oxidation (Fig 2.11). Porosity in lithic breccia is higher than impact melt rocks (2-2.5%) (Table 2.5).

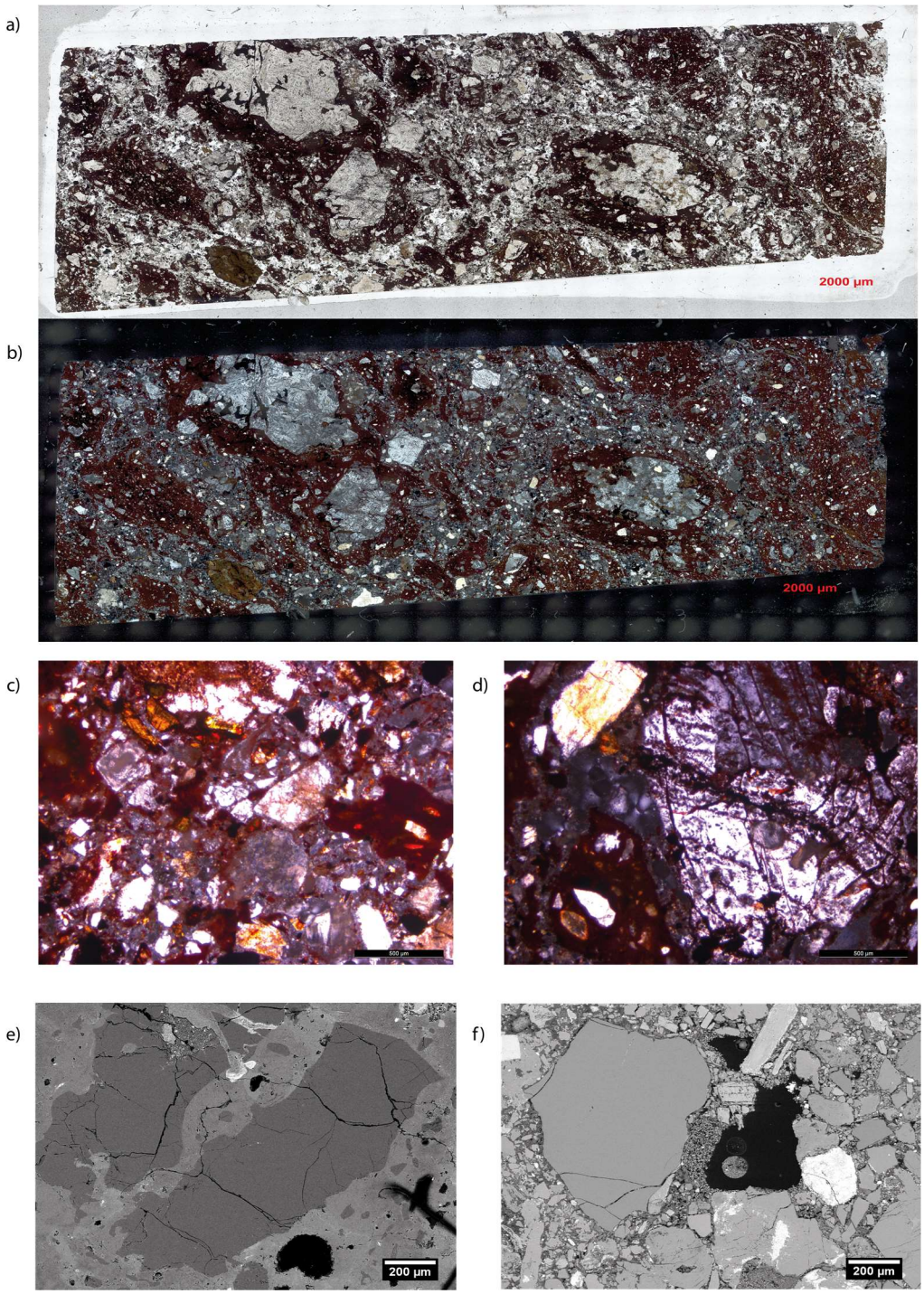


Fig 2.11. Lithic breccia. (a) (a) Optical microscopy mosaic of sample WCIS-14 MK-058B in PPL show the distribution of clasts in the matrix. Scale bar is 2000 µm. (b) Optical microscopy mosaic of sample WCIS-14 058C in PPL show the distribution of clasts in the matrix. Scale bar is 2000 µm. (c) Photomicrograph of sample WCIS-14 MK-058B in XPL showing the altered mineral clasts. Scale bar is 500 µm. (d) Photomicrograph of sample WCIS-14 MK-058B in XPL showing the altered mineral clasts. Scale bar is 500 µm. (e) Photomicrograph of sample WCIS-14 058C in XPL showing the altered mineral clasts. Scale

bar is 500 µm. (e) and (f) SEM BSE images of samples WCIS-14 MK-058B and WCIS-14 MK-058C respectively showing fractured mineral clasts embedded in the matrix.

2.5.3.5. Impact melt-bearing breccia or suevitic breccia (with melt particles)

Impact melt breccias are polymict impact breccia containing melt particles. Suevite (I), Suevite (II), and WCIS-14 Oz-005 are impact melt-bearing breccia or suevitic breccia. Suevite (I) and Suevite (II) are from Ries crater, Germany and WCIS-14 Oz-005 is from West Clearwater Impact Structure, Canada. Both of the samples contain fragments of glasses.

WCIS-14 Oz-005 contain red, oxidised impact melt particles set in a fine-grained matrix (Fig 2.12). Glass component is surrounded by clastic groundmass (Osinski and Grieve, 2017). It contains clasts of quartz and feldspars. The clasts range in size from 100-900 µm. Hematite is present as opaque minerals. Some of the feldspar clasts are altered (Fig 2.12). Quartz clasts are fractured (Fig 2.12). The microfractures range from 0.1 to 4 µm in width (Fig 2.12). The glass fragment contains vesicles. Porosity in this sample is 3.46% (Table 2.5).

Suevite samples contain clasts of vitric or glassy material, quartz, albite, microcline, hornblende, and minor amounts of muscovite and prehnite. Mineral clasts are 100-700 µm in diameter. The clast and lithic fragments are supported by clastic groundmass, which forms up to ~80 % of the volume of which 30-50 % is glass (Fig 2.12) (Osinski et al., 2004). All the mineral clasts are highly fractured, and planar fractures can be observed in some quartz grains, but most of the clast do not contain high-pressure shock features. The microfractures were 0.5-6 µm in width (Fig 2.12). Some of the mineral grains seem to have been weathered. The samples contained macro-fractures with aperture 0.2-0.4 mm and up to 2-5 cm in length (Fig 2.12). Ries Crater suevites are well-studied impact melt-bearing breccia. A detailed petrographic description of suevites can be found in Stähle (1972); Engelhardt et al. (1995); Engelhardt (1997); Osinski et al. (2004); Osinski (2003); Osinski et al. (2016). Suevite samples had the highest porosity among impact melt rocks and impact breccias (10.3%) (Table 2.5).

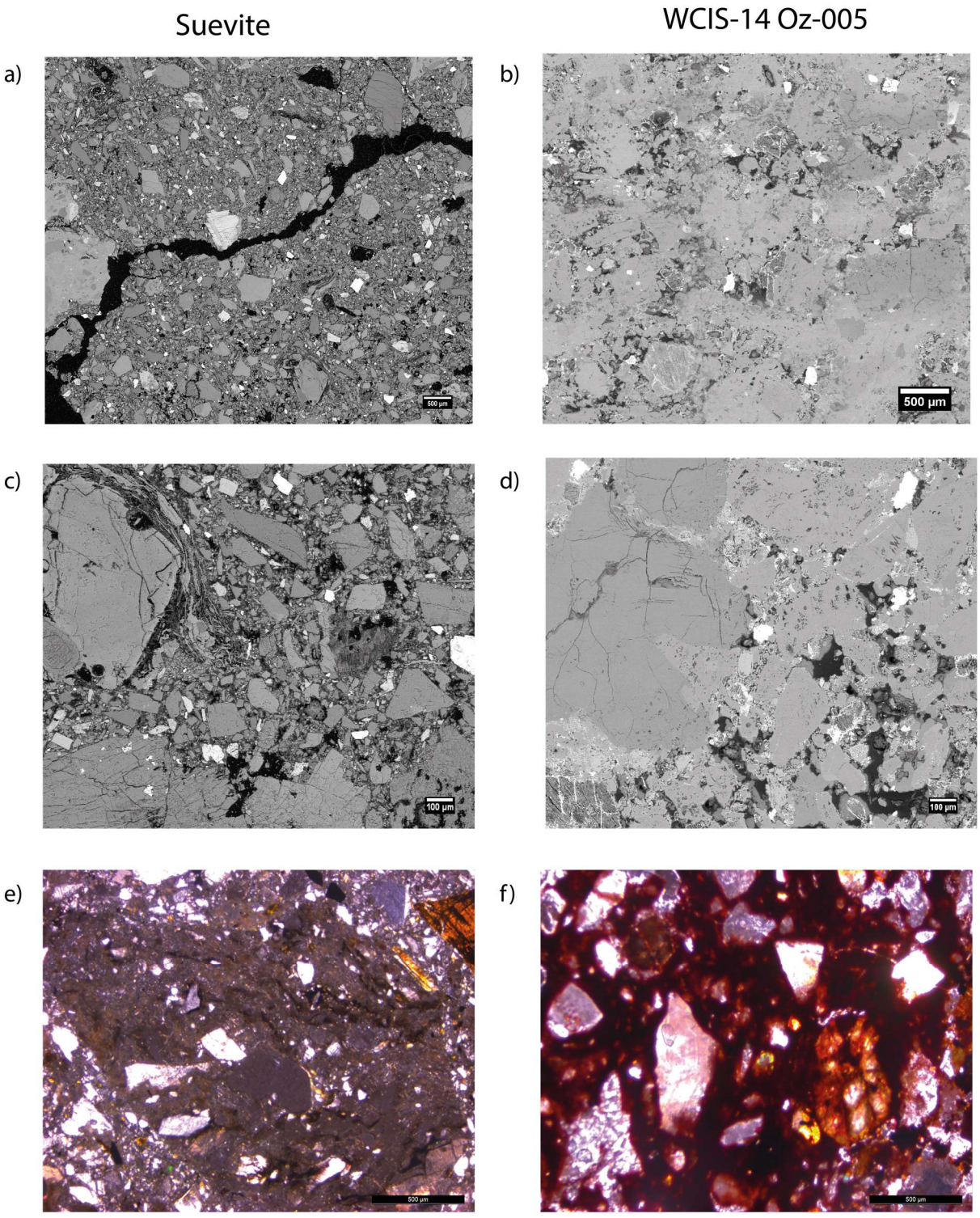


Fig 2.12. Impact melt-bearing breccia. (a) SEM BSE mosaic of the suevite sample showing the clast distribution in the matrix. The curved black lines show a fracture in the sample. Scale bar is 500 µm. (b) SEM BSE mosaic of the sample WCIS-14 Oz-005 showing clasts embedded in the matrix. Scale bar is 500 µm. (c) SEM BSE image of the suevite sample showing fractured mineral clasts embedded in the matrix. Scale bar is 100 µm. (d) SEM BSE mosaic fractured minerals embedded in a very fine-grained matrix. Scale bar is 100 µm. (e)

Photomicrograph of suevite sample in XPL showing clasts embedded in the clastic matrix. Scale bar is 500 µm. (f) Photomicrograph of sample WCIS-14 Oz-005 in XPL showing clasts of quartz and feldspar minerals in the oxidised matrix. Scale bar is 500 µm.

2.6. Conclusions

In this chapter we presented the petrographic analysis of low-shocked Moenkopi and Coconino sandstone from Meteor Crater (Arizona), low-shocked crystalline rocks, impact melt rocks and impact breccias from West Clearwater Impact Structure (Canada), and suevite or impact melt-bearing breccia from Ries crater (Germany). These samples were analysed using petrographic microscopy, scanning electron microscopy (SEM), powder X-ray diffraction (XRD), and X-ray computed tomography (CT) to describe the deformation and changes in rock samples due to impact. By combining these techniques samples were characterised in order to determine the compositional and textural properties of the rock samples, which was used to classify all samples into classes of impactites as well as into shock pressure classes (Stöffler et al., 2018). Macrofractures of 0.1-0.2 mm and microfractures 0.1-5 µm in aperture were observed in all types of impactites. Porosity was reduced by 38% in class 1a Coconino Sandstone and by 88% in class 1a Moenkopi Sandstone compared to their unshocked counterparts. Class 1b Coconino Sandstone has become friable due to pervasive grain fracturing. Shock features such as Planar Fractures, kink bands were present in class 1a crystalline impact samples. Impact melt rocks were classified into three classes based on the presence of clast fragments coarser than 1 mm: clast rich, clast poor, and clast free. Porosity in impact melt ranges from 0.28 to 2.91%. Breccias were classified into two classes: Lithic breccia and impact melt bearing breccia. Lithic breccias are less porous (2.07-2.57%) compared to impact melt bearing breccias (3.46-10.39%). All the impactites samples that are characterised in this chapter are used in a laboratory weathering experiment in Chapter 3.

References

Ai HA and Ahrens TJ. (2004) Dynamic tensile strength of terrestrial rocks and application to impact cratering. *Meteoritics & Planetary Science* 39: 233-246.

Althoff P. (1977) Structural refinements of dolomite and a magnesian calcite and implications for dolomite formation in the marine environment. *American Mineralogist* 62: 772-783.

Bailey S. (1969) Refinement of an intermediate microcline structure. *American Mineralogist: Journal of Earth and Planetary Materials* 54: 1540-1545.

Bish D and Von Dreele R. (1989) Rietveld refinement of non-hydrogen atomic positions in kaolinite. *Clays and Clay Minerals* 37: 289-296.

Boeyens J and Ichharam V. (2002) Redetermination of the crystal structure of calcium sulphate dihydrate, CaSO4· 2H2O. *Zeitschrift für Kristallographie-New Crystal Structures* 217: 9-10.

Brigatti MF and Davoli P. (1990) Crystal-structure refinements of 1M plutonic biotites. *American Mineralogist* 75: 305-313.

Brigatti MF, Frigieri P and Poppi L. (1998) Crystal chemistry of Mg-, Fe-bearing muscovites-2M1. *American Mineralogist* 83: 775-785.

Bruker A and Topas VJB, Karlsruhe. (2003) 1: general profile and structure analysis software for powder diffraction data–User manual.

Buckman J, Bankole SA, Zihms S, et al. (2017) Quantifying Porosity through Automated Image Collection and Batch Image Processing: Case Study of Three Carbonates and an Aragonite Cemented Sandstone. *Geosciences* 7: 70.

Buhl E, Poelchau MH, Dresen G, et al. (2013) Deformation of dry and wet sandstone targets during hypervelocity impact experiments, as revealed from the MEMIN Program. *Meteoritics & Planetary Science* 48: 71-86.

Buscombe D. (2013) Transferable wavelet method for grain-size distribution from images of sediment surfaces and thin sections, and other natural granular patterns. *Sedimentology* 60: 1709-1732.

Cockell CS and Osinski GR. (2007) Impact-induced impoverishment and transformation of a sandstone habitat for lithophytic microorganisms. *Meteoritics & Planetary Science* 42: 1985-1993.

Colville AA and Ribbe PH. (1968) The crystal structure of an adularia and a refinement of the structure of orthoclase. *American Mineralogist: Journal of Earth and Planetary Materials* 53: 25-37.

Downs RT, Hazen R and Finger L. (1994) The high-pressure crystal chemistry of low albite and the origin of the pressure dependency of Al-Si ordering. *American Mineralogist* 79: 1042-1052.

Drits VA, Zviagina BB, McCarty DK, et al. (2010) Factors responsible for crystal-chemical variations in the solid solutions from illite to aluminoceladonite and from glauconite to celadonite. *American Mineralogist* 95: 348-361.

Engelhardt W. (1997) Suevite breccia of the Ries impact crater, Germany: Petrography, chemistry and shock metamorphism of crystalline rock clasts. *Meteoritics & Planetary Science* 32: 545-554.

Engelhardt W, Arndt J, Fecker B, et al. (1995) Suevite breccia from the Ries crater, Germany: Origin, cooling history and devitrification of impact glasses. *Meteoritics & Planetary Science* 30: 279-293.

Ferrière L and Osinski GR. (2013) Shock metamorphism. In: Osinski GR and Pierazzo E (eds) *Impact Cratering: Processes and Products.* John Wiley & Sons, 106-124.

Fitz Gerald JD, Parise JB and MacKinnon ID. (1986) Average structure of an An48 plagioclase from the Hogarth Ranges. *American Mineralogist* 71: 1399-1408.

French BM. (1998) Traces of catastrophe: A handbook of shock-metamorphic effects in terrestrial meteorite impact structures. *Technical Report, LPI-Contrib-954*.

French BM and Koeberl C. (2010) The convincing identification of terrestrial meteorite impact structures: What works, what doesn't, and why. *Earth-Science Reviews* 98: 123-170.

Glinnemann J, King Jr H, Schulz H, et al. (1992) Crystal structures of the low-temperature quartz-type phases of SiO2 and GeO2 at elevated pressure. *Zeitschrift für Kristallographie-Crystalline Materials* 198: 177-212.

Gomez LA and Laubach SE. (2006) Rapid digital quantification of microfracture populations. *Journal of Structural Geology* 28: 408-420.

Grieve RA and Therriault AM. (2013) Impactites: Their characteristics and spatial distribution. *Impact Cratering: Processes and Products*: 90-105.

Gruner JW. (1932) The crystal structure of kaolinite. *Zeitschrift für Kristallographie-Crystalline Materials* 83: 75-88.

Harlow GE. (1982) The anorthoclase structures: the effects of temperature and composition. *American Mineralogist* 67: 975-996.

Healy D, Rizzo RE, Cornwell DG, et al. (2017) FracPaQ: A MATLAB™ toolbox for the quantification of fracture patterns. *Journal of Structural Geology* 95: 1-16.

Kieffer SW. (1971a) I. Shock metamorphism of the Coconino sandstone at Meteor Crater, Arizona. II. The specific heat of solids of geophysical interest. California Institute of Technology.

Kieffer SW. (1971b) Shock Metamorphism of the Coconino Sandstone. *Journal of Geophysical Research*.

Kieffer SW. (1975) From regolith to rock by shock. *The Moon* 13: 301-320.

Kieffer SW, Phakey PP and Christie JM. (1976) Shock processes in porous quartzite: Transmission electron microscope observations and theory. *Contributions to Mineralogy and Petrology* 59: 41-93.

Kring DA. (2017) Guidebook to the geology of Barringer Meteorite Crater, Arizona (aka Meteor Crater): for the 80th Annual Meeting of the Meteoritical Society July 2017. Lunar and Planetary Institute.

Levien L, Prewitt CT and Weidner DJ. (1980) Structure and elastic properties of quartz at pressure. *American Mineralogist* 65: 920-930.

Madden MEE, Kring DA and Bodnar RJ. (2006) Shock reequilibration of fluid inclusions in Coconino sandstone from Meteor Crater, Arizona. *Earth and Planetary Science Letters* 241: 32-46.

Maslen E, Streltsov V, Streltsova N, et al. (1994) Synchrotron X-ray study of the electron density in α-Fe2O3. *Acta Crystallographica Section B: Structural Science* 50: 435-441.

Nelson DO and Guggenheim S. (1993) Inferred limitations to the oxidation of Fe in chlorite: A high-temperature single-crystal X-ray study. *American Mineralogist* 78: 1197-1207.

Osinski G and Grieve R. (2017) " Suevites" of the West Clearwater Lake Impact Structure, Canada: A Demonstration of the Need for a Revised Classification Scheme for Impactites. *Lunar and Planetary Science Conference.*

Osinski GR. (2003) Impact glasses in fallout suevites from the Ries impact structure, Germany: An analytical SEM study. *Meteoritics & Planetary Science* 38: 1641-1667.

Osinski GR, Grieve RA, Bleacher JE, et al. (2018) Igneous rocks formed by hypervelocity impact. *Journal of Volcanology and Geothermal Research*.

Osinski GR, Grieve RA, Chanou A, et al. (2016) The “suevite” conundrum, part 1: The Ries suevite and Sudbury Onaping Formation compared. *Meteoritics & Planetary Science* 51: 2316-2333.

Osinski GR, Grieve RA and Spray JG. (2004) The nature of the groundmass of surficial suevite from the Ries impact structure, Germany, and constraints on its origin. *Meteoritics & Planetary Science* 39: 1655-1683.

Osinski GR and Pierazzo E. (2012) *Impact cratering: Processes and products*: John Wiley & Sons.

Phillips MW, Draheim JE, Popp RK, et al. (1989) Effects of oxidation-dehydrogenation in tschermakitic hornblende. *American Mineralogist* 74: 764-773.

Phillips MW and Ribbe PH. (1973) The structures of monoclinic potassium-rich feldspars. *American Mineralogist: Journal of Earth and Planetary Materials* 58: 263-270.

Phinney W, Simonds C, Cochran A, et al. (1978) West clearwater, Quebec impact structure, part II: petrology. *Lunar and Planetary Science Conference Proceedings.*

Pohl J, Stoeffler D, Gall Hv, et al. (1977) The Ries impact crater. *Impact and explosion cratering: Planetary and terrestrial implications.* 343-404.

Rae A, Collins G, Grieve R, et al. (2017) Complex crater formation: Insights from combining observations of shock pressure distribution with numerical models at the West Clearwater Lake impact structure. *Meteoritics & Planetary Science* 52: 1330-1350.

Rocholl A, Böhme M, Gilg HA, et al. (2018) Comment on "A high-precision 40 Ar/39 Ar age for the Nördlinger Ries impact crater, Germany, and implications for the accurate dating of terrestrial impact events" by Schmieder et al.(Geochimica et Cosmochimica Acta 220 (2018) 146-157. *Geochimica et Cosmochimica Acta*.

Rosa DF. (2012) *The sheet of impact melt at West Clearwater Lake, Northern Quebec*: McGill University (Canada).

Schmieder M, Kennedy T, Jourdan F, et al. (2018) A high-precision 40Ar/39Ar age for the Nördlinger Ries impact crater, Germany, and implications for the accurate dating of terrestrial impact events. *Geochimica et Cosmochimica Acta* 220: 146-157.

Schmieder M, Schwarz WH, Trieloff M, et al. (2015) New 40Ar/39Ar dating of the Clearwater Lake impact structures (Québec, Canada)–Not the binary asteroid impact it seems? *Geochimica et Cosmochimica Acta* 148: 304-324.

Shipman F, Gregson V and Jones A. (1971) *A shock wave study of Coconino Sandstone*: National Aeronautics and Space Administration.

Shoemaker EM and Kieffer SW. (1979) *Guidebook to the geology of Meteor Crater, Arizona*: Center for Meteorite Studies, Arizona State University.

Simonds C, Phinney W, McGee P, et al. (1978) West Clearwater, Quebec impact structure. I-Field geology, structure and bulk chemistry. II-Petrology. *Lunar and Planetary Science Conference Proceedings.* 2633-2693.

Simpson SL. (2015) Geochemical and mineralogical studies of meteorite impact-generated hydrothermal systems on Earth and tracing sources of water: observations from the Rochechouart impact structure, France. University of Glasgow.

Singleton AC, Osinski GR, McCAUSLAND PJ, et al. (2011) Shock-induced changes in density and porosity in shock-metamorphosed crystalline rocks, Haughton impact structure, Canada. *Meteoritics & Planetary Science* 46: 1774-1786.

Sitepu H, O'Connor BH and Li D. (2005) Comparative evaluation of the March and generalized spherical harmonic preferred orientation models using X-ray diffraction data for molybdite and calcite powders. *Journal of Applied Crystallography* 38: 158-167.

Stähle V. (1972) Impact glasses from the suevite of the Nördlinger Ries. *Earth and Planetary Science Letters* 17: 275-293.

Stöffler D, Grieve R, Fettes D, et al. (2007) Impactites. *Metamorphic rocks: A classification and glossary of terms, recommendations of the International Union of Geological Sciences*: 82-92.

Stöffler D, Hamann C and Metzler K. (2018) Shock metamorphism of planetary silicate rocks and sediments: Proposal for an updated classification system. *Meteoritics & Planetary Science* 53: 5-49.

Swope RJ, Smyth JR and Larson AC. (1995) H in rutile-type compounds: I. Single-crystal neutron and X-ray diffraction study of H in rutile. *American Mineralogist* 80: 448-453.

Viani A, Gualtieri AF and Artioli G. (2002) The nature of disorder in montmorillonite by simulation of X-ray powder patterns. *American Mineralogist* 87: 966-975.

Whitmore J, Strom R, Cheung S, et al. (2014) The petrology of the Coconino Sandstone (Permian), Arizona, USA. *Answers Research Journal* 7: 499.

Žunić TB, Šćavničar S and Molin G. (1990) Crystal structure of prehnite from Komiza. *European Journal of Mineralogy*: 731-734.

Chapter 3

3. The effect of impact-generated heterogeneities and discontinuities on the subsequent weathering of impactites: insights from laboratory experiments

Manuscript in preparation

Ankit K. Verma, Mary C. Bourke, Heather A. Viles, Gordon R. Osinski, and Juan Diego Rodriguez-Blanco

Abstract

Impact cratering is an important geological process that affects all planetary bodies in our solar system. As rock breakdown plays a vital role in the evolution of landforms and sediments on a planetary scale, it is crucial to assess the role of inheritance in the subsequent breakdown of impactites (impact rocks). The shock pressure of several gigapascals generated during the impact can exceed the effective strength of target lithology by three to four orders of magnitude and is responsible for melting, vaporisation, shock metamorphism, pore collapse, vesiculation fracturing and fragmentation of rocks. Environmental conditions and heterogeneities in rock properties exert an important control in rock breakdown. Similar to other subaerial rocks, impactites are affected by a range of rock breakdown processes. In order to better understand the role of low-shock inheritance on rock breakdown, a rock breakdown experiment was conducted in a simulated environmental cabinet under conditions similar to terrestrial semi-arid conditions. We cycled temperature (-2 to 35°C) and relative humidity (13-45%) through 39 accelerated diurnal cycles (each of 8 hours duration). We used 41 impactite samples in the experiment that included low shocked sedimentary and crystalline rocks, impact melt rocks and impact breccias. Mechanical (Equotip and weighing), photographic (photographic monitoring), microscopic and solid-state methods (petrographic microscopy, powder X-ray diffraction, scanning electron microscopy, X-ray computed tomography) were used to characterise the rock samples relative to unshocked rocks, and to assess the shock related changes before and after the experiments. The low shocked sedimentary rocks showed a decrease in porosity by 38% (Coconino Sandstone) and 88% (Moenkopi Sandstone) compared to unshocked counterparts. Macrofractures of 0.1-0.2 mm and microfractures 0.1-5 μm in aperture were observed in all types of impactites. The results showed that impactites exhibited an accelerated decline in strength compared to non-impacted control samples. However, rock

type and impact deformation history were key parameters controlling the rate of deterioration.

3.1. Introduction

Impact cratering is a ubiquitous and catastrophic geologic process that has a crucial role in the evolution and modification of all planetary bodies with solid surfaces. During impact, the energy released is much higher than any endogenic geological processes. During an impact event, the impact shock wave is translated into more intense shock-related deformation and melting of target rocks extensively beneath and around the impact crater compared to those located at a far distance (Pierazzo and Melosh, 2000; Kenkmann et al., 2014). In the case of porous rocks like sandstone, this effect is more pronounced (Kieffer, 1971b; Kieffer et al., 1976b).

A range of impactites such as shocked target rocks, impact melt rocks, impact breccias, impact melt-bearing breccias, and tektites are usually found at impact sites. Impactites are classified into autochthonous, parautochthonous and allochthonous based on origin and current location at the impact site. Allochthonous impactites are further classified into proximal and distal based on distance from the impact site. A detailed classification of impactites can be found in Stöffler et al. (2007) and Grieve and Therriault (2013).

During impact, porosity, permeability and density can dramatically change depending on the energy released and the target lithology as well as the distance from the point of impact (Kieffer, 1971b; Cockell and Osinski, 2007; Singleton et al., 2011). The impact metamorphism processes and their effects differ in non-porous crystalline target rocks in comparison to porous sedimentary rocks (Kieffer, 1971b; Cockell and Osinski, 2007; Osinski, 2007; Singleton et al., 2011; Stöffler et al., 2018).

In crystalline rocks, porosity increases with an increase in shock pressure levels (Singleton et al., 2011). This is caused due to fracturing and differential mineral melting during the passage of the shock and subsequent rarefaction wave (Singleton et al., 2011).

For porous sedimentary rocks, such as sandstone, that are subject to low shock pressure levels (<10 GPa) the rock density increases due to pore collapse, comminution and fracturing of grains. Rock density decreases as shock pressures rise ($25 > P > 10$ GPa) due to vesiculation and formation of glasses and melts that weld mineral grains (Kieffer, 1971a;

Kieffer, 1971b). At even higher shock pressures (>30 GPa) the porosity is further reduced as minerals recrystallise from the melt (Cockell and Osinski, 2007).

If impact rocks are subject to longer-term heating and annealing during crater cooling, the porosity and permeability will be affected further. For highly porous substrates (such as sandstones), more of the impact energy is taken up in pore collapse resulting in lesser solid state transformations and higher post-shock temperatures than a similar impact into non-porous crystalline target lithology (Kieffer, 1971b; Madden et al., 2006).

There are two shock-related features that we investigate in this study, micro-fracturing and mineral-scale deformation. First, The role of micro-fracturing as a control on the moisture flux in rocks is held to be important in subsequent rates of rock breakdown (Sousa et al., 2005; Anders et al., 2014). Impact fractures and microcracks, produced during impact, increase secondary porosity and affect the total porosity and permeability of the rocks. However, microfracturing is not well understood in any environment (Anders et al., 2014).

Second, naturally occurring distinct diagnostic mineral deformation features related to impact shock waves such as planer fractures, planar deformation features, feather features, toasting, mosaicism, kink bands, high-pressure mineral phase transformations and impact shock melting at various shock pressures are well documented in the literature (French and Koeberl, 2010; Ferrière and Osinski, 2013; Stöffler et al., 2018), and assigned shock pressure levels by calibrated laboratory experiment (Kieffer, 1971b; Shipman et al., 1971; Kieffer et al., 1976a). What has not been adequately investigated is the role of the mineral-scale deformation features may have on the subsequent breakdown of rocks.

3.1.1. Previous work

Environmental conditions and heterogeneities in rock properties exert an important control in rock breakdown. Earlier studies have demonstrated that pore geometry affects rock susceptibility to weathering and controls the intensity of weathering (Tuğrul, 2004). Several studies (Newsom et al., 2013; Wright, 2013) have reported a unique style of rock breakdown associated with decompression cracks in impacted basalt at Lonar Crater, India. Natural silicate glasses are susceptible to accelerated dissolution when compared to their crystalline counterparts (Wolff-Boenisch et al., 2006). Since, impact generated glasses have a different texture, density and structure (French and Koeberl, 2010), they may weather differently. The structural defects, deformations and change in surface area of minerals makes shocked rocks more susceptible to chemical weathering than unshocked rocks (Boslough and Cygan, 1988;

Bell, 2017). Moreover, microstructures and defects in minerals generated during impact shock (e.g. Planar Fractures (PFs), Planar Deformation Features (PDFs), mosaicism, microfractures) can provide permeable pathways for fluid circulation leading to chemical weathering (Leroux, 2005; Furukawa et al., 2011). Increasing shock pressures also causes devolatilization in minerals (Madden et al., 2006), which may affect the response of rocks to thermal weathering (Farquharson et al., 2017).

To understand the mechanism, style and rate of weathering and the role of a range of environmental factors, geomorphologists conduct weathering experiments in controlled laboratory conditions. A range of weathering and field exposure experiments has been conducted to understand the role of lithology (Warke, 2007; Viles and Goudie, 2007), environment and microclimate (e.g. Goudie and Parker (1998); Warke and Smith (1998); Viles (2005); Viles and Goudie (2007); Smith et al. (2011); Viles et al. (2010), mechanism and style of deterioration (Williams and Robinson, 2001; De Kock et al., 2015; Ghobadi and Babazadeh, 2015), the presence of salts (Goudie and Parker, 1998; Goudie et al., 2002; Smith et al., 2005; Warke, 2007), and porosity and fractures (Sousa et al., 2005; Tuğrul, 2004). These data have emphasised the role of stress history and the inherited weakness that may result from past weathering. Few studies used simulated pre-stressed rocks (sedimentary and crystalline) with different weathering histories and subjected rocks to experimental weathering and field exposure trials in arid conditions (Warke, 2007; Viles et al., 2010; Viles et al., 2018). They found that pre-stressed rocks deteriorate faster than un-stressed rocks. Moreover, the nature of pre-stressing had a significant effect on the rate of breakdown (Warke, 2007; Viles et al., 2010; Viles et al., 2018).

No detailed study has been undertaken to explore the role of impact metamorphism and the effect of inherited heterogeneities and deformation caused by impact process on subsequent on subsequent style and rate of weathering. Here, we present data from the first physical weathering experiment in simulated semi-arid conditions on impactites. The focus of this study is to identify how the inheritance of an impact event affects the subsequent breakdown of impactites exposed at the surface to sub-aerial weathering.

3.2. Materials and methods

3.2.1. Sample source

The primary focus of this study is to understand the effect of impact-related deformation on weathering of sandstone in simulated weathering environmental conditions using low-shocked sedimentary rocks sampled from Meteor Crater (USA). We also report on pilot weathering experiment on a small number of crystalline impacted rocks, impact melt rocks, and impact breccias from West Clear Water Impact structure (Canada) and Ries Crater (Germany) as these are also common rocks in terrestrial impact craters, but they have a different impact history (Fig 2.1). Forty-one samples of impactites and non-impacted rocks were selected for the weathering experiment.

3.2.1.1. Meteor Crater Samples: Sedimentary impacted rocks

Two types of sedimentary rock samples are included in this study. These are Permian Coconino Sandstone, and Triassic Moenkopi Sandstone sampled from the 50, 000 years old 1.2 km diameter Barringer Meteorite Crater aka Meteor Crater in Arizona (Kieffer, 1971a; Shoemaker and Kieffer, 1979). The impacted samples were collected from NW, NE, SE and S Crater walls and the ejecta blanket on the south side of the crater (Fig 2.2). Non-impacted varieties of Coconino and Moenkopi Sandstone samples were included as control samples in the experiment. Non-impacted Moenkopi Sandstone samples were collected from two sites along Meteor Crater road that experience similar environmental conditions, 5 and 9 km from the Meteor Crater (Fig 6.5). Non-impacted Coconino Sandstone samples were collected from Clear creek reservoir 50 km from Meteor Crater (this was one of the closest surface exposures). Eight impacted Coconino sandstone, nine impacted Moenkopi sandstone and two non-impacted (control) samples of both Coconino and Moenkopi Sandstone were used in the weathering experiment (i.e., 21 samples). Impacted samples were named according to Barringer Crater Reference Collection naming convention (*pers. comm*. D. Kring).

3.2.1.2. West Clearwater Impact Structure samples: Crystalline impacted rocks, impact melt rocks, and impact breccias

The ~36 km diameter West Clearwater Impact Structure (WCIS) is about 125 km east of Hudson Bay in Quebec, Canada (Simonds et al., 1978). WCIS is ~286 Ma old and is relatively well preserved with a large ring of islands in the ~30 km diameter lake (Schmieder et al., 2015; Osinski and Grieve, 2017). The samples from this crater were collected during NASA FINESSE (Field Investigation to Enable Solar System Science and Exploration)

expedition in 2014 by one of the co-authors. Target lithologies comprise granitic gneiss, granite, tonalite, granodiorite, quartz monzodiorite with later diabase dykes (Phinney et al., 1978; Simonds et al., 1978; Rosa, 2012; Rae et al., 2017; Osinski and Grieve, 2017). Osinski and Grieve (2017) proposed a general stratigraphy of impactites from the bottom to top in the sequence: Fractured basement > lithic impact breccia > impact melt-bearing breccia or suevite > clast rich impact melt rock > clast poor impact melt rock > clast free impact melt rock.

Impacted granite and tonalite samples were collected from around the rim and impact melt rocks and impact breccias were collected from ring islands. Samples were named according to NASA FINESSE WCIS campaign naming convention.

3.2.1.3. Ries Crater samples: Impact melt-bearing breccia or suevite

The ~26 km diameter Ries Crater in western Bavaria, Germany is one of the best preserved terrestrial mid-sized complex impact structures (Pohl et al., 1977). Ries crater was formed ~15 million years ago in the flat-lying sequence of Mesozoic sedimentary rocks that unconformably overlie Hercynian crystalline basement (Pohl et al., 1977; Osinski, 2003; Rocholl et al., 2018; Schmieder et al., 2018). A single Suevite sample from this crater is used in this study. The sample came from the repository collection of one of the co-authors, and its precise sample location in the field is not known.

3.2.2. Sample preparation

Polished thinsection of 30 μm thickness was prepared for petrographic examination. Powdered samples were prepared in a mortar and pestle for X-ray diffraction analysis. For the weathering experiments, rock samples were cut into cube blocks of 5 cm side length using a wet rock saw at Trinity College Dublin. A few samples which were not big enough for making 5 cm cube blocks, were cut down into the biggest dimension possible (see Table 3.1-3.4).

3.2.3. Characterisation of samples

Characterisation of samples was necessary to describe the deformation and changes in rock samples due to impact. Several laboratory analysis techniques were used to characterise

petrographical properties in rock samples. Samples were assessed to determine compositional and textural properties using a combination of qualitative and quantitative techniques including scanning electron microscopy (SEM), powder X-ray diffraction (XRD), petrographical microscopy and X-ray computed tomography (CT). In order to classify each sample into a shock pressure class, the shock deformation state of quartz was determined in polished thinsection under a petrographic microscope. These features were then matched to the published classification, and the shock pressure class was assigned to the samples (Kieffer, 1971b; Stöffler et al., 2018) based on the presence and absence of specific shock features (e.g. PF, PDFs) in quartz and decreasing quartz content in the samples due to conversion into high-pressure polymorphs and glass. Quantitative powder X-ray diffraction was used to determine the relative proportion of high-pressure mineral polymorphs in the samples. The shock progression seen in the quartz is similar to that found in other studies (Kieffer, 1971b; Engelhardt, 1997; Rosa, 2012; Rae et al., 2017).

3.2.3.1. Quantitative X-ray diffraction (XRD) for identification of mineral phases in rock samples

Quantitative powder X-ray diffraction (XRD) analysis was performed on rock sample to identify and measure relative proportion of minerals and their high-pressure polymorphs formed during impact using the Bruker D5000 in Trinity College Dublin and the Panalytical X'Pert Pro XRD at the Natural History Museum, London. These data allowed us to assign shock pressure class to these samples based on abundances of higher-pressure mineral polymorphs. Furthermore, powder XRD was used to identify salt species present in the field.

3.2.3.2. Petrographic examination using scanning electron microscope (SEM) and petrographic microscope

Petrographic microscopy and SEM were used to analyse and identify the composition (mineral composition, grain size, grain size distribution, grain contact, porosity, grain shape, matrix, sorting), weathering (secondary alteration minerals, grain disintegration, grain shape, secondary porosity, fracture patterns), and impact associated deformation features (e.g., PF, PDFs, microfractures) of the rock. Polished thin sections were examined under Nikon Eclipse LV100 petrographic microscope. Grain size and sorting analysis for sedimentary impactites were done in the MATLAB tool developed by Buscombe (2013). Zeiss Axio Imager 2 microscope was used to obtain mosaic of thin sections to understand the composition and grain-matrix relationship in the thin section.

A Tescan Mira XMU Field Emission scanning electron microscope (SEM) at the Centre for Microscopy Analysis (CMA) in Trinity College Dublin was used to obtain Backscattered Electron (BSE) images of rock thin sections. The SEM was equipped with KE Developments Centaurus system. Thin sections were carbon coated to a thickness of 10 nm to aid conductivity. BSE images were obtained at a working distance of 18 mm. Beam operating conditions were 20 kV of accelerating voltage and probe current of 10 pA.

SEM BSE mosaics (~50 mm^2) were used for porosity determination of impacted and non-impacted samples (Buhl et al., 2013b). SEM BSE mosaics (~50 mm^2) represents significant subsection of the entire thinsection. The area for BSE mosaic was selected manually by locating subsection of thinsection that roughly represented the whole thinsection. Macrofractures were avoided in the field of view BSE mosaic for estimating primary porosity of rock sample in order to avoid any bias in the result. Porosity in rock samples was estimated by quantitative BSE image analysis in freely available software Image J following established methodology (Buckman et al., 2017). BSE images have high contrast which enables discrimination between grains and the lowest intensity (or darkest) epoxy-filled pore spaces. Grey-Scale intensity thresholding was visually applied at the default setting by manually adjusting the intensity in order to capture the maximum degree of observed porosity. The percentage area of thresholded pore space was measured for porosity percentage determination. BSE images were also used to quantify the microfractures in rock samples.

3.2.3.3. X-ray computed tomography (CT)

X-ray CT was used to visualise and quantify macro-fractures (0.1 mm – 1 mm) present in the sample blocks. A Nikon Metrology HMX ST 225 X-ray CT at the Natural History Museum (London) was used to characterise the samples. X-ray CT images were acquired at 200 kV and 200 µA using 0.5 mm copper filter and ultra-focus X-ray head. Approximately 3142 projections were acquired at 2 frames per projection by 0.2 mm detector pixel size. The X-ray CT scanned 2 hours for each sample at 0.046 mm voxel size. The scan was reconstructed into a 16-bit unsigned raw file format which took 1.5 hours for each sample. The resolution of 0.046 mm per voxel is the highest that could be achieved for 5 cm cube rock block with this approach.

X-ray CT was used to characterise macro-fractures both before and after the environmental chamber experiments (De Kock et al., 2015). This technique helped to quantify the presence

of pre-existing micro-fractures and those that may be enhanced or generated by the experiments.

3.2.4. Laboratory weathering experiment

3.2.4.1. Weathering experiment design

In order to understand the role of impact inheritance on rock weathering, an experiment was conducted to simulate physical weathering under terrestrial semi-arid conditions over a short timespan (c 39 diurnal cycles). A Sanyo Fissons-FE300H/MP/R20 environmental cabinet was used to simulate the semi-arid environment conditions found at Meteor Crater in Arizona during spring (Fig A.3.8-A.3.9 in Appendix 3). It is required to ensure the samples have sufficient exposure to manifest a physical response to the conditions. Shorter run times may not produce measurable effects. Viles et al. (2010) ran terrestrial simulations for 12 days on basalt and had a successful outcome. Due to limited availibility of funding and access to the environmental cabinet facility, the experiment was run for 13 days.

In the physical weathering experiment, environmental cycling simulated heating and cooling, wetting and drying, freeze and thaw, and salt weathering processes. Our motivation was to simulate natural weathering conditions to produce an observable rock breakdown in the short experiment timeframe available. Forty-one sample blocks of impactites and non-impacted rocks were used in this experiment.

To provide a pedogenic component to the experimental environment and to isolate the base of the rock from the metallic tray, a ~2 cm thick sand layer was placed in sample trays (Fig 3.1). Building sand (quartz sand) was used in this experiment which had similar albedo and grain size as the sand found at Meteor Crater site. This was done to recreate field-like thermal gradients. The mean grain size of the sand used in the experiment was 270 μm (measured by Malvern Laser Particle Sizer Mastersizer 2000) which is similar to sand sampled from the field site (230 μm, measured by dry sieving). Salt samples (MC51417-3 and MC51417-4) collected in the field at the Meteor Crater site were analysed to identify the salt species. Gypsum salt (calcium sulphate dihydrate, $CaSO_4 \cdot 2H_2O$) was detected in the powder XRD analysis (Fig A.3.10 in Appendix 3) and was used in this experiment to simulate the natural field conditions. Although gypsum is not known to be an aggressive salt in short duration weathering experiment conditions (Charola et al., 2007; Williams and Robinson, 2001),

gypsum salt was mixed into the sand in 1:10 ratio by weight as this sand to salt ratio is known to produce observable breakdown (Goudie and Parker, 1998; Goudie et al., 2002). The rock samples were placed on top of this sand-salt layer to simulate natural conditions in which salt uptake take place by a capillary rise in the field (Fig 3.1). Samples were separated in the tray to prevent possible interactions.

In this simulation, diurnal cycles of temperature and humidity (forced by convection) were accelerated so that each 24 hours was simulated over 8 hours in the environmental cabinet (Fig 3.1). Temperature and relative humidity data obtained from an iButton (Viles, 2011) deployed at Meteor Crater was used in this simulation (Fig A.3.8-A.3.8 in Appendix 3). A full diurnal spring range (-2 to 35°C) which recorded the highest temperature gradient was chosen and compressed into an 8h cycle by reducing the length of time at near-constant temperatures to induce rock breakdown in reasonably realistic circumstances. This was done to preserve a natural rate of temperature change during periods of maximum heating and cooling and to minimise chamber time (Viles et al., 2010). An 8-hour cycle is appropriate as a shorter cycle require accelerating conditions too far from reality, that can have negative consequences on the experiment outcome. The mean rate of change in air temperature (dT/dt) in this experiment was ~0.15°C/min. Thirty-nine cycles were repeated in total. Each cycle lasted 8 hours, and consist of 8 steps, of 1 h duration each step, with a constant cooling and warming rate. The temperature inside the environmental chamber was recorded using an iButton to ensure that the chamber was performing the temperature and relative humidity simulations correctly.

The chamber was configured into two compartments using a metallic shelf (Fig 3.1). Seven sample trays containing six samples (Fig A.3.1-A.3.7 in Appendix 3) in each tray were placed in the chamber (4 sample trays in the top compartment and 3 in the bottom compartment). A 40W halogen incandescent bulb was placed ~30 cm from the samples in each compartment of the chamber (Fig 3.1) to provide direct heating of rock surfaces by radiation to mimic natural condition of heat transfer (Warke and Smith, 1998; Viles et al., 2010). The lamp was switched on for half of each cycle using a programmable timer plug (Fig 3.1). The rain was simulated by spraying both the sand and the sandstone block surface with 25 mL of distilled water every 6 cycles. The spatial position of each sample tray was changed within chamber shelf sixth cycle when the chamber was opened for rain simulation to ensure equal exposure to any slight variations in conditions in the chamber (e.g. direct

radiational heating variation due to the position of the lamp in the chamber). The surface temperature of the rock surface was monitored every sixth cycle with an infrared thermometer to ensure that rock does not get too much heat from an artificial light source.

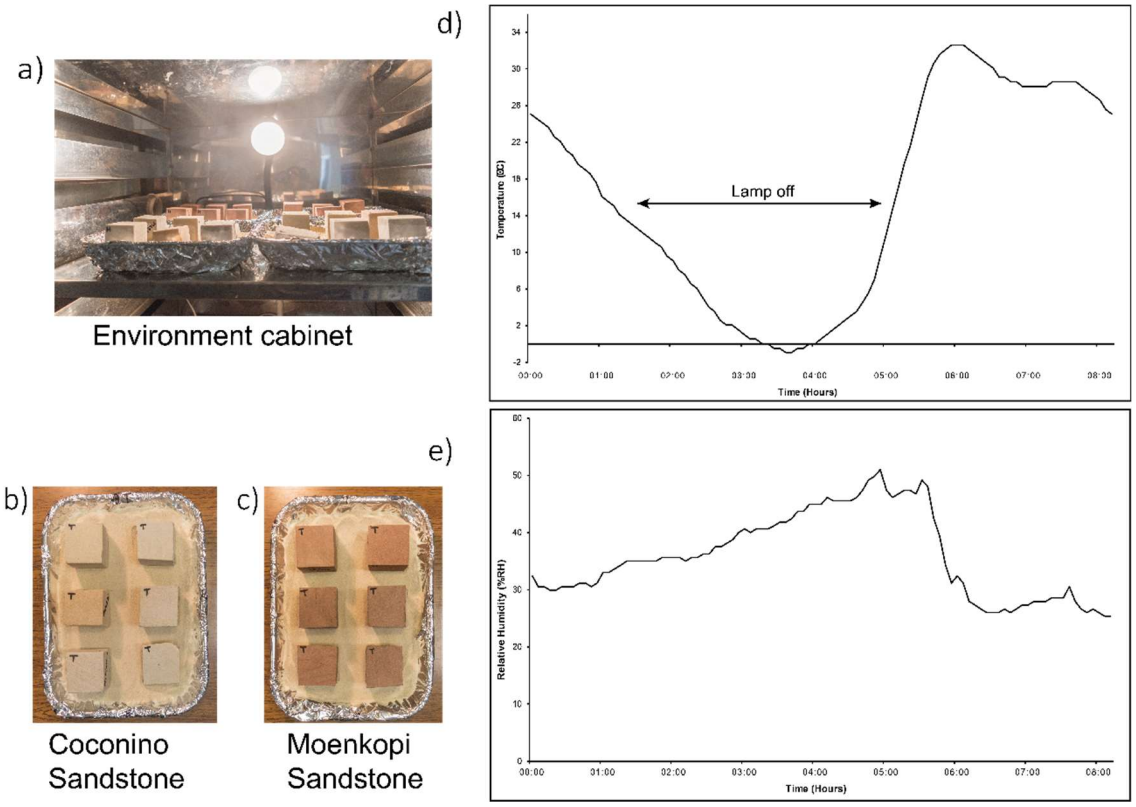


Fig 3.1. Physical weathering experiment protocols. (a) Terrestrial semi-arid condition simulation chamber with a lamp on top. (b) and (c) Rock sample tray. Sample blocks were placed on the sand-salt layer in the tray. (d) and (e) Temperature and humidity cycling of air in the simulation chamber.

3.2.4.2. Change metrics

Large-scale changes were monitored by weighing and photographing the samples before and after the experiments. Before weighing the sample at the end of the experiment, the samples were softly brushed to remove any sand, salt or debris attached to the rock surface. The change in weight is expressed as a percentage of initial block weight. A high-resolution Nikon D5500 24-megapixel camera with 35 mm prime lens was used to take scale photographs of the top and bottom facets of the sample blocks before and after the experiment. For small-scale changes, close up photographs of the rock samples were analysed before and after the rock breakdown experiments to identify and quantify changes

in order to establish the nature, rate, and intensity of breakdown under experimental conditions.

Rock hardness was measured using the Proceq Equotip Piccolo Bambino 2 before and after the experiment to detect any changes in rock strength (Kompatscher, 2004; Aoki and Matsukura, 2007; Viles et al., 2011). The measurement was obtained using D device version (impact body 27 mm long, flat support ring) in HLD mode (Kompatscher, 2004). The hardness measured by equotip are represented as Leeb hardness value (Kompatscher, 2004). Samples were supported by 1 m thick solid granite worktop bench. A rigid connection between the sample and solid support was ensured. The contact surface of the sample and the surface of the solid support was level, flat and smooth clean and dry. This was done to prevent unwanted energy absorption resulting in distortion in test results due to vibration as the impact body as the equotip hits the test point (Kompatscher, 2004). Twenty equotip measurements on each block were taken on different locations on the same surface and averaged. Any decrease in rock surface strength as a result of the generation of new microfractures or modification of an existing one is expected to be reflected in a decrease in Leeb hardness value (Aoki and Matsukura, 2007; Viles et al., 2011).

3.2.4.3. Desalination experiment

In order to quantify the amount of salt taken into macrofractures by capillary action during the experiment a series of desalination experiments were conducted. The samples were placed in individual, non-reactive, transparent, 1L cylindrical containers made up of Nalgene polypropylene copolymer material. The container was filled with 600 ml of distilled water, tightly capped and left for 48h. Samples were then removed and oven dried for 24 h at 50 °C to avoid the potential of inducing thermal breakdown. The experiment was repeated for three cycles. The conductivity of the water in which samples were immersed was measured using a handheld electrical conductivity meter and weight of the sample was recorded at the beginning and the end of each cycle. When there was little to no difference in the water conductivity or weight of the rock sample, then the experiment was stopped. At the end of the desalination, the sample strength was measured by Equotip. The Equotip measurement was carefully obtained on the same surface on which measurements were obtained before and after the weathering experiment. Care was taken to avoid previous Equotip measurement locations.

3.3. Results

3.3.1. Characterisation of rock samples

In this study, sedimentary and crystalline impactites samples were classified into shock pressure classes using XRD, SEM-BSE, and petrographic microscopy observation following classification by (Kieffer, 1971b; Kieffer, 1971a; Madden et al., 2006; Stöffler et al., 2018). Below is a summary of the characterisation of impactite samples (Tables 3.1-3.4). Further detailed of the petrographic analysis can be found in Chapter 2.

Table 3.1. Description of properties of Coconino Sandstone sample blocks used in the weathering experiment. Same sample names with Roman numerals in brackets indicate blocks cut from the same big sample.

Coconino Sandstone (CS)	Shock pressure class	Sample Size (cm)	Type of rock	Porosity (%)	Grain size (mm)	Sorting	Lamination	Visible macro-fracture in hand sample	Petrographic overview
MC51417-5 (I)	1A	~5×5×5	Ejecta	5.81	0.12	0.08	Five sets parallel lamination bands, the width of the band is 1 mm	No	**Class 1a (<5GPa) CS** may have experienced <5GPa of shock pressure during impact. In general, specimens of class 1a shocked CS do not differ in macroscopic appearance from unshocked CS. The grains are weakly to moderately cemented. In thin section, these rocks have less porosity than massive unshocked Coconino Sandstone. Porosity has been reduced in these samples due to compaction caused by slight translation and rotation of individual grains or small group of grains during the passage of shock waves. However, remnant porosity is still visible under a petrographic microscope. Less than 5% of quartz grains show wavy extinction under cross-polars. Class 1a samples retain their original grain size as in found in unshocked samples and 37-65% quartz grains displayed irregular microfractures (Madden et al., 2006).
MC51417-5 (II)	1A	~5×5×5	Ejecta	5.81	0.12	0.08	5 sets parallel lamination bands, width of band is 1 mm	No	
MC51417-6	1A	~5×5×5	Ejecta	14.42	0.09	0.07	No, massive	No	
MC51417-7	1A	~5×5×5	Ejecta	18.5	0.14	0.09	8 bands of width 1 mm parallel, closely spaced 0.5 cm	No	
MC51417-8	1A	~5×4×4	Ejecta	12.27	0.09	0.06	No, massive	No, crumbled corner	
MC51517-2	1A	~5×5×3	Crater wall rock	12.72	0.11	0.07	Four bands of lamination with 1 mm width, closely spaced 0.5 cm	One set of fracture 3 cm in length and 0.2 cm in width only visible on two adjacent surfaces, broke along a fracture or lamination during sample preparation	
MC51517-4	1A	~5×5×5	Crater wall rock	13.69	0.12	0.08	No, massive	One set of fracture 4 cm in length and 0.2 mm width only visible on two adjacent surfaces	
MC51517-8 (I)	1A	~5×5×5	Crater wall rock	13.69	0.16	0.09	No, massive	One set of fracture,5.5 cm in length, 0.2 mm wide, visible only on two adjacent surfaces of the block	
MC51517-8 (II)	1A	~5×5×5	Crater wall rock	13.69	0.16	0.09	One band of ~1 mm thick lamination, massive	No	
MC51417-9	1B	~7×7×3	Ejecta from quary	10.98	0.1	0.07	no, but the friable sample	No	**Class 1b (~5 GPa) CS** is fragile and friable, fine-grained, powdery in texture. The rock is snow white in hand sample and can be broken by gentle hand pressure. The size of the grains is reduced by fracturing, only a fraction of the grains preserves the original grain size. These isolated grains are surrounded by much smaller, highly fractured quartz particles. In class 1b CS ~98% of grains contain

									irregular fractures (Madden et al., 2006). The aperture/width of intragranular microfracture in the quartz grains in low shocked Coconino Sandstone ranged from 0.1-5 um.
CLR-1	unshocked	~5×5×5	Control	20.44	0.09	0.07	No, massive	1.5 cm long fracture, visible on two adjacent surfaces only.	**The unshocked CS** is pale buff, white, fine-grained, saccharoidal, cross-bedded eolian Sandstone Detrital quartz grains in the sandstone are generally well rounded, well sorted. CS contains 94-99 % quartz 0.4 – 5 % kaolinite, and minor feldspar, heavy minerals (rutile, zircon), calcite and hematite as secondary deposits can occur in trace quantity.
CLR-2	unshocked	~5×5×5	Control	20.93	0.09	0.04	No, massive	No	

Table 3.2. Description of properties of Moenkopi Sandstone sample blocks used in the weathering experiment. Same sample names with Roman numerals in brackets indicate blocks cut from the same big sample.

Moenkopi Sandstone (MS)	**Shock Pressure class**	**Sample Size (cm)**	**Type of rock**	**Porosity (%)**	**Grain size (mm)**	**Sorting**	**Lamination**	**Visible macrofracture in Hand sample**	**Petrographic overview**
MC8215-01	1A	~5×5×3	Crater wall rock	0.7	0.09	0.06	No, massive	Two sets of fractures passing through two facets, the first one is 2 cm in length and the second is 6 cm long. The aperture of the fractures is 0.1 mm	**Class 1a (<5GPa) MS** may have experienced <5GPa of shock pressure during impact. In hand specimen, there is no visible difference between class 1a and unshocked MS. No high-pressure polymorphs were identified in XRD analysis and no change in mineralogy was observed in class 1a MS compared to unshocked MS. Macroscopic fractures are present in some of the class 1a MS samples. Due to low shock, this porosity is reduced in class 1a MS. The porosity in low, shocked Moenkopi is 0.5-1%. No irregular grain fracturing due to impact can be seen in class 1a MS. A small amount of the quartz grains shows wavy extinction
MC51317-1	1A	~5×5×5	Crater wall rock	0.58	0.09	0.06	Three sets of sub-parallel cross-laminations	No	
MC51317-2	1A	~5×5×5	Crater wall rock	0.78	0.09	0.06	Three sets of sub-parallel cross-lamination	Six set of fracture along cross-lamination on different facets. the length of fracture ranges from 1-2 cm and aperture 0.1 mm	
MC51317-03	1A	~5×5×5	Crater wall rock	0.50	0.1	0.06	No, massive	No	
MC51317-4 (I)	1A	~5×5×5	Crater wall rock	1.09	0.1	0.07	Three sets of sub-parallel cross laminations	One big 5 cm long and 0.2 mm wide orthogonal fracture visible on all facets. Smaller fractures are ranging from 1-2 cm long 0.1 mm wide visible on multiple facets.	
MC51317-4 (II)	1A	~5×5×3	Crater wall rock	1.09	0.1	0.07	Two sets of sub-parallel cross-laminations	Three sets of fracture ranging from 1.5-5 cm and aperture 0.1-0.2 mm visible on three facets	
MC51317-5	1A	~5×5×5	Ejecta	0.74	0.09	0.07	Four set of sub-parallel cross lamination	No	
MC51317-6	1A	~5×4×5	Ejecta	0.83	0.09	0.07	No, massive	One set of 4 cm long fracture visible on two adjacent facets. the aperture of the fracture is 0.1 mm	
MC51417-1 (I)	1A	~5×5×5	Crater wall rock	0.96	0.09	0.05	Three set of sub-parallel cross lamination	No	
MC51417-1 (II)	1A	~5×5×4.5	Crater wall rock	0.96	0.09	0.05	One set of visible cross lamination	Two set of small fractures on two adjacent faces, ranging in length from 1-2.5 cm and aperture 0.1 mm	
MC51417-2 (I)	1A	~5×5×5	Ejecta	0.71	0.07	0.05	Three sets of sub-	No	

							parallel cross-laminations		
MC51417-2 (II)	1A	~5×5×5	Ejecta	0.71	0.07	0.05	One set of cross-lamination	No	
MC51417-2 (III)	1A	~5×5×2.5	Crater wall rock	0.71	0.07	0.05	Three sets of sub-parallel cross-laminations	No	
CS16-01	Unshocked	~5×5×5	Control	8.39	0.1	0.06	No, massive	No	**Unshocked Moenkopi** sandstone is very fine-grained sandstone which is cemented by carbonates. Moenkopi contains 50-80 % quartz, microcline, muscovite, hematite and kaolinite in minor amounts and remainder being composed of carbonate minerals (calcite and dolomite). Quartz is subrounded, equant, and well sorted and has subhedral grain boundary. The matrix is very fine grained and iron rich. The mean grain size ranges from 0.07-0.1 mm. The grain size ranges from 0.009-0.12 mm. The texture of the rock is grain supported.
CS16-02	Unshocked	~5×5×5	Control	5.23	0.08	0.06	Four set of sub-parallel cross lamination	No	

Table 3.3. Description of properties of crystalline impactite sample blocks used in the weathering experiment.

WCIS target rocks	Shock pressure class	Sample Size (cm)	Type of rock	Porosity (%)	Visible macrofracture in Hand sample	Petrographic overview
WCIS-14 MK-004	1a	~5×5×5	Target rock from around rim (granite)	0.07	Multiple macro-fractures on all surfaces ranging in length from 2-5 cm and 0.1 mm in aperture	**Class 1a granite (<10 GPa)** may have experienced <10 GPa shock pressure during impact. The granite sample has a pinkish grey hue in hand sample. Class 1a granite is medium grained hypidiomorphic, equigranular, with average grain-sizes varying from ~1 mm to up to ~3 mm. The granite samples contain quartz, albite, microcline and in minor amounts muscovite and clinochlore. Intragranular and intergranular fracturing is pervasive in the sample. Planar Fracture is present in quartz grains.
WCIS-14 MK-001a	1a	~3.5×3.5×3	Target rock from around rim (granite)	Negligible	One set of fracture 4 cm in length and 0.1 mm width only visible on two adjacent surfaces	
WCIS-14 Oz-015	1a	~4×3×3	Target rock from around rim (Tonalite)	0.26	No	**Class 1a tonalite (<10 GPa)** have undergone low shock (<10 GPa) deformation during impact. The sample looks greenish in hand sample. Class 1a tonalite is medium grained hypidiomorphic, equigranular, with average grain-sizes varying from ~ 1mm to up to ~3 mm. Class 1a tonalite contains quartz, albite, biotite, hornblende and in minor amounts calcite and clinochlore. Intragranular fracturing is pervasive in the sample. Kink bands can be observed in biotite. Planar Fractures in quartz is present.

Table 3.4. Description of properties of impact melt rock and impact breccia sample blocks used in the weathering experiment. Same sample names with Roman numerals in brackets indicate blocks cut from the same big sample.

Impactites	Sample Size (cm)	Type of rock	Porosity (%)	Visible macrofracture in Hand sample	Petrographic overview
WCIS-14 RW-019	~3.5×3.5×3.5	Clast rich fine-grained impact melt rock	2.91	No	This sample is massive and appears reddish-purple colour in hand sample due to oxidation of matrix. Clast rich melt rocks contain up to 25% fragments coarser than 1 mm. Clast rich impact melt rock contain quartz, andesine, sanidine, and minor muscovite, hematite and montmorillonite. Clasts usually compose 40-60%, and matrix occupies 60-40% of most of the samples (Rosa, 2012). The matrix is composed microlites made of iron oxide and plagioclase (<10 µm). The matrix has reacted with embedded clasts in clast rich impact melt rock. Clasts in the sample have micro-fractures.
WCIS-14 MK-082	~5×5×3	Clast poor fine-grained impact-melt rock	0.15	Multiple macro-fractures on all surfaces ranging in length from 1-5 cm and 0.1 mm in aperture	The clast poor impact melt rocks WCIS-14 MK-015, and WCIS-14 MK-087 appears red to purple in hand sample. Whereas, WCIS-14 MK-082 looks yellowish brown in hand sample. Clast poor impact melt rock contains less than 15% clasts larger than 1 mm across (Simonds et al., 1978, Rosa, 2012). Clast poor impact melt rocks WCIS-14 MK-015, and WCIS-14 MK-087 contain microcline, muscovite, andesine, and montmorillonite in minor quantity. Sample WCIS-14 MK-082 consist of quartz, anorthite, albite, sanidine and minor amounts of montmorillonite. In thin section, WCIS-14 MK-082 appears very different than WCIS-14 MK-015 and WCIS-14 MK-087. The melt matrix (size< 50 µm) in WCIS-14 MK-082 displays interlocking texture, whereas in WCIS-14 MK-015 and WCIS-14 MK-087 matrix displays fine-grained microlites (<10 µm) feldspar. Clasts in all clast poor impact melt rocks are fractured and reacted with the surrounding melt matrix. The matrix is oxidised in the samples. WCIS-14 MK-082 appears to be extensively chemically weathered/altered. WCIS-14 MK-015 may have been affected by hydrothermal alteration as it contains quartz vugs.
WCIS-14 MK-015	~5×5×3	Clast poor fine-grained impact melt rock	0.28	Multiple macro-fractures are ranging from 3-5 cm and 0.1 mm in aperture visible on multiple facets/ surfaces. Two vugs of diameter 0.5 and 1 cm are visible on two facets.	
WCIS-14 MK-087	~3×3×3	Clast poor fine-grained impact-melt rock	0.61	A few fractures ranging in length 1-2 cm with aperture less than 0.1 mm seen on three facets.	
WCIS-14 MK-60	~4×4×4	Clast free impact melt rock	1.51	One fracture 3 cm in length and 0.1 mm visible on one surface only	These samples contain no clast upto the size of 1 mm. These samples appear reddish brown in hand sample. They appear to be more coherent than clast rich- and clast poor- impact melt rocks. These samples contain quartz, anorthite, albite, muscovite, hornblende and minor montmorillonite. The matrix is oxidised and consist of devitrified glass. At high magnification, plagioclase laths (<10 µm) in matrix show interstitial texture. Clasts are fractured and have reacted to melt matrix.
WCIS-14 MK-077	~5×4×3	Clast free impact melt rock	0.21	No	
WCIS-14 MK-058B	~5×5×3	Lithic breccia	2.07	No	Lithic breccia appears red in hand sample. These samples contain larger clast (≥1 mm) embedded in the clastic matrix. The breccia samples consist of quartz, albite, orthoclase, muscovite, montmorillonite and minor hematite. The clasts are fractured and contain shock features. Toasted quartz and PDFs and PFs was observed in quartz and feldspar. In the thin section, matrix appears reddish brown due to oxidation.
WCIS-14 058C	~4×4×4	Lithic breccia	2.57	One set of fracture 4 cm in length and 0.1 mm in aperture visible on only one facet	
WCIS-14 Oz-005	~5×5×3	Impact melt-bearing breccia or suevite	3.46	Multiple small fractures of length 1.5 cm and aperture 0.1mm visible three facets	WCIS-14 Oz-005 contain red, oxidised impact melt particles set in a fine-grained matrix. Glass component is surrounded by clastic groundmass (Osinski and Grieve, 2017). It contains clasts of quartz, feldspar. The clasts range in size from 100-900 micron. Hematite was present as opaque minerals. Some of the feldspar clasts are altered. Quartz clasts were fractured. The microfractures range from 0.1 to 4 microns in width. The glass fragment contains vesicles.
Suevite (I)	~5×5×5	Impact melt-bearing breccia or suevite	10.39	Multiple macro-fractures on all surfaces ranging in length from 1-5 cm and 0.1-0.2 mm in an aperture on all facets of the rocks.	Suevite samples contain clasts of vitric or glassy material, quartz, albite, microcline, hornblende, and minor amounts of muscovite and prehnite. Mineral clasts are 100-700 micron in diameter. The clast and lithic fragments are supported by clastic groundmass which forms up to ~80 % of the volume of which 30-50 % is glass (Osinski et al., 2004). All the mineral clasts are highly fractured, planar fractures were observed in some quartz grains, but most of the clast do not contain high-pressure shock features. The microfractures were 0.5-6 micron in width. Some of the mineral grains are appearing to be weathered. The samples contained macro-fractures in hand sample with aperture 0.2-0.4 mm and up to 2-5 cm in length.
Suevite (II)	~5×5×5	Impact melt-bearing breccia or suevite	10.39	Multiple macro-fractures on all surfaces ranging in length from 1-5 cm and 0.1-0.2 mm in the aperture. In hand sample observation, this sample contains more fractures and vitreous phases compared to Suevite (I)	

3.3.2. Experimental results

Figure 3.1 d and e show that our experimental design was successful in reproducing air and relative humidity changes known in semi-arid terrestrial conditions. At low temperatures (-2 to 5°C), a layer of dew was observed to precipitate on the top surface of the blocks. A gypsum salt crust was noted on the sand layer following water spray. At the end of the experiment, salt efflorescence can be seen on the surface of the blocks in contact with the sand-salt bed. In the following section, results from different types of impactites used in the weathering experiments are reported separately.

3.3.2.1. Sedimentary impactites

3.3.2.1.2. Coconino Sandstone (CS)

Table 3.5. Summary of results from weathering and desalination experiment

Coconino Sandstone	Shock pressure class	Equotip Leeb values before the experiment	Equotip Leeb values after the experiment	% change in Leeb values due to experiment	Equotip Leeb values after desalination	% change in Leeb values due to desalination	Conductivity (µS/cm)	%change in weight due to weathering experiment	%change in weight due to desalination
MC51417-5 (I)	1A	418	383	-8.37%	388	-7.18%	58	-0.12%	-0.07%
MC51417-5 (II)	1A	373	334	-10.46%	334	-10.46%	63	-0.09%	-0.07%
MC51417-6	1A	379	326	-13.98%	345	-8.97%	25	-0.06%	-0.05%
MC51417-7	1A	343	322	-6.12%	331	-3.50%	65	-0.08%	-0.07%
MC51417-8	1A	303	270	-10.89%	285	-5.94%	42	-0.07%	-0.06%
MC51417-9	1B	not measured	not measured	-	not measured	-	81	-0.45%	-0.23%
MC51517-2	1A	393	342	-12.98%	351	-10.69%	78	-7.42%	-0.09%
MC51517-4	1A	345	289	-16.23%	322	-6.67%	43	-0.07%	-0.03%
MC51517-8 (I)	1A	430	399	-7.21%	397	-7.67%	18	-0.05%	-0.04%
MC51517-8 (II)	1A	427	406	-4.92%	397	-7.03%	20	-0.04%	-0.03%
CLR-1	unshocked	386	363	-5.96%	355	-8.03%	31	-0.09%	-0.05%
CLR-2	unshocked	373	357	-4.29%	349	-6.43%	21	-0.10%	-0.05%
Mean percent change	**1A**			**-10.13%**		**-7.57%**		**-0.89%**	**-0.06%**
Mean percent change	**1B**			**not measured**		**not measured**		**-0.45%**	**-0.23%**
Mean percent change	**unshocked**			**-5.13%**		**-7.23%**		**-0.10%**	**-0.05%**

Most of the low shocked CS, assigned to shock pressure class 1a (Table 3.1) exhibited a higher loss in Leeb hardness values compared to unshocked CS following the weathering experiment (Fig 3.2). In terms of weight loss class 1a CS did not show any significant difference compared to unshocked rocks during weathering and desalination experiment (Fig 3.3). Sample MC51517-2 was the exception with the most significant amount of breakdown and debris (Fig 3.3). After desalination experiment class 1a CS (with the exception of MC51517-8 (I) and MC51517-8 (II)) gained strength whereas unshocked CS samples lost strength (Fig 3.2).

CS sample (MC51417-9) the only sample representing class 1b shock pressure class show a much more significant loss in weight in comparison to its unshocked counterpart during weathering and desalination experiment (Fig 3.3). This sample was not tested for rock strength using equotip as it was friable and start breaking with slight hand pressure.

Most of the class 1a and the sample 1b CS showed higher conductivity during desalination experiment (Table 3.5). The higher conductivity showed no correlation to higher porosity. X-ray CT examination did not reveal any new fracture growth or change in existing fracture aperture and length due to weathering experiment.

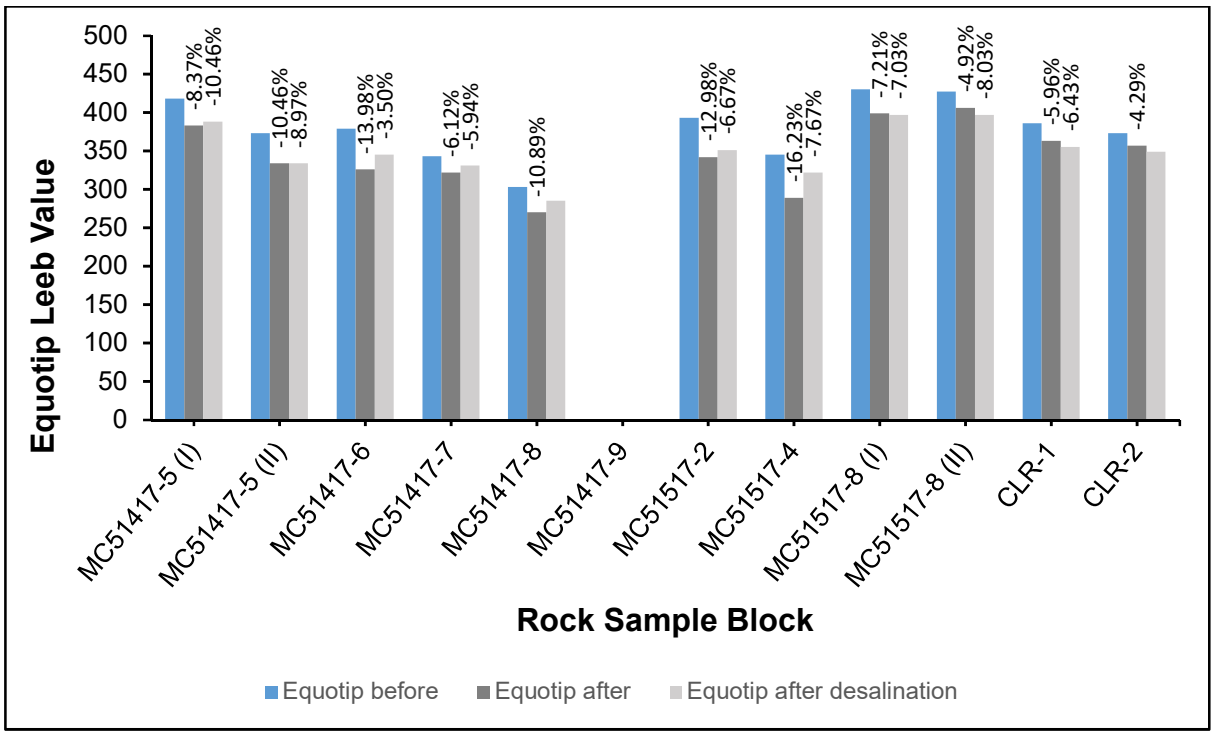


Fig 3.2. Change in Equotip Leeb Hardness value in Coconino Sandstone shock class 1a samples due to the weathering and desalination experiment. The percent value on top of each column is the percent change from the initial Leeb value. Equotip measurements were not obtained for shock class 1b sample MC51417-9 because it was friable.

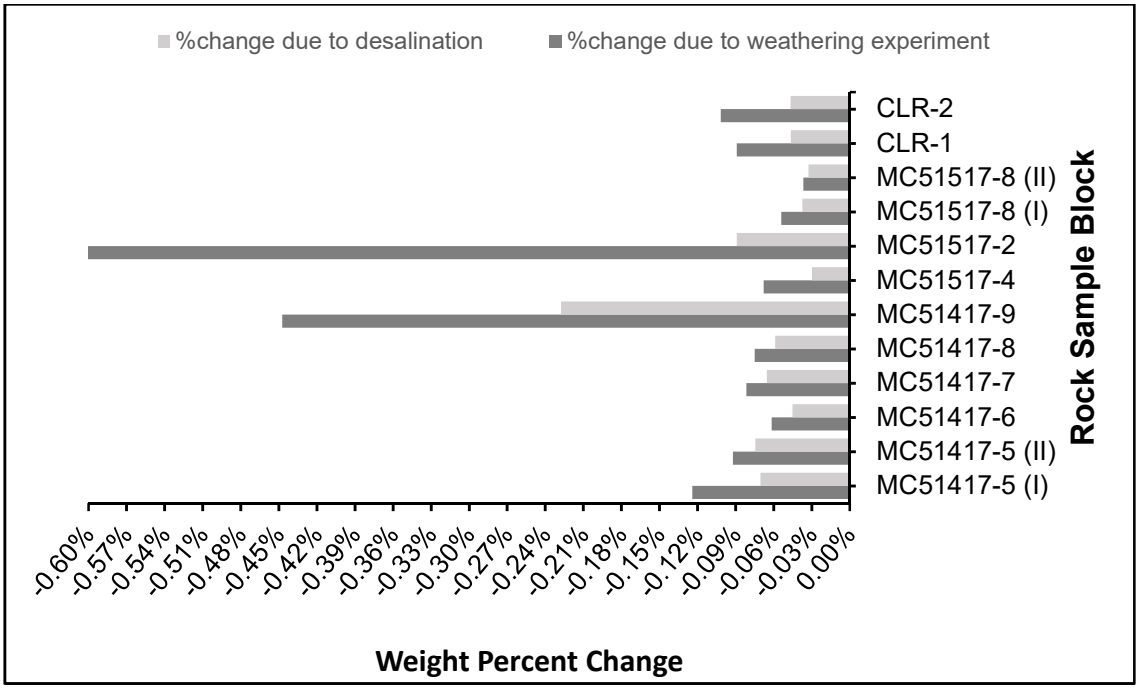


Fig 3.3. Percent weight change in Coconino Sandstone samples due to the weathering and desalination experiment (including shock class 1b sample MC51417-9).

3.3.2.1.2. Moenkopi Sandstone (MS)

Table 3.6. Summary of results from weathering and desalination experiment

Moenkopi Sandstone	Shock Pressure class	Equotip Leeb values before the experiment	Equotip Leeb values after the experiment	% change in Leeb values due to experiment	Equotip Leeb values after desalination	% change in Leeb values due to desalination	Conductivity (µS/cm)	%change in weight due to weathering experiment	%change in weight due to desalination
MC8215-01	1A	461	435	-5.64%	430	-6.72%	103	0.02%	-0.25%
MC51317-1	1A	485	470	-3.09%	464	-4.33%	102	0.20%	-0.16%
MC51317-2	1A	485	466	-3.92%	462	-4.74%	188	0.30%	-0.05%
MC51317-03	1A	489	461	-5.73%	458	-6.34%	80	-0.05%	-0.19%
MC51317-4 (I)	1A	450	449	-0.22%	429	-4.67%	186	0.23%	-0.21%
MC51317-4 (II)	1A	472	462	-2.12%	437	-7.42%	104	-0.07%	-0.21%
MC51317-5	1A	515	490	-4.85%	488	-5.24%	74	-0.01%	-0.17%
MC51317-6	1A	460	433	-5.87%	420	-8.70%	84	0.63%	-0.19%
MC51417-1 (I)	1A	451	432	-4.21%	430	-4.66%	87	-0.08%	-0.12%
MC51417-1 (II)	1A	432	423	-2.08%	398	-7.87%	63	0.19%	-0.12%
MC51417-2 (I)	1A	484	458	-5.37%	462	-4.55%	78	0.07%	-0.13%
MC51417-2 (II)	1A	501	479	-4.39%	473	-5.59%	92	0.02%	-0.13%
MC51417-2 (III)	1A	470	447	-4.89%	443	-5.74%	56	0.14%	-0.13%
CS16-01	unshocked	451	419	-7.10%	418	-7.32%	70	-0.06%	-0.12%
CS16-02	unshocked	503	474	-5.77%	474	-5.77%	70	0.03%	-0.15%
Mean	**1A**			**-4.03%**		**-5.89%**		**0.12%**	**-0.16%**
Mean	**unshocked**			**-6.44%**		**-6.55%**		**-0.02%**	**-0.14%**

All of the low shocked Moenkopi sandstone samples belong to class 1a. In these samples, primary porosity is reduced to ≤1% from ~5-8% in unshocked samples (Table 3.2). Some class 1a samples contain macroscopic fractures visible in hand samples (Table 3.2). Class 1a low shocked MS samples with no visible macro-fractures showed a similar loss in Leeb hardness to unshocked control samples due to weathering and desalination experiment (Fig 3.4). Class 1a MS samples with visible macro-fractures on the bottom surface in hand samples exhibited lower change Leeb hardness compared to unshocked control and other class 1a MS samples (Fig 3.4 and Table 3.2). The macro-fractures on the bottom surface (surface in contact with the sand-salt surface) in class 1a assisted in salt uptake due to capillary action which likely increased strength. These samples gained weight due to salt uptake might be higher than the loss of weight due to granular disintegration (Fig 3.5). In addition, the first conductivity measurement of the water containing these samples had higher conductivity values in comparison with unshocked control counterparts (Table 3.6). After desalination experiment, all the Class 1a MS samples lost strength as the salts were removed from the fractures. Unshocked control samples showed very little to no change (Fig 3.4). After desalination experiment, all the class 1a samples which initially gained weight during the weathering experiment had lost weight (Fig 3.5). Of note is that Class 1a MS containing macro-fractures showed a higher decrease in strength after desalination compared to unshocked and other class 1a MS (Fig 3.4 and Table 3.2).

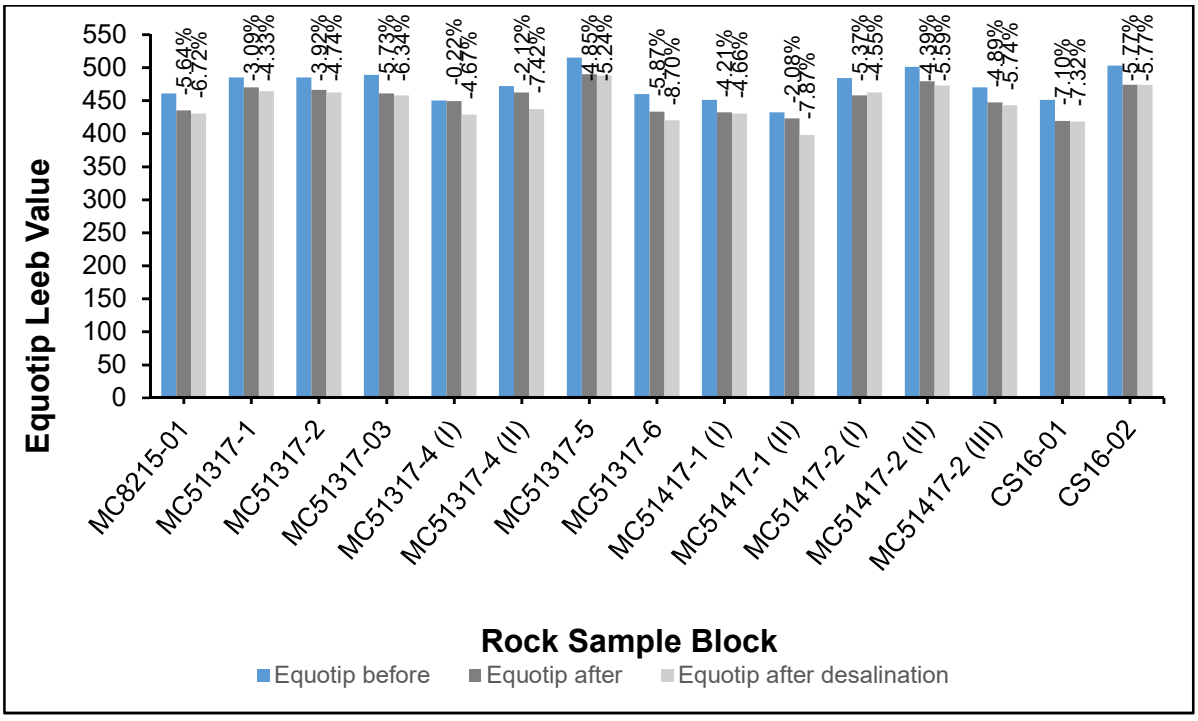


Fig 3.4. Change in Equotip Leeb Hardness value in Moenkopi Sandstone samples due to the weathering and desalination experiment. The percent value on top of each column is the percent change from the initial Leeb value.

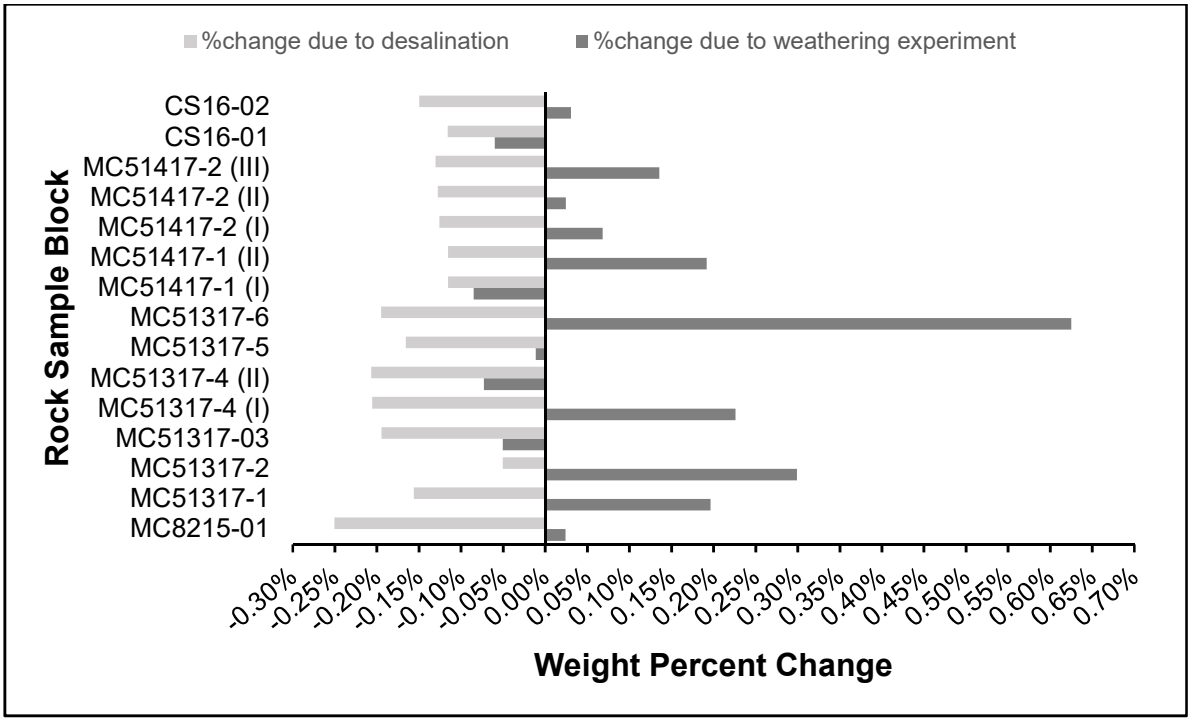


Fig 3.5. Percent weight change in Moenkopi Sandstone samples due to the weathering and desalination experiment.

3.3.2.2. Crystalline Impactites

Table 3.7. Summary of results from weathering and desalination experiment

WCIS target rocks	Shock pressure class	Equotip Leeb values before the experiment	Equotip Leeb values after the experiment	% change in Leeb values due to experiment	Equotip Leeb values after desalination	% change in Leeb values due to desalination	Conductivity (µS/cm)	%change in weight due to weathering experiment	%change in weight due to desalination
WCIS-14 MK-004	1a	855	835	-2.34%	824	-3.63%	22	0.00%	-0.03%
WCIS-14 MK-001a	1a	733	685	-6.55%	656	-10.50%	20	0.01%	-0.06%
WCIS-14 Oz-015	1a	710	708	-0.28%	658	-7.32%	16	0.01%	-0.04%

Two samples of low shocked granite and one sample of low shocked tonalite were used in the weathering experiment of crystalline impactites. These samples belonged to shock pressure class 1a. These rocks did not have an unshocked control counterpart.

Class 1a tonalite sample (WCIS-14 Oz-015) showed minimal change in strength due to weathering experiment but showed a higher change in strength following desalination (Fig 3.6). Class 1a granite samples (WCIS-14 MK-001a and WCIS-14 MK-004) exhibited a higher change in Leeb hardness compared to tonalite (Fig 3.6). The variation between granite samples may be due to impact-induced deformation heterogeneity. All samples showed a lowering of Leeb hardness following desalination (Fig 3.6). While there was negligible weight loss due to weathering experiment or desalination (Fig 3.7). No visible granular fragments were observed, and X-ray CT examination did not show any new fracture growth or change in existing fracture aperture and length.

Shocked crystalline rocks have higher initial Leeb hardness compared to sedimentary impactites that represent the higher strength of crystalline rocks (Table 3.5-3.7). After desalination experiment class 1a granite and tonalite samples (WCIS-14 MK-001a and WCIS-14 Oz-015) showed a higher change in strength compared to unshocked Moenkopi and Coconino Sandstone samples, and most of the low-shocked Moenkopi sandstone (Table 3.5-3.7 and Fig 3.2, 3.4, and 3.6).

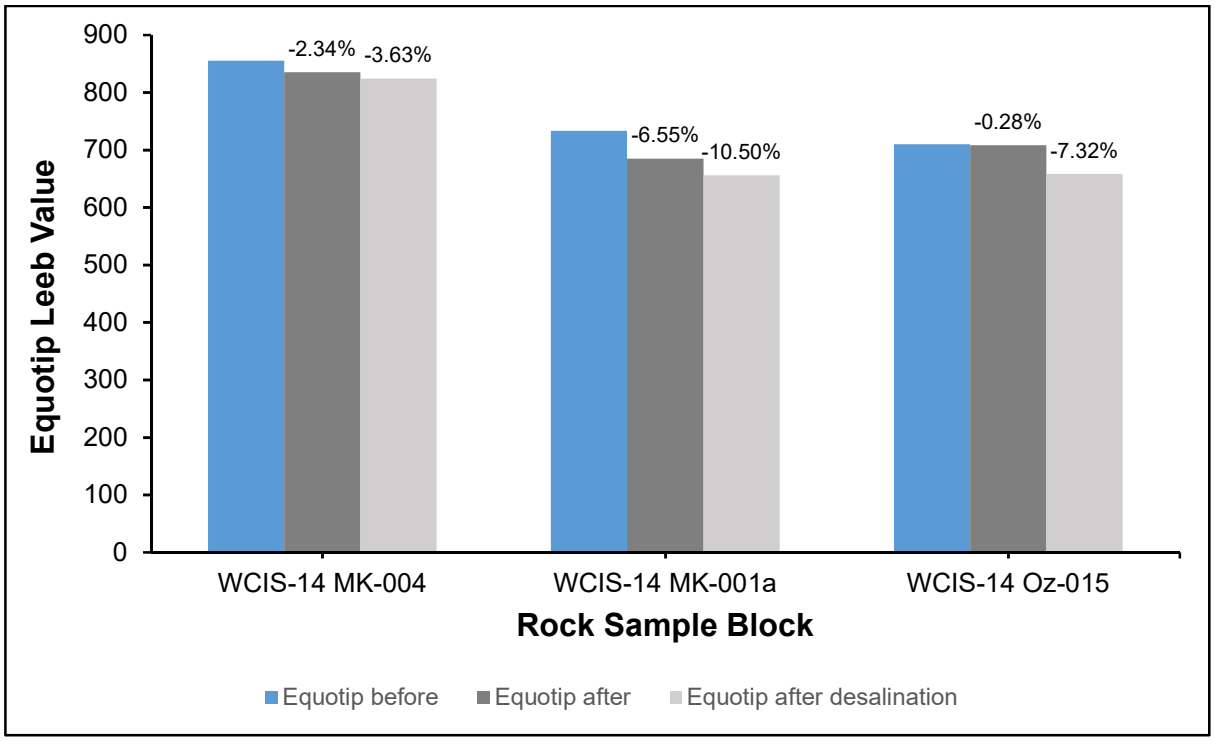


Fig 3.6. Change in Equotip Leeb Hardness value in crystalline impactites samples due to the weathering and desalination experiment. The percent value on top of each column is the percent change from the initial Leeb value.

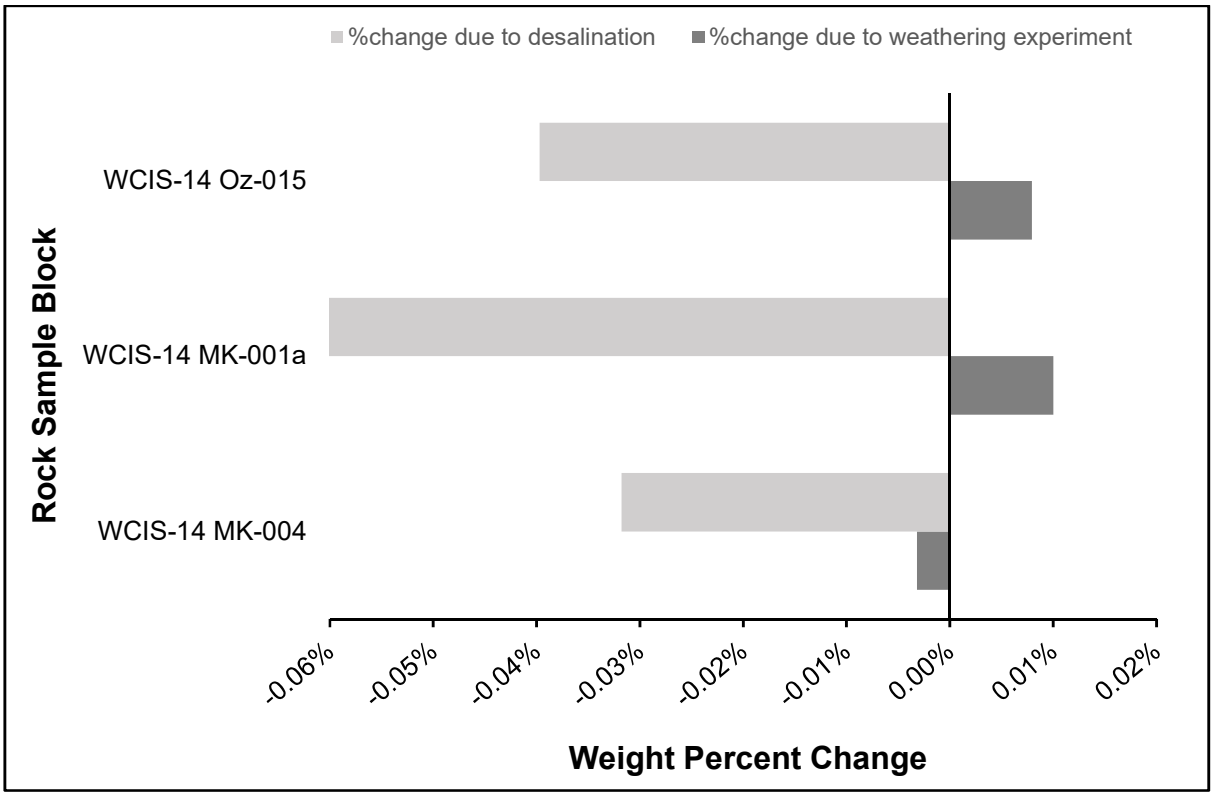


Fig 3.7. Percent weight change in crystalline impactite samples due to the weathering and desalination experiment.

3.3.2.3. Impact melt rocks and impact breccias

Table 3.8. Summary of results from weathering and desalination experiment

Impactites	Type of rock	Equotip Leeb values before the experiment	Equotip Leeb values after the experiment	% change in Leeb values due to experiment	Equotip Leeb values after desalination	% change in Leeb values due to desalination	Conductivity (µS/cm)	%change in weight due to weathering experiment	%change in weight due to desalination
WCIS-14 RW-019	Clast rich fine-grained impact melt rock	643	654	1.71%	578	-10.11%	16	-0.26%	-0.21%
WCIS-14 MK-082	Clast poor fine grained impact-melt rock	603	529	-12.27%	494	-18.08%	27	0.71%	-0.13%
WCIS-14 MK-015	Clast poor fine-grained impact melt rock	730	711	-2.60%	703	-3.70%	16	0.01%	-0.11%
WCIS-14 MK-087	Clast poor fine grained impact-melt rock	642	637	-0.78%	599	-6.70%	7	-0.17%	-0.43%

WCIS-14 MK-60	Clast free impact melt rock	769	740	-3.77%	723	-5.98%	15	-0.15%	-0.11%
WCIS-14 MK-077	Clast free impact melt rock	772	742	-3.89%	729	-5.57%	13	-0.02%	0.00%
WCIS-14 MK-058B	Lithic breccia	623	533	-14.45%	585	-6.10%	21	-0.13%	-0.08%
WCIS-14 058C	Lithic breccia	513	490	-4.48%	483	-5.85%	17	-0.04%	-0.82%
WCIS-14 Oz-005	Impact melt bearing breccia or suevite	476	402	-15.55%	404	-15.13%	27	-0.33%	-0.61%
Suevite (I)	Impact melt bearing breccia or suevite	321	327	1.87%	312	-2.80%	61	1.45%	-1.11%
Suevite (II)	Impact melt bearing breccia or suevite	394	351	-10.91%	324	-17.77%	53	2.01%	-1.28%

3.3.2.3.1. Clast rich fine-grained impact-melt rock

WCIS-14 RW-019 is a clast rich impact melt rock. The sample had an initial Leeb value lower than shocked crystalline impactites (Table 3.7-3.8). RW-019 showed a gain in strength during weathering experiment possibly due to salt uptake (Fig 3.8). After desalination experiment, the sample lost strength (Fig 3.8). This sample lost 0.26% in weight during weathering experiment (Fig 3.9). The sample may have lost more weight due to granular disintegration than gained weight due to salt uptake. The sample shows a slight loss in weight after the desalination (Fig 3.9).

3.3.2.3.2. Clast poor fine-grained impact-melt rock

WCIS-14 MK-015, WCIS-14 MK-087 and WCIS-14 MK-082 are clast poor fine-grained impact melt rocks. WCIS-14 MK-015 have fractures visible in hand sample. The sample had an initial Leeb value similar to crystalline impactites (Table 3.7-3.8). This sample lost strength during weathering experiment (Fig 3.8). The sample also lost strength after desalination (Fig 3.8). The sample exhibits a slight gain in weight due to salt uptake during weathering experiment (Fig 3.9). After desalination, the sample lost more weight than after weathering experiment (Fig 3.9).

WCIS-14 MK-087 had initial Leeb value lower than crystalline rocks (Table 3.7-3.8). This sample lost very little strength during weathering experiment (Fig 3.8). The sample lost strength after desalination (Fig 3.8). The sample lost weight during weathering experiment and lost slightly more weight after desalination (Fig 3.9). The slight differences in the behaviour of both samples could be due to internal variation (e.g. macro-fractures, crystallites arrangement).

WCIS-14 MK-082 had initial Leeb value lower than crystalline impactites (Table 3.7-3.8). The sample lost strength due to the weathering experiment (Fig 3.8). The sample lost even

more strength after desalination (Fig 3.8). The sample gained weight during weathering experiment possibly due to salt uptake (Fig 3.9). The sample lost a little weight after desalination (Fig 3.9).

WCIS-14 MK-082 exhibited the highest rate of deterioration among clast poor impact melt rocks.

3.3.2.3.3. Clast free impact melt rock

WCIS-14 MK-060 and WCIS-14 MK-077 are clast free impact melt rock. The sample had an initial Leeb value similar to crystalline rocks (Table 3.7-3.8). The samples lost strength during weathering experiment and after desalination (Fig 3.8). These samples lost a little weight during weathering experiment (Fig 3.9). The sample WCIS-14 MK-077 lost less weight during the weathering and desalination experiment than WCIS-14 MK-060 (Fig 3.9).

3.3.2.3.4. Lithic breccia

WCIS-14 MK-058B and WCIS-14 058C are lithic breccia which contains no melt. These samples had an initial Leeb value lower than crystalline impactites (Table 3.7-3.8). WCIS-14 058C has lower initial Leeb values compared to WCIS-14 MK-058B (Table 3.8). WCIS-14 MK-058B lost more strength during weathering and desalination experiment in comparison to WCIS-14 058C (Fig 3.8). WCIS-14 MK-058B showed more loss in weight than WCIS-14 058C after weathering experiment (Fig 3.9). After desalination WCIS-14 058C lost more weight than WCIS-14 MK-058B (Fig 3.9).

3.3.2.3.5. Impact melt-bearing breccia or suevite

Suevite (I), Suevite (II), and WCIS-14 Oz-005 are impact melt-bearing breccia or suevitic breccia. These samples had an initial Leeb value lower than crystalline impactites and similar to sedimentary impactites (Table 3.5-3.8). Suevite (II) contains more visible fracture and vitric clasts than Suevite (I). Suevite (II) and WCIS-14 Oz-005 lost strength during weathering experiment, but Suevite (I) gained strength (Fig 3.8). After desalination experiment, all samples lost strength, but Suevite (I) show a little loss in strength (Fig 3.8). Suevite (I) and Suevite (II) gained weight due to salt uptake during weathering experiment due to salt uptake through the macro-fractures (Fig 3.9). However, WCIS-14 Oz-005 lost weight during weathering experiment (Fig 3.9). After desalination, all the samples lost weight (Fig 3.9).

X-ray CT examination did not show any new fracture growth or change in existing fracture aperture and length due to weathering experiment in any of the samples.

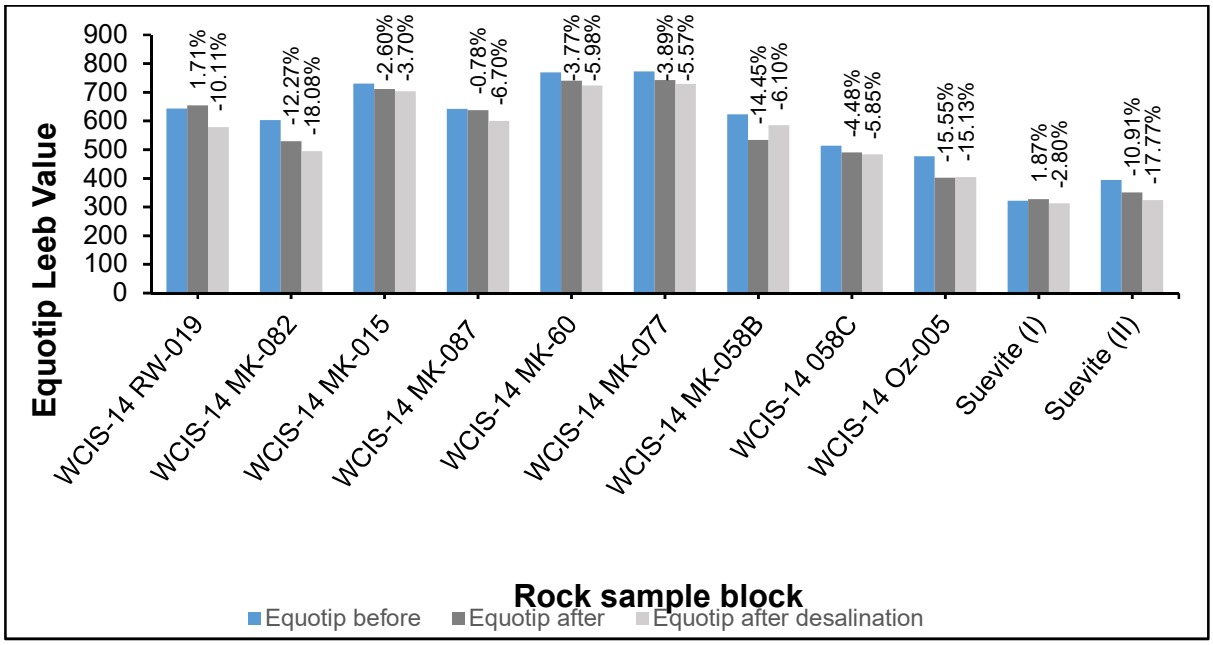


Fig 3.8. Change in Equotip Leeb Hardness value in Impact melt rock and impact breccia samples due to the weathering and desalination experiment. The percent value on top of each column is the percent change from initial leeb value.

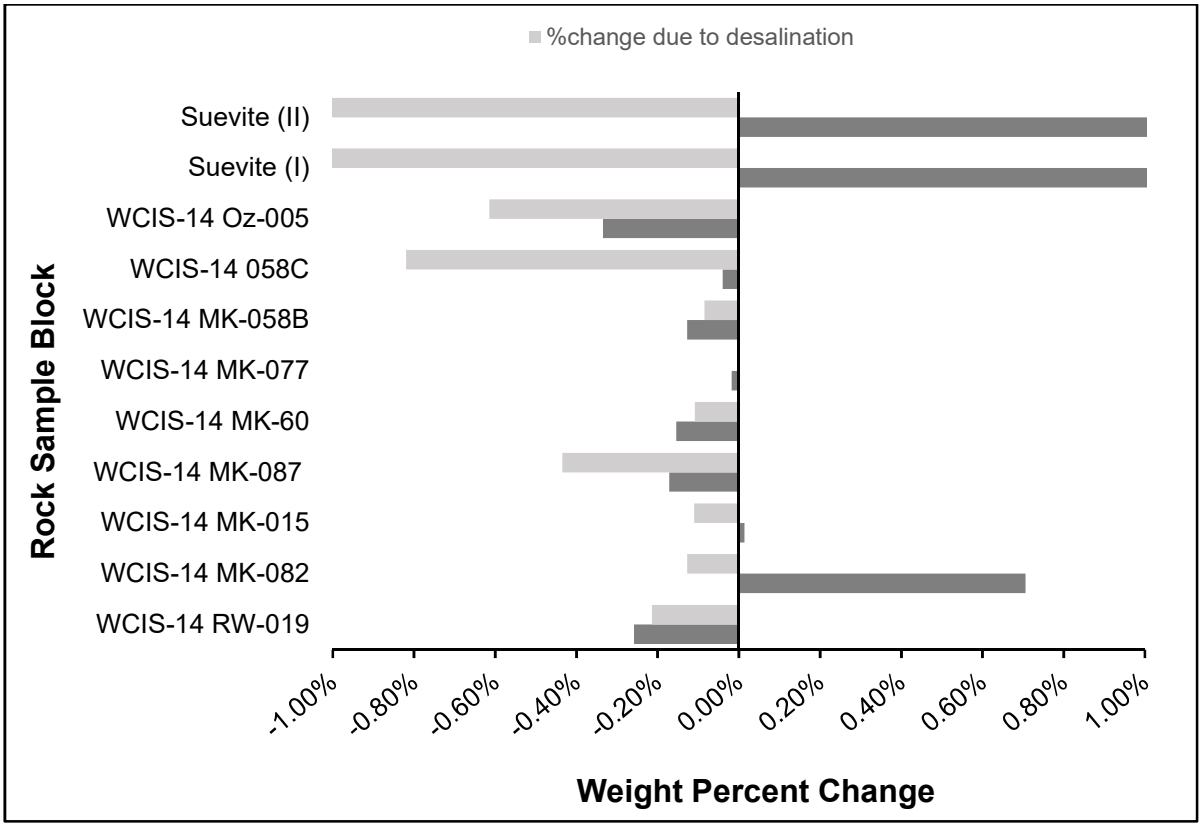


Fig 3.9. Percent weight change in impact melt rock and impact breccia samples due to the weathering and desalination experiment.

3.4. Discussion and interpretation

3.4.1. Role of simulated semi-arid environmental conditions

The decline in strength and loss of weight of the sample blocks under semi-arid terrestrial environment conditions demonstrates that the semi-arid environmental conditions may be sufficient to instigate breakdown. These findings suggest that relatively moderate rates of heating and cooling (dT/dt = ~0.15°C/min in this experiment) in the presence of salt and moisture can induce breakdown in rocks and the often cited 2°C/min thermal shock threshold is not required. Under the semi-arid conditions simulated in this study our experiment shows that rocks with impact inheritance tend to deteriorate faster than non-impacted rocks.

At night-time, cold conditions (low temperatures, lamp off) in the presence of high relative humidity, gypsum may have been mobilised. Lower loss or increase in strength in some impactites with macro-fractures compared to their counterparts with no visible macro-

fractures or non-impacted control samples are noted due to the uptake of salt by the capillary rise through fractures present in the bottom surface in contact with sand-salt layer. Because of its low mobility and solubility compared to other salts (e.g. sodium sulphate, sodium nitrate), gypsum tends to accumulate in the larger macro fracture opening (Charola et al., 2007), the accumulation of salt start to close the macro-fractures openings and inhibits subsequent ingress of salt and moisture (Smith et al., 2011). Similar behaviour was also recorded during initial cycles in laboratory weathering experiments for gypsum treated sandstone blocks by (Williams and Robinson, 2001) and other sodium sulphate treated sandstone (Ghobadi and Babazadeh, 2015) and crystalline rocks (Zhu et al., 2003; Viles et al., 2010; Viles et al., 2018). However, after removal of salts by desalination experiment, these samples exhibited a loss in strength. This suggests that if the length of our experiment were longer, the weakening of blocks that have taken up salt would have occurred. The effectiveness of salt depends on a combination of its solubility, rate of solubility changes with temperature, crystal habit, the rate of crystal growth and volume increases associated with hydration/dehydration changes (Warke, 2007). Due to its low solubility and mobility, gypsum salts are not as aggressive as other more soluble salts such as sodium sulphate and sodium nitrates. However, in the presence of other salt species and more extended exposure in the environment gypsum salts can cause a breakdown in rocks as the initial cementing role of salts is replaced by a deteriorative role (Williams and Robinson, 2001; Charola et al., 2007).

3.4.2. Size and shape of the blocks

Some of the sample blocks used in the weathering experiment were cuboidal instead of a cube, and few of them had a smaller dimension ca. 3 cm. In order to understand the possible effects of variations in size and shape of blocks on weathering experiment results, we tested blocks with slight variation in size and shape. We obtained blocks of different size and shape (cube and cuboid in this experiment) from a few larger samples collected in the field. In the experiment, we found that a small (~ 1-2 cm in side length) variation in size and shape did not affect the response of sample blocks due to the weathering experiment. The block response is more influenced by internal variation (e.g. presence and distribution of flaws such as fractures and laminations, distribution of vitric phases in the sample) than the size and shape of the blocks.

3.4.3. Severity and mode of deterioration

Our weathering experiment simulated natural semi-arid field conditions for a short duration of time. This did not have a significant effect on most of the blocks, and no severe damage was observed compared to those observed in a longer weathering experiment simulations (e.g. (Warke, 2007)

Small amounts (0.03 g) of granular disintegration was noticed in some of the Class 1a MS samples (Fig 3.10), and class 1b CS sample. A few of the impact melt rocks (WCIS-14 MK-082), and impact melt-bearing breccias (Suevite I and Suevite II) also lost material due to granular disintegration. Class 1a Coconino Sandstone lost measurable mass through granular disintegration, but due to the similar colour of the base sand layer, it was difficult to differentiate between the debris and sand used in the experiment.

We also observed salt efflorescence on many sample blocks in contact with the sand-salt layer in the experiment.

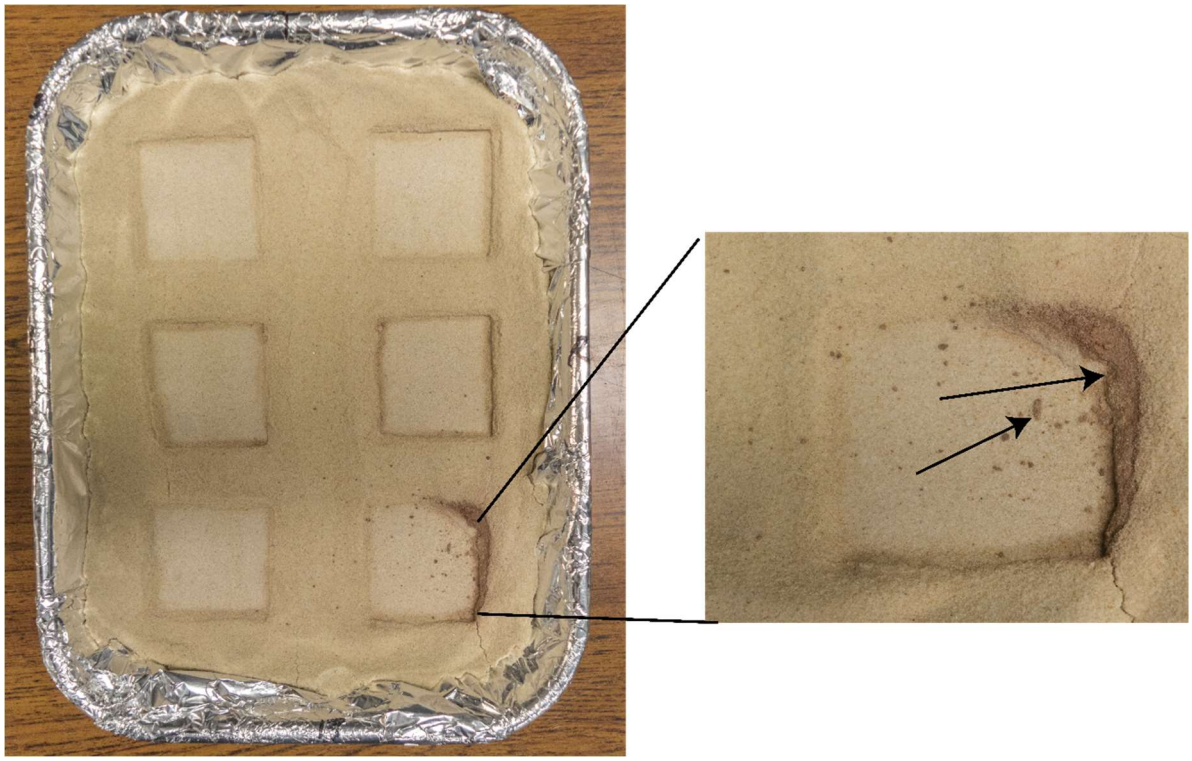


Fig 3.10. The observed breakdown in rock samples. Black arrows show chips and granular disintegrated material in class 1a MS after the sample block is removed from the bed.

3.4.4. Fracture propagation

The sample blocks were monitored using X-ray CT before and after the weathering experiment to understand the role of impact generated macroscopic fractures to subsequent weathering. CT scans were helpful in visualising and quantifying pre-existing fractures in the blocks (Fig 3.11). While no changes in aperture or length of the fractures were observed following the weathering experiment in CT images, some factors may be responsible for this. First, the resolution of CT images (46 μm) may not have been sufficient to resolve any changes in existing fractures or indeed detect a newly generated fracture. Second, the weathering simulation may not have produced any change. Regardless, we are confident that this technology, which can yield higher resolutions, will enable a better understanding of rock response that is normally not accessible to the investigator to assess a change in the short length.

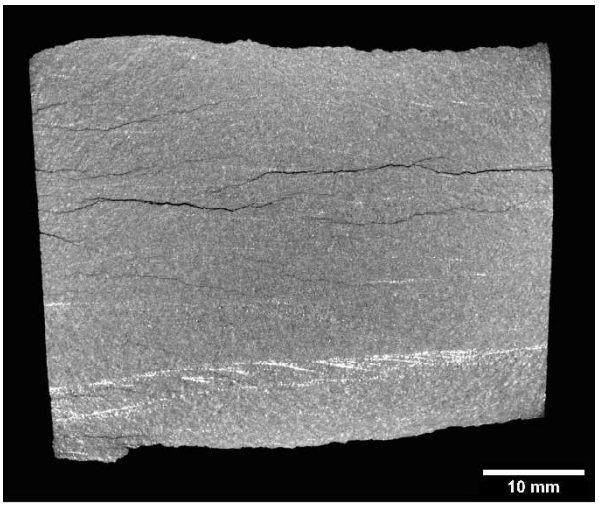


Fig 3.11. Macro-fractures seen in a class 1a MS (MC51317-4_I) block in X-ray CT image. The aperture of fractures ranges from 0.09-0.2 mm. In the bottom portion of the sample, one set of cross laminations is visible. Resolution of the image is 46 μm/voxel.

3.4.5. Lithology

In our experiment, different impactites were subjected to identical weathering conditions. Thus the results can be broadly compared.

There was no significant difference in initial strength of class 1a shocked and unshocked control CS samples. Even though porosity is reduced in class 1a CS compared to unshocked CS (Table 1a), class 1a CS showed an accelerated loss of strength in comparison with unshocked CS. This may be due to the presence of irregular intragranular fractures in quartz

grains. It is likely that intragranular fractures are exploited and enlarged by thermal stressing in the presence of salt and moisture. This would lead to an accelerated weakening in class 1a Coconino Sandstone. In previous studies, it was noted that the CS samples are also weaker along lamination planes (Kieffer, 1971a). The passage of shock wave in the Coconino Sandstone may also have made samples weaker along these laminations (Kieffer, 1975).

At shock pressure class 1b, the passage of shock wave has caused weak lithification in CS due to extensive grain fracturing and comminution (Kieffer, 1975). As a result, the CS has become friable and easily breaks down under slight hand pressure. This sample had lower initial strength compared to class 1a and unshocked CS, as the sample was so soft that equotip measurement was not possible. Primary porosity was reduced in this sample due to compaction and grain rotation. However, similar to sample 1a, secondary porosity due to grain fracturing support the ingress of salt and moisture. The sample easily loses mass due to granular disintegration. This sample showed evidence of more rapid breakdown relative to all other samples. Suggesting, that even in low shocked rocks of specific lithologies, an increase in shock influences breakdown rates, if not styles of breakdown. Future access to samples for experimental work will permit these findings to be validated.

Although not statistically significant, we found that the trend is for weathering of Coconino Sandstone to have been more strongly expressed relative to Moenkopi Sandstone in the low shock pressure deformation class (1a). This can be due to two reasons –

1. Coconino Formation being the closest to the point of impact might have experienced relatively higher shock deformation in low shock pressure regime (0-5 GPa) compared to Moenkopi Formation which represents the free surface of the impact site (Kring, 2017).
2. The finer grain size of Moenkopi Sandstone (0.07-0.1 mm) and low porosity (5-8%) when compared to Coconino Sandstone (grain size = 0.09-0.16 mm, porosity = 20%), may have led to a different response in low shock pressure regime (0-5 GPa). Class 1a MS only exhibits a reduction in porosity, unlike class 1a CS, it is not affected by irregular fracturing in quartz grains. This difference may be key in the subsequent expression of rock breakdown in sandstone.

The response of specific samples during the experiments did not always indicate the final outcome. We found a significant difference in the response of the class 1a MS which initially

showed a decrease in strength but at the end of the cycle, showed a trend to increase in strength, although, not back to initial values. Unshocked Moenkopi Sandstone did not have this trend. We hypothesise that this is due to the higher frequency of macro-fractures in the class 1a MS that creates accommodation space for the precipitation of salts. Class 1a MS that had macrofractures became stronger due to the ingress of salts via macrofractures. However, following de-salination the rock samples exhibited an accelerated decrease in strength compared to unshocked and other class 1a MS. This suggests that macro-fractures in class 1a MS samples are compensating for the loss in porosity and if the experiment were extended in duration, perhaps class 1a samples may have shown higher deterioration relative to unshocked samples.

Unusually class 1a CS gained strength following desalination. This may be due to grain size, composition and packing difference in two different types of sandstone (Israeli and Emmanuel, 2018). However, there is no conclusive explanation for this behaviour of class 1a CS since this was not observed in unshocked CS.

Class 1a crystalline granite and tonalite were much stronger than Coconino and Moenkopi Sandstone. These rocks have coarser grains and smaller macro-fractures than MS samples. These samples had a negligible primary porosity (0.07-0.2 %), however intergranular(?) and intragranular fracturing in these rocks created space for moisture and salt ingress. The smaller pores in crystalline impactites limited the initial salt and moisture penetration whereas macro-fractures aided in ingress of salt and moisture. After a few wetting cycles, cementation of salt in macro-fractures blocked the subsequent ingress of moisture and salt in the fracture openings. These rocks showed a muted response during weathering experiment. After removal of cemented salts by desalination experiment the rocks show a higher loss of strength. This loss of strength was comparable to low shocked sandstone samples. Nevertheless, low shocked crystalline impactites do not lose material as much as low shocked sedimentary impactites due to weathering and desalination experiment because these samples are much stronger than sandstone samples and require longer stressing to start deterioration.

Impact melt-bearing breccias or suevites were weaker than crystalline rocks, lithic breccias and impact melt rocks but have similar strength as class 1a sandstone. Impact melt-bearing breccia exhibited the highest loss in strength and weight among impact breccias and impact melt rocks. They deteriorate faster than class 1a sandstone and crystalline rocks.

Lithic breccias are weaker than crystalline rocks and impact melt rocks but were as strong as class 1a sandstone. The loss of strength in lithic breccias was higher than impact melt rocks but similar to class 1a sandstone and crystalline rocks.

Heterogeneous and anisotropic nature of gains and lithic fragment arrangement by finer grained matrix made impact melt breccia and lithic breccia less cohesive than other impactites. The coefficient of thermal expansion and heat capacity of different crystalline and amorphous phases are different (Fei, 1995; Navrotsky, 1995). Mismatch in the thermal response of neighbouring grains due to these thermal properties may enhance deterioration due to heating and cooling. Because of the heterogeneous arrangement of grains, impact breccias might experience higher thermal fatigue due to thermal cycling.

Impact melt rocks are weaker than crystalline rocks but are stronger than impact melt-bearing breccia, lithic breccia and class 1a sandstone. The impact melt rocks with increasing clast density showed higher loss in strength. The clast free impact melt rock showed lower loss in strength compared clast rich and clast poor impact melt rocks due to weathering and desalination experiment. One clast poor fine-grained impact melt rock (WCIS-14 MK-082) exhibited the highest loss in strength due to weathering and desalination experiment among all the samples. This sample had lower strength than other impact melt rocks (Table 3.8). This sample was stronger than impact melt-bearing breccia and sandstone but weaker than crystalline rocks. The accelerated loss in strength in this sample may because it was more chemically altered than other impact melt rocks.

In this experiment, we found that class 1b Cononino Sandstone will breakdown the fastest followed by impact melt-bearing breccias, altered impact melt rock, lithic breccia, class 1a Coconino Sandstone, class 1a Moenkopi Sandstone, impact melt rock, and class 1a crystalline rock (Fig 3.12). This order of breakdown is proposed based on the observation of deterioration and initial strength of the samples used in this experiment.



Fig 3.12. Relative rates of breakdown observed on sample rocks following experiments. Highest rates are at the bottom. 'T' represents the top surface of the sample block.

3.5. Conclusion

This study is the first systematic attempt to understand the effect of impact generated heterogeneities and deformation on the subsequent weathering of impactites. A physical weathering experiment on impactites was conducted for the first time in an environmental chamber. Several types of impactites were subjected to physical weathering experiment in simulated terrestrial semi-arid environmental conditions. These impactites include low shocked Coconino and Moenkopi Sandstone from Meteor Crater, low shocked Granite and Tonalite, impact melt rocks, lithic breccias, and impact melt-bearing breccia from West Clearwater Impact Structure, and Suevite breccia from Ries Crater.

The major results summarised as follows.

1. Low shock pressure (<5 GPa) causes pore collapse and macro- and micro-fracturing in porous sandstone. The macro- and micro-fractures make sandstone weaker and guide the entry of moisture and salt and so have a control on the intensity of weathering. Low shocked (class 1a and 1b) sandstone exhibits accelerated deterioration than unshocked counterparts.
2. Low shocked crystalline impactites (<10GPa) exhibit similar loss of strength comparable to low shocked sandstone samples. Nevertheless, low shocked crystalline impactites were stronger than low shocked sedimentary impactites. They do not lose material as much as low shocked sedimentary impactites due to weathering and desalination experiment as these samples will require longer stressing to start deterioration.
3. Impact melt bearing breccia were weaker and less cohesive compared to impact melt rocks, lithic breccia and class 1a crystalline and sedimentary impactites. These samples breakdown faster than other samples.
4. Lithic breccias have strength comparable to low shocked sedimentary impactites. The rate of deterioration of these samples are similar to low shocked sedimentary impactites.
5. The impact melt rocks have strength comparable to low shocked crystalline impactites. The impact melt rocks with increasing clast density show accelerated loss in strength. This is because as the clast content decreases, welding action of melt becomes stronger. For example, Clast free impact melt rocks are stronger than clast rich impact melt rocks.

6. Since melt and glasses are more susceptible to chemical alteration than their crystalline counterparts (Wolff-Boenisch et al., 2006). Once the impact melt rocks are chemically altered, their breakdown is faster than low shocked sedimentary and crystalline impactites due to subsequent physical weathering (e.g. WCIS-14 MK-082 in our experiment).
7. Our weathering experiment successfully simulated realistic spring-time semi-arid temperature regimes and demonstrated that the semi-arid environmental conditions might be sufficient to instigate breakdown. Relatively moderate rates of heating and cooling (dT/dt = ~0.15°C/min in this experiment) in the presence of salt and moisture can induce breakdown in rocks and often-cited 2°C/min thermal shock threshold may not be necessary.
8. A small variation in clast shape and size does not significantly affect the response of sample blocks in the weathering experiment. The response of the blocks is more affected by internal variation (e.g. presence and distribution of flaws such as fractures and laminations, distribution of vitric phases in the sample).
9. Granular disintegration and salt efflorescence are two of the observed breakdown features in the sample blocks after the weathering experiment. X-ray CT examination of samples at a resolution of 46 μm revealed no change in existing macro-fractures and no new fractures. The changes in macro-fractures may occur below the detection limit of 46 μm.

We found that impactites exhibited an accelerated decline in strength compared to non-impacted control samples. However, the rock type and impact deformation history are important in controlling the rate of deterioration. As impact craters are widespread on Mars, the enhanced breakdown of impactites are likely to have played an important role in landscape evolution on Mars. Even on airless bodies, the impact generated discontinuities and heterogeneities can be exploited by thermal cycling to produce an accelerated breakdown (Hazeli et al., 2017).

References

Anders MH, Laubach SE and Scholz CH. (2014) Microfractures: A review. *Journal of Structural Geology* 69: 377-394.

Aoki H and Matsukura Y. (2007) A new technique for non-destructive field measurement of rock-surface strength: an application of the Equotip hardness tester to weathering studies. *Earth Surface Processes and Landforms* 32: 1759-1769.

Bell M. (2017) Experimentally Shocked and Altered Basalt: VNIR Spectra of Mars Analog Materials.

Boslough MB and Cygan RT. (1988) Shock-enhanced dissolution of silicate minerals and chemical weathering on planetary surfaces. *Lunar and Planetary Science Conference Proceedings.* 443-453.

Buckman J, Bankole SA, Zihms S, et al. (2017) Quantifying Porosity through Automated Image Collection and Batch Image Processing: Case Study of Three Carbonates and an Aragonite Cemented Sandstone. *Geosciences* 7: 70.

Buhl E, Poelchau MH, Dresen G, et al. (2013) Deformation of dry and wet sandstone targets during hypervelocity impact experiments, as revealed from the MEMIN Program. *Meteoritics & Planetary Science* 48: 71-86.

Buscombe D. (2013) Transferable wavelet method for grain-size distribution from images of sediment surfaces and thin sections, and other natural granular patterns. *Sedimentology* 60: 1709-1732.

Charola AE, Pühringer J and Steiger M. (2007) Gypsum: a review of its role in the deterioration of building materials. *Environmental geology* 52: 339-352.

Cockell CS and Osinski GR. (2007) Impact-induced impoverishment and transformation of a sandstone habitat for lithophytic microorganisms. *Meteoritics & Planetary Science* 42: 1985-1993.

De Kock T, Boone MA, De Schryver T, et al. (2015) A pore-scale study of fracture dynamics in rock using X-ray micro-CT under ambient freeze–thaw cycling. *Environmental science & technology* 49: 2867-2874.

Engelhardt W. (1997) Suevite breccia of the Ries impact crater, Germany: Petrography, chemistry and shock metamorphism of crystalline rock clasts. *Meteoritics & Planetary Science* 32: 545-554.

Farquharson J, Griffiths L, Baud P, et al. (2017) Compressive strength evolution of thermally-stressed Saint Maximin limestone. *AGU Fall Meeting Abstracts.*

Fei Y. (1995) Thermal expansion. *Mineral Physics & Crystallography: a handbook of physical constants* 2: 29-44.

Ferrière L and Osinski GR. (2013) Shock metamorphism. In: Osinski GR and Pierazzo E (eds) *Impact Cratering: Processes and Products.* John Wiley & Sons, 106-124.

French BM and Koeberl C. (2010) The convincing identification of terrestrial meteorite impact structures: What works, what doesn't, and why. *Earth-Science Reviews* 98: 123-170.

Furukawa Y, Sekine T, Kakegawa T, et al. (2011) Impact-induced phyllosilicate formation from olivine and water. *Geochimica et Cosmochimica Acta* 75: 6461-6472.

Ghobadi M and Babazadeh R. (2015) Experimental studies on the effects of cyclic freezing–thawing, salt crystallization, and thermal shock on the physical and mechanical characteristics of selected sandstones. *Rock Mechanics and Rock Engineering* 48: 1001-1016.

Goudie A and Parker A. (1998) Experimental simulation of rapid rock block disintegration by sodium chloride in a foggy coastal desert. *Journal of Arid Environments* 40: 347-355.

Goudie AS, Wright E and Viles HA. (2002) The roles of salt (sodium nitrate) and fog in weathering: a laboratory simulation of conditions in the northern Atacama Desert, Chile. *Catena* 48: 255-266.

Grieve RA and Therriault AM. (2013) Impactites: Their characteristics and spatial distribution. *Impact Cratering: Processes and Products*: 90-105.

Hazeli K, El Mir C, Papanikolaou S, et al. (2017) The Origins of Asteroidal Rock Disaggregation: Interplay of Thermal Fatigue and Microstructure. *Icarus*.

Israeli Y and Emmanuel SJESD. (2018) Impact of grain size and rock composition on simulated rock weathering. 6: 319-327.

Kenkmann T, Poelchau MH and Wulf G. (2014) Structural geology of impact craters. *Journal of Structural Geology* 62: 156-182.

Kieffer S, Schaal R, Gibbons R, et al. (1976a) Shocked basalt from Lonar impact crater, India, and experimental analogues. *Lunar and Planetary Science Conference Proceedings.* 1391-1412.

Kieffer SW. (1971a) I. Shock metamorphism of the Coconino sandstone at Meteor Crater, Arizona. II. The specific heat of solids of geophysical interest. California Institute of Technology.

Kieffer SW. (1971b) Shock Metamorphism of the Coconino Sandstone. *Journal of Geophysical Research*.

Kieffer SW. (1975) From regolith to rock by shock. *The Moon* 13: 301-320.

Kieffer SW, Phakey PP and Christie JM. (1976b) Shock processes in porous quartzite: Transmission electron microscope observations and theory. *Contributions to Mineralogy and Petrology* 59: 41-93.

Kompatscher M. (2004) Equotip-rebound hardness testing after D. Leeb. *Proceedings, Conference on Hardness Measurements Theory and Application in Laboratories and Industries.* 11-12.

Kring DA. (2017) Guidebook to the geology of Barringer Meteorite Crater, Arizona (aka Meteor Crater): for the 80th Annual Meeting of the Meteoritical Society July 2017. Lunar and Planetary Institute.

Leroux H. (2005) Weathering features in shocked quartz from the Ries impact crater, Germany. *Meteoritics & Planetary Science* 40: 1347-1352.

Madden MEE, Kring DA and Bodnar RJ. (2006) Shock reequilibration of fluid inclusions in Coconino sandstone from Meteor Crater, Arizona. *Earth and Planetary Science Letters* 241: 32-46.

Navrotsky A. (1995) Thermodynamic properties of minerals. *Mineral Physics & Crystallography: a handbook of physical constants*: 18-28.

Newsom HE, Wright SP, Misra S, et al. (2013) Comparison of simple impact craters: A case study of Meteor and Lonar Craters. *Impact Cratering: Processes and Products*: 271-289.

Osinski G and Grieve R. (2017) " Suevites" of the West Clearwater Lake Impact Structure, Canada: A Demonstration of the Need for a Revised Classification Scheme for Impactites. *Lunar and Planetary Science Conference.*

Osinski GR. (2003) Impact glasses in fallout suevites from the Ries impact structure, Germany: An analytical SEM study. *Meteoritics & Planetary Science* 38: 1641-1667.

Osinski GR. (2007) Impact metamorphism of CaCO3-bearing sandstones at the Haughton structure, Canada. *Meteoritics & Planetary Science* 42: 1945-1960.

Phinney W, Simonds C, Cochran A, et al. (1978) West clearwater, Quebec impact structure, part II: petrology. *Lunar and Planetary Science Conference Proceedings.*

Pierazzo E and Melosh H. (2000) Melt production in oblique impacts. *Icarus* 145: 252-261.

Pohl J, Stoeffler D, Gall Hv, et al. (1977) The Ries impact crater. *Impact and explosion cratering: Planetary and terrestrial implications.* 343-404.

Rae A, Collins G, Grieve R, et al. (2017) Complex crater formation: Insights from combining observations of shock pressure distribution with numerical models at the West Clearwater Lake impact structure. *Meteoritics & Planetary Science* 52: 1330-1350.

Rocholl A, Böhme M, Gilg HA, et al. (2018) Comment on “A high-precision 40 Ar/39 Ar age for the Nördlinger Ries impact crater, Germany, and implications for the accurate dating of terrestrial impact events” by Schmieder et al.(Geochimica et Cosmochimica Acta 220 (2018) 146-157. *Geochimica et Cosmochimica Acta*.

Rosa DF. (2012) *The sheet of impact melt at West Clearwater Lake, Northern Quebec*: McGill University (Canada).

Schmieder M, Kennedy T, Jourdan F, et al. (2018) A high-precision 40Ar/39Ar age for the Nördlinger Ries impact crater, Germany, and implications for the accurate dating of terrestrial impact events. *Geochimica et Cosmochimica Acta* 220: 146-157.

Schmieder M, Schwarz WH, Trieloff M, et al. (2015) New 40Ar/39Ar dating of the Clearwater Lake impact structures (Québec, Canada)–Not the binary asteroid impact it seems? *Geochimica et Cosmochimica Acta* 148: 304-324.

Shipman F, Gregson V and Jones A. (1971) *A shock wave study of Coconino Sandstone*: National Aeronautics and Space Administration.

Shoemaker EM and Kieffer SW. (1979) *Guidebook to the geology of Meteor Crater, Arizona*: Center for Meteorite Studies, Arizona State University.

Simonds C, Phinney W, McGee P, et al. (1978) West Clearwater, Quebec impact structure. I-Field geology, structure and bulk chemistry. II-Petrology. *Lunar and Planetary Science Conference Proceedings.* 2633-2693.

Singleton AC, Osinski GR, McCAUSLAND PJ, et al. (2011) Shock-induced changes in density and porosity in shock-metamorphosed crystalline rocks, Haughton impact structure, Canada. *Meteoritics & Planetary Science* 46: 1774-1786.

Smith B, Srinivasan S, Gomez-Heras M, et al. (2011) Near-surface temperature cycling of stone and its implications for scales of surface deterioration. *Geomorphology* 130: 76-82.

Smith B, Warke P, McGreevy J, et al. (2005) Salt-weathering simulations under hot desert conditions: agents of enlightenment or perpetuators of preconceptions? *Geomorphology* 67: 211-227.

Sousa LM, del Río LMS, Calleja L, et al. (2005) Influence of microfractures and porosity on the physico-mechanical properties and weathering of ornamental granites. *Engineering Geology* 77: 153-168.

Stöffler D, Grieve R, Fettes D, et al. (2007) Impactites. *Metamorphic rocks: A classification and glossary of terms, recommendations of the International Union of Geological Sciences*: 82-92.

Stöffler D, Hamann C and Metzler K. (2018) Shock metamorphism of planetary silicate rocks and sediments: Proposal for an updated classification system. *Meteoritics & Planetary Science* 53: 5-49.

Tuğrul A. (2004) The effect of weathering on pore geometry and compressive strength of selected rock types from Turkey. *Engineering Geology* 75: 215-227.

Viles H. (2011) Weathering systems. In: Thomas DS (ed) *Arid Zone Geomorphology: Process, Form and Change in Drylands.* III ed.: John Wiley & Sons, 85-101.

Viles H, Ehlmann B, Wilson CF, et al. (2010) Simulating weathering of basalt on Mars and Earth by thermal cycling. *Geophys. Res. Lett.* 37: L18201.

Viles H and Goudie A. (2007) Rapid salt weathering in the coastal Namib desert: implications for landscape development. *Geomorphology* 85: 49-62.

Viles H, Goudie A, Grab S, et al. (2011) The use of the Schmidt Hammer and Equotip for rock hardness assessment in geomorphology and heritage science: a comparative analysis. *Earth Surface Processes and Landforms* 36: 320-333.

Viles H, Messenzehl K, Mayaud J, et al. (2018) Stress histories control rock-breakdown trajectories in arid environments. *Geology* 46: 419-422.

Viles HA. (2005) Microclimate and weathering in the central Namib Desert, Namibia. *Geomorphology* 67: 189-209.

Warke P. (2007) Complex weathering in drylands: implications of 'stress' history for rock debris breakdown and sediment release. *Geomorphology* 85: 30-48.

Warke P and Smith B. (1998) Effects of direct and indirect heating on the validity of rock weathering simulation studies and durability tests. *Geomorphology* 22: 347-357.

Williams R and Robinson D. (2001) Experimental frost weathering of sandstone by various combinations of salts. *Earth Surface Processes and Landforms* 26: 811-818.

Wolff-Boenisch D, Gislason SR and Oelkers EH. (2006) The effect of crystallinity on dissolution rates and CO2 consumption capacity of silicates. *Geochimica et Cosmochimica Acta* 70: 858-870.

Wright S. (2013) Decompression Cracks in Altered Basalt Under Solid-State Shock Pressures: A New Macroscopic Shock Texture. *LPI Contributions* 1737: 3049.

Zhu Lp, Wang Jc and Li By. (2003) The impact of solar radiation upon rock weathering at low temperature: a laboratory study. *Permafrost and Periglacial Processes* 14: 61-67.

Chapter 4

4. A Structure from Motion photogrammetry-based method to generate sub-millimetre resolution Digital Elevation Models for investigating rock breakdown features

Published in Earth Surface Dynamics

Co-author: Mary C. Bourke

Abstract

We have generated sub-millimetre resolution DEMs of weathered rock surfaces using SfM photogrammetry techniques. We apply a close-range Structure from Motion (SfM) photogrammetry-based method in the field and use it to generate high-resolution topographic data for weathered boulders and bedrock. The method was pilot tested on extensively weathered Triassic Moenkopi Sandstone outcrops near Meteor Crater in Arizona. Images were taken in the field using a consumer grade DSLR camera and were processed in commercially available software to build dense point clouds. The point clouds were registered to a local 3D coordinate system (x, y, z) which was developed using a specially designed triangle coded control target and then exported as Digital Elevation Models (DEMs). The accuracy of the DEMs was validated under controlled experimental conditions. A number of checkpoints were used to calculate errors. We also evaluated the effects of image and camera parameters on the accuracy of our DEMs. We report a horizontal error of 0.5 mm and a vertical error of 0.3 mm in our experiments. Our approach provides a low-cost method for obtaining very high-resolution topographic data on weathered rock surfaces (area < 10 m^2). The results from our case study confirm the efficacy of the method at this scale and show that the data acquisition equipment is sufficiently robust and portable. This is particularly important for field conditions in remote locations or steep terrain where portable and efficient methods are required.

4.1. Introduction

Rock breakdown describes a range of geomorphic processes that transform rock masses into soil or regolith and unconsolidated rock materials. It plays a vital role in climate control via atmosphere-lithosphere interaction, biogeochemical cycling and landform evolution on a planetary scale (Goudie and Viles, 2012). The scale of features range from μm (e.g., fractures, weathering pits, fractures) to m scale (e.g., tafoni, scaling and blisters) (Viles, 2001; Bourke and Viles, 2007). In addition, many active rock breakdown processes that

operate over a short geological timescale (10^0-10^2 years) produce observable microscale (mm-cm) breakdown features. To better understand the weathering processes, high resolution (sub-mm to mm) microtopographic data are necessary for in-situ measurement of small-scale weathering features (Viles, 2001). To date, the inability to measure the general geomorphometry of small-scale breakdown features has inhibited our understanding of the causal links at relevant scales. Many small-scale (mm-cm) breakdown features are ambiguous, and it remains challenging to distinguish between similar looking features (e.g. aeolian pits vs dissolution pits) and therefore to establish a clear link between weathering feature form and the formative process. Even for homogenous forms on a surface, it may be difficult to understand the role of individual weathering mechanisms (Viles, 2005; Warke, 2007; Viles et al., 2010; Viles et al., 2018). In addition, extending analysis routines between rock breakdown sites, to better understand features that often show considerable complexity in their intensity, size and shape depending on lithological, geological and micro-environmental factors (Viles, 2001) has been limited by the application of different techniques at different scales and in different locations. Using the same technique (i.e. SfM) across scales will permit similar analysis routines for different scale landscapes (Cullen et al., 2018a).

This will facilitate the investigation of potential feedbacks across various scales boundaries. The morphometric analysis of topography at different scales will aid the interpretation of the complex interrelationship of weathering processes and landscapes and facilitate a better understanding of the multi-scale weathering system (Viles, 2013b).

Quantitative analysis of landforms is necessary for the identification and interpretation of landform genesis and history. In the past few decades, a range of micro-topographic data collection methods has been used in rock breakdown and soil erosion studies. These include: (1) laser scanning techniques (Fardin et al., 2001; Fardin et al., 2004; Bourke et al., 2007a; Bourke et al., 2008; Aguilar et al., 2009; Sturzenegger and Stead, 2009; MŁynarczuk, 2010; Medapati et al., 2013; Chen et al., 2014; Ge et al., 2014; Lai et al., 2014), (2) stereophotogrammetry (Rieke-Zapp and Nearing, 2005; Taconet and Ciarletti, 2007; Aguilar et al., 2009; Bui et al., 2009; Sturzenegger and Stead, 2009; Kim et al., 2015), (3) Micro-roughness meters (MRM) (McCarroll, 1992; McCarroll and Nesje, 1996; White et al., 1998). However, there are significant logistical, technical and for some, financial constraints that have hindered the adoption of these methods, particularly in physically challenging terrains such as remote, difficult to access and steep terrains.

Laser scanning permits collection of high-resolution topographic data at the relevant scale for the study of small-scale rock breakdown features. However, due to difficulties associated with transporting the often-cumbersome instrument in the field (Ehlmann et al., 2008b), this technology has rarely been used to collect data on rock surfaces in situ (Fardin et al., 2004). Additionally, laser scanners require a stable platform, on which to operate and this can be difficult to find in steep terrain (e.g. crater and canyon walls, and mountainous terrain). There are hand-held portable laser scanners available which do not require a stable platform to operate, but the resolution offered by them is currently insufficient to resolve mm-cm scale rock breakdown features (Chan et al., 2016).

Stereophotogrammetry is a method of DEM generation using stereo images of an object/surface. It is widely-applied in terrestrial and planetary terrains (Kim and Muller, 2009; Li et al., 2011). The knowledge of camera internal geometry (i.e. sensor type and size), camera calibration parameters and Ground Control Points (GCPs) with known coordinates along with inertial measurement parameters (i.e., yaw, pitch and roll) are critical requirements for stereo photogrammetry to solve collinearity equation and orient photogrammetric model (Taconet and Ciarletti, 2007; Aguilar et al., 2009).

While both methods have been effectively used to analyse rock breakdown at larger scales, both require expensive software (e.g. SocetSet, PHOTOMOD, FARO Scene, Trimble RealWorks, Leica CYCLONE, VisionLidar) and expert knowledge to process data and generate DEMs, the cost of which may push this technology beyond many academic research budgets.

The micro-roughness meter (MRM) (McCarroll, 1992; McCarroll and Nesje, 1996; White et al., 1998) is operated manually and has been used to characterise and quantify breakdown on rock surfaces. Direct physical access to the rock surface is required, which limits sampling in out of reach locations (McCarroll and Nesje, 1996). While the resolution, precision, and accuracy of MRM (~0.001 to 0.005 mm) is higher than laser scanning and photogrammetry techniques (sub-mm to mm), the topographic data obtained from MRM is one dimensional and limits the analysis to the calculation of profile roughness parameters. The profile roughness parameters only provide information along a profile, not the entire rock surface, which often makes it difficult to determine the exact nature of a topographic feature (Leach, 2013). In comparison, 3D data from laser scanners and photogrammetry enable calculation of areal surface roughness parameters. These parameters have advantages

over traditional profile roughness parameters and have more statistical significance than equivalent profile measurements (Leach, 2013).

4.1.1. Structure from Motion (SfM)

Structure from Motion (SfM) is an established and widely used method to generate 3D models in the geosciences (Favalli et al., 2012; Westoby et al., 2012; Smith et al., 2016). It is increasingly used in geomorphology for characterisation of topographic surfaces and analysis of spatial and temporal geomorphic changes, with an accuracy comparable to existing laser scanning and stereo photogrammetry techniques in close range scenario (Aguilar et al., 2009; Thoeni et al., 2014; Smith et al., 2016; Wilkinson et al., 2016). SfM photogrammetry utilises a sequence of overlapping digital images of a static subject taken from different spatial positions to produce a 3D point cloud. Image metadata for image matching is used to estimate 3D geometry and camera positions using bundle adjustment algorithm (Smith et al., 2016). The workflow uses an automated Scale Invariant Feature Transform (SIFT) image matching method (Smith et al., 2016). The advancement in new image matching algorithms has eased and automated the SfM workflow compared to stereophotogrammetry (Remondino et al., 2014; Smith et al., 2016).

Applications in geomorphology include laboratory flume experiments (Morgan et al., 2017), rockslides and landslide (Niethammer et al., 2012; Russell, 2016), eroding badlands (Smith and Vericat, 2015), fluvial morphology (Javernick et al., 2014; Dietrich, 2015; Bakker and Lane, 2016; Dietrich, 2016a; Dietrich, 2016b), peatland microforms (Mercer and Westbrook, 2016), glacial processe dynamics (Piermattei et al., 2016; Immerzeel et al., 2017), river restoration (Marteau et al., 2016), mapping coral reefs (Casella et al., 2016), beach surveying (Brunier et al., 2016a), soil erosion (Snapir et al., 2014; Balaguer-Puig et al., 2017a; Prosdocimi et al., 2017; Vinci et al., 2017; Heindel et al., 2018), volcanic terrains (James and Robson, 2012; Bretar et al., 2013; Carr et al., 2018), porosity of river bed material (Seitz et al., 2018), grain size estimation of gravel bed rivers (Pearson et al., 2017) and coastal erosion (James and Robson, 2012). In addition, SfM has also been widely used in archaeology for the photogrammetric recording of small-scale rock art and artefacts, and large-scale archaeological sites (Sapirstein, 2016; Sapirstein and Murray, 2017; Jalandoni et al., 2018; Sapirstein, 2018).

The increased uptake of this method is primarily due to its relatively low cost, high portability, and ease of data processing workflow. Much of the SfM workflow is automated

in a range of relatively affordable commercial software (e.g. Agisoft Photoscan, SURE, Photomodeler), closed source free software (e.g. VisualSfM, CMPMVS), and open source software (e.g., Bundler, OpenMVG, OpenMVS, MicMac, SFMToolkit).

There is a considerable amount of available literature on SfM techniques and workflows. A detailed discussion of the technique is found in several available papers, e.g. Westoby et al. (2012); Fonstad et al. (2013); Thoeni et al. (2014); Micheletti et al. (2015a); Micheletti et al. (2015b); Eltner et al. (2016); Ko and Ho (2016); Smith et al. (2016); Schonberger and Frahm (2016); Bedford (2017); Zhu et al. (2017); Ozyesil et al. (2017).

Several studies have reported high accuracy in 3D topographic data obtained using SfM when compared to methods such as Terrestrial Laser Scanner (TLS) or RTK-GPS surveys (Harwin and Lucieer, 2012; Favalli et al., 2012; Andrews et al., 2013; Fonstad et al., 2013; Dietrich, 2014; Nilosek et al., 2014; Caroti et al., 2015; Palmer et al., 2015; Clapuyt et al., 2016; Koppel, 2016; Piermattei et al., 2016; Panagiotidis et al., 2016; Wilkinson et al., 2016). A detailed comparison of cost-benefit, data acquisition rate, spatial coverage, operating conditions, resolution and accuracy analysis between TLS and SfM techniques are found in Smith et al. (2016), and Wilkinson et al. (2016). The recent advances in Structure from Motion approaches (SfM) have yet to be widely applied to micro-scale landforms, such as rock breakdown features.

Here we trial the use of SfM for very high resolution (sub-mm) application. Our approach uses high-resolution digital photography (from consumer grade camera) combined with SfM workflow. We evaluate errors in our DEMs using checkpoints in the field and validate our approach through a series of controlled experiments. We also assess the error propagation with distance from the control target in DEMs generated in our experiment. We find that SfM offers a robust approach to rock breakdown studies.

Our work provides an alternative and additional cost-effective, transportable and fieldwork-friendly method for use in geomorphological studies that require the production of high-resolution topographic models from field sites. Below, we outline the development and test of our approach in the field and under controlled conditions. We provide a detailed guide so that others may adopt our approach in their research.

4.2. Methodology

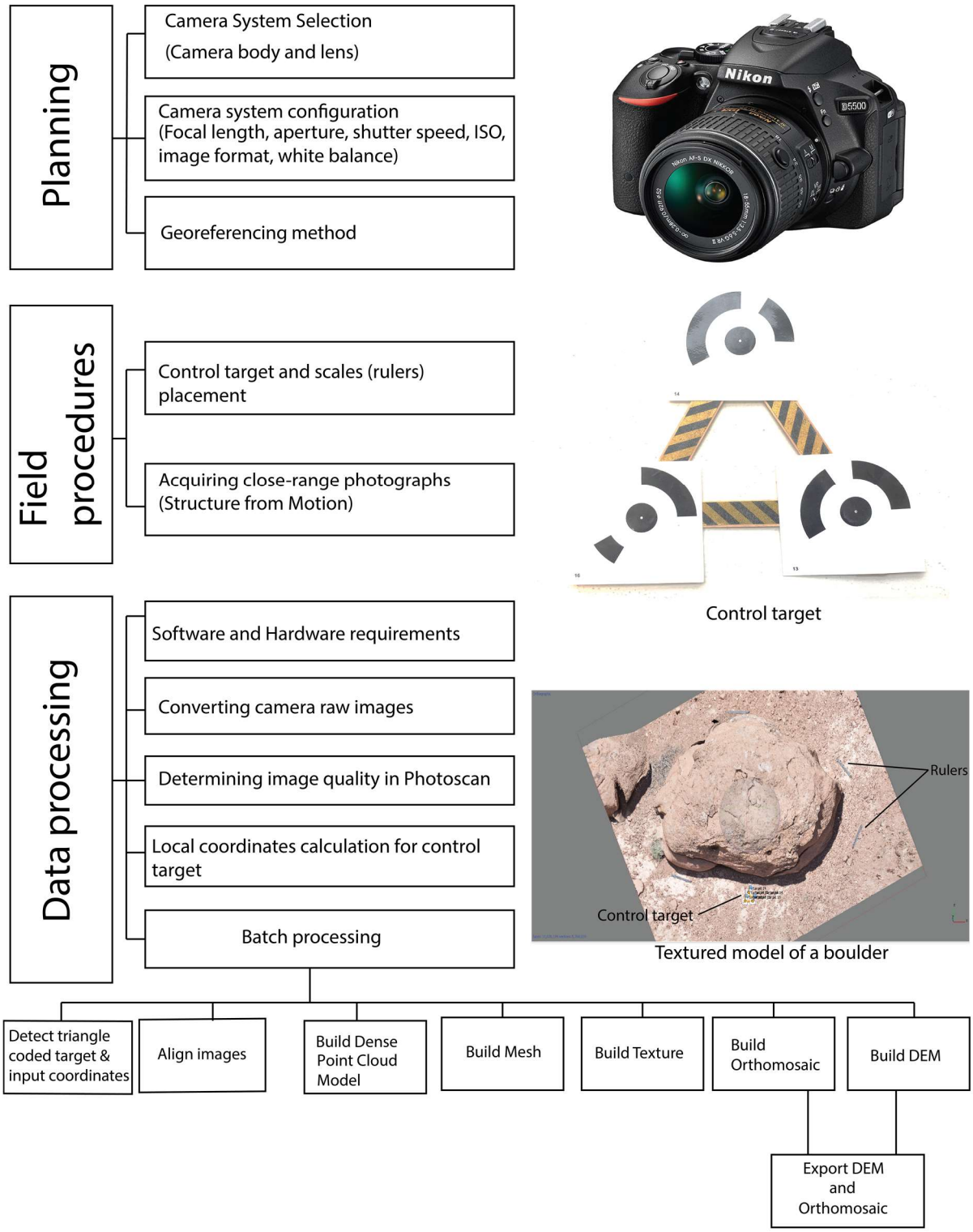


Fig 4.1. A schematic diagram of the typical workflow for Digital Elevation Model (DEM) production described in this study.

4.2.1. Equipment

The quality of image data collection can be improved by careful camera system selection, configuration, and image acquisition. The Camera system plays a vital role in effective resolution, signal-to-noise ratio, and distortion (Mosbrucker et al., 2017). For this work, low-cost, consumer-grade, ultra-compact and lightweight Nikon D5500 DSLR camera was used. A Digital Single Lens Reflex (DSLR) camera system includes a camera body and a lens. This camera has an Advanced Photo System type-C (APS-C) sensor (366.6 mm^2) with no anti-aliasing filter and captures an image with an effective resolution of 24.2 Mega Pixels (MP). A DSLR camera provides flexibility in selecting different kinds of lenses and captures high-resolution images in raw (RAW) format. Images in raw format store more Red Green blue (RGB) pixel information than in Joint Photographic Experts Group (JPEG) format. We used a zoom lens with a variable focal length of 18-55 mm and a 35 mm prime or fixed focal-length lens in this study. A more comprehensive discussion of camera system consideration and configuration for SfM Photogrammetry work is found in Bedford (2017), Mosbrucker et al. (2017), and Sapirstein and Murray (2017).

4.2.2. Control target and local coordinate system

The dense point cloud generated by SfM is not scaled or oriented to a real-world dimension. Therefore, registration to a known coordinate system (geographic or local) using Ground Control Points (GCPs) is required to reference and scale the model. GCP refers to a point with known coordinates (x, y, z). Incorporating GCPs in the SfM workflow is known to reduce systematic errors such as doming and dishing (Javernick et al., 2014; James and Robson, 2014) and permits a check on the accuracy of DEMs. At least three GCPs are required to generate a DEM from a dense point cloud.

For our study, we designed and built a new, portable control target (Fig 4.2). The triangle control target was made from 13 cm long craft sticks covered with textured plastic tape to protect it from shrinking and swelling in humid conditions (Fig 4.2). Each vertex served as a GCP. A set of three 12-bit coded markers were printed from Agisoft Photoscan software, laminated and attached at each vertex (Fig4.2). The advantage of using coded markers is that they can be automatically identified in Photoscan, which minimises the time and reduces error. Goldstein et al. (2015) found that the number and the placement of GCPs affect the

accuracy of SfM derived DEMs. In this work, our area of interest was small (<10 m^2); hence, we determined that three GCPs would be sufficient.

We used our triangle coded control target (GCPs) to calculate local coordinates to scale and reference our DEMs (Fig 4.2). The length of the triangle sides to the GCP centre was measured using an Engineer's scale with 0.5 mm accuracy. The sides of the triangle were 0.133, 0.132, and 0.131 m, respectively, for a, b, and c (Fig 4.2). The angle A (54.03°/1.06 radians) was determined using cosine rule, and the coordinates of each vertex of the triangle were determined using trigonometry (Fig 4.2 and Table 4.1).

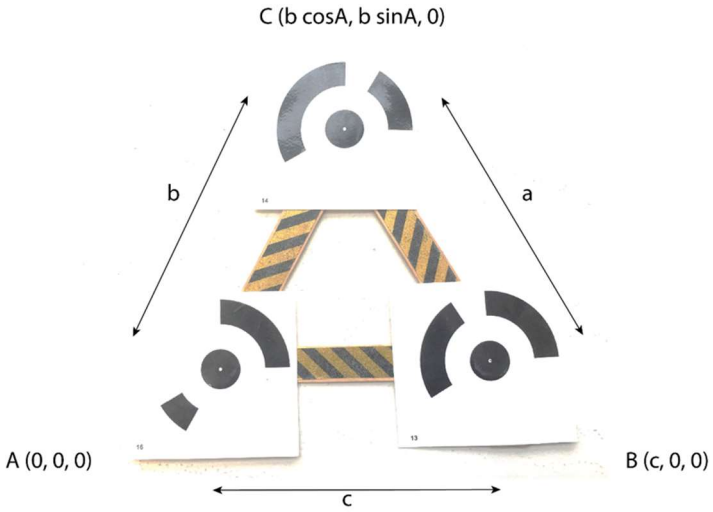


Fig 4.2. Triangle coded control target. Each vertex of this triangle is a GCP.

Table 4.1. Local coordinates for each vertex of triangle coded control target.

Coded marker	Vertices	X (m)	Y (m)	Z (m)
Target 16	A position	0	0	0
Target 13	B position	0.131	0	0
Target 14	C position	0.064489	0.115175	0

4.2.3. Data processing

Following image data acquisition (described below) the data were processed using an Intel Xeon workstation with 32 GB of RAM and 2GB Nvidia Quadro 4000 graphics card. We used commercially available software (Adobe Lightroom CC) to process raw images and

Agisoft PhotoScan for DEM generation. Photoscan is a 'black box' software, so it remains unclear the exact SfM algorithm used.

Photoscan does not support NEF file format (RAW) images generated by the Nikon camera, and they were converted to tiff format. While this step increases processing time, the benefit of capturing images in raw format is that any photometric corrections (i.e., exposure correction) can be performed without losing metadata (Guidi et al., 2014a). Raw images were imported into Lightroom and exported as uncompressed tiff image files with AdobeRGB (1998) colour space (Süsstrunk et al., 1999; Korytkowski and Olejnik-Krugly, 2017) and 16 bits/component bit depth. Image histograms generated in Lightroom confirmed that the images were well exposed, and no photometric correction was required. Each RAW file was 25-30 MB. When converted to uncompressed tiff, this increase to 130-140 MB per image file. Exporting tiff images from Lightroom took about 5-10 minutes in total.

4.2.4. DEM generation workflow in Photoscan

Agisoft Photoscan is a popular software for generating DEMs from SfM photogrammetry technique. Many published studies have already described DEM production workflow in Photoscan (e.g. Leon et al. (2015); James et al. (2017a)), so we only summarise the parameters used in our study here. A detailed step by step guideline for this study is presented in Section A4.1 (Appendix 4). For a more detailed explanation of workflow in Photoscan, we refer readers to Agisoft (2016) and Shervais K. (2016).

Table 4.2. Summary of processing parameters in the development of DEM in Photoscan

Stage 1	**General**	
	Images	Loading images, image quality determination, images with quality index <0.5 discarded
	Identification of markers: scale bar and coordinate input	Coded markers detected, local coordinates entered, scale bar created
	Measurement and scale bar accuracy setting	Measurement and scale bar accuracy adjustment, 0.01 mm for experiments, 0.5 mm for field data
	Masking	Only if images contain unwanted scenes
	Coordinate system	Local Coordinates (m)
Stage 2	**Alignment parameters**	
	Accuracy	Highest
	Pair preselection	Generic
	Key point limit	40,000
	Tie point limit	4,000
	Constrain features by mask	No (yes if images were masked)
	Optimization parameters	
	Parameters	f, cx, cy, k1-k3, p1, p2

Stage 3	**Dense point cloud Reconstruction parameters**	
	Quality	High
	Depth filtering	Mild
Stage 4	**Mesh Model Reconstruction parameters**	
	Surface type	Height field
	Source data	Dense
	Interpolation	Enabled
	Quality	High
	Depth filtering	Mild
	Face count	11,536,078
	Texturing parameters	
	Mapping mode	Generic
	Blending mode	Mosaic
	Texture size	4,096 x 4,096
	DEM Reconstruction parameters	
	Coordinate system	Local Coordinates (m)
	Source data	Dense cloud
	Interpolation	Enabled
	Orthomosaic Reconstruction parameters	
	Coordinate system	Local Coordinates (m)
	Channels	3, uint16
	Blending mode	Mosaic
	Surface	Mesh
	Enable color correction	Yes

4.2.5. Error evaluation experiments

A series of controlled image acquisition experiments were conducted to evaluate the horizontal and vertical errors of the DEMs generated using the GCP developed in this study (Fig 4.3 and 4.4). In addition, we tested the influence of a range of other variables on the accuracy and quality of DEMs. These include: (1) Type of lens, (2) Prior lens profile correction, (3) colour space of images, (4) dense point cloud quality setting in Photoscan, (5) image file format, (6) the position of control target with respect to subject, and (7) masking of images (Table 3).

4.2.5.1. Experiment design

In order to validate the sub-mm horizontal and vertical accuracy of DEM generated, a calibrated error evaluation chart was designed in Adobe Indesign and printed as 1.4 × 1.4 m poster (Fig 4.3). This chart contains four concentric squares and 16 coded scale bars of known length (Fig 4.3). This chart was laid on the relatively flat ground (±1° from the centre of the poster), and 16 wooden cubes of dimension ~5 cm were placed on vertices of each square (Fig 4.3 and 4.5a). We chose wooden blocks because of their non-homogeneous

texture, which is easily reconstructed using photogrammetry. Sixteen coded scale bars were used as checkpoints to estimate horizontal (XY) errors, and sixteen wooden blocks were used to determine vertical (Z) errors. Two triangle coded control targets were designed in the centre and the left corner of the poster (Fig 4.3). An additional four, 25 cm long coded scale bars were placed 60 cm away from the outer scale bar on each side of the poster. The coordinates of the triangle coded target were determined as described in section 4.2.2. The experiment was undertaken outside in overcast lighting conditions.

Three sets of images of the poster and nearby ground surface made up of concrete paving stones with visible edges were acquired using a zoom lens set at 24 mm and a 35 mm prime or fixed focal-length lens. Two sets of images were taken by the zoom lens set at 24 mm and 35 mm prime lens. The third set of images were acquired, using the zoom lens set at 24 mm, to cover the extended area where four additional scale bars were placed outside the poster on the cement surface. All the images were acquired using Nikon D5500 in manual mode. Camera settings were adjusted for the best result for the lighting conditions during the experiment. Aperture was set at f/7.1, the shutter speed was fixed at 1/200 s, and ISO was kept at 100. The focus was set to auto-focus during image acquisition. Images were acquired in raw and then converted into an uncompressed tiff in Adobe Lightroom (section 4.2.3).

RAW images were processed to change a few parameters in the image sets. Ten models were run in Photoscan from the three sets of images acquired. The DEMs were generated using the workflow described in section 4.2.4. Table 4.3 summarises the variables tested in the ten DEMs.

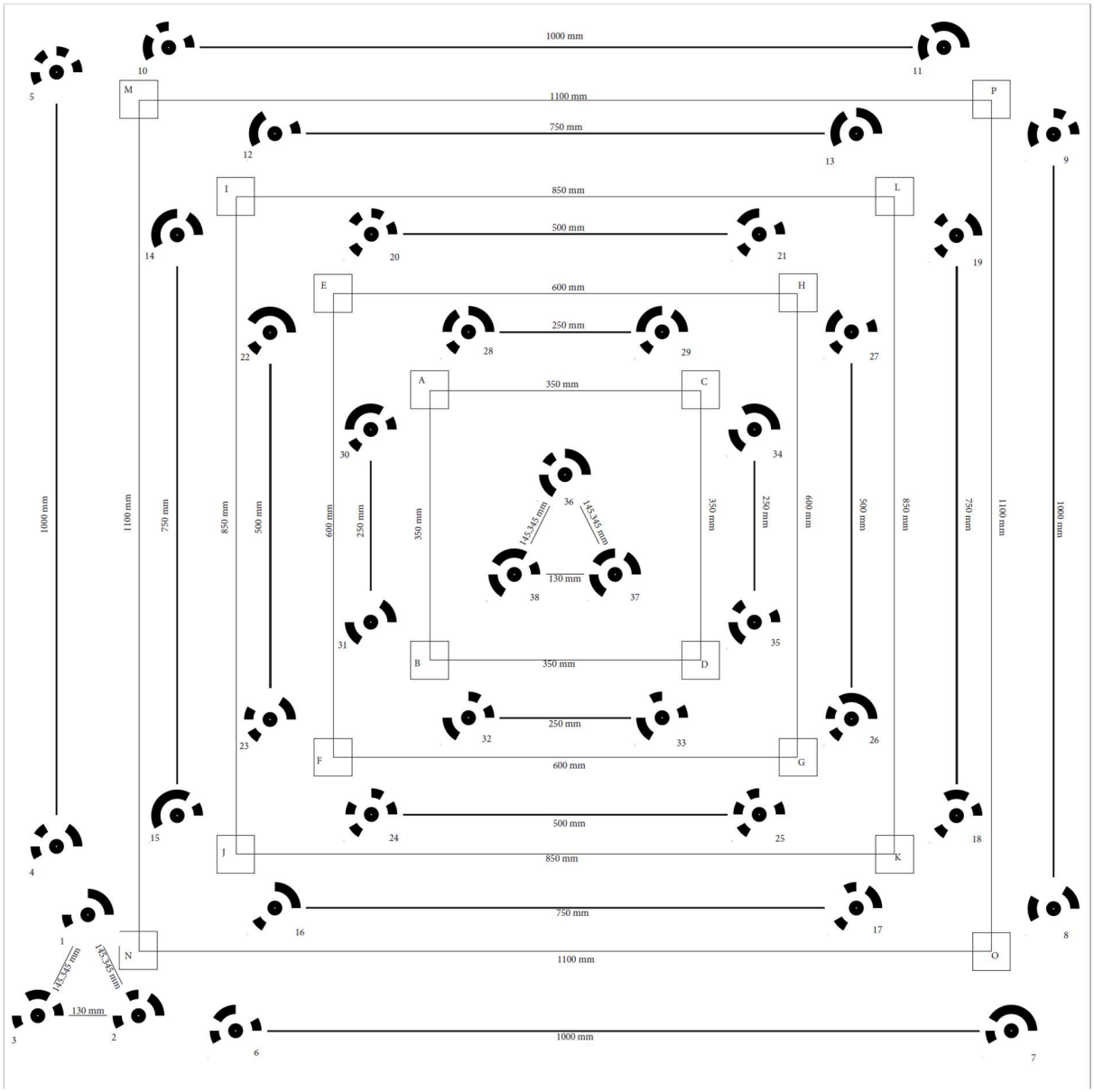


Fig 4.3. Error evaluation chart (1.4 × 1.4 m). Coded scale bars are horizontal checkpoints. Wooden blocks (small squares) at each vertex of bigger squares are vertical checkpoints. Two triangle coded control targets were used to georeferenced DEMs.

Table 4.3. The experimental design used in error evaluation experiment. Cross mark represents the DEMs compared for a variable.

Variables tested →	Type of lens (zoom lens vs prime lens)	Prior lens profile correction in images	Colour space (e.g. ProPhotoRGB, sRGB, AdobeRGB)	Dense point cloud quality setting (e.g.ultra high,high, medium)	Image format (tiff vs jpeg)	Position of the control target	Masking of images
DEMs ↓							
24 mm extended area							
24 mm profile corrected		×					
24 mm without profile corrected	×	×					
35 mm AdobeRGB			×				
35 mm sRGB			×				
35 mm ProPhotoRGB		×	×	×	×		
35 mm jpg					×		
35 mm profile corrected		×					
35 mm masked	×			×		×	×
35 mm corner control target						×	×

4.2.5.2. Estimating errors

The error evaluation chart (Fig 4.3) was used to estimate errors in the following way. The coded scale bars were used as horizontal checkpoints. The distance between coded markers and the centroid of the triangular control target was measured with an accuracy of 0.01 mm in Adobe InDesign. The scale bars were automatically detected in Photoscan. These scale bars were not used to scale or optimise the sparse point cloud in Photoscan. Photoscan estimated the length of coded scale bars based on the referencing information from the control target. The known length of coded scale bars was subtracted from the estimated length in Photoscan to calculate the horizontal error.

To determine the vertical error of the DEMs, the wooden blocks were used as checkpoints (Fig 4.5a). The DEMs and orthophotos were imported in ArcMap 10.4.1 (Fig 4.5). The height of wooden blocks was measured in ArcMap using the Interpolate Line tool (3D

Analyst tool), by drawing a straight line across one of the sides of the wooden block and extending it to the ground surface. Height was estimated as the difference in mean elevation between wooden block top surface and the surrounding ground surface on each side. The actual height of wooden blocks was measured by an electronic digital Vernier Caliper. The Vernier Caliper has an accuracy of 0.03 mm and a measurement repeatability of 0.01 mm. We obtained five measurements along the same side of the wooden block measured in ArcMap. We take the mean of these five measurements to calculate the height of the wooden block. The measured height was subtracted from the estimated DEM height to calculate the vertical error. The distance between the centre of wooden blocks and centroid of the triangle coded target was determined in Adobe Indesign. We used horizontal and vertical checkpoint errors with their distance from the control target to visualise error propagation in DEMs with distance (section 4.3.1).

4.3. Experiment Results

4.3.1. Distribution of horizontal and vertical errors

Error propagation with distance was estimated, and the data are shown in Tables A.4.1-A.4.1 (Appendix 4). The horizontal checkpoint errors for 24 mm extended area and 35 mm masked DEMs (Table A.4.1 in Appendix 4) were used to visualise errors over an area of 6.14 m^2 and 1.96 m^2 respectively as a contour plot (Fig 4.4 a and c). The data show that horizontal errors are almost symmetrical in X and Y direction (Fig 4.4 a and c). We used vertical checkpoints for 24 mm extended area and 35 mm masked DEMs (Table A.4.2 in Appendix 4) to visualise vertical errors as the surface plot over an area of 1.96 m^2 (Figure 4.4 b and d).

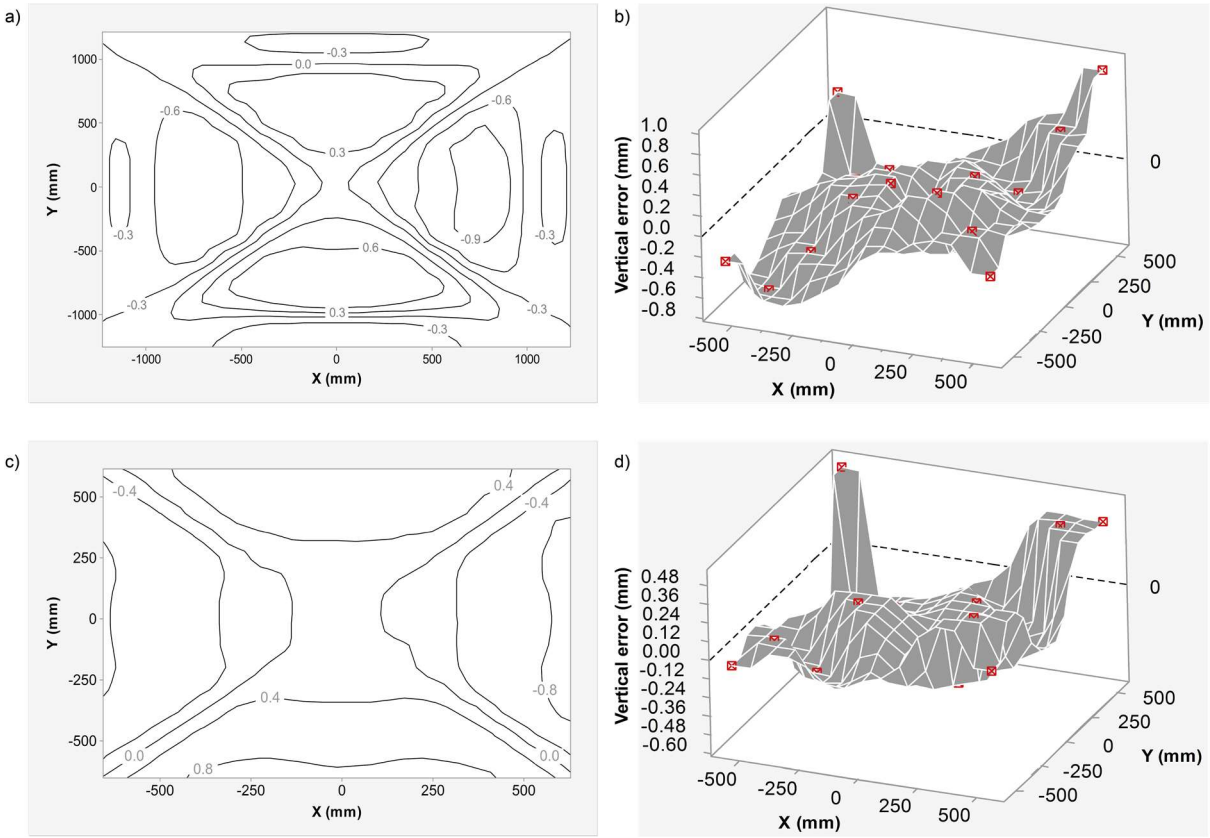


Fig 4.4. (a) Horizontal error contour plot for a DEM generated using images acquired with the zoom lens. Contours represent horizontal (XY) error (in mm) in the DEM. (b) Vertical errors in DEM generated using images from a zoom lens. Red cubes on the surface in the plot shows the location of wooden blocks (vertical checkpoints). (c) Horizontal error contour plot for a DEM generated using images from a prime lens. Contours represent horizontal (XY) error (in mm) in the DEM. (d) Vertical errors in DEM generated using images from a prime lens. Red cubes on the surface in the plot shows the location of wooden blocks (vertical checkpoints).

4.3.2. Role of image variables in DEM error

In this section, we present the findings from our DEM error evaluation experiment. Orthophoto and DEM of the error evaluation chart are shown in Figure 4.5. The summary of ten DEMs produced in the error evaluation experiment is presented in Table 4.4.

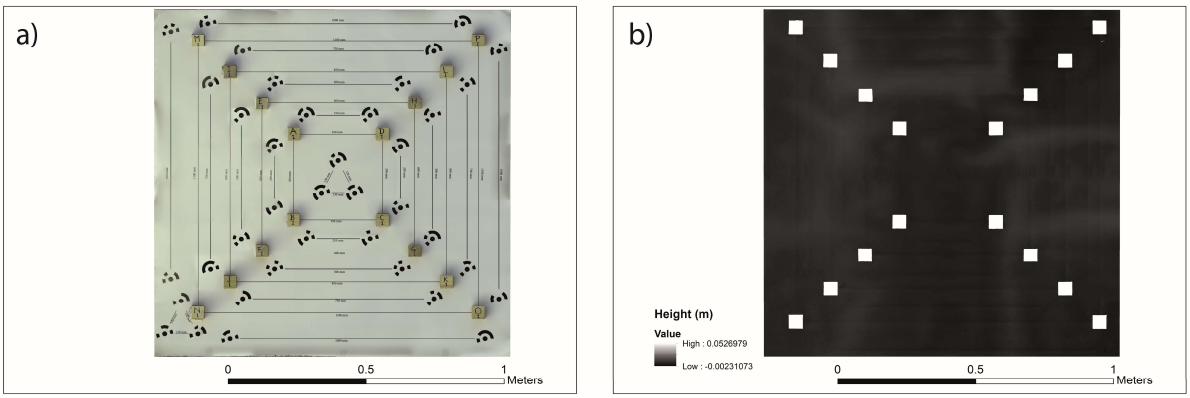


Fig 4.5. (a) Orthophoto of error evaluation chart. Coded scale bars represent horizontal checkpoints. Wooden blocks denote vertical checkpoints. (b) DEM of the error evaluation chart.

Table 4.4. Summary of experimental DEM data. Reprojection Error is the root mean square reprojection error (RMSE) averaged over all tie points on all images. In some publications, reprojection error is also referred to as RMS image residual (James et al., 2017a). In Agisoft manual, reprojection error is defined as the distance between the point on the image where a reconstructed 3D point can be projected, and the original projection of that 3D point detected on the photo (Agisoft, 2016). It is used to quantify how closely an estimate of a 3D point recreates the point's original projection and as a basis for the 3D point reconstruction procedure. Root Mean Square Error (RMSE) XY is the root mean square error for X and Y coordinates for control location/checkpoint. Root Mean Square Error (RMSE) Z is the root mean square error for X and Y coordinates for control location/checkpoint. Projection Accuracy (in pixels) is the root mean square error for X, Y coordinates on an image for control location/checkpoint averaged over all the images.

Below we also explored the role of several parameters on the accuracy of DEMs, and the detailed results are in section A.4.2 (Appendix 4). Horizontal and vertical checkpoint errors are used to compare these DEMs.

DEM	Colour space	No. of images	RMSE X,Y (Check) (mm)	RMSE Z (Check) (mm)	RMSE X,Y (Control) (mm)	RMSE Z (Control) (mm)	Reprojection error (pix)	Projection accuracy (control) (pix)	Accuracy (check) (pix)	Resolution (mm/pix)	Point density (pts/mm^2)	DEM quality setting	Time taken (Hr)
24 mm extended area	ProPhotoRGB	259	0.52	0.35	0.08	0.17	0.81	0.28	0.37	0.51	3780	High	169
24 mm profile corrected	ProPhotoRGB	178	0.56	0.37	0.08	0.16	0.72	0.29	0.35	0.45	4810	High	59
24 mm without profile corrected	ProPhotoRGB	178	0.55	0.35	0.08	0.17	0.77	0.29	0.37	0.45	4910	High	62
35 mm AdobeRGB	AdobeRGB	236	0.59	0.3	0.08	0.09	0.53	0.15	0.19	0.65	2330	Medium	10
35 mm corner coded target	ProPhotoRGB	236	0.59	0.27	0.02	0.54	0.54	0.17	0.2	0.32	9230	High	67
35 mm jpg	ProPhotoRGB	236	0.91	0.34	1.16	3.18	3.19	0.75	1.72	0.67	2180	Medium	8
35 mm masked	ProPhotoRGB	236	0.59	0.28	0.08	0.08	0.62	0.16	0.19	0.32	9760	High	67
35 mm profile corrected	ProPhotoRGB	236	0.59	0.39	0.08	0.07	0.54	0.17	0.2	0.66	2290	Medium	9
35 mm ProPhotoRGB	ProPhotoRGB	236	0.59	0.41	0.08	0.06	0.53	0.16	0.2	0.65	2330	Medium	10
35 mm sRGB	sRGB	236	0.59	0.42	0.08	0.62	0.54	0.16	0.19	0.65	2330	Medium	10

Although, our experiment suggests that there is no statistically significant difference in the accuracy of DEMs generated from prime and zoom lens we find that the use of the prime lens will yield lower errors compared to a zoom lens for SfM photogrammetry. Our results also indicate that prior lens profile correction, placement of control target relative to the subject of interest and masking of images had no statistically significant effect on the accuracy of DEM. However, we report that using Adobe RGB colour space and tiff file compression reduced error in DEMs (Table 4.4). We obtained better resolution and accuracy

using “High” dense point cloud quality setting in Photoscan. Based on our findings, we use these parameters in our field survey.

4.3.3. Repeatability

We used two independent image surveys to test the repeatability of our DEM generation method. We obtained a very high intraclass correlation for horizontal (ICC=0.999), and vertical (ICC=0.911) checkpoint errors between two DEMs produced from two different set of images (24 mm extended area and 24 mm without profile corrected). These DEMs were generated using identical image parameters and settings in Photoscan. Therefore, this method of DEM generation can easily be repeated.

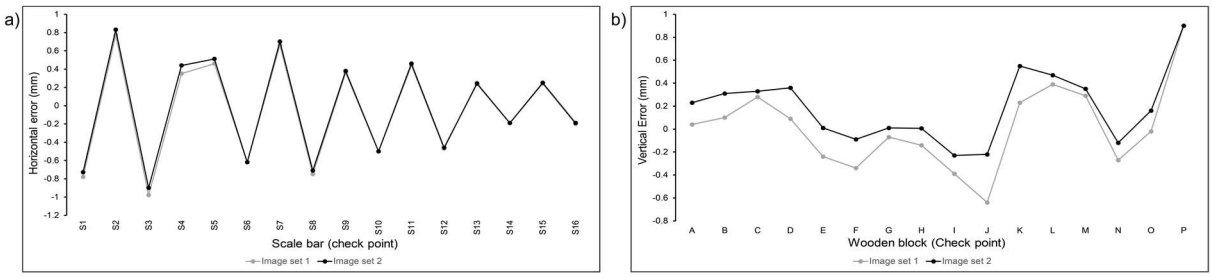


Fig 4.6. a) and b) Horizontal checkpoint and vertical checkpoint errors in DEMs produced from two different image sets to test repeatability.

Additionally, we performed DEM of Difference (DoD) on these two DEMs (24 mm extended area - 24 mm without profile corrected) of the same subject generated from two independent image surveys. The change in vertical elevation for the evaluation chart and surrounding ground surface made up of concrete paving stones was calculated from the DoD, (Fig 4.7). The change in elevation (E) is within Limit of Detection (LoD) and is interpreted as no change (±0.49 mm), and the change above the LoD value is interpreted as change (-0.49>E>0.49 mm). We find that the nearby textured concrete ground surface which had a good number of keypoints during sparse point cloud generation shows no change. The shadow areas within the sides of wooden blocks, the edges of wooden blocks and flat and textureless evaluation chart area that had poor image match and thus low keypoints shows changes. Cullen et al. (2018a) have demonstrated that the reliability of SfM to detect sub-mm changes depends on the texture and complexity of the rock surface. SfM is known to less reliable in reconstructing non-textured, reflective and flat objects or scenes (Agisoft, 2016). We notice that these changes are not related to the distance from the control target but areas with poor image matching due to homogeneous texture and shadows. The rock

surface with non-homogeneous texture will produce better image matches and thus improve model quality and accuracy. The result shows that with our control target approach, it is possible to generate DEM with sub-mm accuracy, but this will depend on the complexity and texture of the surface. Using our approach, Cullen et al. (2018a) successfully generated DEMs of simulated rock surface (~100 cm^2) with sub-mm accuracy.

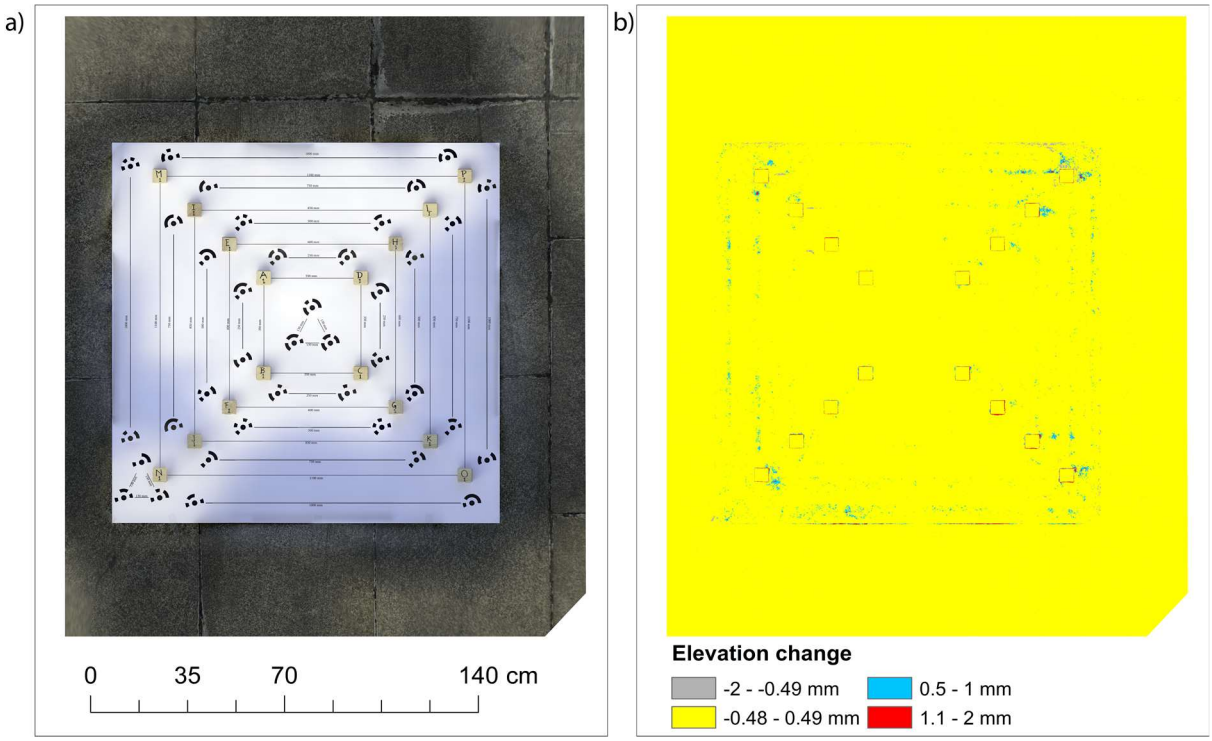


Fig 4.7. (a) The orthophoto showing evaluation test chart and nearby ground surface area. (b) DoD showing a change in surface elevation between two independent DEMs. The yellow coloured area is within the LoD (±0.49 mm) and is interpreted as no change.

4.5.Field application of SfM for DEM generation

We tested the approach on eight Moenkopi Sandstone outcrops (intermediate axis = ~ 2 m) at a field site near Meteor Crater, Arizona. Meteor Crater is located in a relatively low-relief, southern part of the Colorado Plateau near the town of Winslow in north-central Arizona (35° 1' N, 111° 1' W) (Shoemaker and Kieffer, 1979; Shoemaker, 1987). Moenkopi is very fine-grained reddish-brown sandstone (Kring, 2017). These outcrops have weathered to produce surfaces with different shapes, sizes, aspect, slope and contain a range of weathering features such as pits, alveoli, flaking, crumbling, fractures, colouration, and lichen colonisation (see Chapter 6).

4.5.1. Data collection

We used the zoom lens set at 24 mm focal length (36 mm full frame camera equivalent). The focal length of 24 mm was chosen as it provided a greater field of view where there was little space to move around to take images in the field (e.g., very steep slope). Camera aperture was set to f/6.3. A smaller aperture allows less light to reach the camera sensor and gives a larger depth of field (Haukebø, 2015). An image with larger depth of field is sharper and has a larger area in focus and are recommended for photogrammetry work (Bedford, 2017). A higher shutter speed (1/400) was chosen to compensate camera shake due to, e.g., the wind. ISO was kept at 100 to minimise the noise in the images (Mosbrucker et al., 2017). White balance was kept at daylight mode. During photo acquisition, care was taken to ensure that the image was sharp, and everything in the frame was in focus. Matrix metering mode was selected to provide the best exposure and equal brightness throughout the image. Images were taken in autofocus mode to maintain optimal image quality (sharpness). These settings were chosen based on the lighting and field conditions, and field testing demonstrated high image quality at these settings.

Several images were acquired from different vantage points. Firstly, from all around the boulder surface (from a distance of ~2 m) followed by additional close-range (from a distance of < ~1 m) images (see Figure 8). Images were acquired with at least 60% lateral overlap. The theoretical minimum number of images required in SfM workflow is 3 (Favalli et al., 2012; Westoby et al., 2012). However, there is no maximum limit to the number of input images in the SfM workflow. The number of images required to reconstruct accurate dense point cloud depends on the size and complexity (e.g. shape, surface texture, curvature, and slope) of the outcrop. It is always better to take more images as it will permit less sharp images to be discarded before processing.



Fig 4.8. Multi-exposure image showing the different spatial positions from where images were acquired. First images were acquired from a distance of ~2 m then close-up images were taken from a distance of <~1 m. DEM and orthophoto of the imaged boulder are shown in Figure 10 g and h.

For a detailed guideline for ideal image acquisition in the field, we recommend the following: Smith et al. (2016); Bedford (2017); Mosbrucker et al. (2017). For our data collection, a triangle coded control target (Fig 4.2) was placed on the ground parallel to the top surface of the boulder (Fig 4.1). It is crucial for the control target to be flat and approximately parallel to the surface of interest as it defines the orientation of the surface of interest in the DEM. If the adjacent ground is not level, the control target can be placed on top of the target surface. We used four rulers of 30 cm and placed them around the outcrops (Fig 4.1). These rulers were used as checkpoints to estimate horizontal errors in the DEMs. The images were acquired in quick succession in the field to ensure that there was a minimum change in the shadow lengths and lighting conditions. We acquired images during early morning and evening and tried to avoid shadows in the image. The images were shot in raw format. A potential limitation to this in the field is that they take up to twice as much storage space as JPEGs. For an area ~10m^2, placement of GCPs, rulers and image acquisition took approximately 20 minutes. Images were processed as described in section 2.4. DEM and Orthophoto generation took 8-10 hours on “high” dense point cloud quality setting.

4.5.2. Field Results

4.5.2.1.DEMs of Moenkopi outcrops in the field

We generated eight DEMs and orthophotos of weathered Moenkopi outcrop surfaces (Fig 4.9 and 4.10). We find that small weathering features, such as weathering pits (mm scale), are clearly resolved in our DEMs and Orthophotos (Fig 4.9 and 4.10). Details of DEM parameters have been summarized in Table 4.5. Horizontal errors for checkpoints were calculated by measuring the length of rulers from orthophoto in Photoscan and subtracting the known length of the ruler from it. The distance of the checkpoints from the control target was measured in Photoscan. Horizontal error propagation with distance from the control target in DEMs is presented in Table 4.6. The resolution of DEMs ranges from 0.45 to 0.68 mm/pixel. All the Orthophotos have a resolution of 0.5 mm/pixel. Horizontal and vertical RMSE of control points is less than 0.5 mm except for vertical error for boulder S2-M2 (Table 4.5). Horizontal RMSE estimated from checkpoints were also less than 0.5 mm (Table 4.5).

Table 4.5. Field DEM data summary

DEM	Boulder dimension (m)	No. of Images	Resolution (mm/pix)	Reprojection Error (pix)	RMSE XY (control) (mm)	RMSE Z (control) (mm)	Projection accuracy (control) (pix)	RMSE XY (check points) (mm)
S2-M1	2.64 × 1.91	62	0.68	0.45	0.26	0.28	0.23	0.31
S2-M2	1 × 0.9	47	0.49	0.56	0.28	0.88	0.29	0.22
S2-M3	1.82 × 1.23	55	0.61	0.46	0.28	0.14	0.29	0.21
S2-M4	1.31 × 1.04	48	0.45	0.50	0.31	0.64	0.14	0.15
S2-M5	1.38 × 1.05	55	0.55	0.67	0.26	0.1	0.29	0.19
S2-M7	2.5 × 1.6	59	0.51	0.48	0.35	0.39	0.21	0.13
S2-M20	3.2 × 1.8	52	0.60	0.41	0.32	0.28	0.09	0.25
S3-M33	5 × 2.9	66	0.58	0.30	0.32	0.38	0.06	0.27

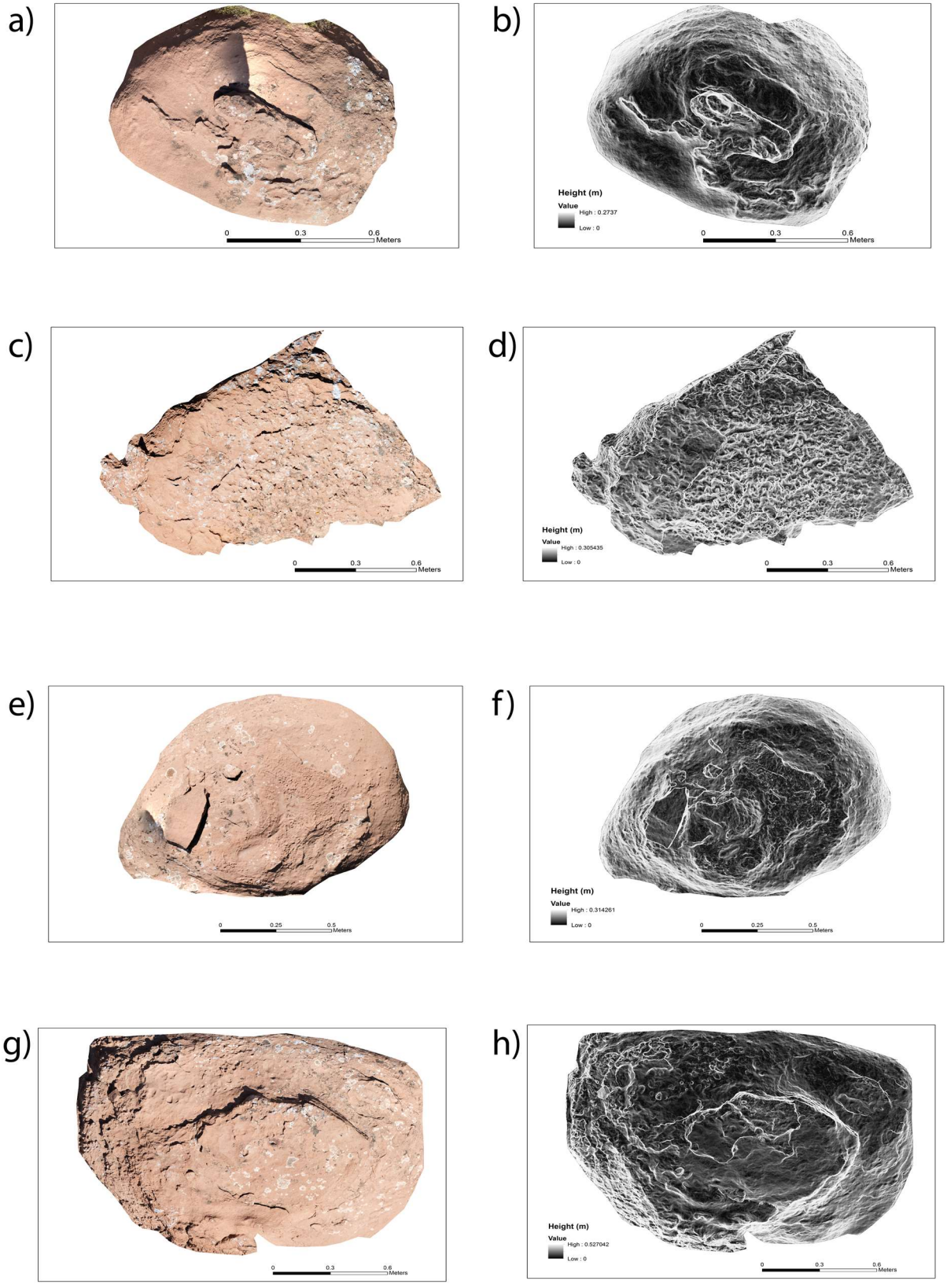


Fig 4.9. Orthophotos and DEMs of Moenkopi outcrops. (a) and (b) Boulder S2-M2. (c) and (d) Boulder S2-M5. (e) and (f) Boulder S2-M4. (g) and (h) Boulder S2-M3.

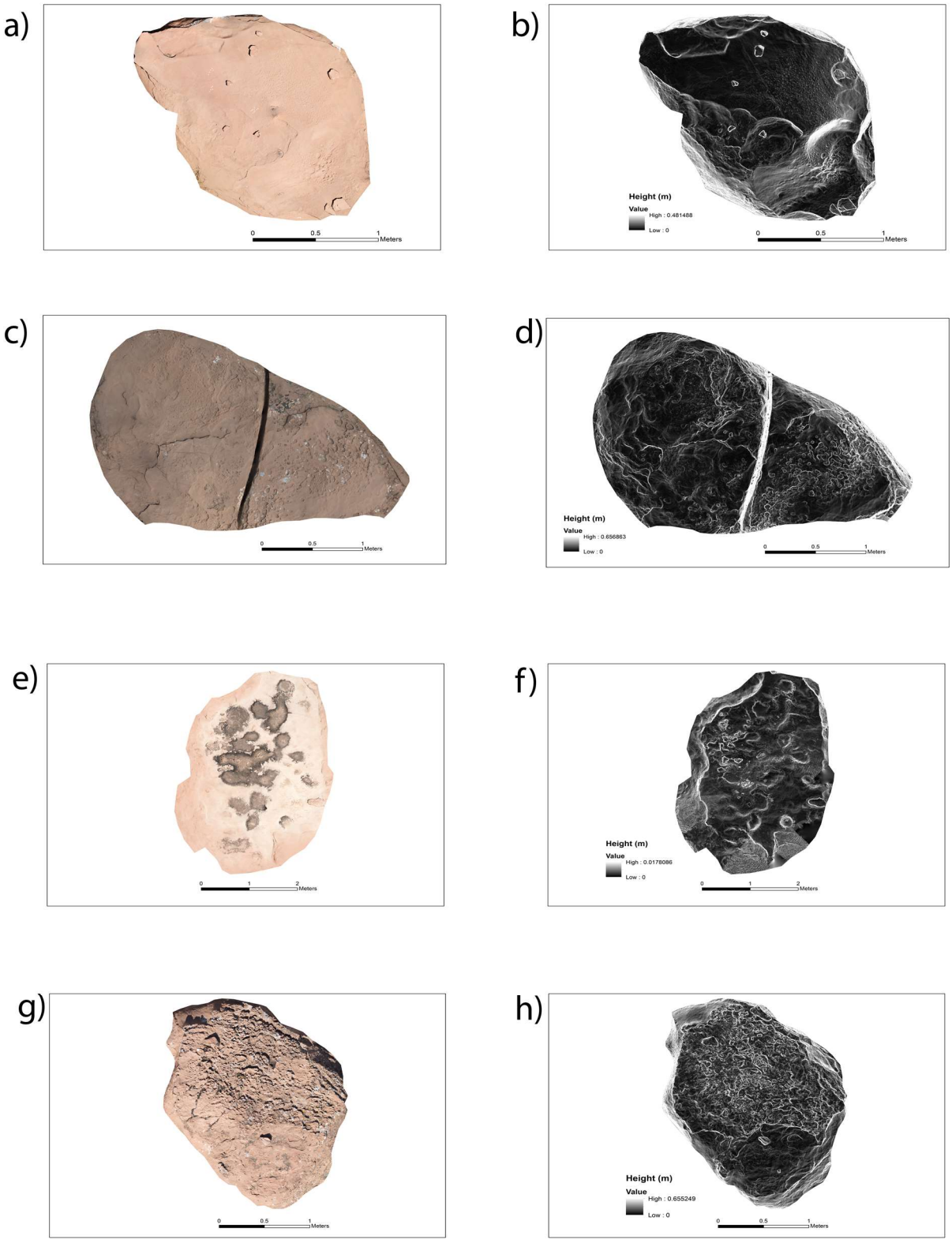


Fig 4.10. Orthophotos and DEMs of Moenkopi outcrops. (a) and (b) Bedrock S2-M7. (c) and (d) Bedrock S2-M20. (e) and (f) Bedrock S3-M33. (g) and (h) Boulder S2-M1.

Table 4.6. Horizontal error propagation with distance from control target in DEMs from the field.

Distance from the target (m)	S2-M1 (mm)	Distance from the target (m)	S2-M2 (mm)	Distance from the target (m)	S2-M3 (mm)
1.39	0.1	0.57	0.2	1.59	0.2
0.8	0.1	0.63	0.2	0.31	0.2
2.5	0.1	1	0.3	1.42	-0.1
3.4	-0.6	1.2	0.2	1.95	0.3

Distance from the target (m)	S2-M4 (mm)	Distance from the target (m)	S2-M5 (mm)	Distance from the target (m)	S2-M7 (mm)
1.1	0.1	1.1	-0.2	2.47	0.1
0.71	0.1	1.18	-0.1	1.9	-0.1
1.24	0.2	1.55	0.1	0.56	0.2
1.43	0.2	1.41	-0.3	1.95	0.1

Distance from the target (m)	S2-M20 (mm)	Distance from the target (m)	S2-M33 (mm)
0.45	0.2	5.66	-0.1
1.48	0.3	4.21	0.4
2.48	0.3	2.17	0.2
2.68	-0.2	2.72	0.3

4.6.Discussion

There are significant technical and logistical challenges that have resulted in geomorphologists not directly capturing the topographic data of outcrops at the microscale (mm) in the field (Ehlmann et al., 2008b). In order to generate high-resolution DEMs (~mm accuracy) of the relatively small boulder and bedrock surfaces (areas < 10 m^2), geographic coordinates cannot be used to register SfM dense point cloud. GPS surveying is used to collect topographic point data from surfaces which can be used to register SfM point dense point cloud to build a DEM. The surveying equipment can be expensive (e.g. dGPS, RTK-GPS, and total station). These survey instruments (except total station) have centimetre accuracy, which is inadequate for generating DEMs of sub-mm accuracy. The equipment can be challenging to transport in poorly accessible field terrains and can rely on satellite signals which may not work in all locations or global locations. In addition, the equipment requires a relatively low gradient, stable surface to set up. A relatively new approach known as 'direct georeferencing' only requires the camera orientation parameters and GPS (Carbonneau and Dietrich, 2016). However, it can only provide centimetre accuracy, which is coarser than needed for small-scale weathering feature analysis.

A total station can be used to determine the coordinates of an unknown point relative to a known coordinate if a direct line of sight can be established between the two points. Coordinates obtained from a total station can be used to register SfM dense point cloud to generate high-resolution DEMs (mm accuracy). However, operating a total station in challenging field conditions have drawbacks similar to those of dGPS survey equipment described above.

A number of previous studies have produced mm-cm resolution DEMs with mm-cm horizontal and vertical accuracy (Favalli et al., 2012; James and Robson, 2012; Bretar et al., 2013; Snapir et al., 2014; Haukebø, 2015; Leon et al., 2015; Micheletti et al., 2015a; Balaguer-Puig et al., 2017a; Prosdocimi et al., 2017; Vinci et al., 2017; Smith and Warburton, 2018). These studies employed relatively complicated methods for georeferencing SfM dense point cloud to generate DEM, for example, Favalli et al. (2012) and Micheletti et al. (2015a) used a laser scanner coordinate system, Snapir et al. (2014) used laser range finder and optical level to find the relative 3D positions of the GCPs, Bretar et al. (2013) employed stereo-photogrammetric method using a measuring tape for scaling the model, Haukebø (2015) measured 3D positions of each camera positions which are

difficult to replicate in the field, James and Robson (2012) utilised distance measured between multiple points on a turntable to scale the model of a sample of size 10 cm in the lab, Prosdocimi et al. (2017) used RTK-GPS to reference DEMs of soil plots (0.25 m^2) in the field, Leon et al. (2015) used handheld GPS and several GCPs to scale the DEMs, and others (Balaguer-Puig et al., 2017a; Vinci et al., 2017; Smith and Warburton, 2018) used a total station to estimate coordinates for GCPs.

The method presented by Snapir et al. (2014) is useful for making DEMs of a horizontal surface, but difficult to replicate on remote and treacherous field terrain (e.g. slope of mountain, crater or canyon wall). This is due to the difficulty of placing several GCPs and determining their relative position with sub-mm accuracy in these terrains. Another problem of using many GCPs for smaller surface (<5 m^2) is that it may cover the area of interest and obscure the DEM of the target surface for further analysis. In this study, we have solved this problem by using a small triangle control target (area ~75 cm^2, Fig 4.2) to georeference the dense point cloud used to generate DEMs with high accuracy. In our experience, we found that using three arbitrary points separated by a longer distance (few metres) and using these points to find relative coordinates with each other can be difficult in the field due to curvature and slope of the rock surfaces (e.g. Heindel et al. (2018)). In comparison, this study achieved sub-mm horizontal (<0.5 mm) and vertical (<1 mm) accuracy in sub-mm resolution DEM using a relatively simple georeferencing approach (section 4.2.2) without any expensive and bulky survey equipment. The DEMs generated following our methodology have sufficient resolution for measurement and quantification of mm-cm scale rock breakdown features.

4.6.1. High-resolution DEMs with low errors

Scaling errors in DEMs are important as they will affect any 2D distance or 3D volume measurements obtained from the DEMs (Carbonneau and Dietrich, 2016). Uncertainties in the DEMs are linked to the accuracy of the SfM model (James et al., 2017b), and knowledge of the source and magnitude of error helps in interpreting the results. The resolution and accuracy of SfM based DEMs also relies on image quality. Low-quality images used in SfM workflow reduces the resolution and accuracy of DEMs (Russell, 2016). It has been found that image acquisition geometry affects the output of SfM models (Carbonneau and Dietrich, 2016; Morgan et al., 2017). We acknowledge that controlling image acquisition geometry in the field will be difficult as the outcrop may not be accessible from all angles for image acquisition (e.g. a boulder on steeply sloping crater wall). The error in DEMs depends mainly on image quality and geometry and the method of georeferencing. Proper planning

of image acquisition and high GCP accuracy can improve the accuracy of DEM. Image matching is a limiting factor for point cloud density, camera calibration, error related to model scaling and orientation in the SfM workflow and DEM accuracy (Mosbrucker et al., 2017). Image matching depends on image quality, lighting condition, surface texture and the complexity of the subject. Image quality depends on good exposure (which depends on camera settings and lighting conditions), sharpness (i.e. the entire subject in the image in focus), noise in the image (higher ISO), camera configuration (camera sensor and lens combination). Improvement in image matching reduces reprojection error which ultimately propagates high accuracy in the dense point cloud and DEM. We have achieved a horizontal accuracy of <0.5 mm for in situ generated DEM of boulders and bedrock. To our knowledge, this accuracy has not been reported before in the literature for SfM generated DEMs of rock outcrops generated in the field.

4.6.2. DEM resolution

The resolution of the DEM depended on the resolution of camera sensor used, the distance of image acquisition from the object, quality of images and quality settings used for processing dense point cloud in Photoscan. Since a 24 MP camera was used and images were acquired <2 m from the boulder/bedrock resulted in DEM of resolution <1 mm/pixel. This resolution could be further increased if "Ultra High" quality settings would have been used while processing dense point cloud in Photoscan. Instead, "High" quality setting was chosen during processing dense point cloud because it cut down the time required to process DEM by 70-80% and resulted in a smaller DEM file size which can be easily handled in external analysis software (e.g. ArcGIS, Landserf).

In our experiment, we found that "medium" dense point quality setting does not dramatically deteriorate the horizontal and vertical accuracy of DEM. The "medium" quality DEM is good enough for geomorphological studies if time and computing power are a constraint. Given optimal lighting and weather conditions, this SfM workflow can outperform laser scanning solutions for small surfaces (<10 m^2). However, the performance of SfM based topographic data is affected by vegetation and shadows and texture of the surface of interest (Micheletti et al., 2015b; Smith et al., 2016).

4.6.3. DEM errors

Our experiment was conducted under controlled conditions to validate sub-mm horizontal and vertical accuracy using our triangle control target georeferencing approach. We obtained

horizontal accuracy <0.60 mm and vertical accuracy of <0.45 mm in our experiment. The use of the prime lens at a fixed focus will yield lower errors compared to a zoom lens for SfM photogrammetry, as suggested by Mosbrucker et al. (2017). Our experimental results suggest that prime lens had slightly better vertical accuracy compared to zoom lens when both lenses were used in autofocus mode. However, there is no statistically significant difference in the accuracy of DEMs generated from prime and zoom lens used at autofocus. The slightly higher errors due to using zoom lens in comparison with prime lenses is acceptable considering that it offers flexibility to choose a focal length (choice depends on the field of view) and its low cost. Most of the less expensive DSLR camera lenses do not come with a focusing scale. Lens set at autofocus is more suitable than those set at the fixed focus for acquiring images of outcrops in challenging and steep terrains such as crater walls. Lens set at autofocus allows us to take sharper images from a very close distance (few centimetres) as well as from farther away (few meters) from the rock outcrop without introducing issues associated with the hyperfocal distance of the camera system. Photoscan does an excellent job performing accurate autocalibration from EXIF data of the images. We found that using AdobeRGB colour space and tiff image compression improves the DEM accuracy. Prior Lens profile correction and the position of the control target had a negligible effect on the accuracy of DEM. Masking of images in our experiment did not reduce the processing time for DEM generation. We find that changing the position of the control target with respect to the area of interest had an almost negligible effect on horizontal and vertical errors. For the field data, the horizontal checkpoint errors derived using rulers for Moenkopi outcrop DEMs in the field (Table 4.6) correspond to the results obtained in our experiment (Fig 4.4a). In some cases, the horizontal error was found to be lower in the field for a certain distance from the control target (Table 4.6) compared to the results obtained in the experiment (Fig 4.4a). This could be due to better image texture of weathered outcrops in the field compared to the reduced texture of our experiment subject (Fig 4.3). This is evident in the reprojection error and projection accuracy (Table 4.4 and 4.5). Some of the field DEMs have lower reprojection and projection error than the DEMs generated in the experiment. Photoscan provides an option to improve the reprojection errors and thus the overall error in DEMs if errors are high due to poor image matching. This can be performed using “gradual selection” tool in Photoscan to filter and remove tie points with high reprojection errors after image matching during stage 2 (see Table 4.2) of processing DEM (Agisoft, 2016).

4.6.4. Portable and affordable

For many projects, it is the budget, ease of use, and portability that require researchers to choose one technique over others. To date, relatively few studies have undertaken a cost-benefit, data acquisition rate, spatial coverage, operating conditions, resolution and accuracy analysis of the SfM with other topography data collection methods. Some researchers (e.g. Smith et al. (2016) and Wilkinson et al. (2016)) have proposed that SfM photogrammetry ranks highly as it is the cheapest and has the highest resolution compared to other topographic data collection methods (e.g. total station, differential GPS (dGPS), Terrestrial Laser Scanning (TLS), stereophotogrammetry). They also found that the speed of data acquisition and accuracy for SfM method is comparable to TLS and stereophotogrammetry in a close-range scenario. Our work supports their findings but goes further and outlines an approach to produce sub-mm resolution DEMs with sub-mm accuracy using ground-based, close-range SfM photogrammetry. The cost of the camera system (camera + zoom lens) used in this study is €460. The triangle control target used in this study cost less than €10. The educational licence of Agisoft Photoscan was purchased for €600 (a one-time investment). The total cost of field equipment and software used in this study is well within the budget of a small research project. In addition, the total weight of the camera system and control target used is less than 1 kg. Our approach can be used in any scenario where high resolution, accurate DEMs and orthophotos are required (e.g., scaled laboratory experiments or small-scale features in the field). In addition, we have demonstrated an SfM photogrammetry approach that is relatively affordable, field-portable, fast and efficient method without requiring any prior information on camera position, orientation or internal camera parameters or the need for additional survey equipment.

4.6.5. Importance of microtopographic data in the rock breakdown

We propose that the generation of microscale topographic data by methods described here will be important for the advancement of rock breakdown studies. Specific rock breakdown processes can leave a unique morphological signature on rock surfaces (Bourke and Viles, 2007). More often, the synergies linking breakdown processes, mechanisms and agents operate over a range of spatial and temporal scales (Viles, 2013b) and can result in a palimpsest of features that represent a change in, e.g., weathering conditions (Ehlmann et al., 2008b). As such, the breakdown is non-linear, and processes can exploit inheritance features and overprint them over time. Micro-scale DEMs will permit us to move from a predominant specific geomorphometry approach to a general geomorphometry approach, where, e.g., the relationships can be investigated. In addition, our approach will ease the

cumbersome task of collecting morphometric data on individual weathering features in the field (e.g. Norwick and Dexter (2002); Bruthans et al. (2018)).

There are a number of areal surface roughness and geomorphometric parameters that can be applied to quantify rock breakdown (Leach, 2013; Lai et al., 2014; Davis et al., 2015; Du Preez, 2015; Trevisani and Rocca, 2015; Verma and Bourke, 2017). The ability to quantify surface change across an area rather than limited to specific points will aid interpretation of the causal links between controls and resultant landform development. This is particularly relevant for the recent developments in monitoring micro-climates (Mol and Viles, 2012; Coombes et al., 2013) of rock breakdown environments or dynamic environments such as intertidal rock platforms (e.g., Cullen et al. (2018a)).

Our companion paper (Cullen et al., 2018a) shows the potential application of our approach and provides a comparison between the traditional method of measuring erosion on rock shore platforms using a Traversing/Micro Erosion Meter (T/MEM) with Structure from Motion (SfM) Photogrammetry. The results indicated that SfM Photogrammetry offers several advantages over the T/MEM allowing measurement of erosion at different scales on rock surfaces with low roughness while also providing a means for identifying different processes and styles of erosion. In addition, the work demonstrated accuracy in the repeatability of measurements.

Diagnostic indices that reveal morphometric differences has been attempted at the landscape scale (e.g., Lyew-Ayee et al. (2007)). The production of a high-resolution dataset for microscale weathering features offers an opportunity to test analysis routines such as semi-variogram, areal surface roughness and fractal analysis to identify patterns of the breakdown features at different scales (Inkpen et al., 2000; Viles, 2001; Fardin et al., 2004; Bourke et al., 2008; Leach, 2013). Areal surface fractal analysis of rock surfaces would help to elucidate on equifinality in the production of breakdown features and issue of distinguishing fossil from current forming features (Viles, 2001; Fardin et al., 2004).

Our approach permits the comparative study of weathering features in different environments and the same environment over time. The ability to replicate our approach to assemble a time-series of data (as outlined in a companion paper, Cullen et al. (2018a), will facilitate the determination of weathering rates in the field at seasonal and annual temporal

scales. This will assist with issues in extrapolating from the laboratory to the field where rates of weathering have traditionally been overestimated (Viles, 2001).

4.7.Conclusion

We have developed and tested a triangle coded control target which is used to register SfM generated dense point clouds to produce DEMs. We applied SfM photogrammetry on eight Moenkopi Sandstone outcrops near Meteor Crater, Arizona. We found that the deployment of existing techniques to generate high-resolution data not suitable for use in our remote and poorly accessible field terrains (e.g. crater wall, canyon). In this study, we have demonstrated that this challenge can be overcome by SfM photogrammetry. A triangle coded control target (GCPs) was specifically developed to a) compute local coordinates and b) used to georeference the 3D point cloud generated by SfM photogrammetry. This allowed generation of a sub-mm resolution DEM with sub-mm accuracy. We validated sub-mm accuracy in DEMs with an experimental approach. Our study demonstrated that it is possible to use our method to generate DEMs of rock outcrops (< 10 m^2) in the field to sub-mm horizontal and vertical accuracy. In optimal conditions (good lighting, weather and vegetation-free) local coordinate georeferencing workflow may outperform TLS for certain applications. Development of a triangle coded control target not only helped to generate sub-mm resolution DEM but also permitted the automation of the SfM batch process workflow, generating a DEM as the end product. We anticipate that the ease of production of sub-mm resolution DEM without the use of any bulky survey equipment has the potential to transform the existing approach to small-scale topographic data acquisition and offers a promising solution to data collection challenges in the confined laboratory and difficult field conditions. The SfM workflow in this study provides an easy, simple, quick and relatively affordable method to generate 3D topographic data for weathering features in hard to access terrains. The high-resolution DEMs of rocks surfaces in this study facilitate faster data collection and offers a potential solution to overcome many challenges in the field, including short and long-term monitoring of micro to mesoscale erosion in dynamic environments (Cullen et al., 2018a).

References

AGISOFT, L. 2016. Agisoft PhotoScan user manual, Professional edition, version 1.2. 2016.

AGUILAR, M., AGUILAR, F. & NEGREIROS, J. 2009. Off-the-shelf laser scanning and close-range digital photogrammetry for measuring agricultural soils microrelief. *Biosystems engineering,* 103**,** 504-517.

ANDREWS, D., BEDFORD, J. & BRYAN, P. 2013. A comparison of laser scanning and structure from motion as applied to the great barn at harmondsworth, uk. *ISPRS-International Archives of the Photogrammetry, Remote Sensing and Spatial Information Sciences,* 5**,** W2.

BAKKER, M. & LANE, S. N. 2016. Archival photogrammetric analysis of river–floodplain systems using Structure from Motion (SfM) methods. *Earth Surface Processes and Landforms,* 42**,** 1274-1286.

BALAGUER-PUIG, M., MARQUÉS-MATEU, Á., LERMA, J. L. & IBÁÑEZ-ASENSIO, S. 2017. Estimation of small-scale soil erosion in laboratory experiments with Structure from Motion photogrammetry. *Geomorphology,* 295**,** 285-296.

BEDFORD, J. 2017. *Photogrammetric Applications for Cultural Heritage. Guidance for Good Practice*, Historic England.

BOURKE, M., NICOLI, J., VILES, H. & HOLMLUND, J. 2007. The persistence of fluvial features on clasts: results of wind tunnel abrasion experiments. *Lunar and Planetary Science Conference.* League City, Texas.

BOURKE, M., VILES, H., NICOLI, J., LYEW-AYEE, P., GHENT, R. & HOLMLUND, J. 2008. Innovative applications of laser scanning and rapid prototype printing to rock breakdown experiments. *Earth Surface Processes and Landforms,* 33**,** 1614-1621.

BOURKE, M. C. & VILES, H. A. 2007. *A photographic atlas of rock breakdown features in geomorphic environments*.

BRETAR, F., ARAB-SEDZE, M., CHAMPION, J., PIERROT-DESEILLIGNY, M., HEGGY, E. & JACQUEMOUD, S. 2013. An advanced photogrammetric method to

measure surface roughness: Application to volcanic terrains in the Piton de la Fournaise, Reunion Island. *Remote Sensing of Environment,* 135**,** 1-11.

BRUNIER, G., FLEURY, J., ANTHONY, E. J., GARDEL, A. & DUSSOUILLEZ, P. 2016. Close-range airborne Structure-from-Motion Photogrammetry for high-resolution beach morphometric surveys: Examples from an embayed rotating beach. *Geomorphology,* 261**,** 76-88.

BRUTHANS, J., FILIPPI, M., SLAVÍK, M. & SVOBODOVÁ, E. 2018. Origin of honeycombs: Testing the hydraulic and case hardening hypotheses. *Geomorphology,* 303**,** 68-83.

BUI, Q.-B., MOREL, J.-C., REDDY, B. V. & GHAYAD, W. 2009. Durability of rammed earth walls exposed for 20 years to natural weathering. *Building and Environment,* 44**,** 912-919.

CARBONNEAU, P. E. & DIETRICH, J. T. 2016. Cost-effective non-metric photogrammetry from consumer-grade sUAS: implications for direct georeferencing of structure from motion photogrammetry. *Earth Surface Processes and Landforms,* 42**,** 473-486.

CAROTI, G., ZARAGOZA, I. M.-E. & PIEMONTE, A. 2015. Accuracy assessment in structure from motion 3D reconstruction from UAV-born images: The influence of the data processing methods. *The International Archives of Photogrammetry, Remote Sensing and Spatial Information Sciences,* 40**,** 103.

CARR, B. B., CLARKE, A. B., ARROWSMITH, J. R., VANDERKLUYSEN, L. & DHANU, B. E. 2018. The emplacement of the active lava flow at Sinabung Volcano, Sumatra, Indonesia, documented by structure-from-motion photogrammetry. *Journal of Volcanology and Geothermal Research*.

CASELLA, E., COLLIN, A., HARRIS, D., FERSE, S., BEJARANO, S., PARRAVICINI, V., HENCH, J. L. & ROVERE, A. 2016. Mapping coral reefs using consumer-grade drones and structure from motion photogrammetry techniques. *Coral Reefs***,** 1-7.

CHAN, T. O., LICHTI, D. D., BELTON, D., KLINGSEISEN, B. & HELMHOLZ, P. 2016. Survey Accuracy Analysis of a Hand-held Mobile LiDAR Device for Cultural

Heritage Documentation. *Photogrammetrie-Fernerkundung-Geoinformation,* 2016**,** 153-165.

CHEN, Y., CAO, P., MAO, D., PU, C. & FAN, X. 2014. Morphological analysis of sheared rock with water–rock interaction effect. *International Journal of Rock Mechanics and Mining Sciences,* 70**,** 264-272.

CLAPUYT, F., VANACKER, V. & VAN OOST, K. 2016. Reproducibility of UAV-based earth topography reconstructions based on Structure-from-Motion algorithms. *Geomorphology,* 260**,** 4-15.

COOMBES, M. A., NAYLOR, L. A., VILES, H. A. & THOMPSON, R. C. 2013. Bioprotection and disturbance: seaweed, microclimatic stability and conditions for mechanical weathering in the intertidal zone. *Geomorphology,* 202**,** 4-14.

CULLEN, N. D., VERMA, A. K. & BOURKE, M. C. 2018. A comparison of structure from motion photogrammetry and the traversing micro-erosion meter for measuring erosion on shore platforms. *Earth Surf. Dynam.,* 6**,** 1023-1039.

DAVIS, L. G., BEAN, D. W., NYERS, A. J. & BRAUNER, D. R. 2015. GLiMR: A GIS-based method for the geometric morphometric analysis of artifacts. *Lithic Technology,* 40**,** 199-217.

DIETRICH, J. 2015. *Applications of structure-from-motion photogrammetry to fluvial geomorphology.* Ph.D., University of Oregon.

DIETRICH, J. T. 2014. *Applications of Structure-from-Motion Photogrammetry to Fluvial Geomorphology This dissertation has been accepted and approved in partial fulfillment of the requirements for the Doctor of Philosophy degree in the Department of Geography by: Mark Fonstad Chairperson Patricia McDowell Core Member.* University of Oregon.

DIETRICH, J. T. 2016a. Bathymetric Structure-from-Motion: extracting shallow stream bathymetry from multi-view stereo photogrammetry. *Earth Surface Processes and Landforms,* 42**,** 355-364.

DIETRICH, J. T. 2016b. Riverscape mapping with helicopter-based Structure-from-Motion photogrammetry. *Geomorphology,* 252**,** 144-157.

DU PREEZ, C. 2015. A new arc–chord ratio (ACR) rugosity index for quantifying three-dimensional landscape structural complexity. *Landscape ecology,* 30**,** 181-192.

EHLMANN, B. L., VILES, H. A. & BOURKE, M. C. 2008. Quantitative morphologic analysis of boulder shape and surface texture to infer environmental history: A case study of rock breakdown at the Ephrata Fan, Channeled Scabland, Washington. *Journal of Geophysical Research: Earth Surface* 113.

ELTNER, A., KAISER, A., CASTILLO, C., ROCK, G., NEUGIRG, F. & ABELLÁN, A. 2016. Image-based surface reconstruction in geomorphometry–merits, limits and developments. *Earth Surface Dynamics,* 4**,** 359-389.

FARDIN, N., FENG, Q. & STEPHANSSON, O. 2004. Application of a new in situ 3D laser scanner to study the scale effect on the rock joint surface roughness. *International Journal of Rock Mechanics and Mining Sciences,* 41**,** 329-335.

FARDIN, N., STEPHANSSON, O. & JING, L. 2001. The scale dependence of rock joint surface roughness. *International Journal of Rock Mechanics and Mining Sciences,* 38**,** 659-669.

FAVALLI, M., FORNACIAI, A., ISOLA, I., TARQUINI, S. & NANNIPIERI, L. 2012. Multiview 3D reconstruction in geosciences. *Computers & Geosciences,* 44**,** 168-176.

FONSTAD, M. A., DIETRICH, J. T., COURVILLE, B. C., JENSEN, J. L. & CARBONNEAU, P. E. 2013. Topographic structure from motion: a new development in photogrammetric measurement. *Earth Surface Processes and Landforms,* 38**,** 421-430.

GE, Y., KULATILAKE, P. H., TANG, H. & XIONG, C. 2014. Investigation of natural rock joint roughness. *Computers and Geotechnics,* 55**,** 290-305.

GOUDIE, A. S. & VILES, H. A. 2012. Weathering and the global carbon cycle: geomorphological perspectives. *Earth-Science Reviews,* 113**,** 59-71.

GUIDI, G., GONIZZI, S. & MICOLI, L. 2014. Image pre-processing for optimizing automated photogrammetry performances. *ISPRS Annals of the Photogrammetry, Remote Sensing and Spatial Information Sciences,* 2**,** 145.

HARWIN, S. & LUCIEER, A. 2012. Assessing the accuracy of georeferenced point clouds produced via multi-view stereopsis from unmanned aerial vehicle (UAV) imagery. *Remote Sensing,* 4**,** 1573-1599.

HAUKEBØ, A. R. 2015. *Modelling of Marine Icing with Close Range Photogrammetry.* Masters thesis, UiT The Arctic University of Norway.

HEINDEL, R. C., CHIPMAN, J. W., DIETRICH, J. T. & VIRGINIA, R. A. 2018. Quantifying rates of soil deflation with Structure-from-Motion photogrammetry in west Greenland. *Arctic, Antarctic, and Alpine Research,* 50**,** SI00012.

IMMERZEEL, W., KRAAIJENBRINK, P. & ANDREASSEN, L. 2017. Use of an unmanned aerial vehicle to assess recent surface elevation change of Storbreen in Norway. *Cryosphere Discuss. doi,* 10.

INKPEN, R., COLLIER, P. & FONTANA, D. J. Z. F. G. S. 2000. Close-range photogrammetric analysis of rock surfaces. 67-81.

JALANDONI, A., DOMINGO, I. & TAÇON, P. S. 2018. Testing the value of low-cost structure-from-motion (SfM) photogrammetry for metric and visual analysis of rock art. *Journal of Archaeological Science: Reports,* 17**,** 605-616.

JAMES, M. & ROBSON, S. 2012. Straightforward reconstruction of 3D surfaces and topography with a camera: Accuracy and geoscience application. *Journal of Geophysical Research: Earth Surface,* 117.

JAMES, M. R. & ROBSON, S. 2014. Mitigating systematic error in topographic models derived from UAV and ground-based image networks. *Earth Surface Processes and Landforms,* 39**,** 1413-1420.

JAMES, M. R., ROBSON, S., D'OLEIRE-OLTMANNS, S. & NIETHAMMER, U. 2017a. Optimising UAV topographic surveys processed with structure-from-motion:

Ground control quality, quantity and bundle adjustment. *Geomorphology,* 280**,** 51-66.

JAMES, M. R., ROBSON, S. & SMITH, M. 2017b. 3-D uncertainty-based topographic change detection with structure-from-motion photogrammetry: precision maps for ground control and directly georeferenced surveys. *Earth Surface Processes and Landforms,* 42**,** 1769-1788.

JAVERNICK, L., BRASINGTON, J. & CARUSO, B. 2014. Modeling the topography of shallow braided rivers using Structure-from-Motion photogrammetry. *Geomorphology,* 213**,** 166-182.

KIM, D. H., GRATCHEV, I. & BALASUBRAMANIAM, A. 2015. A photogrammetric approach for stability analysis of weathered rock slopes. *Geotechnical and Geological Engineering,* 33**,** 443-454.

KIM, J.-R. & MULLER, J.-P. 2009. Multi-resolution topographic data extraction from Martian stereo imagery. *Planetary and Space Science,* 57**,** 2095-2112.

KO, J. & HO, Y.-S. 3D Point Cloud Generation Using Structure from Motion with Multiple View Images. The Korean Institute of Smart Media Fall Conference, 2016. 91-92.

KOPPEL, P. 2016. Agisoft Photoscan: Point Cloud accuracy in close range configuration. Koppel Engineering.

KORYTKOWSKI, P. & OLEJNIK-KRUGLY, A. 2017. Precise capture of colors in cultural heritage digitization. *Color Research & Application,* 42**,** 333-336.

KRING, D. A. 2017. Guidebook to the geology of Barringer Meteorite Crater, Arizona (aka Meteor Crater): for the 80th Annual Meeting of the Meteoritical Society July 2017. Lunar and Planetary Institute.

LAI, P., SAMSON, C. & BOSE, P. 2014. Surface roughness of rock faces through the curvature of triangulated meshes. *Computers & Geosciences,* 70**,** 229-237.

LEACH, R. 2013. *Characterisation of areal surface texture*, Springer.

LEON, J. X., ROELFSEMA, C. M., SAUNDERS, M. I. & PHINN, S. R. 2015. Measuring coral reef terrain roughness using 'Structure-from-Motion'close-range photogrammetry. *Geomorphology,* 242**,** 21-28.

LI, R., HWANGBO, J., CHEN, Y. & DI, K. 2011. Rigorous photogrammetric processing of HiRISE stereo imagery for Mars topographic mapping. *IEEE Transactions on Geoscience and Remote Sensing,* 49**,** 2558-2572.

LYEW-AYEE, P., VILES, H. & TUCKER, G. 2007. The use of GIS-based digital morphometric techniques in the study of cockpit karst. *Earth Surface Processes and Landforms* 32**,** 165-179.

MARTEAU, B., VERICAT, D., GIBBINS, C., BATALLA, R. J. & GREEN, D. R. 2016. Application of Structure-from-Motion photogrammetry to river restoration. *Earth Surface Processes and Landforms,* 42**,** 503-515.

MCCARROLL, D. 1992. A new instrument and techniques for the field measurement of rock surface roughness. *Zeitschrift fur Geomorphologie,* 36**,** 69-79.

MCCARROLL, D. & NESJE, A. 1996. Rock surface roughness as an indicator of degree of rock surface weathering. *Earth Surface Processes and Landforms,* 21**,** 963-977.

MEDAPATI, R. S., KREIDL, O. P., MACLAUGHLIN, M., HUDYMA, N. & HARRIS, A. Quantifying surface roughness of weathered rock-examples from granite and limestone. Geo-Congress 2013: Stability and Performance of Slopes and Embankments III, 2013. 120-128.

MERCER, J. J. & WESTBROOK, C. J. 2016. Ultrahigh-resolution mapping of peatland microform using ground-based structure from motion with multiview stereo. *Journal of Geophysical Research: Biogeosciences,* 121**,** 2901-2916.

MICHELETTI, N., CHANDLER, J. H. & LANE, S. N. 2015a. Investigating the geomorphological potential of freely available and accessible Structure-from-Motion photogrammetry using a smartphone. *Earth Surface Processes and Landforms,* 40**,** 473-486.

MICHELETTI, N., CHANDLER, J. H. & LANE, S. N. 2015b. Structure from Motion (SfM) Photogrammetry. *In:* COOK, S. J., CLARKE, L.E. & NIELD, J.M. (ed.) *Geomorphological Techniques.* British Society for Geomorphology.

MŁYNARCZUK, M. 2010. Description and classification of rock surfaces by means of laser profilometry and mathematical morphology. *International Journal of Rock Mechanics and Mining Sciences,* 47**,** 138-149.

MOL, L. & VILES, H. A. 2012. The role of rock surface hardness and internal moisture in tafoni development in sandstone. *Earth Surface Processes and Landforms,* 37**,** 301-314.

MORGAN, J. A., BROGAN, D. J. & NELSON, P. A. 2017. Application of Structure-from-Motion photogrammetry in laboratory flumes. *Geomorphology,* 276**,** 125-143.

MOSBRUCKER, A. R., MAJOR, J. J., SPICER, K. R. & PITLICK, J. 2017. Camera system considerations for geomorphic applications of SfM photogrammetry. *Earth Surface Processes and Landforms,* 42**,** 969-986.

NIETHAMMER, U., JAMES, M., ROTHMUND, S., TRAVELLETTI, J. & JOSWIG, M. 2012. UAV-based remote sensing of the Super-Sauze landslide: Evaluation and results. *Engineering Geology,* 128**,** 2-11.

NILOSEK, D., WALVOORD, D. J. & SALVAGGIO, C. 2014. Assessing geoaccuracy of structure from motion point clouds from long-range image collections. *Optical Engineering,* 53**,** 113112-113112.

NORWICK, S. A. & DEXTER, L. R. 2002. Rates of development of tafoni in the Moenkopi and Kaibab formations in Meteor Crater and on the Colorado Plateau, northeastern Arizona. *Earth Surface Processes and Landforms,* 27**,** 11-26.

OZYESIL, O., VORONINSKI, V., BASRI, R. & SINGER, A. 2017. A Survey on Structure from Motion. *arXiv preprint arXiv:1701.08493*.

PALMER, L. M., FRANKE, K. W., ABRAHAM MARTIN, R., SINES, B. E., ROLLINS, K. M. & HEDENGREN, J. D. 2015. Application and Accuracy of Structure from

Motion Computer Vision Models with Full-Scale Geotechnical Field Tests. *IFCEE 2015.*

PANAGIOTIDIS, D., SUROVÝ, P. & KUŽELKA, K. 2016. Accuracy of Structure from Motion models in comparison with terrestrial laser scanner for the analysis of DBH and height influence on error behaviour. *J. FOR. SCI,* 62**,** 357-365.

PEARSON, E., SMITH, M., KLAAR, M. & BROWN, L. 2017. Can high resolution 3D topographic surveys provide reliable grain size estimates in gravel bed rivers? *Geomorphology,* 293**,** 143-155.

PIERMATTEI, L., CARTURAN, L., DE BLASI, F., TAROLLI, P., DALLA FONTANA, G., VETTORE, A. & PFEIFER, N. 2016. Suitability of ground-based SfM–MVS for monitoring glacial and periglacial processes. *Earth Surface Dynamics,* 4**,** 425-443.

PROSDOCIMI, M., BURGUET, M., DI PRIMA, S., SOFIA, G., TEROL, E., COMINO, J. R., CERDÀ, A. & TAROLLI, P. 2017. Rainfall simulation and Structure-from-Motion photogrammetry for the analysis of soil water erosion in Mediterranean vineyards. *Science of the Total Environment,* 574**,** 204-215.

REMONDINO, F., SPERA, M. G., NOCERINO, E., MENNA, F. & NEX, F. 2014. State of the art in high density image matching. *The Photogrammetric Record,* 29**,** 144-166.

RIEKE-ZAPP, D. H. & NEARING, M. A. 2005. Digital close range photogrammetry for measurement of soil erosion. *The Photogrammetric Record,* 20**,** 69-87.

RUSSELL, T. S. 2016. Calculating the Uncertainty of a Structure from Motion (SfM) Model, Cadman Quarry, Monroe, Washington. University of Washington.

SAPIRSTEIN, P. 2018. A high-precision photogrammetric recording system for small artifacts. *Journal of Cultural Heritage,* 31**,** 33-45.

SAPIRSTEIN, P. & MURRAY, S. J. J. O. F. A. 2017. Establishing best practices for photogrammetric recording during archaeological fieldwork. 42**,** 337-350.

SAPIRSTEIN, P. J. J. O. A. S. 2016. Accurate measurement with photogrammetry at large sites. 66**,** 137-145.

SCHONBERGER, J. L. & FRAHM, J.-M. Structure-from-motion revisited. Proceedings of the IEEE Conference on Computer Vision and Pattern Recognition, 2016. 4104-4113.

SEITZ, L., HAAS, C., NOACK, M. & WIEPRECHT, S. 2018. From picture to porosity of river bed material using Structure-from-Motion with Multi-View-Stereo. *Geomorphology,* 306**,** 80-89.

SHERVAIS K., A. D. J. 2016. Structure from Motion (SfM) Photogrammetry Data Exploration and Processing Manuel. Available: https://d32ogoqmya1dw8.cloudfront.net/files/getsi/teaching_materials/high-rez-topo/student_materials/sfm_data_processing_exploration.pdf.

SHOEMAKER, E. M. 1987. Meteor Crater, Arizona. *Geological Society of America, Centennial Field Guide,* 2**,** 399-404.

SHOEMAKER, E. M. & KIEFFER, S. W. 1979. *Guidebook to the geology of Meteor Crater, Arizona*, Center for Meteorite Studies, Arizona State University.

SMITH, M., CARRIVICK, J. & QUINCEY, D. 2016. Structure from motion photogrammetry in physical geography. *Progress in Physical Geography,* 40**,** 247-275.

SMITH, M. & WARBURTON, J. 2018. Microtopography of bare peat: a conceptual model and objective classification from high-resolution topographic survey data. *Earth Surface Processes and Landforms,* 43**,** 1557-1574.

SMITH, M. W. & VERICAT, D. 2015. From experimental plots to experimental landscapes: topography, erosion and deposition in sub-humid badlands from Structure-from-Motion photogrammetry. *Earth Surface Processes and Landforms,* 40**,** 1656-1671.

SNAPIR, B., HOBBS, S. & WAINE, T. 2014. Roughness measurements over an agricultural soil surface with Structure from Motion. *ISPRS Journal of Photogrammetry and Remote Sensing,* 96**,** 210-223.

STURZENEGGER, M. & STEAD, D. 2009. Close-range terrestrial digital photogrammetry and terrestrial laser scanning for discontinuity characterization on rock cuts. *Engineering Geology,* 106**,** 163-182.

SÜSSTRUNK, S., BUCKLEY, R. & SWEN, S. Standard RGB color spaces. Color and Imaging Conference, 1999. Society for Imaging Science and Technology, 127-134.

TACONET, O. & CIARLETTI, V. 2007. Estimating soil roughness indices on a ridge-and-furrow surface using stereo photogrammetry. *Soil and Tillage Research,* 93**,** 64-76.

THOENI, K., GIACOMINI, A., MURTAGH, R. & KNIEST, E. 2014. A comparison of multi-view 3D reconstruction of a rock wall using several cameras and a laser scanner. *The International Archives of Photogrammetry, Remote Sensing and Spatial Information Sciences,* 40**,** 573.

TREVISANI, S. & ROCCA, M. 2015. MAD: robust image texture analysis for applications in high resolution geomorphometry. *Computers & Geosciences,* 81**,** 78-92.

VERMA, A. K. & BOURKE, M. C. 2017. An in-situ Investigation of the Effect of Impact Processes on Rock Breakdown Using sub-mm Resolution DEMs at Meteor Crater, Arizona *9th International Conference on Geomorphology, India*

VILES, H. 2010. Simulating weathering of basalt on Mars and Earth by thermal cycling. *Geophys. Res. Lett.,* 37**,** L18201.

VILES, H., MESSENZEHL, K., MAYAUD, J., COOMBES, M. & BOURKE, M. 2018. Stress histories control rock-breakdown trajectories in arid environments. *Geology,* 46**,** 419-422.

VILES, H. A. 2001. Scale issues in weathering studies. *Geomorphology,* 41**,** 63-72.

VILES, H. A. 2005. Microclimate and weathering in the central Namib Desert, Namibia. *Geomorphology,* 67**,** 189-209.

VILES, H. A. 2013. Synergistic Weathering Processes *In:* SHRODER, J. F. (ed.) *Treatise on Geomorphology.* San Diego: Academic Press.

VINCI, A., TODISCO, F., BRIGANTE, R., MANNOCCHI, F. & RADICIONI, F. 2017. A smartphone camera for the structure from motion reconstruction for measuring soil surface variations and soil loss due to erosion. *Hydrology Research,* 48**,** 673-685.

WARKE, P. 2007. Complex weathering in drylands: implications of 'stress' history for rock debris breakdown and sediment release. *Geomorphology,* 85**,** 30-48.

WESTOBY, M., BRASINGTON, J., GLASSER, N., HAMBREY, M. & REYNOLDS, J. 2012. 'Structure-from-Motion'photogrammetry: A low-cost, effective tool for geoscience applications. *Geomorphology,* 179**,** 300-314.

WHITE, K., BRYANT, R. & DRAKE, N. 1998. Techniques for measuring rock weathering: application to a dated fan segment sequence in southern Tunisia. *Earth Surface Processes and Landforms,* 23**,** 1031-1043.

WILKINSON, M., JONES, R., WOODS, C., GILMENT, S., MCCAFFREY, K., KOKKALAS, S. & LONG, J. 2016. A comparison of terrestrial laser scanning and structure-from-motion photogrammetry as methods for digital outcrop acquisition. *Geosphere,* 12**,** 1865-1880.

ZHU, S., SHEN, T., ZHOU, L., ZHANG, R., FANG, T. & QUAN, L. 2017. Accurate, Scalable and Parallel Structure from Motion. *arXiv preprint arXiv:1702.08601*.

Chapter 5

5. The effect of low impact shock deformation on the subsequent breakdown of sandstone in a semi-arid environment

Co-authors: Mary C. Bourke and David A. Kring

Abstract

This study investigates the effects of low impact shock (<5 GPa) on the subsequent nature of breakdown of Moenkopi Sandstone at Meteor Crater in Arizona. A comparative field study was undertaken between low shocked Moenkopi Sandstone crater wall rock and ejecta on the North, North East, and South crater wall at Meteor Crater and unshocked boulders and bedrock at three control sites that have the same rock formation and similar climatic history but were not affected by impact shock. These three sites along Meteor Crater road were 9, 5, and 4 km respectively away from the N rim of Meteor Crater. We used the Schmidt hammer to collect rock hardness data and Structure from Motion (SfM) to generate high-resolution digital elevation models (DEMs). The DEMs generated were analysed using a range of areal surface roughness parameters and morphometric geomorphic feature classification. We found no statistically significant difference in terms of rock hardness, roughness and morphometric geomorphic features between low-shocked and unshocked Moenkopi Sandstone. However, we do find a statistically significant difference in terms of rock hardness, roughness and morphometric features at multiple scales between N and S-SW facing crater wall slopes for Moenkopi Sandstone at Meteor Crater. Field study revealed that there is no obvious difference in nature of weathering between low shocked and unshocked Moenkopi Sandstone. However, our findings suggest that aspect related microclimate is a dominant control in subsequent weathering of low shocked Moenkopi Sandstone.

5.1. Introduction

Rock breakdown refers to a range of weathering and erosion processes that transform rock masses into the soil and unconsolidated rock materials (Bourke and Viles, 2007). In an arid environment, rock breakdown is crucial to the process of landscape denudation (Warke, 2013). The scale of breakdown features range from μm (e.g., fractures, weathering pits) to m scale (e.g., tafoni, scaling and blisters) (Viles, 2001; Bourke and Viles, 2007).

A considerable amount of literature is available on weathering (Moses et al., 2014; Bland and Rolls, 1998b; Bourke and Viles, 2007; Viles, 2011) and references therein). Many studies have been conducted to understand the efficacy of rock breakdown in desert environments (Goudie et al., 1979; Heslop, 2003; Smith et al., 2005; Viles and Goudie, 2007; Viles et al., 2010; Viles, 2005; Goudie and Parker, 1998; Goudie and Viles, 2000; Goudie et al., 2002; Laity, 2009b; Warke, 2007; Laity and Bridges, 2009; Laity et al., 2001; Bridges and Laity, 2001; Cooke et al., 2006; Smith et al., 2000; Laity, 1995; Laity, 2009a; Laity, 2011; Viles et al., 2018). Rock breakdown studies have been undertaken in a range of terrestrial desert environment (see for example Heslop (2003), Viles and Goudie (2007), Warke (2007), McKay et al. (2009)). Haloclasty, thermoclasty and aeolian abrasion are considered as dominant processes responsible for the mechanical breakdown of rock in an arid environment (Warke, 2013). Role of water-based weathering processes such as slaking and cryoclasty, and the chemical weathering has been considered important in the breakdown of rock as our understanding of moisture and the thermal regime in arid environment deepened (Warke, 2013). In the arid environment, availability of sufficient moisture in the form of dew, fog or occasional rainfall support colonisation of algae and cyanobacteria (Warke, 2013). They are considered responsible for bioweathering and biokarst development on and below rock surfaces (Smith et al., 2000).

Rock breakdown is generally a slow process in semi-arid environment (recession rates 0.5-2.5 mm/100 years; Wells et al. (2008)) and depends on several factors such as lithology and rock properties, environment and microclimate, presence of salt, and stress history (Bland and Rolls, 1998b; Cooke et al., 2006; Heslop, 2003; Smith et al., 2005; McKinley and Warke, 2007; Warke, 2007; Sharma, 2010; Viles et al., 2010; Viles, 2011; Warke, 2013; Viles et al., 2018).

Rock properties are one of the most critical factors that control breakdown (Goudie, 2016). The influence of rock properties on rock breakdown and landform development is termed rock control (Goudie, 2016). The importance of rock control has been recognised for a long time in rock breakdown research, but only a limited number of studies have attempted to quantify its influence (McKinley and Warke, 2007; Tuğrul, 2004).

Rock properties can be measured at a range of scales (µm to m), from lineaments and fractures to rock micro-pores (Goudie, 2016). The scale of analysis is vital in understanding the role of rock control in rock breakdown as the relationship between rock control and rock breakdown operating at different spatial and temporal scales can be non-uniform (Viles, 2013b; Viles, 2001).

In recent years a few researchers have emphasised on the effect of stress history (inherited weakness from an extended period of past weathering) on subsequent weathering (Warke, 2007; Viles et al., 2010; Viles et al., 2018). They found that rocks with a stress history deteriorate faster than un-stressed rocks. Moreover, the nature of pre-stressing has a significant effect on the rate of breakdown (Warke, 2007; Viles et al., 2010; Viles et al., 2018).

At micro and macro scale (μm to cm) porosity is one of the most important rock properties for controlling rock breakdown since it influences the permeability of fluid and salt transport through the rock (McKinley and Warke, 2007; Goudie, 2016). Rock porosity can be due to pores or fractures and is affected by subsequent physical and chemical weathering (Sausse et al., 2001; Cardell et al., 2008; Viles et al., 2010; Jin et al., 2011; Labus and Bochen, 2012; Navarre-Sitchler et al., 2013; De Kock et al., 2015).

An important geologic process that affects rock properties is impact cratering. Impact cratering is a catastrophic and instantaneous geologic process that affects the petrographic and petrophysical properties of rocks (Kieffer, 1971a; French, 1998; Osinski and Pierazzo, 2012). Shock pressure of several gigapascals during impact exceeds the effective strength of target lithology by three to four orders of magnitude leading to melting, vaporisation, shock metamorphism, fracturing and fragmentation of rocks as well as deformation and high-pressure mineral phase transformations (Melosh, 1989; Grieve and Therriault, 2013; Gillet and Goresy, 2013; Kenkmann et al., 2014). There is also a large volume of rocks in impact craters that show no sign of shock metamorphism and plastic deformation but are deformed at the sub-shock level by brittle fracturing mechanisms (Kieffer, 1971b; Kieffer, 1975; Madden et al., 2006; Rosa, 2012; Kenkmann et al., 2014; Rae et al., 2017).

Impact in sandstone targets significantly changes the porosity, permeability, density and cohesion. The nature of the change depends on the energy released during impact and the location of the rock from the point of impact (Kieffer, 1971b; Cockell and Osinski, 2007; Singleton et al., 2011; Madden et al., 2006).

In addition to environmental conditions, heterogeneities in rock properties exert an important control on rock breakdown. Studies have demonstrated that pore geometry affects rock susceptibility to weathering and controls the intensity of weathering (Tuğrul, 2004; McKinley and Warke, 2007).

In the case of porous sandstone, density increases due to pore collapse at low shock pressure levels (<10 GPa) and decreases as shock pressure increases (>10 GPa, <25 GPa) due to vesiculation and formation of glasses (Kieffer, 1971a; Kieffer, 1971b). At lower shock

pressure (<10 GPa), sandstones are weakly lithified due to comminution and fracturing of grains but become strongly lithified or cohesive due to the formation of glasses and melts that weld mineral grains at higher shock pressure (>10 GPa) (Kieffer, 1975). Low shock pressures (<10 GPa) causes pore collapse in sandstone whereas high shock pressures (>10, <25 GPa) can produce vesiculation (Kieffer, 1971a; Kieffer, 1971b; Cockell and Osinski, 2007). At even higher shock pressures (>30 GPa) the porosity is reduced as minerals recrystallise from the melt (Cockell and Osinski, 2007). If impact rocks are subject to longer-term heating and annealing during crater cooling, the porosity and permeability will be affected further (Kieffer et al., 1976b). For highly porous substrates (such as sandstones), more of the impact energy is taken up in pore collapse resulting in lesser solid-state transformations and higher post-shock temperatures than a similar impact into non-porous crystalline target lithology (Kieffer, 1971b; Madden et al., 2006).

There are numerous studies of the erosion and degradation of crater landforms on Earth and Mars (Grant and Schultz, 1993a; Grant and Schultz, 1993b; Grant et al., 2006; Grant et al., 2008; Golombek et al., 2006; Kumar et al., 2010; Golombek et al., 2014; Osinski and Pierazzo, 2012; Komatsu et al., 2014) and references therein), but relatively few have examined the inherited effects of impacts on the nature of subsequent rock breakdown (Boslough, 1991; Frattini et al., 2014). In particular, there are no detailed studies on the role of low impact shock on the subsequent style and rate of rock breakdown. Here the role of low impact shock inheritance on the subsequent nature of breakdown of sandstone is qualitatively and quantitatively assessed.

5.1.1. Sandstone weathering

Sandstone is one of the commonly found sedimentary rocks on Earth. Sandstone consists of sand-sized grains (1/16 to 2 mm diameter), dominantly quartz supported by a matrix of other minerals. Quartz is exceptionally resistant to chemical weathering, though it does dissolve in certain conditions (Ollier and Pain, 1996). Quartz has no cleavage, which makes it resistant to physical weathering and attrition during transport by wind (Ollier and Pain, 1996). Sandstone rich in clay and feldspar is more prone to chemical weathering than quartz-rich sandstone (Taylor and Eggleton, 2001).

The sandstone of evaporitic and basaltic composition have also been reported in Meridiani Planum and Gale Crater on Mars (Grotzinger et al., 2005; Grotzinger et al., 2014; Grotzinger et al., 2015; Stack et al., 2015). They are sourced from mafic-rich precursors so are rich in

olivine, pyroxene, and calcic plagioclase (Grotzinger et al., 2014), compared to quartz and feldspar-rich sandstone found on Earth. Mafic minerals contain cleavage planes and are softer compared to quartz, making them more susceptible to chemical weathering and physical abrasion (Taylor and Eggleton, 2001; Hausrath et al., 2008; Hausrath and Brantley, 2010; Cornwall et al., 2015). These sandstone targets are also affected by impact processes (Boslough, 1991; Golombek et al., 2014; Newsom et al., 2014; Treiman et al., 2015). Thus, Martian sandstone should be more susceptible to breakdown than terrestrial sandstone.

Sandstone is weathered by the attack on the cement and matrix, removing support of the sand grains (Ollier and Pain, 1996). Sand grains of quartz is little affected; however feldspar and mica present in the sandstone are easily weathered (Taylor and Eggleton, 2001). Calcareous sandstone is affected by solution, and because of initial porosity, the solution penetrates deeper (Ollier and Pain, 1996). Clay matrix sandstones weather by breakdown and eluviation of clay (Ollier and Pain, 1996). Iron-oxide cements generally weather due to hydration of iron oxide to hydroxides (Ollier and Pain, 1996).

Considerable literature has accumulated which discusses nature, role and relationship of various weathering processes in development of these breakdown features in sandstone (Mottershead, 1994; Wray, 1997; Turkington, 1998; Williams and Robinson, 2001; Turkington and Paradise, 2005; Wells et al., 2008; Labus and Bochen, 2012; Mol and Viles, 2012). Israeli and Emmanuel (2018) showed that grain size is important in the rate of weathering. Labus and Bochen (2012) found in an experiment that the character of grain contacts is an important factor influencing sandstone weathering. The most resistant are sandstones of concave-convex contacts; less resistant are the ones with straight grain contacts.

The works of many authors emphasise the role of rock porosity and pore size distribution as in sandstone weathering (Tuğrul, 2004; McKinley and Warke, 2007) and references therein). Due to high porosity in sandstone ample water is absorbed, and in cold regions, it causes frost weathering (Ollier and Pain, 1996). Thermal expansion due to insolation is important in causing sandstone weathering as quartz, for example, has a coefficient of volumetric expansion of 0.36 between 20 and 100° C (Turkington and Paradise, 2005). Sandstone often displays extensive bedding and cross-bedding, and joints. Variations in-water holding ability due to joints, bedding and porosity, make lines of weakness for physical weathering (Ollier and Pain, 1996). Sandstone displays diverse assemblages of breakdown features created by a combination of processes that appear to act together or in sequence, causing weakening and disintegration of the rock (Turkington and Paradise, 2005). Examples include

exfoliation, flaking and crumbling, case hardening, granular disintegration, polygonal cracking, tafoni, weather-pits, Gnammas and fluting (Fitzner et al., 2003; Bourke and Viles, 2007). While discussing rock breakdown features in the arid environment, there is often confusion over the processes forming these features. This confusion arises because of the equifinality of breakdown features. Several breakdown forms are the result of different processes occurring in synergy (Viles, 2013b).

The aim of this study is to compare nature of breakdown between low impact shocked (<5GPa) Moenkopi Sandstone (MS) from Meteor Crater and unshocked Moenkopi Sandstone from three control sites that share similar climatic history to Meteor Crater. In this paper, we compared the weathering between Meteor Crater and the control sites using rock hardness measurements and rock surface texture analysis methods. In addition, we also explore the effect of aspect on the breakdown of Moenkopi Sandstone at Meteor Crater.

5.2.Study Site

5.2.1. Meteor Crater

5.2.1.1. Introduction

Meteor Crater (aka Barringer Meteorite Impact Crater) was the first recognised impact crater on Earth. Scientific investigation at Meteor Crater began more than a century ago (Foote, 1891). G.K. Gilbert, who investigated the theory of meteorite impact for lunar craters, was one of the first geologists to study Meteor Crater. He advocated a volcanic origin for Meteor Crater (Gilbert, 1896). A few years later, Barringer, a mining geologist and his business partner Tilghman suggested an impact origin for Meteor Crater (Barringer, 1905; Tilghman, 1905). The Gilbert-Barringer controversy raged for many decades until detailed studies at Meteor Crater by Shoemaker (1959); (1960). Shoemaker (1960) compared Meteor Crater and Teapot Ess crater (Nevada) formed by the nuclear explosion, to explore the impact mechanics of Canyon Diablo asteroid (Shoemaker, 1987). The debate for the origin of Meteor Crater was finally settled with the discovery of coesite and stishovite (high-pressure polymorphs of quartz) in breccia from the crater (Chao et al., 1960; Chao et al., 1962). A detailed review of Meteor Crater origin studies can be found in Masaitis (2006).

Meteor Crater is a simple impact crater and one of the best-preserved impact sites on Earth (Fig 5.1). This ~50,000 year old crater was formed by the hypervelocity impact (12 km/s) of

an iron asteroid named Canyon Diablo (Melosh and Collins, 2005) in a ~1070 m thick sequence of Paleozoic and Mesozoic sedimentary rocks of the Colorado Plateau underlain by Precambrian crystalline basement (Chapman, 2007; Newsom et al., 2013; Kring, 2017). It is located in a relatively low-relief portion of the southern part of the Colorado Plateau approximately 55 km east of Flagstaff near the town of Winslow in north-central Arizona (35° 01' N, 111° 01' W) (Shoemaker, 1987).



Fig 5.1. Meteor Crater in Arizona (looking toward East crater wall).

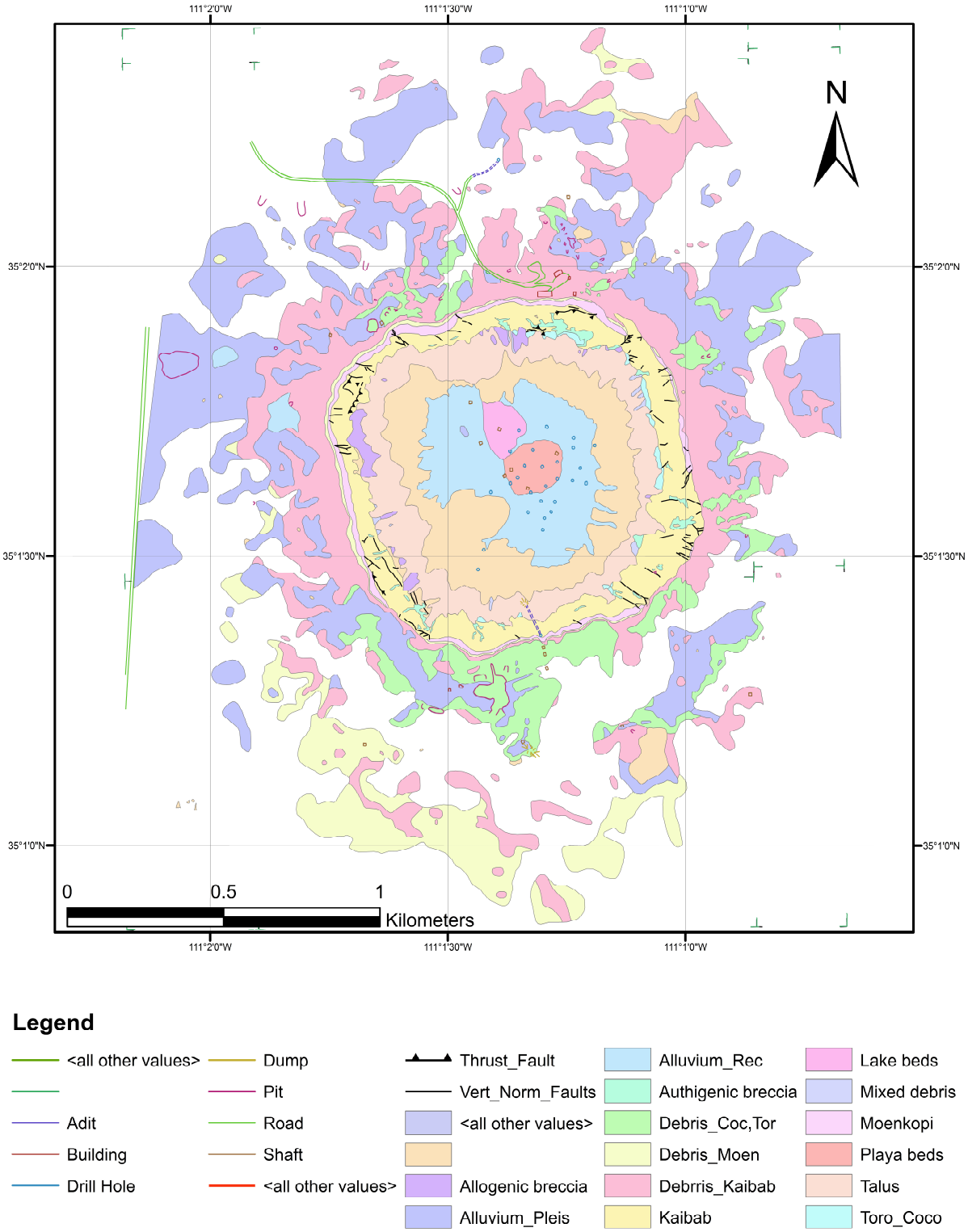


Fig 5.2. Geologic map of Meteor Crater produced by Shoemaker (1960).

5.2.1.2.Geologic setting

Meteor Crater is a bowl-shaped, near-circular impact structure on Earth and has a diameter of 1.2 km (Kring, 2017). The rim crest rises 30-60 m above the surrounding terrain, and the depth of the bowl-shaped depression is ~180 m (Roddy et al., 1975; Pilon et al., 1991; Kring, 2017). The average slopes of upper crater walls are ~40 to 50° (Kring, 2017). Adjacent to the crater is the ~18-25 m deep sinuous Canyon Diablo (Fig 5.3) which pre-dates Meteor Crater impact event (Shoemaker, 1960; Kring, 1997). Canyon Diablo is formed by northeast flowing Little Colorado River.

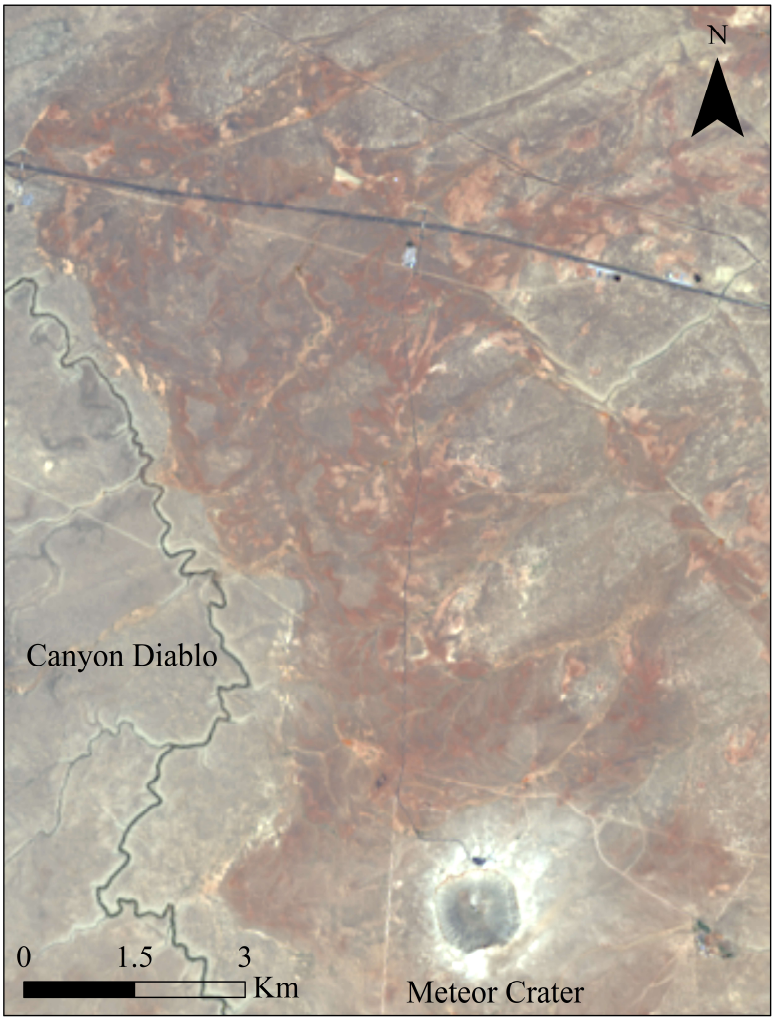


Fig 5.3. Landsat 8 image showing the location of Meteor Crater and Canyon Diablo.

Meteor crater lies near the anticlinal bend of a gentle monoclinal fold (Shoemaker, 1987). The strata along crater walls are cross-cut by tear faults in four locations, which controlled the square shape in plan view (Kring, 2017). Faulting at the time of the crater-forming event

along two mutually perpendicular joint sets in SE-NW and SW-NE (present before impact) caused uplift to various degrees in the crater wall (Shoemaker and Kieffer, 1979; Newsom et al., 2013; Kring, 2017). Kring (2015) measured the bearing of 80 vegetation lines that delineate joints on the north and south side of the crater and found that the dominant joint direction is in agreement with regional joint direction, i.e., NW-SE. The crater is underlain by relatively flat-lying Permian and Triassic beds (Faure and Mensing, 2007; Newsom et al., 2013). Three principal formations are the Coconino Sandstone (Permian), the Kaibab Limestone (Permian) and the Moenkopi Formation (Triassic) comprises 99% of the target lithology and subsequent ejecta (Faure and Mensing, 2007; Newsom et al., 2013; Kring, 2017). Outcrops and boulders of Moenkopi and Kaibab are extensively exposed in the region and close to the crater. This is due to minimal vegetation and erosion in the semi-arid climate and a thin and sparse soil cover in the region. Kaibab Formation is also well exposed in the walls of Canyon Diablo which is close to the crater.

At present, below the crater floor lies ~30 m thick lens of lacustrine sediments, beneath which is a ~200 m thick lens of impact breccia and an underlying >750 m thick sequence of Paleozoic sedimentary rock beds. Crystalline basement rocks are ~1070 m below the surface (Kumar and Kring, 2008; Kring, 2017). Shoemaker and Kieffer (1979) mapped three breccia units within the crater: authigenic breccia, allogenic breccia, and mixed debris (Fig 5.2).

Authigenic breccias are monomict formed due to disruptive shear within rock formations (Kring, 2017). These breccias are locally present along faults in the crater walls (Fig 5.2) (Shoemaker and Kieffer, 1979; Kring, 2017).

Allogenic breccias are made up chiefly of fragments from a single formation but can also contain fragments from other formations (Shoemaker and Kieffer, 1979; Kring, 2017). These breccias occur in upper crater wall as well as in the breccia lens beneath the lake bed. The breccia lens contains fragments of shocked Coconino Sandstone, lechatelierite (melt derived from Coconino) and meteoritic material. In the crater wall, breccias are dominated by debris from Kaibab Formation (Shoemaker and Kieffer, 1979; Kring, 2017).

A layer of mixed debris occurs as 10.5 m thick layer, rests on top of allogenic breccia and beneath talus and lake beds and in patches along upper crater wall (Shoemaker and Kieffer, 1979; Kring, 2017). The mixed debris is composed of fragments derived from all formations and include all five stages of shocked Coconino Sandstone (as classified by Kieffer (1971b)) and oxidised meteoritic material. Shoemaker and Kieffer (1979) suggested that this breccia

unit was formed by fallout debris blasted to a great height and then redeposited on top of the crater. The material in this unit is well mixed.

5.2.1.3. Target rocks

Colorado Plateau near Meteor Crater is made up of ~1070 m thick sedimentary rocks overlying a crystalline basement. The ~100 m thick Devonian Martin Formation unconformably overlies the basement rock (Kring, 2017). It is unconformably covered by ~23 m Mississippian Redwell Formation (Kring, 2017). These units are overlain by ~2 m thick Permian Molas Formation followed by ~85 m Permian Naco Formation (Kring, 2017). The Naco Formation is covered by the ~550 m thick Permian Supai Formation (Kring, 2017). These units are not exposed in the crater wall. Although seismic refraction survey by Ackermann et al. (1975) revealed the impact fractures extend to at least ~800 m beneath the crater floor till Martin Formation.

Three distinct rock layers (i.e. Coconino, Kaibab and Moenkopi Formations) are visible on the crater sidewalls (see Fig 5.4). The boundary between these rock layers is easy to identify due to the difference in their appearance in the outcrops. Permian Coconino is partly exposed on the present-day middle to lower crater wall (Fig 5.2); it consists of fine-grained, saccharoidal, white, cross-bedded, quartzose sandstone of aeolian origin; the thickness of Coconino is 210 to 240 m around the crater (Shoemaker and Kieffer, 1979; Kumar et al., 2010; Kring, 2017). In outcrop, Coconino Sandstone appears as white to light cream colour (Munsell value ranges from 10YR 8/1 to 10YR 8/2). Coconino sandstone is composed of >95% quartz, traces of clay minerals, and heavy minerals (Shipman et al., 1971; Kieffer, 1971a; Kieffer, 1971b; See et al., 2002; Madden et al., 2006; Whitmore et al., 2014). Grains are well rounded with an average size of 0.12 to 0.15 mm (Ahrens and Gregson, 1964; Shipman et al., 1971). The non-impacted Coconino Sandstone have a porosity of 24-25% (Ahrens and Gregson, 1964; Shipman et al., 1971). The bulk density of the sandstone is 2.08 ± 0.03 g/cm^3 (Ai and Ahrens, 2004), and grain density is 2.65 g/cm^3 (Shipman et al., 1971). In an experiment, Ai and Ahrens (2004) found that radial cracks appear at ~30 MPa and complete fragmentation at ~40 MPa in Coconino Sandstone.

The Permian Toroweap formation conformably overlies Coconino formation (Fig 5.2) is 1 to 3 m thick and consists of a white to yellowish-brown, medium to coarse-grained calcareous sandstone interbedded with thin dolomite beds (Shoemaker and Kieffer, 1979; Kumar and Kring, 2008; Kring, 2017). It is conformably overlain by 79 to 81 m thick

Permian Kaibab formation which is composed of dolomitic limestone (Fig 5.2), fossiliferous marine sandy dolomite, and thin calcareous sandstone horizons (Shoemaker, 1987; Kring, 2007; Kring, 2017). The Kaibab Formation consists of three member beds: Alpha (yellowish, vuggy textured, dolomite interbedded with a few white sandstone beds), Beta (yellowish massive dolomite), Gamma (white to yellowish massive dolomite) from top to the bottom i.e., Gamma is the oldest member and Alpha is the youngest member (Shoemaker and Kieffer, 1979; Kring, 2007; Kumar et al., 2010; Kring, 2017). The mineral composition within Kaibab Formation varies as it is composed of limestone, dolomite and sandstone, major minerals include carbonate ranging from 20 to 97% and minor quartz, plagioclase, microcline and opaque minerals (Kring, 2017). The average bulk density of Kaibab Formation is 2.24 g/cm^{3,} and grain density is 2.79 g/cm^3 (Watkins and Walters, 1966). The porosity in non-impacted Kaibab Formation ranges from 12-24% (Watkins and Walters, 1966).

Thin Triassic Moenkopi Formation unconformably overlies Kaibab Formation (Fig 5.2), is a dark reddish-brown 3 to 6 m thick fissile shale and siltstone. The Moenkopi has two members: Moqui Member (fissile dark-brown shale) and Wupatki Member (pale reddish-brown, cross-bedded, sandstone and siltstone) (Kring, 2007; Kumar and Kring, 2008; Newsom et al., 2013; Kring, 2017). Moenkopi Sandstone is composed of quartz, microcline, kaolinite, muscovite, hematite, calcite and dolomite. The matrix in the sandstone is stained by iron. The average grain size is 0.05-0.06 mm. Porosity in non-impacted Moenkopi Sandstone ranges from 7-18% (Kring, 2017). Dry bulk density in Moenkopi Sandstone ranges from 2.19-2.48 g/cm^3 and grain density 2.68-3.63 g/cm^3 (Watkins and Walters, 1966).

The inverted sequence of these sedimentary rocks is present in the hinge zone and overturned flap and further outward in the ejecta blanket. The Kaibab and Moenkopi Formations are exposed in the upper part of the crater wall as well as in the near vicinity of the crater (Shoemaker, 1987). Additional details of these lithologies can be found elsewhere (chapter 2 of Kring (2017) and references therein).

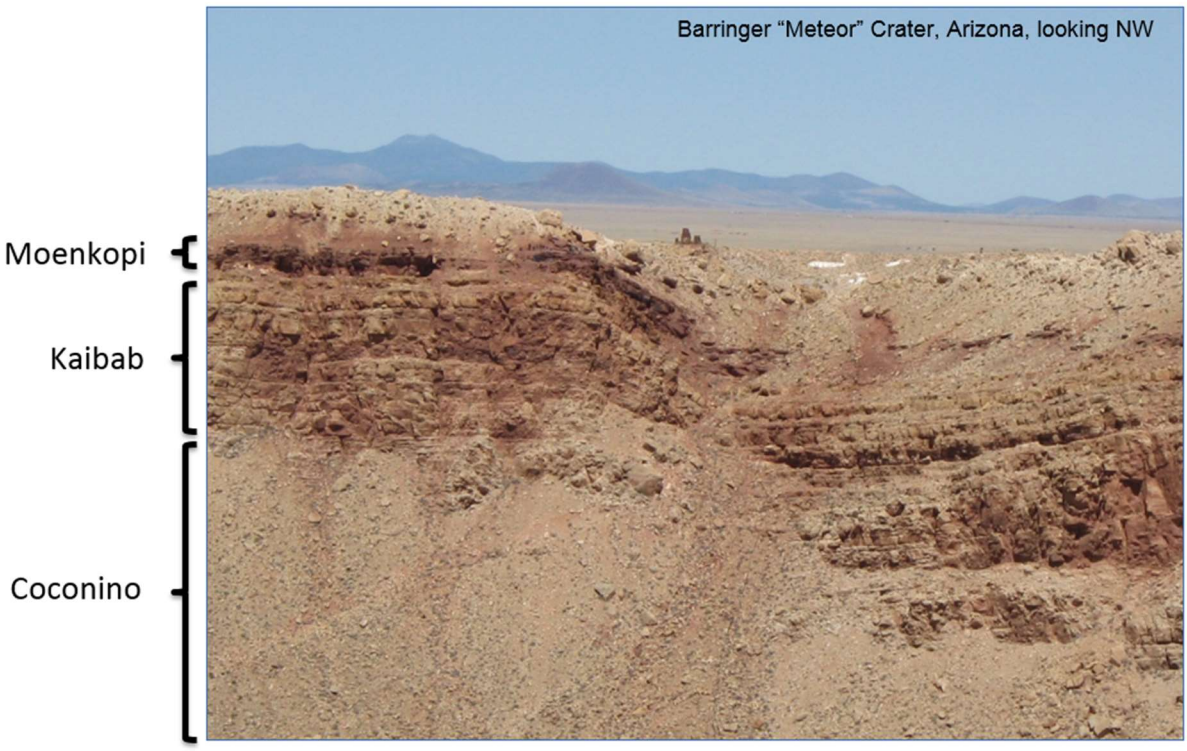


Fig 5.4. North-West crater wall showing three prominent rock formations exposed in the crater wall.

5.2.1.4. Age of the crater

Meteor Crater is a very well preserved crater for impacts on Earth. The lack of erosion on sharp edges of ejecta fragments in a desert environment led Barringer (1905) to suggest that Meteor Crater was 2,000 to 3,000 years old. Similarly, Tilghman (1905) suggested that Meteor Crater was 10,000 to 5,000 years old based on the pristine structure of the crater. Blackwelder (1932) suggested that Meteor Crater was formed between 40,000 to 70,000 years ago based on his study of the thickness of lake sediments inside the crater; the volume of fine-grained debris and alluvium on the crater walls floor; gully incision into crater walls and dissolution weathering of Kaibab ejecta blocks. Kaye (1963) measured ^{59}Ni in 4 pieces of Canyon Diablo meteorite and determined a terrestrial age of <40,000 years. Ives et al. (1964) obtained an age of 24,000 ± 2,000 years by radiocarbon dating gastropod shells from a sample of lake beds obtained from dump around the main shaft in the crater floor. Shoemaker and Kieffer (1979) originally estimated late Pleistocene age between ~20 ka to ~30 ka of Meteor Crater based on the stratigraphy of Quaternary sediments within the crater. Sutton (1985) determined an average age of 49,000 ± 3000 by thermoluminescence

measurements of quartz in four impact-shocked Coconino sandstone (from classes 3 and 4 of Kieffer (1971b) classification) breccia in the crater floor and three shocked Kaibab dolomite derived from the fallout layer (Sutton, 1985). Phillips et al. (1991) obtained a mean exposure age of 49,700 ± 850 years using cosmogenic ^{36}Cl accumulation in exhumed rocks normally buried Kaibab Formation, as well as ^{14}C in rock varnish. The mean ^{36}Cl date is supported by ^{14}C dates in the oldest rock varnish (Phillips et al., 1991). They sampled three boulders from the crater rim and two from the ejecta blanket surrounding the crater of siliceous dolomite of the Kaibab Formation. In a parallel study Nishiizumi et al. (1991) sampled four of the same boulders from crater walls and six rock samples from the summits of large blocks on the crater rim in a layer of ejecta derived from Permian Kaibab formation and dated the surface exposure of these boulders from in situ production of ^{10}Be and ^{26}Al. They derived a minimum age of 49,200 ± 1,700 years. The remarkable agreement of the age of Meteor Crater derived from three independent methods (Sutton, 1985; Nishiizumi et al., 1991; Phillips et al., 1991) has led the scientific community to accept that Meteor Crater was formed 49,000 to 50,000 years ago.

5.2.1.5.Distribution of Ejecta

Meteor Crater has a relatively well-preserved ejecta blanket, extending out 800 to 1150 m from the crater rim (Fig 5.2). Roddy et al. (1975) estimated that 175 million tons of rock were ejected from the crater. Ejecta blanket is well preserved up to the radial distance of >1 km from the crater wall and is distributed over ~7.5 km^2. It consists of fragmented material from Coconino, Kaibab and Moenkopi Formations (Kumar and Kring, 2008; Kring, 2017).

The ejecta blanket consists of exhibiting a generally inverted stratigraphy (Pilon et al., 1991). The lowest unit in the debris contains fragments from Moenkopi Formation (Shoemaker, 1987). A layer of Kaibab debris rests on top of the Moenkopi debris (Shoemaker, 1987). There is sharp contact between this two debris unit within the crater, but at distances of 0.8 km from the crater rim, there is slight mixing of Moenkopi and Kaibab fragments at the contact (Shoemaker, 1987). Patches of a third debris unit, composed of sandstone fragments from the Coconino and Toroweap, overlies with sharp contact on the Kaibab debris unit (Shoemaker, 1987).

At Meteor Crater ejecta has been distributed asymmetrically, Coconino debris is prevalent on the south side of the crater, whereas Kaibab dolomite dominates elsewhere around the crater (Kring et al., 2011). The thickness of the ejecta blanket is found to be greatest on the

south side and thins with the distance from the crater rim (Kring, 2017). In NE of the crater, the thickness of ejecta blanket ranges from 3 m close to the crater rim to 10 m at the distal end of the ejecta blanket (Roddy et al., 1975; Pilon et al., 1991). The coarsest material within the ejecta blanket is concentrated near the crater rim (Kring, 2017).

5.2.1.6. Past and present environment

The climatic conditions at the time of the impact were relatively warmer than in general within the Wisconsin period of glaciation. The late Pleistocene age of the crater occurs within the Pinedale interstadial (Kring (1997); Fig 5).

Lacustrine sediments on the crater floor indicate that an ephemeral lake was present in the crater during wet intervals in the late Pleistocene epoch. These coincide with the late Wisconsin glaciation event. This lake dried up due to a decrease in the annual amount of precipitation in northern Arizona caused by the retreat of Laurentide ice sheet from North America about 10,000 years ago (Faure and Mensing, 2007). At the centre of the crater floor, 30 meters of lacustrine sediments and debris from weathered wall rock accumulated as the lake dried up (Shoemaker and Kieffer, 1979; Kring, 2017).

Meteor Crater is close to the San Francisco volcanic field consisting of 400 cinder cones (Shoemaker and Kieffer, 1979). The ages of the eruption in the San Francisco volcanic field range from 6.13 Ma to 1000 years (S.J. Reynolds, 1986), with the Sunset Crater eruption being the youngest one. The Sunset Crater eruption began in 1064 A.D. and lasted for nearly 200 years (Shoemaker and Kieffer, 1979). The interbedded volcanic ash deposits with lacustrine sediments and beneath colluvium on the crater floor may be associated with the Sunset Crater eruption (Shoemaker and Kieffer, 1979; Kring, 2017).

The area immediately around the crater is drained by Little Colorado river. Before the impact event, the area in the vicinity of the crater was probably drained by a network of shallow streams flowing towards the Little Colorado River in the northeast (Kring, 1997). Environmental reconstruction of the area in the vicinity of the crater based on megaflora and megafauna fossil information suggests that these shallow streams may have been sustained for a longer period providing a higher amount of moisture at that time than the present (Kring, 1997). Ground Penetrating Radar (GPR) survey conducted by Pilon et al. (1991) located the water table ~65 m below the crater floor. Shoemaker and Kieffer (1979) found that the impact event occurred during an interval in which the groundwater table was 30-40

m higher than at present. They also suggested that the talus deposits in the crater are mid-Wisconsin in age and that the debris flow deposits are late Wisconsin.

At present, the vegetation around Meteor Crater is dominated by grassland consisting of shrubs like sagebrush, snakeweed, rabbit-brush, groundsel, and cliffrose (Kring, 1997). These grasses can also be seen in the crater with a subtle difference in vegetation type and coverage due to different microclimatic zones within the crater due to its topography (Whiteman et al., 2008). Junipers occur inside the south crater wall and on the south rim of the crater (Barringer, 1905; Kring, 1997). Vegetation patterns in the Colorado Plateau have changed many times during the Holocene and Pleistocene, but in general, the genera of the plant involved have been the same (Kring, 1997).

The mean total rainfall averages ~194 mm and mean annual snowfall averages ~285 mm, recorded at a weather station ~25 km away from Meteor Crater, in and around the crater over the past 123 years (the Western Regional Climate Center). Palucis et al. (2011) report annual precipitation of 300 to 450 mm consisting of the approximately equal amount of rain and snow at Meteor Crater.

During winter, the maximum daily temperature difference increases by 15° C from the floor to rim (Whiteman et al. (2008); Fig 1). Diurnal air temperature differences across the crater are created by shadows cast by the rim and the effects of differential insolation on opposing sidewalls (Whiteman et al. (2008); Fig 2). At night when temperature inversions formed within the crater, the temperature differences between sidewalls at the same height became small (Whiteman et al., 2008). On crater rim level, however, the SW rim could be 3°C colder than the NE rim when a large-scale cold air drainage flow from the SW affected the crater (Whiteman et al., 2008). During the daytime, temperature differences reach 4°C when one sidewall was exposed to sunlight, and the opposing sidewall was in shadow. The N and W sidewalls were relatively warmer in the morning, and the E sidewall was relatively warmer in the afternoon (Whiteman et al., 2008). Whiteman et al. (2008) conducted a month-long meteorological field experiment called Meteor Crater Experiment (METCRAX 2006) in October 2006 in Meteor Crater. They found out that during the daytime, horizontal-axis eddies were shed by the crater rim and large vertical-axis eddies formed over the crater floor.

5.2.1.7.Erosion and crater degradation

The vicinity of Meteor Crater is dominated by the erosion of very fine-grained Moenkopi Formation (Kring, 1997). Gullies are formed on the crater walls, and the crater floor is filled

with alluvium and windblown material since the crater was formed. The alcove-channel-fan morphology of the gullies on the interior crater walls suggests that they were formed by fluvial processes (Kumar et al., 2010). Intense precipitation in the form of rain and snow at Meteor Crater may have played a role in the development of these gullies (Palucis et al., 2011). Grant and Schultz (1993a) used field mapping, air photos, and Landsat Thematic Mapper (TM) imagery and determined morphometry of radial gullies draining the flanks of Meteor Crater, measuring 1-5 m wide, 1-2 m deep, and have a density of 8.6 km/km^2, 3.4 km/km^2, and 0.0 km/km^2. Most gullies occur in relict debris chutes along the steep walls and give drainage densities of 13.7 km/km^2 and 4.3 km/km^2 inside Meteor Crater (Grant and Schultz, 1993a; Grant and Schultz, 1993b). Present-day precipitation is probably limited to the production of small gullies and modification of pre-existing gullies; most of the erosion and gullies may have an older origin (Kumar et al., 2010). The total mass of materials transported by fluvial processes appears to be twice than that removed by eolian deflation (Grant and Schultz, 1993a).

Sandy dolomite of the Kaibab formation is by far the most resistant to weathering of all the rock types at Meteor Crater (Nishiizumi et al., 1991). Hence, the dolomite, which forms ledges on the crater walls and prominent knobs in the ejecta, was expected to have the most prolonged continuous exposure at the surface (Nishiizumi et al., 1991). The fallout layer containing highly shocked Coconino Sandstone was much more easily eroded than the Kaibab layer and had been entirely removed from most of the crater rim (Nishiizumi et al., 1991). A previous study by Norwick and Dexter (2002) reported tafoni developed on the Moenkopi and Kaibab Formation in Meteor Crater and found that the size of the tafoni enlarges with age in the Colorado Plateau region.

An estimate of 15-20 m of erosion in crater rim was made by (Shoemaker and Kieffer, 1979). The lower parts of the crater walls are mantled with Pleistocene talus and debris flow deposits. Lower Inner crater wall is covered by talus deposits while leaving 80-100 m of the upper crater wall is exposed to the erosion (Poelchau et al., 2009).

An average erosion rate of 30 cm/1,000 years was found near Whale Rock on the west rim of the crater (Nishiizumi et al., 1991). On the other hand, the mean denudation rate for the last 23,000 years is 5 cm/1,000 years (Nishiizumi et al., 1991).

In contrast, Grant and Schultz (1993b) reported smaller amounts of erosion around the crater, although they focused their studies on debris farther from the rim crest and on shallower slopes. Their estimate was based on the production of coarse erosional lag deposits and the

sediment budget of multiple drainage systems on the flank of the crater. They estimated <1 m of erosion beyond 0.25-0.5 crater radii from the crater rim, although the loss of 2 to 3 m of material occurred in small areas. These estimates of erosion are smaller than those in previous studies, but Grant and Schultz (1993b) suggest that there are true variations with radial distances from the crater rim. Higher erosion rates determined by Shoemaker and Kieffer (1979), (Roddy et al., 1975), and (Nishiizumi et al., 1991) reflect erosional conditions on or near the steep rim crest, whereas their results indicate erosional conditions on the shallower flanks of the ejecta blanket.

5.2.2. Control sites

The Moenkopi Formation is extensively exposed at the surface of the Mogollon Slope surrounding Meteor Crater. We selected three sites of Moenkopi sandstone that were not affected by impact shock outside Meteor Crater as control sites. The samples collected from these sites were analysed in a preliminary study to make sure that Moenkopi Sandstone at these sites did not experience any impact shock related deformation (Chapter 2). At these sites, Moenkopi Formation bedrocks/boulders are well exposed. These sites are easily accessible by road. The first control site is approximately 9 kilometres to the north of Meteor Crater (Fig 5.5). The second and third control site is located along the Meteor Crater road, 5 and 4 kilometres, respectively from the Crater (Fig 5.5).

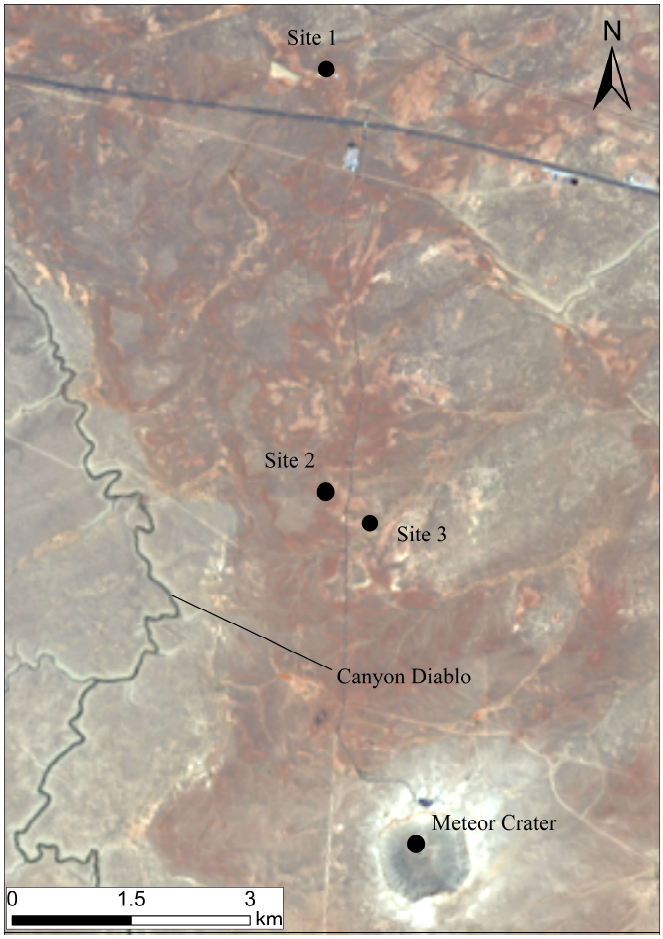


Fig 5.5. This map shows the location of the Meteor Crater and control sites. Image source: Landsat 8.

5.3. Methodology

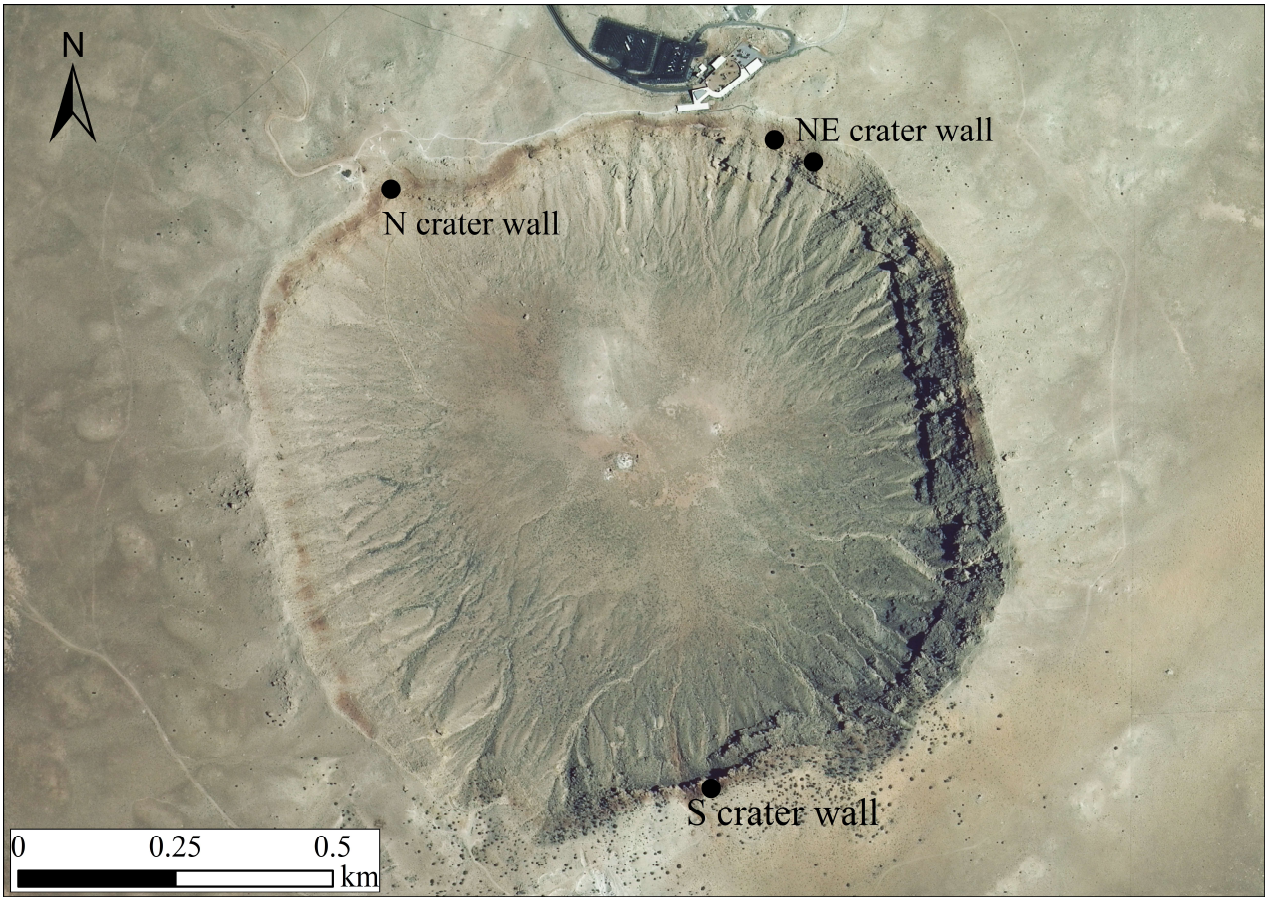


Fig 5.6. Map showing the location of Schmidt Hammer and Structure from Motion data, and Moenkopi Sandstone sampling locations at Meteor Crater. Image source: The USGS National Map.

5.3.1. Contemporary microclimate at the study site

5.3.1.1. Microclimatic sensor installation in the field

Meteor crater experiences semi-arid climatic conditions (Whiteman et al., 2008; Lehner et al., 2016). Five miniature (<1cm diameter) microclimatic iButton sensors were set up at Meteor Crater site. This was necessary to ascertain the contemporary microclimatic conditions under which the breakdown features are being formed. Hygrochron (records air temperature and relative humidity) type 8-bit iButton sensors were deployed in the field. The resolution of relative humidity (RH) and air temperature measurement was 0.6% RH and 0.5 °C respectively. Safe places (e.g., away from the sight of tourists and places where iButtons are easy to retrieve) were chosen while deploying iButtons in Moenkopi outcrops, keeping in mind natural and anthropogenic disturbances. Two iButtons were deployed on the North, and North East crater walls and three iButtons were deployed outside Meteor Crater (Fig 5.7). These iButtons (hygrochrons) (Viles, 2011) measured and logged temperature and

relative humidity data for 11 months at 2-hour intervals. Two-hour interval was chosen because 8-bit iButton sensors are limited to recording 8192 reading. Data recording at a smaller time interval (<2 hours) for one year was not possible as there was not enough memory on the iButton sensor. The battery in three iButton sensors (hygrochrons - H 04, H 05, and H 19) could not survive for one year in the field, and the data was lost for these sensors (Fig 5.7). We were able to retrieve data from two iButtons (hygrochrons – H 06 and H 10) deployed at NE crater wall at Meteor Crater and a site close to Bar T Bar ranch road in the field (Fig 5.7).

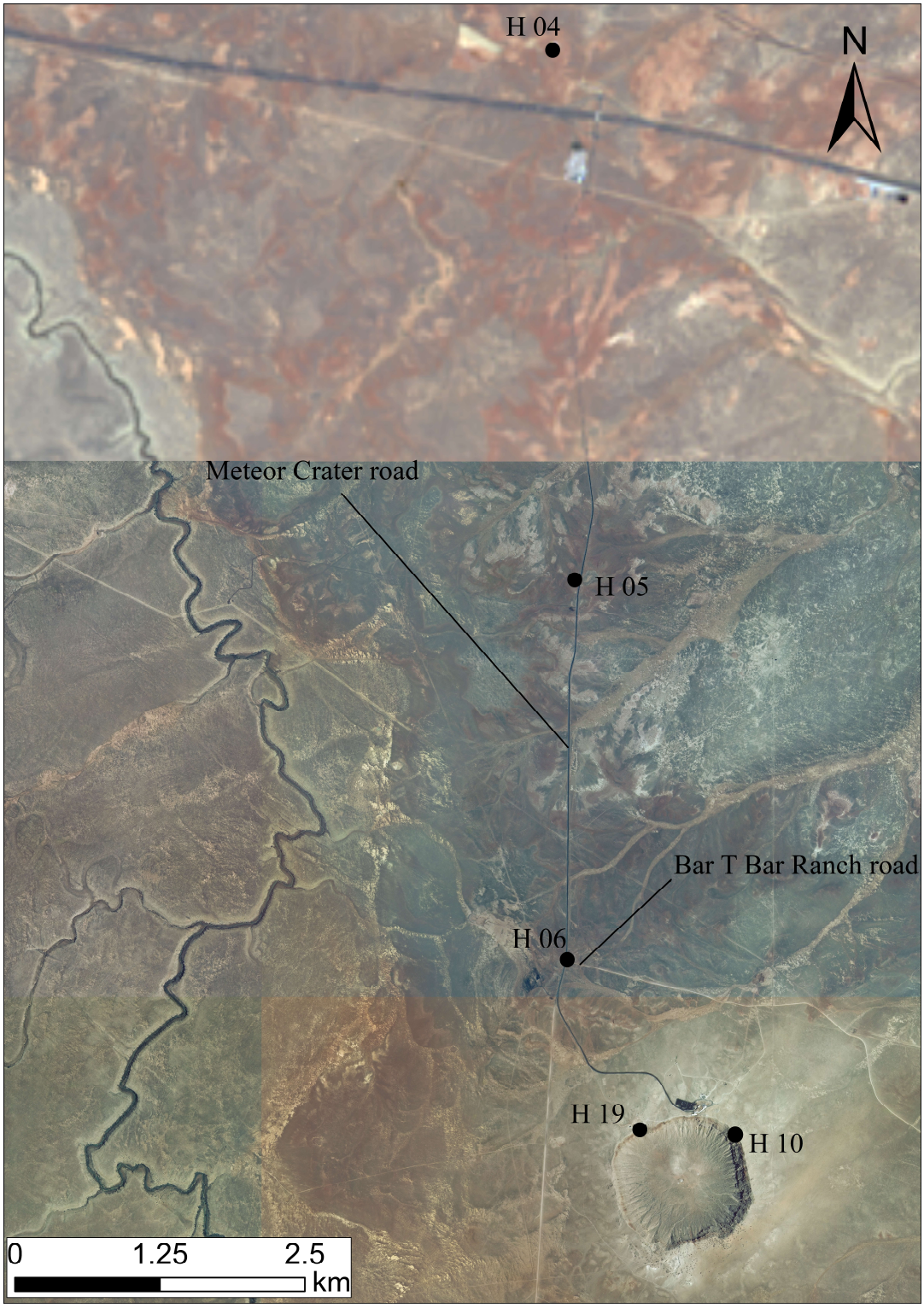


Fig 5.7. Map showing locations where iButton sensors (hygrochrons) were installed in the field. USGS orthoimage image is overlayed on Landsat 8 image. Image: The USGS National Map and Landsat 8.

5.3.1.2. The Meteor Crater Experiment - METCRAX I and METCRAX II data

In order to assess a difference in aspect related microclimate, we analysed air temperature and relative humidity data from two meteorological experiments METCRAX I (2006) (Whiteman et al., 2008) and METCRAX II (2013) (Lehner et al., 2016) that were conducted at Meteor Crater. In addition, solar radiation and shadow progression models at Meteor crater were generated from METCRAX I data.

During METCRAX I experiment, air temperatures were measured at the 5-minute interval while the METCRAX II experiment took the air temperature and relative humidity reading every 2.5-minute interval. The air temperature and humidity data measurements were obtained using HOBO Pro Temp/Ext Temp temperature and humidity data loggers, installed along several transects along all the crater sidewalls at Meteor Crater.

5.3.1.3. Solar insolation modelling

Incoming solar radiation was modelled for 12 months in a year at Meteor Crater in ArcGIS 10.6.1. The model does not incorporate real atmospheric conditions throughout the year such as clouds and humidity that affect energy received at the ground, but parameters were adjusted to model approximate average conditions at the Meteor Crater. The area solar radiation tool was used to calculate solar insolation across entire Meteor Crater. The model was created using Palucis and McEnulty (2010) 1 m/pixel DEM of Meteor Crater. The sky size was input as 200 cells, and a whole year with monthly interval time configuration was selected. The 0.5-hour time interval through the day was used for calculation of sky sectors for sun maps. The z factor was one as x,y and z units were similar. The number of azimuth direction used when calculating the viewshed was 32. The number of divisions used to create sky sectors in the sky map was 8. The diffuse model type was created for the uniform sky. The fraction of radiation that passes through the atmosphere, transmissivity, was 0.5 and diffuse proportion of 0.3 used. The output radiation rasters will always be the floating-point type and have units of watt-hours per square meter (WH/m^2).

5.3.2. Rock breakdown features documentation at Meteor Crater and the control sites

Before collecting data on rock breakdown features in the field, reconnaissance fieldwork was conducted to inspect breakdown features on Moenkopi Sandstone outcrops at Meteor Crater and the control sites. This was done in order to constrain the feature and to

design/select suitable data collection and analysis techniques (see sections 5.3.5 and 5.3.6). It was important to determine the scale at which breakdown features occur at field sites in order to plan microtopographic data collection methods. Survey of style and scale of breakdown features also helped to choose roughness analysis parameters and window scale for roughness analysis (section 5.3.6). Rock breakdown features survey also helped to assess the morphometric feature analysis performed in section 5.4.6. Bedrocks and boulders at control sites lie on a relatively flat area of Mogollon slope (±5°). Most of the outcrops were flat and generally had one dominant facet (approximately parallel to the ground). In order to avoid the effect of aspect on weathering only dominant facet (approximately parallel to the ground) of outcrops were sampled for photo documentation, Schmidt hammer and Structure from Motion data collection. Similarly, at Meteor Crater, dominantly exposed facet (near parallel to local crater wall slope) of crater wall rocks and ejecta boulders on crater walls were sampled. The facets sampled receive maximum insolation compared to other facet and were suited for taking images as these surfaces were well illuminated during most of the day.

5.3.3. Petrophysical characterisation of Moenkopi Sandstone

A total of nine Moenkopi Sandstone samples were collected at Meteor Crater (see Fig 2.2 for locations) and two Moenkopi Sandstone samples at control sites (see Fig 5.5 for locations). The mineralogical composition and petrographic properties of these Moenkopi Sandstone samples were determined using a petrographic microscope and powdered X-ray diffraction (XRD). X-ray computed tomography (CT) was used to visualise and measure the size of fractures in the Moenkopi samples. Porosity in Moenkopi Sandstone was determined using a scanning electron microscope (SEM) backscattered electron (BSE) images. The BSE images were processed to determine porosity. Detailed information on the sampling and analysis methods can be found in Chapter 2.

5.3.4. Rock hardness measurements

Rock surface hardness was measured at Meteor Crater and the three control sites (Fig 5.5; Table 5.2) in Arizona using the N-type Schmidt hammer (Viles et al., 2011). At Meteor Crater, Schmidt Hammer (SH) rebound values were obtained at North, North-East, and South crater wall (Fig 5.6). SH rebound values were used to estimate the mechanical strength of the rock surface. SH rebound values are highly correlated with rock surface hardness that is further related to the mechanical strength of rock surface. SH rebound data was collected

according to the International Society of Rock Mechanics (ISRM) suggested method (Aydin, 2015). Twenty SH rebound measurements were collected for each outcrop and values were averaged. For a very small number of outcrops with small and insufficient surface area, ten SH measurements were obtained. SH values vary with moisture and surface texture inhomogeneity, so the measurements were taken on the dry and relatively smooth surface. SH values are further affected by lichen cover, weak and fractured rocks, and small surface area and size of rock outcrop (<15 cm). In order to minimise errors from these factors, we only took measurements on outcrops bigger than > 50 cm, avoided heavily lichen-covered surface and weakly fractured and flaked areas on rock surfaces. All the measurements were obtained in similar weather conditions (on dry summer days).

5.3.5. Structure from Motion: Digital Elevation Model generation

High-resolution topographic data of rock surfaces was collected using Structure from Motion (SfM) photogrammetry (Favalli et al., 2012; Westoby et al., 2012; Smith et al., 2016) technique to compare the roughness of weathering features and geomorphic morphometric forms at range of scales between Meteor Crater and Control sites. A number of Moenkopi Sandstone outcrops were selected at Meteor Crater and the three control sites for DEM generation (Fig 5.5-5.6; Table 5.3). We used a 24.2 Megapixels Nikon D5500 camera with a variable zoom lens fixed at 24 mm focal length, on a tripod where possible to reduce effects of the handshake, to obtain images of rock outcrops. At Meteor Crater, the crater walls are very steep, so a tripod was not used at Meteor Crater. Approximately 100 images of each block were obtained. This number of images was required to capture the full extent of the outcrops in the field. Several images were acquired from different vantage points. Firstly, from all around (~1-2 m) the boulder surface followed by additional close-range images (<50 cm). Images were acquired with at least 60% lateral overlap.

We used the zoom lens set at 24 mm focal length (36 mm full frame camera sensor equivalent). The focal length of 24 mm was chosen as it provided a greater field of view where there was little space to move around to take images in the field (e.g., very steep slope). Camera aperture was set to f/6.3. A smaller aperture allows less light to reach the camera sensor and gives a larger depth of field (Haukebø, 2015). An image with larger depth of field is sharper and has a larger area in focus and are recommended for photogrammetry work (Bedford, 2017). A higher shutter speed (1/400) was chosen to compensate camera shake due to, e.g., the wind. ISO was kept at 100 to minimise the noise in the images (Mosbrucker et al., 2017). White balance was kept at daylight mode. During photo

acquisition, care was taken to ensure that the image was sharp, and everything in the frame was in focus. Matrix metering mode was selected to provide the best exposure and equal brightness throughout the image. Images were taken in autofocus mode to maintain optimal image quality throughout all the images. These settings were chosen based on the lighting and field conditions, and field testing demonstrated high image quality at these settings.

For our data collection, a triangle coded control target (Verma and Bourke, 2019) was placed on the ground or top of the outcrop parallel to the top surface of the boulder. It is crucial for the control target to be flat and approximately parallel to the surface of interest as it defines the orientation of the surface of interest in the DEM. We used four rulers of 30 cm and placed them around the outcrops. These rulers were used as checkpoints to verify horizontal errors in the DEMs (see Chapter 4). The images were acquired in quick succession in the field to ensure that there was a minimum change in the shadow lengths and lighting conditions. We acquired images during early morning and evening and tried to avoid shadows in the image. The images were shot in raw format. A potential limitation to this in the field is that they take up to twice as much storage space as JPEGs. For an area ~10m^2, placement of GCPs, rulers and image acquisition took approximately 20 minutes. Images were processed as described in Verma and Bourke (2019).

Image acquisition and DEM generation were performed according to guidelines provided in Verma and Bourke (2019). DEM and Orthophoto generation took 8-10 hours on "high" dense point cloud quality setting. DEMs were generated in Agisoft Photoscan with a resolution of 0.5 mm and precision of 0.5-1 mm.

A detailed guideline for DEM generation from SfM photogrammetry can be found in Chapter 4 (Verma and Bourke, 2019).

5.3.6. Analysis of boulder DEMs to quantify breakdown features

Rock breakdown processes result in a range of breakdown features (Bourke and Viles, 2007). These breakdown features have varying geometry and morphologies. Often geologists observe rock breakdown features and qualitatively describe in the field (Heslop, 2003; Thornbush, 2012). Usually, dimensions of these features are manually measured (Norwick and Dexter, 2002). These two-dimensional manual measurements of complex and heterogeneously distributed hundreds and thousands of individual breakdown features are cumbersome, biased and not sufficient to compare the nature of breakdown features at different field locations. Many of the breakdown features have a third dimension – they are

volumetric. Areal surface roughness analysis can be used to characterise the 3D forms of breakdown features automatically, with high detail and accuracy, without human bias at multiple scales (Medapati et al., 2013; Chen et al., 2014; Lai et al., 2014). Roughness analysis captures complex breakdown features at different scales and offers a potential to quantitatively compare breakdown features between low shocked Moenkopi Sandstone at Meteor Crater and unshocked Moenkopi Sandstone at control sites (Chen et al., 2014). DEMs of rock surfaces generated using SfM photogrammetry were used as input for areal surface roughness analysis and morphometric geomorphic feature classification in commercially available and widely used Geographic Information System (GIS) platforms Arc GIS 10.4.1 and freely available open source Landserf 2.3 (Copyright, Jo Wood, 1996-2009). A range of areal surface roughness parameters such as Standard Deviation of Height (Sq), Standard deviation of slope (Sdq), Maximum Height (Sz), Vector Ruggedness Measure (VRM), and morphometric geomorphic feature classification was performed on moving windows of 1.5, 5.5, 10.5, 15.5, 20.5, 25.5, and 50.5 mm to quantify the boulder surface breakdown features. The roughness analysis was performed in ArcMap. Morphometric classification of geomorphic forms was performed in Landserf. These analysis parameters are described in detail below.

The aim of this study was first to explore if there is any difference in areal surface roughness due difference in nature of weathering features between low shocked and unshocked Moenkopi Sandstone. The second aim was to assess which roughness parameters and scale better characterise different breakdown features.

5.3.6.1. Areal Surface Roughness Parameters

Four roughness parameters were selected to calculate areal surface roughness using DEMs of the rock outcrops at multiple scales. These parameters were selected based on ease of calculation in commonly available ArcGIS software. These parameters were also tested to assess which roughness parameters were more suitable in the study of rock weathering.

5.3.6.1.1. Standard deviation of height (Sq)

The standard deviation of height is a measure of surface roughness that captures the local dispersion of elevation within a sample window area. The standard deviation of height is equivalent to the root mean square height

$$Sq = \sqrt{\frac{1}{A}\iint_A \left(z_{ij} - \bar{z}\right)^2 dx\, dy}$$

Where A is the area, z_{ij} is the height of the cell, and $\bar{z}$ is the mean height of cells within the analysis neighbourhood window. Sq parameter was calculated at multiple window scale (1.5, 5.5, 10.5, 15.5, 20.5, 25.5, and 50.5 mm) in Benthic Terrain Modeler tool in Arc Map (Walbridge et al., 2018). Sq is always a positive value.

5.3.6.1.2. Standard deviation of slope (Sdq)

The standard deviation of slope is equivalent to the root mean square gradient. Sdq is the root mean square of slopes at all points within a sampling window area. Sdq is mathematically calculated as -

$$Sdq = \sqrt{\frac{1}{A}\int\int \left(\frac{dz^2}{dx} + \frac{dz^2}{dy}\right) dx\, dy}$$

Where A is the area, z is vertical height, and x, y are horizontal dimensions. First, the slope of the DEM was calculated using Spatial Analyst Tools in Arc Map. Then, the standard deviation of the slope was calculated at multiple window scale (1.5, 5.5, 10.5, 15.5, 20.5, 25.5, and 50.5 mm) in Benthic Terrain Modeler tool in Arc Map (Walbridge et al., 2018).

Sdq is measured in degrees. Sdq of a completely flat surface is 0. When a sub-sample surface has any slope, its Sdq value becomes larger.

5.3.6.1.3. Maximum height (Sz)

Maximum height is defined as the height between the highest peak and deepest valley within a sampling window area.

$$Sz = Sp - Sv$$

Sp represents the maximum peak height, i.e., the height of the highest point of the surface in a sampling window. The Sv represents the maximum pit/valley height, i.e. the height of the lowest point of the surface in a sampling window. Sz was calculated using neighbourhood focal statistics tool at multiple scales (1.5, 5.5, 10.5, 15.5, 20.5, 25.5, and 50.5 mm) in ArcMap.

5.3.6.1.4. Vector Ruggedness Measure (VRM)

Vector Ruggedness Measure (VRM) measures terrain ruggedness as the variation in 3D orientation within a sampling window area (Sappington et al., 2007; Walbridge et al., 2018). VRM was adapted from a method first proposed by Hobson (1972) and later developed by Sappington et al. (2007). For each grid cell in the window, vector analysis is used to calculate the dispersion of vectors normal (orthogonal) to grid cells using the three-dimensional location of the cell centre, the local slope, and the local aspect within the specified neighborhood (Sappington et al., 2007; Walbridge et al., 2018). A resultant vector for the window is evaluated and divided by the number of cells in the moving window (Walbridge et al., 2018). The resultant magnitude of the vector is subtracted from 1 to obtain a dimensionless that ranges from 0 (no variation) to 1 (total variation)(Walbridge et al., 2018). Typical values are small (≤0.4) for data of natural surfaces (Walbridge et al., 2018). Vector Ruggedness Measure (VRM) was calculated at multiple moving window sizes in Benthic Terrain Modeler tool in Arc Map (Walbridge et al., 2018).

5.3.6.2. Morphometric classification of geomorphic features

DEMs allow high-resolution characterisation of 3D forms at a range of scales. Surface features were classified into six classes of simple mathematical morphometric forms (viz. ridge, channel, peak, pass, planar and pit) using landscape analysis method adopted from Fisher et al. (2004). Each morphometric form is equivalent to a "landform" which in the context of analysis of a boulder surface may correspond to a specific surface breakdown feature, e.g., planar surface caused by flaking, ridges representing alveoli rims (Fisher et al., 2004; Ehlmann et al., 2008b). We refer the reader to Fisher et al. (2004) and Ehlmann et al. (2008b) for the mathematical background of this classification. Percentage frequency of each morphometric features was calculated over multiple window sizes in Landserf 2.3. We used threshold values of slope and curvatures of 5.0 and 0.1, respectively, as suggested in Fisher et al. (2004) and Ehlmann et al. (2008b). This data was used to compare the morphometric breakdown forms on Moenkopi Sandstone outcrops at multiple scales from Meteor Crater and the control sites.

5.3.7. Statistical analysis of the data

Once Schmidt Hammer hardness, roughness and morphometric analysis were completed for each boulder/bedrock, these results were compared between Meteor Crater and the three control sites to determine if differences were significant.

The SH data, roughness data and morphometric data were not normally distributed, so were analysed with a non-parametric, Kruskal-Wallis test statistic in IBM SPSS Statistics 24 (White et al., 1998; Nicholson, 2008), at the 0.05 significance level. Dunn's pairwise tests were carried out as post-hoc to Kruskal-Wallis test, and significance values were adjusted by the Bonferroni correction for multiple tests. Data were tested for normality using Shapiro-Wilk test before application of statistical tests.

5.4. Results

5.4.1. Microclimate at the study site

5.4.1.1. Microclimatic data retrieved from iButtion sensors

In winters, the air temperature ranges from a minimum of -8°C to a maximum of 7°C (diurnal minimum and maximum temperature) while during summer the daily air temperatures can range between 18 to 44 °C at the north-east rim of the crater (Fig 5.8). Relative humidity can vary from 20 to 80% in a single day in winters while in summers diurnal range can be between 10 to 40% (Fig 5.9). The air temperature and relative humidity range suggest freeze and thaw weathering in winters and insolation weathering in summers (Bland and Rolls, 1998a). Meteor Crater site receives moisture in the form of rain throughout the year and snowfall in winters. The mean total rainfall averages ~194 mm and mean annual snowfall averages ~285 mm, recorded at a weather station ~25 km away from Meteor Crater, in and around the crater over the past 123 years (The Western Regional Climate Center). Since the control sites are located close to Meteor Crater in relatively flat-lying, low-relief plains of the Mogollon slope (Fig 5.2), these sites experience similar microclimatic as Meteor Crater. The temperature and humidity data from outside Meteor Crater, close to Bar-T-Bar ranch road, show similar trends in temperature and relative humidity compared to Meteor Crater data (Fig 5.8-5.11). The small difference could be due to the difference in elevation and aspect where the temperature and relative humidity were collected.

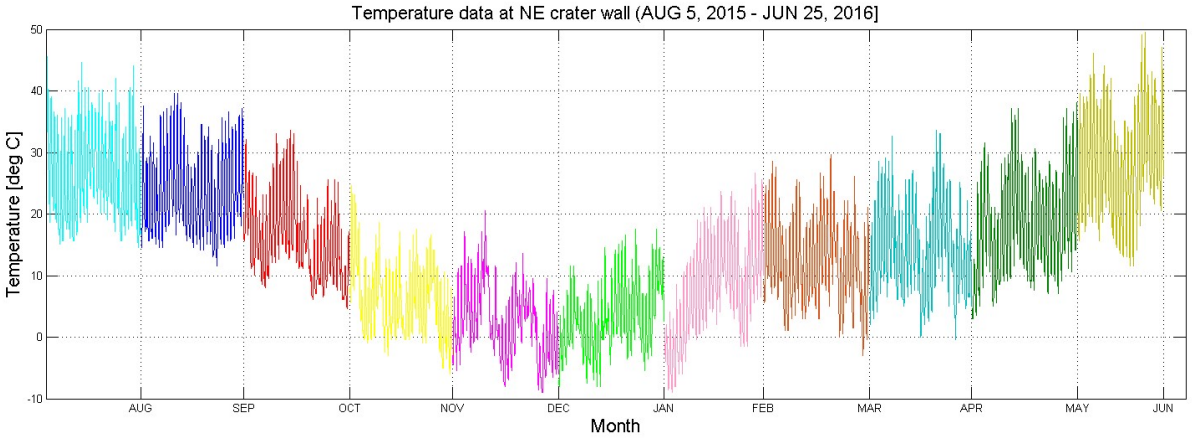


Fig 5.8. Air temperature data retrieved from iButton H 10 installed at Meteor Crater (see Fig 5.7 for location). Different colours on the plot represent temperature data from different months.

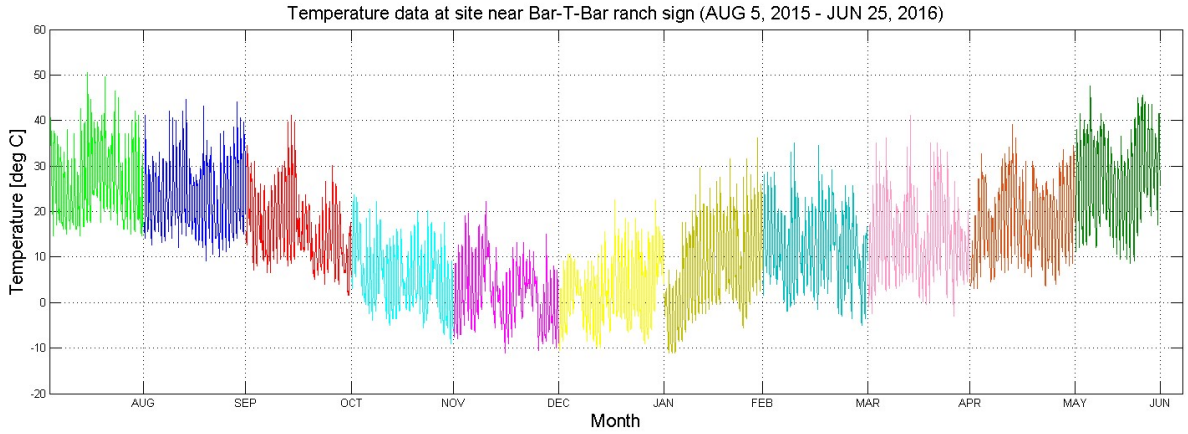


Fig 5.9. Air temperature data retrieved from iButton H 06 installed close to Bar T Bar Ranch road junction (see Fig 5.7 for location). Different colours on the plot represent temperature data from different months.

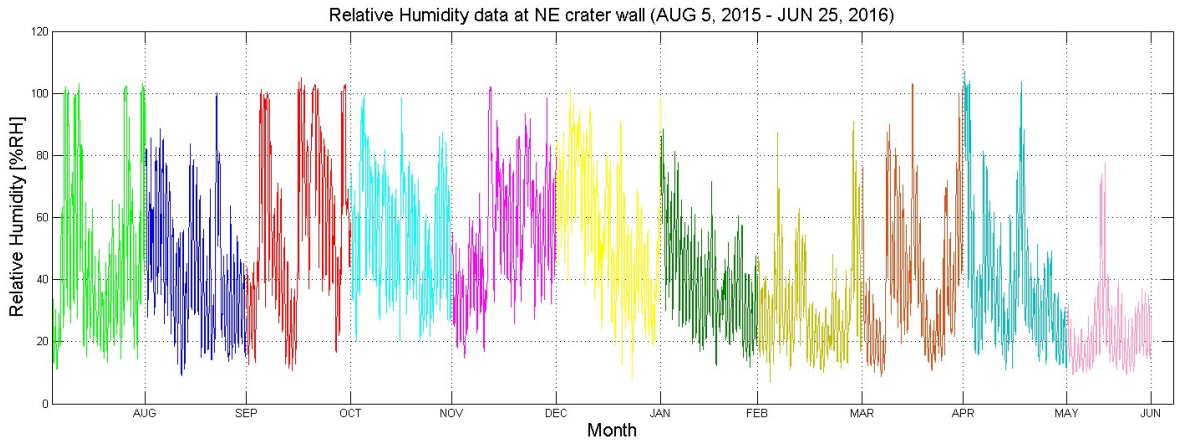


Fig 5.10. Relative humidity data retrieved from iButton H 10 installed at Meteor Crater (see Fig 5.7 for location). Different colours on the plot represent relative humidity data from different months.

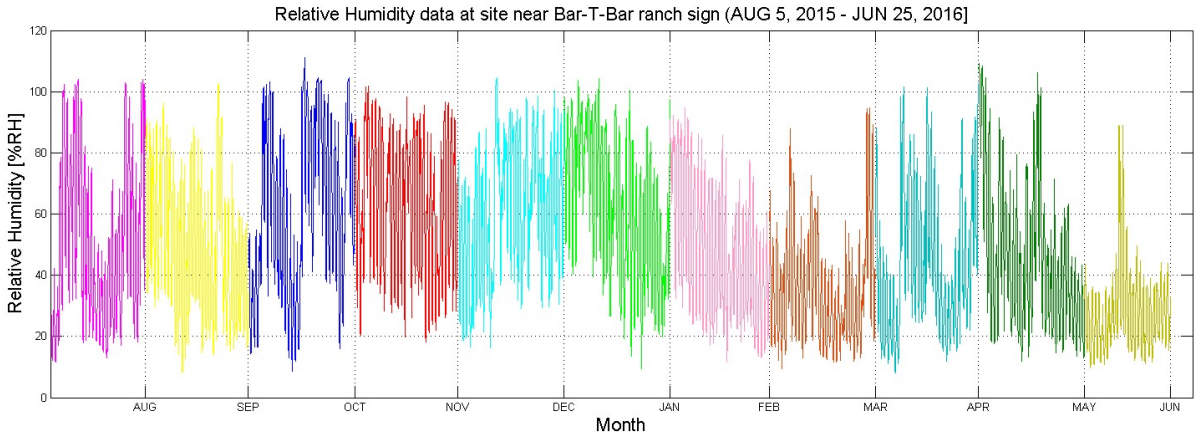


Fig 5.11. Relative humidity data retrieved from iButton H 06 installed close to Bar T Bar ranch road junction (see Fig 5.7 for location). Different colours on the plot represent relative humidity data from different months.

5.4.1.2.Microclimatic data from METCRAX I and METCRAX II

METCRAX I experiment investigated temperature inversions and the formation of atmospheric seiches in the crater. A yearlong temperature data from NE crater rim and crater floor showed that temperature inversions are strongest in midwinter and temperature differences can exceed 15°C between the crater rim and crater floor (Whiteman et al., 2008). The minimum temperature differences also show that diurnal lapse conditions in the crater, with no events in the period of data recording when the night-time inversion persisted throughout the day (Whiteman et al., 2008). The outer slopes of the Meteor crater experienced lower temperatures than the same altitudes inside the crater (Whiteman et al.,

2008). The upper 70% of the crater wall on the south and west side experienced lower temperatures than the north and east side at Meteor Crater (Whiteman et al., 2008). The maximum temperatures were higher on the inner north and south sidewalls since they were subject to strong afternoon insolation (Fig 5.17). Whiteman et al. (2008) found that outer sidewalls experienced warmer maximum temperatures than on the inner sidewalls at the south and west side of the crater. At elevations above 1591 m, the crater sidewalls are approximately isothermal (Whiteman et al., 2008). During the middle of the day, crater walls at higher altitude have lower air temperatures as temperature decreases with altitude in the well-mixed atmosphere (Whiteman et al., 2008). Sudden temperature fall at the individual sites in the afternoon (and abrupt temperature jumps in the morning) indicate the times of local sunset and sunrise at the sites on crater wall as shadows propagate across the crater (Fig 5.15) (Whiteman et al., 2008). A temperature jump developed at crater rim level due to rapid cooling inside the crater than the atmosphere just above the crater (Whiteman et al., 2008). This results in the development of a deep near-isothermal layer in the upper 80% of the crater atmosphere during nighttime (Whiteman et al., 2008).

Temperature data from METCRAX I and METCRAX II experiments close to the Moenkopi outcrops locations on N, NE and S crater walls (Fig 5.6) showed that S crater wall experienced slightly lower air temperatures than N and NE crater walls during most of the day and night in October (Fig 5.12-5.14). S crater wall becomes slightly warmer than the N and NE crater wall for a brief period during the day (after 1430 MST) due to shadow propagation effects in the crater basin (Fig 5.15). Relative humidity data from the METCRAX II experiment near the Moenkopi outcrops on NE and S crater wall showed that S crater wall received more relative humidity than NE crater wall (Fig 5.14). This might be one of the reasons for more flora and lichen colonisation on the south side of the crater.

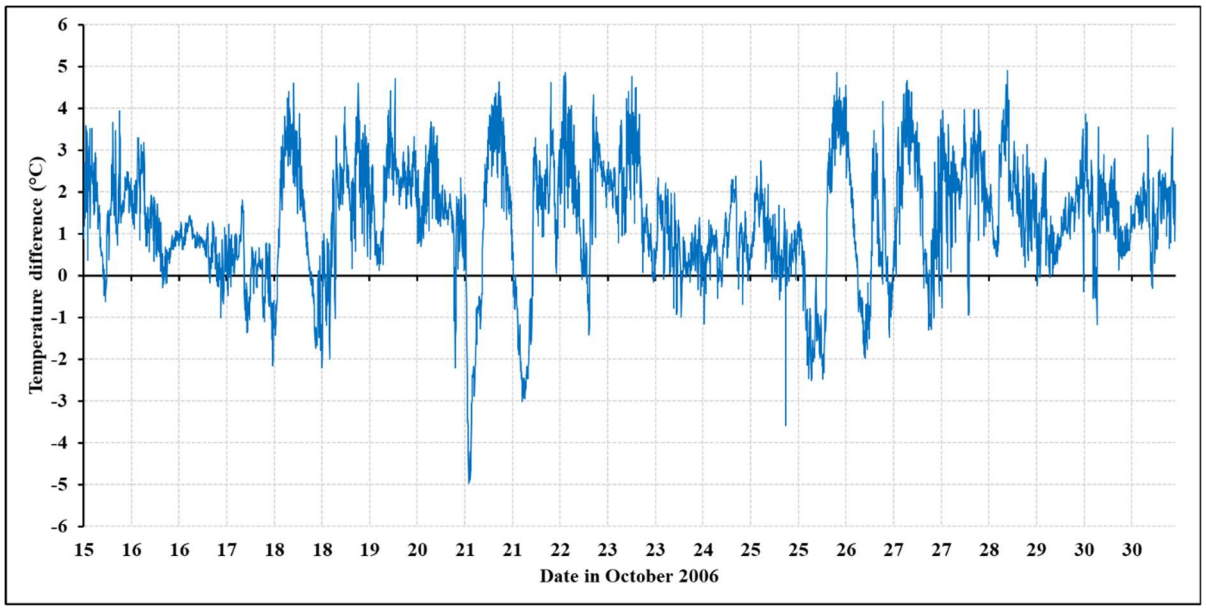


Fig 5.12. METCRAX I air temperature data collected every 5 minutes interval for 15 days in October in 2006. This graph represents the difference in air temperature between N (south facing) and S (north facing) crater wall. This temperature data was collected from the elevation of ~1700 m (~140 m above crater floor). During the night, temperature differences between the same elevations on the crater walls are small. During the day, temperature differences rise to 4 °C when a crater wall is in sunlight, and the opposing crater wall is shadowed. In general, the north walls are relatively warmer in the morning than south crater walls.

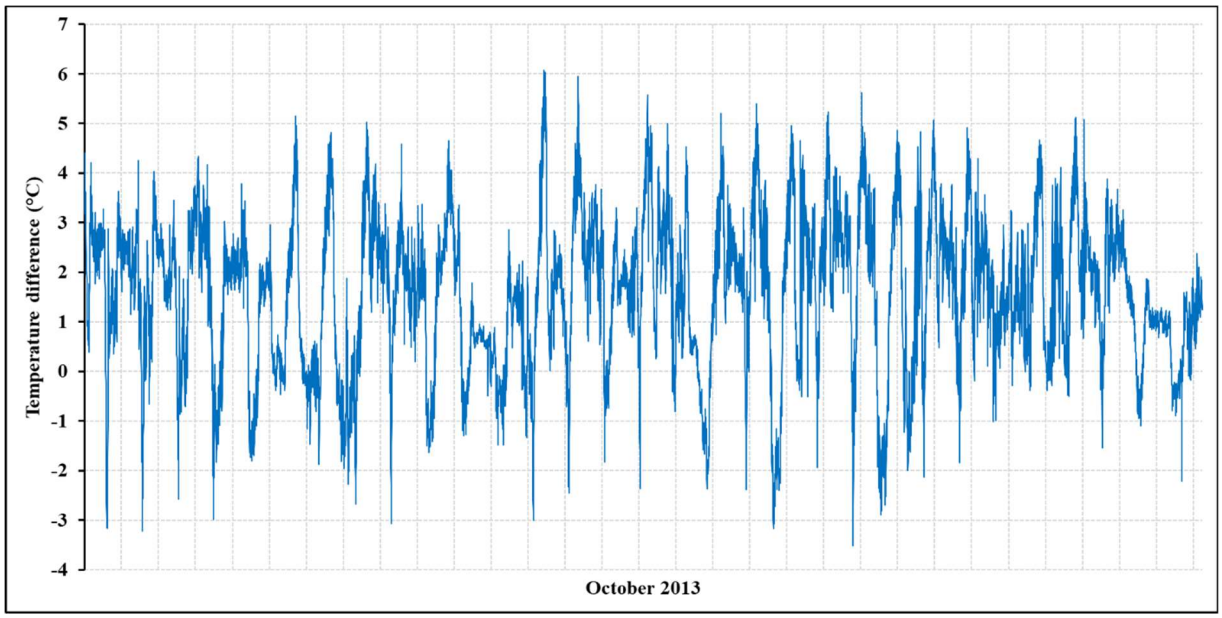


Fig 5.13. METCRAX II air temperature data collected every 2.5 minutes interval for October in 2013. This graph represents the difference in air temperature between NE (south-west facing) and S (north facing) crater wall. This temperature data was collected from the

elevation of ~1700 m (~140 m above crater floor). In general, the north-east crater wall is warmer than the south crater wall for the most part of the day. However, for a brief period in the afternoon (after 1430 MST till sunset), the south crater wall gets slightly warmer due to shadow progression.

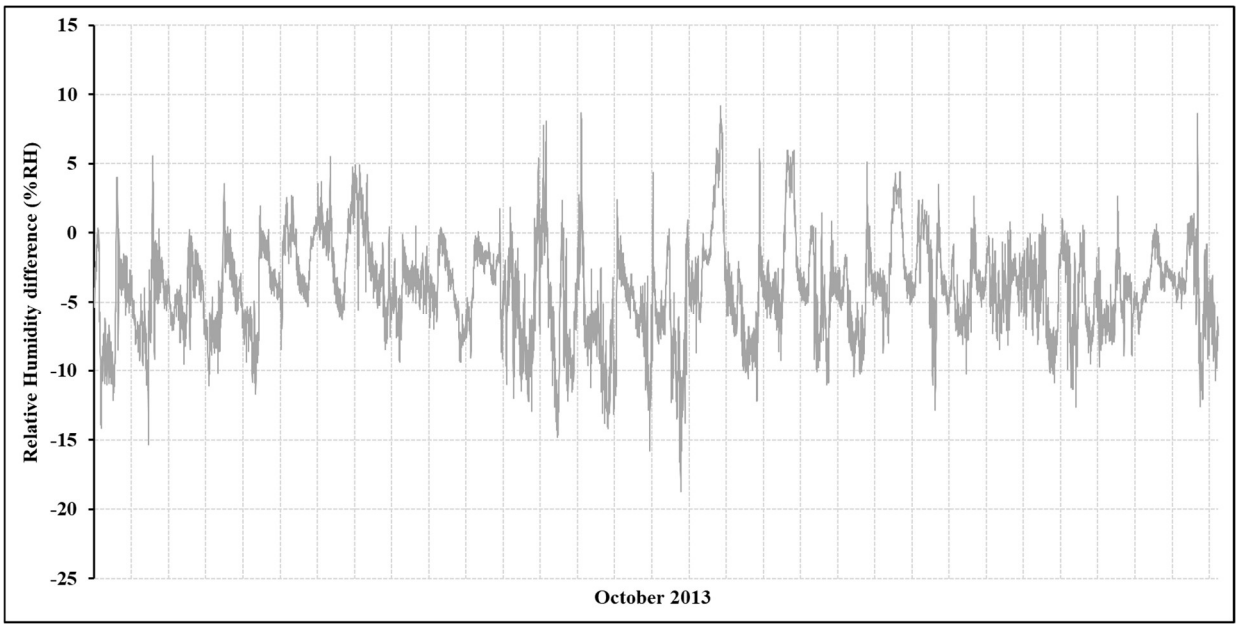


Fig 5.14. METCRAX II relative humidity data collected every 2.5 minutes interval for October in 2013. This graph represents the difference in relative humidity between NE (south-west facing) and S (north facing) crater wall. This temperature data was collected from the elevation of ~1700 m (~140 m above crater floor). In general, the south crater wall has more relative humidity than north-east crater wall.

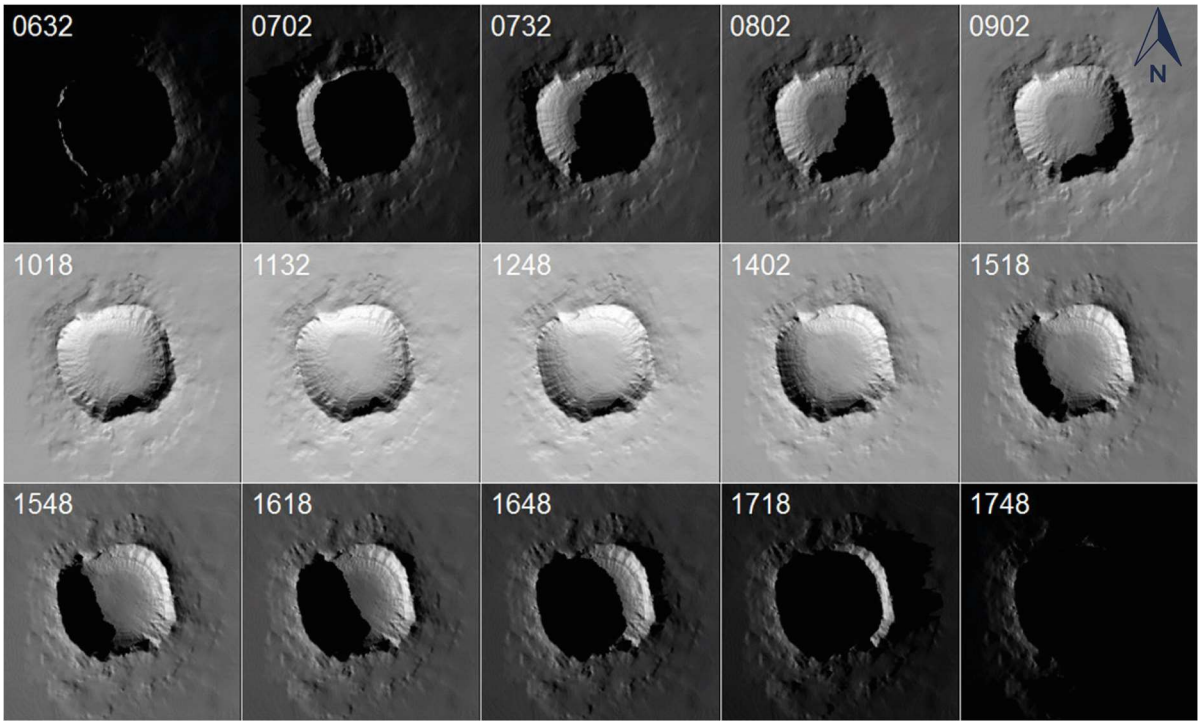


Fig 5.15. The METCRAX I experiment documented the diurnal air temperature differences caused by oblique sunlight and shadows on the crater walls. The figure shows the modelled progression of sunlight and shadows in the crater on October 15, 2006, within units of Mountain Standard Time (MST). Image source: Image was published in Kring (2017) and was originally produced by David Whiteman of METCRAX team.

The solar radiation map presented in Fig 5.16 shows the effect of the sun over Meteor Crater in every month for the year 2017. The solar insolation model exhibits strong contrasts in insolation related to aspect and seasonal changes, over the entire crater (Fig 5.16). During summer (May to July), overall insolation reaches a maximum, and north- and south-facing slopes receive the slightly different amount of solar radiation. However, in the fall, winter and spring months, difference in insolation between north and south facing slopes are the largest.

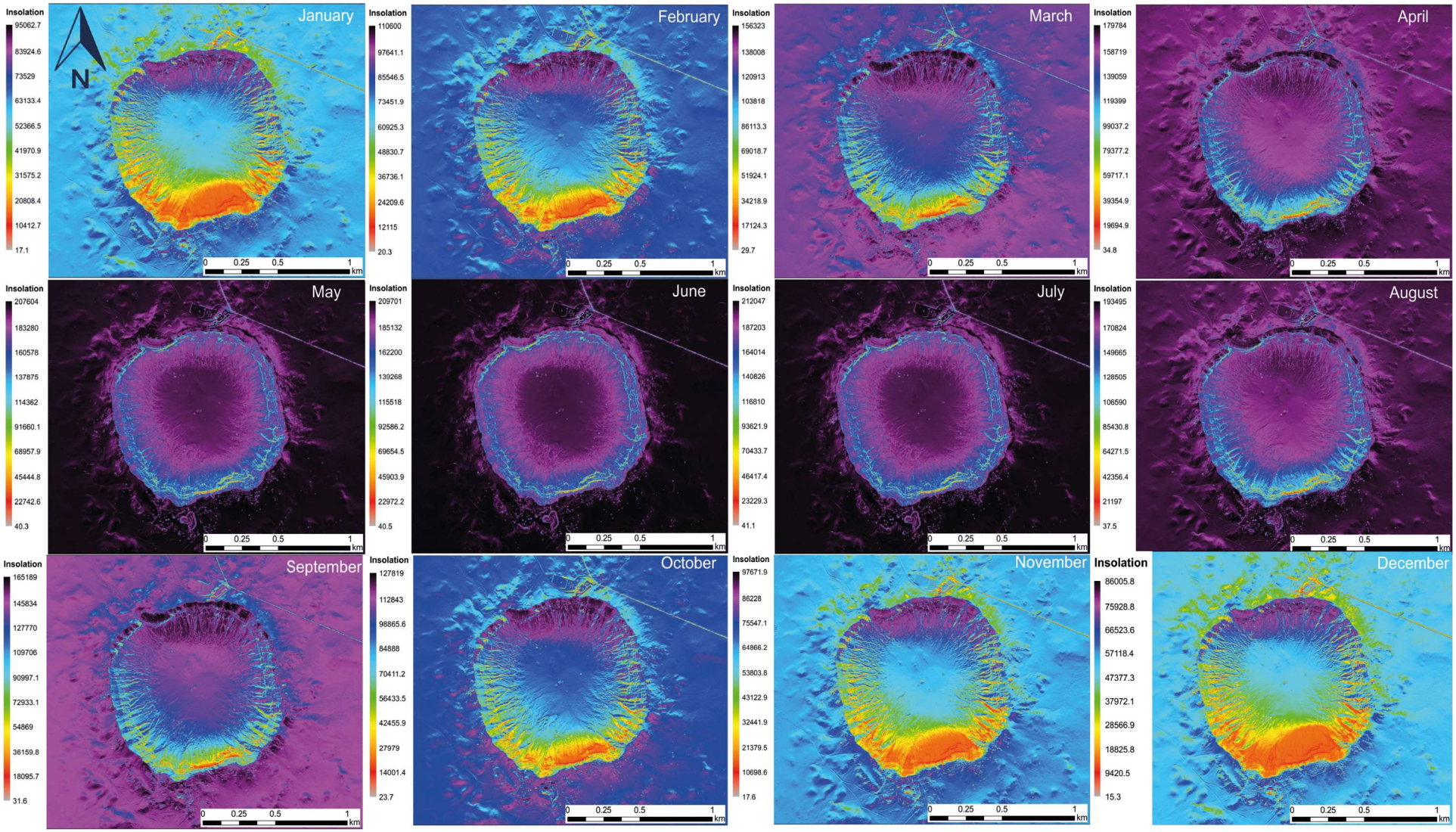


Fig 5.16. Solar insolation model for all the months in the year 2017. The unit of the map is watt-hours per square meter (WH/m^2). NOTE: The grey to red colour represents the lowest amount of solar insolation whereas black to magenta colour represents the highest amount of solar insolation received.

Sebastian Hoch from METCRAX I team modelled global radiation (direct + diffuse) received by inclined surfaces in and around Arizona's Meteor Crater, for 15 October 2006 (Whiteman et al., 2008; Hoch et al., 2010). The astronomical sunrise and sunset were at 0639 MST and 1740 MST, respectively (Fig 5.15). Soon after solar noon, the maximum global solar radiation was achieved at the crater (Fig 5.17) (Whiteman et al., 2008). The shading caused by crater sidewalls delayed sunrise at both the crater floor (0800 MST) and upper south sidewall (1018 MST) and resulted to an earlier sunset (crater floor: 1620 MST, upper south: 1648 MST) (Fig 5.17) (Whiteman et al., 2008). Maximum insolation occurs at the crater floor during solar noon, due to slope and aspect the upper south crater wall delays the maximum insolation until 1400 MST (Fig 5.17).

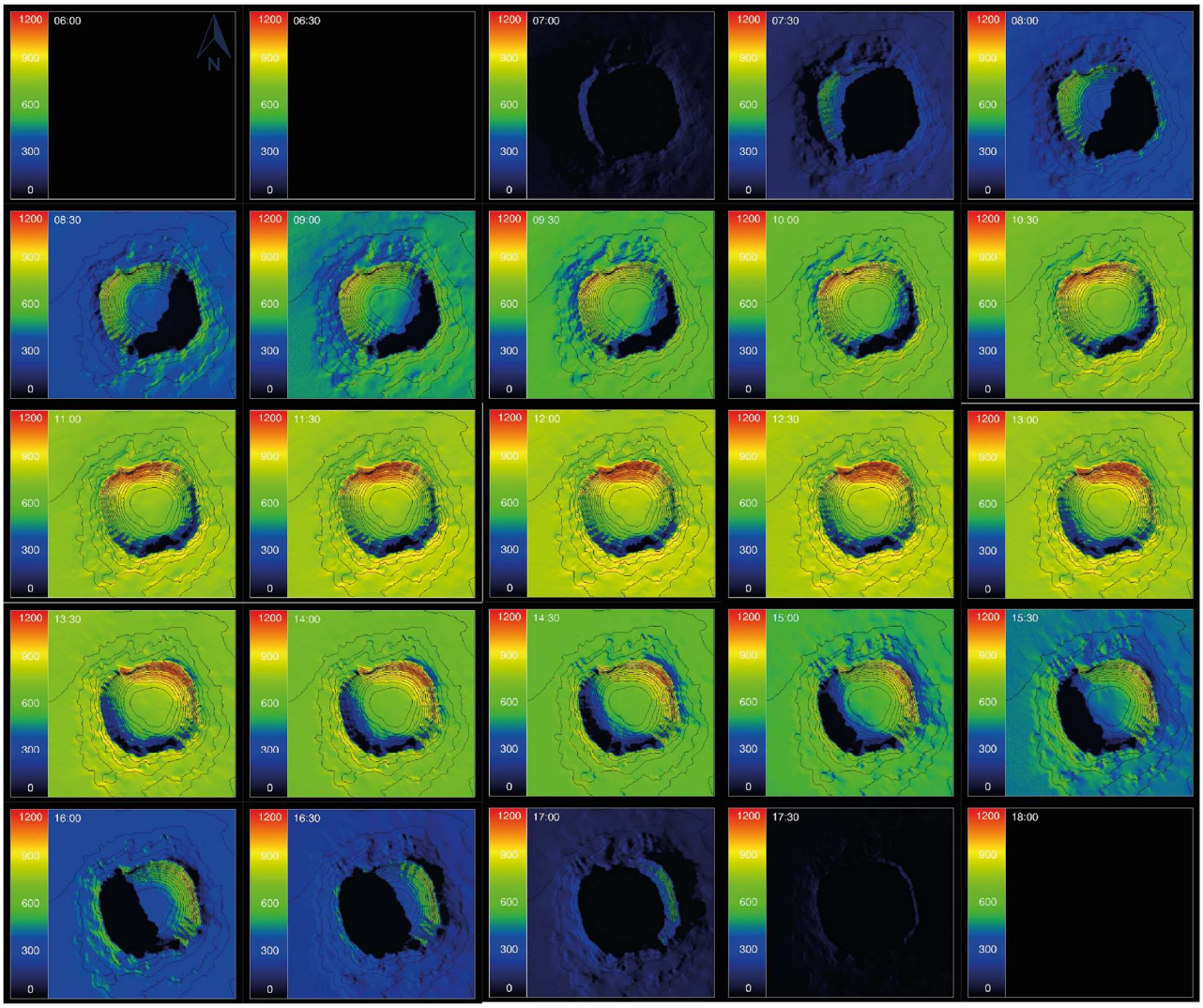


Fig 5.17. The METCRAX I experiment documented the diurnal air temperature differences caused by oblique sunlight and shadows on the crater walls. The figure shows the modelled

global radiation (direct + diffuse) received by inclined surfaces in and around Arizona's Meteor Crater, for 15 October 2006, with timestamps in units of Mountain Standard Time (MST). The unit of solar radiation is watt/m^2 (W/m^2). This differential solar radiation created differential air temperatures that were measured at the crater. Source: This model was made by Sebastian Hoch from the METCRAX team. Image source: This unpublished image was provided by David Whiteman of METCRAX team.

5.4.2. Photo documentation of breakdown features

Photo documentation, qualitative assessment, and identification of breakdown features were undertaken at Meteor Crater and control sites (Fig 5.18-5.19). A range of rock breakdown features was observed at the Meteor Crater and the control sites. Rock breakdown features observed at both the Meteor Crater and the control site include flaking, granular disintegration, cracks, alveoli, grus, exfoliation, splitting, tafoni, pachydermal weathering, spalling, crumbling, multiple splits, aeolian etching, and lichen-associated breakdown. All of these features were present on boulders and bedrocks at both Meteor Crater and the control site. Table 5.1 presents the detailed description of breakdown features observed in Moenkopi Sandstone at Meteor Crater and the control sites.

Table 5.1. Rock breakdown features observed at the field site

Type	Breakdown features	Description	Occurrence	Weathering processes
1-Loss of rock material (LS)	Alveoli	Alveoli are small (<1m) cavernous weathering features that occur in groups. Individual alveoli are separated from neighbours by narrow, thin walls, which looks like honeycomb (Bourke and Viles, 2007)	Facet of boulder and bedrock	Salt weathering, aeolian erosion, frost weathering (Mustoe, 1982; Rodriguez-Navarro et al., 1999)
	Tafoni	Tafoni are large (>1m) cavernous weathering features. They are often developed towards the base of large outcrop with near-circular arch-shaped opening and characterised by flaking backwall, concave inner wall, the overhanging lip in front, and debris covered floor (Heslop, 2003; Bourke and Viles, 2007).	Facet of boulder and bedrock	Salt weathering, frost weathering, chemical weathering (Goudie, 2004; Heslop, 2003; Brandmeier et al., 2011)
	Back weathering	Back weathering is a uniform loss of mm to cm scale rock material parallel to the original rock surface. Back weathering can occur due to loss of scales, crumbs, rock layers (Fitzner and Heinrichs, 2001)	Facet of boulder and bedrock	Mechanical and chemical weathering (Bland and Rolls, 1998a; Fitzner and Heinrichs, 2001; Bourke and Viles, 2007)
	Weathering pits	Weathering pits are small closed circular depression features on a horizontal and gently inclined rock surface that have a diameter ranging several cm. Depression backwall contains soil deposits and debris	Facet of boulder and bedrock	Frost weathering, chemical weathering, salt weathering, biochemical weathering (Goudie, 2004)
	Micropitting	Micropitting are small (mm-cm) pit type features. Micropitting develops from microscale irregularities within the rock surface which may be lithologically controlled (e.g. vesicles in volcanic rocks) (Bourke and Viles, 2007)	Facet of boulder and bedrock	Chemical and biochemical weathering (Bourke and Viles, 2007; Thornbush, 2012)
	Breakout	Breakout is the loss of large-scale rock fragments (cm^3 to dm^3).		Mechanical weathering (Bland and Rolls, 1998a; Bourke and Viles, 2007)
	Aeolian etching	Less resistant minerals or laminations within a facet preferentially attacked by windblown dust and sand	Facet of ejecta boulder and	Aeolian abrasion (Laity, 2009b)

		forming mm-cm etching patterns (Bourke and Viles, 2007).	crater wall rock at the south side of Meteor Crater	
2- Discoloration/deposition (DD)	Discolouration	Discolouration on the rock surface is produced by µm thick coating on the rock surface. The reddish-brown to the black colour coating can be due deposition of manganese and iron (Bourke and Viles, 2007)	Facet of boulder and bedrock	Chemical and biochemical weathering (Taylor and Eggleton, 2001)
	Soiling	Loose coating of µm to mm thick dust/soil layer on the rock surface. Soiling can occur over cm^2 to m^2 area.	Facet of boulder and bedrock	Aeolian erosion (Bourke and Viles, 2007).
	Efflorescence	Efflorescence is deposition of a layer of crystalline salt on the rock surface. It occurs when the water leaves behind salt deposits on the rock surface. It appears as a white, µm-mm thick salt coating. (Bourke and Viles, 2007). Powdered XRD analysis revealed the presence of gypsum at field sites.	Facet of boulder and bedrock	Salt weathering (Pel et al., 2004)
	Lichen colonisation	The occurrence of lichens on the rock surface. The lichen cover can be µm-mm thick and covering area ranging from cm^2 to m^2.	Facet of boulder and bedrock	Biochemical weathering (Chen et al., 2000)
	Colonisation by higher plants	Small plants tend to grow from fracture or joints on the bedrock.	Facet of boulder and bedrock	Biochemical weathering (Warke, 2013)
3-Detachment of rock material (DT)	Flaking	Flaking is the removal of mm to cm sections of the near-surface layer of rock.	Facet of boulder and bedrock	Mechanical weathering (Bland and Rolls, 1998a; Bourke and Viles, 2007)
	Granular disintegration	Granular disintegration occurs at mm scales where a range of rock breakdown processes acts together to detach individual grains from a rock surface producing a rough surface. The product of granular disintegrating is fine-grained debris that is easily eroded by wind and water, where not eroded they remain as loose debris near the outcrop. (Bourke and Viles, 2007)	Facet of boulder and bedrock	Salt weathering, chemical weathering, biochemical weathering (Goudie and Viles, 2015)
	Crumbling	Crumbling is a detachment of larger compact rock pieces (cm^3 to dm^3)in the form of crumbs (Fitzner and Heinrichs, 2001)	Facet of boulder and bedrock	Mechanical weathering (Bourke and Viles, 2007; Warke, 2013)
	Exfoliation	Exfoliation is mm-cm cracking in rocks approximately parallel to the surface of rock (Thomas et al., 2005).	Facet of boulder and bedrock	Insolation weathering (Leask and Wilson, 2003)
	Splitting	Splitting is the breaking of a bolder/outcrop into smaller parts. It occurs on clast scale where the combination of mechanical weathering processes enhances pre-existing weakness within boulder/bedrock to produce split rocks (Bourke and Viles, 2007)	Entire boulder and bedrock	Mechanical weathering (Bourke and Viles, 2007)
	Spalling	Spalling is the peeling off cm long platy fragments from rock surface (Bourke and Viles, 2007)	Facet of boulder and bedrock	Chemical weathering (Bourke and Viles, 2007)
4-Fissures/deformation (FD)	Cracks	Cracks or fissures are mm to cm wide lines of weakness along which rock surface splits without breaking apart (Bourke and Viles, 2007).	Facet of boulder and bedrock or entire outcrop	Insolation weathering (Bourke and Viles, 2007)
	Polygonal cracking	Polygonal cracking (also known as pachydermal weathering, (Thomas et al., 2005) occurs mm-cm wide cracks connected to form a polygon with 5 to 6 sides. It looks similar to desiccation cracks. Individual polygons have an interior angle of about 120° (Bourke and Viles, 2007; Chan et al., 2008)	Facet of boulder and bedrock	Frost weathering, insolation weathering, wetting and drying (Chan et al., 2008)

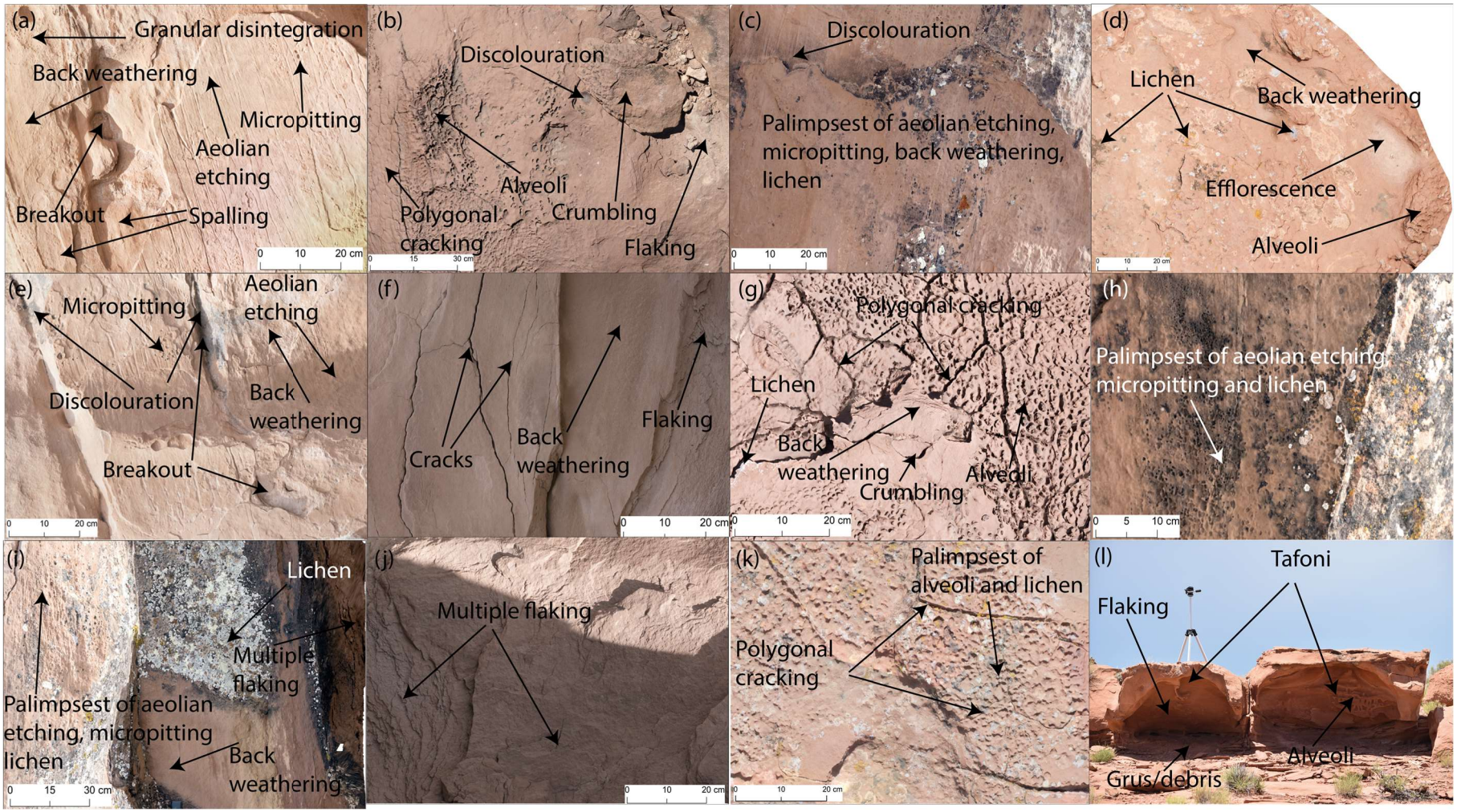


Fig 5.18. Rock breakdown features observed at Meteor Crater and the control sites. All the images except (l) are orthophotos. These orthophotos of Moenkopi Sandstone except (l) are from Meteor Crater.

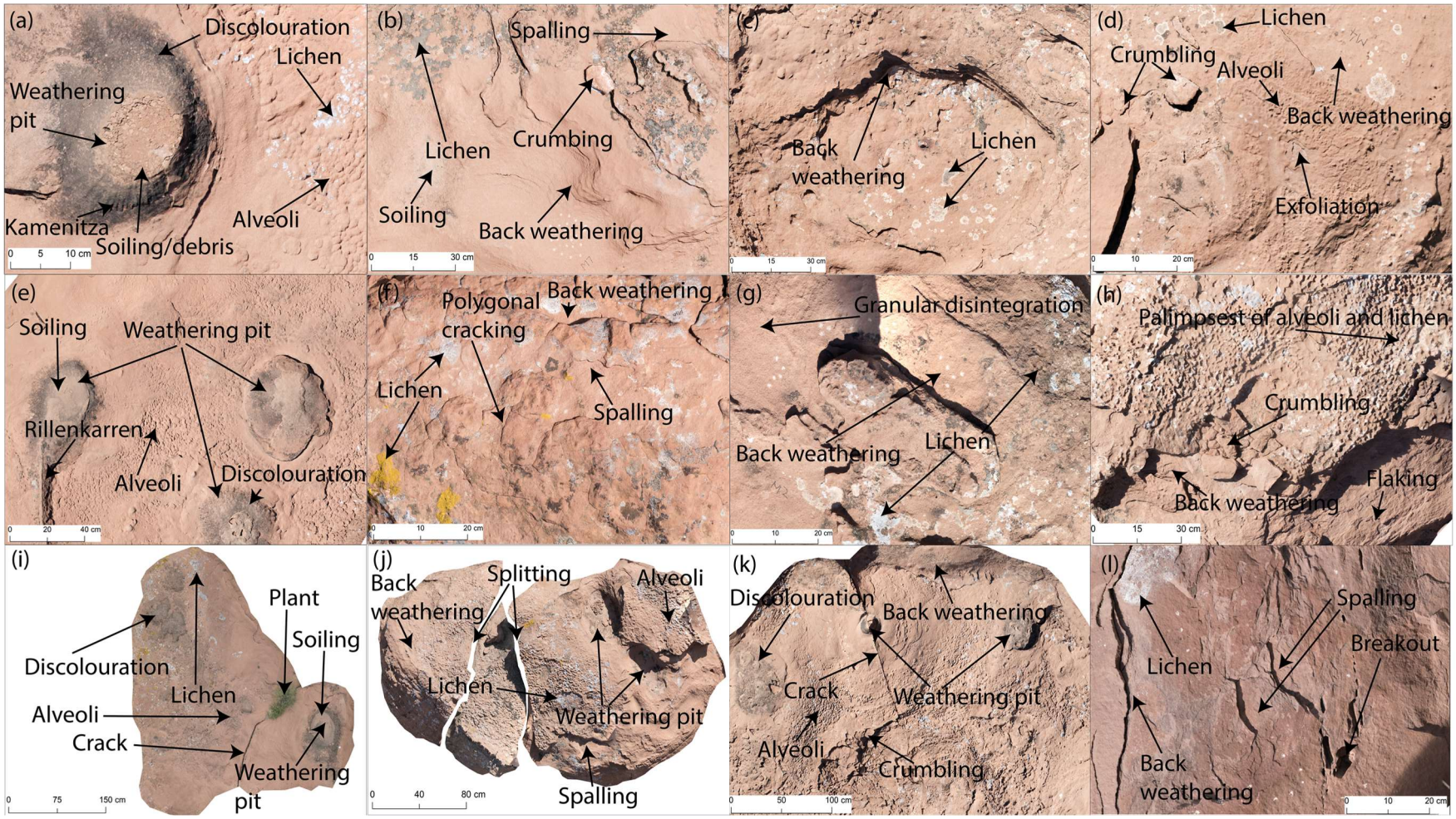


Fig 5.19. Rock breakdown features observed at the control sites. All the images are orthophotos. All the images are the orthophotos.

5.4.3. Petrographic properties of unshocked and shocked Moenkopi Sandstone

The petrographic properties of Moenkopi Sandstone are presented in detail in chapter 2 and are summarised here for self-consistency of this paper format.

Unshocked Moenkopi sandstone (MS) is very fine-grained sandstone which is cemented by carbonates. Moenkopi contains 50-80 % quartz, microcline, muscovite, hematite and kaolinite in minor amounts and remainder being composed of carbonate minerals (calcite and dolomite). Quartz is subrounded, equant, and well sorted and has subhedral grain boundary. The matrix is very fine grained and iron rich. The mean grain size ranges from 0.07-0.1 mm. The grain size ranges from 0.009-0.12 mm. The texture of the rock is grain supported. The porosity in unshocked Moenkopi Sandstone ranges 5-8.5%. The pore diameter ranges from 3 to 300 μm. Some of the Moenkopi Samples contain cross laminations in hand samples. The powdered X-ray Diffraction of efflorescence sample from two of the Moenkopi Sandstone outcrops revealed the presence of Gypsum salt in the field. This suggests ongoing salt weathering process in Moenkopi Sandstone.

Class 1a (<5GPa) Shocked Moenkopi Sandstone (MS) may have experiences <5GPa of shock pressure during impact. In hand specimen, there is no visible difference between class 1a and unshocked MS. No high-pressure polymorphs were identified in XRD analysis and no change in mineralogy was observed in class 1a MS compared to unshocked MS. Macroscopic fractures with an aperture of 4-200 μm and length from 0.5 to 5 cm are present in some of the class 1a MS samples. Due to low shock, porosity is reduced by 88% in class 1a MS compared to unshocked MS. The porosity in low shocked Moenkopi is 0.5-1%. The pore diameter ranges from 3 to 180 μm. No irregular grain fracturing due to impact can be seen in class 1a MS. A small amount of the quartz grains show wavy extinction.

More comprehensive and detailed information on all the samples of Moenkopi Sandstone is presented in Chapter 2.

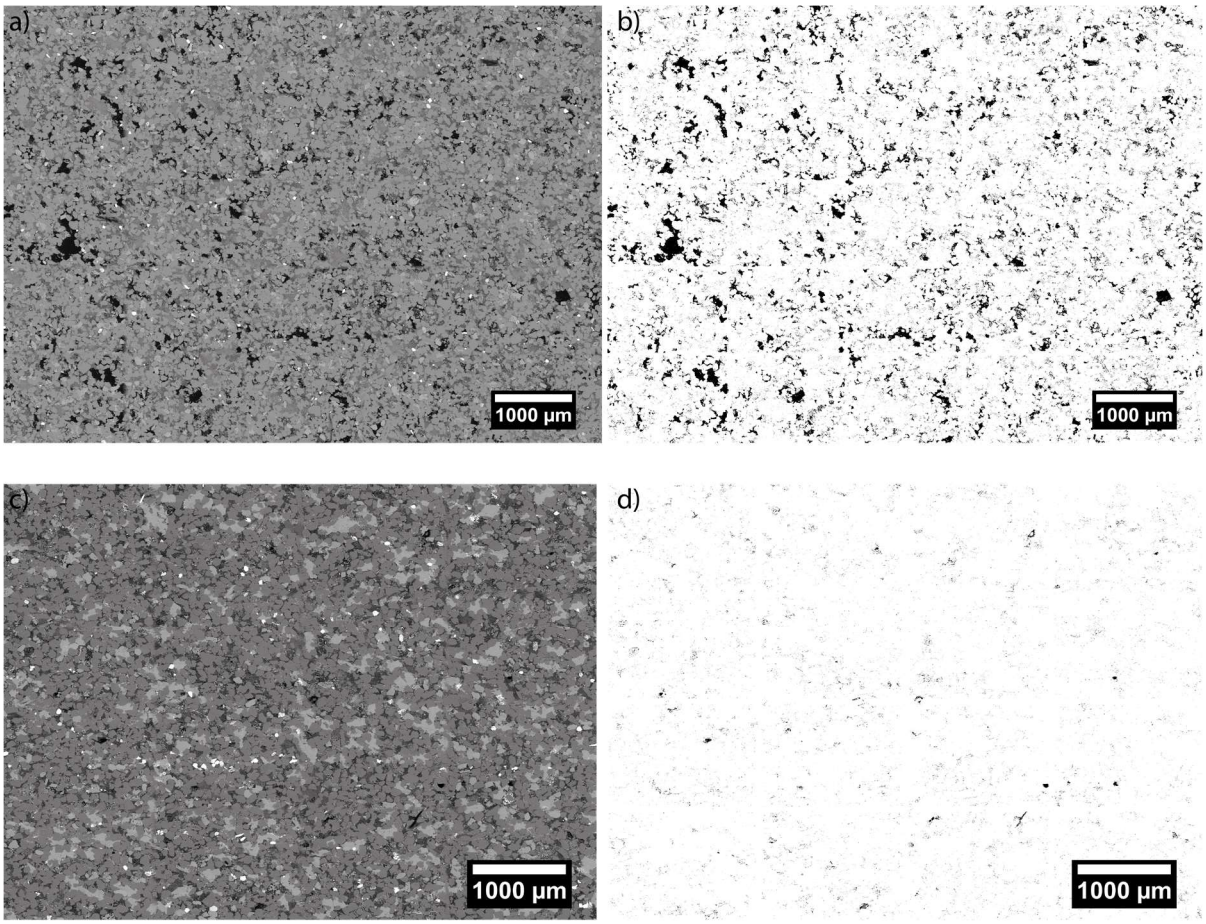


Fig 5.20. Moenkopi sandstone. (a) BSE image of unshocked MS showing pores. Black substrate represents pore spaces. (b) thresholded image minus (a) showing pores in black colour. (c) BSE image of class 1a MS showing reduced porosity. (d) thresholded image minus (c) displaying fewer pore spaces in black.

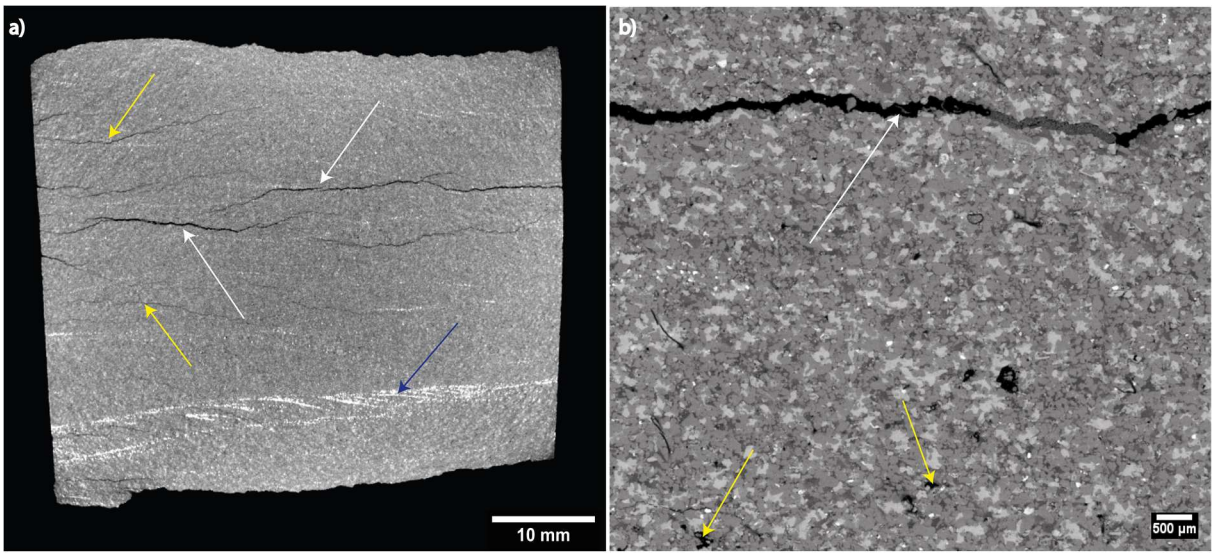


Fig 5.21. Fractures in low shocked Moenkopi Sandstone. a) The X-ray CT image on the left showing the distribution of fractures with apertures ranging from 0.09 to 0.2 mm. The white

arrows show fractures with ~0.2 mm aperture and yellow arrows show fractures with ~0.09 mm. The blue arrow shows the cross-lamination in the sample. b) The SEM BE image of the same sample shows collapsed pores (shown by yellow arrows) and inter-granular fracture (shown by white arrows) of aperture 0.15 mm.

5.4.4. Rock Hardness

In terms of rock surface hardness, the mean Schmidt Hammer (SH) rebound values (Table 5.2, Fig. 5.22) do not reveal a significant difference between Meteor Crater and the three control sites at $p<0.05$ level. Rock hardness varies with the breakdown features present on the rock surface. Rock surface with intensive flaking features had lower hardness value compared to rock surfaces with alveoli. Detailed statistical analysis of SH rebound data can be found in Appendix 5.

Table 5.2. Schmidt hammer statistics and averages per boulder. Schmidt hammer rebound values are mean standard (±standard deviation).

Location	No. of rock outcrops Sampled	Schmidt hammer rebound value
Control Site 1	30	38.8 ± 5.6
Control Site 2	31	37.5 ± 6.6
Control Site 3	39	38.5 ± 7.0
Meteor Crater	22	37.9 ± 7.7

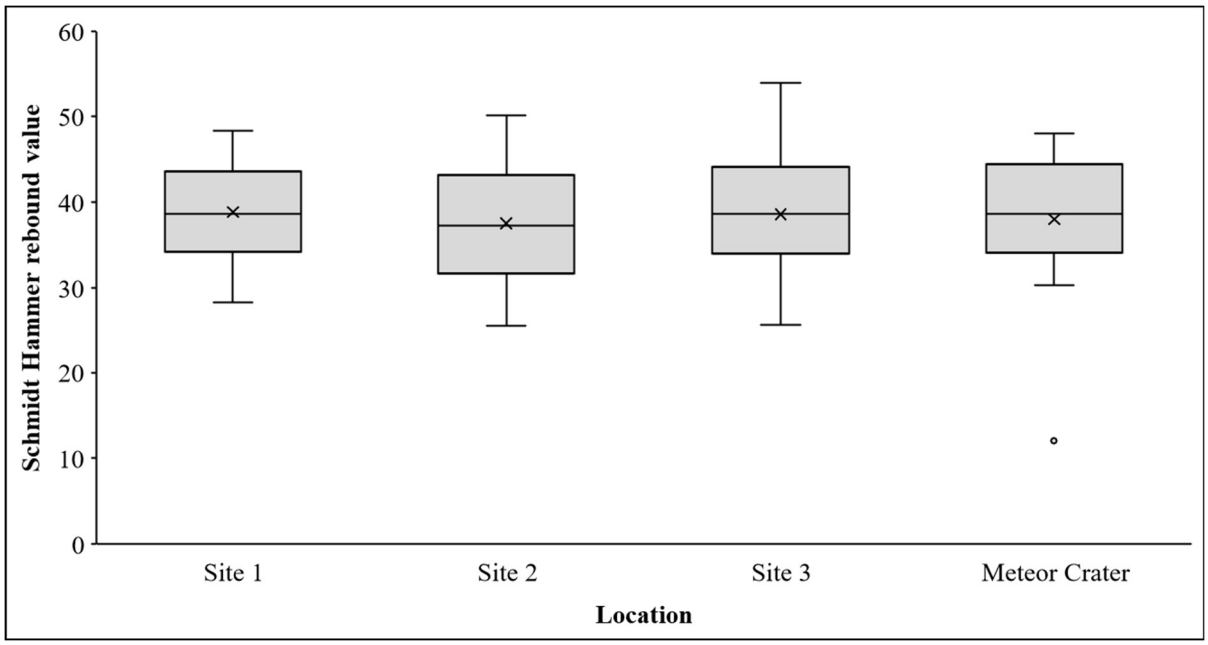


Fig 5.22. Box and whisker plot showing a summary of Schmidt hammer data (min, max, and inter-quartile range) for Meteor Crater and the three control sites. The 'x' represents the mean of the SH rebound values at each site. The hollow circle represents an outlier SH rebound value at Meteor Crater.

5.4.5. Areal surface roughness analysis

The results of four areal surface roughness analysis: the standard deviation of height (Sq), the standard deviation of slope (Sdq), Maximum height (Sz), and Vector Ruggedness Measure (VRM) at seven window scale sizes (1.5, 5.5, 10.5, 15.5, 20.5, 25.5, 50.5 mm) are presented in the following sections. The spatial resolution of DEMs that were analysed to calculate these parameters was 0.5 mm; the resolution was kept constant for DEMs from all the sites.

Table 5.3. Summary of DEM analysis conducted.

Site	No. of DEMs	Areal surface roughness and morphometric feature classification				
		Sq	Sdq	Sz	VRM	Morphometric feature classification
Control Site 1	13	✓	✓	✓	✓	✓
Control Site 2	15	✓	✓	✓	✓	✓
Control Site 3	22	✓	✓	✓	✓	✓
Meteor Crater	21	✓	✓	✓	✓	✓

In the following sections, we present the results from roughness analysis on all the DEMs from Meteor Crater and control sites. The data and detailed statistical analysis of roughness analysis can be found in Appendix 5.

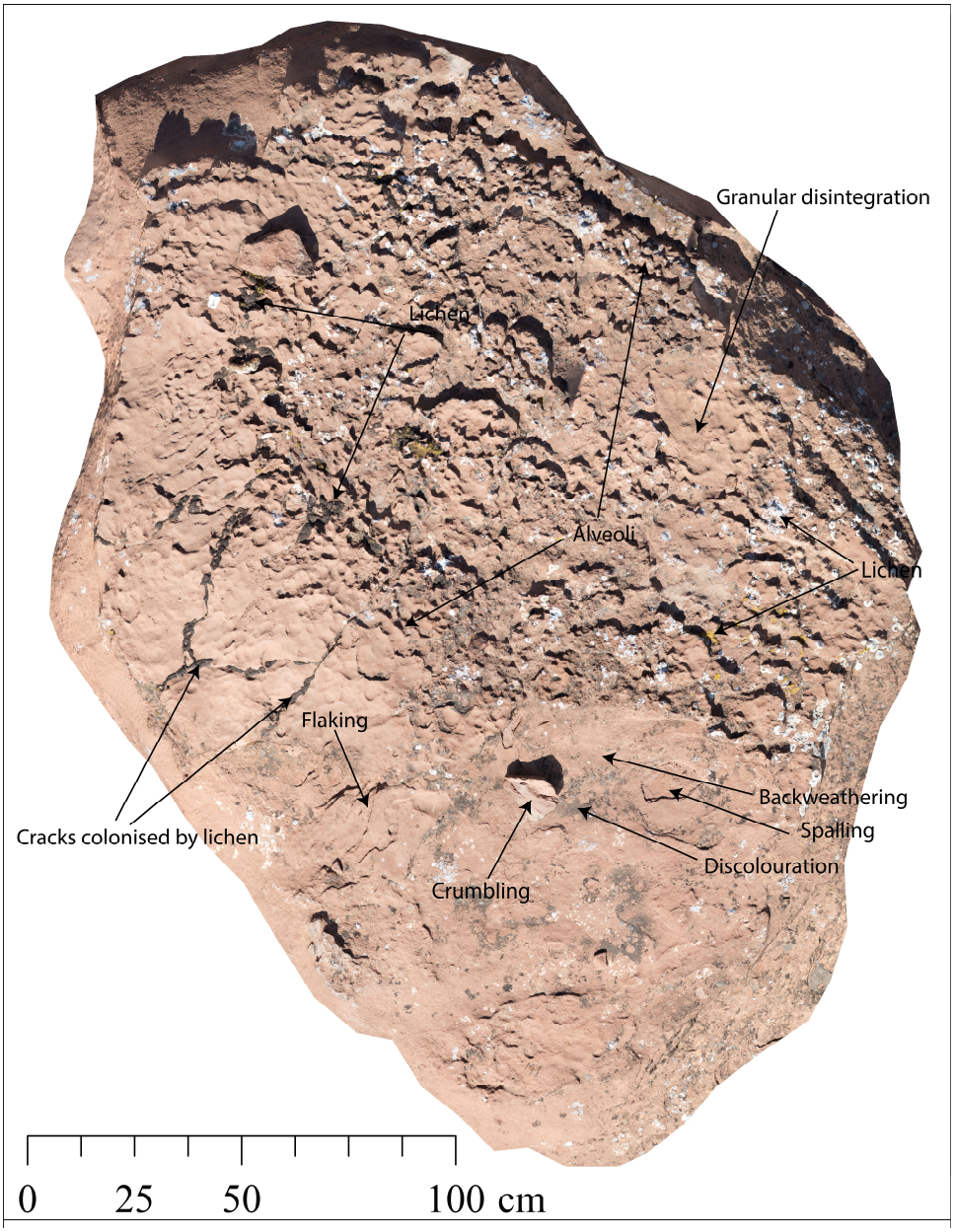


Fig 5.23. Weathering features on a boulder from site 2. The roughness analysis of this boulder is presented as an example in the following sections.

5.4.5.1. Standard Deviation of height (Sq)

The distribution of Sq for all seven window scale sizes had no statistically significant difference between Meteor Crater and the three control sites. Fig 5.24 shows the median of Sq from all the sites at seven window scale sizes. One general trend can be seen in the data is that Sq increases as the window scale size increases for all the sites. Fig 5.25-5.26 shows

the Sq analysis on a boulder from site 2 (Fig 5.23) as an example. Analysis of other samples is in Appendix 5. The roughness (Sq value) is increasing as the window scale increases. The variation in Sq value is smaller at 1.5 mm window scale, so it is unable to detect breakdown features larger than 1.5 mm (Fig 5.25). At higher window sizes, 5.5 to 25.5 mm, the edges and walls of alveoli and flaking features (mm-cm scale) can be distinguished (Fig 5.25). At 50.5 mm window size, the visibility of cm-scale features such as breakouts and crumbling are more prominent, and edges and walls of neighbouring smaller alveoli and flaking features are not distinguishable (Fig 5.26).

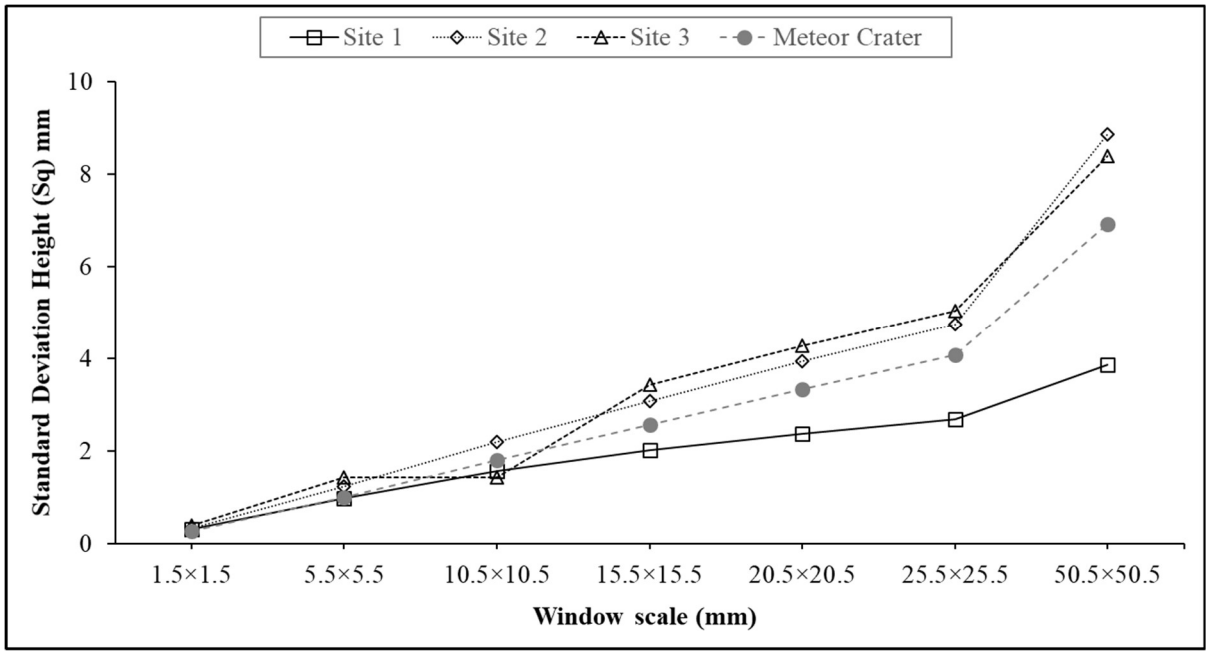


Fig 5.24. The plot of median values of Sq according to moving-window size.

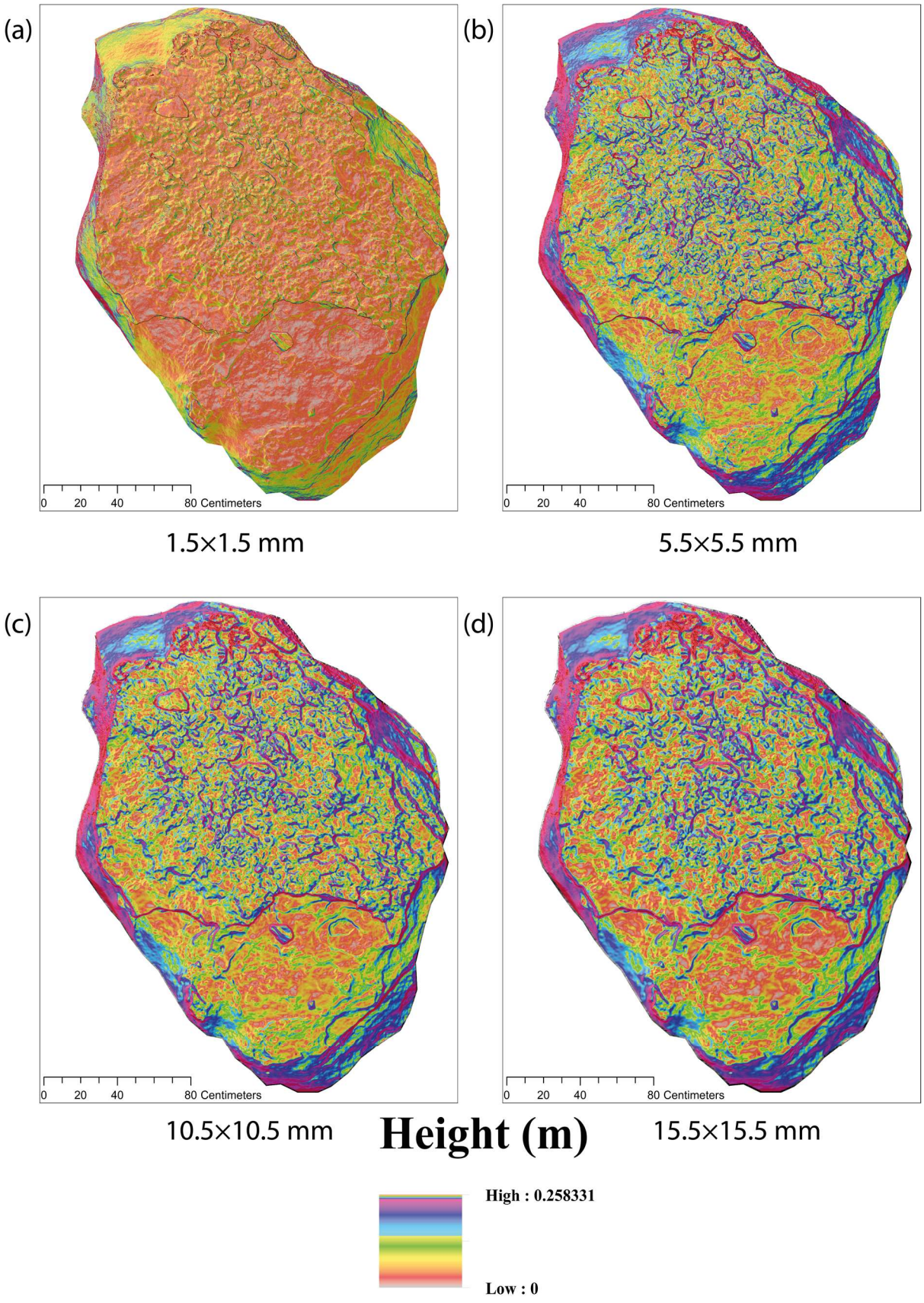


Fig 5.25. Sq output calculated at four moving window sizes for a boulder at Site 2 (Fig 5.23).

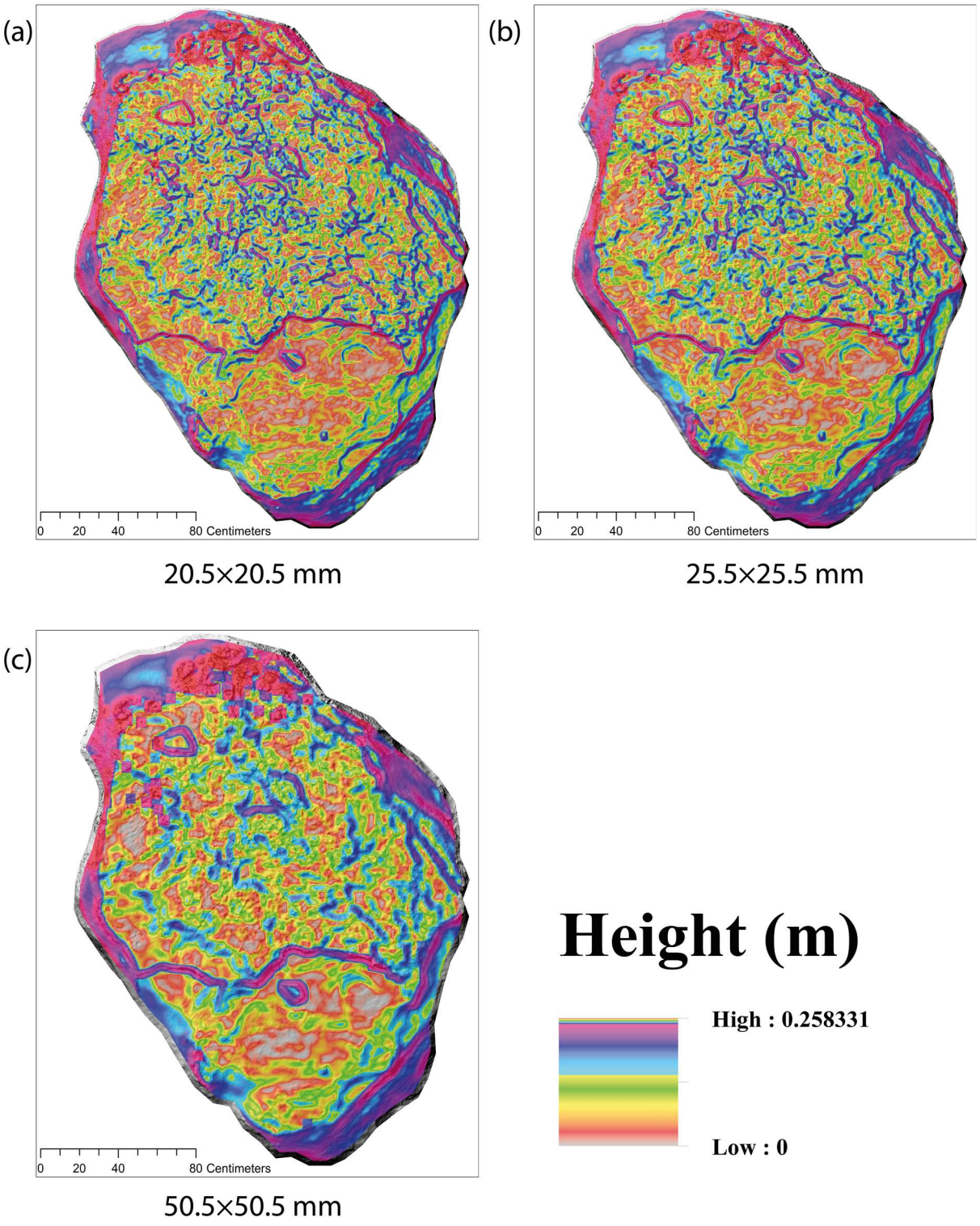


Fig 5.26. Sq output calculated at three moving window sizes for a boulder at Site 2 (Fig 5.23).

5.4.5.2. Standard Deviation of slope (Sdq)

The distribution of Sdq at all seven window scales reveal no statistical significance between Meteor Crater and the three control sites. The median of Sdq for Site 1 at all window scales was slightly higher than the values for Meteor Crater and control sites 2 and 3 (Fig 5.27). The distribution of Sdq was very similar for Site 3 and Meteor Crater at all window scales. Similar to Sq, Sdq increases with an increase in window scale size. At smaller scales, 1.5 to 5.5 mm, the edges and walls of alveoli and flaking (mm-cm scale) are less distinct from neighbouring features. At the larger scale, 10.5 to 25.5 mm, the boundaries of breakdown features are easily distinguishable (Fig. 5.28). At scale 50.5 mm, cm scale crumbling, and breakout features standout from neighbouring breakdown features (Fig 5.29). Sharp alveoli edges and walls can still be distinguishable from neighbouring breakdown features, but mm scale flaking and smoothened alveoli are difficult to distinguish (Fig 5.29).

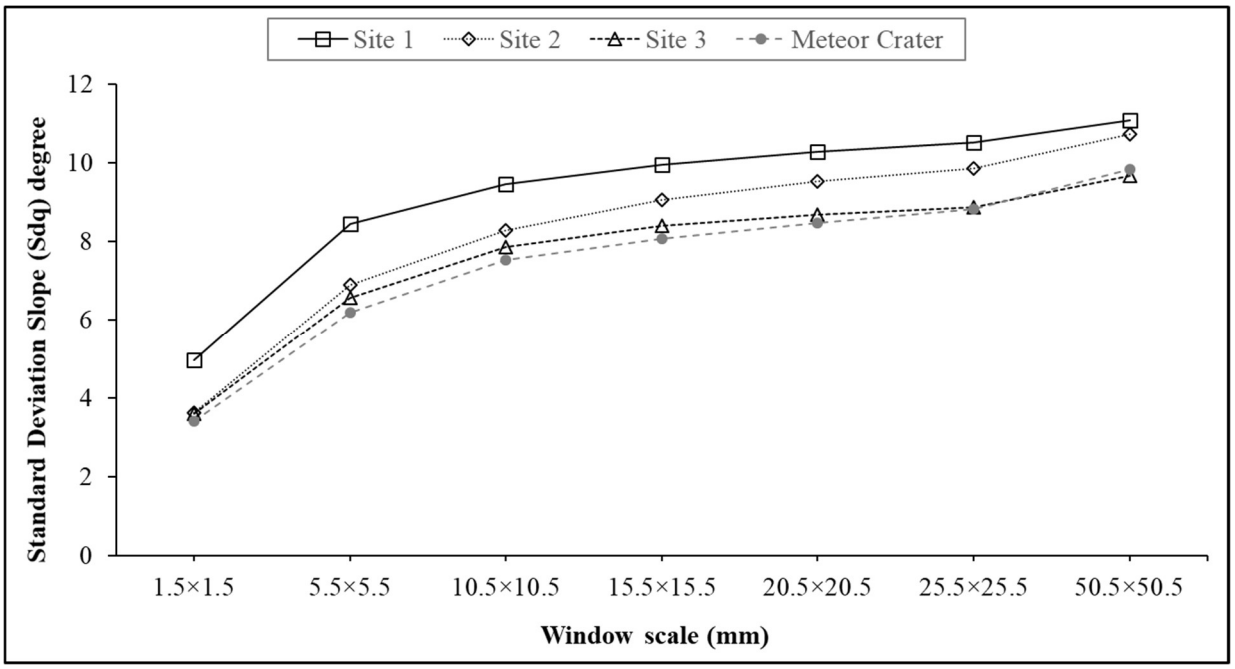


Fig 5.27. The plot of median values of Sdq according to moving-window size.

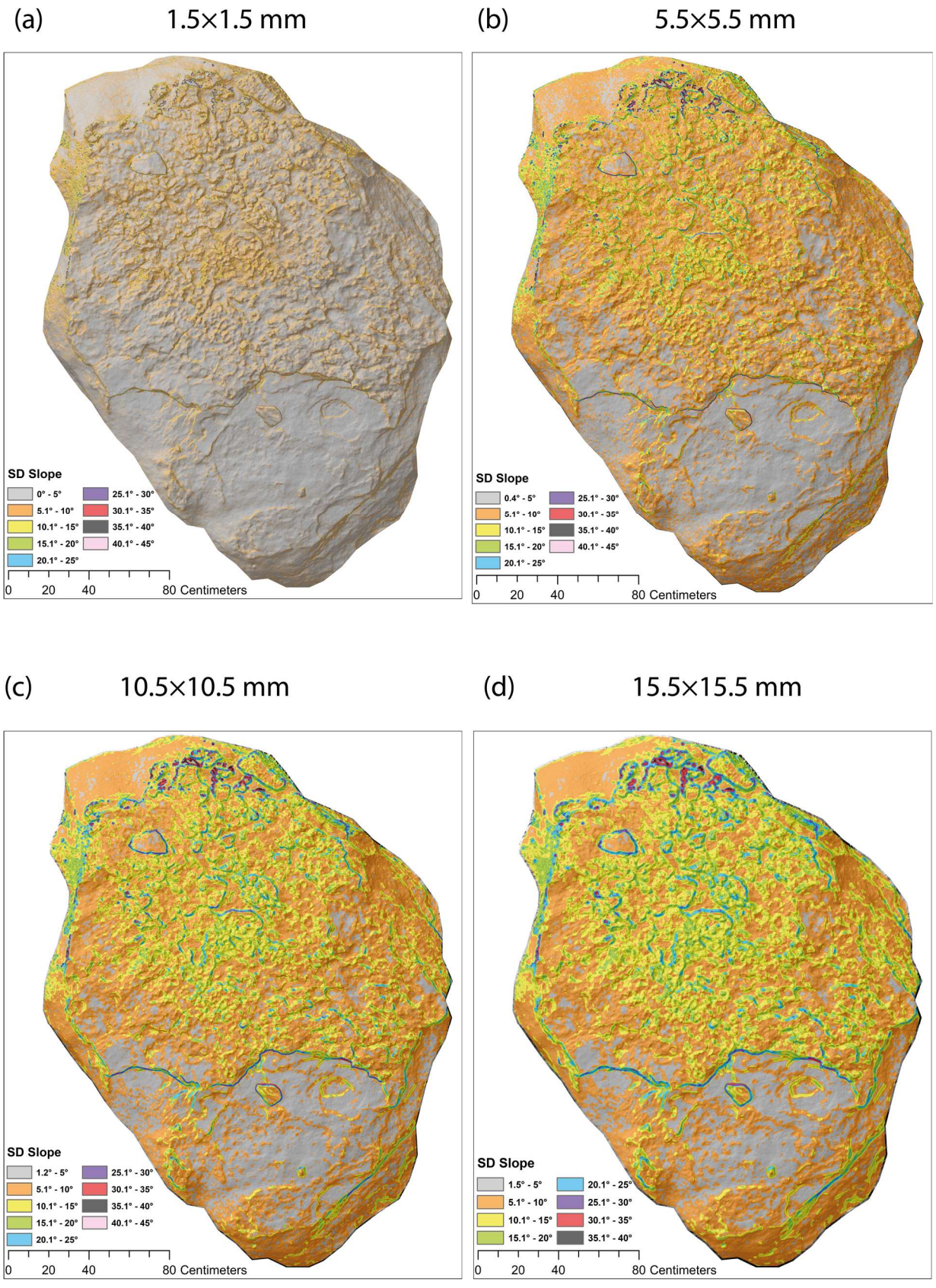
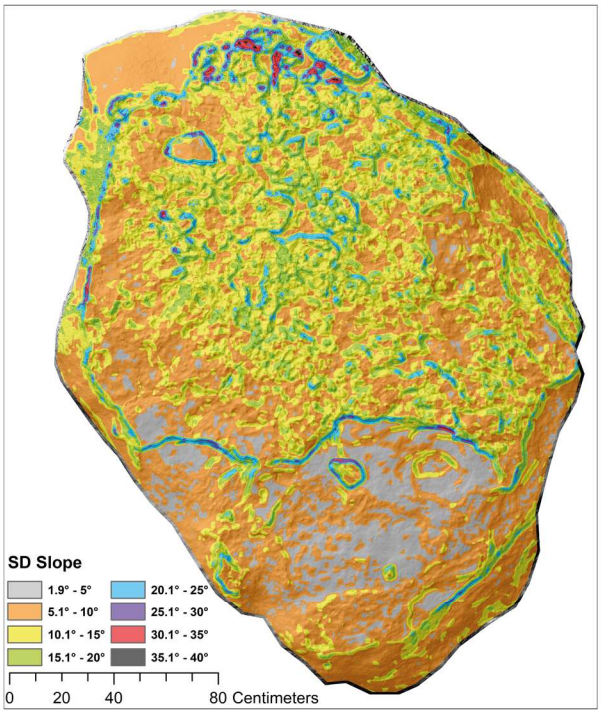
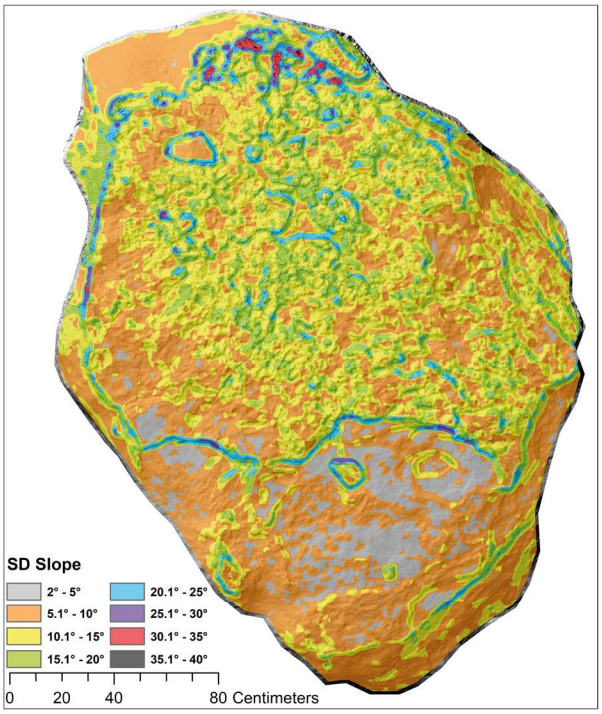


Fig 5.28. Sdq output calculated at four moving window sizes for a boulder at Site 2 (Fig 5.23).

(a) 20.5×20.5 mm



(b) 25.5×25.5 mm



(c) 50.5×50.5 mm

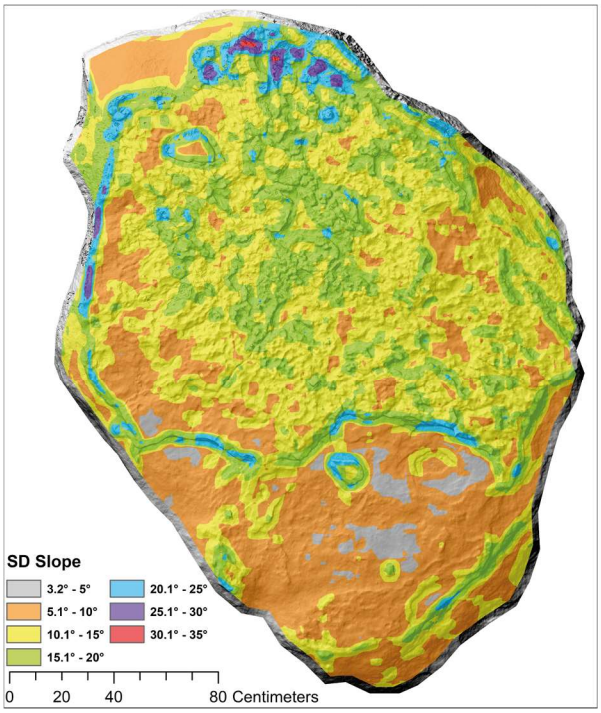


Fig 5.29. Sdq output calculated at three moving window sizes for a boulder at Site 2 (Fig 5.23).

5.4.5.3. Maximum height (Sz)

We found no statistically significant difference in Sz for all window scales between Meteor Crater and the control sites. Similar to Sq and Sdq, Sz increases with the increase in window scale (Fig 5.30). The distribution of Sz at all window scale for Site 1 and Meteor Crater is very similar (Fig 5.30). The variation in Sz value is smaller at 1.5 mm window scale, so it is unable to detect breakdown features larger than 1.5 mm (Fig 5.31). At higher window sizes, 5.5 to 25.5 mm, the edges and walls of alveoli and flaking features (mm-cm scale) can be distinguished (Fig 5.31). At 50.5 mm window size, the visibility of cm-scale features such as breakouts and crumbling are more prominent, and edges and walls of neighbouring smaller alveoli and flaking features are not distinguishable (Fig 5.32).

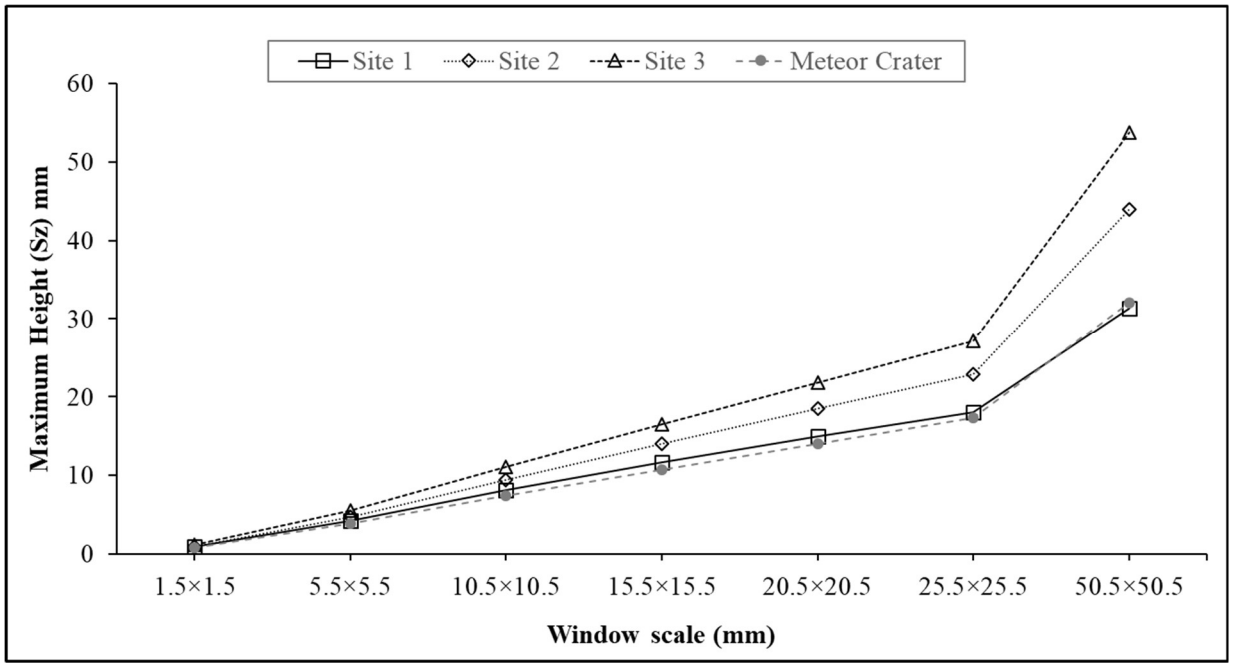


Fig 5.30. The plot of median values of Sz according to moving-window size.

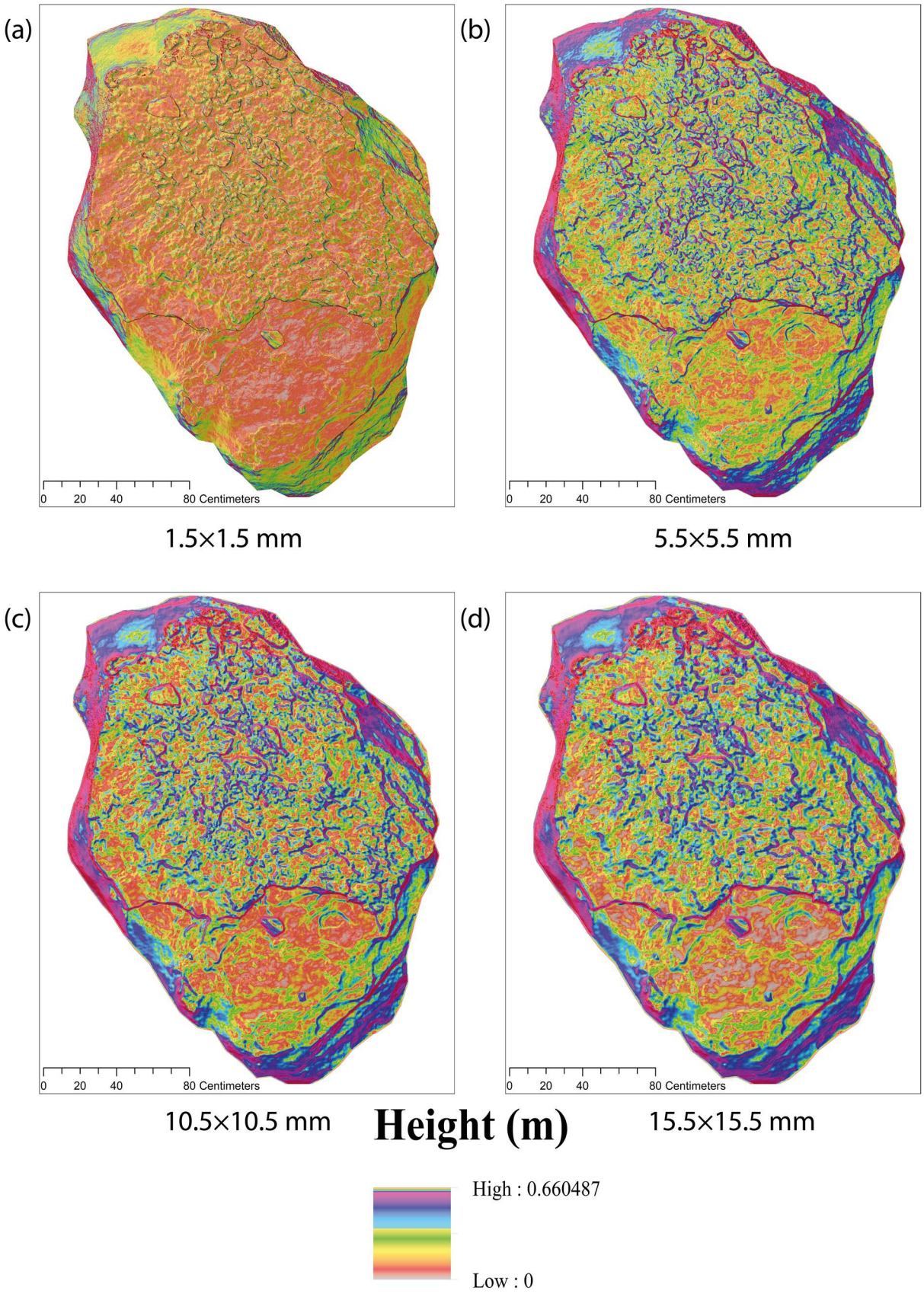


Fig 5.31. Sz output calculated at four moving window sizes for a boulder at Site 2 (Fig 5.23).

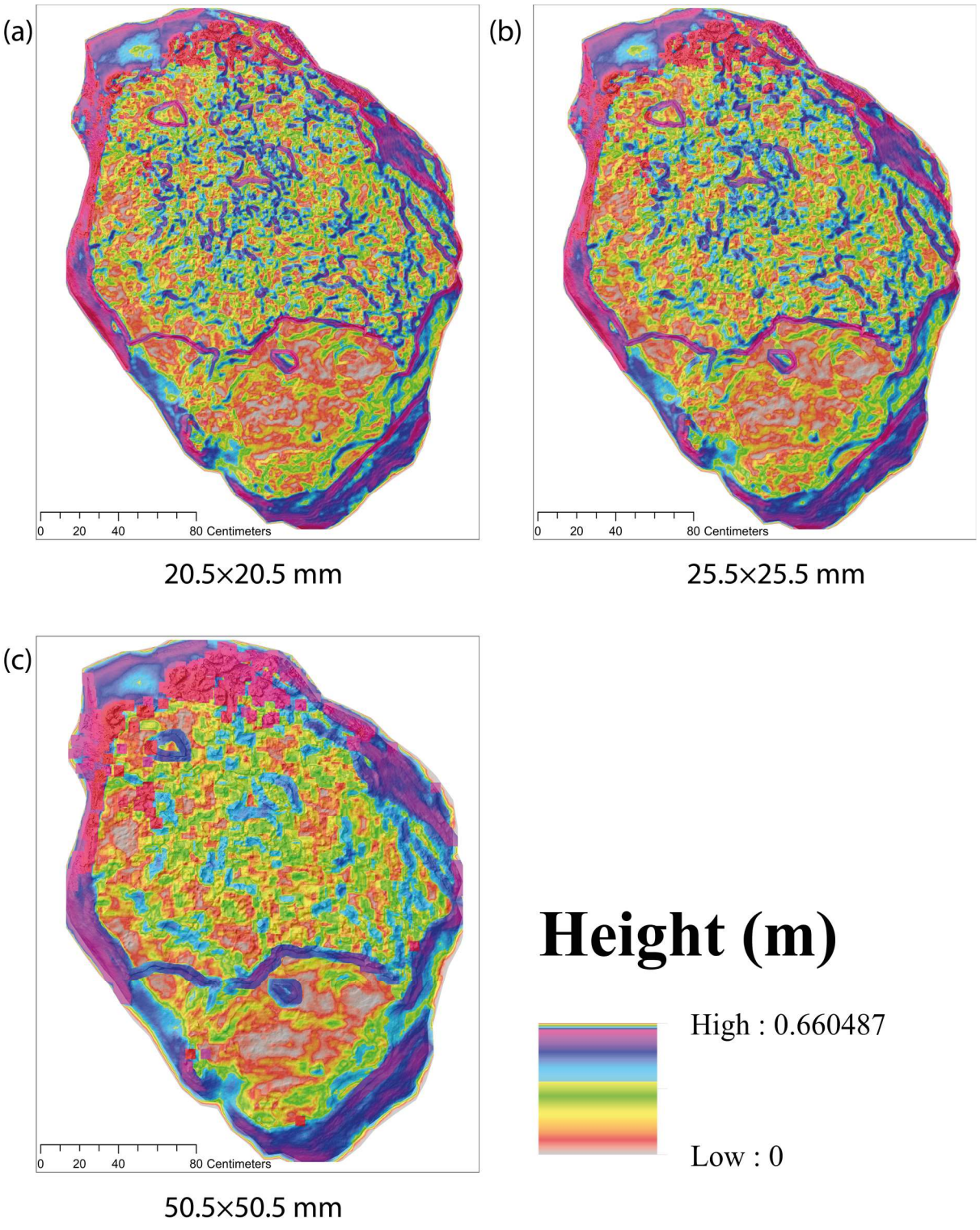


Fig 5.32. Sz output calculated at three moving window sizes for a boulder at Site 2 (Fig 5.23).

5.4.5.4. Vector Ruggedness Measure (VRM)

VRM at window scale 1.5 mm revealed statistical significance difference between Site 1 and Site 2 (control sites). However, there was no statistically significant difference between Meteor Crater and two other control sites (Site 2 and Site 3). At higher window scale, 5.5 to 50.5 mm, no statistically significant difference was found between Meteor Crater and the three control sites. The median of VRM for Site 1 at all window scale was slightly higher than the values for Meteor Crater and the other two control sites. VRM increases as window scale increases (Fig 5.33). Fig 5.34-5.35 shows VRM calculated for a boulder on seven moving window sizes.

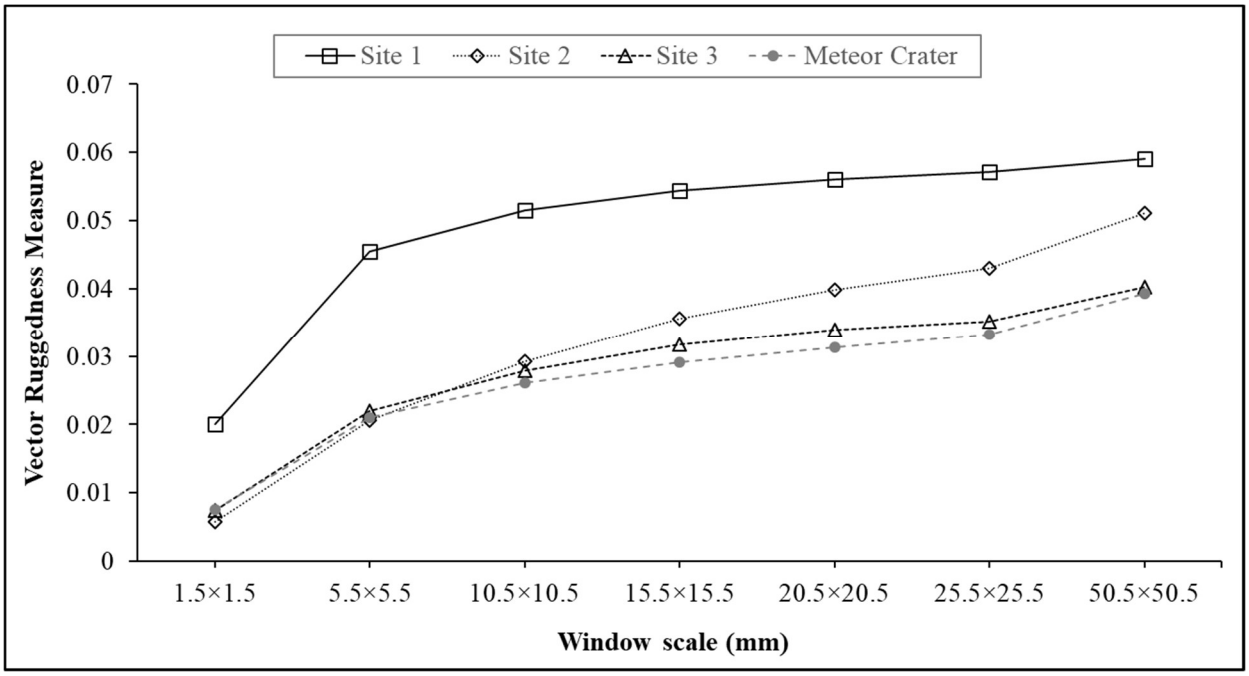


Fig 5.33. The plot of median values of VRM according to moving-window size.

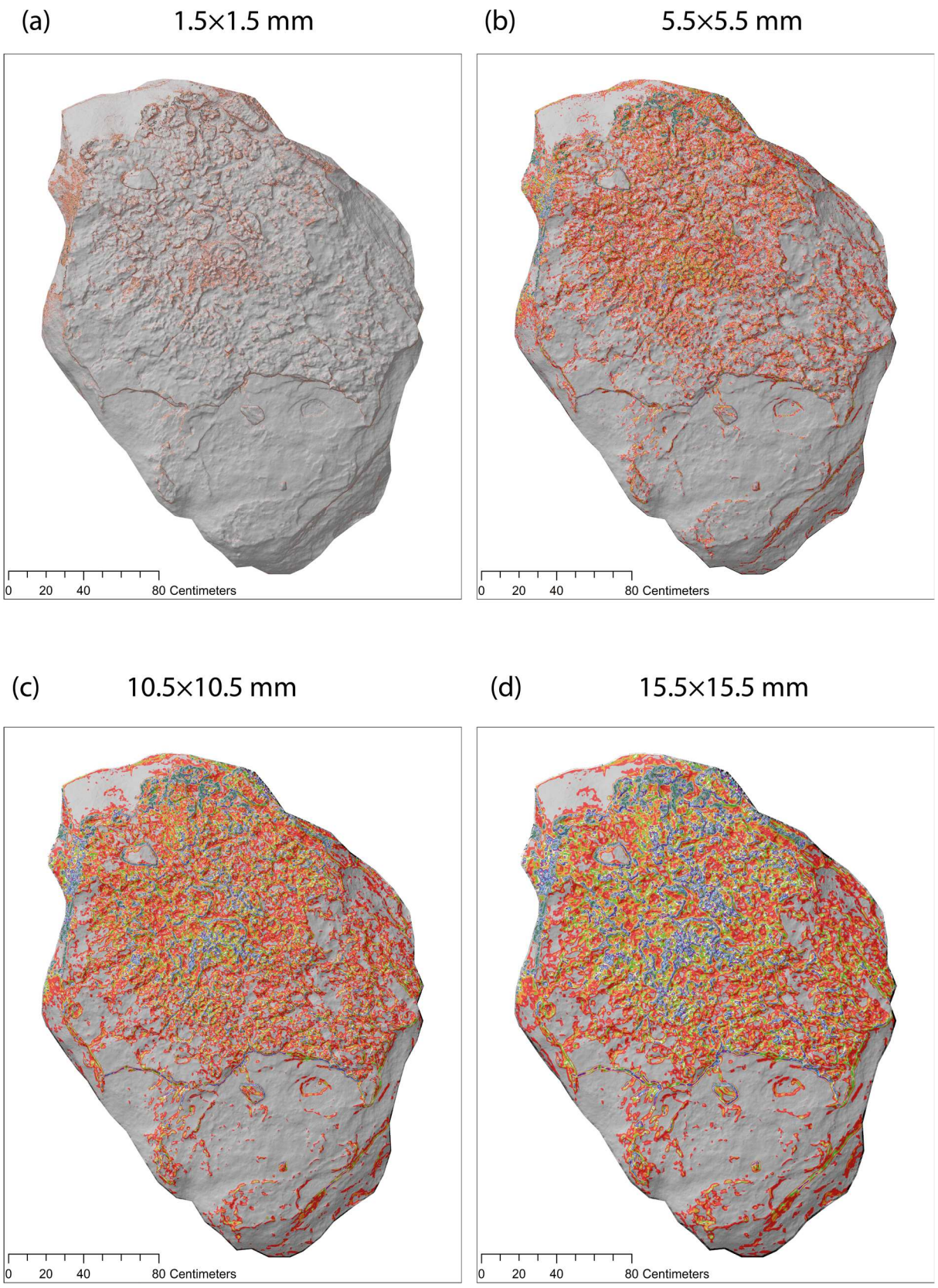


Fig 5.34. VRM output calculated at four moving window sizes for a boulder at Site 2 (Fig 5.23).

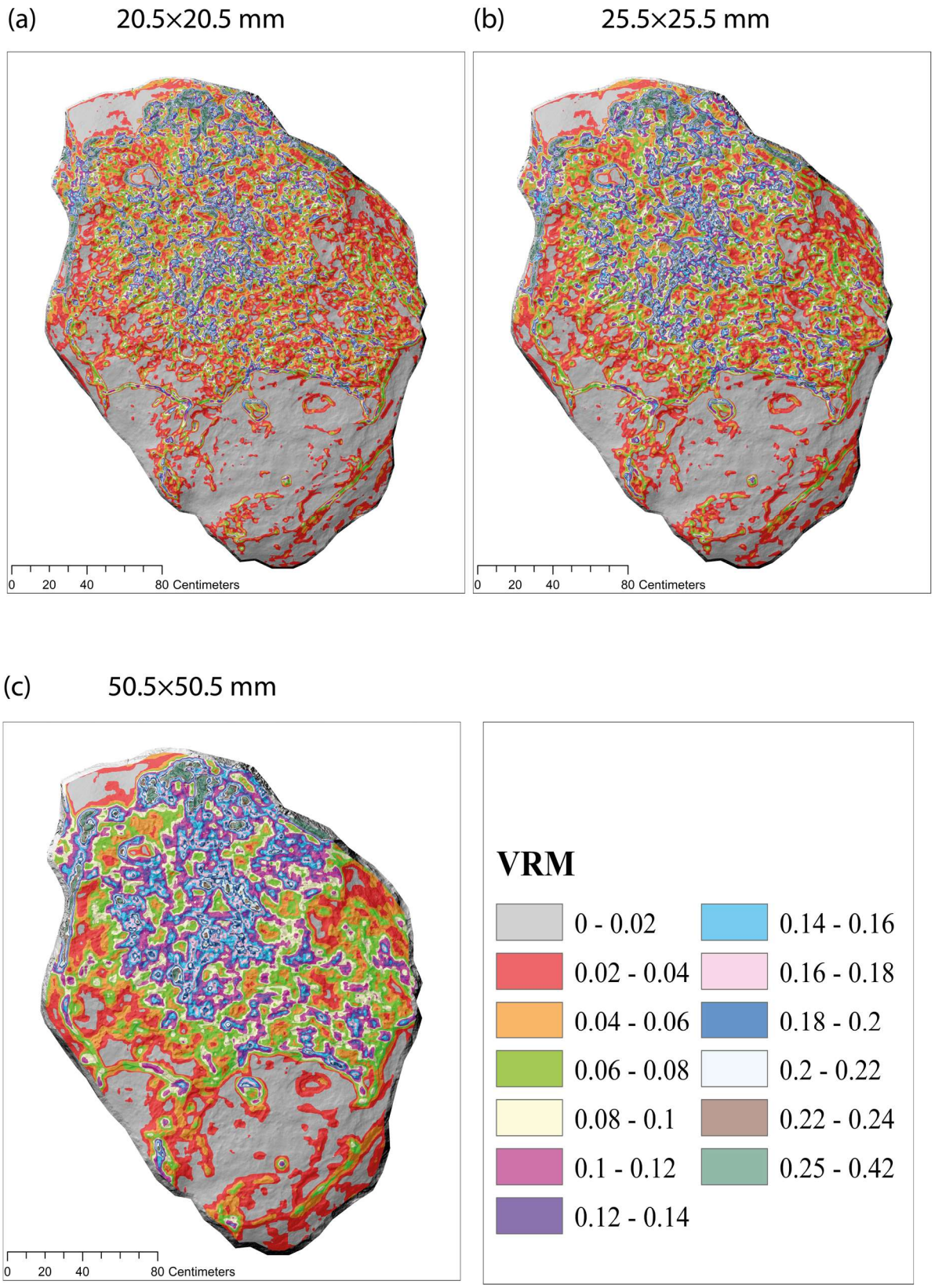


Fig 5.35. VRM output calculated at three moving window sizes for a boulder at Site 2 (Fig 5.23).

5.4.6. Morphometric feature classification

In percent area of morphometric geomorphic feature classes, at all window scale and all feature classes, there were no statistically significant differences between Meteor Crater and the three control sites. The median of percent area of the pit, pass, and the ridge was slightly higher for site 1 compared to Meteor Crater and two other control sites (Fig 5.36). The median of percent area of planar features was slightly higher for Meteor Crater compared to the three control sites (Fig 5.36). Fig 5.37-5.38 shows morphometric feature calculated for a boulder on seven moving window sizes. Detailed statistical analysis and data tables for morphometric feature analysis is presented in Appendix 5.

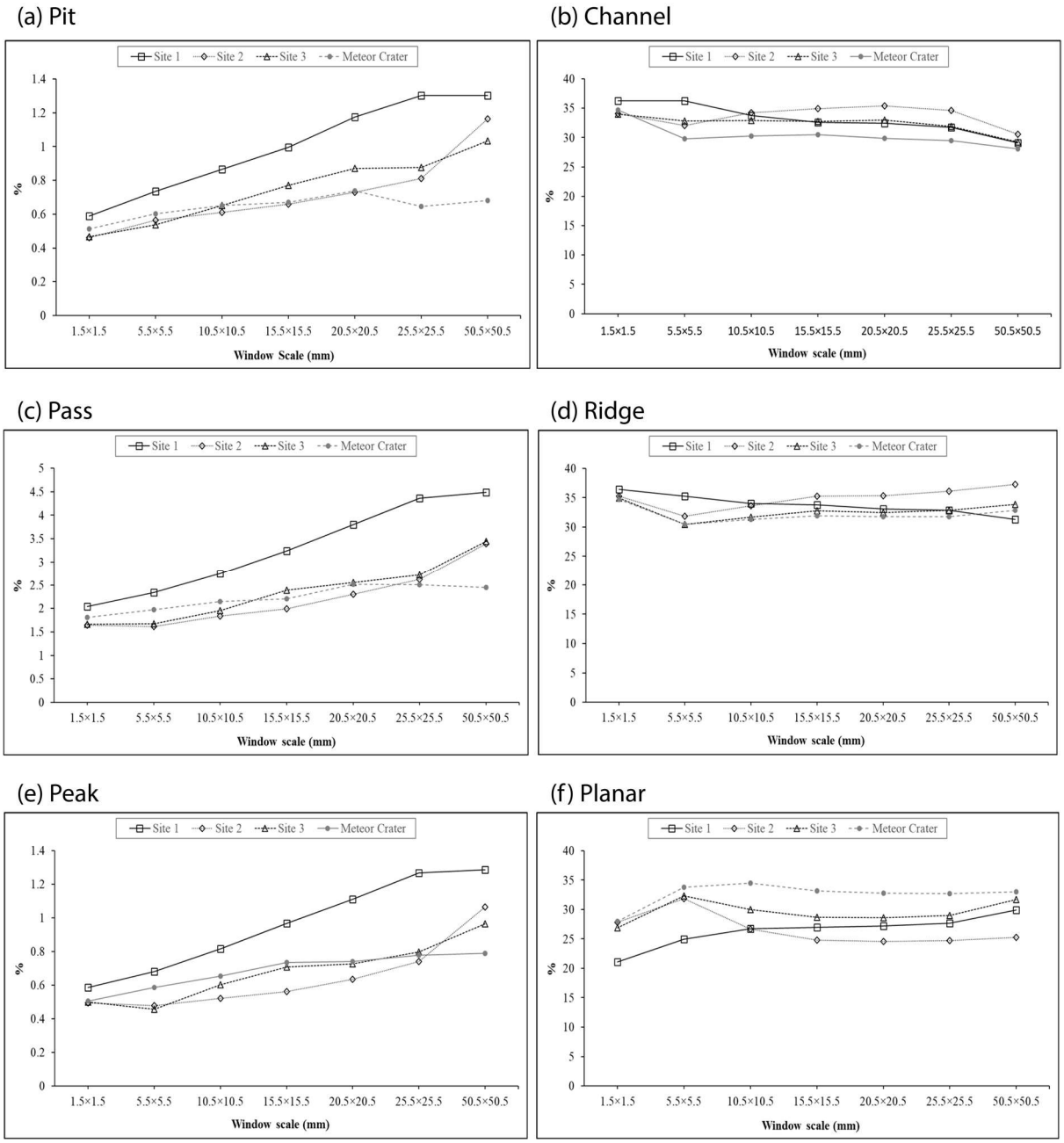


Fig 5.36. The plot of median values of area percent frequency of morphometric classes as a function of scale window size used. Note y-axes vary between plots. Classes are (a) pit, (b) channel, (c) pass, (d) ridge, (e) peak, and (f) planar.

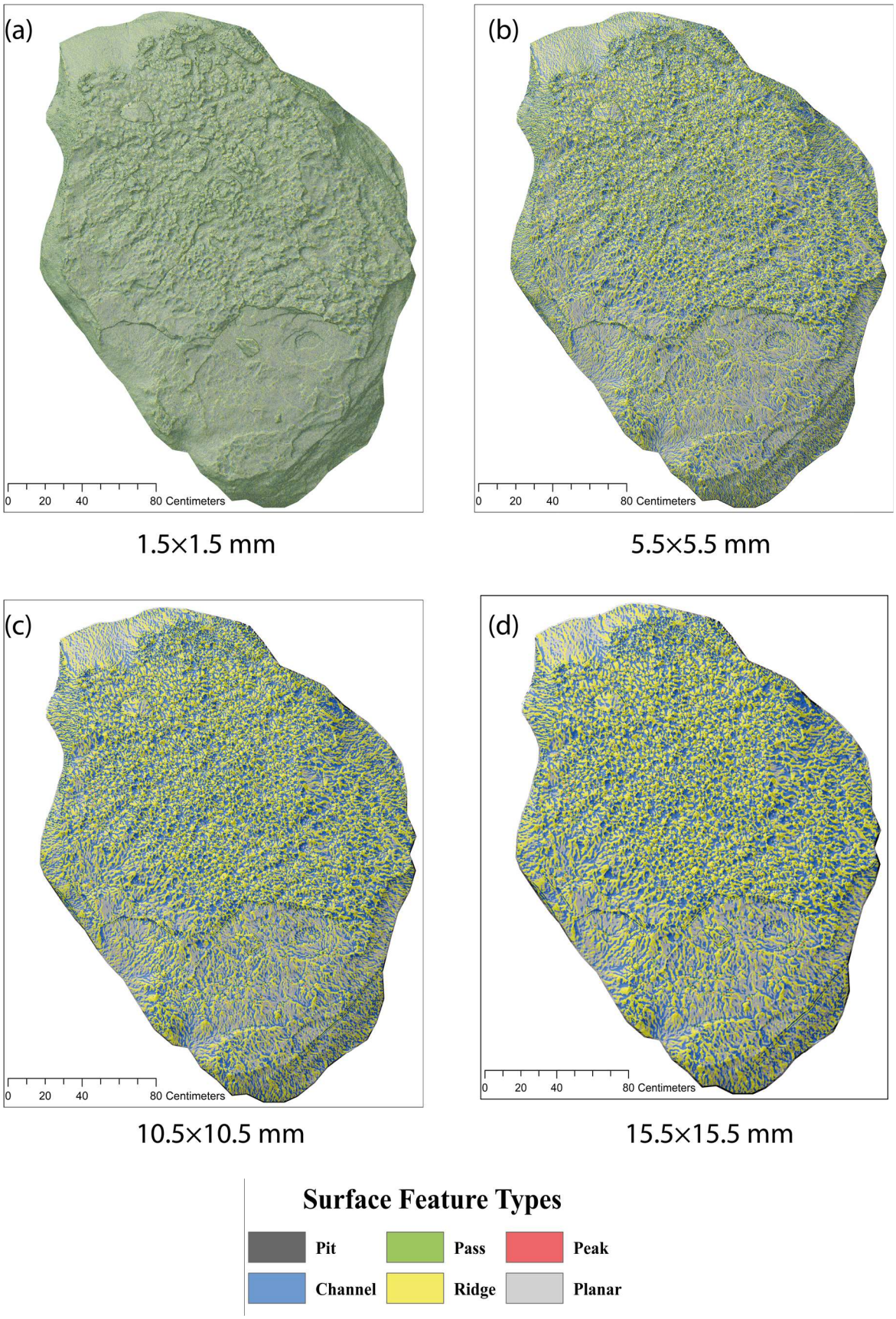


Fig 5.37. Morphometric feature classification output calculated at four moving window sizes for a boulder at Site 2 (Fig 5.23).

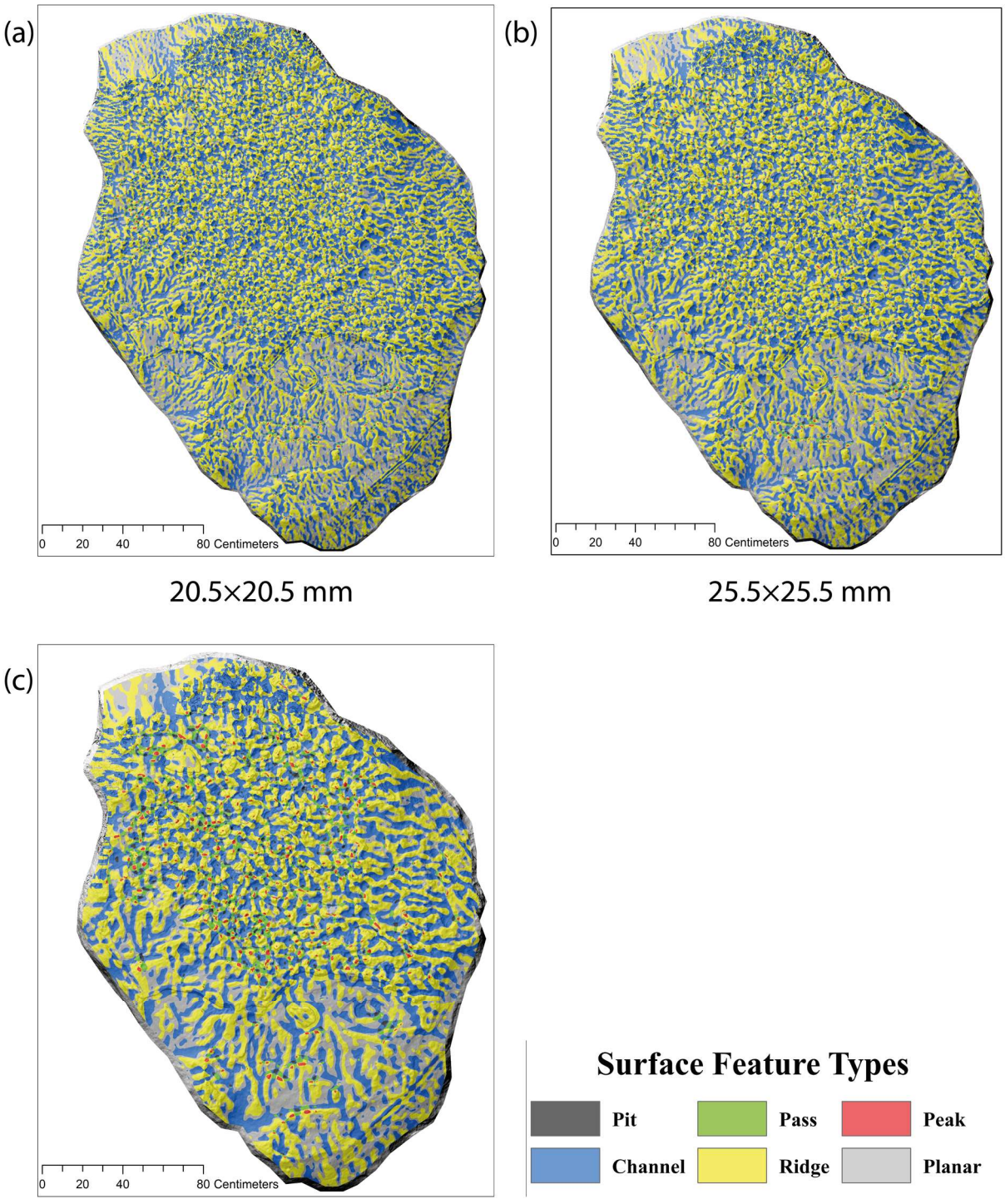


Fig 5.38. Morphometric feature classification output calculated at three moving window sizes for a boulder at Site 2 (Fig 5.23).

5.4.7. Effects of crater wall aspect on weathering

The effect of wall aspect on breakdown was explored at Meteor Crater. We compared SH rebound values, roughness parameters and morphometric feature classes between North facing (S crater wall), South facing (N crater wall), and SW facing (NE crater wall) outcrops. The results are presented in Tables 5.4 and 5.5.

We found a statistically significant difference in SH rebound value between S, SW and N facing outcrops at Meteor Crater. In terms of rock surface roughness, there was no statistically significant difference in Sq and Sz at any window scale between S, SW, and N facing outcrops at Meteor Crater. There was a statistically significant difference in Sdq at 5.5×5.5 - 50.5×50.5 mm window scale between S-SW and N facing outcrops. We find a difference in Sdq at 1.5×1.5 mm window scale between SW and N facing outcrops but no difference between S and N facing outcrops at Meteor Crater.

For VRM, we find statistical significance difference at 15.5×15.5 – 50.5×50.5 mm window scale between S-SW and N facing outcrops. At window scale 5.5×5.5 -10.5×10.5 mm, there was a significant difference between S and N facing outcrops but no difference between SW and N facing outcrops. At the lowest window scale 1.5×1.5 mm there was a significant difference between SW and N facing outcrops but no significant difference between S and N facing outcrops at Meteor Crater.

There was no statistically significant difference found in any of the roughness parameters at all window scale and SH rebound value between S and SW facing outcrops.

Table 5.4. Data for roughness analysis at Meteor Crater calculated at multiple window sizes. The values are mean standard (±standard deviation).

Moenkopi Sandstone at Meteor Crater			
	SW facing (NE crater wall)	**N facing (S crater wall)**	**S facing (N crater wall)**
SH rebound value	36.8±4.0	45.5±2.1	31.7±10.0
Sq (1.5×1.5 mm) mm	0.34±0.19	0.22±0.05	0.30±0.07
Sq (5.5×5.5 mm) mm	1.15±0.47	0.80±0.42	1.09±0.27
Sq (10.5×10.5 mm) mm	1.98±0.69	1.48±0.35	1.97±0.52
Sq (15.5×15.5 mm) mm	2.72±0.86	2.11±0.51	2.81±0.78
Sq (20.5×20.5mm) mm	3.41±1.02	2.73±0.67	3.61±1.04
Sq (25.5×25.5 mm) mm	4.07±1.18	3.31±0.82	4.38±1.30
Sq (50.5×50.5 mm) mm	7.06±1.97	5.97±1.54	7.89±2.52
Sdq (1.5×1.5 mm)	3.9±1.0°	2.8±0.5°	3.6±0.5°
Sdq (5.5×5.5 mm)	7.3±2.0°	5.1±0.6°	6.7±0.8±
Sdq (10.5×10.5 mm)	8.7±2.4°	6.0±0.6°	8.0±0.9°
Sdq (15.5×15.5 mm)	9.5±2.5°	6.5±0.6°	8.7±0.9°

Sdq (20.5×20.5mm)	9.9±2.6°	6.9±0.7°	9.2±1.0°
Sdq (25.5×25.5 mm)	10.2±2.6°	7.1±0.7°	9.6±1.0°
Sdq (50.5×50.5 mm)	11.1±2.4°	7.8±0.8°	10.7±1.0°
VRM (1.5×1.5 mm)	0.01±0.01	0	0.01±0
VRM (5.5×5.5 mm)	0.03±0.02	0.01±0	0.03±0.01
VRM (10.5×10.5 mm)	0.04±0.03	0.02±0.01	0.04±0.01
VRM (15.5×15.5 mm)	0.05±0.04	0.02±0.01	0.04±0.01
VRM (20.5×20.5mm)	0.05±0.04	0.02±0.01	0.05±0.01
VRM (25.5×25.5 mm)	0.06±0.04	0.03±0.01	0.05±0.01
VRM (50.5×50.5 mm)	0.06±0.04	0.03±0.01	0.06±0.01
Sz (1.5×1.5 mm) mm	1.04±0.53	0.67±0.15	0.93±0.22
Sz (5.5×5.5 mm) mm	4.53±1.86	3.21±0.72	4.33±1.06
Sz (10.5×10.5 mm) mm	8.31±3.0	6.23±1.41	8.30±2.08
Sz (15.5×15.5 mm) mm	11.8±3.99	9.15±2.08	12.1±3.09
Sz (20.5×20.5mm) mm	15.1±4.95	12.0±2.75	15.8±4.09
Sz (25.5×25.5 mm) mm	18.3±5.9	14.8±3.4	19.3±5.0
Sz (50.5×50.5 mm) mm	33.3±10.6	28.1±6.6	36.1±9.7

Percent morphometric feature classification revealed interesting results at different window scales. For pit at 5.5×5.5 mm and 20.5×20.5 mm, we find a significant difference between SW and N facing outcrops but no difference between S and N facing outcrops. For pass at 5.5×5.5, we find a significant difference between SW and N facing outcrops but no difference between S and N facing outcrops. For Ridge at 20.5×20.5 mm and 25.5×25.5 mm, we find a significant difference between SW and N facing outcrops but no difference between S and N facing outcrops.

We did not find any significant difference in terms of morphometric features at all window scale between S and SW facing outcrops.

Table 5.5. Data for area percent morphometric feature classification at Meteor Crater calculated at multiple window sizes. The are values are mean standard (±standard deviation).

Moenkopi Sandstone at Meteor Crater			
	SW facing	**N facing**	**S facing**
Pit (1.5×1.5 mm)	0.55±0.4%	0.96±0.41%	0.67±0.35
Pit (5.5×5.5 mm)	0.52±0.26%	1.14±0.52%	0.72±0.35%
Pit (10.5×10.5 mm)	0.57±0.29%	1.30±0.63%	0.77±0.40%
Pit (15.5×15.5 mm)	0.61±0.33%	1.36±0.69%	0.78±0.43%
Pit (20.5×20.5mm)	0.63±0.36%	1.39±0.68%	0.77±0.44%
Pit (25.5×25.5 mm)	0.66±0.41%	1.39±0.64%	0.77±0.47%
Pit (50.5×50.5 mm)	0.75±0.55%	1.44±0.54%	0.73±0.57%
Channel (1.5×1.5 mm)	35.38±2.79%	30.68±3.66%	34.37±2.04%
Channel (5.5×5.5 mm)	31.65±6.14%	28.84±2.51%	31.87±2.39%
Channel (10.5×10.5 mm)	32.45±6.46%	28.77±2.52%	31.30±2.42%
Channel (15.5×15.5 mm)	32.38±6.06%	28.43±2.41%	30.83±2.24%
Channel (20.5×20.5mm)	31.88±5.66%	28.13±2.34%	30.36±2.14%

Channel (25.5×25.5 mm)	31.43±5.25%	27.72±2.40%	30.08±2.02%
Channel (50.5×50.5 mm)	28.67±3.69%	26.12±2.73%	29.30±1.92%
Pass (1.5×1.5 mm)	1.89±1.12%	3.31±1.46%	2.34±1.20%
Pass (5.5×5.5 mm)	1.72±0.97%	3.82±1.89%	2.43±1.22%
Pass (10.5×10.5 mm)	1.85±1.02%	4.38±2.33%	2.55±1.33%
Pass (15.5×15.5 mm)	2.01±1.10%	4.65±2.58%	2.65±1.40%
Pass (20.5×20.5mm)	2.16±1.23%	4.81±2.61%	2.67±1.50%
Pass (25.5×25.5 mm)	2.32±1.38%	4.87±2.61%	2.66±1.50%
Pass (50.5×50.5 mm)	2.74±1.97%	4.99±2.33%	2.66±1.80%
Ridge (1.5×1.5 mm)	35.12±2.34%	30.78±3.66%	34.61±2.28%
Ridge (5.5×5.5 mm)	31.14±4.15%	28.99±2.64%	33.22±2.75%
Ridge (10.5×10.5 mm)	32.37±4.62%	29.27±2.45%	33.14±2.82%
Ridge (15.5×15.5 mm)	33.05±4.66%	29.23±2.21%	33.21±2.76%
Ridge (20.5×20.5mm)	33.49±4.45%	29.05±1.96%	33.40±2.76%
Ridge (25.5×25.5 mm)	33.61±4.13%	29.12±1.81%	33.46±2.92%
Ridge (50.5×50.5 mm)	34.67±3.23%	30.04±1.97%	34.56±4.02%
Peak (1.5×1.5 mm)	0.54±0.33%	0.97±0.42%	0.68±0.34%
Peak (5.5×5.5 mm)	0.54±0.27%	1.17±0.62%	0.76±0.37%
Peak (10.5×10.5 mm)	0.60±0.31%	1.32±0.78%	0.78±0.39%
Peak (15.5×15.5 mm)	0.65±0.34%	1.40±0.78%	0.80±0.40%
Peak (20.5×20.5mm)	0.69±0.39%	1.44±0.82%	0.81±0.40%
Peak (25.5×25.5 mm)	0.74±0.44%	1.50±0.83%	0.81±0.40%
Peak (50.5×50.5 mm)	0.90±0.59%	1.65±0.74%	0.85±0.54%
Planar (1.5×1.5 mm)	26.52±4.60%	33.30±8.91%	27.33±4.61%
Planar (5.5×5.5 mm)	34.44±9.75%	36.03±7.01%	31.0±5.21%
Planar (10.5×10.5 mm)	32.16±10.42%	34.96±7.14%	31.46±5.22%
Planar (15.5×15.5 mm)	31.31±10.20%	34.92±7.19%	31.74±4.89%
Planar (20.5×20.5mm)	31.14±9.74%	35.18±7.23%	32.0±4.66%
Planar (25.5×25.5 mm)	31.23±9.13%	35.40±7.32%	32.22±4.56%
Planar (50.5×50.5 mm)	32.26±5.78%	35.76±7.12%	31.89±5.01%

5.5. Discussion

5.5.1. Rock hardness, roughness and morphometric features

We found no significant difference in SH rebound value, roughness parameters, and morphometric geomorphic features at all seven window sizes between Meteor Crater and the control sites. Roughness analysis revealed that in general, the median of all roughness parameters increases with increase in window size and follow a linear trend. SH rebound value shows a weak negative correlation to surface roughness. McCarroll (1992) has demonstrated the importance of the rock surface roughness at the point of impact on controlling the SH rebound value. The smoother the outcrop surface roughness, the higher the SH rebound value due to the greater amount of surface contact made by the SH plunger tip.

Morphometric feature class abundance tends to show a relationship with rock surface roughness at all window scales. The smoother rock surfaces had a slightly higher percent area of planar, pit, peak, and pass features whereas rougher surfaces had a higher percent of

the ridge and channel features. The increased percentage of ridges on slightly rough outcrops at all window scales may be due to the sharp edges and sidewalls of mm to cm scale weathering features (e.g. alveoli, flaking, crumbling, pachydermal weathering). The higher roughness of the outcrops is related to channels and ridges because these morphometric features are related to weathering features where the material is lost, generating greater local differences in microtopography at mm-cm scale.

We find that surface roughness analysis and morphometric geomorphic feature classification provide a way to compare *in situ* rock surface textures in order to compare weathering in low shocked and unshocked Moenkopi Sandstone. Both roughness analysis and morphometric feature classification can be useful in assessing spatial and temporal rock breakdown processes.

We find that the direct DEM generation of in-situ rock surfaces for roughness analysis is advantageous over indirect DEM generation methods such as in the field used by Ehlmann et al. (2008b). Ehlmann et al. (2008b) used the molding and casting technique to capture microtopography of the rock surface in the field. They used plaster of paris to cast 15 × 15 cm weathered rock surface. The molds were bought back from the field and scanned using Konica Minolta VI-9i three-dimensional digitiser, and the 3D point cloud data obtained from scan was converted into DEMs. These techniques lead to an artificial reduction in absolute roughness (Bourke et al., 2008; Ehlmann et al., 2008b). A possible explanation for this smoothness of the cast is due to the failure in capturing mm scale breaks in slope and disturbance of the uppermost mm of the rock surface during applying and removing molds (Ehlmann et al., 2008b). Consequently, we do not recommend this approach for the comparison of rock outcrops at different field locations.

In addition, the sampling of smaller rock surface areas (<0.5m^2) for roughness analysis reduces the statistical significance. Smaller sampling area (<0.5m^2) on large outcrop facet may not represent the distribution of style of weathering features present on the entire facet. Smaller sampling areas will produce biased results when compared with entire rock facet sampling. In situ SfM DEM generation techniques can be used to produce sub-mm resolution microtopographic data of larger rock surface areas (up to 10 m^2) (Verma and Bourke, 2019) than the indirect DEM generation techniques which are limited to smaller areas (~225 cm^2) (Ehlmann et al., 2008b). We also find that the direct SfM DEM generation

technique is accurate and less time-consuming compared to the indirect technique (Ehlmann et al., 2008b; Verma and Bourke, 2019).

5.5.2. Recommendation of roughness parameters for breakdown feature analysis

Roughness parameters measure variation in local relief at the scale specified by the size of the neighbourhood window. At 1.5×1.5 mm window size generally, the roughness parameters for MS outcrops at Meteor Crater and the control site have generally similar values. At the smallest window scale, roughness parameters were only able to detect granular detachment and mm scale flaking but not cm scale features. As the window scale increases to 5.5×5.5 mm, the ability to detect cm-scale weathering increases as well. However, at highest window scale 50.5×50.5 mm, weathering features smaller than 2 cm in size (diameter/length) are smoothed out due to higher window scale and less likely to be detected by height-based roughness parameters (e.g. Sq and Sz).

All roughness parameters were normalised (normalised values = (raster value - raster min) / (raster max - raster min)) to dimensionless values ranging from 0 (smoothest) to 1 (roughest) so that their performance could be compared. Fig 5.40 shows the behaviour of roughness parameters at 10.5×10.5 mm window scale across a profile on a boulder from control site 2 (Fig 5.39).

Sq is a measure of height variability within the moving window (Leach, 2013). When the window size is similar to the weathering features slope length, Sq provides a measure of local relief. For much larger window sizes (50.5×50.5 mm), Sq measure the roughness of the landscape at that coarser scale (Gallant, 2000). With large window sizes, Sq identifies breaks of slope and could be used to detect regional relief. At fine resolutions and small window sizes, it remains good at identifying small features. The Sq parameter represents an overall measure of the texture comprising the surface. Sq parameter is insensitive in differentiating the nature of morphometric peaks, valleys, pits and the spacing of these morphometric features. Thus, Sq may be ambiguous in that many surfaces with extremely different spatial and height symmetry weathering features (e.g., micropitting vs alveoli) may have the same Sq value but have very different distribution on the rock surface.

The Sz parameter is similar to Sq in that it measures variation in local relief but has a disadvantage of sometimes changing abruptly as individual peaks and pits/valleys enter and leave the moving window (Leach, 2013). This can result in visible overlapping rectangular regions in the results at higher window scale (Fig 5.32 c) (Gallant, 2000).

Sz parameter has a very high positive correlation with Sq parameter (Table 5.6). The Sz parameters should be used with caution as it is sensitive to isolated peaks and pits/valleys which may not be significant. Also, Sz parameter is always successful in finding unusual conditions such as sharp edges, dips on the rock surface that may be indicative of a weathering feature.

Sdq is a general measurement of the slopes which encompass the surface and may be used to tell the difference in surfaces with similar Sq and Sz values roughness values. Sdq may find application for highly weathered rock surfaces, the surface containing similar looking morphometric features (e.g. micropitting and alveoli, multiple flakes and exfoliation) but with a very different distribution. Both the amplitude and spacing of weathering texture affects Sdq. Thus, for a given Sq and Sz, wider spaced weathering features may indicate a lower Sdq value than a rock surface with the same Sq and Sz, but finer spaced weathering features, as demonstrated in Fig 5.40. Sdq parameters have a moderate positive correlation between Sq and Sz parameters (Table 5.6).

VRM effectively captures variability in slope and aspect into a single measure and is less correlated with the slope (Sappington et al., 2007; Walbridge et al., 2018). VRM appears to decouple terrain ruggedness from slope better than current ruggedness indices, such as Terrain Ruggedness Index (TRI) or Land Surface Ruggedness Index (LSRI) (Sappington et al., 2007). VRM and Sdq parameters have a very high positive correlation (Table 5.6). Both VRM and Sdq are good at identifying fine-scale weathering features.

Sdq and VRM correctly identify steep, smooth slopes and areas of surface clutter (e.g., alveoli) while also identifying breaks of slope across different scales. In addition to the excellent performance at a variety of scales, both Sdq and VRM are simple to calculate in BTM toolbox (Walbridge et al., 2018), although any noise or error in the original DEM may be enhanced as they are calculated from height values (Grohmann et al., 2011).

Fig 5.40 demonstrates how different roughness parameter for the same surface (same scale) have different behaviour. At the places with little variation in microtopography Sq and Sz parameter are less effective compared to Sdq and VRM parameters. Nonetheless, once weathering features are visually identified, the Sq and Sz parameters may be used to indicate

significant deviations in the texture characteristics. In combination with Sdq or VRM parameters, Sq or Sz parameters can be useful in distinguishing different weathering features at a given scale.

Table 5.6. The matrix of correlation coefficients for all roughness parameters at multiple scales obtained using the Pearson correlation in R. The Pearson correlation coefficient (PCC) which describes the strength of the relationship and its sign, '-1' being the strongest negative relationship, '0' expressing no correlation and '1' representing the strongest positive relationship. The numerical value in brackets represents the window scale in mm.

Roughness Parameter	Sq (1.5)	Sq (5.5)	Sq (10.5)	Sq (15.5)	Sq (20.5)	Sq (25.5)	Sq (50.5)	Sdq (1.5)	Sdq (5.5)	Sdq (10.5)	Sdq (15.5)	Sdq (20.5)	Sdq (25.5)	Sdq (50.5)	VRM (1.5)	VRM (5.5)	VRM (10.5)	VRM (15.5)	VRM (20.5)	VRM (25.5)	VRM (50.5)	Sz (1.5)	Sz (5.5)	Sz (10.5)	Sz (15.5)	Sz (20.5)	Sz (25.5)	Sz (50.5)
Sq (1.5×1.5)	1.00																											
Sq (5.5×5.5)	0.99	1.00																										
Sq (10.5×10.5)	0.97	1.00	1.00																									
Sq (15.5×15.5)	0.95	0.98	1.00	1.00																								
Sq (20.5×20.5)	0.93	0.97	0.99	1.00	1.00																							
Sq (25.5×25.5)	0.91	0.96	0.98	0.99	1.00	1.00																						
Sq (50.5×50.5)	0.73	0.78	0.82	0.85	0.87	0.88	1.00																					
Sdq (1.5×1.5)	0.40	0.37	0.35	0.33	0.31	0.30	0.22	1.00																				
Sdq (5.5×5.5)	0.43	0.42	0.41	0.40	0.38	0.37	0.29	0.96	1.00																			
Sdq (10.5×10.5)	0.44	0.44	0.44	0.43	0.42	0.41	0.35	0.91	0.99	1.00																		
Sdq (15.5×15.5)	0.45	0.45	0.45	0.45	0.44	0.44	0.38	0.88	0.97	1.00	1.00																	
Sdq (20.5×20.5)	0.45	0.46	0.46	0.46	0.46	0.45	0.40	0.86	0.96	0.99	1.00	1.00																
Sdq (25.5×25.5)	0.45	0.46	0.47	0.47	0.47	0.46	0.42	0.84	0.95	0.99	1.00	1.00	1.00															
Sdq (50.5×50.5)	0.47	0.48	0.49	0.50	0.50	0.50	0.46	0.81	0.93	0.97	0.99	0.99	1.00	1.00														
VRM (1.5×1.5)	0.46	0.39	0.35	0.33	0.31	0.29	0.19	0.88	0.82	0.75	0.71	0.69	0.68	0.65	1.00													
VRM (5.5×5.5)	0.46	0.41	0.38	0.36	0.34	0.32	0.22	0.91	0.90	0.86	0.83	0.81	0.80	0.77	0.97	1.00												
VRM (10.5×10.5)	0.44	0.41	0.39	0.37	0.36	0.34	0.25	0.89	0.94	0.92	0.90	0.89	0.88	0.85	0.90	0.98	1.00											
VRM (15.5×15.5)	0.44	0.41	0.40	0.39	0.37	0.36	0.28	0.88	0.95	0.94	0.93	0.92	0.91	0.89	0.85	0.95	0.99	1.00										
VRM (20.5×20.5)	0.43	0.41	0.41	0.40	0.38	0.37	0.29	0.87	0.94	0.95	0.94	0.93	0.92	0.91	0.82	0.93	0.99	1.00	1.00									
VRM (25.5×25.5)	0.43	0.42	0.41	0.40	0.39	0.38	0.31	0.86	0.94	0.95	0.95	0.94	0.93	0.92	0.80	0.92	0.98	0.99	1.00	1.00								
VRM (50.5×50.5)	0.44	0.43	0.43	0.43	0.42	0.42	0.35	0.83	0.93	0.95	0.95	0.95	0.94	0.94	0.77	0.89	0.96	0.98	0.99	0.99	1.00							
Sz (1.5×1.5)	1.00	0.98	0.97	0.95	0.93	0.91	0.73	0.42	0.45	0.46	0.46	0.47	0.47	0.48	0.48	0.48	0.46	0.45	0.45	0.45	0.45	1.00						
Sz (5.5×5.5)	0.99	0.99	0.98	0.97	0.96	0.94	0.77	0.42	0.46	0.47	0.48	0.48	0.49	0.50	0.46	0.46	0.46	0.45	0.46	0.46	0.47	0.99	1.00					
Sz (10.5×10.5)	0.96	0.97	0.97	0.96	0.95	0.94	0.78	0.43	0.46	0.48	0.48	0.49	0.49	0.51	0.44	0.45	0.45	0.45	0.45	0.46	0.47	0.96	0.99	1.00				
Sz (15.5×15.5)	0.94	0.95	0.96	0.95	0.95	0.94	0.79	0.41	0.45	0.47	0.48	0.48	0.49	0.51	0.41	0.42	0.42	0.43	0.43	0.44	0.46	0.94	0.98	0.99	1.00			
Sz (20.5×20.5)	0.91	0.93	0.94	0.94	0.94	0.93	0.79	0.40	0.44	0.46	0.47	0.48	0.49	0.50	0.39	0.40	0.40	0.41	0.42	0.43	0.45	0.92	0.96	0.98	1.00	1.00		
Sz (25.5×25.5)	0.89	0.92	0.93	0.93	0.93	0.93	0.80	0.40	0.43	0.45	0.47	0.47	0.48	0.50	0.37	0.39	0.39	0.40	0.41	0.41	0.44	0.90	0.95	0.97	0.99	1.00	1.00	
Sz (50.5×50.5)	0.83	0.86	0.88	0.90	0.90	0.90	0.80	0.37	0.41	0.44	0.45	0.46	0.47	0.50	0.31	0.33	0.35	0.36	0.38	0.39	0.42	0.83	0.90	0.94	0.97	0.98	0.99	1.00



Fig 5.39. Location of profile extracted on the boulder surface to compare the behaviour of the roughness parameter along the same profile in relation to weathering features.

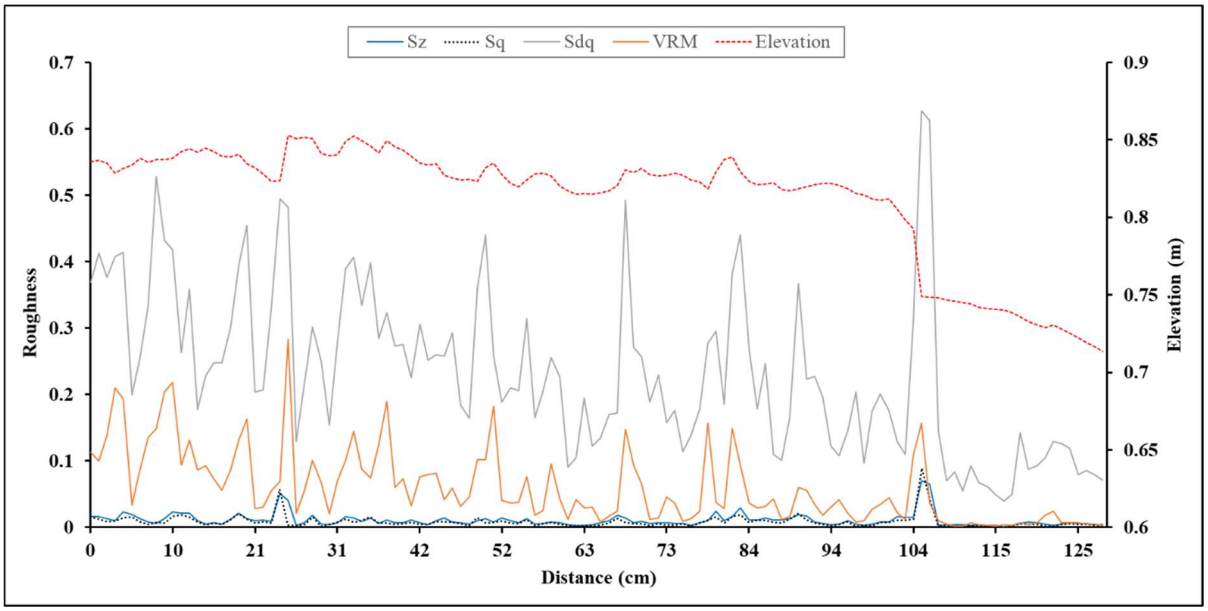


Fig 5.40. Morphometric profile for four roughness parameters across the weathering features on a boulder in Fig 5.39.

Based on our results, we recommend roughness parameters for suitable for detection of weathering features ranging mm-cm scale in Table 5.7.

Table 5.7. Roughness analysis recommendation at different scales for four groups of rock breakdown features: 1. Loss of rock material (LS), 2. Depositions (D), 3. Detachment of rock material (DT), and 4. Fissures/deformation (FD).

Roughness parameter	1.5×1.5 mm	5.5×5.5 mm	10.5×10.5 mm	15.5×15.5 mm	20.5×20.5 mm	25.5×25.5 mm	50.5×50.5 mm
Sq	D, DT	D, LS, DT	LS, DT	LS, DT	LS, DT	LS, DT	LS, DT
Sz	D, DT	D, LS, DT	LS, DT	LS, DT	LS, DT	LS, DT	LS, DT
Sdq	DT, FD	LS, DT, FD	LS, DT, FD	LS, DT, FD	LS, DT, FD	LS, DT, FD	LS, DT, FD
VRM	LS, DT	LS, DT, FD	LS, DT, FD	LS, DT, FD	LS, DT, FD	LS, DT, FD	LS, DT, FD

We recommend the use of a height roughness parameter (Sq, Sz) with Sdq or VRM. Based on our results and PCC matrix in Table 6.6, any combination of height parameter (Sq or Sz) with Sdq or VRM at 10.5, 25.5, and 50.5 mm window scale should be optimum for comparing weathering features observed at a similar scale to this study.

5.5.3. Effect of low shock on the breakdown of Moenkopi Sandstone

The petrophysical analysis of Moenkopi Sandstone revealed that it had undergone low shock damage. The porosity of low shocked Moenkopi Sandstone has been decreased by 88% compared to unshocked Moenkopi Sandstone. The pore throat size has been significantly decreased due to pore collapse. In low shocked MS macrofractures of aperture 4 to 200 μm are formed due to the passage of low-pressure shock waves (<5GPa).

Numerical models (Bryan et al., 1978; Roddy et al., 1980; Collins et al., 2004), laboratory experiments (Ai and Ahrens, 2004; Buhl et al., 2013a; Buhl et al., 2013b; Kowitz et al., 2013a; Kowitz et al., 2013b) geophysical surveys (Ackermann et al., 1975; Regan and Hinze, 1975; Pilon et al., 1991; Turolski, 2013) and field studies (Roddy et al., 1975; Kumar and Kring, 2008; Kring, 2017) at Meteor Crater support the idea of pervasive fracturing of target rocks in and around craters extending both radially as well as depth below the crater to a distance equal to half crater diameter. Preferential erosion has been observed along these fracture system and deformation zones in the crater walls (Kumar et al., 2010; Frattini et al., 2014). The impact related zones of weaknesses in the interior crater wall would have likely

played an important role in groundwater flow and discharge on the crater wall, causing enhanced and preferential erosion of fractured and fragmented rocks (Kumar et al., 2010).

In our physical weathering experiment on MS in environmental conditions similar to that found at Meteor Crater, it was found that the MS with macrofractures provides pathways for moisture and salt ingress (Chapter 3). The secondary porosity formed due to the fracturing of MS may be compensating for a decrease in primary porosity in low shocked MS. The macrofractures of the aperture of several micrometres extending up to several cms also provides a larger surface area for fluid migration than the reduced pore throats in low shock deformed MS in which original porosity is reduced due to pore collapse. The macrofratures in MS may be affecting the total permeability of Moenkopi Sandstone at Meteor Crater. The characterisation of permeability of MS at both Meteor Crater and control sites may help to understand this phenomenon. However, this in-depth investigation of permeability differences due to low shock deformation was beyond the scope of this study.

Field study revealed that there is no noticeable difference in nature of weathering between low shocked and unshocked Moenkopi Sandstone. However, we find that aspect related microclimate could be dominant control in subsequent weathering of low shocked Moenkopi Sandstone.

There was no statistically significant difference in terms of rock surface hardness, roughness and morphometric features in Moenkopi Sandstone between Meteor Crater and the control sites. Exposure duration of outcrops is a complex function of local topography (Viles, 2011; Viles, 2013a). At Meteor Crater, the inner crater wall where low shocked Moenkopi Sandstone were studied is quite steep, suggesting that these outcrops have probably been exposed for only short periods due to active mass wasting along the crater wall slope (Kumar et al., 2010; Palucis et al., 2011; Kring, 2017). It should be noted that the crater wall rocks and ejecta boulders on crater walls investigated in this study have been exposed much later than 50, 000 years. Nishiizumi et al. (1991) estimated ^{10}Be-^{26}Al exposure age of four crater wall rocks ranging from 15-24 ka. In another study, Phillips et al. (1991) ^{14}C dated rock varnish on Moenkopi Sandstone from NW crater wall (close to Moenkopi Sandstone on N crater wall in this study) and found it to be ~ 25, 000 years old. This suggests that present crater wall has been exposed, for only half of the age of crater itself, after crushed and fallout materials were eroded from crater wall. The exposure age of Moenkopi Sandstone at control sites are not precisely known.

In comparison, the local topography of the control sites has been more stable and static, exposing the rocks for extended periods (Norwick and Dexter, 2002). However, it can be assumed that their approximate age is older than 50, 000 years and no more than several hundred thousand years (Norwick and Dexter, 2002). Thus, the MS outcrops at the control sites have more time to undergo weathering. However, this has no noticeable effect on the nature of weathering features observed at Meteor Crater and control sites. A detailed cosmogenic exposure age dating of rock surfaces at the Meteor Crater and the control sites is required in future studies to explore this observation.

In addition to shock deformation, microclimate at the crater may have also played an important role in weathering at Meteor Crater. There was a lake formed on the crater floor immediately after the impact. The lake persisted for about ~40,000 years before disappearing ~11,000 years ago (Kring, 2017; Kring, 1997). The lake provided locally humid micro-climatic conditions and thus would have supplied more moisture within the crater than compared to the control sites (Grant and Schultz, 1990). Within the Meteor Crater, microclimate varies due to the aspect (Whiteman et al., 2007; Whiteman et al., 2008). Wetter conditions at Meteor Crater in the past due to the presence of the lake on crater floor would have contributed in a variation of moisture flux on the different side of crater walls. The precipitation and moisture distribution on the crater walls depend on the aspect and local topography inside the crater. This means rocks exposed on the different side of crater walls might have experienced different microclimatic conditions in the past, which would have resulted in the difference in the rate at which weathering processes operated locally. So, in addition to shock history, stress history due to past weathering is also crucial in this context of ongoing weathering at Meteor Crater. In order to understand stress history due to past weathering, the knowledge of exposure age of rocks is required. A detailed study of exposure ages of rocks is needed in future to understand the complex past weathering regime at Meteor Crater. In this study, we have focussed on contemporary microclimatic conditions to compare weathering at Meteor Crater and the control site. The results from this study suggest that microclimate is more important control in weathering of Moenkopi Sandstone than the low shock deformation.

In our physical weathering experiment, it was found that low shocked (<5 GPa) Coconino Sandstone show an accelerated change in strength compared to unshocked Coconino Sandstone (chapter 3). Enhanced breakdown of low shocked (<5GPa) and higher shocked (5-60 GPa) rocks and brecciated rocks at crater can explain several observations such as

differential erosion and degradation of impact craters on Earth and Mars (Pan and Ehlmann, 2018), lack or absence of higher shocked rocks on surface at older terrestrial craters (French, 1998; Osinski and Pierazzo, 2012), contradiction in the erosion rate estimated by researchers at Meteor Crater (Nishiizumi et al., 1991; Roddy et al., 1975; Roddy, 1978; Grant and Schultz, 1993b; Ramsey, 2002), lack of Coconino ejecta from E-W and N side of the Meteor Crater (Ramsey, 2002; Kring, 2017), wider and deeper alcoves in Coconino Sandstone compared to other rock formations at Meteor Crater (Kumar et al., 2010). However, in order to clearly explain these differences, a future investigation is required.

We propose a hypothesis that shock damage in rocks (0-60 GPa) combined with different microclimatic conditions causes enhancement in weathering at impact sites.

5.5.4. Effect of aspect on the breakdown of Moenkopi Sandstone

We found a significant difference in weathering between S-SW facing and N facing Moenkopi outcrops by analysing SH rebound value, roughness and morphometric geomorphic features. The S-SW facing outcrops (N-NE crater wall) have lower SH rebound value and higher roughness than N facing (S crater wall outcrops). This difference in weathering between S-SW facing and N facing outcrops on the crater wall can be attributed to aspect related microclimate.

Incoming solar insolation received from the sun is the primary energy source that drives rock surface temperature changes. Understanding solar insolation received by outcrops is key to understanding fundamental mechanical weathering processes (e.g. insolation weathering). Landscape scales and topographic variation are significant factors that determine the spatial variability of solar insolation. The difference in elevation, slope and aspect, terrain reflectance, surface albedo and shadows cast by crater walls all affect the amount of insolation received at different locations within the crater (Hoch et al., 2010). This inconsistency in insolation also varies with time of day and time of year that in turn contributes to variability of microclimate including factors such as air and rock surface temperature regimes, evapotranspiration, snowmelt patterns, soil moisture, and light and moisture availability for photosynthesis (lichen and plant growth) (Burnett et al., 2008).

Heating of rock due to solar radiation is dependent on slope, and aspect (Bland and Rolls, 1998b). The slope of the upper North crater wall is about 50-60° and is ~150 m higher than crater floor. The air temperature difference exceeds 15°C during winter in 165 m deep Meteor Crater (Whiteman et al., 2008). Upper north crater wall receives solar radiation for a maximum period due to shadow effect (Fig 5.15-5.17) (Whiteman et al., 2008). Leask and

Wilson (2003) suggested that rock surface temperature changes rapidly in a crater-like depression when the sun disappears behind or appears from behind nearby topography. Events like this create a difference between rock surface temperature and air temperature. The rapid change in rock surface temperature induces stresses in the outer layer of rock (Leask and Wilson, 2003; Smith et al., 2011) resulting in exfoliation, flaking or granular disintegration (Bourke and Viles, 2007). This is in agreement with the weathering features observed at N-NE crater wall sites.

In a study at Big Creek in central Idaho, Lifton et al. (2009) investigated the role of aspect on rock strength in a valley. They found a significant difference between the SH rebound values of the north and south facing sides of Big Creek. They found that the south-facing slope had lower SH rebound values than north-facing slopes of the valley. They suggested two explanation for this phenomenon: (i) during the summer, diurnal heating and cooling of rocks on south-facing slopes by solar radiation creates strong thermal gradients and enough stress to cause fracturing and (ii) during the winter, the south-facing slopes receive more solar radiation and therefore experience more freeze-thaw cycles than do the shaded north-facing slopes. Lifton et al. (2009) reported that north-facing slopes typically have more vegetative cover than south-facing slopes in the Big Creek valley, thus providing protective shading to the rock outcrops. We observed a similar phenomenon in this study at Meteor Crater, where S-SW facing Moenkopi Sandstone was more weathered than N facing Moenkopi. Similar to Big Creek, N facing slopes at Meteor Crater also have more vegetative cover due to the higher amount of moisture availability (Kring, 1997; Grant and Schultz, 1990). Similar observations were made in the hyper-arid Namib Desert and Antarctic dry valleys where lichen and vegetation presence were related microclimate (Miotke, 1980; Viles, 2005). The greater plant cover may retard the erosion on south crater walls (north facing). Burnett et al. (2008) also found that south-facing slopes in canyons in north-eastern Arizona receive more insolation resulting in generally warmer and drier conditions and are only moist for a few months in the winter when evapotranspiration is lowest and after the snowmelt episodes in spring. Contradictory to this, they found the north facing slope wetter and holding sufficient moisture throughout the year.

In contrast to this, Burnett et al. (2008) had observed the opposite of the rock strength phenomenon on sandstone in canyon slopes in N.E. Arizona than the Lifton et al. (2009) study and our observation at Meteor Crater. Their SH rebound data showed values on the north-facing slopes were lower than those on the south facing slopes of the valley. They

suggested that greater weathering and lower rock strength on north-facing slopes is consistent with a strong control of rock resistance to breakdown through hydration weathering since north facing slopes have lower insolation and more soil moisture retention. Accordingly, the proportion of cliff area is much higher, and non-cliff slopes are slightly steeper on south-facing slopes, where weathering is reduced, and rock strength is higher.

Tesson et al. (2017) investigated rockfalls on the young crater walls (<100 kyrs) on Mars. They mapped a total of 1584 recent rockfalls in 45 relatively fresh craters. Their finding suggests that mid-latitude craters have more numerous rockfalls on equator-facing slopes compared to pole-facing slopes. At equatorial latitudes, there are more rockfalls on N-S oriented slopes compared to E-W ones. They found that Northern mid-latitude (from 20°N to 40°N) south facing crater wall slopes are the ones where the temperature contrast is perceived to be at a maximum between night and day, and therefore where thermo-elastic stress is the strongest. This is in agreement with our solar insolation model for northern mid-latitude on Earth (at Meteor Crater). They concluded that rockfall in impact craters occur on the surface of Mars where thermal stress is the strongest whereas slopes, where water ice is expected, have fewer rockfall events. Therefore, thermo-elastic stress linked to high-temperature contrasts in diurnal cycles seems to play a much more significant role in rock breakdown than freeze/thaw cycles of water on modern Mars.

There is a difference in nature of weathering in Moenkopi Sandstone within Meteor Crater, which might be associated to aspect related microclimate differences; in contrast, it appears that low shock deformations in Moenkopi Sandstone are not major control in subsequent weathering.

5.6. Conclusion

This study is the first comprehensive field study that investigates the effect of low impact shock (<5GPa) on subsequent rock breakdown at Meteor Crater. Meteor Crater is one of the best preserved and youngest craters in semi-arid environmental conditions. Moenkopi Sandstone target at Meteor Crater was chosen to investigate the effect of low impact shock on the nature of breakdown. The low shocked Moenkopi Sandstone ejecta and crater wall rocks at Meteor Crater were compared with exposures of unshocked Moenkopi Sandstone at three control sites near Meteor Crater sharing similar climatic history. Rock hardness measurements and Structure from Motion (SfM) topographic data on Moenkopi outcrops

from each site were collected to compare the strength and nature of breakdown. SfM data was used to generate sub-mm resolution Digital Elevation Models (DEMs) of rock surfaces. These DEMs were analysed using areal surface roughness parameters, and morphometric classification parameters for windows of side length 1.5, 5.5, 10.5, 15.5, 20.5, 25.5, and 50.5 mm.

The major findings are summarised below.

1. Areal surface roughness parameters, Standard deviation of Height, Standard Deviation of Slope, Maximum height, for Moenkopi Sandstone reveal no statistical significance difference at all window scales between Meteor Crater and Control sites. In percent area of morphometric feature classes (pit, channel, pass, ridge, peak, and planar), at all the window scales, there were no significant differences between Meteor Crater and control sites. Vector Ruggedness Measure (VRM) show a significant difference at window scale of 1.5 mm between control sites (Site 1 and Site 2), however for rest of the window scales for VRM, there were no significant differences between the control sites and Meteor Crater. This suggests that there is no obvious difference in the nature of breakdown features between low shocked and unshocked Moenkopi Sandstone.
2. Rock hardness measurement reveals no statistically significant difference between Meteor Crater and control sites. This led to the conclusion that there is no statistically significant difference in rock hardness between low shocked Moenkopi at Meteor Crater and unshocked Moenkopi sandstone at control sites.
3. The approach of direct DEM generation of in-situ rock surfaces for roughness analysis and morphometric feature classification in this study is advantageous over indirect DEM generation methods in the field used in previous studies. Unlike, indirect DEM generation techniques, the SfM based DEM generation approach used in this study does not lead to an artificial reduction in absolute roughness. Our SfM DEM generation technique is accurate and less time-consuming compared to indirect technique and can be used to compare rock surface weathering at other sites to compare weathering in different lithologies and different environmental conditions.
4. Surface roughness is a useful tool for rock surface texture analysis due to weathering. Quantitative computation of surface roughness of rock surface provides valuable information for understanding rock breakdown features. Among the four common methods that were used to examine the surface roughness, the method of Sdq and

VRM roughness parameters are the most obvious in detecting a small break or sudden change in microrelief than height roughness parameters (Sq and Sz). We recommend using a height roughness parameter (Sq, Sz) with Sdq or VRM. For rock breakdown features survey at a similar scale as ours, any of the combination of height parameter (Sq or Sz) with Sdq or VRM at 10.5, 25.5, and 50.5 mm window scale should be optimum for studying breakdown features.

5. We found a statistically significant difference in terms of rock hardness, and most of the roughness and morphometric features at multiple scales between S-SW facing and N facing crater wall slopes. The SH rebound values are lower and roughness values are higher for S-SW facing slopes compared to N facing slopes. This could be related to the difference in aspect related microclimate. The S-SW facing crater slopes receive higher solar insolation than N facing slopes throughout the year.
6. Even though porosity has been reduced in low-shocked Moenkopi Sandstone at Meteor Crater, the fractures in the outcrops may have increased the permeability is responsible for the movement of salt and moisture. Fractures create conduits for salt and moisture ingress in low shocked Moenkopi Sandstone. The secondary porosity formed due to the fracturing may be compensating for a decrease in primary porosity in low shocked Moenkopi Sandstone. This indicates that low-shocked generated deformation combined with aspect related microclimatic variations are responsible for weathering of Moenkopi sandstone at Meteor Crater.

References

ACKERMANN, H., GODSON, R. & WATKINS, J. 1975. A seismic refraction technique used for subsurface investigations at Meteor Crater, Arizona. *Journal of Geophysical Research,* 80**,** 765-775.

AHRENS, T. J. & GREGSON, V. 1964. Shock compression of crustal rocks: Data for quartz, calcite, and plagioclase rocks. *Journal of Geophysical Research,* 69**,** 4839-4874.

AI, H. A. & AHRENS, T. J. 2004. Dynamic tensile strength of terrestrial rocks and application to impact cratering. *Meteoritics & Planetary Science,* 39**,** 233-246.

AYDIN, A. 2015. ISRM suggested method for determination of the Schmidt hammer rebound hardness: revised version. *The ISRM Suggested Methods for Rock Characterization, Testing and Monitoring: 2007-2014.* Springer.

BARRINGER, D. M. 1905. Coon Mountain and its crater. *Proceedings of the Academy of Natural Sciences of Philadelphia***,** 861-886.

BEDFORD, J. 2017. *Photogrammetric Applications for Cultural Heritage. Guidance for Good Practice*, Historic England.

BLACKWELDER, E. 1932. THE AGE OFMETEOR CRATER.

BLAND, W. & ROLLS, D. 1998a. Mechanical weathering processes. *Weathering: an introduction to the scientific principles.* Arnold, Hodder Headline, PLC.

BLAND, W. & ROLLS, D. 1998b. *Weathering: an introduction to the scientific principles*, Arnold, Hodder Headline, PLC.

BOSLOUGH, M. 1991. Shock modification and chemistry and planetary geologic processes. *Annual Review of Earth and Planetary Sciences,* 19**,** 101-130.

BOURKE, M., VILES, H., NICOLI, J., LYEW-AYEE, P., GHENT, R. & HOLMLUND, J. 2008. Innovative applications of laser scanning and rapid prototype printing to rock breakdown experiments. *Earth Surface Processes and Landforms,* 33**,** 1614-1621.

BOURKE, M. C. & VILES, H. A. 2007. *A photographic atlas of rock breakdown features in geomorphic environments*.

BRANDMEIER, M., KUHLEMANN, J., KRUMREI, I., KAPPLER, A., KUBIK, P. J. E. S. P. & LANDFORMS 2011. New challenges for tafoni research. A new approach to understand processes and weathering rates. 36**,** 839-852.

BRIDGES, N. & LAITY, J. Rock Abrasion and Ventifact Formation on Mars from Field Analog Theoretical and Experimental Studies. Field Trip and Workshop on the Martian Highlands and Mojave Desert Analogs, 2001. 13.

BRYAN, J., BURTON, D., CUNNINGHAM, M. & LETTIS JR, L. 1978. Two-dimensional computer simulation of hypervelocity impact cratering: some preliminary results for Meteor Crater, Arizona. California Univ.

BUHL, E., KOWITZ, A., ELBESHAUSEN, D., SOMMER, F., DRESEN, G., POELCHAU, M. H., REIMOLD, W. U., SCHMITT, R. T. & KENKMANN, T. 2013a. Particle size distribution and strain rate attenuation in hypervelocity impact and shock recovery experiments. *Journal of Structural Geology,* 56**,** 20-33.

BUHL, E., POELCHAU, M. H., DRESEN, G. & KENKMANN, T. 2013b. Deformation of dry and wet sandstone targets during hypervelocity impact experiments, as revealed from the MEMIN Program. *Meteoritics & Planetary Science,* 48**,** 71-86.

BURNETT, B. N., MEYER, G. A. & MCFADDEN, L. D. J. J. O. G. R. E. S. 2008. Aspect-related microclimatic influences on slope forms and processes, northeastern Arizona. 113.

CARDELL, C., BENAVENTE, D. & RODRÍGUEZ-GORDILLO, J. J. M. C. 2008. Weathering of limestone building material by mixed sulfate solutions. Characterization of stone microstructure, reaction products and decay forms. 59**,** 1371-1385.

CHAN, M. A., YONKEE, W. A., NETOFF, D. I., SEILER, W. M. & FORD, R. L. 2008. Polygonal cracks in bedrock on Earth and Mars: Implications for weathering. *Icarus,* 194**,** 65-71.

CHAO, E., FAHEY, J., LITTLER, J. & MILTON, D. 1962. Stishovite, SiO2, a very high pressure new mineral from Meteor Crater, Arizona. *Journal of Geophysical Research,* 67**,** 419-421.

CHAO, E. C., SHOEMAKER, E. M. & MADSEN, B. M. 1960. First natural occurrence of coesite. *Science,* 132**,** 220-222.

CHAPMAN, M. 2007. *The geology of Mars: evidence from earth-based analogs*, Cambridge University Press.

CHEN, J., BLUME, H.-P. & BEYER, L. J. C. 2000. Weathering of rocks induced by lichen colonization—a review. 39**,** 121-146.

CHEN, Y., CAO, P., MAO, D., PU, C. & FAN, X. 2014. Morphological analysis of sheared rock with water–rock interaction effect. *International Journal of Rock Mechanics and Mining Sciences,* 70**,** 264-272.

COCKELL, C. S. & OSINSKI, G. R. 2007. Impact-induced impoverishment and transformation of a sandstone habitat for lithophytic microorganisms. *Meteoritics & Planetary Science,* 42**,** 1985-1993.

COLLINS, G. S., MELOSH, H. J., IVANOV, B. A. J. M. & SCIENCE, P. 2004. Modeling damage and deformation in impact simulations. 39**,** 217-231.

COOKE, R. U., WARREN, A. & GOUDIE, A. S. 2006. *Desert geomorphology*, CRC Press.

CORNWALL, C., BANDFIELD, J. L., TITUS, T. N., SCHREIBER, B. & MONTGOMERY, D. 2015. Physical abrasion of mafic minerals and basalt grains: Application to martian aeolian deposits. *Icarus,* 256**,** 13-21.

DE KOCK, T., BOONE, M. A., DE SCHRYVER, T., VAN STAPPEN, J., DERLUYN, H., MASSCHAELE, B., DE SCHUTTER, G. & CNUDDE, V. 2015. A pore-scale study of fracture dynamics in rock using X-ray micro-CT under ambient freeze–thaw cycling. *Environmental science & technology,* 49**,** 2867-2874.

EHLMANN, B. L., VILES, H. A. & BOURKE, M. C. 2008. Quantitative morphologic analysis of boulder shape and surface texture to infer environmental history: A case study of rock breakdown at the Ephrata Fan, Channeled Scabland, Washington. *Journal of Geophysical Research: Earth Surface* 113.

FAURE, G. & MENSING, T. M. 2007. Meteorites and Impact Craters. *Introduction to Planetary Science.* Springer.

FAVALLI, M., FORNACIAI, A., ISOLA, I., TARQUINI, S. & NANNIPIERI, L. 2012. Multiview 3D reconstruction in geosciences. *Computers & Geosciences,* 44**,** 168-176.

FISHER, P., WOOD, J. & CHENG, T. 2004. Where is Helvellyn? Fuzziness of multi-scale landscape morphometry. *Transactions of the Institute of British Geographers,* 29**,** 106-128.

FITZNER, B., HEINRICHS, K. & LA BOUCHARDIERE, D. 2003. Weathering damage on Pharaonic sandstone monuments in Luxor-Egypt. *Building and Environment,* 38**,** 1089-1103.

FITZNER, B. & HEINRICHS, K. J. A.-U. C. G. 2001. Damage diagnosis at stone monuments-weathering forms, damage categories and damage indices. 12-13.

FOOTE, A. E. 1891. ART. XLIV.--A New Locality for Meteoric Iron with a Preliminary Notice of the Discovery of Diamonds in the Iron. *American Journal of Science (1880-1910),* 42**,** 413.

FRATTINI, P., CROSTA, G., DE BLASIO, F., CASTELLANZA, R., UTILI, S. & LUCAS, A. Crater Shock Damage Zone and Landslide Size Distribution in Valles Marineris, Mars. Lunar and Planetary Science Conference, 2014. 2024.

FRENCH, B. M. 1998. Traces of catastrophe: A handbook of shock-metamorphic effects in terrestrial meteorite impact structures. *Technical Report, LPI-Contrib-954*.

GALLANT, J. P. W. J. C. 2000. *Terrain analysis: principles and applications*, John Wiley & Sons.

GILBERT, G. K. 1896. The origin of hypotheses, illustrated by the discussion of a topographic problem. *Science,* 3**,** 1-13.

GILLET, P. & GORESY, A. E. 2013. Shock events in the solar system: the message from minerals in terrestrial planets and asteroids. *Annual Review of Earth and Planetary Sciences,* 41**,** 257-285.

GOLOMBEK, M., GRANT, J., CRUMPLER, L., GREELEY, R., ARVIDSON, R., BELL, J., WEITZ, C., SULLIVAN, R., CHRISTENSEN, P. & SODERBLOM, L. 2006. Erosion rates at the Mars Exploration Rover landing sites and long-term climate change on Mars. *Journal of Geophysical Research: Planets (1991–2012),* 111.

GOLOMBEK, M., WARNER, N., GANTI, V., LAMB, M., PARKER, T., FERGASON, R. & SULLIVAN, R. 2014. Small crater modification on Meridiani Planum and implications for erosion rates and climate change on Mars. *Journal of Geophysical Research: Planets,* 119**,** 2522-2547.

GOUDIE, A. 2004. *Encyclopedia of geomorphology*, Psychology Press.

GOUDIE, A., COOKE, R. & DOORNKAMP, J. 1979. Formation of silt from quartz dune sand by salt-weathering processes in deserts. *Journal of Arid Environments*.

GOUDIE, A. & PARKER, A. 1998. Experimental simulation of rapid rock block disintegration by sodium chloride in a foggy coastal desert. *Journal of Arid Environments,* 40**,** 347-355.

GOUDIE, A. & VILES, H. 2015. Weathering on the Namib Plains: Marble and Granite. *Landscapes and Landforms of Namibia.* Springer.

GOUDIE, A. S. & VILES, H. A. 2000. The thermal degradation of marble. *Acta Univ. Carol. Geogr.,* 35**,** 7-16.

GOUDIE, A. S., WRIGHT, E. & VILES, H. A. 2002. The roles of salt (sodium nitrate) and fog in weathering: a laboratory simulation of conditions in the northern Atacama Desert, Chile. *Catena,* 48**,** 255-266.

GOUDIE, A. S. J. E.-S. R. 2016. Quantification of rock control in geomorphology. 159**,** 374-387.

GRANT, J., ARVIDSON, R. E., CRUMPLER, L., GOLOMBEK, M. P., HAHN, B., HALDEMANN, A., LI, R., SODERBLOM, L., SQUYRES, S. W. & WRIGHT, S. 2006. Crater gradation in Gusev crater and Meridiani Planum, Mars. *Journal of Geophysical Research: Planets,* 111.

GRANT, J. & SCHULTZ, P. Amounts and styles of ejecta erosion at Meteor Crater, Arizona. Lunar and Planetary Science Conference, 1990.

GRANT, J. A. & SCHULTZ, P. H. 1993a. Degradation of selected terrestrial and Martian impact craters. *Journal of Geophysical Research: Planets (1991–2012),* 98**,** 11025-11042.

GRANT, J. A. & SCHULTZ, P. H. 1993b. Erosion of ejecta at Meteor Crater, Arizona. *Journal of Geophysical Research: Planets (1991–2012),* 98**,** 15033-15047.

GRANT, J. A., WILSON, S. A., COHEN, B. A., GOLOMBEK, M. P., GEISSLER, P. E., SULLIVAN, R. J., KIRK, R. L. & PARKER, T. J. 2008. Degradation of Victoria crater, Mars. *Journal of Geophysical Research: Planets,* 113.

GRIEVE, R. A. & THERRIAULT, A. M. 2013. Impactites: Their characteristics and spatial distribution. *Impact cratering: Processes and products***,** 90-105.

GROHMANN, C. H., SMITH, M. J., RICCOMINI, C. J. I. T. O. G. & SENSING, R. 2011. Multiscale analysis of topographic surface roughness in the Midland Valley, Scotland. 49**,** 1200-1213.

GROTZINGER, J. P., ARVIDSON, R., BELL, J., CALVIN, W., CLARK, B., FIKE, D., GOLOMBEK, M., GREELEY, R., HALDEMANN, A. & HERKENHOFF, K. 2005. Stratigraphy and sedimentology of a dry to wet eolian depositional system, Burns formation, Meridiani Planum, Mars. *Earth and Planetary Science Letters,* 240**,** 11-72.

GROTZINGER, J. P., CRISP, J. A. & VASAVADA, A. R. 2015. Curiosity's Mission of Exploration at Gale Crater, Mars. *Elements,* 11**,** 19-26.

GROTZINGER, J. P., SUMNER, D., KAH, L., STACK, K., GUPTA, S., EDGAR, L., RUBIN, D., LEWIS, K., SCHIEBER, J. & MANGOLD, N. 2014. A habitable fluvio-lacustrine environment at Yellowknife Bay, Gale Crater, Mars. *Science,* 343**,** 1242777.

HAUKEBØ, A. R. 2015. *Modelling of Marine Icing with Close Range Photogrammetry.* Masters thesis, UiT The Arctic University of Norway.

HAUSRATH, E. & BRANTLEY, S. 2010. Basalt and olivine dissolution under cold, salty, and acidic conditions: What can we learn about recent aqueous weathering on Mars? *Journal of Geophysical Research: Planets,* 115.

HAUSRATH, E. M., NAVARRE-SITCHLER, A. K., SAK, P. B., STEEFEL, C. I. & BRANTLEY, S. L. 2008. Basalt weathering rates on Earth and the duration of liquid water on the plains of Gusev Crater, Mars. *Geology,* 36**,** 67-70.

HESLOP, E. E. M. 2003. *Clast breakdown in the Atacama Desert, Chile :An intergrated field and laboratory approach.* D.Phil, University of Oxford.

HOCH, S. W., WHITEMAN, C. D. J. J. O. A. M. & CLIMATOLOGY 2010. Topographic effects on the surface radiation balance in and around Arizona's Meteor Crater. 49**,** 1114-1128.

ISRAELI, Y. & EMMANUEL, S. J. E. S. D. 2018. Impact of grain size and rock composition on simulated rock weathering. 6**,** 319-327.

IVES, P. C., LEVIN, B., ROBINSON, R. D. & RUBIN, M. 1964. US Geological Survey radiocarbon dates VII. *Radiocarbon,* 6**,** 37-76.

JIN, L., ROTHER, G., COLE, D. R., MILDNER, D. F., DUFFY, C. J. & BRANTLEY, S. L. J. A. M. 2011. Characterization of deep weathering and nanoporosity development in shale—A neutron study. 96**,** 498-512.

KAYE, J. 1963. Cosmogenic radioactivities in iron meteorites. *Carnegie Institute of Technology Progress Report 1962–1963***,** 62-77.

KENKMANN, T., POELCHAU, M. H. & WULF, G. 2014. Structural geology of impact craters. *Journal of Structural Geology,* 62**,** 156-182.

KIEFFER, S. W. 1971a. *I. Shock metamorphism of the Coconino sandstone at Meteor Crater, Arizona. II. The specific heat of solids of geophysical interest.* California Institute of Technology.

KIEFFER, S. W. 1971b. Shock Metamorphism of the Coconino Sandstone. *Journal of Geophysical Research*.

KIEFFER, S. W. 1975. From regolith to rock by shock. *The Moon,* 13**,** 301-320.

KIEFFER, S. W., PHAKEY, P. P. & CHRISTIE, J. M. 1976. Shock processes in porous quartzite: Transmission electron microscope observations and theory. *Contributions to Mineralogy and Petrology,* 59**,** 41-93.

KOMATSU, G., KUMAR, P. S., GOTO, K., SEKINE, Y., GIRI, C., MATSUI, T. J. P. & SCIENCE, S. 2014. Drainage systems of Lonar Crater, India: Contributions to Lonar Lake hydrology and crater degradation. 95**,** 45-55.

KOWITZ, A., GÜLDEMEISTER, N., REIMOLD, W., SCHMITT, R. & WÜNNEMANN, K. 2013a. Diaplectic quartz glass and SiO 2 melt experimentally generated at only 5 GPa shock pressure in porous sandstone: Laboratory observations and meso-scale numerical modeling. *Earth and Planetary Science Letters,* 384**,** 17-26.

KOWITZ, A., SCHMITT, R. T., UWE REIMOLD, W., HORNEMANN, U. J. M. & SCIENCE, P. 2013b. The first MEMIN shock recovery experiments at low shock pressure (5–12.5 GPa) with dry, porous sandstone. 48**,** 99-114.

KRING, D. Botanical Signature of Tectonic Fractures in the Target Rocks of Barringer Meteorite Crater, Arizona. Lunar and Planetary Science Conference, 2015. 1036.

KRING, D., BALCERSKI, J., BLAIR, D., CHOJNACKI, M., DONOHUE, P., DRUMMOND, S., GARBER, J., HOPKINS, M., HUBER, M. & JARET, S. Asymmetrical Distribution of Impact Ejected Lithologies at Barringer Meteorite Crater (aka Meteor Crater). Lunar and Planetary Science Conference, 2011. 1746.

KRING, D. A. 1997. Air blast produced by the Meteor Crater impact event and a reconstruction of the affected environment. *Meteoritics & Planetary Science,* 32**,** 517-530.

KRING, D. A. 2007. *Guidebook to the geology of barringer meteorite crater, arizona (aka Meteor Crater)*, Lunar and Planetary Institute Houston.

KRING, D. A. 2017. Guidebook to the geology of Barringer Meteorite Crater, Arizona (aka Meteor Crater): for the 80th Annual Meeting of the Meteoritical Society July 2017. Lunar and Planetary Institute.

KUMAR, P. S., HEAD, J. W. & KRING, D. A. 2010. Erosional modification and gully formation at Meteor Crater, Arizona: Insights into crater degradation processes on Mars. *Icarus,* 208**,** 608-620.

KUMAR, P. S. & KRING, D. A. 2008. Impact fracturing and structural modification of sedimentary rocks at Meteor Crater, Arizona. *Journal of Geophysical Research: Planets (1991–2012),* 113.

LABUS, M. & BOCHEN, J. 2012. Sandstone degradation: an experimental study of accelerated weathering. *Environmental Earth Sciences,* 67**,** 2027-2042.

LAI, P., SAMSON, C. & BOSE, P. 2014. Surface roughness of rock faces through the curvature of triangulated meshes. *Computers & Geosciences,* 70**,** 229-237.

LAITY, J., BRIDGES, N. & BOYLE, T. Ventifact Formation in the Mojave Desert: Field Analogs for Martian Processes. Field Trip and Workshop on the Martian Highlands and Mojave Desert Analogs, 2001. 4004.

LAITY, J. E. 1995. Wind abrasion and ventifact formation in California. *Desert aeolian processes.* Springer.

LAITY, J. E. 2009a. Landforms, landscapes, and processes of aeolian erosion. *Geomorphology of Desert Environments.* Springer.

LAITY, J. E. 2011. Wind erosion in drylands. *Arid Zone Geomorphology: Process, Form and Change in Drylands, Third Edition***,** 539-568.

LAITY, J. E. & BRIDGES, N. T. 2009. Ventifacts on Earth and Mars: Analytical, field, and laboratory studies supporting sand abrasion and windward feature development. *Geomorphology,* 105**,** 202-217.

LAITY, J. J. 2009b. *Deserts and desert environments*, John Wiley & Sons.

LEACH, R. 2013. *Characterisation of areal surface texture*, Springer.

LEASK, H. & WILSON, L. Heating and cooling of rocks on Mars: consequences for weathering. Lunar and Planetary Science Conference, 2003. 1320.

LEHNER, M., WHITEMAN, C. D., HOCH, S. W., CROSMAN, E. T., JEGLUM, M. E., CHERUKURU, N. W., CALHOUN, R., ADLER, B., KALTHOFF, N. & ROTUNNO, R. J. B. O. T. A. M. S. 2016. The METCRAX II field experiment: A study of downslope windstorm-type flows in Arizona's Meteor Crater. 97**,** 217-235.

LIFTON, Z. M., THACKRAY, G. D., VAN KIRK, R. & GLENN, N. F. J. G. 2009. Influence of rock strength on the valley morphometry of Big Creek, central Idaho, USA. 111**,** 173-181.

MADDEN, M. E. E., KRING, D. A. & BODNAR, R. J. 2006. Shock reequilibration of fluid inclusions in Coconino sandstone from Meteor Crater, Arizona. *Earth and Planetary Science Letters,* 241**,** 32-46.

MASAITIS, V. 2006. Review of the Barringer crater studies and views on the crater's origin. *Solar System Research,* 40**,** 500-512.

MCCARROLL, D. 1992. A new instrument and techniques for the field measurement of rock surface roughness. *Zeitschrift fur Geomorphologie,* 36**,** 69-79.

MCKAY, C. P., MOLARO, J. L. & MARINOVA, M. M. 2009. High-frequency rock temperature data from hyper-arid desert environments in the Atacama and the Antarctic Dry Valleys and implications for rock weathering. *Geomorphology,* 110**,** 182-187.

MCKINLEY, J. & WARKE, P. J. G. S., LONDON, SPECIAL PUBLICATIONS 2007. Controls on permeability: implications for stone weathering. 271**,** 225-236.

MEDAPATI, R. S., KREIDL, O. P., MACLAUGHLIN, M., HUDYMA, N. & HARRIS, A. Quantifying surface roughness of weathered rock-examples from granite and limestone. Geo-Congress 2013: Stability and Performance of Slopes and Embankments III, 2013. 120-128.

MELOSH, H. & COLLINS, G. 2005. Planetary science: Meteor Crater formed by low-velocity impact. *Nature,* 434**,** 157.

MELOSH, H. J. 1989. Impact cratering: A geologic process. *Research supported by NASA. New York, Oxford University Press (Oxford Monographs on Geology and Geophysics, No. 11), 1989, 253 p.,* 1.

MIOTKE, F. 1980. Microclimate and weathering processes in the area of Darwin Mountains and Bull Pass, Dry Valleys. *Antarctic Journal of the United States,* 15**,** 14-16.

MOL, L. & VILES, H. A. 2012. The role of rock surface hardness and internal moisture in tafoni development in sandstone. *Earth Surface Processes and Landforms,* 37**,** 301-314.

MOSBRUCKER, A. R., MAJOR, J. J., SPICER, K. R. & PITLICK, J. 2017. Camera system considerations for geomorphic applications of SfM photogrammetry. *Earth Surface Processes and Landforms,* 42**,** 969-986.

MOSES, C., ROBINSON, D. & BARLOW, J. 2014. Methods for measuring rock surface weathering and erosion: a critical review. *Earth-Science Reviews,* 135**,** 141-161.

MOTTERSHEAD, D. 1994. *Spatial variations in intensity of alveolar weathering of a dated sandstone structure in a coastal environment, Weston-super-Mare, UK*, John Wiley & Sons: Chichester.

MUSTOE, G. 1982. The origin of honeycomb weathering. *Geological Society of America Bulletin,* 93**,** 108-115.

NAVARRE-SITCHLER, A. K., COLE, D. R., ROTHER, G., JIN, L., BUSS, H. L. & BRANTLEY, S. L. J. G. E. C. A. 2013. Porosity and surface area evolution during weathering of two igneous rocks. 109**,** 400-413.

NEWSOM, H. E., MANGOLD, N., KAH, L. C., WILLIAMS, J. M., ARVIDSON, R. E., STEIN, N., OLLILA, A. M., BRIDGES, J. C., SCHWENZER, S. P. & KING, P. L. 2014. Gale crater and impact processes–Curiosity's first 364 Sols on Mars. *Icarus*.

NEWSOM, H. E., WRIGHT, S. P., MISRA, S. & HAGERTY, J. J. 2013. Comparison of simple impact craters: A case study of Meteor and Lonar Craters. *Impact Cratering: Processes and Products***,** 271-289.

NICHOLSON, D. T. J. G. 2008. Rock control on microweathering of bedrock surfaces in a periglacial environment. 101**,** 655-665.

NISHIIZUMI, K., KOHL, C., SHOEMAKER, E., ARNOLD, J., KLEIN, J., FINK, D. & MIDDLETON, R. 1991. In situ 10 Be-26 Al exposure ages at meteor Crater, Arizona. *Geochimica et Cosmochimica Acta,* 55**,** 2699-2703.

NORWICK, S. A. & DEXTER, L. R. 2002. Rates of development of tafoni in the Moenkopi and Kaibab formations in Meteor Crater and on the Colorado Plateau, northeastern Arizona. *Earth Surface Processes and Landforms,* 27**,** 11-26.

OLLIER, C. & PAIN, C. 1996. *Regolith, soils and landforms*, John Wiley & Sons.

OSINSKI, G. R. & PIERAZZO, E. 2012. *Impact cratering: Processes and products*, John Wiley & Sons.

PALUCIS, M. & MCENULTY, T. J. N. R. 2010. Meteor Crater, AZ: A terrestrial analog to study gully formation on Mars. 10**,** G9V40S4C.

PALUCIS, M. C., DIETRICH, W. E. & HOWARD, A. 2011. The role of debris flows in the origin and evolution of gully systems on crater walls: Martian analogs in Meteor Crater, Arizona (USA). *Italian Journal of Engineering and Environment*.

PAN, L. & EHLMANN, B. L. J. J. O. G. R. P. 2018. Aqueous Processes from Diverse Hydrous Minerals in the Vicinity of Amazonian-Aged Lyot Crater.

PEL, L., HUININK, H., KOPINGA, K., VAN HEES, R., ADAN, O. J. C. & MATERIALS, B. 2004. Efflorescence pathway diagram: understanding salt weathering. 18**,** 309-313.

PHILLIPS, F. M., ZREDA, M. G., SMITH, S. S., ELMORE, D., KUBIK, P. W., DORN, R. I. & RODDY, D. J. 1991. Age and geomorphic history of Meteor Crater, Arizona, from cosmogenic 36 Cl and 14 C in rock varnish. *Geochimica et Cosmochimica Acta,* 55**,** 2695-2698.

PILON, J., GRIEVE, R. & SHARPTON, V. 1991. The subsurface character of Meteor Crater, Arizona, as determined by ground-probing radar. *Journal of Geophysical Research: Planets,* 96**,** 15563-15576.

POELCHAU, M. H., KENKMANN, T. & KRING, D. A. 2009. Rim uplift and crater shape in Meteor Crater: Effects of target heterogeneities and trajectory obliquity. *Journal of Geophysical Research: Planets,* 114.

RAE, A., COLLINS, G., GRIEVE, R., OSINSKI, G. & MORGAN, J. 2017. Complex crater formation: Insights from combining observations of shock pressure distribution with numerical models at the West Clearwater Lake impact structure. *Meteoritics & Planetary Science,* 52**,** 1330-1350.

RAMSEY, M. S. J. J. O. G. R. P. 2002. Ejecta distribution patterns at Meteor Crater, Arizona: On the applicability of lithologic end-member deconvolution for spaceborne thermal infrared data of Earth and Mars. 107.

REGAN, R. D. & HINZE, W. J. J. J. O. G. R. 1975. Gravity and magnetic investigations of Meteor Crater, Arizona. 80**,** 776-788.

RODDY, D., BOYCE, J., COLTON, G. & DIAL JR, A. Meteor Crater, Arizona, rim drilling with thickness, structural uplift, diameter, depth, volume, and mass-balance calculations. Lunar and Planetary Science Conference Proceedings, 1975. 2621-2644.

RODDY, D. J. Pre-impact geologic conditions, physical properties, energy calculations, meteorite and initial crater dimensions and orientations of joints, faults and walls at Meteor Crater, Arizona. Lunar and Planetary Science Conference, 9 th, Houston, Tex, 1978. 3891-3930.

RODDY, D. J., SCHUSTER, S. H., KREYENHAGEN, K. N. & ORPHAL, D. L. Computer code simulations of the formation of Meteor Crater, Arizona-Calculations MC-1 and MC-2. Lunar and Planetary Science Conference Proceedings, 1980. 2275-2308.

RODRIGUEZ-NAVARRO, C., DOEHNE, E. & SEBASTIAN, E. 1999. Origins of honeycomb weathering: the role of salts and wind. *Geological Society of America Bulletin,* 111**,** 1250-1255.

ROSA, D. F. 2012. *The sheet of impact melt at West Clearwater Lake, Northern Quebec*, McGill University (Canada).

S.J. REYNOLDS, F. P. F., J. W. WELTY, M. S. RODDY, D. A. CURRIER, A. V. ANDERSON, AND S. B. KEITH. 1986. Compilation of radiometric age determinations in Arizona. *Arizona Burau of Geologis and Mineral Technology Bulletin*.

SAPPINGTON, J. M., LONGSHORE, K. M. & THOMPSON, D. B. J. T. J. O. W. M. 2007. Quantifying landscape ruggedness for animal habitat analysis: a case study using bighorn sheep in the Mojave Desert. 71**,** 1419-1426.

SAUSSE, J., JACQUOT, E., FRITZ, B., LEROY, J. & LESPINASSE, M. J. T. 2001. Evolution of crack permeability during fluid–rock interaction. Example of the Brezouard granite (Vosges, France). 336**,** 199-214.

SEE, T. H., HÖRZ, F., MITTLEFEHLDT, D. W., VARLEY, L., MERTZMAN, S. & RODDY, D. 2002. Major Element Analysis of the Target Rocks at Meteor Crater, Arizona.

SHARMA, V. K. 2010. *Introduction to process geomorphology*, CRC Press.

SHIPMAN, F., GREGSON, V. & JONES, A. 1971. *A shock wave study of Coconino Sandstone*, National Aeronautics and Space Administration.

SHOEMAKER, E. M. 1959. Impact mechanics at Meteor crater, Arizona. US Geological Survey].

SHOEMAKER, E. M. 1960. Penetration mechanics of high velocity meteorites, illustrated by Meteor Crater, Arizona. *Meteorite Craters, Benchmark Papers in Geology,* 1**,** 170.

SHOEMAKER, E. M. 1987. Meteor Crater, Arizona. *Geological Society of America, Centennial Field Guide,* 2**,** 399-404.

SHOEMAKER, E. M. & KIEFFER, S. W. 1979. *Guidebook to the geology of Meteor Crater, Arizona*, Center for Meteorite Studies, Arizona State University.

SINGLETON, A. C., OSINSKI, G. R., MCCAUSLAND, P. J. & MOSER, D. E. 2011. Shock-induced changes in density and porosity in shock-metamorphosed crystalline

rocks, Haughton impact structure, Canada. *Meteoritics & Planetary Science,* 46**,** 1774-1786.

SMITH, B., SRINIVASAN, S., GOMEZ-HERAS, M., BASHEER, P. & VILES, H. 2011. Near-surface temperature cycling of stone and its implications for scales of surface deterioration. *Geomorphology,* 130**,** 76-82.

SMITH, B., WARKE, P., MCGREEVY, J. & KANE, H. 2005. Salt-weathering simulations under hot desert conditions: agents of enlightenment or perpetuators of preconceptions? *Geomorphology,* 67**,** 211-227.

SMITH, B., WARKE, P. & MOSES, C. 2000. Limestone weathering in contemporary arid environments: a case study from southern Tunisia. *Earth Surface Processes and Landforms,* 25**,** 1343-1354.

SMITH, M., CARRIVICK, J. & QUINCEY, D. 2016. Structure from motion photogrammetry in physical geography. *Progress in Physical Geography,* 40**,** 247-275.

STACK, K., GROTZINGER, J., GUPTA, S., KAH, L., LEWIS, K., MCBRIDE, M., MINITTI, M., RUBIN, D., SCHIEBER, J. & SUMNER, D. Sedimentology and Stratigraphy of the Pahrump Hills Outcrop, Lower Mount Sharp, Gale Crater, Mars. Lunar and Planetary Science Conference, 2015. 1994.

SUTTON, S. 1985. Thermoluminescence measurements on shock-metamorphosed sandstone and dolomite from Meteor Crater, Arizona: 2. Thermoluminescence age of meteor crater. *Journal of Geophysical Research: Solid Earth,* 90**,** 3690-3700.

TAYLOR, G. & EGGLETON, R. A. 2001. *Regolith geology and geomorphology*, John Wiley & Sons.

TESSON, P.-A., CONWAY, S. & MANGOLD, N. 2017. Role of thermo-elastic stress on rockfall triggering in martian impact craters. *9th International Conference on Geomorphology.* New Delhi, India.

THOMAS, M., CLARKE, J. & PAIN, C. 2005. Weathering, erosion and landscape processes on Mars identified from recent rover imagery, and possible Earth analogues. *Aust. J. Earth Sci.,* 52**,** 365-378.

THORNBUSH, M. J. 2012. A site-specific index based on weathering forms visible in Central Oxford, UK. *Geosciences,* 2**,** 277-297.

TILGHMAN, B. C. 1905. Coon Butte, Arizona. *Proceedings of the Academy of Natural Sciences of Philadelphia***,** 887-914.

TREIMAN, A. H., BISH, D. L., VANIMAN, D. T., CHIPERA, S. J., BLAKE, D. F., MING, D. W., MORRIS, R. V., BRISTOW, T. F., MORRISON, S. M. & BAKER, M. B. 2015. Mineralogy, Provenance, and Diagenesis of a Potassic Basaltic Sandstone on Mars: CheMin X-ray Diffraction of the Windjana Sample (Kimberley Area, Gale Crater). *Journal of Geophysical Research: Planets*.

TUĞRUL, A. 2004. The effect of weathering on pore geometry and compressive strength of selected rock types from Turkey. *Engineering Geology,* 75**,** 215-227.

TURKINGTON, A. 1998. Cavernous weathering in sandstone: lessons to be learned from natural exposure. *Quarterly Journal of Engineering Geology and Hydrogeology,* 31**,** 375-383.

TURKINGTON, A. V. & PARADISE, T. R. 2005. Sandstone weathering: a century of research and innovation. *Geomorphology,* 67**,** 229-253.

TUROLSKI, A. 2013. *Near-surface geophysical imaging of complex structures: Meteor Crater, AZ and Jemez Pueblo, NM.*

VERMA, A. K. & BOURKE, M. C. 2019. A method based on structure-from-motion photogrammetry to generate sub-millimetre-resolution digital elevation models for investigating rock breakdown features. *Earth Surf. Dynam.,* 7**,** 45-66.

VILES, H. 2011. Weathering systems. *In:* THOMAS, D. S. (ed.) *Arid zone geomorphology: process, form and change in drylands.* III ed.: John Wiley & Sons.

VILES, H., EHLMANN, B., WILSON, C. F., CEBULA, T., PAGE, M. & BOURKE, M. 2010. Simulating weathering of basalt on Mars and Earth by thermal cycling. *Geophys. Res. Lett.,* 37**,** L18201.

VILES, H. & GOUDIE, A. 2007. Rapid salt weathering in the coastal Namib desert: implications for landscape development. *Geomorphology,* 85**,** 49-62.

VILES, H., GOUDIE, A., GRAB, S. & LALLEY, J. 2011. The use of the Schmidt Hammer and Equotip for rock hardness assessment in geomorphology and heritage science: a comparative analysis. *Earth Surface Processes and Landforms,* 36**,** 320-333.

VILES, H., MESSENZEHL, K., MAYAUD, J., COOMBES, M. & BOURKE, M. 2018. Stress histories control rock-breakdown trajectories in arid environments. *Geology,* 46**,** 419-422.

VILES, H. A. 2001. Scale issues in weathering studies. *Geomorphology,* 41**,** 63-72.

VILES, H. A. 2005. Microclimate and weathering in the central Namib Desert, Namibia. *Geomorphology,* 67**,** 189-209.

VILES, H. A. 2013a. Linking weathering and rock slope instability: non-linear perspectives. *Earth Surface Processes and Landforms,* 38**,** 62-70.

VILES, H. A. 2013b. Synergistic Weathering Processes *In:* SHRODER, J. F. (ed.) *Treatise on Geomorphology.* San Diego: Academic Press.

WALBRIDGE, S., SLOCUM, N., POBUDA, M. & WRIGHT, D. J. J. G. 2018. Unified geomorphological analysis workflows with benthic terrain modeler. 8**,** 94.

WARKE, P. 2007. Complex weathering in drylands: implications of 'stress' history for rock debris breakdown and sediment release. *Geomorphology,* 85**,** 30-48.

WARKE, P. 2013. 4.12 Weathering in Arid Regions.

WATKINS, J. & WALTERS, L. 1966. Laboratory physical property measurements on core and surface samples from six lunar analog test sites. *Investigations of in situ physical properties of surface and subsurface site materials by engineering geophysical techniques, annual report, fiscal year***,** 259-267.

WELLS, T., HANCOCK, G. & FRYER, J. J. E. G. 2008. Weathering rates of sandstone in a semi-arid environment (Hunter Valley, Australia). 54**,** 1047-1057.

WESTOBY, M., BRASINGTON, J., GLASSER, N., HAMBREY, M. & REYNOLDS, J. 2012. 'Structure-from-Motion'photogrammetry: A low-cost, effective tool for geoscience applications. *Geomorphology,* 179**,** 300-314.

WHITE, K., BRYANT, R. & DRAKE, N. 1998. Techniques for measuring rock weathering: application to a dated fan segment sequence in southern Tunisia. *Earth Surface Processes and Landforms,* 23**,** 1031-1043.

WHITEMAN, C. D., HOCH, S. W., HAHNENBERGER, M., MUSCHINSKI, A., HOHREITER, V., BEHN, M., CHEON, Y., ZHONG, S., YAO, W. & FRITTS, D. 2008. METCRAX 2006: Meteorological experiments in Arizona's Meteor crater. *Bulletin of the American Meteorological Society,* 89**,** 1665-1680.

WHITEMAN, C. D., HOCH, S. W., HAHNENBERGER, M. & ZHONG, S. METCRAX 2006–first results from the meteor crater experiment. Preprints, 29th Conf. Alpine Meteor, 2007. 4-8.

WHITMORE, J., STROM, R., CHEUNG, S. & GARNER, P. A. 2014. The petrology of the Coconino Sandstone (Permian), Arizona, USA. *Answers Research Journal,* 7**,** 499.

WILLIAMS, R. & ROBINSON, D. 2001. Experimental frost weathering of sandstone by various combinations of salts. *Earth surface processes and landforms,* 26**,** 811-818.

WRAY, R. 1997. A global review of solutional weathering forms on quartz sandstones. *Earth-Science Reviews,* 42**,** 137-160.

Chapter 6

6 Synthesis

6.1. Overview

In order to understand the effect of impact processes on rock breakdown, it is necessary first to understand the geology and lithology of the (unshocked) target in the region where the impact has occurred, and deformations and heterogeneities in target rocks due to impact. The results of laboratory analysis and experiments on impactites and the field studies of breakdown features in low-shocked sandstone provide new information on the role of heterogeneities and deformations due to impact processes. Overall this has advanced the understanding of impact processes in subsequent rock breakdown.

This thesis is the first detailed and comprehensive study exploring the role of impact inheritance on the breakdown of impactites. This thesis discusses and advances the understanding of the effects of low shock deformations and heterogeneities produced by impact processes in subsequent rock breakdown.

6.2. Contribution and broader implication of this research

The study of the effect of impact processes on rock breakdown in this thesis contributes to the field of rock breakdown and impact cratering in three ways.

First, it extends our knowledge of heterogeneities and deformations produced in rocks in low impact shock environment. Second, it advances the field of rock breakdown by providing insight into the effect of these low impact shock generated heterogeneities and deformations in rocks on subsequent nature and rate of breakdown. Third, it contributes to the development and application of SfM photogrammetry and X-ray CT methods in the study of rock breakdown.

1) Petrographic studies using a combination of techniques revealed changes in a range of impactite samples that experienced low shock level (<10 GPa). The porosity in low-shocked sandstone has decreased compared to unshocked samples. Intragranular fractures are pervasive in most of the low impact shocked impactite samples except low-shocked Moenkopi samples. Macrofractures (<0.2mm) was found in all impactite samples. The effect of low-shock on Moenkopi Sandstone has been explored for the first time, which revealed a decrease in porosity by 88% and macrofractures of 0.1-0.2 mm in aperture compared to unshocked Moenkopi Sandstone. The low shocked damage

characteristics found in Coconino Sandstone, crystalline rocks, impact melt rocks, impact breccias, and impact melt-bearing breccias is in agreement with previous studies (Kieffer, 1971b; Madden et al., 2006; Rosa, 2012; Rae et al., 2017; Osinski and Grieve, 2017; Engelhardt et al., 1995; Engelhardt, 1997; Osinski et al., 2004; Tolometti and Osinski, 2018). A negative correlation between mechanical strength and clast size in impact melt rock was found, as the clast size decreases the mechanical strength slightly increases. Impact melt bearing breccias have the lowest mechanical strength compared to impact melt rocks and impact breccias. Impact breccias have an intermediate mechanical strength between impact melt rocks and impact melt-bearing breccias.

2) The physical weathering experiment conducted on impactites in this study is the first systematic and novel attempt to understand the effect of impact generated heterogeneities and deformation on the subsequent physical weathering of impactites. The results from physical weathering experiment showed that in general impactites exhibited an accelerated decline in strength decline in strength compared to non-impacted samples. However, rock type and impact inheritance are key parameters in controlling the rate of breakdown. Unlike Coconino Sandstone, the low shocked Moenkopi Sandstone samples exhibited no accelerated decline in strength compared to their unshocked counterparts in the experiment timeframe. The field survey conducted at Meteor Crater site is the first-ever field study to compare the effects of low shock damage (<5 GPa) on the nature of subsequent breakdown of sandstone. Rock hardness measurement reveals no statistically significant difference between Meteor Crater and control sites. Areal surface roughness parameters, Standard deviation of Height, Standard Deviation of Slope, Maximum height, Vector Ruggedness Measure for Moenkopi Sandstone reveal no statistical significance difference at all window scales between Meteor Crater and Control sites. In percent area of morphometric feature classes (pit, channel, pass, ridge, peak, and planar), at all the window scales, there were no significant differences between Meteor Crater and control sites. This led to the conclusion that there is no statistically significant difference in nature of weathering between low shocked Moenkopi at Meteor Crater and unshocked Moenkopi sandstone at control sites. However, a significant difference in terms of rock hardness, and all the roughness parameters and morphometric features at multiple scales between S-SW facing and N facing crater wall slopes was found. This could be related to the difference in aspect related microclimate. The S-SW facing crater slopes receive higher solar insolation than N facing slopes throughout the year. Even though porosity has been

reduced in low-shocked Moenkopi Sandstone at Meteor Crater, the fractures in the outcrops may have increased the permeability is responsible for the movement of salt and moisture. Fractures create conduits for salt and moisture ingress in low shocked Moenkopi rocks. The secondary porosity formed due to the fracturing may be compensating for a decrease in primary porosity in low shocked Moenkopi Sandstone. This indicates that low-shocked generated deformation combined with aspect related microclimatic variations are responsible for weathering of Moenkopi sandstone at Meteor Crater.

3) Methodological contribution of SfM photogrammetry and X-ray CT in rock breakdown studies -

SfM Photogrammetry: The development of SfM photogrammetry to generate sub-mm resolution Digital Elevation Models (DEMs) with sub-mm accuracy in this thesis is a significant advancement for the micro-topographic data collection on weathered rock surfaces (area <10 m^2) in remote locations and steep terrains. The method can be used to collect direct in-situ topographic data, which overcomes the limitations of 'smoothing' that occurs during indirect topographic data collection methods (e.g. (Ehlmann et al., 2008b). It can also be used to compare the textural properties of weathered rock surfaces between different sites. This is demonstrated in Chapter 6, where the roughness and morphometric forms at Meteor Crater and control sites are compared. The inability to measure the general geomorphometry of breakdown features has inhibited understanding causal links at relevant scales of the palimpsest of weathering features. In this thesis, we have demonstrated the application of areal height and slope roughness and rugosity parameters in the study of rock breakdown. The areal surface roughness and morphometric analysis at a range of scales performed on rock surfaces in Chapter 6 is an advancement to 2D profile based roughness analysis which only provides information along a profile, not entire rock surface which often makes it difficult to determine the exact nature of a topographic feature (Leach, 2013). This method can be used in any scenario where high resolution, accurate DEMs and orthophoto are required (e.g., scaled laboratory experiments or mm to cm-scale features in the field). This method is superior to scaled digital image technique used by Heslop (2003) to measure changes during weathering experiment as this technique produces scaled orthophoto data. This is in addition to sub-mm resolution topographic data that can be used to identify and quantify changes before and after weathering experiments or field exposure trials. The high-resolution DEMs of rocks surfaces in this study facilitate more rapid data collection and offers a potential solution to overcome many challenges in the field, and for short and long-

term monitoring of micro to mesoscale erosion in dynamic environments. Recently, this has been demonstrated by Cullen et al. (2018b) who adapted this method for an experiment to measure erosion on simulated rock shore platforms (Appendix I) and Mc Keown et al. (2017b) in an experimental study to measure mm scale surface features in sand caused by sublimation of CO_2 ice.

X-ray CT: The X-ray CT method used in Chapter 3 to monitor rock samples before and after the weathering experiment to understand the role of impact generated macroscopic fractures to subsequent weathering is useful for visualising and quantifying the presence of pre-existing micro-fractures and those that may be enhanced or generated by the experiments. Moreover, high-resolution X-ray CT scans provide a non-destructive method for porosity and permeability analysis. In future studies, this non-destructive technique will enable a better understating of rock response that is usually not accessible to the investigator in short length weathering experiments.

6.3. Implication of Laboratory experiments on Weathering at Meteor Crater

We found that the trend is for weathering of Coconino Sandstone to have been more strongly expressed relative to Moenkopi Sandstone in the low shock pressure deformation class (1a). The low shocked Moenkopi showed no significant difference in weathering in short-term laboratory experiment compared to the control sample.

This can be due to two reasons –

1. Coconino Formation being the closest to the point of impact might have experienced relatively higher shock deformation in low shock pressure regime (0-5 GPa) compared to Moenkopi Formation which represents the free surface of the impact site (Kring, 2017).
2. The finer grain size of Moenkopi Sandstone (0.07-0.1 mm) and low porosity (5-8%) when compared to Coconino Sandstone (grain size = 0.09-0.16 mm, porosity = 20%), may have led to a different response in low shock pressure regime (0-5 GPa). Class 1a MS only exhibits a reduction in porosity, unlike class 1a CS, it is not affected by irregular fracturing in quartz grains. This difference may be key in the subsequent expression of rock breakdown in sandstone.

Findings from our laboratory experiment suggest that macrofractures in class 1a MS samples may be compensating for the loss in porosity and if the experiment were extended in duration, perhaps class 1a samples may have shown higher deterioration relative to unshocked samples. But this proposition is not reflected in field study comparing rock breakdown features in low shocked Moenkopi and unshocked Moenkopi Sandstone at a larger scale (cm-m scale). The results from field studies revealed that there is no statistically significant difference in rock breakdown between low shocked and unshocked Moenkopi Sandstone. The results from field and laboratory study agree with each other in terms that in both studies, no significant difference was found in the breakdown of low shocked Moenkopi Sandstone compared to unshocked Moenkopi Sandstone.

Breakdown of rocks in the natural environment is a complex and non-linear dynamic process, and inheritance from past rock breakdown processes affects the contemporary breakdown of rocks (Warke, 1996b; Warke, 2007; Viles, 2010; Viles, 2013b; Viles et al., 2018). The effect of processes at smaller scales (μm-mm) must modify process rates at a larger scale (cm-m) (Turkington and Paradise, 2005). The exploitation of pores, capillaries, and microfractures by salt weathering may affect long-term weathering rate of sandstone. However, salt weathering may also affect the effective pore size distribution within the sandstone and thus modify the solution ingress/egress regime, consequently affecting salt precipitation patterns and rates of loss of rock surface material (Turkington and Paradise, 2005; Johnston et al., 2019). Furthermore, inheritance from past weathering of the sandstone is likely to control the evolution of microfractures and secondary porosity–permeability, a feedback loop that cannot be ignored (Turkington and Paradise, 2005; Warke, 2007; Viles et al., 2018). Thus, a detailed investigation of permeability and cosmogenic exposure ages of Moenkopi Sandstone is required in future in order to understand the complex relationship of weathering history and shock damage on contemporary weathering.

6.4.The implication for rock breakdown on Early Mars

Even though regolith and rocks on Mars have different mineralogy than rocks used in our experiment, the results of this work have implications for Martian rock breakdown. The shock effects will produce broadly similar deformations and heterogeneities in the rocks that will affect the subsequent weathering of rocks. It is known from laboratory experiments that shocked mafic, and impact glasses dissolves faster than the unshocked crystalline counterparts (Boslough and Cygan, 1988; Cygan et al., 1989; Bell, 2015; Bell, 2017). These shock activated minerals require less time to alter and intermittent warming events due to

impact, and volcanic events might be enough to weather these minerals (Halevy and Head III, 2014; Palumbo and Head, 2018). Most of the altered material dates from the Noachian and Early Hesperian (Poulet et al., 2005; Tornabene et al., 2013), period of heaviest meteorite bombardment, so these materials have continued to be exposed for subsequent shock modification, and shock activated weathering process occurring in synergy for billions of years (Boslough, 1991; Tyburczy and Aherns, 1988). These two processes in combination may be responsible for abundant dust and colour of Martian fines on Mars (Boslough et al., 1986; Boslough, 1991).

During Noachian and Hesperian periods, when the Martian climate was different from today, and it is intuitive to suggest that fluids were available to react with rocks (Carter et al., 2015; Zolotov and Mironenko, 2016). To date, inheritance has not been considered in the discussion of surface features on Mars, particularly the inheritance of weakness in rocks due to impact. The results of the experimental work suggest that impactites would have broken down faster than non-impact rocks. It is also likely; this would have been expressed along a shock magnitude continuum (although this has yet to be demonstrated). This latter point is supported somewhat by the work of other researchers to understand shock enhanced weathering of mafic and plagioclase minerals. They found that the rate of dissolution of minerals is controlled by the shock level, and shocked minerals alter faster than the unshocked minerals (Boslough and Cygan, 1988; Bell, 2017). In addition, it has been found that the significant volume of impact glasses formed during impact would react faster than their crystalline counterparts (Wolff-Boenisch et al., 2006; Tornabene et al., 2013; Cannon and Mustard, 2015). Enhanced weathering of impactites in Noachian cratered terrain may be the reason for the abundance of hydrated silicates and clay minerals in these regions (Poulet et al., 2005). Even under less hydrous scenarios for an early Mars, the impact-induced fracture planes at the mineral and clast scale would have been important controls to induce rapid breakdown under ‘cold-icy’ thermal cycles.

Sedimentary rocks on Mars are more common than previously thought: with the advancement in remote sensing data collection during the last 20 years, sedimentary rocks have been identified at various locations on that planet (Malin and Edgett, 2000). However, these rocks have a mafic to ultramafic composition and are different in mineralogy than commonly found sedimentary rocks on Earth (McLennan and Grotzinger, 2008). Meridiani Planum has several impact craters in sedimentary target rocks (e.g. Victoria Crater; (Squyres et al., 2009; Hayes et al., 2011). As different rock types experience a different level of shock

damage depending on porosity, mineralogy, volatile saturation, and distance from the point of impact during impact (Kieffer, 1971a), sedimentary rocks can be more affected compared to crystalline rocks experiencing the same shock pressure level. Even a low shock pressure (<10 GPa) causes more damage in sedimentary rocks (e.g. sandstone; (Kieffer, 1971b) than in crystalline rocks (e.g. basalt; (Kieffer et al., 1976a). This study supports this finding where we find that sandstone that has experienced the same level of low shock pressure will breakdown faster than crystalline rocks.

The difference in rock types and facies may produce a difference in impact shock-related damage, and this will subsequently lead to a differential rate of rock breakdown. This suggests that the erosion/degradation of crater landforms will differ depending on the lithology of the target rock. Regional and local differences in lithology may lead to a differential rate of breakdown. Weak lithification caused due to low impact shock would produce weak rock materials that could be easily removed by fluvial and aeolian erosional processes (Kieffer, 1975; Grant et al., 2008). For example, Class 1b Coconino Sandstone has become so soft and friable that it can be easily removed in the field by aeolian or fluvial processes. Similar aeolian erosion of weaker sandstone (aeolianite) rocks are also reported at Victoria Crater on Mars (Grant et al., 2008). Despite the discovery of several hundreds of potential paleolakes, relatively rarity of the preserved delta deposits on Mars is a mystery (Fassett and Head III, 2008; Howard, 2007; Hoke et al., 2014). This sparse presence of delta deposits may be explained by resurfacing by a combination of impact processes and aeolian erosion. Impact processes produce weaker and friable impacted rock material that is subsequently removed by aeolian processes and limit their preservation.

The age of the Martian surface is determined by crater count statistics (Hartmann and Neukum, 2001). The crater chronology models are based on crater size-frequency distribution on the surface of Moon, which is linked to the radiometric age of lunar samples and meteorites (Hartmann and Neukum, 2001; Werner and Tanaka, 2011). Enhanced weathering and erosion of shocked ejecta and impactites in different lithologies may affect the preservation of crater diameters or indeed may control the enhanced modification of crater rims. These factors have not received sufficient attention in the literature.

Regolith on the lunar surface consists of minerals shocked at various levels and impact glass (Kieffer, 1975), but The Moon lacks an atmosphere or hydrosphere with which the regolith can react. On airless bodies, thermal gradients are considerably high compared to planetary

bodies with the atmosphere (Molaro and Byrne, 2012). Impact-induced deformation and discontinuities will subsequently affect the thermal breakdown of rocks and production of regolith on asteroids and planetary bodies without an atmosphere (Delbo, 2014; Viles, 2014; Hazeli et al., 2017).

6.5.Suggested future work

The subaerial breakdown of impactites is currently an understudied area of research. Here are suggested areas for future investigation:

6.5.1. Photogrammetry and roughness analysis

The topographic data produced using SfM photogrammetry method developed in Chapter 4 can be combined and registered with visible/near-infrared (VNIR), thermal infrared (TIR) and short-wave infrared (SWIR) hyperspectral imaging (Hinchcliffe et al., 2017). This will not only help to quantify the loss of materials, rock surface roughness, alteration but also able to relate breakdown features with chemical and biological weathering. This will help to better understand the link between mechanical, chemical and biological weathering.

Furthermore, a range of new areal surface roughness parameters such as function related parameters, material ratio parameters, volume parameters, hybrid parameters, spatial parameters and areal fractal parameters could be borrowed from the field of metrology and applied in the rock breakdown research (Leach, 2013). These parameters have several advantages over traditional profile roughness parameters as they have more statistical significance than equivalent profile measurements. The ability to quantify surface change across an area rather than limited to specific points will aid interpretation of the causal links between controls and resultant landform development. This is particularly relevant for the recent developments in monitoring micro-climates (Mol and Viles, 2012; Coombes et al., 2013) of rock breakdown environments. In addition, these parameters can be useful in determining the exact nature of the topographic feature. Many small-scale (mm-cm) breakdown features are ambiguous, and it remains challenging to distinguish between similar-looking features (e.g. aeolian pits vs dissolution pits) and therefore to establish a clear link between weathering feature form and the formative process. Even for homogenous forms on a surface, it may be difficult to understand the role of individual weathering mechanisms (Viles, 2005; Warke, 2007; Viles et al., 2010; Viles et al., 2018). Between rock

breakdown sites, features often show considerable complexity in their intensity, size and shape depending on lithological, geological and micro-environmental factors (Viles, 2001). Areal surface fractal analysis of rock surfaces would help to elucidate equifinality in the production breakdown features and problems of identifying fossil vs current forming features (Viles, 2001; Fardin et al., 2004). However, most of the existing GIS packages (e.g. ArcGIS, QGIS) does not include theses roughness parameters so users may need to code the parameters in ArcGIS using Python scripting or MATLAB.

6.5.2. Physical weathering experiments

The physical weathering experiment conducted in chapter 3 of this thesis revealed some interesting results regarding the breakdown of impactites. This experiment only included low shocked sandstone and felsic crystalline rocks, and few impact melt rocks and impact breccias. Increasing shock pressures also cause devolatilization in minerals (Madden et al., 2006), which may affect the response of rocks to thermal weathering (Farquharson et al., 2017).

In future, physical weathering experiments longer in length (>15 days) and different environmental conditions can be designed to include a range of lithologies that have experienced different levels of shock pressures (0-60 GPa).

Similar to experiments conducted by (Viles et al., 2010) in Mars conditions, physical weathering experiments can be conducted in the present and early Mars environmental conditions on basalt that has undergone different levels of shock deformations (Kieffer et al., 1976a). This will help us understand better the role of shock processes in the subsequent breakdown in past and presents Martian conditions.

In addition to strength test, weight, photographic and CT scan monitoring of changes used in the chapter 3, Acoustic Emission, ultrasonic sensors, thermocouples, strain gauge rosettes, moistures sensors (Menéndez and David, 2013; Eppes et al., 2016; David et al., 2017) should be used for monitoring continuous changes in rock strength, microcracking, moisture and temperature. This will provide a better insight into the role of heterogeneities and deformations due to impact in fluid and salt uptake.

6.5.3. Chemical Weathering experiments

Mineralogy and crystal structure plays an important role in chemical alterations of rocks. During impact, at high pressures (>25 GPa) mineral polymorphs, glasses and melts are produced (Stöffler et al., 2018). Natural silicate glass is susceptible to accelerated dissolution than their crystalline counterparts (Wolff-Boenisch et al., 2006). Since, impact-generated glasses have a different texture, density and structure (French and Koeberl, 2010), they may weather/alter differently. The structural defects, deformations and change in surface area of minerals makes shocked rocks more susceptible to chemical weathering than unshocked rocks (Boslough and Cygan, 1988; Bell, 2017).

Moreover, microstructures and defects in minerals generated during impact shock (e.g. Planar Fractures, Planar Deformation Features, mosaicism, microfractures) can provide permeable pathways for fluid circulation leading to chemical weathering (Leroux, 2005; Furukawa et al., 2011). Previously, Boslough and Cygan (1988) and Cygan et al. (1989) conducted experiments on artificially shocked silicate minerals to investigate the role of shock pressure on dissolution. They found enhancement in dissolution with an increase in shock pressure experienced by minerals. However, the effect of impact shock in rocks is more complex compared to individual minerals because shock damage in rocks depends on their porosity, mineral composition and distribution, duration of shock pressure, and fluid saturation (Kieffer, 1971a).

The role of high impact shock-related changes in rocks on chemical weathering can be explored by conducting chemical weathering experiments in controlled conditions. A series of chemical weathering experiments could be conducted on naturally and artificially shocked and unshocked basaltic materials that have experienced a range of shock pressure (i.e. 0-60 GPa). These experiments can be conducted in varying environmental conditions (e.g. temperature, atmospheric pressure, redox conditions (oxic/anoxic atmosphere), humidity, pH value). Naturally shocked rocks are sometimes affected by other subsequent geological processes. Thus, using experimentally shocked basalt samples in weathering experiment will help us better understand the role of shock on weathering. Shocked basaltic samples can be characterised by well-established techniques such as X-ray diffraction, raman, infrared and laser induced breakdown spectroscopy (LIBS), including the use of scanning electron microscopy electron backscatter diffraction (EBSD), backscatter electron (BSE) and cathodoluminescence (CL) detectors before and after the weathering experiment.

6.5.4. Field studies

Potential future work at Meteor Crater will examine the influence of stratigraphic structures (e.g., crossbedding) present in Coconino and Moenkopi Sandstone on shock damaging and subsequent rock breakdown. Biochemical weathering of impacted Moenkopi and Kaibab Formations will be explored to understand the effect of shock damage on biomediation.

Field studies should be conducted at other impact sites in different lithology and climatic conditions. Newsom et al. (2013) and Wright (2013) reported a unique style of rock breakdown associated with decompression cracks in impacted basalt at Lonar Crater, India. Lonar Crater could be studied to understand the influence of impact processes in subsequent weathering of basalt. Lonar Crater is the only best-preserved crater in basaltic target rocks on Earth (Osae et al., 2005). The in-situ comparative study could be performed on shocked basaltic outcrops at Lonar Crater in India using Raman, infrared and LIBS spectroscopy (Kieffer et al., 1976a; Ehlmann et al., 2008a). The results obtained from laboratory weathering experiment and field studies could also be compared with in-situ remote sensing data collected from current and future rovers on Mars.

Additional field studies at Lonar Crater can explore potential topics -

1) Basaltic lithology exposed at around Lonar Crater is complex, reflecting on the multi events of lava emplacement and cooling (see Maloof et al. (2010) and Komatsu et al. (2014)). A future study will assess how this original lithology of the basalt was deformed due to the impact and how it affects the subsequent rock breakdown.

2) Role of hydrology. In comparison to Meter Crater, Lonar Crater has been more affected by the hydrological processes in its history. Even today, Lonar Crater is hydrologically quite active with enhanced precipitation, the presence of an inner crater lake, and groundwater movement (Komatsu et al., 2014). Future rock breakdown studies should consider those "water" processes.

3) Regional climatic influence modulated by the crater topography. Somewhat similar to our finding of the microclimate influence on the rock breakdown at the Meteor Crater, Lonar Crater exhibits a possible influence of the southwest monsoon in the form of enhanced drainage development on the southwestern section of the ejecta blanket (Komatsu et al., 2014). A Future field study will explore if rock breakdown is also enhanced at the localities of Lonar Crater where more moist wind hits.

References

Bell M. (2015) Experimentally Shocked and Altered Basalt: Laboratory Analogs for Calibration of Mars Remote Sensing and In Situ Data.

Bell M. (2017) Experimentally Shocked and Altered Basalt: VNIR Spectra of Mars Analog Materials.

Boslough M. (1991) Shock modification and chemistry and planetary geologic processes. *Annual review of Earth and planetary sciences* 19: 101-130.

Boslough M, Venturini E, Morosin B, et al. (1986) Physical properties of shocked and thermally altered nontronite: Implications for the Martian surface. *Journal of Geophysical Research: Solid Earth* 91.

Boslough MB and Cygan RT. (1988) Shock-enhanced dissolution of silicate minerals and chemical weathering on planetary surfaces. *Lunar and Planetary Science Conference Proceedings.* 443-453.

Cannon KM and Mustard JF. (2015) Preserved glass-rich impactites on Mars. *Geology* 43: 635-638.

Carter J, Loizeau D, Mangold N, et al. (2015) Widespread surface weathering on early Mars: A case for a warmer and wetter climate. *Icarus* 248: 373-382.

Coombes MA, Naylor LA, Viles HA, et al. (2013) Bioprotection and disturbance: seaweed, microclimatic stability and conditions for mechanical weathering in the intertidal zone. *Geomorphology* 202: 4-14.

Cullen ND, Verma AK and Bourke MC. (2018) A comparison of Structure from Motion Photogrammetry and the Traversing Micro Erosion Meter for measuring erosion on rock shore platforms. *Earth Surf. Dynam. Discuss.* 2018: 1-26.

Cygan RT, Casey WH, Boslough MB, et al. (1989) Dissolution kinetics of experimentally shocked silicate minerals. *Chemical geology* 78: 229-244.

David C, Sarout J, Dautriat J, et al. (2017) Ultrasonic monitoring of spontaneous imbibition experiments: Precursory moisture diffusion effects ahead of water front. 122: 4948-4962.

Delbo M. (2014) Thermal fatigue as the origin of regolith on small asteroids. *Nature* 508: 233-236.

Ehlmann B, Mustard J and Kumar P. (2008a) Infrared spectra of impact products from Lonar Crater: The effects of weathering and implications for Mars. *Lunar and Planetary Science Conference.* 2437.

Ehlmann BL, Viles HA and Bourke MC. (2008b) Quantitative morphologic analysis of boulder shape and surface texture to infer environmental history: A case study of rock breakdown at the Ephrata Fan, Channeled Scabland, Washington. *Journal of Geophysical Research: Earth Surface* 113.

Engelhardt W. (1997) Suevite breccia of the Ries impact crater, Germany: Petrography, chemistry and shock metamorphism of crystalline rock clasts. *Meteoritics & Planetary Science* 32: 545-554.

Engelhardt W, Arndt J, Fecker B, et al. (1995) Suevite breccia from the Ries crater, Germany: Origin, cooling history and devitrification of impact glasses. *Meteoritics & Planetary Science* 30: 279-293.

Eppes MC, Magi B, Hallet B, et al. (2016) Deciphering the role of solar-induced thermal stresses in rock weathering. 128: 1315-1338.

Fardin N, Feng Q and Stephansson O. (2004) Application of a new in situ 3D laser scanner to study the scale effect on the rock joint surface roughness. *International Journal of Rock Mechanics and Mining Sciences* 41: 329-335.

Farquharson J, Griffiths L, Baud P, et al. (2017) Compressive strength evolution of thermally-stressed Saint Maximin limestone. *AGU Fall Meeting Abstracts.*

Fassett CI and Head III JWJI. (2008) Valley network-fed, open-basin lakes on Mars: Distribution and implications for Noachian surface and subsurface hydrology. 198: 37-56.

French BM and Koeberl C. (2010) The convincing identification of terrestrial meteorite impact structures: What works, what doesn't, and why. *Earth-Science Reviews* 98: 123-170.

Furukawa Y, Sekine T, Kakegawa T, et al. (2011) Impact-induced phyllosilicate formation from olivine and water. *Geochimica et Cosmochimica Acta* 75: 6461-6472.

Grant JA, Wilson SA, Cohen BA, et al. (2008) Degradation of Victoria crater, Mars. *Journal of Geophysical Research: Planets* 113.

Halevy I and Head III JW. (2014) Episodic warming of early Mars by punctuated volcanism. *Nature Geoscience* 7: 865.

Hartmann WK and Neukum G. (2001) Cratering chronology and the evolution of Mars. *Chronology and evolution of Mars.* Springer, 165-194.

Hayes A, Grotzinger J, Edgar L, et al. (2011) Reconstruction of eolian bed forms and paleocurrents from cross-bedded strata at Victoria Crater, Meridiani Planum, Mars. *Journal of Geophysical Research: Planets* 116.

Hazeli K, El Mir C, Papanikolaou S, et al. (2017) The Origins of Asteroidal Rock Disaggregation: Interplay of Thermal Fatigue and Microstructure. *Icarus*.

Heslop EEM. (2003) Clast breakdown in the Atacama Desert, Chile :An intergrated field and laboratory approach. University of Oxford.

Hinchcliffe G, Bollard-Breen B, Cowan DA, et al. (2017) Advanced photogrammetry to assess lichen colonisation in the hyper-arid Namib Desert. *Frontiers in Microbiology* 8: 2083.

Hoke MR, Hynek BM, Di Achille G, et al. (2014) The effects of sediment supply and concentrations on the formation timescale of Martian deltas. 228: 1-12.

Howard ADJG. (2007) Simulating the development of Martian highland landscapes through the interaction of impact cratering, fluvial erosion, and variable hydrologic forcing. 91: 332-363.

Johnston B, McKinley J and Warke P. (2019) Comparative investigation of the spatial distribution of past weathering impacts on sandstone masonry. *Geomorphology* 324: 25-35.

Kieffer S, Schaal R, Gibbons R, et al. (1976) Shocked basalt from Lonar impact crater, India, and experimental analogues. *Lunar and Planetary Science Conference Proceedings.* 1391-1412.

Kieffer SW. (1971a) I. Shock metamorphism of the Coconino sandstone at Meteor Crater, Arizona. II. The specific heat of solids of geophysical interest. California Institute of Technology.

Kieffer SW. (1971b) Shock Metamorphism of the Coconino Sandstone. *Journal of Geophysical Research*.

Kieffer SW. (1975) From regolith to rock by shock. *The Moon* 13: 301-320.

Komatsu G, Kumar PS, Goto K, et al. (2014) Drainage systems of Lonar Crater, India: Contributions to Lonar Lake hydrology and crater degradation. 95: 45-55.

Kring DA. (2017) Guidebook to the geology of Barringer Meteorite Crater, Arizona (aka Meteor Crater): for the 80th Annual Meeting of the Meteoritical Society July 2017. Lunar and Planetary Institute.

Leach R. (2013) *Characterisation of areal surface texture*: Springer.

Leroux H. (2005) Weathering features in shocked quartz from the Ries impact crater, Germany. *Meteoritics & Planetary Science* 40: 1347-1352.

Madden MEE, Kring DA and Bodnar RJ. (2006) Shock reequilibration of fluid inclusions in Coconino sandstone from Meteor Crater, Arizona. *Earth and Planetary Science Letters* 241: 32-46.

Malin MC and Edgett KS. (2000) Sedimentary rocks of early Mars. *Science* 290: 1927-1937.

Maloof AC, Stewart ST, Weiss BP, et al. (2010) Geology of lonar crater, India. *Bulletin* 122: 109-126.

Mc Keown L, Bourke M and McElwaine JJSr. (2017) Experiments on sublimating carbon dioxide ice and implications for contemporary surface processes on Mars. 7: 14181.

McLennan S and Grotzinger J. (2008) The sedimentary rock cycle of Mars. *The Martian Surface-Composition, Mineralogy, and Physical Properties* 1: 541.

Menéndez B and David CJEes. (2013) The influence of environmental conditions on weathering of porous rocks by gypsum: a non-destructive study using acoustic emissions. 68: 1691-1706.

Mol L and Viles HA. (2012) The role of rock surface hardness and internal moisture in tafoni development in sandstone. *Earth Surface Processes and Landforms* 37: 301-314.

Molaro J and Byrne S. (2012) Rates of temperature change of airless landscapes and implications for thermal stress weathering. *Journal of Geophysical Research: Planets (1991–2012)* 117.

Newsom HE, Wright SP, Misra S, et al. (2013) Comparison of simple impact craters: A case study of Meteor and Lonar Craters. *Impact Cratering: Processes and Products*: 271-289.

Osae S, Misra S, Koeberl C, et al. (2005) Target rocks, impact glasses, and melt rocks from the Lonar impact crater, India: Petrography and geochemistry. *Meteoritics & Planetary Science* 40: 1473-1492.

Osinski G and Grieve R. (2017) " Suevites" of the West Clearwater Lake Impact Structure, Canada: A Demonstration of the Need for a Revised Classification Scheme for Impactites. *Lunar and Planetary Science Conference.*

Osinski GR, Grieve RA and Spray JG. (2004) The nature of the groundmass of surficial suevite from the Ries impact structure, Germany, and constraints on its origin. *Meteoritics & Planetary Science* 39: 1655-1683.

Palumbo AM and Head JW. (2018) Impact cratering as a cause of climate change, surface alteration, and resurfacing during the early history of Mars. *Meteoritics & Planetary Science* 53: 687-725.

Poulet F, Bibring J-P, Mustard J, et al. (2005) Phyllosilicates on Mars and implications for early Martian climate. *Nature* 438: 623-627.

Rae A, Collins G, Grieve R, et al. (2017) Complex crater formation: Insights from combining observations of shock pressure distribution with numerical models at the West Clearwater Lake impact structure. *Meteoritics & Planetary Science* 52: 1330-1350.

Rosa DF. (2012) *The sheet of impact melt at West Clearwater Lake, Northern Quebec*: McGill University (Canada).

Squyres SW, Knoll AH, Arvidson RE, et al. (2009) Exploration of Victoria crater by the Mars rover Opportunity. *Science* 324: 1058-1061.

Stöffler D, Hamann C and Metzler K. (2018) Shock metamorphism of planetary silicate rocks and sediments: Proposal for an updated classification system. *Meteoritics & Planetary Science* 53: 5-49.

Tolometti G and Osinski G. (2018) The Impact Melt Sheet at West Clearwater Impact Structure: A Petrographic and Geochemical Analysis. *Lunar and Planetary Science Conference.*

Tornabene LL, Osinski GR, McEwen AS, et al. (2013) An impact origin for hydrated silicates on Mars: A synthesis. *Journal of Geophysical Research: Planets* 118: 994-1012.

Turkington AV and Paradise TR. (2005) Sandstone weathering: a century of research and innovation. *Geomorphology* 67: 229-253.

Tyburczy JA and Aherns T. (1988) Dehydration kinetics of shocked serpentine. *Lunar and planetary science conference proceedings.* 435-441.

Viles H. (2010) Simulating weathering of basalt on Mars and Earth by thermal cycling. *Geophys. Res. Lett.* 37: L18201.

Viles H, Ehlmann B, Wilson CF, et al. (2010) Simulating weathering of basalt on Mars and Earth by thermal cycling. *Geophys. Res. Lett.* 37: L18201.

Viles H, Messenzehl K, Mayaud J, et al. (2018) Stress histories control rock-breakdown trajectories in arid environments. *Geology* 46: 419-422.

Viles HA. (2001) Scale issues in weathering studies. *Geomorphology* 41: 63-72.

Viles HA. (2005) Microclimate and weathering in the central Namib Desert, Namibia. *Geomorphology* 67: 189-209.

Viles HA. (2013) Synergistic Weathering Processes In: Shroder JF (ed) *Treatise on Geomorphology.* San Diego: Academic Press, 12-26.

Viles HAJN. (2014) Solar system: Cracking up on asteroids. 508: 190.

Warke P. (2007) Complex weathering in drylands: implications of 'stress' history for rock debris breakdown and sediment release. *Geomorphology* 85: 30-48.

Warke PA. (1996) Inheritance effects in the weathering of debris under hot arid conditions.

Werner S and Tanaka K. (2011) Redefinition of the crater-density and absolute-age boundaries for the chronostratigraphic system of Mars. *Icarus* 215: 603-607.

Wolff-Boenisch D, Gislason SR and Oelkers EH. (2006) The effect of crystallinity on dissolution rates and CO2 consumption capacity of silicates. *Geochimica et Cosmochimica Acta* 70: 858-870.

Wright S. (2013) Decompression Cracks in Altered Basalt Under Solid-State Shock Pressures: A New Macroscopic Shock Texture. *LPI Contributions* 1737: 3049.

Zolotov MY and Mironenko MV. (2016) Chemical models for martian weathering profiles: Insights into formation of layered phyllosilicate and sulfate deposits. *Icarus* 275: 203-220.

Appendices

Appendix 1. A comparison of Structure from Motion Photogrammetry and the Traversing Micro Erosion Meter for measuring erosion on rock shore platforms

Published in Earth Surface Dynamics

Authors: Niamh D. Cullen, Ankit K. Verma and Mary C. Bourke

Abstract

For decades researchers have used the Micro Erosion Meter and it successor the Traversing Micro Erosion Meter to measure microscale rates of vertical erosion (downwearing) on shore platforms. Difficulties with 'upscaling' of microscale field data in order to explain long-term platform evolution have led to calls to introduce other methods which allow measurement of platform erosion at different scales. Structure from Motion Photogrammetry is fast emerging as a reliable, cost-effective tool for geomorphic change detection, providing a valuable means for detecting micro to meso-scale geomorphic change over different terrain types. Here we present the results of an experiment where we test the efficacy of Structure from Motion Photogrammetry for measuring change on shore platforms due to different erosion processes (sweeping abrasion, scratching and percussion). Key to this approach is the development of the Coordinate Reference System used to reference and scale the models, and which can be easily deployed in the field. Experiments were carried out on three simulated platform surfaces with low to high relative rugosity to assess the influence of surface roughness. We find that a Structure from Motion Photogrammetry can be used to reliably detect micro (sub-mm) and meso (cm) scale erosion on shore platforms with a low Rugosity Index. As topographic complexity increases, the scale of detection is reduced. We also provide a detailed comparison of the two methods across a range of categories including cost, data collection, analysis and output. We find that Structure from Motion offers several advantages over the Micro Erosion Meter, most notably the ability to detect and measure erosion of shore platforms at different scales.

A.1.1. Introduction

There are numerous methods employed for measuring natural rates of change on rock surfaces. For decades researchers were restricted to direct measurement of change relative to a datum, however this method has been largely superseded by techniques which fall into

two general categories; contact methods which utilise erosion meters, and non-contact methods such as Terrestrial Laser Scanning (TLS) and Structure from Motion (SfM) Photogrammetry (Moses et al., 2014). On shore platforms, the Micro Erosion Meter (MEM) and its successor the Transverse Micro Erosion Meter (TMEM) are the most frequently applied instruments for quantifying micro-scale erosion. However, SfM Photogrammetry is fast emerging as a valuable tool for detecting and quantifying geomorphic change across a range of scales and environments and represents a potential alternative to the MEM and TMEM for measuring erosion on shore platforms if a suitable level of resolution, accuracy and repeatability can be achieved. There is a large body of literature focussed on each of these methods (e.g. Hanna, 1966; Trudgill, 1975; Trudgill et al., 1981; Stephenson and Kirk, 2001; Snavely, 2006.; Trenhaile, 2006; Stephenson and Finlayson, 2009; Stephenson et al., 2010; Westoby et al., 2012; Gómez-Gutiérrez et al., 2014; Kaiser et al., 2014; Carrivick et al., 2016; Smith et al., 2016). A brief overview of the two methods is given below.

A.1.1.1. The Micro Erosion Meter and the Traversing Micro Erosion Meter

The MEM was developed and described by Hanna (1966) and High and Hanna (1970) as a tool for measuring relatively slow lowering rates of bedrock surfaces. Since its inception, the MEM and its modified successor, the TMEM (Trudgill et al., 1981) (hereafter T/MEM) have been used by numerous researchers to measure rates of surface lowering on shore platforms of varying lithologies. The spatial and temporal variability of measured erosion rates for shore platforms have allowed a more detailed understanding of processes operating on shore platform, contributing to the ongoing debate on the origin of shore platforms and the relative contributions of marine, biological and subaerial processes which drive their evolution (See Stephenson and Finlayson, 2009: , for a more detailed review of the contribution of the T/MEM to rock coast research). The popularity of the T/MEM stems from the ability to detect sub-mm changes over very short (hours) as is the case with platform swelling and timescales comparative with the duration of many research projects (1-3 years), which are also considered representative of longer-term (decadal) measurements (Stephenson et al., 2010). Add to this, the often cited low cost of construction and portability of the instrument and its popularity among rock coast researchers is easily understood.

Moses et al. (2014) outlined some limitations associated with the T/MEM that had been identified by previous research (e.g. Spate et al., 1985; Ellis, 1986; Andrews and Williams,

2000; Trenhaile, 2003; Foote et al., 2006; Swantesson et al., 2006). Authors studying erosion on (relatively soft) chalk platforms noted that the probe might cause erosion of the platform surface. This 'probe erosion' was also noted early on by Spate (1985). However, this does not constitute a problem where erosion rates are rapid (Foote et al., 2006; Swantesson et al., 2006). In addition, Moses et al., (2014) also pointed to previous research which showed that where rapid rates of erosion occur, this may result in the loosening or dislodgement of the bolts on which the T/MEM is placed on annual (Ellis, 1986; Andrews, 2000), or decadal timescales (Stephenson and Kirk, 1996). Trenhaile (2003) noted that although the T/MEM records small amounts of platform downwearing, it cannot record wave quarrying of larger blocks or loss of rock fragments due to frost riving.

Additional significant limitations have also been identified. For example, the location of a T/MEM measurement station is limited to surfaces with low topographic complexity. This is an issue for shore platforms with highly variable meso and macro scale roughness and which only broadly conform to the Sunamura's (1992) traditional Type A and Type B classification. Excluding these more complex platform morphologies significantly limits our ability to quantify rates and identify processes and styles of shore platform erosion across the complete spectrum of platform morphologies. Second, while decades of measuring micro-scale erosion using the T/MEM have provided valuable insights into rates and processes of downwearing on shore platforms, there are difficulties associated with 'up-scaling' these field data to explain meso and macro-scale landform development (Warke and McKinley, 2011). Stephenson and Naylor (2011) noted a tendency towards micro and macro scale studies of shore platform erosion. A recent study that reviewed 95 publications on shore platforms (Cullen and Bourke, 2018) also highlighted this concentration of micro and macro scale studies.

In comparison, meso-scale processes have received less attention, although research at this scale has increased significantly in the last two decades (Cullen and Bourke, 2018). Indeed, Stephenson et al. (2010) advocated the introduction of new techniques which capture the full range of scales of erosion on shore platforms. SfM Photogrammetry is one such technique that has this potential.

A.1.1.2. Structure from Motion Photogrammetry

Significant developments in digital photogrammetry techniques over the last decade have revolutionised the collection of 3D topographic data in the geosciences. Traditional photogrammetry requires a knowledge of the 3D location and orientation of the camera and accurate 3D information of control points in the scene of interest. While methods which allow the accurate calibration of non-metric cameras and reliable automation of the photogrammetric process have enhanced the use of photogrammetry in the geosciences (e.g. Chandler, 1999; Chandler et al., 2002; Carbonneau et al., 2004), it still requires expert understanding and practice (Carrivick et al., 2016). In the last decade, there have been significant workflow advancements which have dramatically reduced the expertise required. Structure from Motion (SfM) photogrammetry, uses a standard camera for collecting image data of a three-dimensional (3D) landform.

Multiple overlapping images are taken from different spatial positions and used to reconstruct the 3D geometry of the target. Unlike traditional photogrammetry, the SfM workflow does not require prior knowledge of the 3D location, the camera orientation or 3D information on control points before reconstruction of scene geometry. Rather, Scale Invariant Feature Detection (SIFT) (Lowe, 2004) is used to match points between images, and a least square bundle adjustment algorithm is used to align images and produce a 'sparse' point cloud representing the most prominent features in the images. A further development utilises Multi-View Stereo (SfM-MVS) algorithms (e.g. Furukawa et al., 2010) to intensify the sparse cloud and merge the resulting 3D point cloud into a single dense point-based model. This can then be used to generate a high-resolution ortho-photo, mesh or Digital Elevation Model (DEM). Successive point clouds and DEMs of the same location or feature can be analysed utilising widely available GIS software (e.g. ESRI ArcGIS desktop or QGIS) and other programs (e.g. CloudCompare) used for geomorphic change detection to quantify erosion and deposition. A large amount of literature has been published on SfM, and the reader is referred to Walkden and Hall (2005); Westoby et al. (2012); (Fonstad et al., 2013); Thoeni et al. (2014); Micheletti et al. (2015a); Micheletti et al. (2015c); Smith et al. (2016); Carrivick et al. (2016); Özyeşil et al. (2017) and Verma and Bourke (2018) for more detailed discussions of SfM techniques and workflows.

The SfM-MVS workflow has been widely applied in the geosciences at varying scales of resolution from small scale (mm - cm's) scale studies of soil erosion to morphodynamic studies of beaches, coastal cliffs and braided rivers (e.g. Lim et al., 2010; Javernick et al.,

2014; Kaiser et al., 2014; Brunier et al., 2016a; Brunier et al., 2016b; Balaguer-Puig et al., 2017b). SfM-MVS offers several advantages over traditional surveying techniques, specifically its relatively low cost and portability of required equipment, i.e. a camera, compared to that of TLS. In addition, the availability of free and relatively low cost commercial software, a semi-automated workflow and the decreasing cost of high-end desktop computers have resulted in the increasing application of this method in geomorphological research. While SfM MVS offer significant advantages at a range of scales, it it worth noting that the scale of some processes operating on shore platforms, for example, platform swelling, operate at resolution currently not obtainable using SfM MVS, and other tried and tested approaches (i.e. the T/MEM) remain the most suitable method of measurement .

It is worth noting that the accuracy and resolution of SfM-MVS derived DEMs relies heavily on the quality of the images used and the accuracy of the coordinate reference system. For work on shore platforms, the accuracy of the DEM is limited by the accuracy of the Ground Control Points (GCPs) used. These are often determined using a Differential GPS (dGPS) or total stations which have reported accuracies of centimetres and millimetres respectively. However, a number of rock breakdown processes, such as granular disintegration (Viles, 2001) and features, such as weathering pits (Viles, 2001; Bourke et al., 2007b; Thornbush, 2012) occur at cm to sub-mm scale.

Our work has three foci: First, to test the SfM-MVS for measuring micro-scale erosion on shore platforms. Second to determine the potential of SfM-MVS for meso-scale geomorphic change detection. Third, to provide a robust assessment and comparison of the two methods (T/MEM and SfM-MVS) for measuring erosion on shore platforms. Key to our approach is to adapt the local coordinate reference system (CRS), and SfM-MVS workflow developed by Verma and Bourke (2018). Their system was developed to generate sub-mm scale DEMs of rock surfaces (<10 m^2) in difficult to access terrains (e.g., cliffs and steep-sided impact crater walls). Their method can produce high resolution (sub-mm) DEMs with sub-mm accuracy. We advance this work through the design and manufacture of a field-hardy Coordinate Reference System (CRS) which can be quickly deployed, repeatedly at the same site. Our approach will enable the application of SfM-MVS for geomorphic change detection on shore platforms at both the micro and meso scale.

In this paper, we present the results of a series of experiments on simulated platform surfaces using our newly developed CRS.

A.1.2. Methods

A.1.2.1. A manufactured Coordinate Reference System for SfM-MVS

We have adapted the local coordinate reference system of Verma and Bourke (2018) which utilises a precisely measured equilateral triangle with a coded marker (downloaded from Agisoft Photoscan) attached at each vertex (Figure 1a and b). The x, y and z coordinates of each coded marker are calculated using trigonometry and serve as the GCPs for generating the DEMs in the SfM-MVS workflow. When used for a small surface area (≤ 6.76 m^2), this method has been proved to produce high resolution (0.5 mm per pixel) DEMs with sub-mm accuracy (Verma and Bourke: 2018).

We mounted the coded markers onto a specifically designed stainless-steel platform (Fig. a and b) based on the design of Verma and Bourke (2018). The platform consists of a 15 cm equilateral triangle with three square steel plates (4 cm x 4 cm x 0.5 cm) and a specially machined leg. Each plate is engineered so that the centre of a plate is fixed precisely (± 0.01mm) on one vertex of the triangular base. The centre of each plate is also permanently marked during manufacture to aid the application of coded markers. The base of the leg is machined to fit a stainless-steel square head bolt to a depth of 1.5 cm and is fixed at the centre of gravity on the underside of the triangular base plate.

In the field, the square headed bolt is fixed to the platform by drilling a hole and fixing the bolt with marine grade epoxy resin, using a digital inclinometer to make sure the bolt head is level. This is similar to the approach used to install T/MEM stations. When mounted onto the bolt, this design secures the base plate with the coordinate system in place with a high degree of relocation precision (see section 3.2). This permits repeated measurements and the georeferencing of DEMs for high resolution change detection of field sites.

A.1.2.2. The experiments

The experiments were designed to capture different scales of erosion from the granular scale (sub-mm) abrasion of the platform surface to the removal of rock fragments (mm -cm). The accuracy of the SfM-MVS generated DEMs used to calculate DEMs of Difference (DoDs)

for geomorphic change detection were assessed by means of horizontal and vertical checkpoints. We also investigated the influence of surface roughness on the accuracy of DEMs and resultant DoDs.

The experiment was set up outdoors on a level table (1.2 m x 0.6 m). Two scaled coded markers (0.25 m) and a series of 2.5 cm x 2.5 cm and 1 cm x 1 cm checkboard pattern, non-coded markers and eight, evenly spaced wooden blocks of known dimensions were fixed onto the table surface (Figure 1 C). These were used to calculate the horizontal and vertical error of the DEMs (as recommended by Verma and Bourke: 2018). Four simulated platform surface blocks were constructed using moulds and gypsum plaster. Stainless steel, square-headed bolts for mounting the CRS, as described above, were installed on each block. A digital inclinometer (Examobile Bubble Level for iPhone) was used to ensure the surface of the bolt was level. The surface of the experimental blocks was constructed to represent a range of micro (<mm - mm) to meso scale >mm - cm) roughness that is observed in the field. These include low (B1), medium (B2) and high (B2) relative surface roughness (Figure 1 D-F). All blocks were sprayed with matte grey paint to allow easy identification of 'erosion' areas and provide additional visual validation of the models. A set of three 1 cm x 1 cm checkboard non-coded markers were fixed to each experimental block to serve as additional checkpoints for horizontal error. One block (B-con) was used as a control. The remaining three blocks (B1, B2 and B3) were used to carry out the experiment. Each block was placed at the centre of the table when acquiring images.

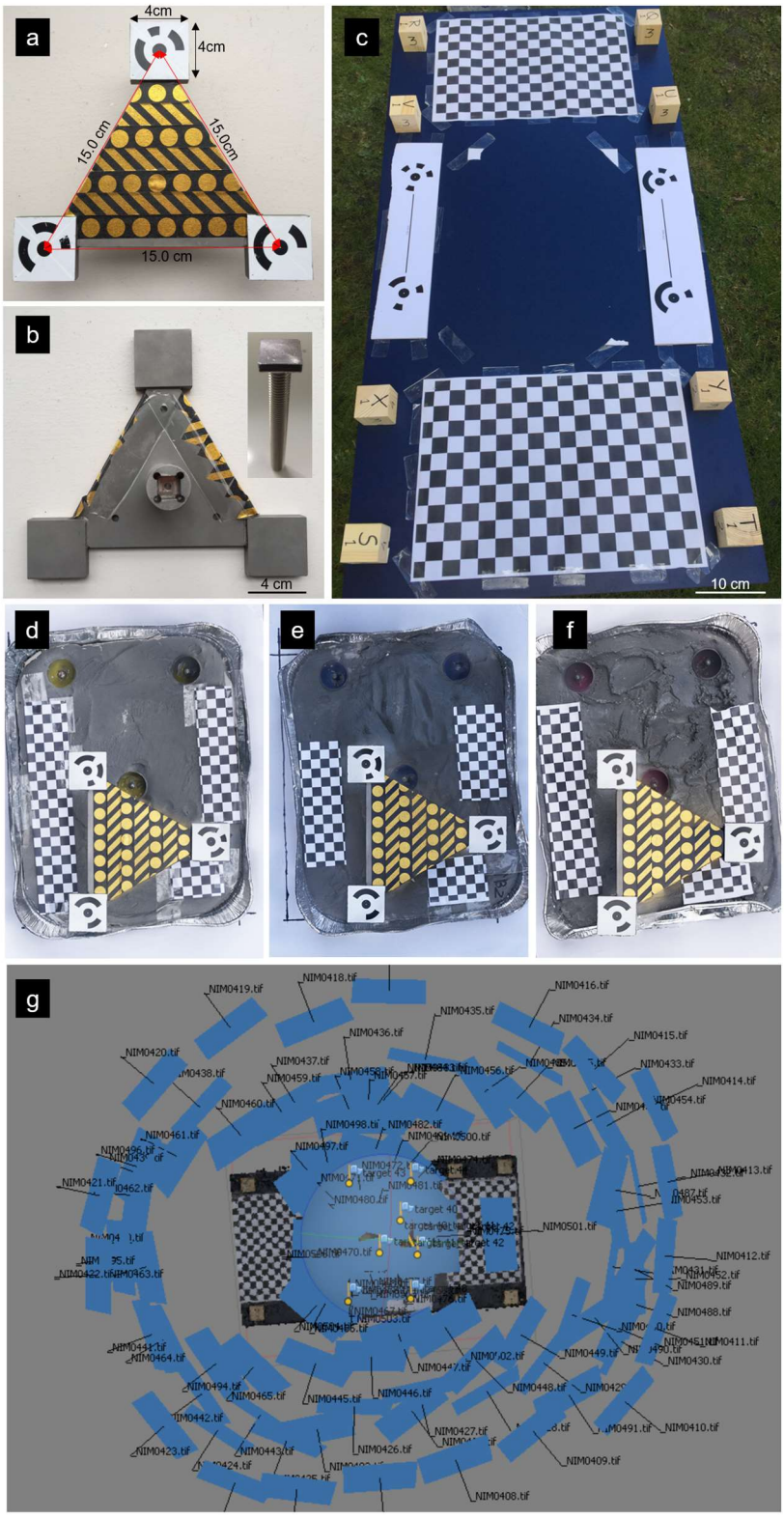


Fig A.1.1. The experimental setup. a) The CRS top view with scale shown and b) underside with the square headed bolt (inset) c) The experimental platform with markers and wooden blocks used to calculate the horizontal and vertical error. d, e, f) The simulated platform and g) example of the camera positions for image acquisition.

A.1.2.3. Data collection

In order to replicate field conditions as closely as possible, all images of the experimental blocks were acquired outdoors during a single day. The CRS was placed on the pre-installed square head bolt (Stig Fasteners , SQHM8x75), and orientation was noted. We used a Nikon D5500 with a variable zoom lens set up at 24 mm focal length, on a tripod to reduce effects of handshake. Approximately 100 images of each block were obtained. This number of images was required to capture the full extent of the table with the non-coded markers and the wooden blocks used for the error analysis. We expect that 40-50 images would be sufficient to generate a high-resolution DEM for a smaller area (e.g. <0.5 m^2) in the field. In this study, ~70 images were acquired at a distance of ~1m from the experimental blocks with the camera mounted on a tripod to reduce the effect of handshake on image quality, and then a series (25-30 images) of close-range shots at <0.5 m (Figure 1). All three experimental blocks and the control block were imaged on the table prior to simulating erosion on the blocks.

Recent work has demonstrated the potential efficacy of smaller-scale physical erosion processes (e.g. abrasion, scratching, perussion impact) on high energy Atlantic shore platforms (Cullen and Bourke, 2018). However accurate quantification of these features has not been possible. We, therefore, tested simulations of three known types of erosion: 1. Sweeping abrasion was simulated by gently abrading the surface of all three blocks with medium grit sandpaper to variable depths up to approximately 1 mm. 2. Scratches were simulated using a screwdriver 3. Impact percussion marks were simulated on one block using a hammer and chisel.

The CRS was removed and replaced between each stage of data collection, as would be practical for carrying out repeat surveys in the field. Images of the blocks were taken following simulated erosion as outlined above.

A.1.2.4. Repeatability

The utility of this approach for microscale change detection using the CRS developed for this study is contingent on the exact replacement of the CRS during successive surveys in the field. To test the repeatability of this approach, we used a control block to acquire images for DEM generation using the data collection and processing procedure outlined above. At

the end of the experiment, the CRS was replaced and the second series of images were acquired for DEM generation for comparison. DEM accuracy and error propagation were calculated as described below.

A.1.2.5. Data processing

A.1.2.5.1. Digital Elevation Models

All the images were acquired in the raw format during the experiment. RAW images were converted to 14-bit uncompressed tiff format with AdobeRGB colour space in Adobe Lightroom. We used Agisoft Photoscan (version 1.4.1). Image quality (Q) was assessed using the Estimate Image Quality tool in AgiSoft and images with Q values < 0.5 were removed. The CRS was used to scale and georeference the model. Baseline DEMs and orthophoto mosaics for each block were generated and exported at the highest, common pixel resolution (0.3mm/pixel) and common pixel coordinates.

A.1.2.5.2. DEMs of Difference

DEMs were exported in ArcMap, and a polygon shapefile was drawn over the area of interest for each block. The area of interest, i.e. the erosion area of the simulated platform surface, was extracted for analysis using the Extract by Mask' tool in Spatial Analyst tools. DoDs were generated using the Raster was Math tool (minus) in ArcMap (version 10.5) using Eq. (1),

$$B1\ DoD_1 = B1\ DEM_1 - B1\ DEM_0 \quad (1)$$

where the subscript refers to the experimental stage.

A.1.2.5.3. Rugosity

To permit evaluation of the impact of different degrees of surface roughness on the accuracy and reliability of our generated DEMs, a rugosity index for each block was calculated in ArcMap using the standard Surface Area ratio method (Risk, 1972; Dahl, 1973) where,

$$Rugosity = \frac{Contoured\ area}{Planar\ area} \quad (2)$$

A rugosity index (RI) of 1 indicates a planar surface while increasingly higher values indicate increasingly 'rougher' surfaces. The contoured area for each block was calculated using the relevant baseline DEM. A TIN surface was generated using the Raster to TIN tool in ArcMap. The contoured surface area for the specified region was calculated using the Polygon Volume tool in ArcMap. The planar surface area of the same region was derived using the calculate geometry tool assuming negligible change in slope over the specified area. The RI was calculated using Eq. (2).

A.1.2.5.4. DEM accuracy and error propagation

The coded and non-coded markers fixed to the table were used as checkpoints to determine the horizontal (XY) error of the DEMs produced using the CRS developed by Verma and Bourke (2018). For each DEM, the model and its respective orthophoto were imported into ArcMap (version 10.5) and the distance between 30 randomly selected checkpoints and the two coded scale bars (Figure 1) were measured using the measurement tool. The horizontal error was calculated as the Root Mean Square Error (RMSE) of the difference between the measured length and known length.

To determine the vertical accuracy of the DEMs, eight wooden blocks were used as checkpoints (Figure 1). The DEMs and orthophotos were imported in ArcMap where the height of wooden blocks were measured using the Interpolate Line tool, by drawing a line across one of the sides of the wooden block and extending it to the table surface. We ensured that the line drawn was straight. Height was estimated as the difference in mean elevation between wooden block top surface and the surrounding table surface on each side. The actual height of wooden blocks was measured by an electronic digital Vernier Caliper. The Vernier Caliper has an accuracy of 0.03 mm and measurement repeatability of 0.01 mm. We obtained five measurements along the same side of wooden block measured in ArcMap. We used the mean of these five measurements to calculate the height of the wooden block. The actual height was subtracted from the estimated DEM height to calculate the vertical error.

The calculation of a DoD can result in propagation of error associated with the DEMs used in the computation process. As such, an error analysis is required to increase confidence in the DoD results. This is particularly important when the scale of geomorphic change being detected is of similar magnitude to uncertainties of the DEMs used in the DoD calculation.

We determined the minimum level of detection as the most suitable method of error analysis for this study as the development of shore platforms is primarily an erosional process and as such, the spatial coherence of erosion and deposition (Wheaton et al., 2010) is unsuitable as a method for error analysis in this study. Additionally, while probabilistic approaches produce reliable estimates of morphological change (e.g. Brasington et al., 2000; Brasington et al., 2003; Lane et al., 2003), small changes in elevation, such as those measured in this experiment, may be disguised as noise (Williams, 2012). The minimum Level of Detection (LoD) uses the quadratic composition of errors in the original DEMs to estimate the propagated error of the calculated DoD (Brasington et al., 2003; Lane et al., 2003; Wheaton et al., 2010; Gómez-Gutiérrez et al., 2014; Williams, 2012):

$$E_{DoD_{1-2}} = \sqrt{(E_{DEM_1}{}^2 + E_{DEM_2}{}^2)} \quad (3)$$

Where $E_{DoD_{1-2}}$ refers to the LoD calculated as the square root of the combined squared errors of the DEMs used to generate the DoD. If values of E_{DEM_1} and E_{DEM_2} are known, this method can be applied at a global or local scale where the spatial variability of the error terms are known (Lane et al., 2003). We applied Eq. (3) to determine the minimum threshold of detection for each DEM (Williams, 2012) for each stage of the experiment. Changes detected that fall within the limits of detection (+ LOD_{min} or – LOD_{min}) calculated using Eq. (1) are considered noise and interpreted as no change.

A.1.3. Results

A.1.3.1. Accuracy and error propagation

DEM generation resulted in a maximum and minimum horizontal (XY) RMSE of 0.23 mm and 0.03 mm respectively. Maximum vertical (Z) RMSE was 0.52 mm with a minimum of 0.23 mm. The minimum limit of detection was calculated at 0 ± 0.27 mm while the maximum LoD was 0 ± 0.71 mm.

Table 1. The horizontal (XY) and vertical (Z) RMSE error for the control block (B-con) and the experimental blocks B1, B2 and B3. LoD for each DoD is also shown.

DEM	XY RMSE (mm)	Z RMSE (mm)	LoD (0 ± mm)

B-con			
1	0.03	0.45	N/A
2	0.12	0.23	0.27
B1			
Stage 0	0.23	0.37	N/A
Stage 1	0.12	0.39	0.54
Stage 2	0.22	0.44	0.56
Stage 3	0.12	0.52	0.71
B2			
Stage 0	0.1	0.40	N/A
Stage 1	0.2	0.46	0.53
Stage 2	0.1	0.35	0.49
Stage 3	0.2	0.45	0.56
B3			
Stage 0	0.2	0.39	N/A
Stage 1	0.1	0.37	0.54
Stage 2	0.1	0.39	0.54
Stage 3	0.1	0.45	0.60

6.4.6. A1.3.2. Repeatability

The change in vertical elevation for the control block calculated from the DoD is shown in Figure 2 below. The maximum change in elevation (- 0.29 mm) is within the LoD and is interpreted as no change.

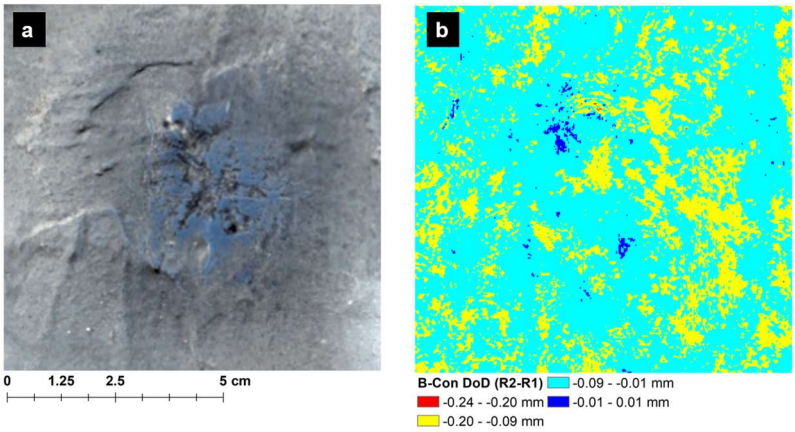


Figure 1. (a) The control block (B-Con) orthophoto and (b) DoD showing a change in surface elevation between successive DEMs. Note that detected change is within the calculated LoD (± 0.27 mm).

6.4.7. A.1.3.3. Rugosity

The RI calculated for each block is shown in Table 2. The control block (B-con) had the lowest rugosity (planar surface) while B1 had a very low RI followed by B2 and B3 in order of increasing rugosity.

Table 2. Contoured surface area (SA), planar surface area and Rugosity Index (RI) for each of the experimental blocks.

Block ID	**Contoured SA** (cm^2)	**Planar SA** (cm^2)	**R Index**
B-con	8.9	8.9	1.00
B1	9.0	8.9	1.01
B2	11.7	10.9	1.07
B3	9.9	8.2	1.21

6.4.7.1.A.1.3.3.1. Very low rugosity platform: B1

The results for experimental block B1 are shown in Figure 3 (a-i). The surface area of B1 used in the analysis is shown in (a) where light grey indicates the area of abrasion. For B1 Abrasion, a maximum negative surface change of 1.06 mm was detected, while an increase of 0.30 mm was observed (b) before the LoD was applied. The area of negative surface change between 0.1 mm and 1.06 mm corresponds to the actual area abraded. After thresholding at the LoD, the area of change detected is significantly lower (less than half) the area where the actual change occurred. No increase in surface elevation was detected. For B1 Scratches, the scratched surface is shown in d (black arrows). Before thresholding, the maximum negative change on the surface of B2 was 0.35 mm while an increase in surface elevation of 0.26 mm was detected. Negative changes corresponded well to the observed locations of scratches. After thresholding at the LoD, no changes were detected on the block surface (f). For B1 impact percussions, the locations where block fragments were removed are shown in G (black arrows). Maximum negative change detected, i.e. predicted the depth of percussions, was 1.49 mm, while a positive change in surface elevation of 0.30 mm was detected before thresholding (H). After thresholding, no positive change in surface elevation was detected and predicted negative change corresponded well to the actual location of percussions (i).

To summarise, for a simulated platform with a very low RI, sweeping abrasion and chips were reliably detected in the thresholded DoD. Scratch depths were less than the LoD and as such were not detected in the thresholded model.

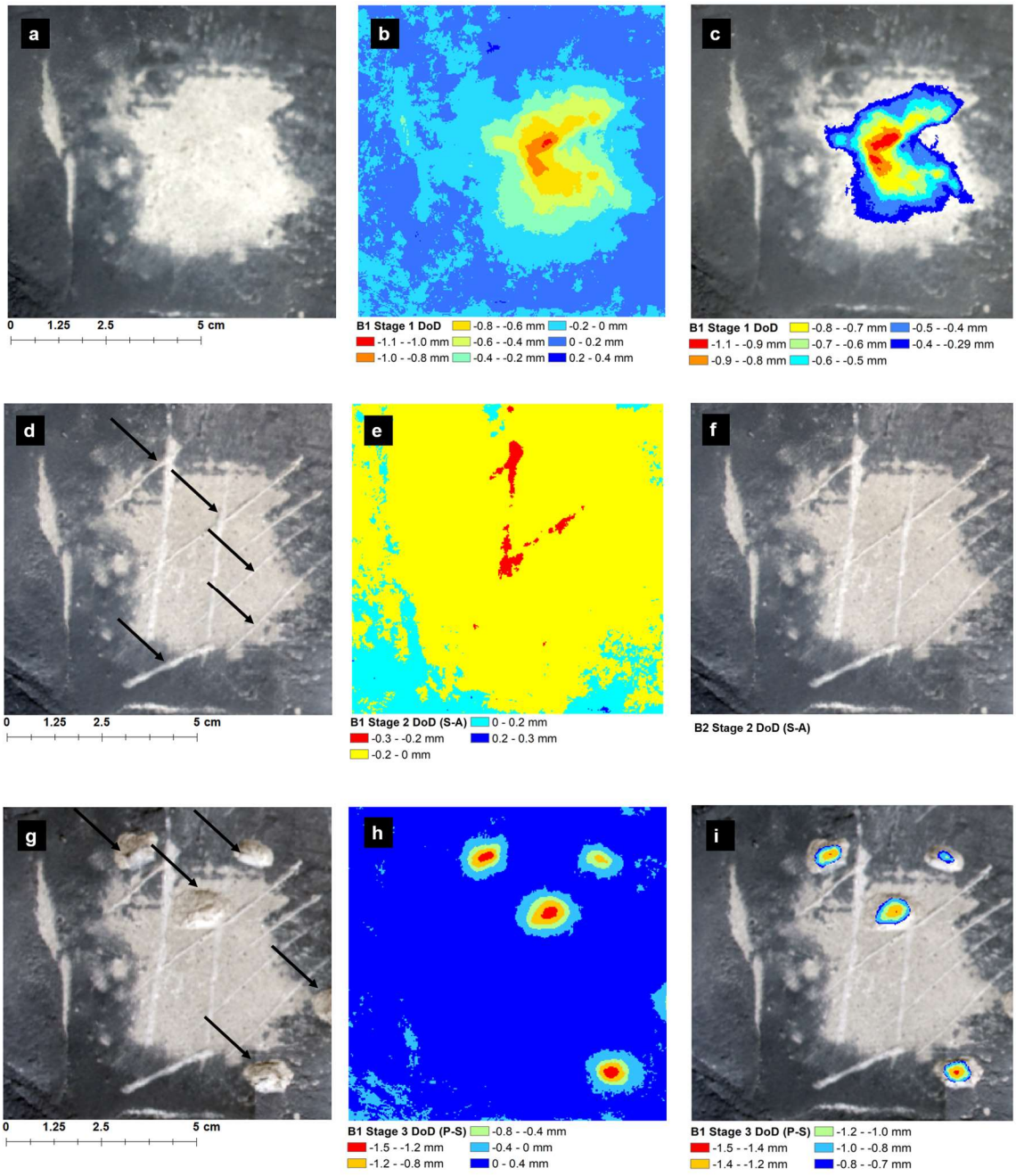


Figure 2. (a) B1 Stage 1 Orthophoto showing abraded surface of simulated platform surface (light grey). (b DoD for B1 Stage 1 before thresholding at LoD and the thresholded DoD (c. (d) B1 Stage 2 orthophoto showing location of scratches, (e) B1 Stage 2 DoD before thresholding and (f) DoD shown in E thresholded at LoD. (g) B1 Stage 3 orthophoto showing locations of percussions. (h) B1 Stage 2 DoD before thresholding at the LoD and the thresholded DoD (I).

The topographic profiles of erosion features on B1 for stages 1, 3 and 3 are shown in Figure 4. The profiles show the geometry (i.e. max depth and width) of erosion features on B1 which are similar in scale for all experimental blocks.

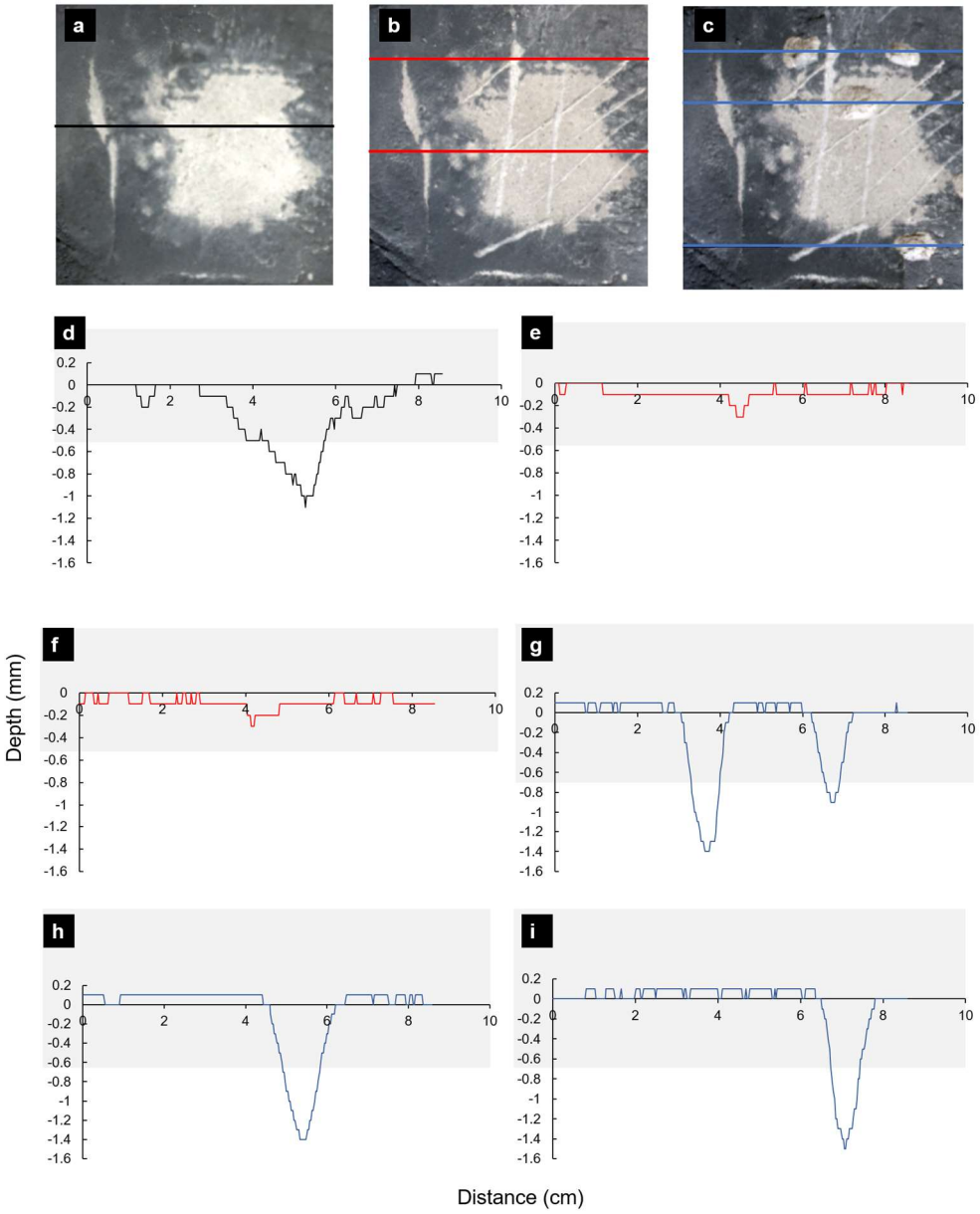


Figure 3. Location and topographic profiles of 'erosion' features on the simulated platform surface of B1 for (a) stage 1 (profile shown in d), (b) stage 2 (e and f, top and bottom respectively shown in b) and (c) stage 3 (g, h and i, top, middle and bottom profiles respectively shown in b). Grey shaded areas in d-i show the LoD.

A.1.3.3.2. Moderate rugosity platform (B2)

The results for experimental block B2 are shown in Figure 5 (a-i). The abraded surface area is indicated by lighter tone areas in Figure 5a. While this abrasion is visible in the DOD (Figure 5b), a significant component of the detected change occurred where no change was expected. This corresponds to 'shadow zones' associated with topographic highs. This result was not affected by thresholding at the LoD (Fig. 5c).

Scratches are evident in Figure 5d. Furthermore, the location of negative change corresponds well to the location of scratches (Fig. 5e). However, similar to B1, a small area of change is detected around the deepest scratch where none is expected (Fig. 5f). The impact percussion features are shown in (Fig. 5g). The maximum negative change in the surface elevation detected (i.e. the depth of percussions), was 3.35 mm, while the maximum positive change was 0.57 mm (h). Following thresholding, no positive change in elevation was detected (Fig. 5i) and negative change corresponded well to the actual location of percussions.

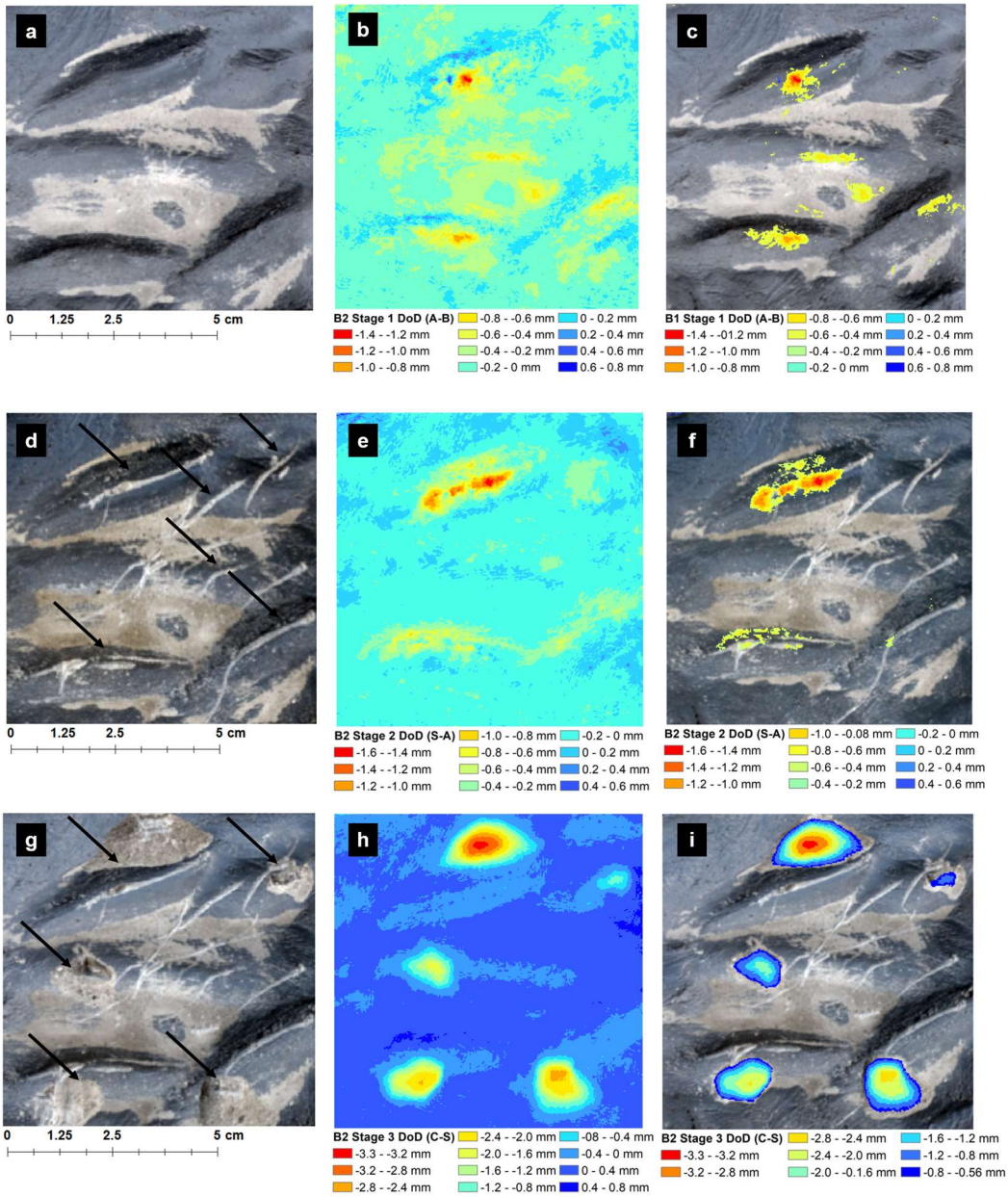


Figure 5. (a) B2 Stage 1 Orthophoto showing abraded area (light grey) of simulated platform surface, (b) B2 Stage 1 DoD before thresholding at LoD and the thresholded DoD (c). (d) B2 Stage 2 orthophoto showing scratched surface of B2 (black arrows). (e) B2 Stage 2 DoD before thresholding and (f) DoD shown in E thresholded at LoD. Note change detected in shadow zones in F (white arrow) where none is expected. (g) B2 Stage 3 orthophoto percussed surface. (h) DoD before thresholding at LoD and (i) DoD thresholded using calculated LoD.

To summarise, for a simulated platform with a moderate RI, only scratches and impacts were detected in the thresholded DoD.

A.1.3.3.3. Relatively high rugosity platform (B3)

The results for B3 are shown in Figure 6 (a-i). The light-toned areas in (a) indicate the abraded surface of the experimental block. In general, the maximum negative change detected (red and orange areas in b) correspond well to the abraded area. However, there are significant increases and decreases (>3 mm) in surface elevation where no change was expected. As above, the largest of these errors generally occurred in 'shadow zones'. Thresholding did not significantly improve the resultant DoD (i). For scratches (Fig. 6d)there was a reduction in surface elevation of 3.45 mm detected where no change was expected. As with the previous stage, these changes were observed to occur in shadow zones. Thresholding at the LoD did not improve the resultant DoD, and both increases and decreases were recorded where no change was expected (white arrows in i). The location percussions are shown in Figure 6g. Maximum negative change detected corresponded mainly to the location of percussion however negative change was recorded where none was expected (h). As before, an abnormal change occurred in shadow zones. Thresholding improved the resultant DoD (i), and the majority of negative change observed corresponded well to the location of percussions, except in some small areas (white arrows in i), associated with shadow zones. Maximum percussion depth was recorded at 5.43 mm.

To summarise, for a simulated platform with a relatively high RI, only impacts were reliably detected in the thresholded DoD. However, there were errors (larger than in B2) in the data, which are concentrated in topographic 'shadows'.

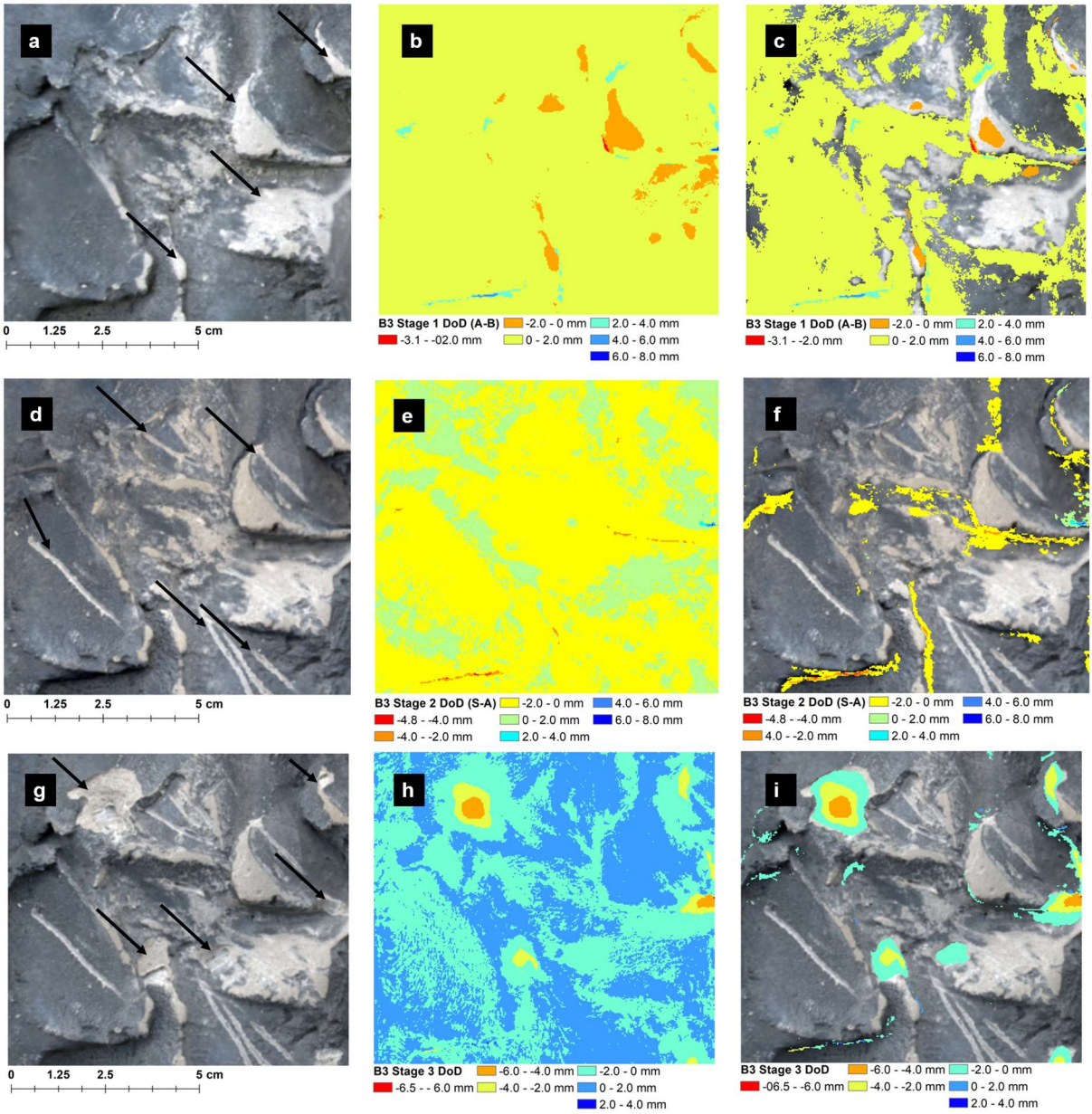


Figure 6. (a) B3 Stage 1 Orthophoto showing abraded surface area (light grey) of simulated platform surface. (b) DoD for B3 Stage 3 before thresholding and (c) DoD at LoD shown at 50% transparency overlain onto the orthophoto shown in A. Note significant geomorphic change detected in shadow zones (white arrows) where no change is expected. (d) B3 Stage 2 orthophoto showing scratched the surface of the simulated platform (black arrows), (e) DoD before thresholding and (f) DoD thresholded at LoD. As in C, note change higher than the LoD detected in shadow zones (white arrows) in f where no change is expected. (g) B3 Stage 3 orthophoto showing the location of percussions (black arrows), (h) B3 Stage 3 DoD before thresholding at LoD and (i) B3 Stage 3 DoD thresholded using calculated LoD. Note shadow zones (white arrows) where DoD indicates change, but none is expected.

A.1.3.4. Comparison of the T/MEM and SfM-MVS for measuring erosion on shore platforms

The T/MEM has, over decades, cemented its position as a low-cost method for measuring microscale erosion on shore platforms, while SfM-MVS is fast emerging as a valuable tool in the geomorphologists toolkit for the detection and measurement of geomorphic change at a range of scales. Both approaches have advantages and limitations, and the choice for use one method over another will depend on a number of factors such as cost, the ease of data collection, quality and value of the data required to answer a specific research question.

We have compared our experience of using the T/MEM to that of the SfM-MVS (based on the CRS and workflow used in this study) as a means for detecting geomorphic change on shore platforms under the following headings. We evaluated both techniques for; ease of data acquisition (including both installation and data collection), data processing, hardware costs, software costs, model resolution, accuracy and overall ease of use. Our reported installation, data collection and data processing times refer to a single measurement station. Hardware costs for the TMEM are based on initial outlay for SDS drill, drill bits, the TMEM platform and engineers gauge. Hardware for the SfM-MVS workflow described in this study refers to initial outlay for the manufacture of CRS and cost of the camera. Basic hardware costs (e.g. computer for processing) are not included. Overall ease of use for each method is based on our experience of data acquisition in the field (installation and collection) and data processing. An overall comparison is provided based on the above factors in addition to the value of the data obtained.

A comparison of the TMEM and the SfM-MVS approach as a means for detecting geomorphic change on shore platforms is shown in Figure 7. Both methods have clear advantages and disadvantages, and the comparison is intended to be a guide to assist researchers in choosing the most appropriate method for specific project deliverables.

A.1.3.4.1. Installation

To install a single T/MEM measurement station, three holes are drilled at the apex of an equilateral triangle and pins set into each hole with a marine grade epoxy resin. The time needed to install a single TMEM station varies between 20 and 80 minutes depending on

operator experience and rock hardness. For the workflow used in this study, the time needed to install a single bolt to mount the CRS will take approximately one-third of the time.

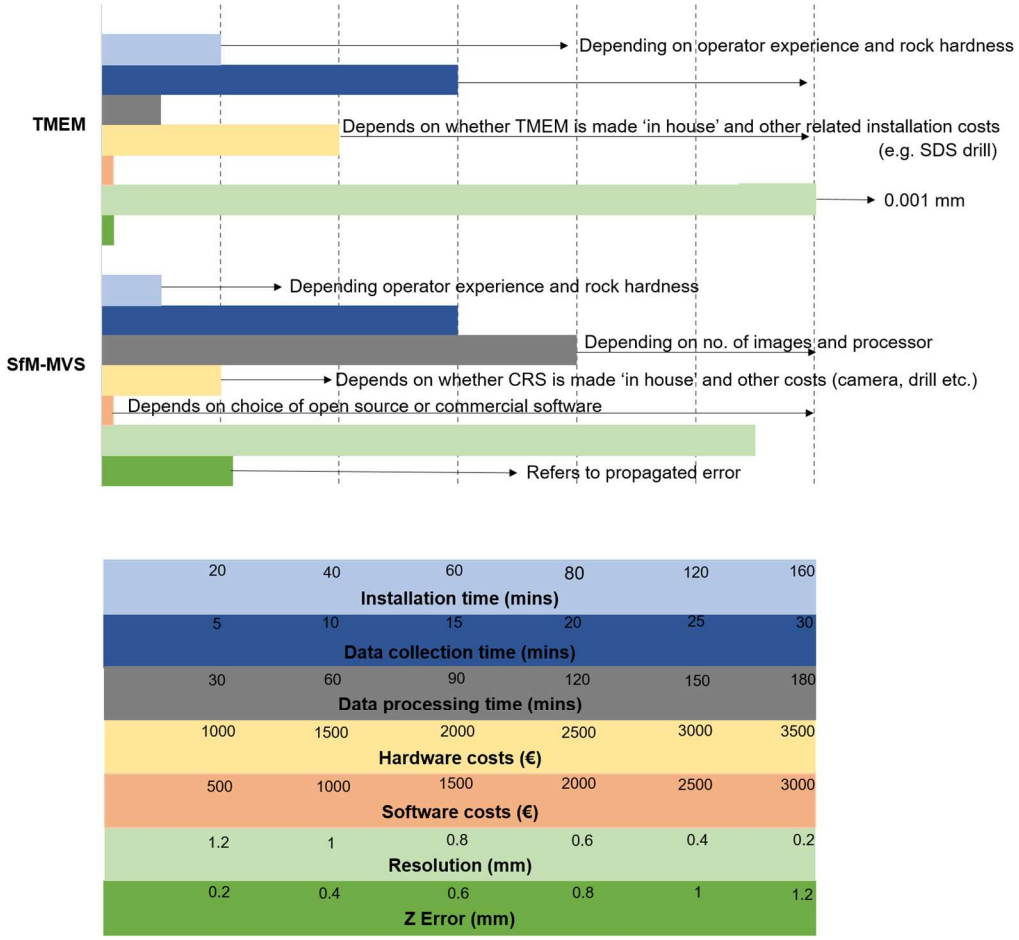


Figure *7.* Comparison of TMEM and the SfM – MVS workflow presented in this study under different categories. Values showed (cost, time etc) increase from left to right apart from 'Resolution' where decreasing values from left to right indicate increasing resolution.

A.1.3.4.2. Data collection

In our experience, the time needed to collect data from a single station (based on 100 measurements) using a TMEM varies between 15-30 mins (grey bar in figure 7). This will depend on whether the digital gauge being used has a USB memory, which automatically stores measurements as they are taken (e.g. Stephenson, 1997), or whether measurements

are recorded manually which increases the time required. In comparison, acquiring the 40-50 images as are necessary for SfM-MVS took approximately 15 minutes.

A.1.3.4.2. Data processing

The time required to process TMEM data will depend on the number of measurements collected and the method used to record data in the field, i.e. whether they are stored automatically (e.g. Stephenson, 1997) or manually. Automatic recording reduces the time needed to process data however manual processing can take up to 30 minutes per station (based on 100 measurements). Data processing takes significantly longer for SfM-MVS (2-3 hours per DEM) depending on a number of images and the processor used.

A.1.3.4.3. Hardware costs

The cost of a TMEM platform varies considerably depending on whether it is made in-house or commercially. In-house construction is considerably less (~€900 for materials and labour), while a commercial TMEM costs approximately €2000 (based on 2017 prices). The cost of the digital gauge also varies depending on the manufacturer, model, resolution, accuracy and Ingress Protection (IP) needed and range from €200-€500. Most rock types will also require an SDS drill with masonry bits which cost in the region of €600. The cost of the 316 stainless steel pins also varies depending on whether they are constructed 'in-house' or purchased commercially.

A.1.3.4.4. Software costs

Software cost for TMEM data processing is negligible while there are free open source software available for processing of images for SfM–MVS (e.g. Visual SfM). However, commercial packages such as Agisoft Photoscan can cost between €600 and €3500 depending on the licence type (e.g. Pro, Standard, Educational, Stand alone or Floating).

A.1.3.4.5. Resolution and Error

Depending on the digital gauge used, TMEM measurements can have a resolution of up to 0.001 mm with a reported measurement error of ± 0.005 mm (Sappington et al., 2007;

Gómez-Pujol et al., 2007). This resolution permits detection of change at a scale not currently achievable using the SfM MVS approach described here. Resolution for SfM-MVS (achieved in this study) was 0.3 mm per pixel. For some DEMs it was less than this (0.15 mm per pixel) however differencing of DEMs requires that pixel resolution be the same for both DEMs being compared. The CRS and SfM-MVS workflow employed for this study achieved maximum XY and Z RMSE errors of 0.2 mm and 0.5 mm respectively.

A.1.4. Discussion

The T/MEM has contributed significantly to our understanding of microscale erosion processes on shore platforms. Measurements of microscale platform erosion using a T/MEM are limited to repeated point measurements over time which provides a mean rate of surface downwearing within the measurement area for that measurement period with the dominant process(es) being inferred from the spatial and temporal variation in downwearing rates (Trenhaile, 2003). However, the method's inability to measure erosion at different scales was noted by Stephenson and Finlayson (2009) as a limitation and the authors advocated the introduction of new methods for measuring shore platform erosion at a range of scales. We have developed a CRS which can be quickly deployed by researchers in the field for detection of micro and meso-scale erosion on shore platforms using SfM-MVS Photogrammetry and a geomorphic change detection approach. The CRS described in this study permits rigorous georeferencing of DEMs derived using the SfM-MVS workflow. Although we demonstate the potential of the method on a simulated shore platform, the approach is not limited to shore platforms and has potential as a means for measuring bedrock erosion at similar scales in other environemnts (see Turowski and Cook, 2017: for examples).

We have demonstrated that SfM-MVS Photogrammetry can be used to reliably detect sub-mm changes on shore platforms where the platform surface has a low RI. This approach successfully detected 0.3 mm downwearing of the simulated platform surface of B1 caused by abrasion of the surface. While we were also able to identify shallow scratches on the surface of the experimental block, applying the LoD obscured this finding due to the shallow depth of scratches (< 0.3 mm). However, we were able to detect loss of mm-cm sized rock effectively. This demonstrates that our approach offers a method for cross scalar analysis of erosion on shore platforms, offering a much-needed means to examine relationships between micro and meso-scale processes of shore platform erosion and morphologies.

Our results indicate that as RI increases, the reliability of SfM-MVS for detection of fine scale (sub-mm) erosion is reduced due to increased topographic complexity. Despite areas of reduced elevation, i.e. erosion, aligning well with areas where the surface had been abraded, there were areas of change where clearly none was expected. Despite this, our approach successfully detected the loss of rock fragments on the simulated platform surface of B2 (higher RI) once the LoD was applied. Similarly, for B3, which had the highest RI, fine-scale erosion and scratches were not detected reliably, and while the loss of rock fragments was detected, the effect of complex topography in creating shadows zones produced abnormal change. The orthophotos were important in this regard as they provided visual validation of the models and highlighted the influence of shadow zones in introducing error into the models. The additional uncertainty introduced into the models due to the surface complexity was not accounted for using the LoD approach. This resulted in abnormal change detection associated with meso scale (> 1mm) slopes and troughs. Indeed, this is a well recognised limitation of SfM MVS approach to geomorphic change detection, and appropriate solutions (e.g. precision mapping) have been proposed. While the strong influence of surface complexity may be considered a limitation, it should be noted that the T/MEM is largely restricted to measurements of downwearing on small surface areas with low topographic complexity. As such, it does not exclude this approach as an alternative for measuring change on this type of surface.

Precision mapping (James et al., 2017c) offers a potential approach to address this as there is an opportunity to increase confidence in the accuracy of point clouds derived for more complex platform morphologies. While the LoD assumes a global uniform distribution of error, precision mapping explicitly accounts for the spatially variable precision characteristic of photo-based surveys (James et al., 2017c) and has been demonstrated to improve change detection in areas with complex topography. Future work will test this approach.

Another possible contributor to the erroneous results may be variable lighting conditions and specular reflection. In a study by Guidi et al. (2014b) demonstrated that the use of polarising filter and digital pre-processing with HDR imaging could help to homogenise brightness over the subject subsequently improving image matching We recommend these approaches to overcome this problem.

This study and our experience in the field using a TMEM suggest that the time required for data collection (installation and acquisition) collection is shorter using an SfM-MVS

approach compared to the TMEM. The requirement of just one bolt per measurement site for the CRS described here, compared to three bolts per measurement site for the TMEM, reduces the time needed for initial installation in the field. Add to that the time required to collect images for the SfM-MVS workflow compared to the time needed to obtain 100 TMEM measurements, and SfM–MVS has notable advantages. This reduced installation and data acquisition time are of particular worth for shore platforms with meso to macro tidal ranges, where time in the intertidal zone is limited to, at most, a couple of hours either side of low tide. For larger platforms, where a number of measurement stations are located in the intertidal zone, time is a limiting factor, and methods which allow rapid installation data collection are preferable. Regarding data processing, the time required depends on the gauge used to collect the TMEM data, i.e. manual or automatic and the desired output (point measurements or 3D surface). Regardless, the processing time required for SfM-MVS is significantly higher (2-3 hours per DEM generated). Nevertheless, batch processing options in Photoscan mean that DEM generation process/steps can be automated and the user time on the computer is reduced. With respect to image acquisition for SfM-MVS, we used a Nikon D5500 and had included this in our overall analysis however expensive cameras are not a prerequisite. For example, in a recent experimental study of surface features in sand caused by sublimation of CO_2 ice, of a similar scale to this study, Mc Keown et al. (2017a) used an iPhone to acquire images and utilised the same CRS developed by Verma and Bourke (2018) to scale and reference DEMs, achieving similar accuracy and resolution (<1 mm).

It is important to note that the resolution of the SfM MVS approach, while capable of detecting sub-mm scale change, is still 2 orders of magnitude lower than that achievable with a T/MEM. The T/MEM offers considerable resolution and accuracy for measurements of very small surface changes, which is particularly useful for measuring very slow rates of downwearing and detection of very small changes due to processes which operate at much finer spatial scales such as platform swelling (e.g. Stephenson and Kirk, 2001; Gómez-Pujol et al., 2007; Trenhaile, 2006; Hemmingsen et al., 2007; Porter and Trenhaile, 2007). For faster-eroding rocks, the precision obtainable using a T/MEM is not required (Stephenson and Finlayson, 2009). While the highest common resolution of the DEMs produced for this study were 0.3 mm/pixel, this is demonstrated to be sufficient for measuring micro-scale and meso scale erosion on surfaces with low RI and loss of rock fragments on more topographically complex surfaces.

In terms of data output, the TMEM produces a series of surface point measurements. These can be compared directly to point measurements made from previous surveys or plotted as a digital elevation model for 3D visualisation of the surface at the bolt site (e.g. Sappington et al., 2007; Stephenson, 1997). The spatial and temporal variation in downwearing rates can be used to infer the efficacy of erosion processes. In this, we suggest that SfM–MVS has a clear and important geomorphic advantage. The technique produces point clouds and DEMs which can be used to identify and classify surface features as well as detect geomorphic change at different scales. This added value in the approach is significant. Orthophotograph mosaics offer additional means for validating meso scale changes on the rock surface and identifying erosion styles.

A.1.5. Conclusions

1. This study demonstrates that SfM can be used to detect sub-mm changes due to erosion on shore platforms. However, we find that as the complexity of the rock surface topography increases, the reliability of SfM to detect sub-mm changes decreases. We note that the application of TMEM is also limited to relatively planar surfaces. Future work will test the precision mapping approach of James et al. (2017c) to determine the spatial distribution of error and increase confidence in results on more topographically complex platform surfaces.

2. While TMEM has higher resolution and accuracy compared to SfM, if offers a limited number of point measurments over a small area. In comparison, SfM produces 3D topographic data from dense point clouds and DEMs which can be used to identify, classify and quantify different styles and scales of erosion.

3. In this study, we have provided a detailed comparison between TMEM and SfM methods to measure change due to erosion of rock surfaces in the coastal environment. The approach is not limited to shore platforms and has potential as a means for measuring erosion at similar scales in a range of environments.

References

ANDREWS, C. & WILLIAMS, R. B. 2000. Limpet erosion of chalk shore platforms in southeast England. *Earth Surface Processes and Landforms,* 25**,** 1371-1381.

BALAGUER-PUIG, M., MARQUÉS-MATEU, Á., LERMA, J. L. & IBÁÑEZ-ASENSIO, S. 2017. Estimation of small-scale soil erosion in laboratory experiments with Structure from Motion photogrammetry. *Geomorphology*.

BOURKE, M. C., BREARLEY, J. A., HAAS, R. & VILES, H. A. 2007. *A photographic atlas of rock breakdown features in geomorphic environments*, Planetary Science Institute.

BRASINGTON, J., LANGHAM, J. & RUMSBY, B. 2003. Methodological sensitivity of morphometric estimates of coarse fluvial sediment transport. *Geomorphology,* 53**,** 299-316.

BRASINGTON, J., RUMSBY, B. & MCVEY, R. 2000. Monitoring and modelling morphological change in a braided gravel-bed river using high resolution GPS-based survey. *Earth Surface Processes and Landforms,* 25**,** 973-990.

BRUNIER, G., FLEURY, J., ANTHONY, E. J., GARDEL, A. & DUSSOUILLEZ, P. 2016a. Close-range airborne Structure-from-Motion Photogrammetry for high-resolution beach morphometric surveys: Examples from an embayed rotating beach. *Geomorphology,* 261**,** 76-88.

BRUNIER, G., FLEURY, J., ANTHONY, E. J., POTHIN, V., VELLA, C., DUSSOUILLEZ, P., GARDEL, A. & MICHAUD, E. 2016b. Structure-from-Motion photogrammetry for high-resolution coastal and fluvial geomorphic surveys. *Géomorphologie: relief, processus, environnement,* 22**,** 147-161.

CARBONNEAU, P. E., LANE, S. N. & BERGERON, N. E. 2004. Catchment-scale mapping of surface grain size in gravel bed rivers using airborne digital imagery. *Water resources research,* 40.

CARRIVICK, J. L., SMITH, M. W. & QUINCEY, D. J. 2016. *Structure from Motion in the Geosciences*, John Wiley & Sons.

CHANDLER, J. 1999. Effective application of automated digital photogrammetry for geomorphological research. *Earth Surface Processes and Landforms,* 24**,** 51-63.

CHANDLER, J., ASHMORE, P., PAOLA, C., GOOCH, M. & VARKARIS, F. 2002. Monitoring river-channel change using terrestrial oblique digital imagery and automated digital photogrammetry. *Annals of the Association of American Geographers,* 92**,** 631-644.

CULLEN, N. D. & BOURKE, M. C. 2018. Clast abrasion of a rock shore platform on the Atlantic coast of Ireland. *Earth Surface Processes and Landforms,* 43 (12) 2627-2641.

DAHL, A. L. 1973. Surface area in ecological analysis: quantification of benthic coral-reef algae. *Marine Biology,* 23**,** 239-249.

ELLIS, N. 1986. *Morphology, process and rates of denudation on the chalk shore platform of East Sussex.* Brighton Polytechnic, PhD Thesis.

FONSTAD, M. A., DIETRICH, J. T., COURVILLE, B. C., JENSEN, J. L. & CARBONNEAU, P. E. 2013. Topographic structure from motion: a new development in photogrammetric measurement. *Earth Surface Processes and Landforms,* 38**,** 421-430.

FOOTE, Y., PLESSIS, E., ROBINSON, D., HÉNAFF, A. & COSTA, S. 2006. Rates and patterns of downwearing of chalk shore platforms of the Channel: comparisons between France and England. *Zeitschrift Fur Geomorphologie,* 144**,** 93-115.

FURUKAWA, Y., CURLESS, B., SEITZ, S. M. & SZELISKI, R. Towards internet-scale multi-view stereo. Computer Vision and Pattern Recognition (CVPR), 2010 IEEE Conference on, 2010. IEEE, 1434-1441.

GÓMEZ-GUTIÉRREZ, Á., SCHNABEL, S., BERENGUER-SEMPERE, F., LAVADO-CONTADOR, F. & RUBIO-DELGADO, J. 2014. Using 3D photo-reconstruction methods to estimate gully headcut erosion. *Catena,* 120**,** 91-101.

GÓMEZ-PUJOL, L., STEPHENSON, W. J. & FORNÓS, J. J. 2007. Two-hourly surface change on supra-tidal rock (Marengo, Victoria, Australia). *Earth Surface Processes and Landforms,* 32**,** 1-12.

GUIDI, G., GONIZZI, S. & MICOLI, L. Image pre-processing for optimizing automated photogrammetry performances. ISPRS Technical Commission V Symposium, 2014. ISPRS, 145-152.

HANNA, F. 1966. A technique for measuring the rate of erosion of cave passages. *Proceedings University of Bristol Spelaeology Society.*

HEMMINGSEN, S. A., EIKAAS, H. S. & HEMMINGSEN, M. A. 2007. The influence of seasonal and local weather conditions on rock surface changes on the shore platform at Kaikoura Peninsula, South Island, New Zealand. *Geomorphology,* 87**,** 239-249.

JAMES, M. R., ROBSON, S. & SMITH, M. W. 2017. 3-D uncertainty-based topographic change detection with structure-from-motion photogrammetry: precision maps for ground control and directly georeferenced surveys. *Earth Surface Processes and Landforms*.

JAVERNICK, L., BRASINGTON, J. & CARUSO, B. 2014. Modeling the topography of shallow braided rivers using Structure-from-Motion photogrammetry. *Geomorphology,* 213**,** 166-182.

KAISER, A., NEUGIRG, F., ROCK, G., MÜLLER, C., HAAS, F., RIES, J. & SCHMIDT, J. 2014. Small-scale surface reconstruction and volume calculation of soil erosion in complex Moroccan gully morphology using structure from motion. *Remote Sensing,* 6**,** 7050-7080.

LANE, S. N., WESTAWAY, R. M. & MURRAY HICKS, D. 2003. Estimation of erosion and deposition volumes in a large, gravel-bed, braided river using synoptic remote sensing. *Earth Surface Processes and Landforms,* 28**,** 249-271.

LIM, M., ROSSER, N. J., ALLISON, R. J. & PETLEY, D. N. 2010. Erosional processes in the hard rock coastal cliffs at Staithes, North Yorkshire. *Geomorphology,* 114**,** 12-21.

LOWE, D. G. 2004. Distinctive image features from scale-invariant keypoints. *International journal of computer vision,* 60**,** 91-110.

MC KEOWN, L., BOURKE, M. & MCELWAINE, J. 2017. Experiments On Sublimating Carbon Dioxide Ice And Implications For Contemporary Surface Processes On Mars. *Scientific reports,* 7**,** 14181.

MICHELETTI, N., CHANDLER, J. H. & LANE, S. N. 2015a. Investigating the geomorphological potential of freely available and accessible Structure-from-Motion photogrammetry using a smartphone. *Earth Surface Processes and Landforms,* 40**,** 473-486.

MICHELETTI, N., CHANDLER, J. H. & LANE, S. N. 2015b. Structure from Motion (SfM) Photogrammetry. *Geomorphlogical Techniques.* Loondon: British Society for Geomorphology.

MOSES, C., ROBINSON, D. & BARLOW, J. 2014. Methods for measuring rock surface weathering and erosion: a critical review. *Earth-Science Reviews,* 135**,** 141-161.

ÖZYEŞIL, O., VORONINSKI, V., BASRI, R. & SINGER, A. 2017. A survey of structure from motion*. *Acta Numerica,* 26**,** 305-364.

PORTER, N. J. & TRENHAILE, A. 2007. Short-term rock surface expansion and contraction in the intertidal zone. *Earth Surface Processes and Landforms,* 32**,** 1379-1397.

RISK, M. J. 1972. Fish diversity on a coral reef in the Virgin Islands. *Atoll Research Bulletin.* Washington,: The Smithsonian Institution,.

SAPPINGTON, J. M., LONGSHORE, K. M. & THOMPSON, D. B. J. T. J. O. W. M. 2007. Quantifying landscape ruggedness for animal habitat analysis: a case study using bighorn sheep in the Mojave Desert. 71**,** 1419-1426.

SMITH, M., CARRIVICK, J. & QUINCEY, D. 2016. Structure from motion photogrammetry in physical geography. *Progress in Physical Geography,* 40**,** 247-275.

SNAVELY, N. 2006. Bundler: SfM for unordered image collections. GitHub.

SPATE, A., JENNINGS, J., SMITH, D. & GREENAWAY, M. 1985. The micro-erosion meter: use and limitations. *Earth Surface Processes and Landforms,* 10**,** 427-440.

STEPHENSON, W. & FINLAYSON, B. 2009. Measuring erosion with the micro-erosion meter—contributions to understanding landform evolution. *Earth-Science Reviews,* 95**,** 53-62.

STEPHENSON, W., KIRK, R., HEMMINGSEN, S. & HEMMINGSEN, M. 2010. Decadal scale micro erosion rates on shore platforms. *Geomorphology,* 114**,** 22-29.

STEPHENSON, W. & NAYLOR, L. 2011. Within site geological contingency and its effect on rock coast erosion. *Journal of Coastal Research,* 61**,** 831-835.

STEPHENSON, W. J. 1997. Improving the traversing micro-erosion meter. *Journal of Coastal Research***,** 236-241.

STEPHENSON, W. J. & KIRK, R. M. 1996. Measuring erosion rates using the micro-erosion meter: 20 years of data from shore platforms, Kaikoura Peninsula, South Island, New Zealand. *Marine Geology,* 131**,** 209-218.

STEPHENSON, W. J. & KIRK, R. M. 2001. Surface swelling of coastal bedrock on inter-tidal shore platforms, Kaikoura Peninsula, South Island, New Zealand. *Geomorphology,* 41**,** 5-21.

SWANTESSON, J., MOSES, C., BERG, G. & JANSSON, K. M. 2006. Methods for measuring shoreplatform micro-erosion; a comparison of the micro-erosion meter and the laser scanner. *Zeitschrift fur Geomorphologie Supplementband,* 144**,** 1-17.

THOENI, K., GIACOMINI, A., MURTAGH, R. & KNIEST, E. 2014. A comparison of multi-view 3D reconstruction of a rock wall using several cameras and a laser scanner. *The International Archives of Photogrammetry, Remote Sensing and Spatial Information Sciences,* 40**,** 573.

THORNBUSH, M. J. 2012. A site-specific index based on weathering forms visible in Central Oxford, UK. *Geosciences,* 2**,** 277-297.

TRENHAILE, A. 2006. Tidal wetting and drying on shore platforms: an experimental study of surface expansion and contraction. *Geomorphology,* 76**,** 316-331.

TRENHAILE, A. S. 2003. Modeling shore platforms: present status and future developments. *In:* LAKHAN, V. C. (ed.) *Advances in Coastal Modeling. Amsterdam: Elsevier.* Elsevier Science B.V. .

TRUDGILL, S. 1975. Measurement of erosional weight loss of rock tablets. *British Geomorphological Research Group Technical Bulletin.*

TRUDGILL, S., HIGH, C. & HANNA, F. 1981. Improvements to the micro-erosion meter. *British Geomorphological Research Group Technical Bulletin.*

TUROWSKI, J. M. & COOK, K. L. 2017. Field techniques for measuring bedrock erosion and denudation. *Earth Surface Processes and Landforms,* 42**,** 109-127.

VERMA, A. K. & BOURKE, M. C. A Structure from Motion photogrammetry-based method to generate sub-millimetre resolution Digital Elevation Models for investigating rock breakdown features. *Earth Surf. Dynam. Discuss., https://doi.org/10.5194/esurf-2018-53, in review, 2018.* .

VILES, H. A. 2001. Scale issues in weathering studies. *Geomorphology,* 41**,** 63-72.

WALKDEN, M. & HALL, J. 2005. A predictive mesoscale model of the erosion and profile development of soft rock shores. *Coastal Engineering,* 52**,** 535-563.

WARKE, P. A. & MCKINLEY, J. 2011. Scale issues in geomorphology. *Geomorphology,* 130**,** 1-4.

WESTOBY, M., BRASINGTON, J., GLASSER, N., HAMBREY, M. & REYNOLDS, J. 2012. 'Structure-from-Motion'photogrammetry: A low-cost, effective tool for geoscience applications. *Geomorphology,* 179**,** 300-314.

WHEATON, J. M., BRASINGTON, J., DARBY, S. E. & SEAR, D. A. 2010. Accounting for uncertainty in DEMs from repeat topographic surveys: improved sediment budgets. *Earth Surface Processes and Landforms,* 35**,** 136-156.

WILLIAMS, R. 2012. DEMs of difference. *Geomorphological Techniques.* Online ed. London, UK: British Society for Geomorphology.

Appendix 2. Supplementary material for chapter 2

A.2.1. Grain size distribution plots

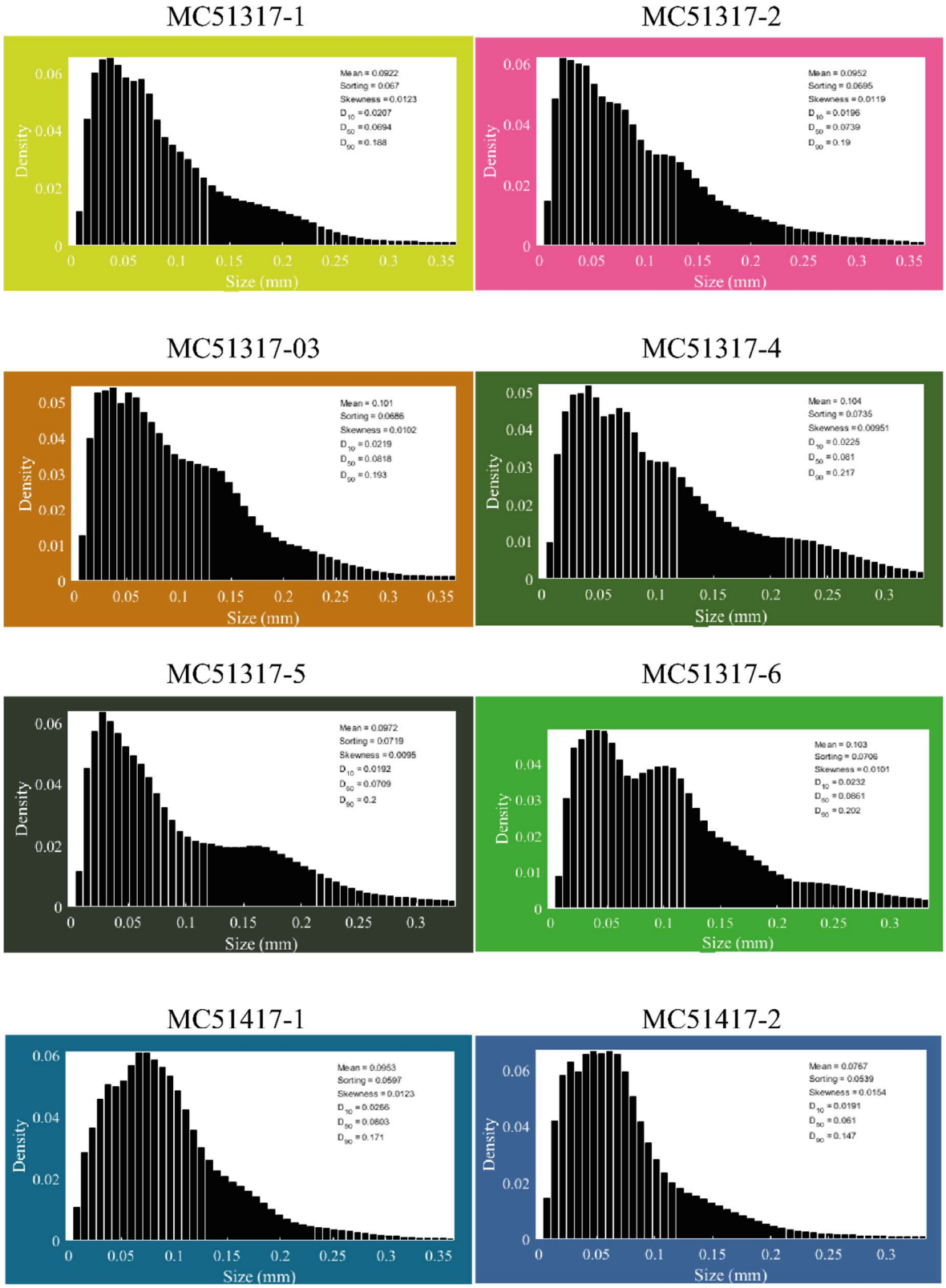


Fig A.2.1. Moenkopi Sandstone

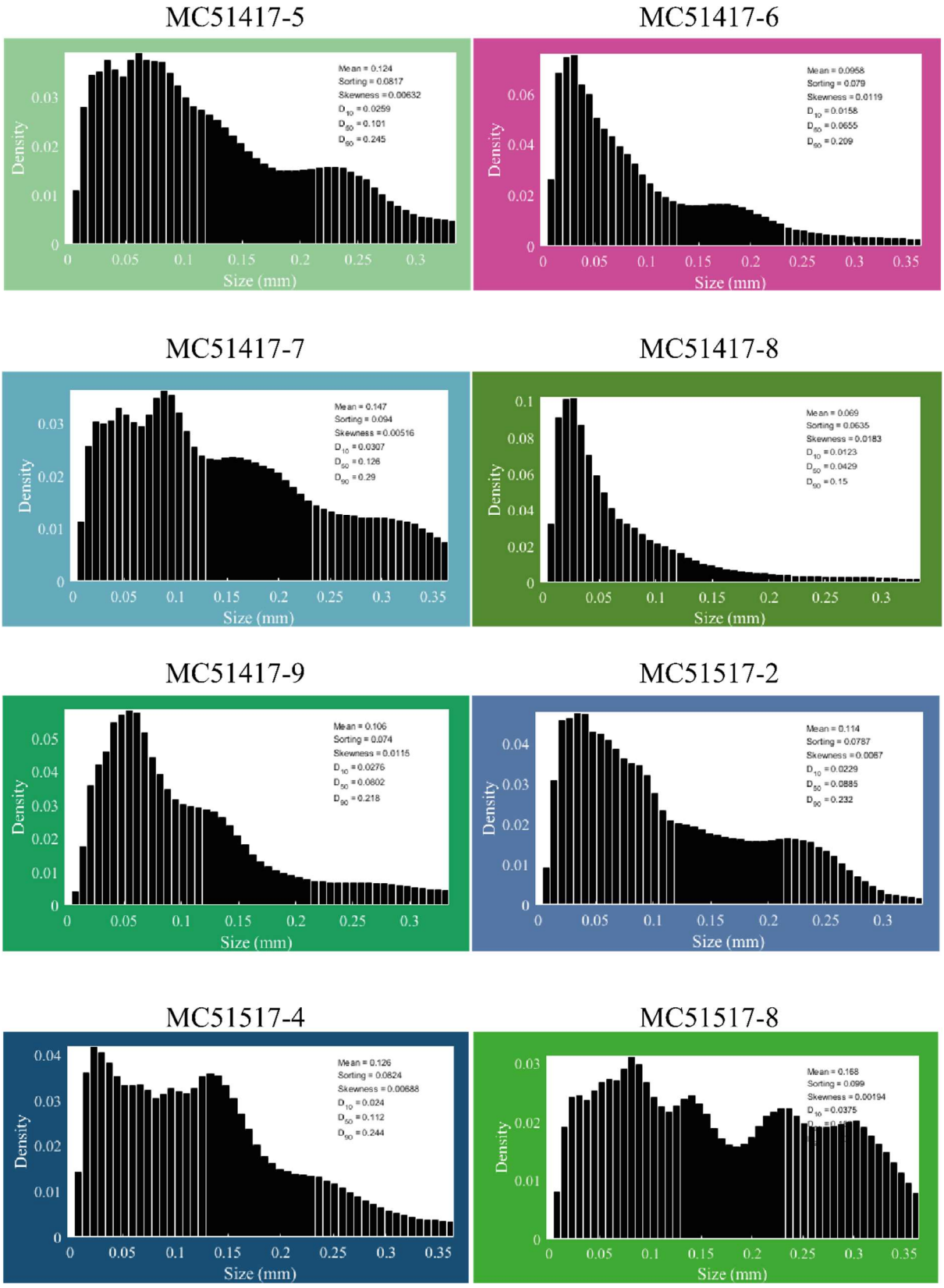


Fig A.2.2. Coconino Sandstone

A.2.2. Powder X-ray diffraction analysis

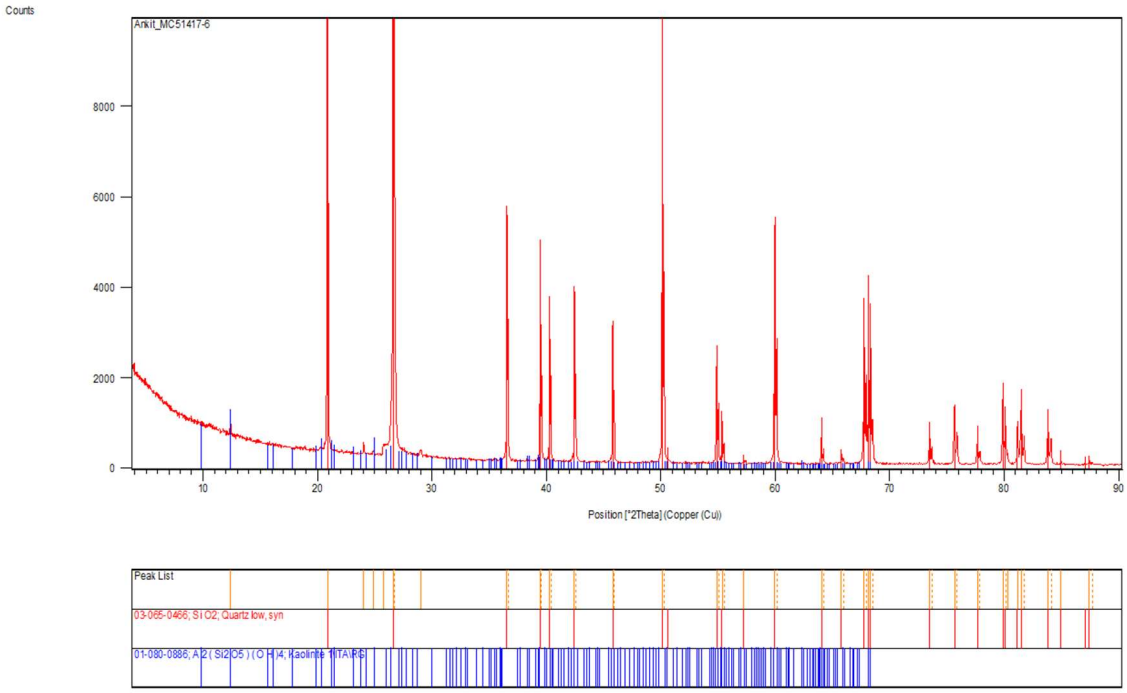


Fig A.2.3. Coconino Sandstone sample - MC51417-6

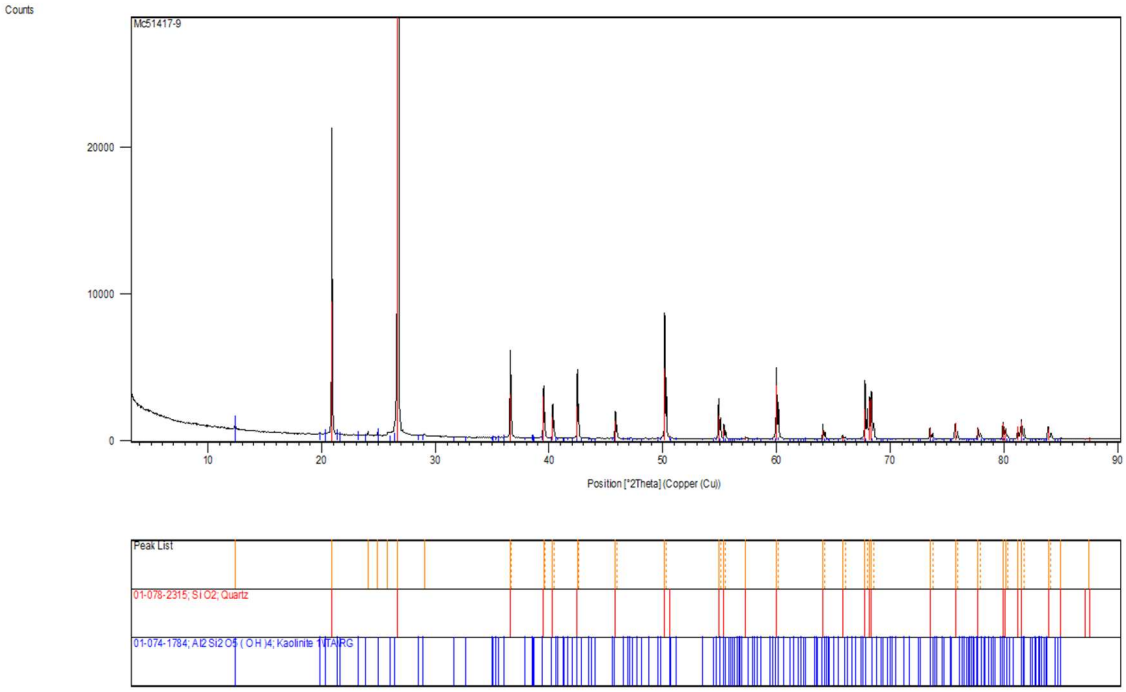


Fig A.2.4. Coconino Sandstone sample - MC51417-9

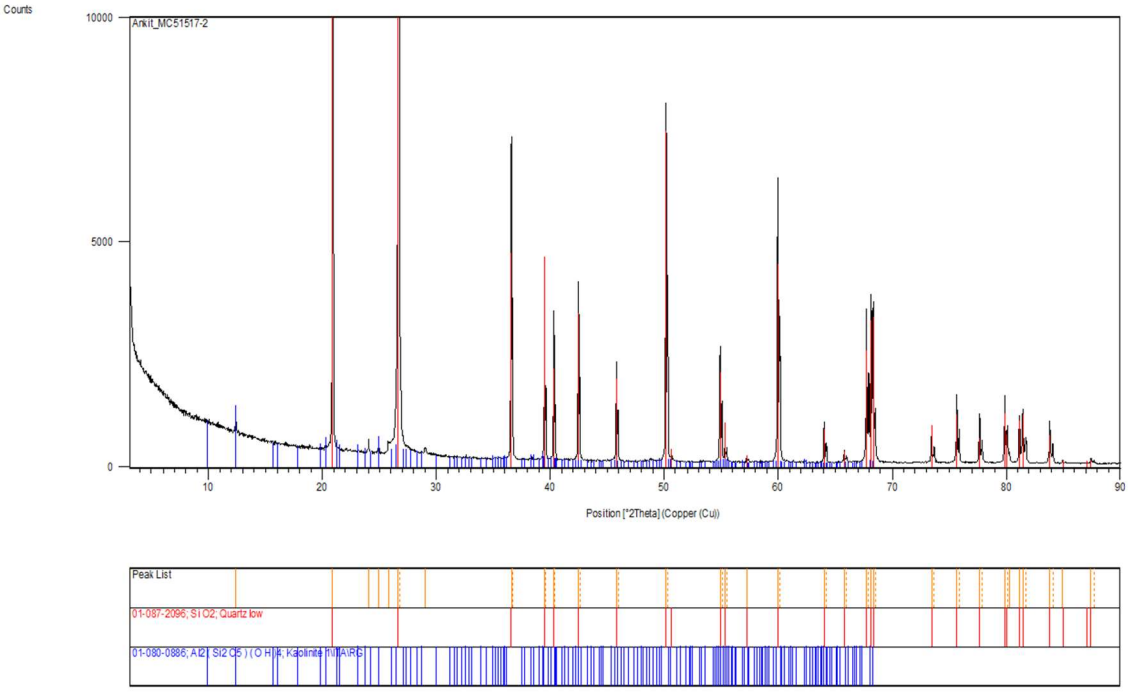


Fig A.2.5. Coconino Sandstone sample - MC51517-2

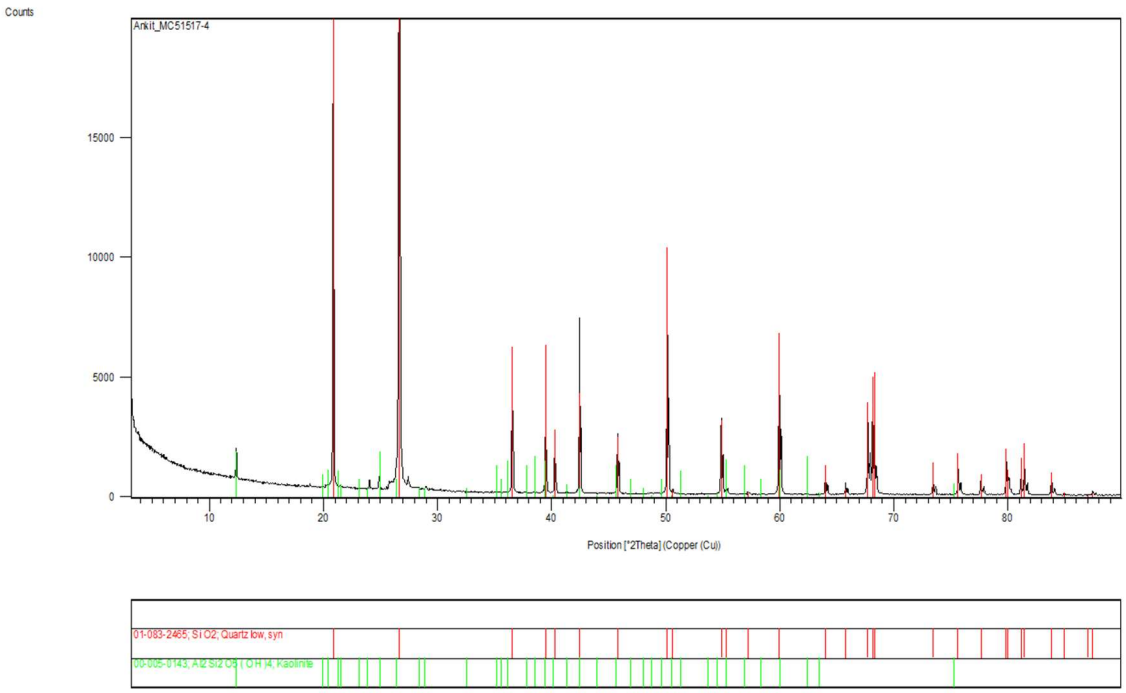


Fig A.2.6. Coconino Sandstone sample - MC51517-4

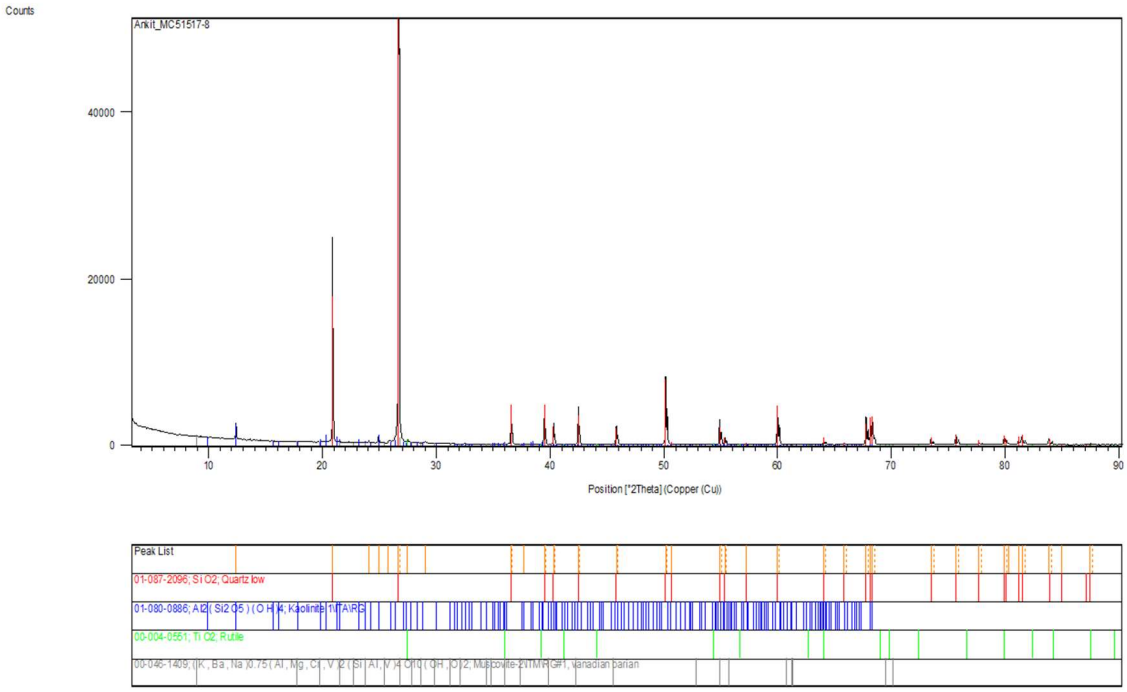


Fig A.2.7. Coconino Sandstone sample - MC51517-8

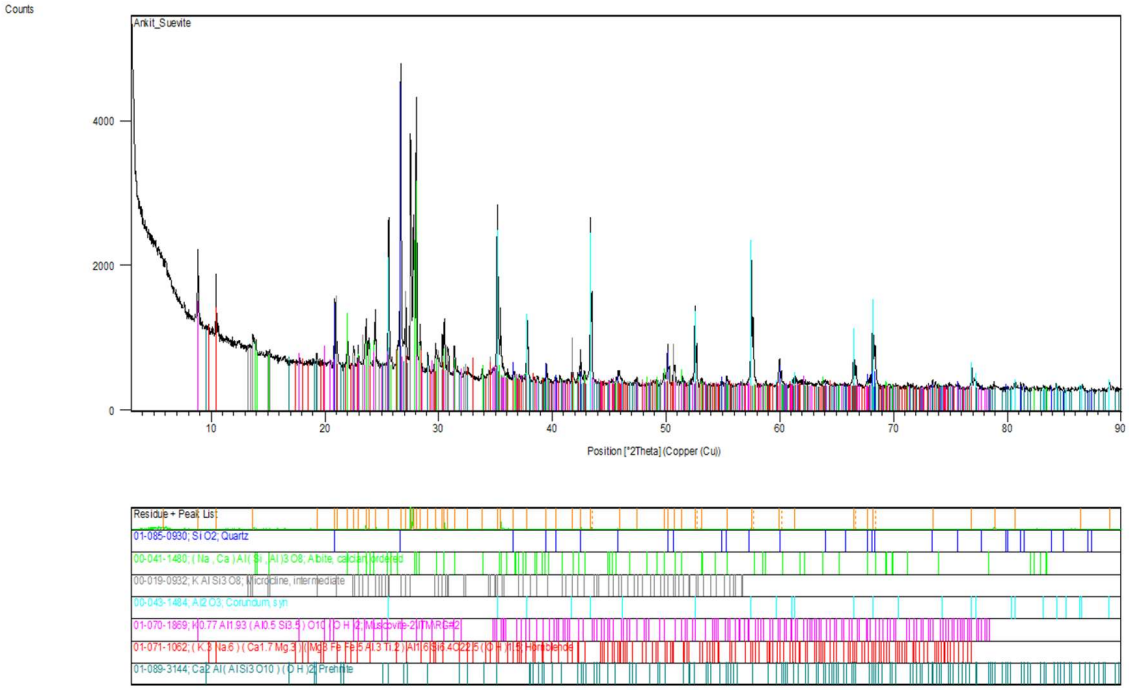


Fig A.2.8. Suevite sample

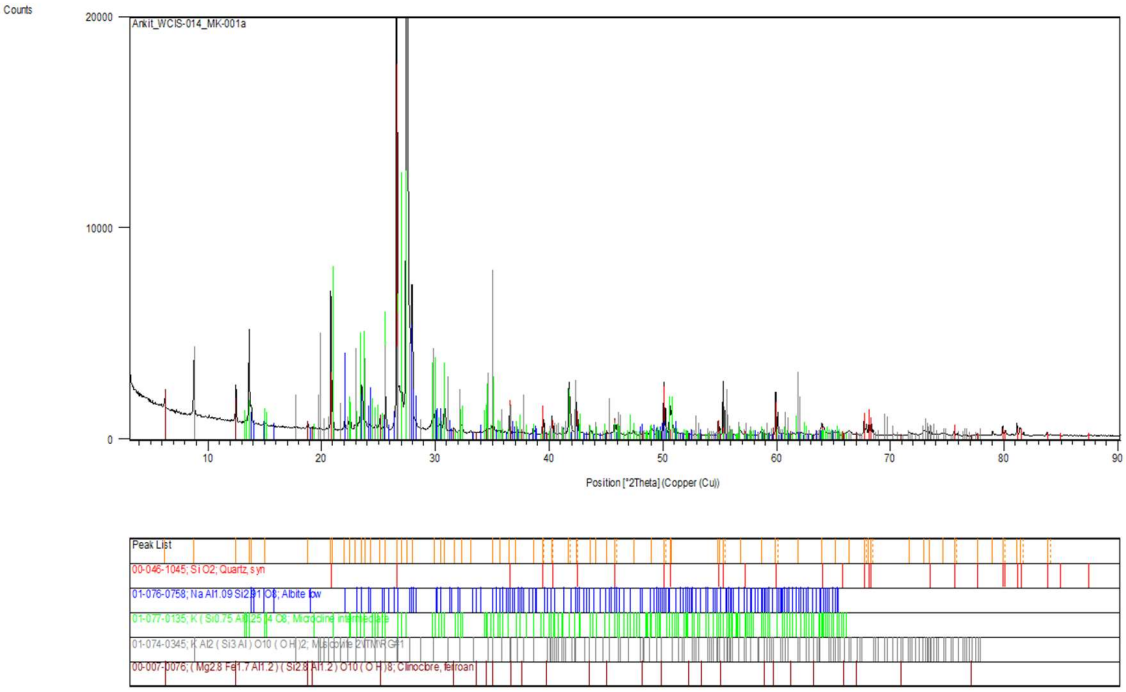


Fig A.2.9. Granite sample - WCIS-14 MK-001a

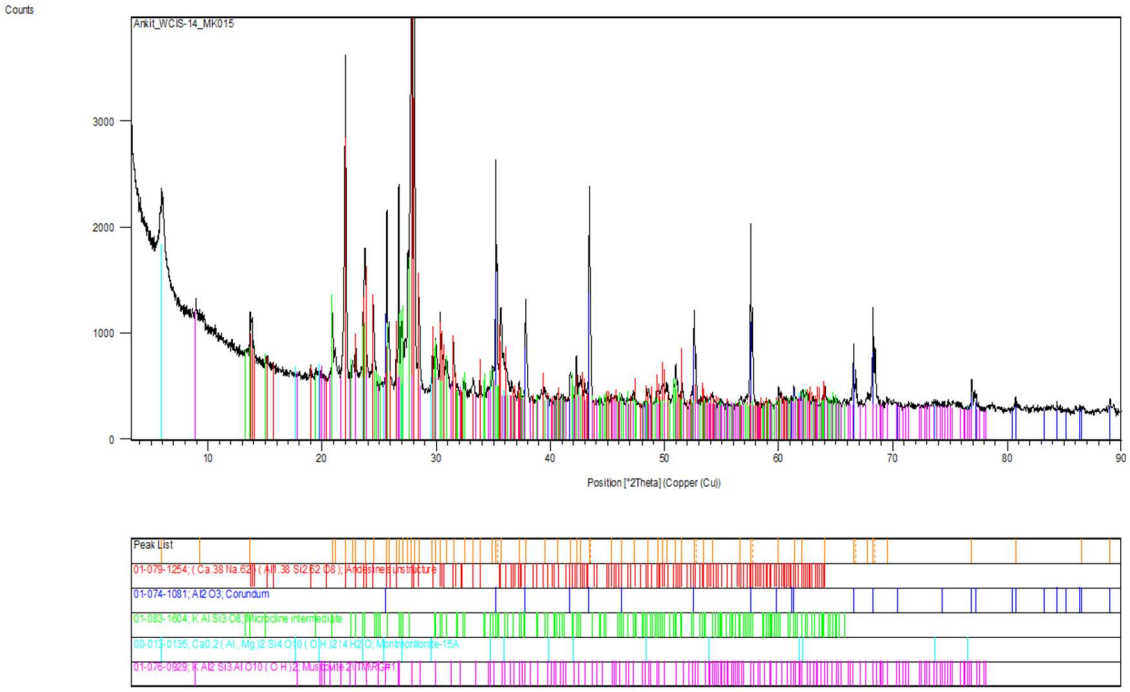


Fig A.2.11. Clast poor fine-grained impact melt rock sample - WCIS-14 MK-015

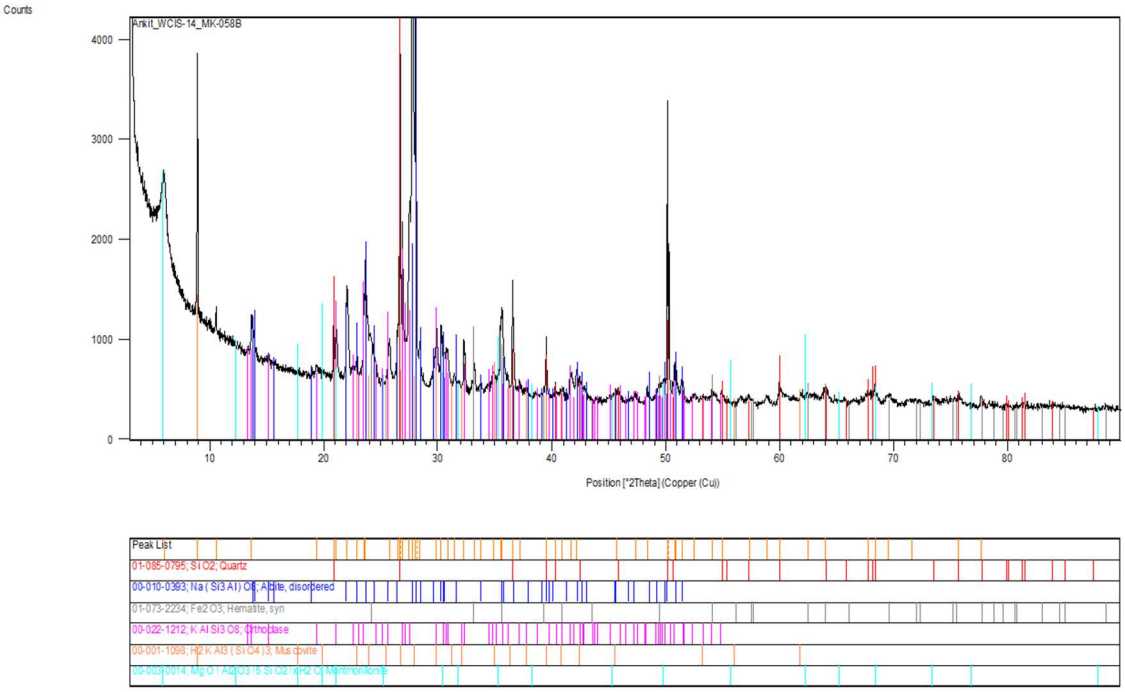


Fig A.2.12. Lithic breccia sample - WCIS-14 MK-058B

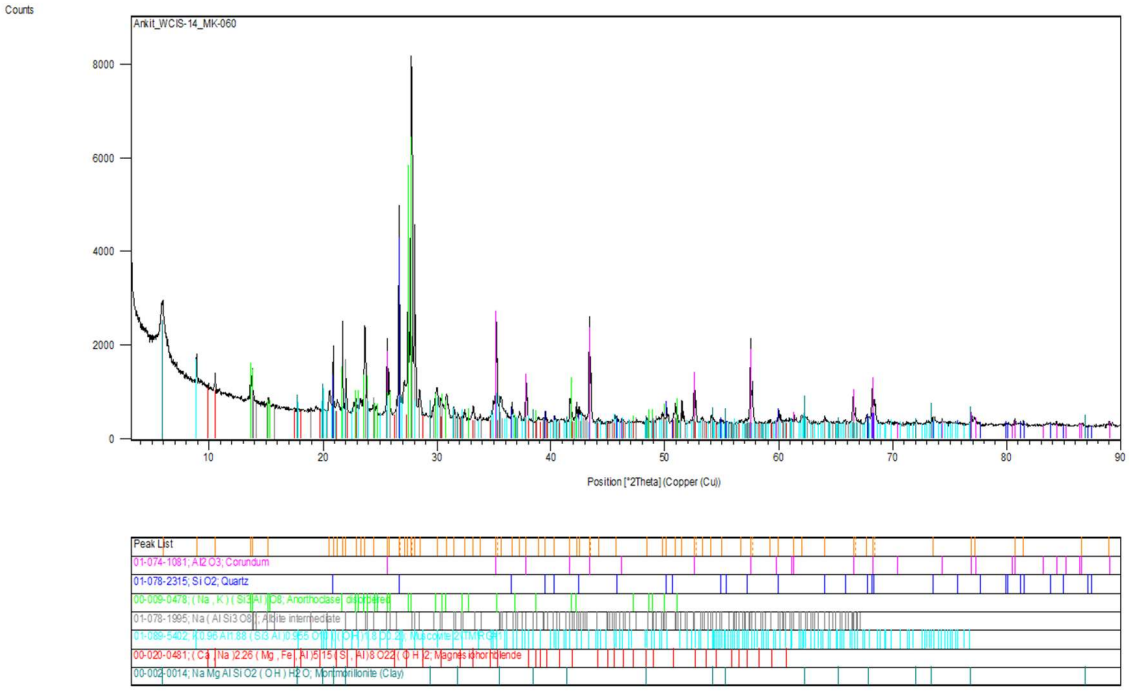


Fig A.2.13. Clast free impact melt rock sample - WCIS-14 MK-060

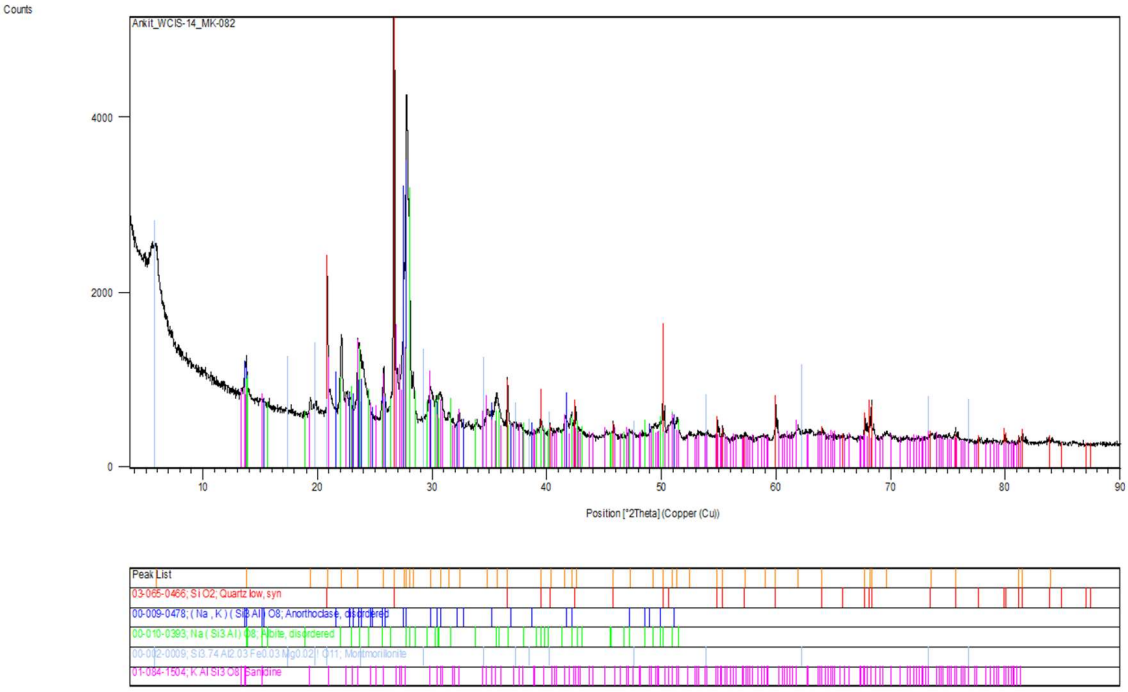


Fig A.2.14. Clast poor fine grained impact-melt rock sample - WCIS-14 MK-082

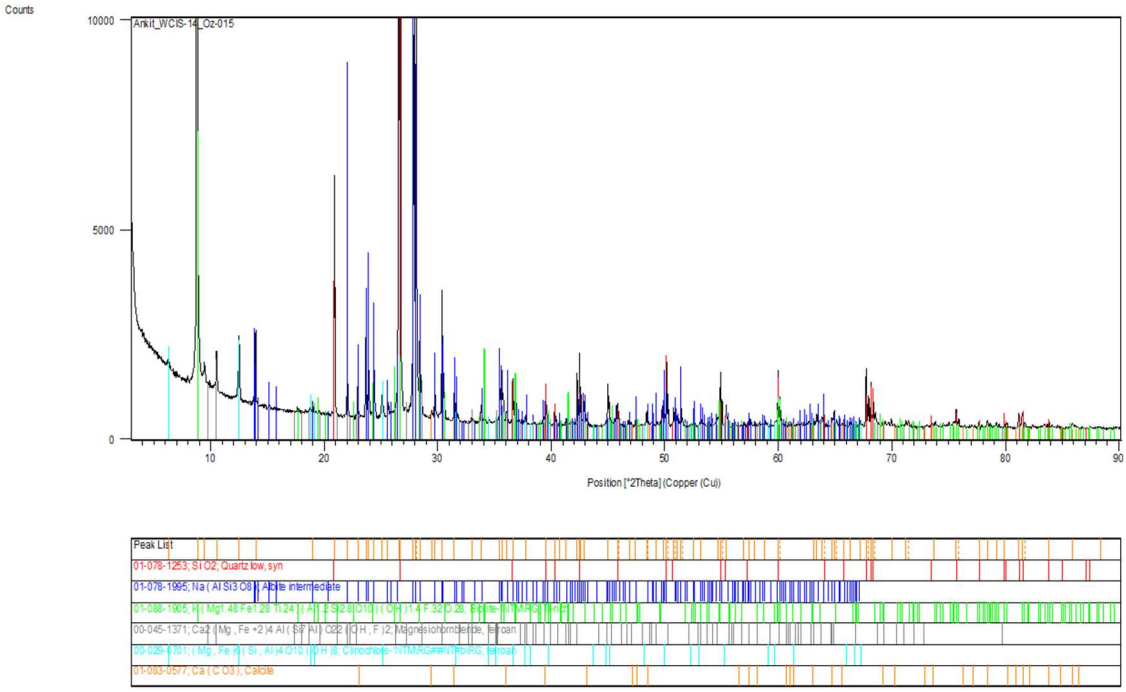


Fig A.2.15. Tonalite sample- WCIS-14 Oz-015

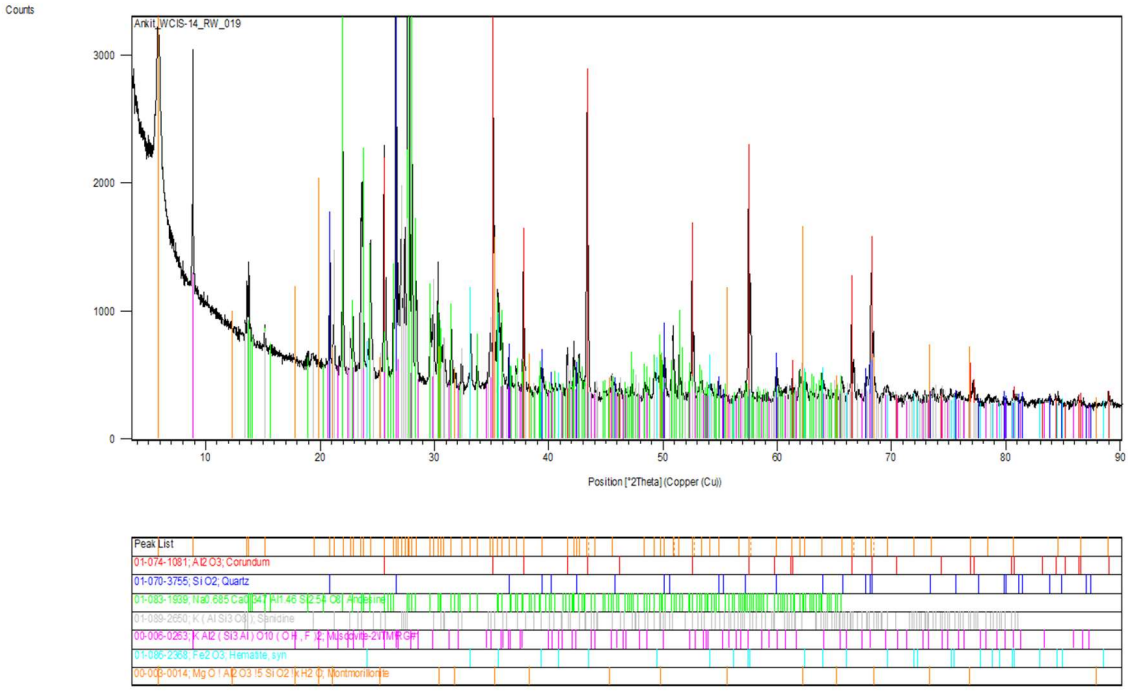


Fig A.2.16. Clast rich fine-grained impact melt rock sample - WCIS-14 RW-019

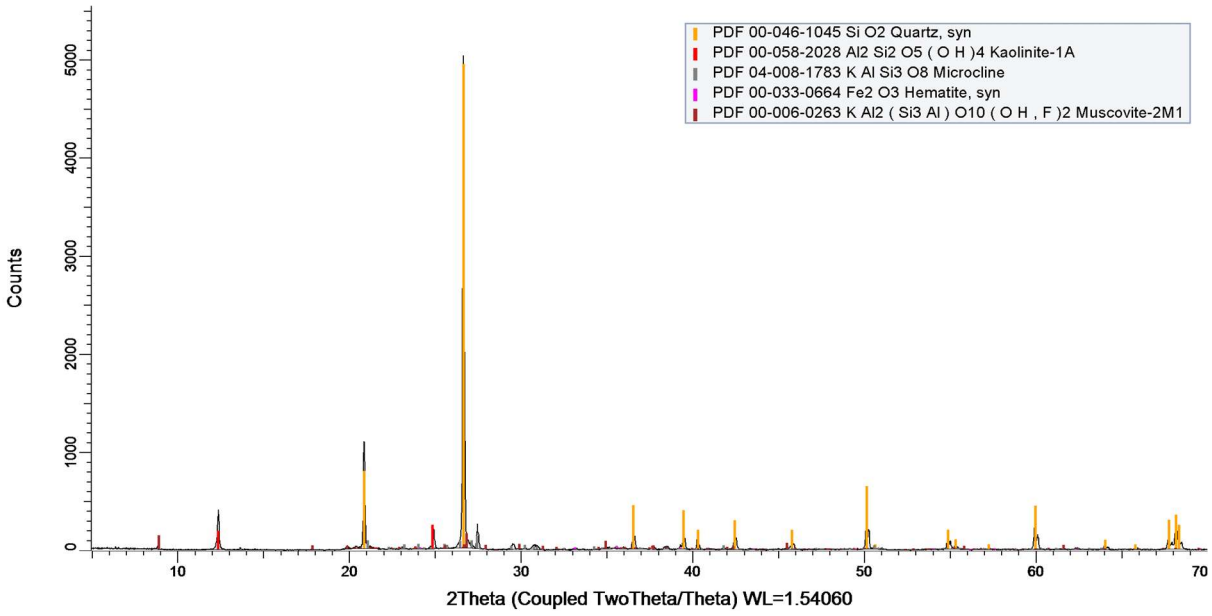
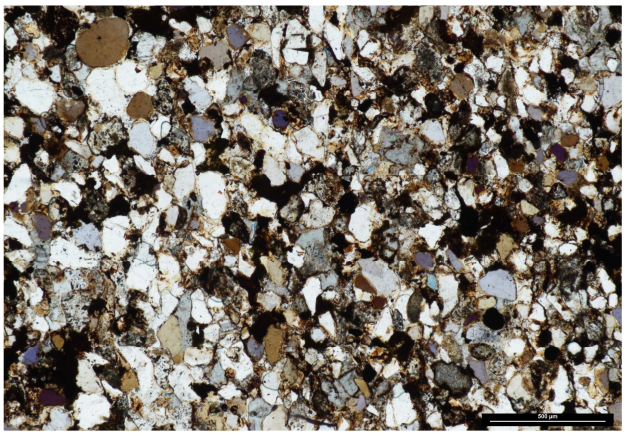
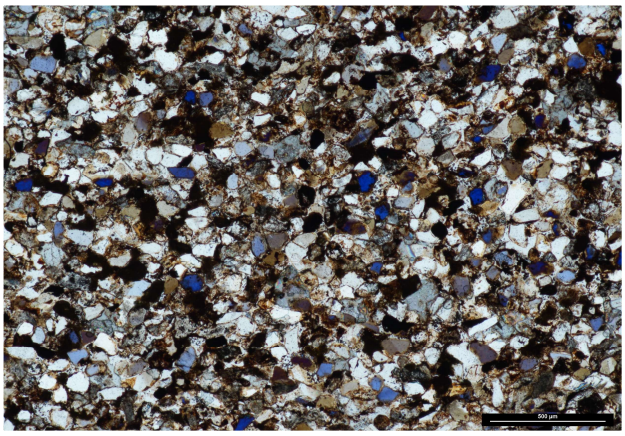


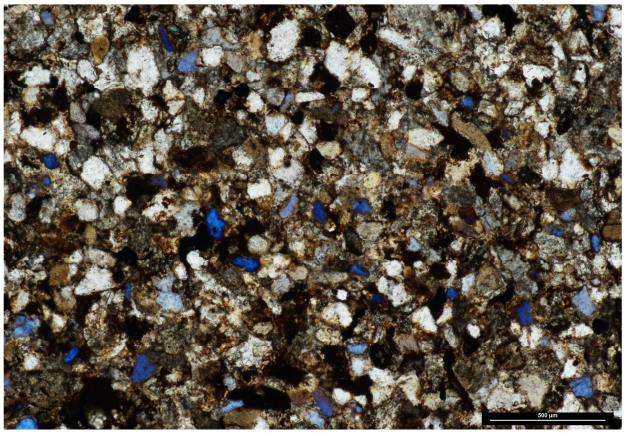
Fig A.2.17. Moenkopi Sandstone sample - MC8215



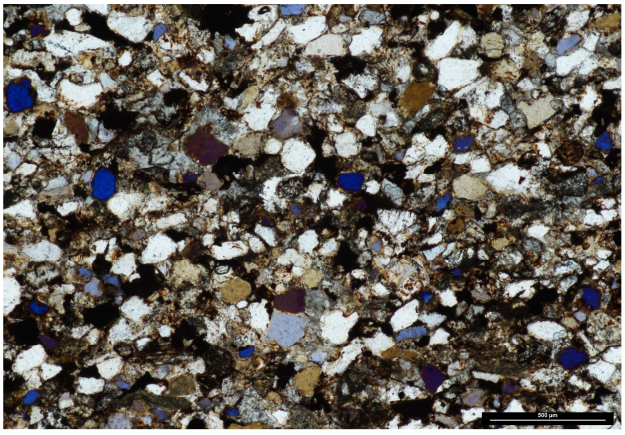
MC51317-1 PPL. Scale bar is 500 µm



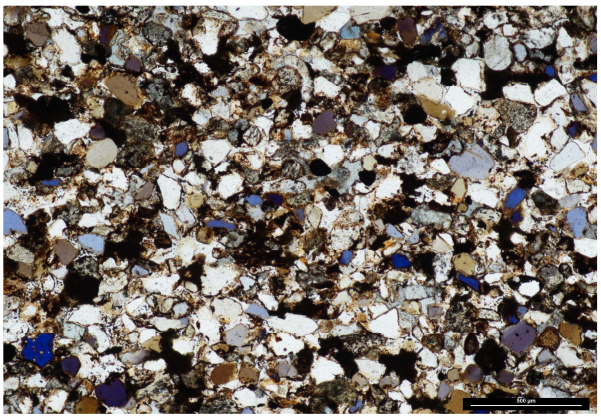
MC51317-2 XPL. Scale bar is 500 µm



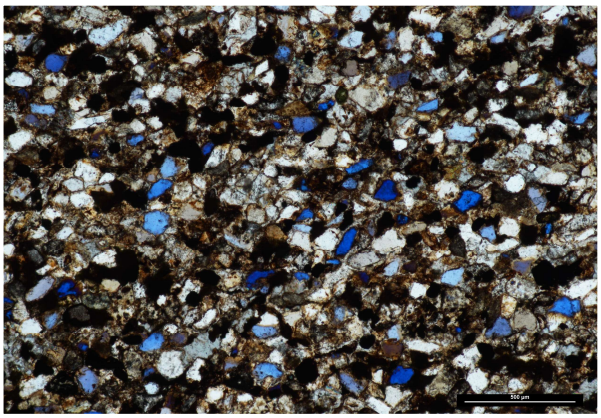
MC51317-03 XPL. Scale bar is 500 µm



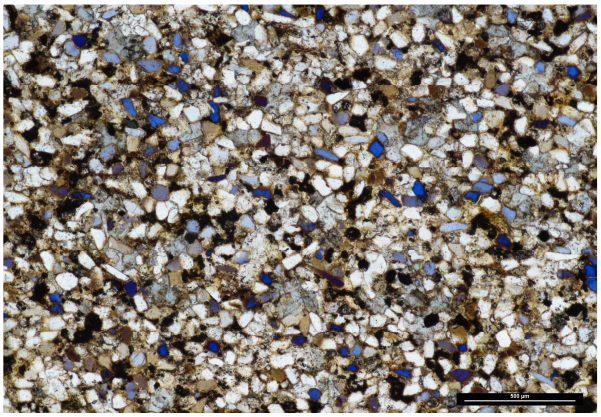
MC51317-4 XPL. Scale bar is 500 µm



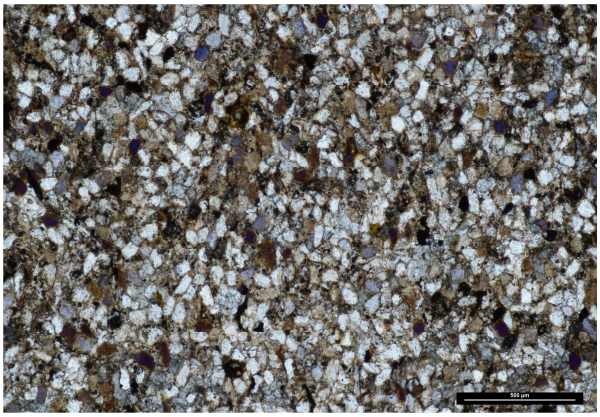
MC51317-5 XPL. Scale bar is 500 µm



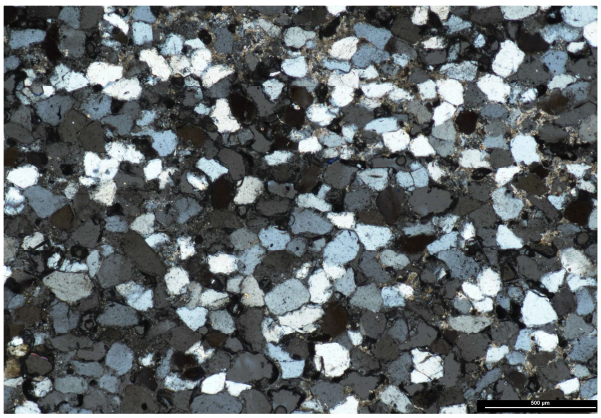
MC51317-6 XPL. Scale bar is 500 µm



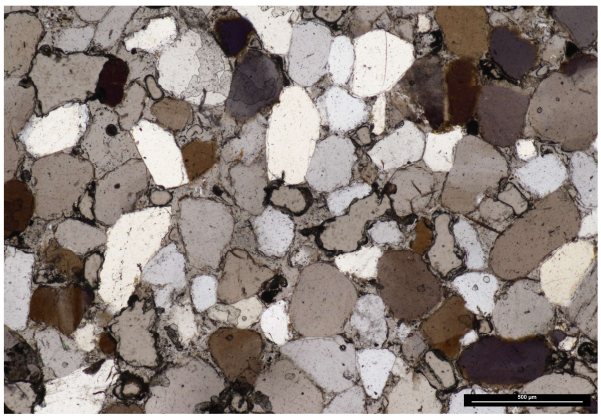
MC51417-1 XPL. Scale bar is 500 µm



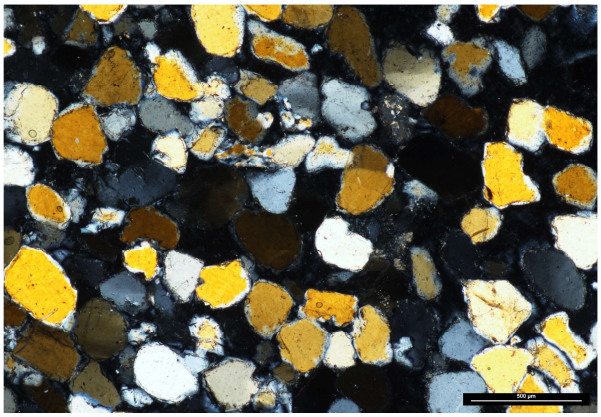
MC51417-2 XPL. Scale bar is 500 µm



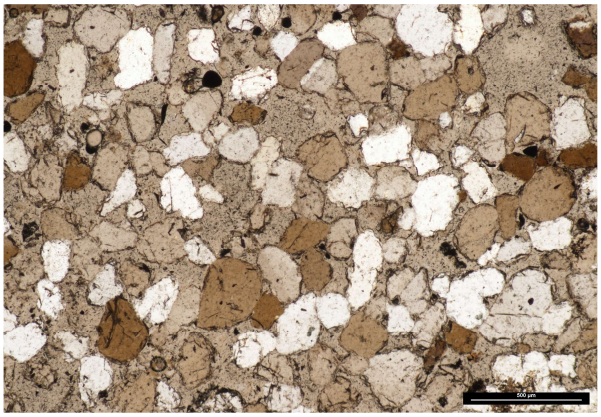
MC51417-5 XPL. Scale bar is 500 µm



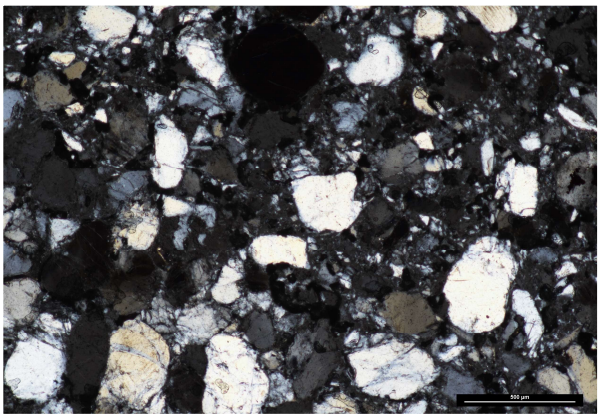
MC51417-6 XPL. Scale bar is 500 µm



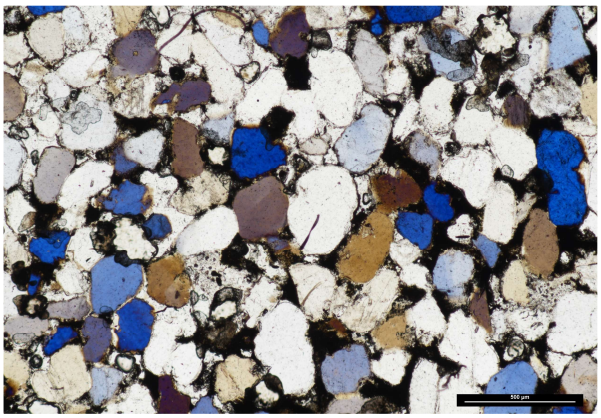
MC51417-7 XPL. Scale bar is 500 µm



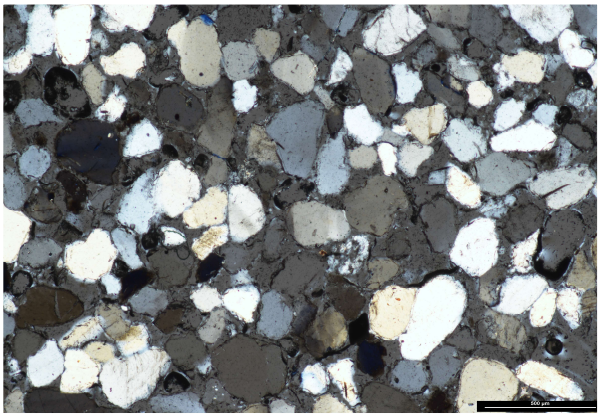
MC51417-8 XPL. Scale bar is 500 µm



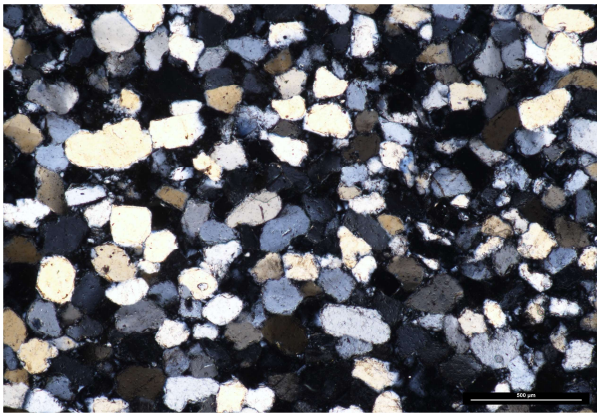
MC51417-9 XPL. Scale bar is 500 µm



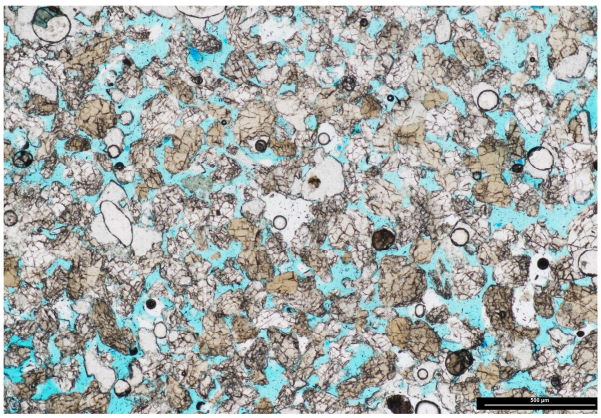
MC51517-2 XPL. Scale bar is 500 µm



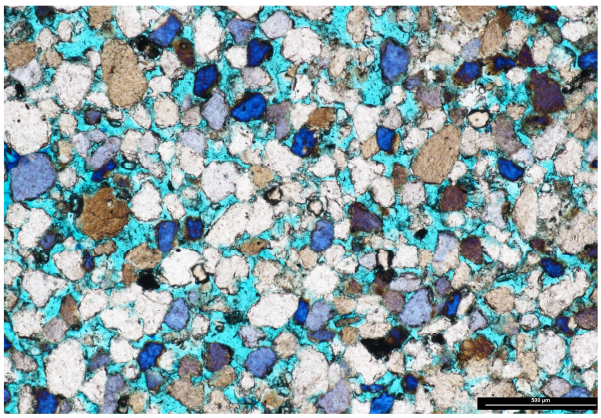
MC51517-4 XPL. Scale bar is 500 µm



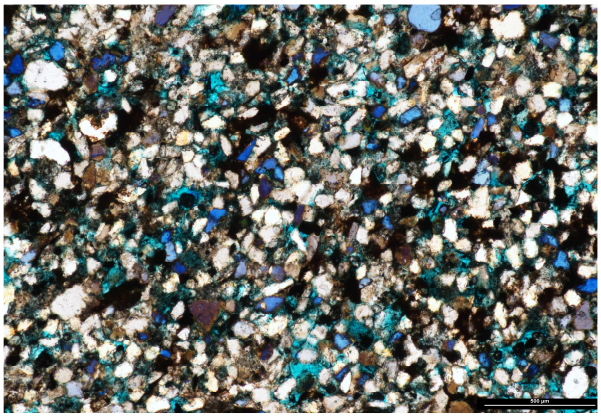
MC51517-8 XPL. Scale bar is 500 µm



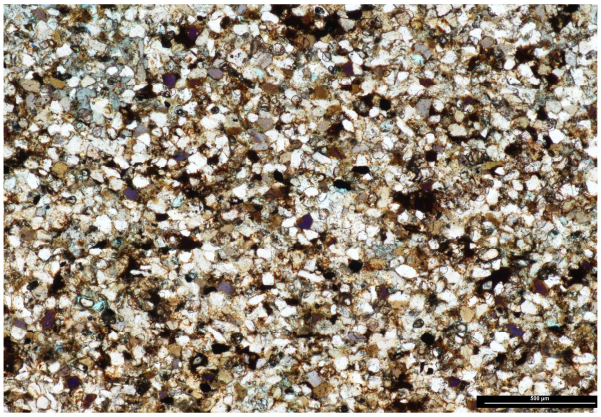
CLR-02 XPL. Scale bar is 500 µm



CLR-01 XPL. Scale bar is 500 µm



CS16-01 XPL. Scale bar is 500 µm



CS16-02 XPL. Scale bar is 500 µm

Appendix 3. Supplementary material for chapter 3

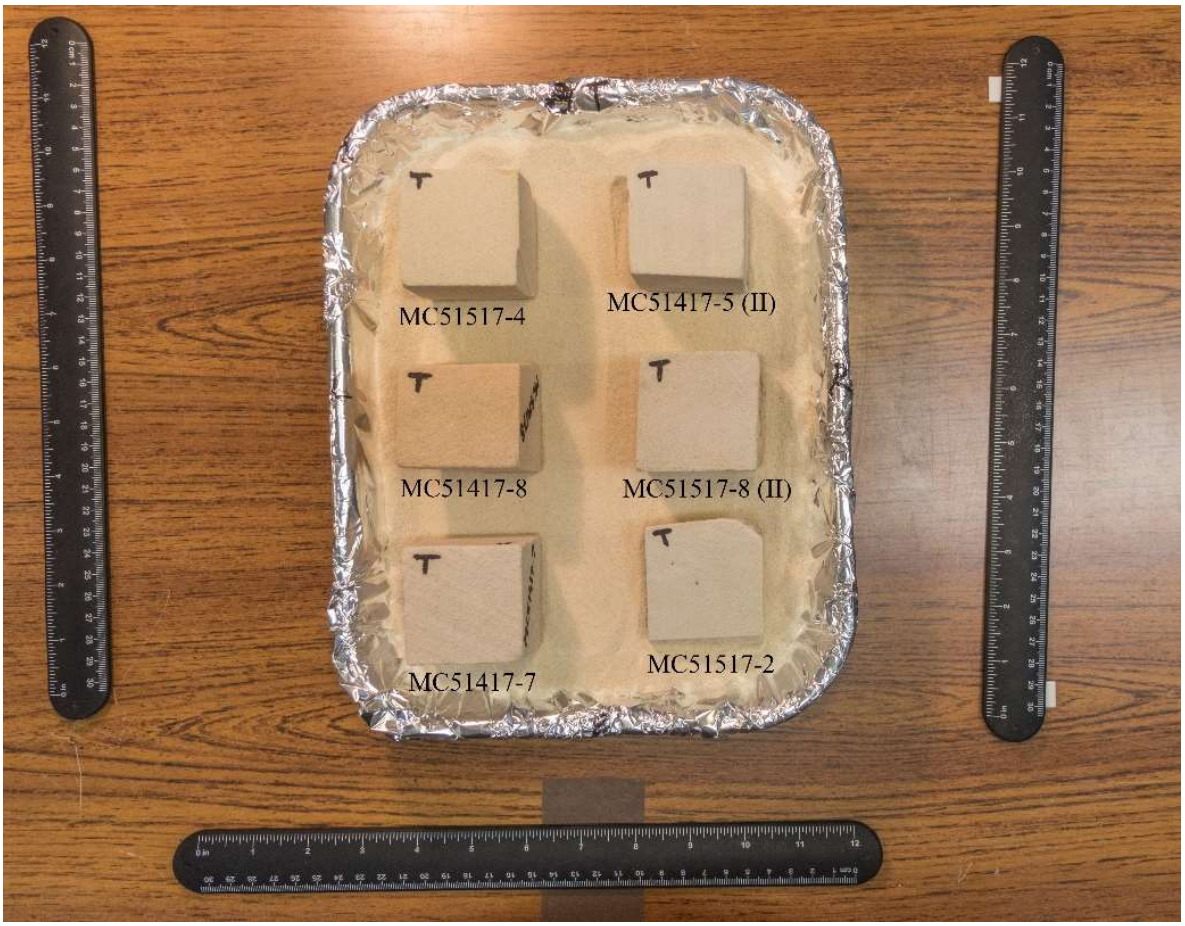


Fig A.3.1. Tray 1 containing Coconino Sandstone sample blocks on top of the sand-salt bed. Three 30 cm rulers are for scale.

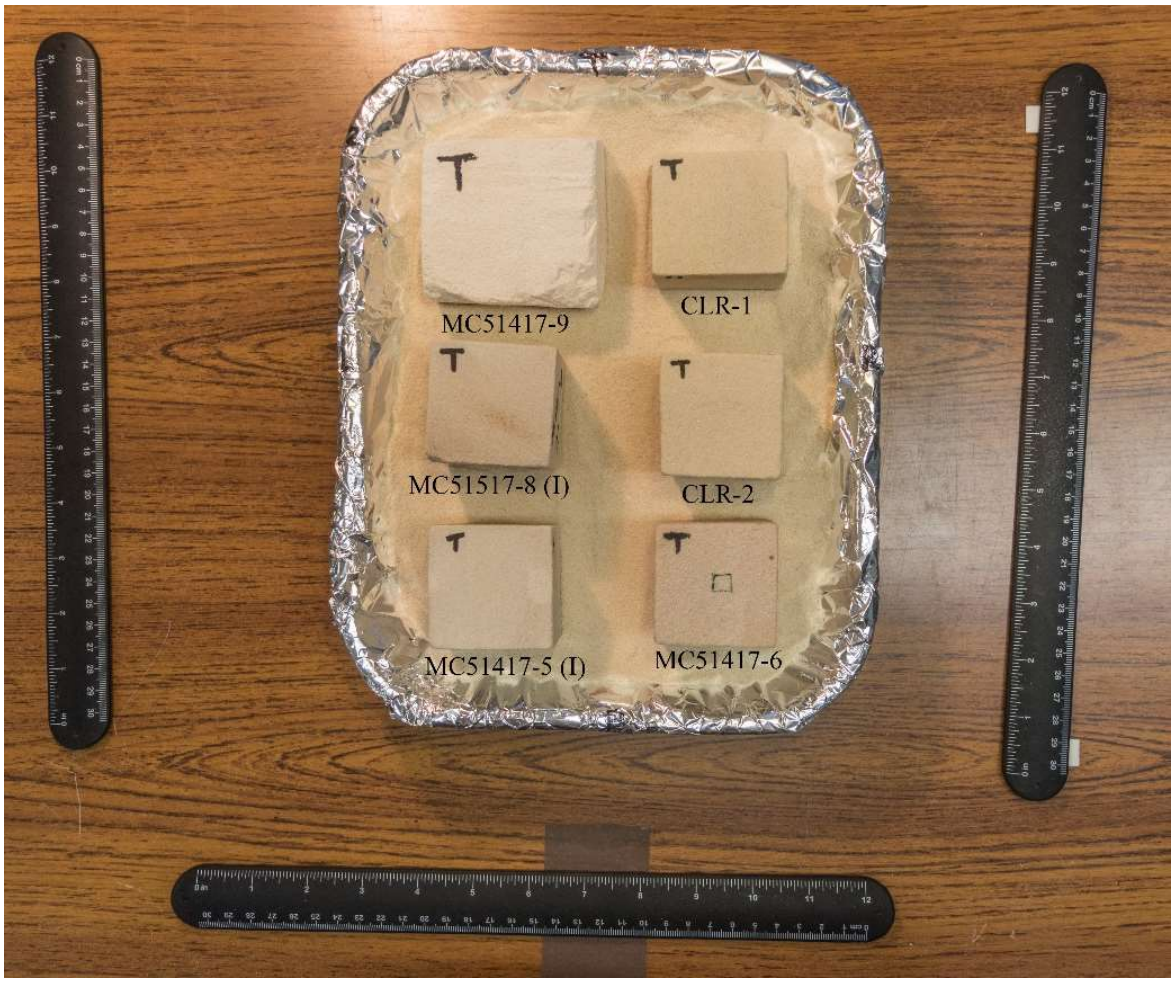


Fig A.3.2. Tray 2 containing Coconino Sandstone sample blocks on top of the sand-salt bed. Three 30 cm rulers are for scale.

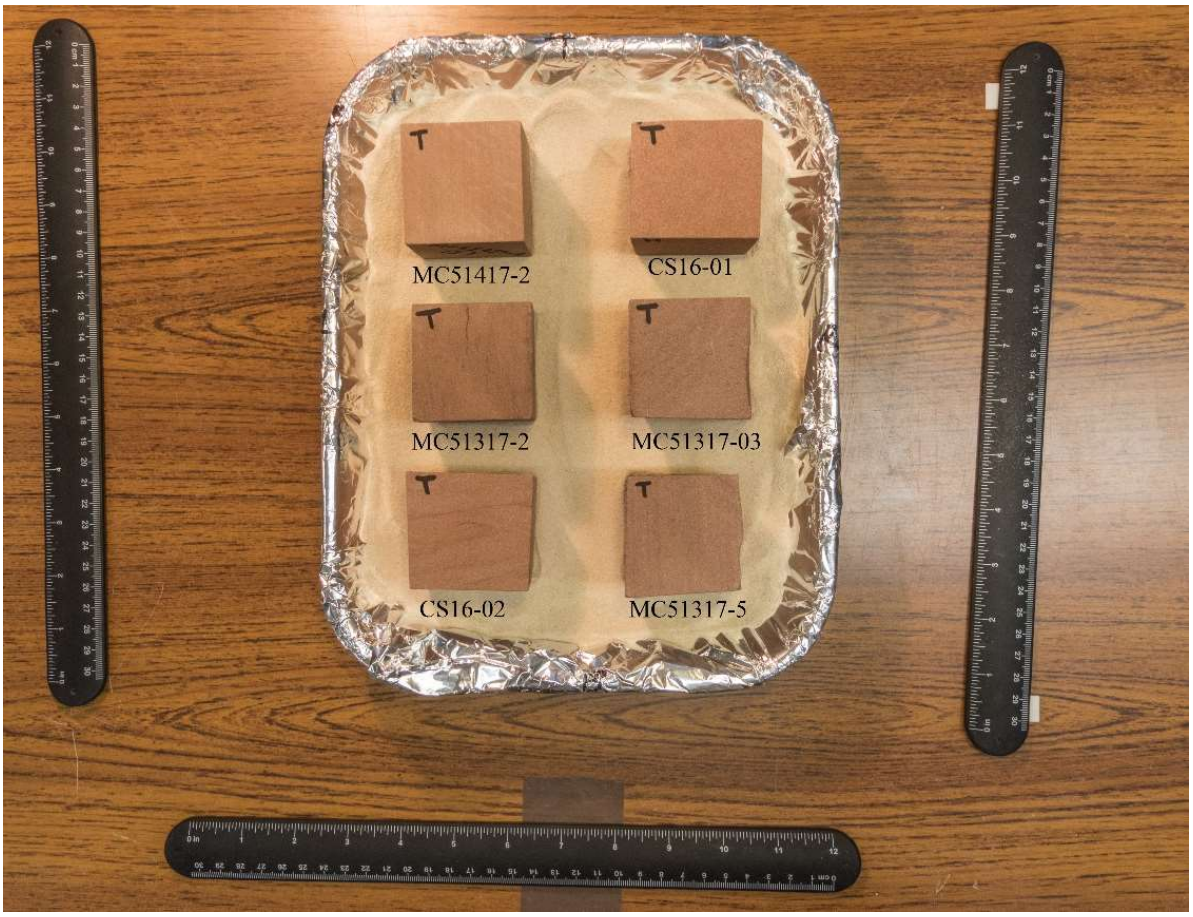


Fig A.3.3. Tray 3 containing Moenkopi Sandstone sample blocks on top of the sand-salt bed. Three 30 cm rulers are for scale.

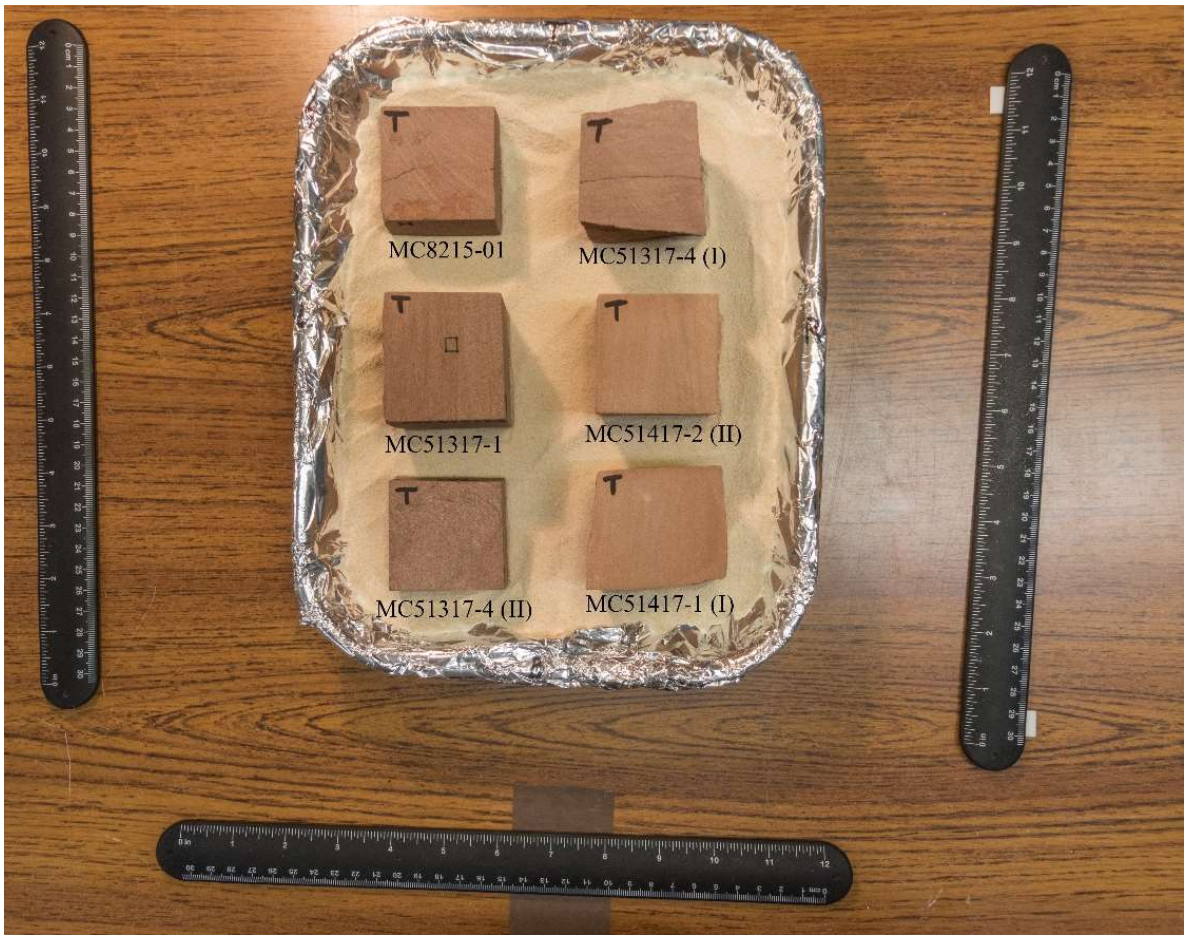


Fig A.3.4. Tray 4 Moenkopi Sandstone sample blocks on top of the sand-salt bed. Three 30 cm rulers are for scale.

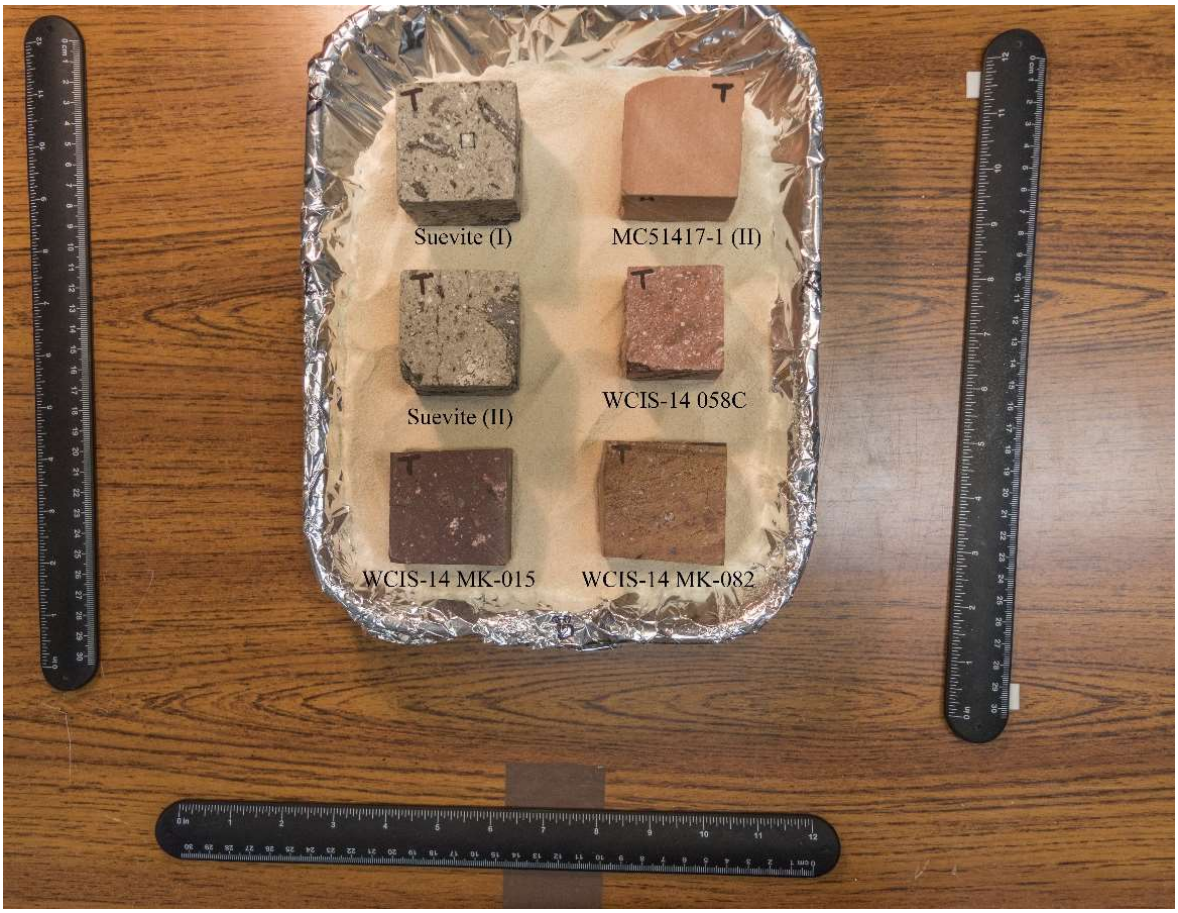


Fig A.3.5. Tray 5 containing Moenkopi Sandstone, impact melt rock, and impact breccia sample blocks on top of the sand-salt bed. Three 30 cm rulers are for scale.



Fig A.3.6. Tray 6 containing crystalline rock, impact melt rock, and impact breccia sample blocks on top of the sand-salt bed. Three 30 cm rulers are for scale.

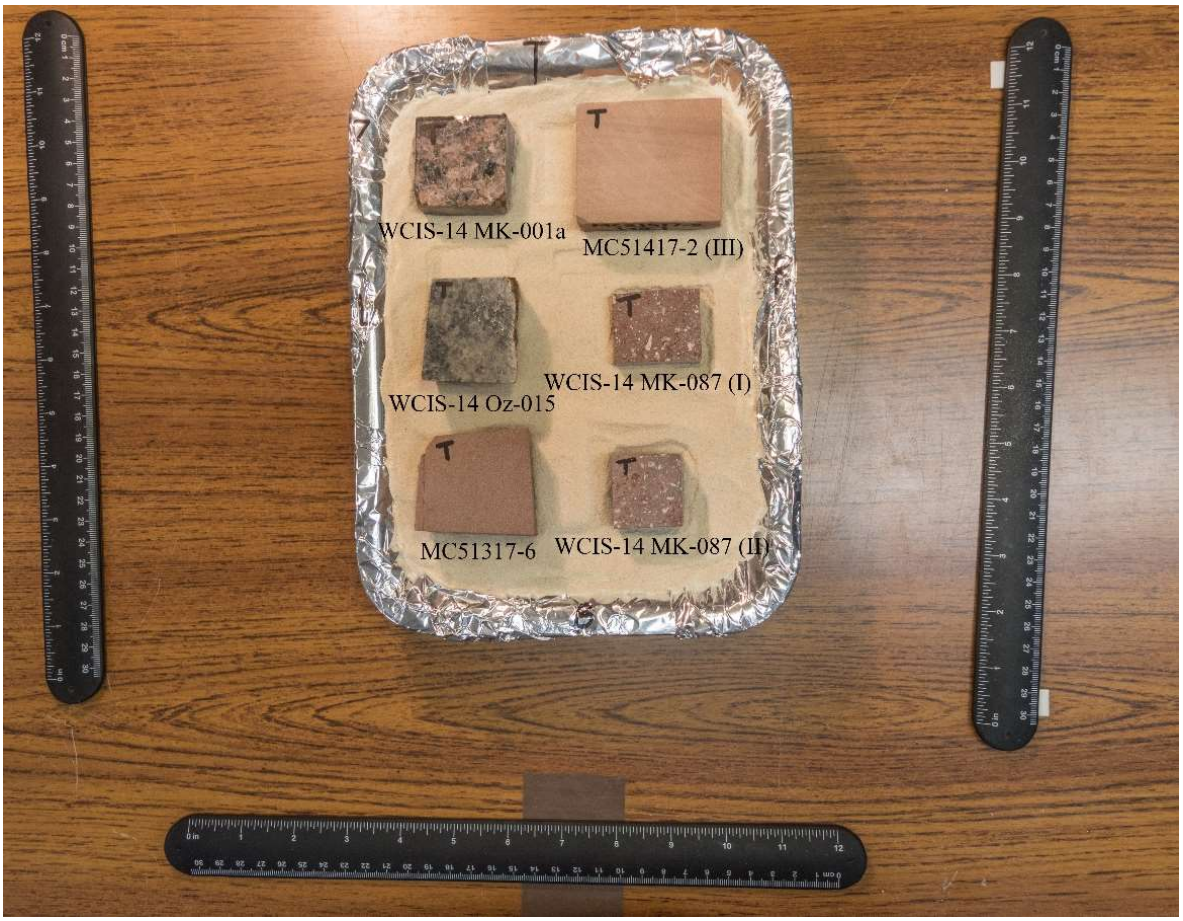


Fig A.3.7. Tray 7 containing Moenkopi Sandstone, crystalline rock, and impact melt rock sample blocks on top of the sand-salt bed. Three 30 cm rulers are for scale.

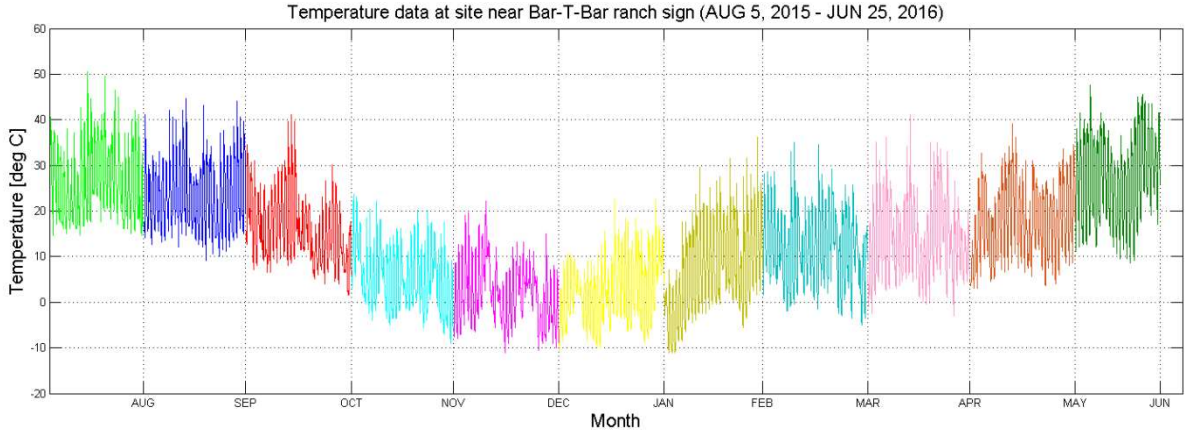


Fig A.3.8. Temperature data for 11 months obtained from an iButton at Meteor Crater site. The iButton was programmed to collect data every two hours. Temperature data from March 17, 2016 was used to conduct the physical weathering experiment.

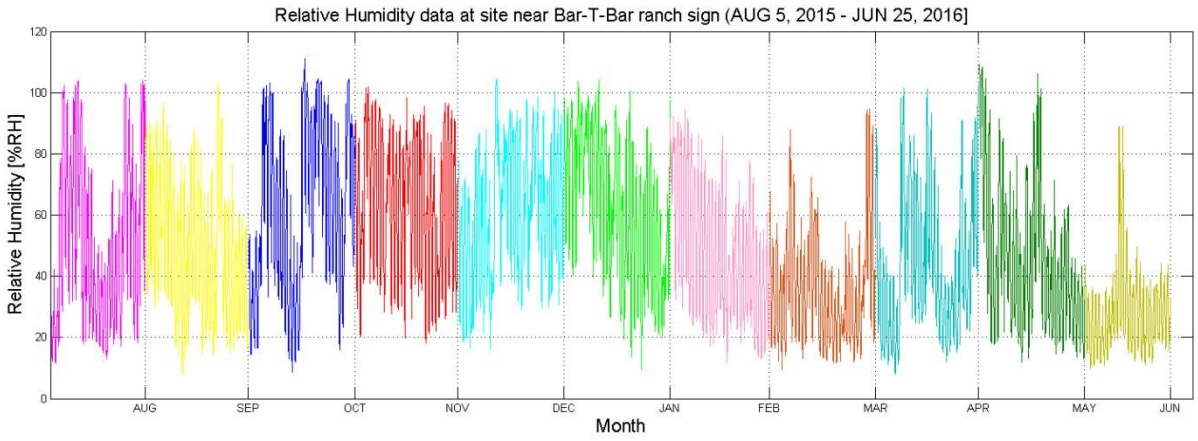


Fig A.3.9. Relative humidity data for 11 months obtained from an iButton at Meteor Crater site. The iButton was programmed to collect data every two hours. Relative humidity data from March 17, 2016 was used to conduct the physical weathering experiment.

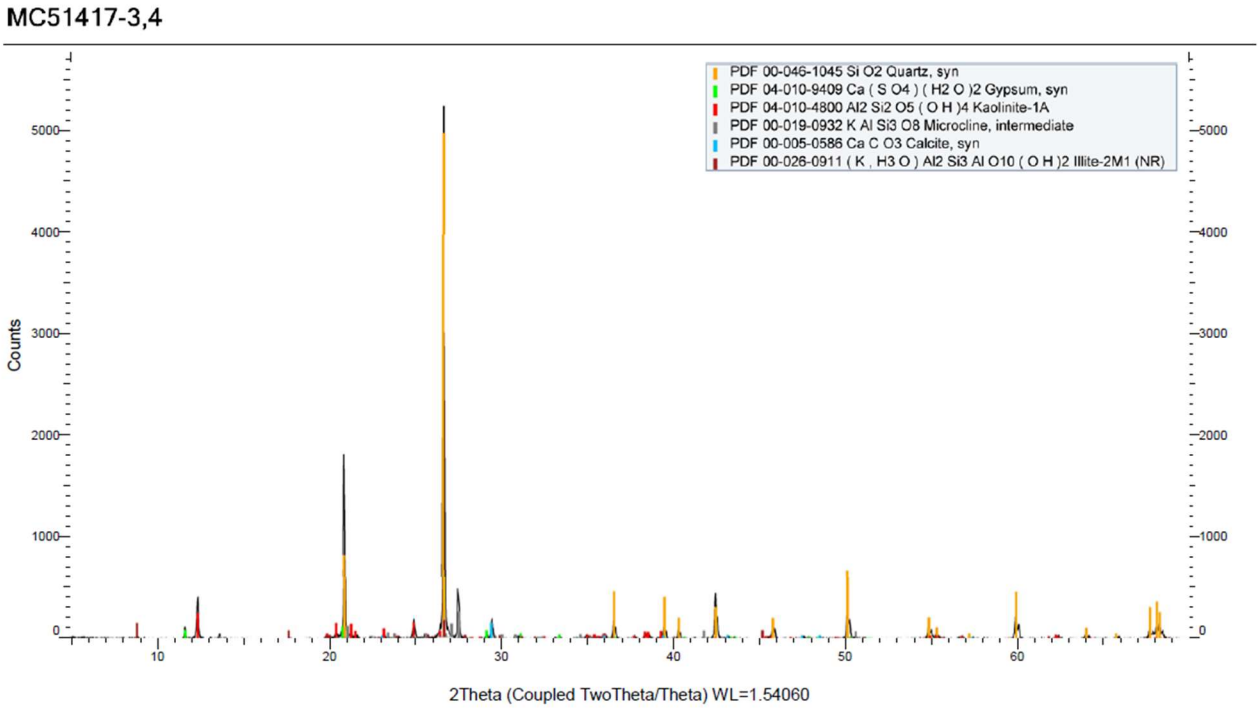


Fig A.3.10. Powder X-ray diffraction analysis on salt efflorescence sample (MC51417-3,4) scrapped from Moenkopi Sandstone at Meteor Crater. Light green peaks correspond to gypsum salt present at Meteor Crater.

Appendix 4. Supplementary material for chapter 4

A.4.1. Guideline for DEM generation workflow in Photoscan

Stage 1: All images are loaded and reviewed in Photoscan. Data with image quality value higher than 0.5 were selected (Agisoft, 2016). The coded GCPs were detected automatically before starting batch processing of images. Local coordinates for each GCP target was entered into Photoscan. The measurement accuracy was adjusted to 0.01 mm for marker accuracy and scale bar accuracy in reference settings for experiments. This value was 0.5 mm for control target in the field. Unwanted scenes in the background or foreground of images (e.g. sky and plants) can lead to incorrect point matching. Photoscan offers a solution to mask out unwanted areas. While this can be a time-consuming process, it can be minimised with careful image acquisition.

Stage 2: Images alignment and optimisation: The program matches the common point in images and determines the camera position for each photo. A 3D sparse point cloud is generated using a least square solution (Thoeni et al., 2014; Agisoft, 2016). The error between measured GCP coordinates and estimated GCP coordinates is determined through the least squares solution (Thoeni et al., 2014). Photos were aligned with the highest alignment accuracy, generic pair pre-selection and the default per-image key and tie point limits. To generate the most accurate 3D model, it is crucial to overcome systematic dishing and doming distortions in the SfM model by correcting lens distortions (Carbonneau and Dietrich, 2016). SfM workflow performs a self-calibration using Exchangeable Image File Format (EXIF) metadata from digital images. Each image is treated as unique during the self-calibration process. The GCP errors were minimised using the camera calibration parameters to refine any distortion in the model during optimisation. PhotoScan adjusts estimated point coordinates and camera parameters, during optimisation, thus reducing the sum of reprojection error and reference coordinate misalignment error (Agisoft, 2016). Although a 3D sparse point cloud is not required for DEM generation, it is required for dense point cloud reconstruction.

Stage 3: Dense Point cloud generation: The dense point cloud is built, using estimated camera positions from sparse point cloud generated during image alignment process. A range of quality options are available, and we selected “High”. This decision was based

on the time required to achieve the required quality for our work. Choosing “Ultra high” can result in higher point density but increases processing time. We used “Mild” depth filtering as we wanted to reconstruct smaller breakdown features (Agisoft, 2016). The dense point cloud was used to generate the DEM.

Stage 4: Mesh and texture: Photoscan reconstructed a 3D polynomial mesh based on dense point cloud representing the rock surface. After mesh, the texture was generated. Mesh is not required for exporting DEM, but a textured mesh model is needed to generate a high-resolution orthophoto.

Table A.4.1. Horizontal checkpoint errors in DEMs produced in error evaluation experiment.

		24 mm extended area (mm)	24 mm profile corrected (mm)	24 mm without profile corrected (mm)	35 mm AdobeRGB (mm)	35 mm corner marker (mm)	35 mm jpg (mm)	35 mm masked (mm)	35 mm profile corrected (mm)	35 mm ProPhotoRGB (mm)	35 mm sRGB (mm)
Scale bar no.	**Coded scale bar**										
S1	target 4_target 5	-0.78	-0.77	-0.73	-0.82	-0.64	0.48	-0.84	-0.82	-0.83	-0.82
S2	target 6_target 7	0.77	0.8	0.83	0.91	1.09	1.8	0.9	0.91	0.9	0.94
S3	target 8_target 9	-0.98	-0.95	-0.9	-0.91	-0.74	0.18	-0.93	-0.91	-0.93	-0.91
S4	target 10_target 11	0.35	0.42	0.44	0.45	0.61	1.72	0.43	0.45	0.43	0.47
S5	target 12_target 13	0.46	0.49	0.51	0.5	0.63	1.44	0.48	0.49	0.49	0.51
S6	target 14_target 15	-0.62	-0.65	-0.62	-0.69	-0.55	0.25	-0.7	-0.68	-0.69	-0.69
S7	target 16_target 17	0.66	0.66	0.7	0.73	0.86	1.46	0.72	0.73	0.72	0.75
S8	target 18_target 19	-0.75	-0.75	-0.71	-0.72	-0.59	-0.05	-0.73	-0.72	-0.73	-0.71
S9	target 20_target 21	0.36	0.34	0.38	0.42	0.52	1.06	0.42	0.42	0.42	0.43
S10	target 22_target 23	-0.5	-0.53	-0.5	-0.53	-0.44	0.09	-0.54	-0.53	-0.54	-0.53
S11	target 24_target 25	0.44	0.43	0.46	0.5	0.59	0.92	0.49	0.51	0.49	0.51
S12	target 26_target 27	-0.47	-0.49	-0.46	-0.48	-0.4	-0.23	-0.49	-0.48	-0.49	-0.48
S13	target 28_target 29	0.25	0.25	0.24	0.28	0.32	0.58	0.27	0.26	0.27	0.29
S14	target 30_target 31	-0.19	-0.2	-0.19	-0.23	-0.19	0.08	-0.24	-0.22	-0.24	-0.23
S15	target 32_target 33	0.24	0.25	0.25	0.28	0.32	0.5	0.27	0.28	-0.24	0.28
S16	target 34_target 35	-0.2	-0.21	-0.19	-0.24	-0.2	0.09	-0.25	-0.24	-0.24	-0.24
S17	target 43_target 44	-0.33									
S18	target 45_target 46	-0.33									
S19	target 47_target 48	-0.27									
S20	Target 49_target 50	-0.27									

Table A.4.2. Vertical checkpoint errors in DEMs produced in error evaluation experiment.

	24 mm extended area (mm)	24 mm profile corrected (mm)	24 mm profile without corrected (mm)	35 mm AdobeRGB (mm)	35 mm corner marker (mm)	35 mm jpg (mm)	35 mm masked (mm)	35 mm profile corrected (mm)	35 mm ProPhotoRGB (mm)	35 mm sRGB (mm)
Wooden Block										
A	0.04	0.14	0.23	-0.19	-0.1	0.16	-0.05	-0.39	-0.3	-0.34
B	0.1	0.37	0.31	-0.09	0.26	-0.16	0.19	-0.19	-0.33	-0.55
C	0.28	0.28	0.33	-0.02	-0.2	-0.006	0.01	-0.05	-0.2	-0.31
D	0.09	0.26	0.36	-0.14	0.13	-0.33	0.06	-0.12	-0.16	-0.18
E	-0.24	-0.37	0.01	-0.42	-0.2	-0.56	-0.13	-0.79	-0.68	-0.67
F	-0.34	-0.1	-0.09	-0.48	-0.19	-0.12	-0.2	-0.35	-0.45	-0.67
G	-0.07	-0.009	0.01	-0.32	-0.1	-0.11	-0.13	-0.19	-0.31	-0.27
H	-0.14	-0.01	0.006	-0.41	-0.17	-0.29	-0.22	-0.56	-0.54	-0.61
I	-0.39	-0.43	-0.23	-0.37	-0.46	-0.44	-0.46	-0.79	-0.84	-0.48
J	-0.64	0.03	-0.22	-0.17	0.15	-0.2	0.05	-0.35	-0.39	-0.33
K	0.23	0.54	0.55	0.03	0.33	0.16	0.4	-0.09	0.04	0.004
L	0.39	0.68	0.47	0.25	0.47	0.28	0.45	0.16	0.2	0.39
M	0.29	0.36	0.35	0.35	0.49	0.49	0.52	0.14	0.25	0.29
N	-0.27	-0.03	-0.12	-0.17	-0.09	-0.48	-0.06	-0.14	-0.24	-0.06
O	-0.02	0.09	0.16	-0.07	0.14	-0.06	0.16	-0.11	-0.02	-0.09
P	0.9	0.8	0.9	0.59	0.35	0.68	0.43	0.54	0.63	0.58

A.4.2. Role of image variables in DEM error

A4.2.1. Type of lens (prime vs zoom)

The DEMs generated from images acquired with prime lens and zoom lens were compared to explore the effect of the type of lens on DEM accuracy. For this purpose, 24 mm without profile corrected and 35 mm masked DEMs were used (Table 4). Horizontal errors were similar in DEMs generated from images taken with both lenses (Figure S1a). Horizontal RMSE for zoom lens DEM was 0.55 mm, and for prime lens, DEM was 0.59 mm. However, Vertical RMSE for the prime lens DEM (0.28 mm) was a little lower than zoom lens DEM (0.35 mm). We determined the intra-class correlation (ICC) for all the horizontal and vertical checkpoint errors (Figure S1 a and b). For horizontal checkpoint errors, ICC is 0.998. For vertical errors, it is 0.847. Reprojection error and projection accuracy were slightly lower for prime lens DEM (Table 4 and Figure S2 b and d). Dense point cloud density for the prime lens was about two times higher than for a zoom lens.

We find therefore that the use of the prime lens will yield lower errors compared to a zoom lens for SfM photogrammetry, as suggested by Mosbrucker et al. (2017). Although, this experiment suggests that there is no statisticsal significant difference in the accuracy of DEMs generated from prime and zoom lens. The slightly higher errors due to using zoom lens is acceptable considering that it offers flexibility to choose a focal length (choice depends on the field of view) and its low cost.

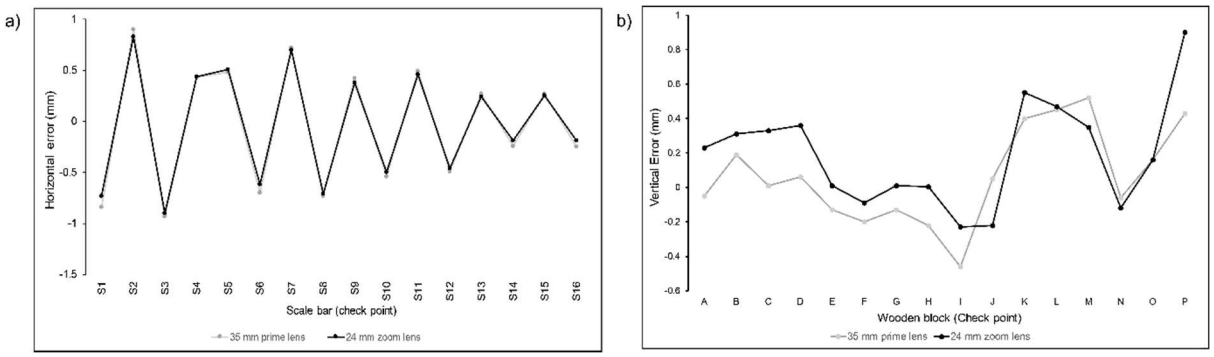


Fig A.4.1. Comparison of horizontal and vertical checkpoint errors in DEM due to the type of lens. (a) Horizontal checkpoint error. (b) Vertical checkpoint error.

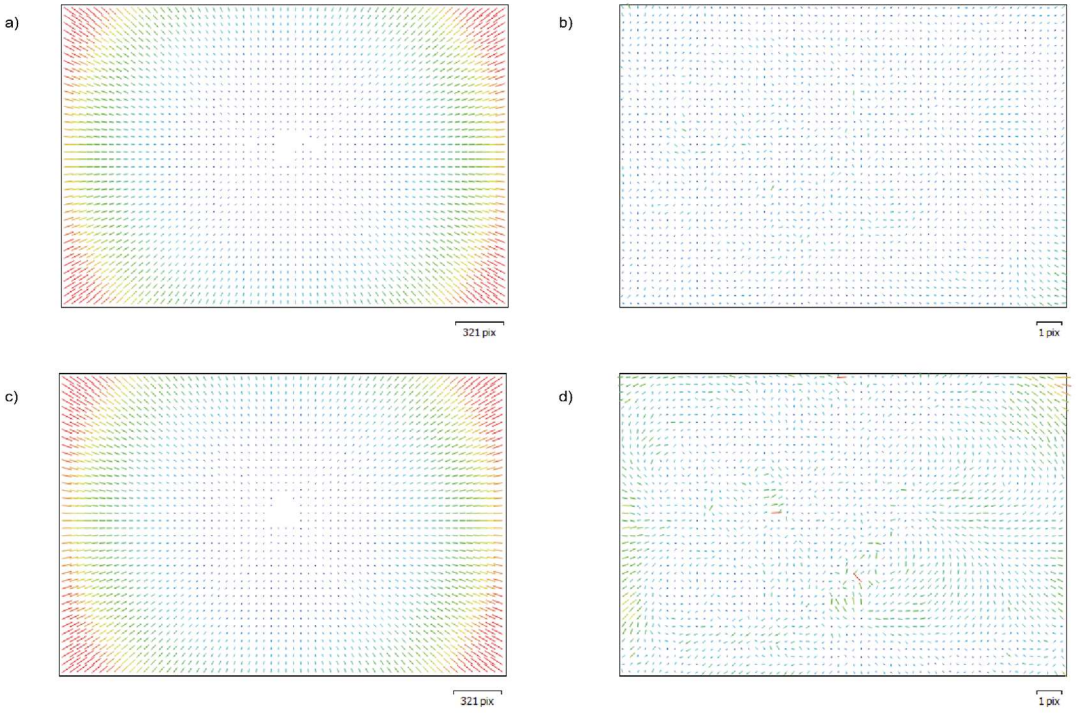


Fig A.4.2. (a) Distortion plot for 35 mm prime lens (b) Residual error plot for 35 mm prime lens. (c) Distortion plot for zoom lens set at 24 mm. (d) Residual error plot for zoom lens set at 24 mm. In image b) and d) residual vectors are magnified by x331.

A.4.2.2. Prior lens profile correction

The effect of prior lens profile correction in Adobe Lightroom on the accuracy of DEM was explored. We used 35 mm profile corrected, 35 mm ProPhotoRGB, 24 mm profile corrected and 24 mm without profile corrected DEMs for comparison (Table 4). Images acquired from 35 mm lens and 24 mm lens were corrected for lens distortion in Lightroom. The horizontal and vertical checkpoint was very similar for a zoom lens (Figure S3 c and d). ICC for horizontal (0.999) and vertical errors (0.947) were very high. For a prime lens, lens profile correction did not affect horizontal and vertical checkpoint error (Figure S3 a and b). ICC for horizontal (0.988) and vertical errors (0.981) were very high for fixed focus lens as well. All the others DEM parameters presented in Table 4 were not affected due to lens profile correction. We find that there was no significant difference observed in DEM accuracy due to prior lens profile correction in images.

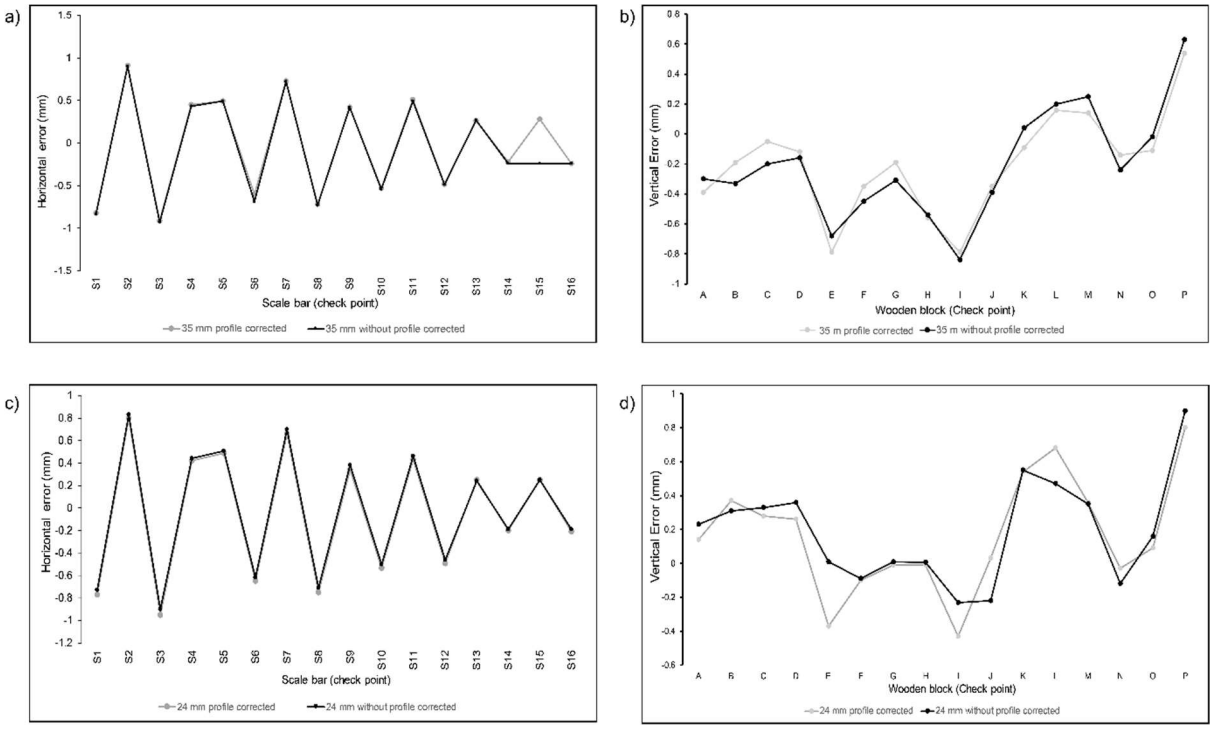


Fig A.4.3. Comparison of horizontal and vertical checkpoint errors in DEM due to lens profile correction. (a) and (b) Horizontal and vertical checkpoint errors for a zoom lens. (c) and (d) Horizontal and vertical checkpoint errors for a prime lens.

A.4.2.3. Colour space of images

In this experiment, the effect of colour space (Katoh, 2005;Korytkowski and Olejnik-Krugly, 2017) on DEM accuracy was investigated. Images acquired from 35 mm prime lens in sRGB, AdobeRGB, and proPhotoRGB was used to make DEMs. We compared 35 mm ProPhotoRGB, 35 mm sRGB, 35 mm AdobeRGB DEMs (Table 4). Horizontal checkpoint errors were very similar for all the DEMs (Figure S4 a). However, vertical errors for AdobeRGB DEM were slightly lower than ProPhotoRGB and sRGB DEMs (Figure S4 b). ICC for horizontal and vertical errors were 0.995 and 0.960. There was negligible difference between ProPhotoRGB and sRGB DEMs, but AdobeRGB DEM had slightly higher vertical accuracy. Mosbrucker et al. (2017) suggested that AdobeRGB images take less time to match points. In this experiment, all the colour spaces (images) took equal time to match points. AdobeRGB and sRGB images have 1% higher tie points than ProPhotoRGB images, but the dense point cloud density and DEM resolution was same for all colour space images. AdobeRGB images had lower reprojection errors compared to ProPhotoRGB and sRGB images. We, therefore, recommend using AdobeRGB colour space for images.

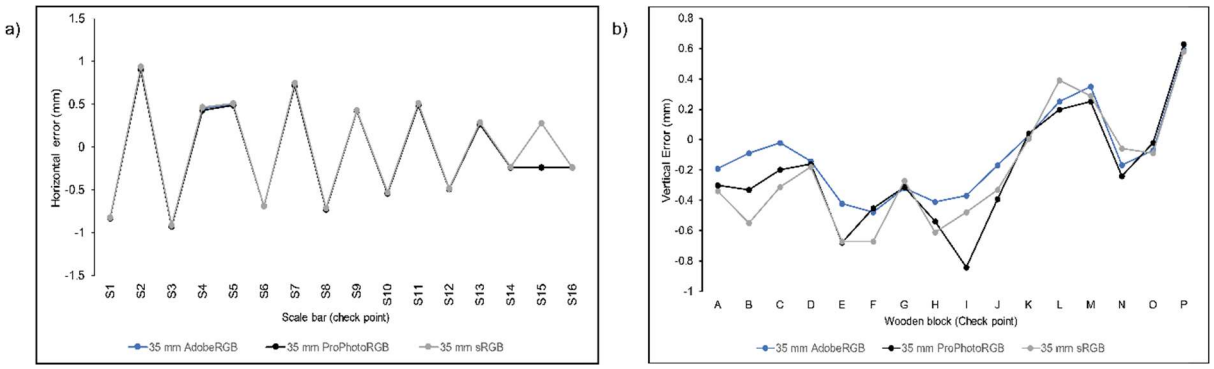


Fig A.4.4. Comparison of horizontal and vertical checkpoint errors in DEM due to colour space. (a) Horizontal checkpoint error. (b) Vertical checkpoint error.

A.4.2.4. Dense point cloud quality setting in Photoscan

In this experiment, the effect of dense point quality setting (or in other words point density) on DEM accuracy was assessed. We compared “high” and “medium” dense point cloud quality setting in Photoscan. We used 35 mm masked and 35 mm ProPhotoRGB DEM for comparison (Table 4). “High” quality setting produced four times higher point density and two times higher DEM resolution compared to “medium”

quality setting. Horizontal errors for both quality settings were very similar (Figure S5 a). However, vertical errors for “high” quality setting were lower than “medium” quality setting (Figure S5 b). ICC for horizontal error (0.989) was very high but for vertical accuracy (0.782) was lower. It took 6.7 times longer to produce “high” quality DEM compared to “medium” quality DEM. Both the DEMs had vertical RMSE less than 0.5 mm.

If time is a constraint, then we recommend choosing “medium” dense point cloud quality setting to generate DEM as there is no significant loss of DEM accuracy.

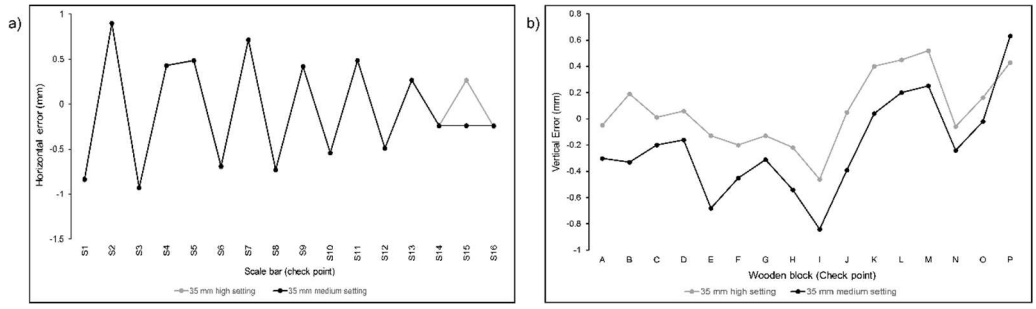


Fig A.4.4.5. Comparison of horizontal and vertical checkpoint errors in DEM due to dense point cloud quality setting in Photoscan. (a) Horizontal checkpoint error. (b) Vertical checkpoint error.

A.4.2.5. Image file format (jpg vs tiff)

The effect of image file format (compression) on the accuracy of DEM was compared in this experiment. We examined 35 mm jpg and 35 mm ProPhotoRGB DEMs (Table 4). Jpg format images produced higher horizontal errors in DEM compared to tiff format images (Figure S6 a). Vertical errors were slightly lower for jpg DEM compared to tiff DEM (Figure S6 b). ICC for horizontal errors (0.685) was very low and vertical errors (0.890) was high. Reprojection error for jpg DEM was about six times higher, and projection error was eight times higher compared to DEM generated using uncompressed tiff images (Table 4). Jpg image format significantly increases error in DEMs. We recommend using tiff format images.

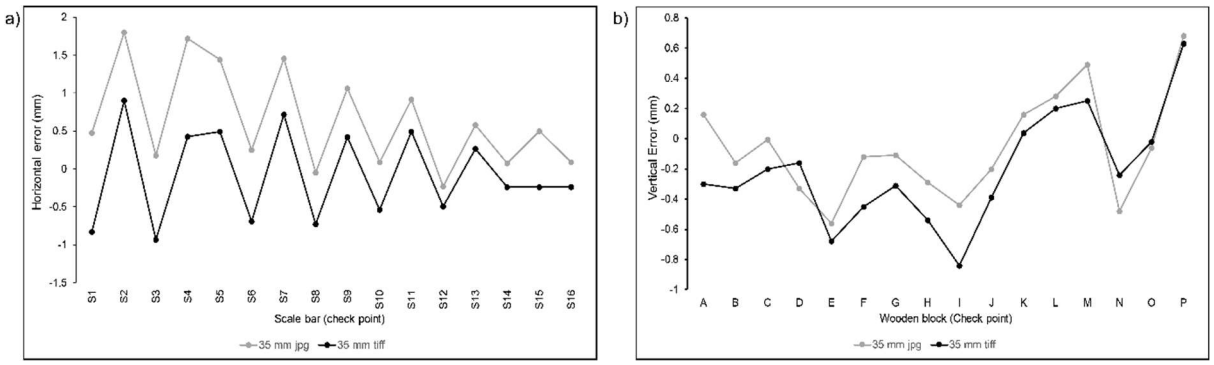


Fig A.4.6. Comparison of horizontal and vertical checkpoint errors in DEM due to image file format (compression). (a) Horizontal check point error. (b) Vertical checkpoint error.

A.4.2.6. The position of the control target with respect to subject

In this experiment, the effect of the position of the control target with respect to subject of interest on DEM accuracy was explored. We compared 35 mm corner target and 35 mm masked DEMs (Table 4). We find that the position of the control target had an almost negligible effect on horizontal and vertical errors (Figure S7 a and b). ICC for horizontal errors (0.988) and vertical errors (0.982) was very high.

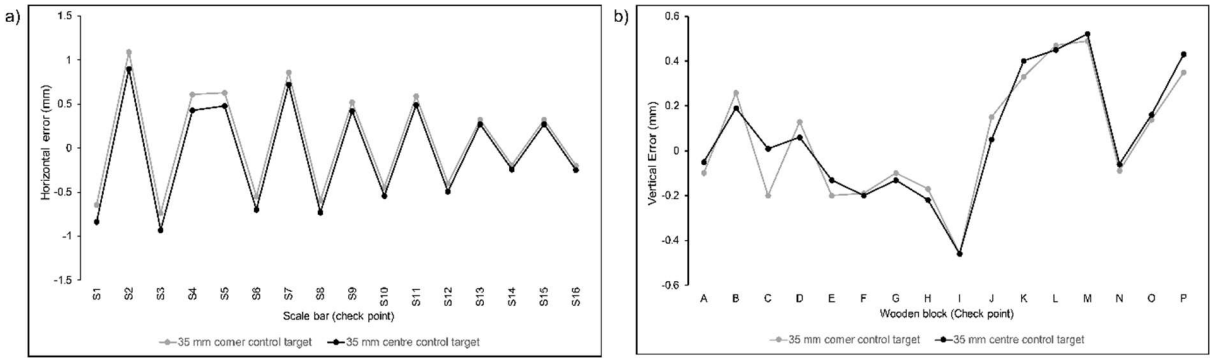


Fig A.4.7. Comparison of horizontal and vertical checkpoint errors in DEM due to the position of the control target. (a) Horizontal checkpoint error. (b) Vertical checkpoint error.

A.4.2.7. Masking

The role of masking of images was compared on the DEM error in this experiment. We used 35 mm corner target and 35 mm masked DEMs for this comparison (Table 4). Masking had an almost negligible effect on Horizontal and Vertical errors in DEM (Figure S7 a and b). In this experiment, masking of images did not reduce the time in the generation of DEM.

References

Photoscan, A.: Agisoft Photoscan User Manual Professional Edition, Version 1.2, Agisoft LLC, 2016.

Carbonneau, P. E., and Dietrich, J. T.: Cost-effective non-metric photogrammetry from consumer-grade sUAS: implications for direct georeferencing of structure from motion photogrammetry, Earth Surface Processes and Landforms, 2016.

Katoh, N.: Extended colour space for capturing devices, Proc. 10th Congress of the International Colour Association, AIC Colour, 2005, 647-652,

Korytkowski, P., and Olejnik-Krugly, A.: Precise capture of colors in cultural heritage digitization, Color Research & Application, 42, 333-336, 2017.

Mosbrucker, A. R., Major, J. J., Spicer, K. R., and Pitlick, J.: Camera system considerations for geomorphic applications of SfM photogrammetry, Earth Surface Processes and Landforms, 2017.

Thoeni, K., Giacomini, A., Murtagh, R., and Kniest, E.: A comparison of multi-view 3D reconstruction of a rock wall using several cameras and a laser scanner, The International Archives of Photogrammetry, Remote Sensing and Spatial Information Sciences, 40, 573, 2014.

Appendix 5. Supplementary Material for chapter 5

A.5.1. Digital Elevation Models (DEM) data

Table A.5.1. Summary of DEM parameters from control site 1.

Rock	No. of Images	Average distance between camera and rock (m)	Orthophoto resolution (mm/pix)	DEM resolution (mm/pix)	Point density (pt/m^2)	Reprojection Error (pix)	XY error (mm)	Z error (mm)	Projection error (pix)
S1.2-M1	50	2.01	0.5	0.5	1.27E+07	0.28	0.32	0.39	0.18
S1.2-M2	39	1.75	0.5	0.5	1.45E+07	0.28	0.36	0.40	0.12
S1.2-M3	56	2.22	0.5	0.5	9.96E+06	0.31	0.31	0.20	0.18
S1.2-M4	61	2.40	0.5	0.5	6.02E+06	0.32	0.42	0.69	0.15
S1-M2	29	2.23	0.5	0.5	9.80E+06	0.44	0.31	0.39	0.13
S1-M4	52	1.66	0.5	0.5	1.39E+07	0.45	0.82	0.29	0.22
S1-M8	55	1.69	0.5	0.5	1.54E+07	0.44	0.36	0.26	0.19
S1-M10	31	1.31	0.5	0.5	2.21E+07	0.51	0.25	0.27	0.33
S1-M13	49	1.78	0.5	0.5	1.44E+07	0.44	0.33	0.95	0.16

Table A.5.2. Summary of DEM parameters from control site 2.

Rock	No. of Images	Average distance between camera and rock (m)	Orthophoto resolution (mm/pix)	DEM resolution (mm/pix)	Point density (pt/m^2)	Reprojection error (pix)	XY error (mm)	Z error (mm)	Projection error (pix)
S2-M7	59	1.66	0.5	0.5	3.82E+06	0.48	0.36	0.39	0.21
S2-M12	102	1.52	0.5	0.5	4.18E+06	0.53	0.35	0.25	0.21
S2-M13	166	1.70	0.5	0.5	4.33E+06	0.49	0.32	0.11	0.29
S2-M16	108	2.77	0.5	0.5	1.63E+06	0.51	0.39	0.12	0.18
S2-M17	73	1.55	0.5	0.5	4.38E+06	0.65	0.30	0.12	0.24
S2-M18	63	1.60	0.5	0.5	3.90E+06	0.58	0.34	0.18	0.17
S2-M19	41	1.42	0.5	0.5	4.39E+06	0.68	0.34	0.13	0.23
S2-M20	52	2.04	0.5	0.5	2.75E+06	0.41	0.32	0.28	0.09
S2-M22	70	1.98	0.5	0.5	2.64E+06	0.47	0.33	0.09	0.19

Table A.5.3. Summary of DEM parameters from control site 3.

Rock	No. of Images	Average distance between camera and rock (m)	Orthophoto resolution (mm/pix)	DEM resolution (mm/pix)	Point density (pt/m^2)	Reprojection error (pix)	XY error (mm)	Z error (mm)	Projection error (pix)
S3-M1	72	1.90	0.5	0.5	3.26E+06	0.51	0.35	0.33	0.24
S3-M6	38	1.62	0.5	0.5	3.96E+06	0.52	0.33	0.14	0.20
S3-M7	47	1.91	0.5	0.5	3.18E+06	0.45	0.35	0.24	0.10
S3-M8	54	1.63	0.5	0.5	3.86E+06	0.48	0.35	0.17	0.26
S3-M9	77	1.54	0.5	0.5	4.00E+06	0.58	0.37	0.55	0.31
S3-M10	61	2.11	0.5	0.5	3.40E+06	0.44	0.36	0.54	0.11
S3-M14	83	1.87	0.5	0.5	3.06E+06	0.43	0.24	0.10	0.22
S3-M18	78	2.22	0.5	0.5	1.99E+06	0.43	0.31	0.29	0.20
S3-M20	61	2.19	0.5	0.5	2.23E+06	0.41	0.35	0.68	0.18
S3-M21	40	2.11	0.5	0.5	2.29E+06	0.42	0.35	0.15	0.21
S3-M22	77	2.68	0.5	0.5	1.58E+06	0.47	0.41	0.14	0.09
S3-M23	44	1.77	0.5	0.5	3.01E+06	0.41	0.36	0.16	0.23
S3-M24	53	1.62	0.5	0.5	4.06E+06	0.47	0.40	0.44	0.38
S3-M25	57	1.95	0.5	0.5	2.58E+06	0.44	0.35	0.28	0.21
S3-M27	110	2.35	0.5	0.5	1.97E+06	0.34	0.30	0.63	0.13
S3-M28	123	3.12	0.5	0.5	945822	0.29	0.32	0.21	0.12
S3-M29	47	1.29	0.5	0.5	5.80E+06	0.49	0.33	0.81	0.23
S3-M31	111	7.23	0.5	0.5	214974	0.31	0.35	0.14	0.15

S3-M32	89	2.23	0.5	0.5	2.05E+06	0.29	0.33	0.11	0.15
S3-M33	66	1.92	0.5	0.5	2.91E+06	0.30	0.32	0.39	0.06
S3-M35	43	3.09	0.5	0.5	1.06E+06	0.46	0.36	0.13	0.16

Table A.5.4. Summary of DEM parameters from Meteor Crater.

Rock	No. of Images	Average distance between camera and rock (m)	Orthophoto resolution (mm/pix)	DEM resolution (mm/pix)	Point density (pt/m^2)	Reprojection Error (pix)	XY error (mm)	Z error (mm)	Projection error (pix)
M13-01	71	1.30	0.5	0.5	6.27E+06	0.57	0.29	0.28	1.05
M13-02	44	1.89	0.5	0.5	3.56E+06	0.33	0.17	0.56	0.88
M13-03	150	1.63	0.5	0.5	4.10E+06	0.39	0.53	0.12	5.57
M13-04	82	1.15	0.5	0.5	8.95E+06	0.64	0.32	0.82	1.78
M13-05	100	1.17	0.5	0.5	7.77E+06	0.49	0.14	0.13	1.10
M13-06	110	1.28	0.5	0.5	6.17E+06	0.48	0.18	0.45	1.35
M13-07	86	1.30	0.5	0.5	6.26E+06	0.41	0.23	0.16	1.30
M13-08	135	1.37	0.5	0.5	5.38E+06	0.49	0.33	0.63	1.97
M13-09	76	1.34	0.5	0.5	6.04E+06	0.58	0.26	0.42	1.38
M13-10	101	1.40	0.5	0.5	5.22E+06	0.68	3.29	0.15	33.31
M14-11	73	0.70	0.5	0.5	1.36E+07	0.97	0.63	0.33	0.95
M14-12	36	0.83	0.5	0.5	8.42E+06	0.68	0.51	0.56	0.74
M14-13	71	1.17	0.5	0.5	5.22E+06	0.96	0.31	0.21	0.95
M14-14	63	0.94	0.5	0.5	6.89E+06	0.81	0.40	0.17	0.89
M14-15	64	0.91	0.5	0.5	9.14E+06	0.81	0.37	0.89	1.22
M14-16	51	1.02	0.5	0.5	1.09E+07	0.59	0.26	0.21	0.56
M14-18	87	3.58	0.5	0.5	8.18E+06	0.80	0.39	0.75	0.97
M14-19	68	0.88	0.5	0.5	1.09E+07	0.92	0.30	0.52	1.19
M14-21	37	1.60	0.5	0.5	3.85E+06	0.51	0.25	0.14	1.28
MC-M1-01	27	1.12	0.5	0.5	8.35E+06	0.62	0.33	0.31	0.19

A.5.2. Rock Hardness Schmidt Hammer rebound data

Table A.5.5. Mean Schmid Hammer (SH) rebound data for site 1.

Location	Schmidt Hammer Rebound value
Site 1	48.4
Site 1	42.2
Site 1	46
Site 1	33.4
Site 1	48.3
Site 1	40.95
Site 1	30.6
Site 1	41.95

Site 1	31.9
Site 1	37.7
Site 1	36.05
Site 1	39.5
Site 1	45.4
Site 1	40.25
Site 1	33.65
Site 1	36
Site 1	34.05
Site 1	35.5
Site 1	34.25
Site 1	30.45
Site 1	28.25
Site 1	37.5
Site 1	35.25
Site 1	36.05
Site 1	45.25
Site 1	43.75
Site 1	43.55
Site 1	42.15
Site 1	40

Table A.5.6. Mean SH rebound data for site 2.

Location	**Schmidt Hammer Rebound value**
Site 2	28.55
Site 2	33.35
Site 2	27.3
Site 2	40.1
Site 2	43.15
Site 2	46.35
Site 2	41.65
Site 2	37.95
Site 2	47.05
Site 2	41.9
Site 2	25.45
Site 2	46.65
Site 2	47.1
Site 2	50.1
Site 2	40.65
Site 2	37.45
Site 2	41.15
Site 2	33.95
Site 2	33.95

Site 2	37.1
Site 2	43.2
Site 2	31.95
Site 2	33.3
Site 2	30.7
Site 2	31.52
Site 2	36.65
Site 2	45.55
Site 2	29.6
Site 2	30.75
Site 2	37.25

Table A.5.6.7. Mean SH rebound data for site 3

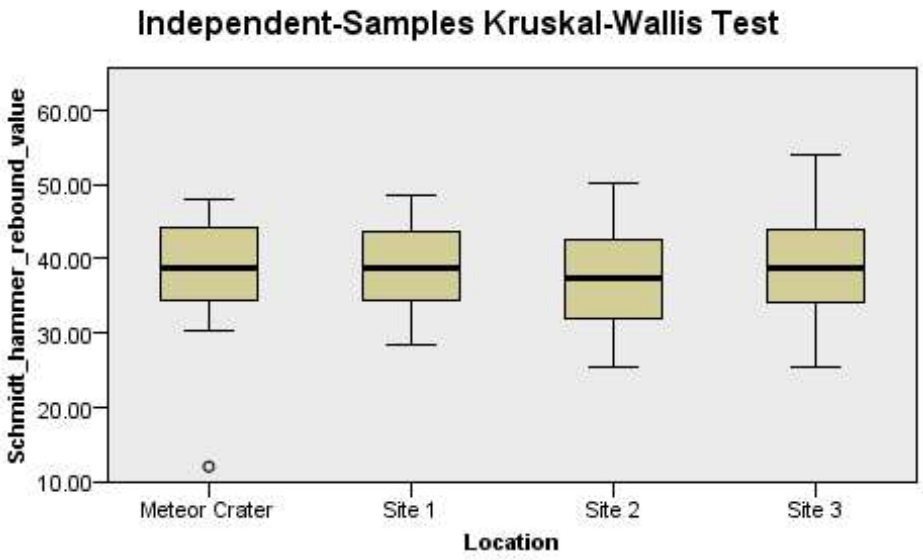
Location	Schmidt Hammer Rebound value
Site 3	33.5
Site 3	34.75
Site 3	35.9
Site 3	39.85
Site 3	28.8
Site 3	34.8
Site 3	34.2
Site 3	38.55
Site 3	34
Site 3	40.2
Site 3	39.85
Site 3	44.25
Site 3	44.5
Site 3	35.15
Site 3	26.6
Site 3	43.45
Site 3	44.7
Site 3	42.25

Site 3	25.5
Site 3	33.9
Site 3	28
Site 3	38.6
Site 3	38.7
Site 3	33.25
Site 3	44.1
Site 3	38.8
Site 3	31.1
Site 3	27.45
Site 3	48.3
Site 3	51.7
Site 3	53.95
Site 3	52.6
Site 3	41.85
Site 3	36.75
Site 3	34.45
Site 3	46.3
Site 3	47
Site 3	39.8

Table A.5.8. Mean SH rebound data for Meteor Crater.

Location	Schmidt Hammer Rebound value
Meteor Crater	45.35
Meteor Crater	38.35
Meteor Crater	32.25
Meteor Crater	32.35
Meteor Crater	35.1
Meteor Crater	38.85
Meteor Crater	34.35
Meteor Crater	38.95
Meteor Crater	39.1
Meteor Crater	33.5
Meteor Crater	45.6
Meteor Crater	44.75
Meteor Crater	47.1
Meteor Crater	42.5
Meteor Crater	48
Meteor Crater	37.85

Meteor Crater	35.45
Meteor Crater	12
Meteor Crater	38.3
Meteor Crater	44.29
Meteor Crater	41.65
Meteor Crater	30.3



Total N	122
Test Statistic	.907
Degrees of Freedom	3
Asymptotic Sig. (2-sided test)	.824

1. The test statistic is adjusted for ties.
2. Multiple comparisons are not performed because the overall test does not show significant differences across samples.

A.5.3. Areal Surface Roughness

Neighbourhood size	Window scale (mm)
3×3	1.5×1.5
11×11	5.5×5.5
21×21	10.5×10.5
31×31	15.5×15.5
41×41	20.5×20.5
51×51	25.5×25.5
101×101	50.5×50.5

A.5.3.1. Standard Deviation of Height (Sq)

Table A.5.9. Sq parameters for site 1

Outcrop							
	Sq (3×3)	**Sq (11×11)**	**Sq (21×21)**	**Sq (31×31)**	**Sq (41×41)**	**Sq (51×51)**	**Sq (101×101)**
S1.2-M1	8.59E-05	2.67E-04	4.64E-04	6.49E-04	8.26E-04	9.96E-04	1.79E-03
S1.2-M2	1.27E-04	3.64E-04	5.99E-04	8.24E-04	1.05E-03	1.26E-03	2.32E-03
S1.2-M3	1.16E-04	3.88E-04	6.99E-04	1.00E-03	1.29E-03	1.58E-03	2.91E-03
S1.2-M4	1.40E-04	4.87E-04	8.72E-04	1.24E-03	1.60E-03	1.95E-03	3.63E-03
S1-M2	1.81E-04	5.81E-04	1.01E-03	1.41E-03	1.78E-03	2.14E-03	3.72E-03
S1-M4_1	7.76E-04	2.16E-03	3.17E-03	3.83E-03	4.32E-03	4.70E-03	5.97E-03
S1-M4_2	3.14E-04	9.71E-04	1.56E-03	2.01E-03	2.37E-03	2.67E-03	3.84E-03
S1-M8_1	2.31E-03	5.58E-03	7.51E-03	8.72E-03	9.59E-03	1.03E-02	1.27E-02
S1-M8_2	3.14E-04	8.87E-04	1.38E-03	1.80E-03	2.17E-03	2.51E-03	3.86E-03
S1-M10	8.47E-04	2.33E-03	3.60E-03	4.68E-03	5.64E-03	6.55E-03	1.06E-02
S1-M13_1	7.13E-04	2.03E-03	3.14E-03	4.01E-03	4.75E-03	5.41E-03	8.28E-03
S1-M13_2	3.52E-04	1.09E-03	1.83E-03	2.51E-03	3.17E-03	3.82E-03	6.99E-03
S1-M13_3	1.04E-03	3.06E-03	4.84E-03	6.40E-03	7.83E-03	9.17E-03	1.52E-02

Table A.5.10. Sq parameters for site 2.

Outcrop							
	Sq (3×3)	**Sq (11×11)**	**Sq (21×21)**	**Sq (31×31)**	**Sq (41×41)**	**Sq (51×51)**	**Sq (101×101)**
S2-M1	5.04E-04	1.77E-03	3.03E-03	4.11E-03	5.06E-03	5.89E-03	9.09E-03
S2-M2	2.46E-04	9.21E-04	1.71E-03	2.45E-03	3.16E-03	3.84E-03	6.86E-03
S2-M3	3.88E-04	1.45E-03	2.67E-03	3.81E-03	4.90E-03	5.94E-03	1.06E-02
S2-M4	2.74E-04	1.03E-03	1.91E-03	2.75E-03	3.54E-03	4.30E-03	7.74E-03
S2-M5	3.48E-04	1.31E-03	2.40E-03	3.40E-03	4.32E-03	5.19E-03	9.08E-03
S2-M6	2.04E-04	7.67E-04	1.41E-03	2.00E-03	2.54E-03	3.04E-03	5.03E-03
S2-M7	1.93E-04	6.74E-04	1.21E-03	1.70E-03	2.16E-03	2.60E-03	4.51E-03
S2-M12	3.61E-04	1.39E-03	2.43E-03	3.43E-03	4.37E-03	5.27E-03	9.31E-03
S2-M13	4.29E-04	1.52E-03	2.72E-03	3.82E-03	4.87E-03	5.87E-03	1.04E-02
S2-M16	3.25E-04	1.14E-03	1.94E-03	2.65E-03	3.29E-03	3.89E-03	6.46E-03
S2-M17	1.14E-03	3.67E-03	5.81E-03	7.40E-03	8.66E-03	9.70E-03	1.34E-02
S2-M18	4.09E-04	1.47E-03	2.61E-03	3.62E-03	4.52E-03	5.35E-03	8.65E-03
S2-M19	4.36E-04	1.69E-03	3.15E-03	4.52E-03	5.79E-03	6.96E-03	1.17E-02
S2-M20	2.52E-04	8.84E-04	1.56E-03	2.18E-03	2.75E-03	3.28E-03	5.56E-03
S2-M22_1	3.16E-04	1.12E-03	1.98E-03	2.76E-03	3.47E-03	4.12E-03	2.23E-02
S2-M22_2	3.20E-04	1.06E-03	1.79E-03	2.43E-03	3.02E-03	3.57E-03	5.90E-03

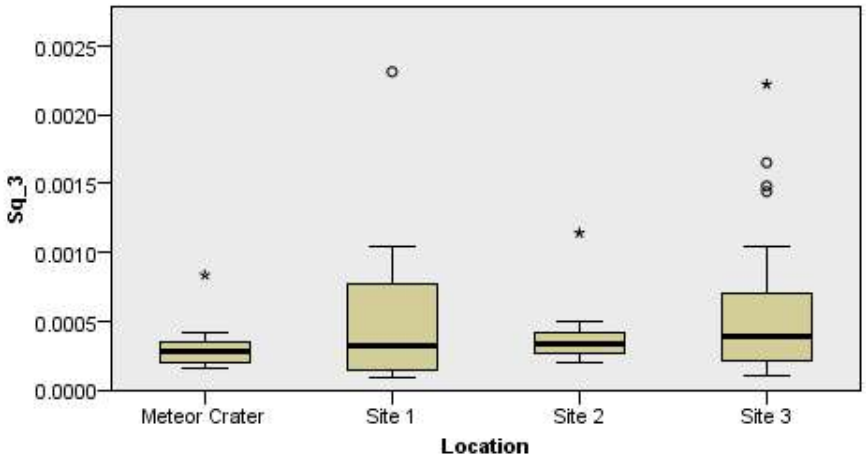
Table A.5.11. Sq parameter for Site 3.

Outcrop							
	Sq (3×3)	**Sq (11×11)**	**Sq (21×21)**	**Sq (31×31)**	**Sq (41×41)**	**Sq (51×51)**	**Sq (101×101)**
S3-M1_1	5.16E-04	1.82E-03	3.19E-03	4.42E-03	5.53E-03	6.53E-03	1.06E-02
S3-M1_2	5.85E-04	1.95E-03	3.21E-03	4.24E-03	5.12E-03	5.91E-03	8.97E-03
S3-M1_3	2.22E-03	6.82E-03	1.01E-02	1.24E-02	1.40E-02	1.54E-02	2.00E-02
S3-M6	1.44E-03	4.15E-03	6.19E-03	7.67E-03	8.83E-03	9.82E-03	1.34E-02
S2-M7	4.66E-04	1.52E-03	2.54E-03	3.44E-03	4.26E-03	5.04E-03	8.39E-03
S3-M8	5.96E-04	1.94E-03	3.24E-03	4.39E-03	5.43E-03	6.43E-03	1.10E-02
S3-M9	1.65E-03	5.05E-03	7.75E-03	9.84E-03	1.16E-02	1.30E-02	1.85E-02
S3-M10	5.76E-04	1.92E-03	3.21E-03	4.31E-03	5.30E-03	6.21E-03	9.97E-03
S3-M14	1.95E-04	6.31E-04	1.05E-03	1.42E-03	1.76E-03	2.09E-03	3.59E-03
S3-M18	1.47E-04	5.27E-04	9.49E-04	1.34E-03	1.71E-03	2.06E-03	3.60E-03
S3-M20	1.62E-04	5.48E-04	9.58E-04	1.32E-03	1.66E-03	1.98E-03	3.38E-03
S3-M21	3.84E-04	1.43E-03	2.63E-03	3.76E-03	4.82E-03	5.83E-03	1.04E-02
S3-M22	8.08E-04	2.78E-03	4.57E-03	6.04E-03	7.31E-03	8.44E-03	1.28E-02
S3-M23	2.94E-04	1.10E-03	2.05E-03	2.95E-03	3.80E-03	4.62E-03	8.35E-03
S3-M24	2.46E-04	9.06E-04	1.67E-03	2.39E-03	3.09E-03	3.75E-03	6.74E-03
S3-M25	2.45E-04	8.56E-04	1.48E-03	2.02E-03	2.50E-03	2.94E-03	4.85E-03
S3-M27	1.72E-04	6.26E-04	1.16E-03	1.67E-03	2.18E-03	2.67E-03	5.05E-03
S3-M28	1.16E-04	4.26E-04	7.88E-04	1.14E-03	1.48E-03	1.82E-03	3.37E-03
S3-M29	1.04E-03	3.07E-03	4.86E-03	6.41E-03	7.84E-03	9.19E-03	1.55E-02
S3-M31	2.84E-04	9.91E-04	1.84E-03	2.67E-03	3.48E-03	4.28E-03	8.03E-03
S3-M32	2.38E-04	7.44E-04	1.19E-03	1.58E-03	1.95E-03	2.29E-03	3.89E-03
S3-M33	1.09E-04	3.81E-04	6.82E-04	9.73E-04	1.26E-03	1.54E-03	2.90E-03
S3-M35	1.48E-03	4.88E-03	7.42E-03	9.21E-03	1.06E-02	1.18E-02	1.58E-02

Table A.5.12. Sq parameter for Meteor Crater.

Outcrop							
	Sq (3×3)	**Sq (11×11)**	**Sq (21×21)**	**Sq (31×31)**	**Sq (41×41)**	**Sq (51×51)**	**Sq (101×101)**
M13-01	2.91E-04	1.02E-03	1.77E-03	2.39E-03	2.91E-03	3.38E-03	5.50E-03
M13-02	1.83E-04	6.45E-04	1.18E-03	1.68E-03	2.16E-03	2.63E-03	4.83E-03
M13-03	1.65E-04	5.65E-04	1.02E-03	1.45E-03	1.87E-03	2.27E-03	4.13E-03
M13-04	4.19E-04	1.34E-03	2.24E-03	2.98E-03	3.62E-03	4.20E-03	6.61E-03
M13-05	2.73E-04	9.84E-04	1.82E-03	2.62E-03	3.41E-03	4.17E-03	7.78E-03
M13-06	3.06E-04	1.14E-03	2.14E-03	3.10E-03	4.04E-03	4.96E-03	9.34E-03
M13-07	4.19E-04	1.46E-03	2.58E-03	3.58E-03	4.52E-03	5.42E-03	9.47E-03
M13-08	8.35E-04	2.33E-03	3.47E-03	4.40E-03	5.24E-03	6.02E-03	9.52E-03
M13-09	2.55E-04	9.63E-04	1.80E-03	2.60E-03	3.37E-03	4.11E-03	7.46E-03
M13-10	3.42E-04	1.07E-03	1.78E-03	2.41E-03	2.99E-03	3.53E-03	6.00E-03
M14-11	2.22E-04	8.28E-04	1.53E-03	2.20E-03	2.83E-03	3.43E-03	6.18E-03
M14-12	1.57E-04	5.70E-04	1.03E-03	1.46E-03	1.87E-03	2.26E-03	4.04E-03
M14-13	2.71E-04	9.63E-04	1.77E-03	2.55E-03	3.31E-03	4.06E-03	7.60E-03
M14-14	1.82E-04	6.63E-04	1.21E-03	1.72E-03	2.21E-03	2.68E-03	4.79E-03
M14-15	2.75E-04	1.01E-03	1.85E-03	2.64E-03	3.40E-03	4.13E-03	7.24E-03
M14-16	3.80E-04	1.26E-03	2.24E-03	3.15E-03	4.03E-03	4.88E-03	8.68E-03
M14-17	2.02E-04	7.39E-04	1.34E-03	1.90E-03	2.43E-03	2.93E-03	5.25E-03
M14-18	3.20E-04	1.18E-03	2.18E-03	3.12E-03	4.01E-03	4.87E-03	8.74E-03
M14-19	3.93E-04	1.46E-03	2.72E-03	3.93E-03	5.10E-03	6.23E-03	1.14E-02
M14-20	2.53E-04	8.32E-04	1.41E-03	1.92E-03	2.39E-03	2.82E-03	4.65E-03
M14-21	2.84E-04	1.05E-03	1.96E-03	2.83E-03	3.70E-03	4.55E-03	8.61E-03
MC-M1-01	1.88E-04	6.84E-04	1.26E-03	1.80E-03	2.33E-03	2.83E-03	5.17E-03

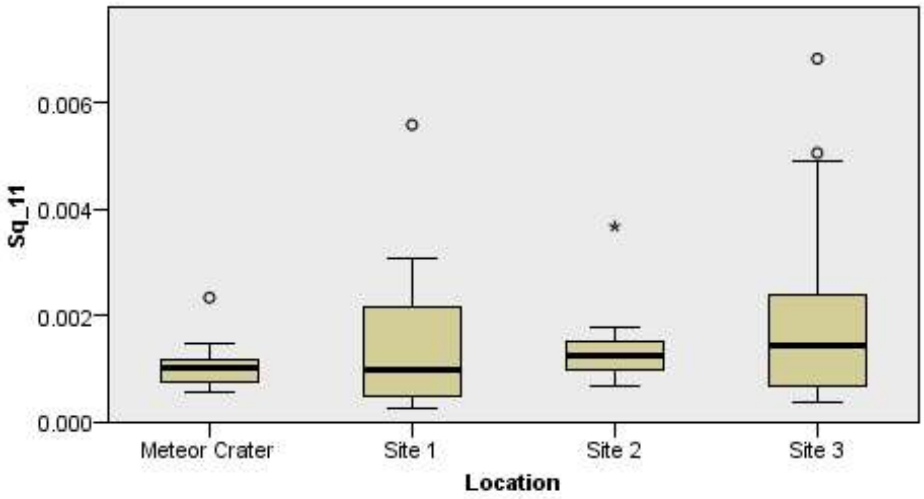
Independent-Samples Kruskal-Wallis Test



Total N	74
Test Statistic	2.844
Degrees of Freedom	3
Asymptotic Sig. (2-sided test)	.416

1. The test statistic is adjusted for ties.
2. Multiple comparisons are not performed because the overall test does not show significant differences across samples.

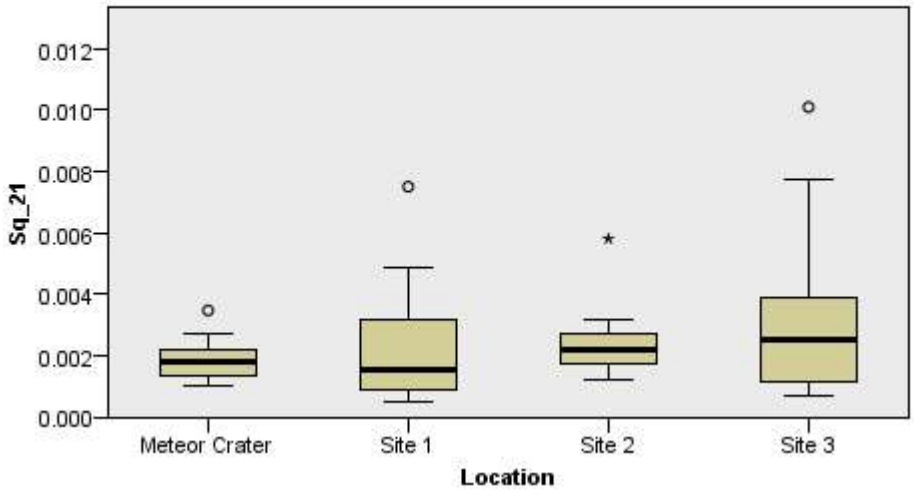
Independent-Samples Kruskal-Wallis Test



Total N	74
Test Statistic	3.286
Degrees of Freedom	3
Asymptotic Sig. (2-sided test)	.350

1. The test statistic is adjusted for ties.
2. Multiple comparisons are not performed because the overall test does not show significant differences across samples.

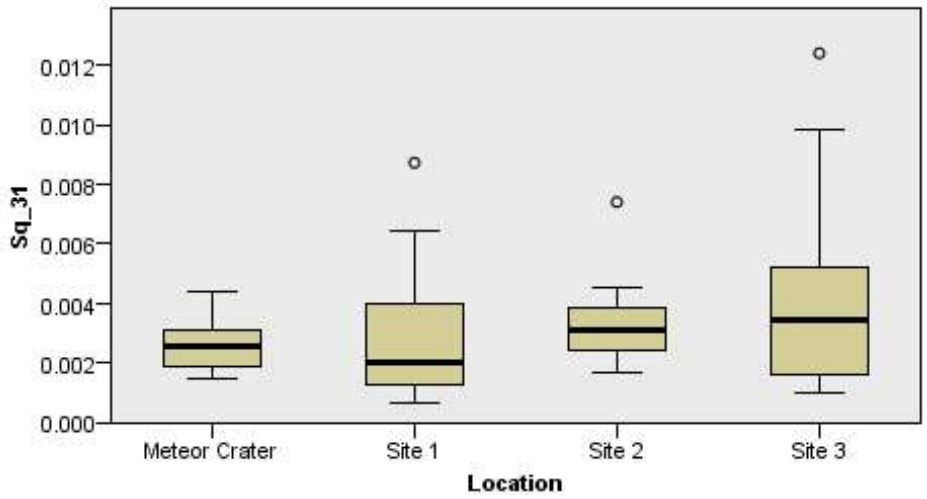
Independent-Samples Kruskal-Wallis Test



Total N	74
Test Statistic	3.619
Degrees of Freedom	3
Asymptotic Sig. (2-sided test)	.306

1. The test statistic is adjusted for ties.
2. Multiple comparisons are not performed because the overall test does not show significant differences across samples.

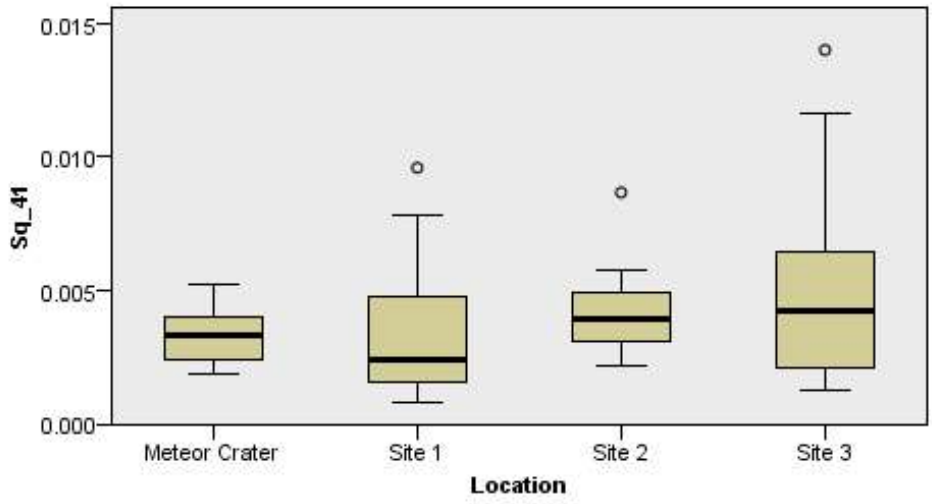
Independent-Samples Kruskal-Wallis Test



Total N	74
Test Statistic	3.849
Degrees of Freedom	3
Asymptotic Sig. (2-sided test)	.278

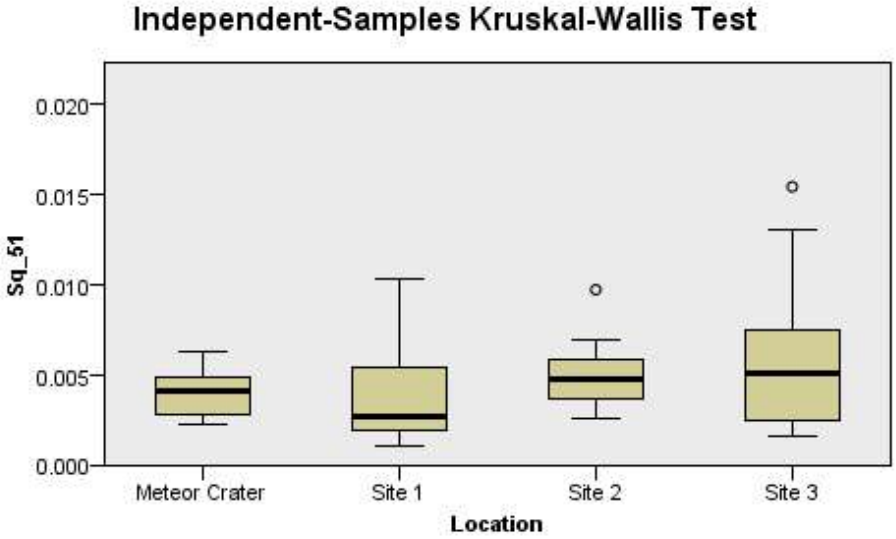
1. The test statistic is adjusted for ties.
2. Multiple comparisons are not performed because the overall test does not show significant differences across samples.

Independent-Samples Kruskal-Wallis Test



Total N	74
Test Statistic	4.382
Degrees of Freedom	3
Asymptotic Sig. (2-sided test)	.223

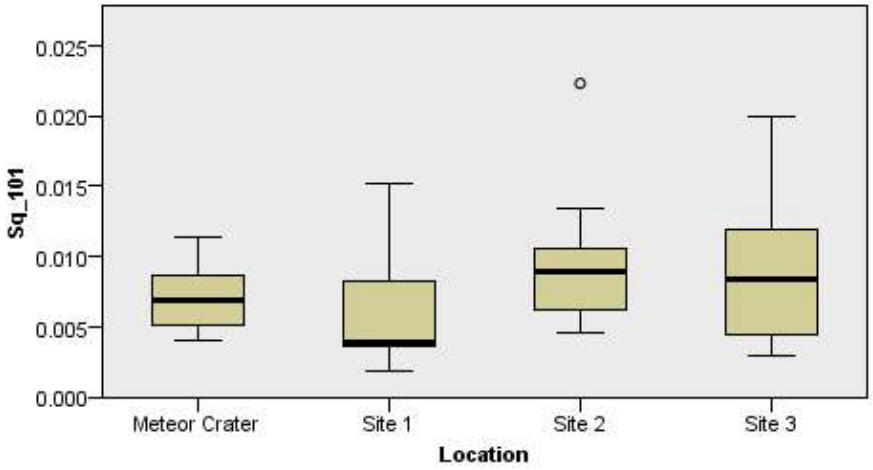
1. The test statistic is adjusted for ties.
2. Multiple comparisons are not performed because the overall test does not show significant differences across samples.



Total N	74
Test Statistic	4.587
Degrees of Freedom	3
Asymptotic Sig. (2-sided test)	.205

1. The test statistic is adjusted for ties.
2. Multiple comparisons are not performed because the overall test does not show significant differences across samples.

Independent-Samples Kruskal-Wallis Test



Total N	74
Test Statistic	6.149
Degrees of Freedom	3
Asymptotic Sig. (2-sided test)	.105

1. The test statistic is adjusted for ties.
2. Multiple comparisons are not performed because the overall test does not show significant differences across samples.

5.3.2. Standard deviation of slope (Sdq)

Table A.5.13. Sdq parameter for Site 1.

Outcrop							
	Sdq (3×3)	**Sdq (11×11)**	**Sdq (21×21)**	**Sdq (31×31)**	**Sdq (41×41)**	**Sdq (51×51)**	**Sdq (101×101)**
S1.2-M1	2.80	4.41	4.89	5.12	5.28	5.39	5.68
S1.2-M2	4.53	7.12	7.74	8.03	8.22	8.35	8.72
S1.2-M3	3.36	5.48	6.18	6.60	6.90	7.14	7.92
S1.2-M4	3.21	5.90	6.86	7.36	7.70	7.95	8.71
S1-M2	2.75	4.52	5.15	5.53	5.80	6.01	6.53
S1-M4_1	6.28	11.38	13.07	13.83	14.25	14.52	15.07
S1-M4_2	5.71	10.19	11.78	12.55	13.01	13.32	14.08
S1-M8_1	5.59	10.05	11.71	12.58	13.11	13.48	14.36
S1-M8_2	3.62	6.54	7.71	8.36	8.79	9.10	9.88
S1-M10	4.98	8.79	10.30	11.11	11.64	12.02	12.98
S1-M13_1	5.15	8.46	9.46	9.96	10.29	10.52	11.09
S1-M13_2	6.40	10.22	11.26	11.78	12.12	12.37	13.03
S1-M13_3	5.58	9.64	11.00	11.72	12.22	12.60	13.89

Table A.5.14. Sdq parameter for Site 2.

Outcrop							
	Sdq (3×3)	**Sdq (11×11)**	**Sdq (21×21)**	**Sdq (31×31)**	**Sdq (41×41)**	**Sdq (51×51)**	**Sdq (101×101)**
S2-M1	4.06	7.46	9.11	10.10	10.77	11.26	12.53
S2-M2	3.10	5.65	6.92	7.67	8.19	8.60	9.83
S2-M3	3.69	6.84	8.50	9.47	10.12	10.59	11.84
S2-M4	3.17	6.03	7.47	8.26	8.77	9.14	10.26
S2-M5	3.84	7.74	9.91	11.09	11.81	12.27	13.20
S2-M6	2.80	5.60	7.16	8.07	8.68	9.13	10.32
S2-M7	2.54	4.33	5.17	5.68	6.05	6.33	7.21
S2-M12	3.39	6.54	8.10	8.90	9.41	9.75	10.59
S2-M13	3.05	5.53	6.72	7.41	7.88	8.23	9.26
S2-M16	4.26	7.43	8.57	9.22	9.67	9.99	10.87
S2-M17	4.86	9.90	12.19	13.29	13.93	14.35	15.24
S2-M18	3.80	7.47	9.34	10.36	11.00	11.43	12.47
S2-M19	3.57	7.30	9.43	10.68	11.50	12.07	13.43
S2-M20	3.55	6.29	7.50	8.22	8.72	9.09	10.18
S2-M22_1	3.96	7.33	9.03	10.03	10.69	11.16	12.36
S2-M22_2	4.04	6.94	8.04	8.66	9.07	9.38	10.21

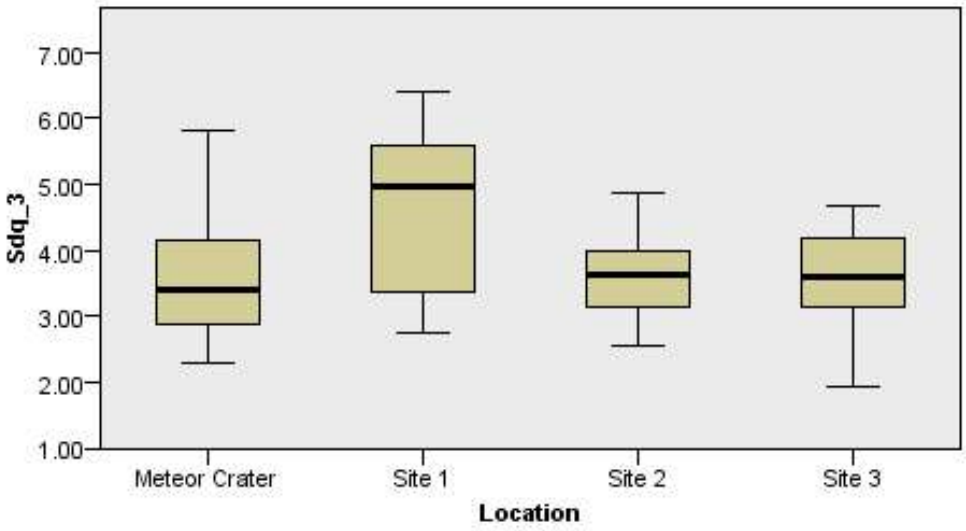
Table A.5.15. Sdq parameter for Site 3.

Outcrop							
	Sdq (3×3)	**Sdq (11×11)**	**Sdq (21×21)**	**Sdq (31×31)**	**Sdq (41×41)**	**Sdq (51×51)**	**Sdq (101×101)**
S3-M1_1	4.38	8.00	9.70	10.62	11.17	11.54	12.36
S3-M1_2	4.43	8.65	10.58	11.53	12.09	12.46	13.35
S3-M1_3	3.76	7.02	8.57	9.44	10.01	10.44	11.71
S3-M6	4.67	8.47	10.16	11.12	11.75	12.21	13.39
S2-M7	4.16	6.92	7.87	8.42	8.82	9.14	10.16
S3-M8	3.56	6.07	7.17	7.83	8.29	8.64	9.68
S3-M9	3.98	7.75	9.63	10.67	11.32	11.76	12.85
S3-M10	3.43	5.62	6.56	7.13	7.54	7.85	8.75
S3-M14	2.80	4.78	5.57	6.02	6.32	6.55	7.25
S3-M18	3.12	5.38	6.19	6.62	6.89	7.09	7.63
S3-M20	4.27	7.10	7.98	8.42	8.69	8.87	9.36
S3-M21	4.18	7.87	9.72	10.77	11.45	11.93	13.13
S3-M22	4.54	8.59	10.44	11.49	12.16	12.63	13.74
S3-M23	3.59	6.56	8.18	9.17	9.83	10.30	11.34
S3-M24	3.13	5.56	6.74	7.42	7.87	8.20	9.08
S3-M25	3.97	7.31	8.81	9.53	9.94	10.19	10.76
S3-M27	3.29	5.28	5.90	6.26	6.52	6.72	7.39
S3-M28	2.68	4.80	5.48	5.86	6.14	6.35	7.04
S3-M29	3.60	6.25	7.21	7.72	8.06	8.33	9.28
S3-M31	1.94	2.98	3.39	3.67	3.89	4.07	4.68
S3-M32	3.03	5.21	5.94	6.34	6.63	6.86	7.63
S3-M33	2.91	4.95	5.54	5.85	6.08	6.26	6.91
S3-M35	4.13	7.33	8.34	8.87	9.21	9.45	10.09

Table A.5.16. Sdq parameter for Meteor Crater.

Outcrop							
	Sdq (3×3)	**Sdq (11×11)**	**Sdq (21×21)**	**Sdq (31×31)**	**Sdq (41×41)**	**Sdq (51×51)**	**Sdq (101×101)**
M13-01	4.89	9.99	12.19	13.10	13.56	13.82	14.32
M13-02	4.17	6.80	7.65	8.10	8.39	8.60	9.21
M13-03	3.77	6.39	7.41	7.98	8.36	8.65	9.46
M13-04	5.81	11.20	13.28	14.21	14.74	15.08	15.85
M13-05	3.51	6.18	7.37	8.04	8.50	8.85	9.88
M13-06	2.77	4.87	5.89	6.47	6.88	7.19	8.16
M13-07	3.35	6.41	7.86	8.64	9.14	9.49	10.40
M13-08	3.22	5.90	7.23	7.96	8.45	8.80	9.79
M13-09	2.87	6.06	7.73	8.63	9.20	9.61	10.65
M13-10	5.06	9.37	11.05	11.86	12.37	12.71	13.60
M14-11	2.29	4.62	5.62	6.15	6.49	6.73	7.38
M14-12	2.72	5.30	6.34	6.85	7.16	7.37	7.84
M14-13	3.75	6.14	6.95	7.37	7.67	7.89	8.60
M14-14	2.59	4.51	5.26	5.65	5.92	6.13	6.80
M14-15	2.78	5.18	6.24	6.87	7.32	7.67	8.75
M14-16	4.15	7.11	8.17	8.78	9.22	9.57	10.75
M14-17	3.46	6.88	8.42	9.22	9.71	10.05	10.92
M14-18	3.48	6.56	7.86	8.57	9.06	9.43	10.54
M14-19	3.11	6.22	7.66	8.49	9.08	9.55	11.05
M14-20	4.57	8.13	9.50	10.25	10.76	11.14	12.21
M14-21	3.28	5.65	6.63	7.20	7.61	7.92	8.90
MC-M1-01	3.11	5.43	6.20	6.58	6.83	7.00	7.40

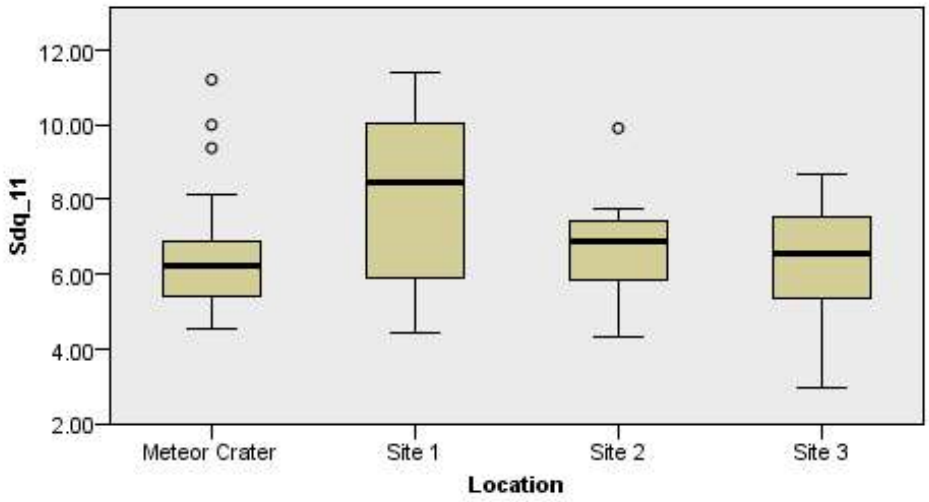
Independent-Samples Kruskal-Wallis Test



Total N	74
Test Statistic	6.479
Degrees of Freedom	3
Asymptotic Sig. (2-sided test)	.091

1. The test statistic is adjusted for ties.
2. Multiple comparisons are not performed because the overall test does not show significant differences across samples.

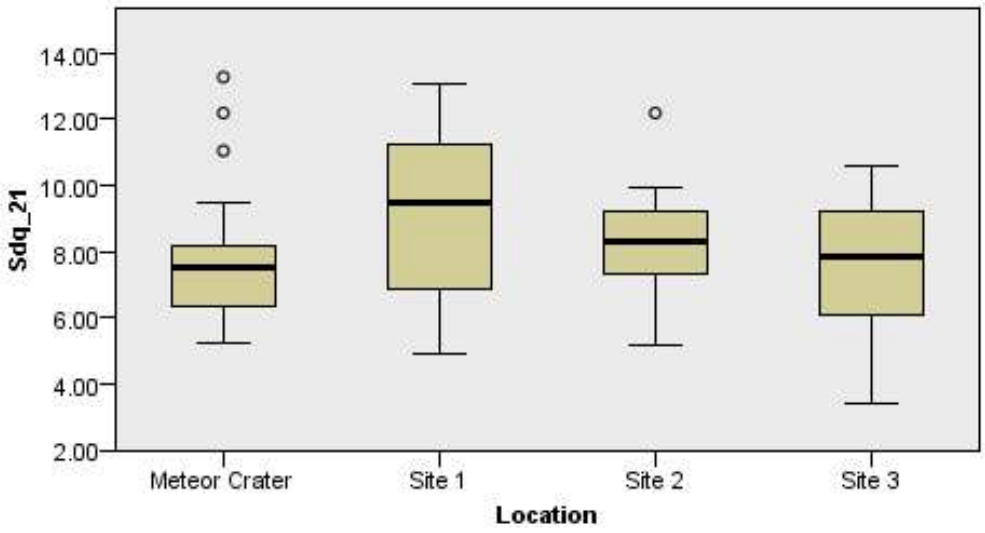
Independent-Samples Kruskal-Wallis Test



Total N	74
Test Statistic	4.027
Degrees of Freedom	3
Asymptotic Sig. (2-sided test)	.259

1. The test statistic is adjusted for ties.
2. Multiple comparisons are not performed because the overall test does not show significant differences across samples.

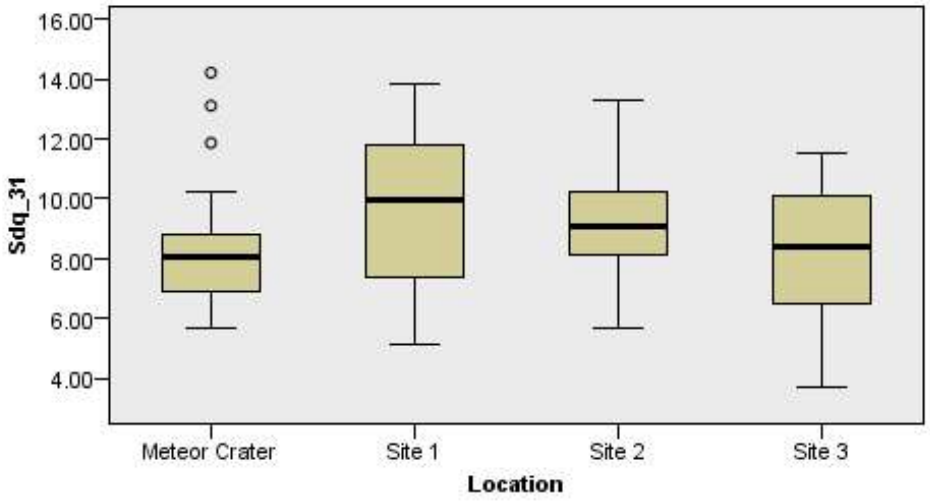
Independent-Samples Kruskal-Wallis Test



Total N	74
Test Statistic	3.029
Degrees of Freedom	3
Asymptotic Sig. (2-sided test)	.387

1. The test statistic is adjusted for ties.
2. Multiple comparisons are not performed because the overall test does not show significant differences across samples.

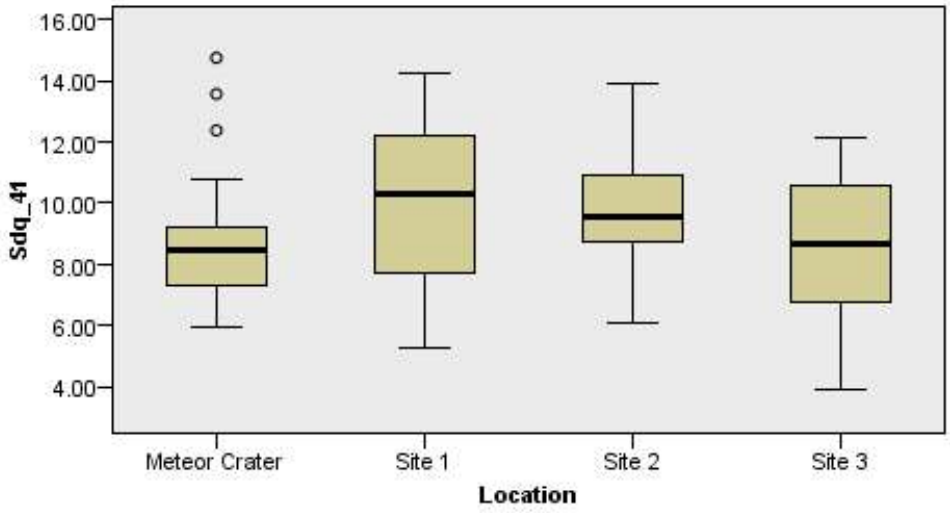
Independent-Samples Kruskal-Wallis Test



Total N	74
Test Statistic	3.258
Degrees of Freedom	3
Asymptotic Sig. (2-sided test)	.353

1. The test statistic is adjusted for ties.
2. Multiple comparisons are not performed because the overall test does not show significant differences across samples.

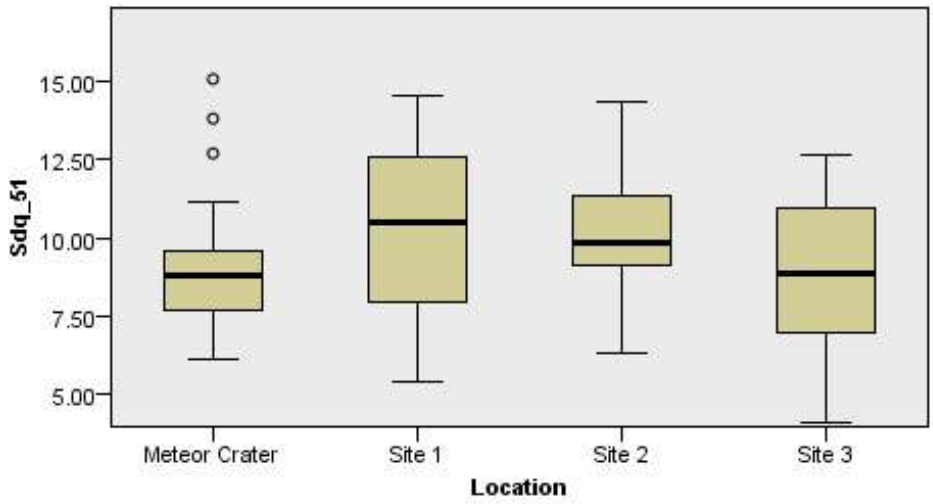
Independent-Samples Kruskal-Wallis Test



Total N	74
Test Statistic	3.402
Degrees of Freedom	3
Asymptotic Sig. (2-sided test)	.334

1. The test statistic is adjusted for ties.
2. Multiple comparisons are not performed because the overall test does not show significant differences across samples.

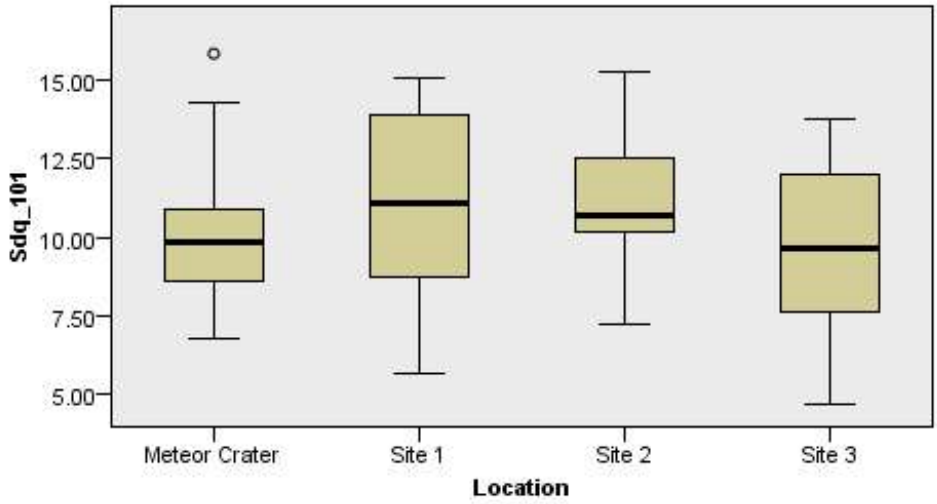
Independent-Samples Kruskal-Wallis Test



Total N	74
Test Statistic	3.442
Degrees of Freedom	3
Asymptotic Sig. (2-sided test)	.328

1. The test statistic is adjusted for ties.
2. Multiple comparisons are not performed because the overall test does not show significant differences across samples.

Independent-Samples Kruskal-Wallis Test



Total N	74
Test Statistic	3.804
Degrees of Freedom	3
Asymptotic Sig. (2-sided test)	.283

1. The test statistic is adjusted for ties.
2. Multiple comparisons are not performed because the overall test does not show significant differences across samples.

A.5.3.3. Maximum height (Sz)

Table A.5.17. Sz parameter for Site 1.

Outcrop							
	Sz (3×3)	**Sz (11×11)**	**Sz (21×21)**	**Sz (31×31)**	**Sz (41×41)**	**Sz (51×51)**	**Sz (101×101)**
S1.2-M1	1.33E-04	1.10E-03	2.02E-03	2.87E-03	3.68E-03	4.48E-03	8.19E-03
S1.2-M2	3.94E-04	1.52E-03	2.67E-03	3.73E-03	4.75E-03	5.73E-03	1.04E-02
S1.2-M3	3.56E-04	1.57E-03	2.96E-03	4.28E-03	5.56E-03	6.80E-03	1.26E-02
S1.2-M4	4.33E-04	1.97E-03	3.73E-03	5.41E-03	7.04E-03	8.64E-03	1.62E-02
S1-M2	5.30E-04	2.45E-03	5.00E-03	7.61E-03	1.02E-02	1.29E-02	2.52E-02
S1-M4_1	2.33E-03	9.94E-03	1.78E-02	2.39E-02	2.89E-02	3.33E-02	5.21E-02
S1-M4_2	9.59E-04	4.28E-03	8.14E-03	1.17E-02	1.50E-02	1.80E-02	3.07E-02
S1-M8_1	6.76E-03	2.30E-02	3.70E-02	4.76E-02	5.60E-02	6.33E-02	9.35E-02
S1-M8_2	9.51E-04	3.92E-03	7.23E-03	1.04E-02	1.36E-02	1.66E-02	3.14E-02
S1-M10	2.53E-03	1.07E-02	1.98E-02	2.82E-02	3.61E-02	4.37E-02	7.75E-02
S1-M13_1	2.15E-03	1.01E-02	1.99E-02	2.90E-02	3.73E-02	4.50E-02	7.65E-02
S1-M13_2	1.08E-03	4.60E-03	8.55E-03	1.23E-02	1.60E-02	1.97E-02	3.71E-02
S1-M13_3	3.14E-03	1.31E-02	2.37E-02	3.35E-02	4.28E-02	5.16E-02	8.99E-02

Table A.5.18. Sz parameter for Site 2.

Outcrop							
	Sz (3×3)	**Sz (11×11)**	**Sz (21×21)**	**Sz (31×31)**	**Sz (41×41)**	**Sz (51×51)**	**Sz (101×101)**
S2-M1	1.47E-03	6.80E-03	1.34E-02	2.02E-02	2.69E-02	3.33E-02	6.28E-02
S2-M2	7.66E-04	3.80E-03	1.84E-03	1.14E-02	1.52E-02	1.90E-02	3.82E-02
S2-M3	1.17E-03	5.70E-03	1.13E-02	1.70E-02	2.26E-02	2.83E-02	5.74E-02
S2-M4	8.44E-04	4.13E-03	8.11E-03	1.20E-02	1.58E-02	1.95E-02	3.75E-02
S2-M5	1.05E-03	5.13E-03	9.99E-03	1.46E-02	1.89E-02	2.31E-02	4.25E-02
S2-M6	6.23E-04	3.05E-03	6.01E-03	8.93E-03	1.18E-02	1.47E-02	2.91E-02
S2-M7	5.89E-04	2.90E-03	5.90E-03	9.03E-03	1.22E-02	1.55E-02	3.18E-02
S2-M12	1.09E-03	5.29E-03	1.04E-02	1.53E-02	2.02E-02	2.50E-02	4.82E-02
S2-M13	1.26E-03	6.03E-03	1.20E-02	1.81E-02	2.41E-02	3.00E-02	5.92E-02
S2-M16	9.55E-04	4.28E-03	8.09E-03	1.18E-02	1.55E-02	1.92E-02	3.67E-02
S2-M17	3.21E-03	1.40E-02	2.65E-02	3.86E-02	5.04E-02	6.19E-02	1.16E-01
S2-M18	1.21E-03	5.94E-03	1.22E-02	1.87E-02	2.56E-02	3.26E-02	6.80E-02
S2-M19	1.30E-03	6.39E-03	1.25E-02	1.85E-02	2.43E-02	2.99E-02	5.68E-02
S2-M20	7.61E-04	3.60E-03	7.02E-03	1.03E-02	1.35E-02	1.65E-02	3.07E-02
S2-M22_1	9.39E-04	4.47E-03	8.93E-03	1.35E-02	1.80E-02	2.26E-02	4.54E-02
S2-M22_2	9.52E-04	4.34E-03	8.49E-03	1.27E-02	1.69E-02	2.12E-02	4.12E-02

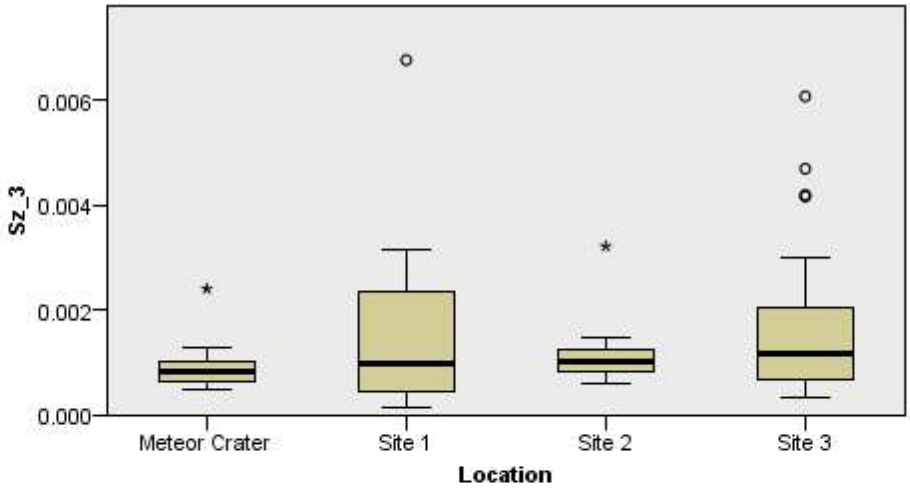
Table A.5.19. Sz parameter for Site 3.

Outcrop							
	Sz (3×3)	**Sz (11×11)**	**Sz (21×21)**	**Sz (31×31)**	**Sz (41×41)**	**Sz (51×51)**	**Sz (101×101)**
S3-M1_1	1.53E-03	7.51E-03	1.58E-02	2.47E-02	3.40E-02	4.34E-02	8.94E-02
S3-M1_2	1.72E-03	7.44E-03	1.36E-02	1.94E-02	2.49E-02	3.02E-02	5.43E-02
S3-M1_3	6.07E-03	2.27E-02	3.62E-02	4.62E-02	5.46E-02	6.20E-02	9.42E-02
S3-M6	4.16E-03	1.82E-02	3.55E-02	5.26E-02	6.90E-02	8.47E-02	1.52E-01
S2-M7	1.37E-03	6.53E-03	1.33E-02	2.05E-02	2.77E-02	3.49E-02	7.13E-02
S3-M8	1.73E-03	8.07E-03	1.60E-02	2.37E-02	3.11E-02	3.82E-02	7.13E-02
S3-M9	4.69E-03	1.80E-02	3.06E-02	4.18E-02	5.21E-02	6.19E-02	1.08E-01
S3-M10	1.66E-03	8.15E-03	1.74E-02	2.70E-02	3.63E-02	4.51E-02	8.54E-02
S3-M14	5.86E-04	2.49E-03	4.46E-03	6.25E-03	7.93E-03	9.55E-03	1.70E-02
S3-M18	4.45E-04	2.11E-03	4.10E-03	6.02E-03	7.89E-03	9.72E-03	1.86E-02
S3-M20	4.94E-04	2.26E-03	4.34E-03	6.40E-03	8.47E-03	1.06E-02	2.15E-02
S3-M21	1.16E-03	5.62E-03	1.11E-02	1.65E-02	2.18E-02	2.72E-02	5.37E-02
S3-M22	2.35E-03	1.04E-02	1.94E-02	2.80E-02	3.64E-02	4.44E-02	8.17E-02
S3-M23	9.02E-04	4.42E-03	8.71E-03	1.29E-02	1.70E-02	2.11E-02	4.11E-02
S3-M24	7.44E-04	3.62E-03	7.14E-03	1.06E-02	1.40E-02	1.74E-02	3.37E-02
S3-M25	7.35E-04	3.41E-03	6.60E-03	9.73E-03	1.28E-02	1.59E-02	3.18E-02
S3-M27	5.19E-04	2.45E-03	4.75E-03	7.00E-03	9.21E-03	1.14E-02	2.19E-02
S3-M28	3.59E-04	1.73E-03	3.36E-03	4.96E-03	6.52E-03	8.05E-03	1.54E-02
S3-M29	3.01E-03	1.31E-02	2.48E-02	3.58E-02	4.61E-02	5.57E-02	9.83E-02
S3-M31	8.74E-04	4.02E-03	7.76E-03	1.14E-02	1.50E-02	1.84E-02	3.49E-02
S3-M32	7.18E-04	2.94E-03	5.05E-03	6.91E-03	8.65E-03	1.03E-02	1.79E-02
S3-M33	3.37E-04	1.54E-03	2.90E-03	4.22E-03	5.49E-03	6.74E-03	1.27E-02
S3-M35	4.19E-03	1.80E-02	3.40E-02	4.98E-02	6.48E-02	7.86E-02	1.30E-01

Table A.5.20. Sz parameter for Meteor Crater.

Outcrop							
	Sz (3×3)	**Sz (11×11)**	**Sz (21×21)**	**Sz (31×31)**	**Sz (41×41)**	**Sz (51×51)**	**Sz (101×101)**
M13-01	8.95E-04	4.06E-03	7.35E-03	1.01E-02	1.27E-02	1.51E-02	2.59E-02
M13-02	5.66E-04	2.62E-03	5.01E-03	7.27E-03	9.43E-03	1.15E-02	2.10E-02
M13-03	5.02E-04	2.26E-03	4.29E-03	6.23E-03	8.11E-03	9.94E-03	1.86E-02
M13-04	1.26E-03	5.32E-03	9.40E-03	1.29E-02	1.60E-02	1.89E-02	3.17E-02
M13-05	8.30E-04	3.91E-03	7.59E-03	1.12E-02	1.46E-02	1.81E-02	3.43E-02
M13-06	9.26E-04	4.48E-03	8.78E-03	1.30E-02	1.71E-02	2.12E-02	4.07E-02
M13-07	1.24E-03	5.68E-03	1.08E-02	1.57E-02	2.03E-02	2.48E-02	4.57E-02
M13-08	2.40E-03	8.91E-03	1.49E-02	2.01E-02	2.50E-02	2.98E-02	5.25E-02
M13-09	7.73E-04	3.75E-03	7.29E-03	1.07E-02	1.40E-02	1.73E-02	3.24E-02
M13-10	1.02E-03	4.27E-03	7.68E-03	1.08E-02	1.38E-02	1.67E-02	3.04E-02
M14-11	6.88E-04	3.34E-03	6.52E-03	9.61E-03	1.26E-02	1.56E-02	2.97E-02
M14-12	4.87E-04	2.31E-03	4.42E-03	6.43E-03	8.36E-03	1.02E-02	1.90E-02
M14-13	8.20E-04	3.82E-03	7.36E-03	1.08E-02	1.42E-02	1.75E-02	3.34E-02
M14-14	5.51E-04	2.64E-03	5.16E-03	7.61E-03	1.00E-02	1.24E-02	2.38E-02
M14-15	8.33E-04	3.96E-03	7.68E-03	1.13E-02	1.48E-02	1.83E-02	3.48E-02
M14-16	1.15E-03	5.07E-03	9.59E-03	1.39E-02	1.81E-02	2.22E-02	4.14E-02
M14-17	6.13E-04	2.88E-03	5.49E-03	7.94E-03	1.03E-02	1.25E-02	2.29E-02
M14-18	9.80E-04	4.68E-03	9.06E-03	1.33E-02	1.73E-02	2.13E-02	4.00E-02
M14-19	1.20E-03	5.73E-03	1.11E-02	1.62E-02	2.12E-02	2.61E-02	4.87E-02
M14-20	7.71E-04	3.42E-03	6.39E-03	9.18E-03	1.19E-02	1.45E-02	2.64E-02
M14-21	8.76E-04	4.20E-03	8.18E-03	1.20E-02	1.58E-02	1.95E-02	3.70E-02
MC-M1-01	5.93E-04	2.84E-03	5.51E-03	8.07E-03	1.06E-02	1.30E-02	2.42E-02

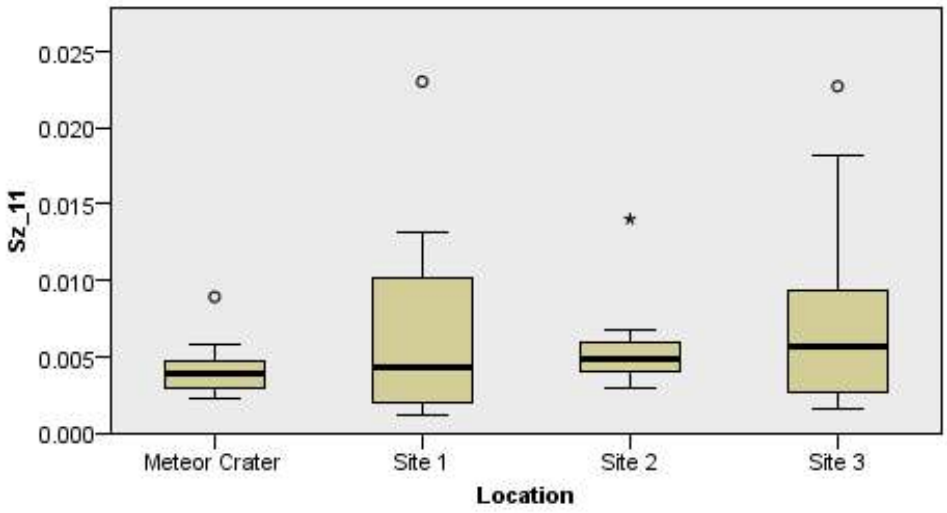
Independent-Samples Kruskal-Wallis Test



Total N	74
Test Statistic	2.631
Degrees of Freedom	3
Asymptotic Sig. (2-sided test)	.452

1. The test statistic is adjusted for ties.
2. Multiple comparisons are not performed because the overall test does not show significant differences across samples.

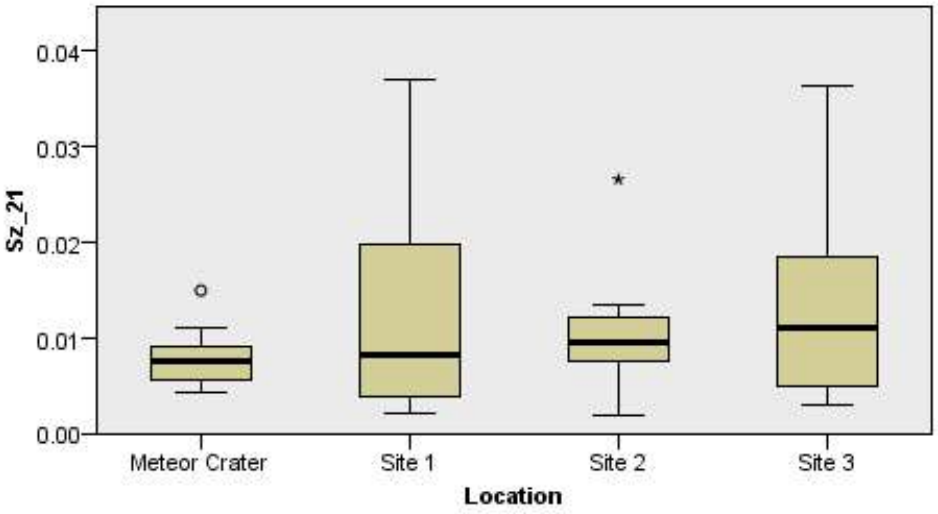
Independent-Samples Kruskal-Wallis Test



Total N	74
Test Statistic	3.356
Degrees of Freedom	3
Asymptotic Sig. (2-sided test)	.340

1. The test statistic is adjusted for ties.
2. Multiple comparisons are not performed because the overall test does not show significant differences across samples.

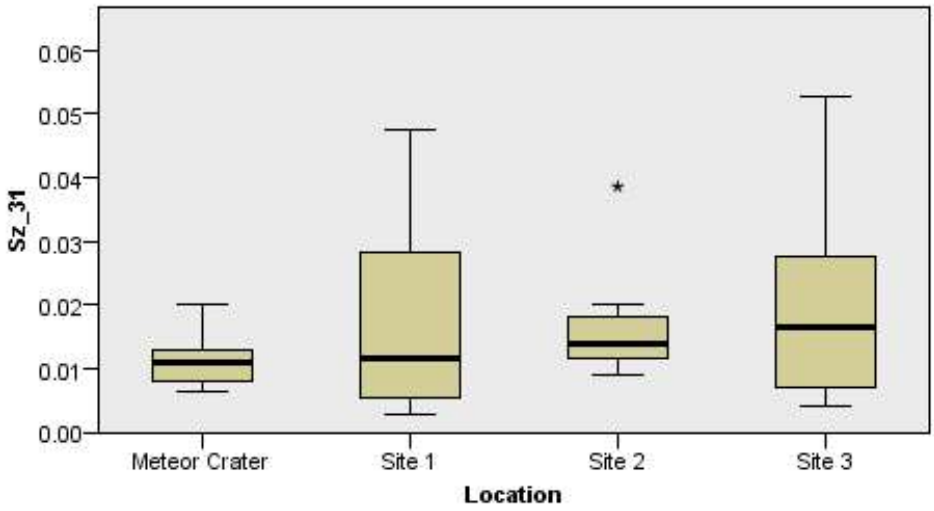
Independent-Samples Kruskal-Wallis Test



Total N	74
Test Statistic	3.122
Degrees of Freedom	3
Asymptotic Sig. (2-sided test)	.373

1. The test statistic is adjusted for ties.
2. Multiple comparisons are not performed because the overall test does not show significant differences across samples.

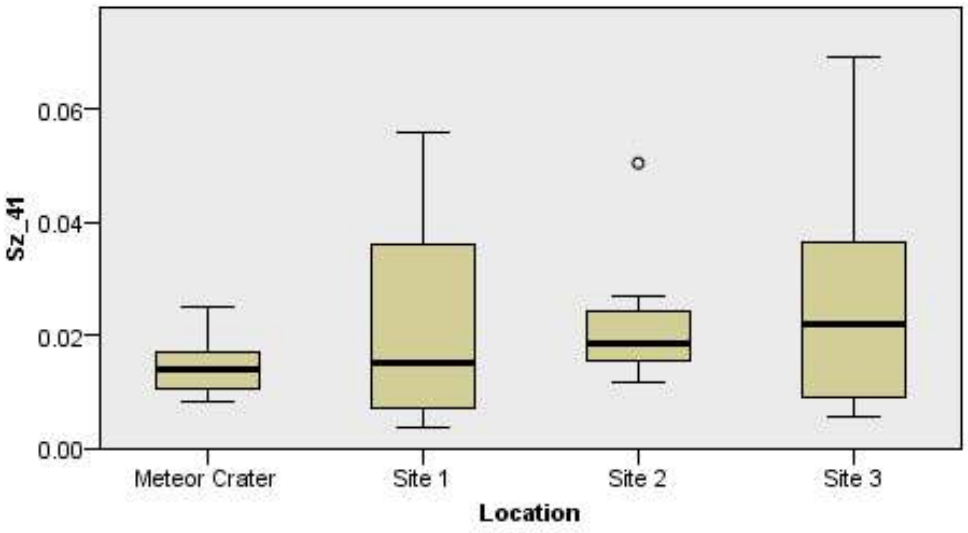
Independent-Samples Kruskal-Wallis Test



Total N	74
Test Statistic	4.486
Degrees of Freedom	3
Asymptotic Sig. (2-sided test)	.214

1. The test statistic is adjusted for ties.
2. Multiple comparisons are not performed because the overall test does not show significant differences across samples.

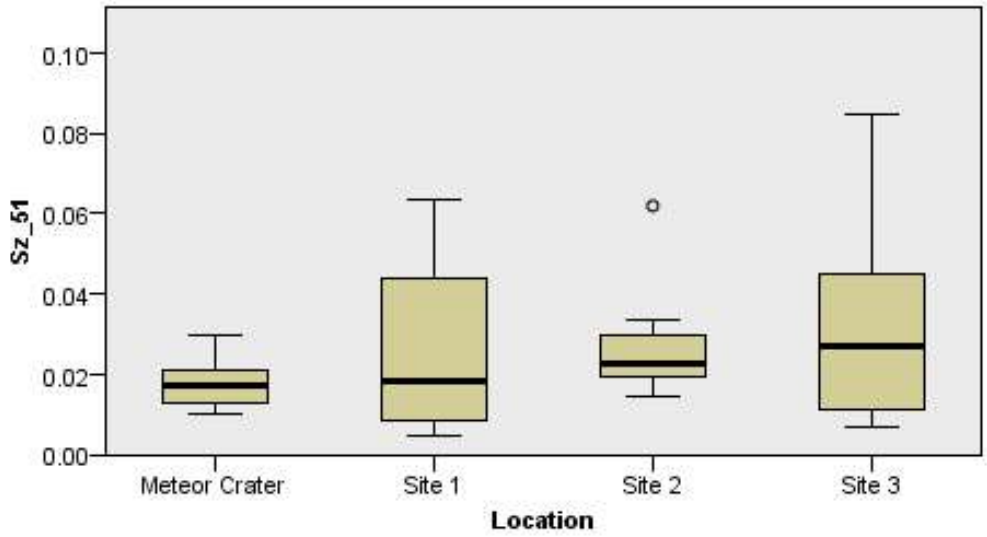
Independent-Samples Kruskal-Wallis Test



Total N	74
Test Statistic	4.971
Degrees of Freedom	3
Asymptotic Sig. (2-sided test)	.174

1. The test statistic is adjusted for ties.
2. Multiple comparisons are not performed because the overall test does not show significant differences across samples.

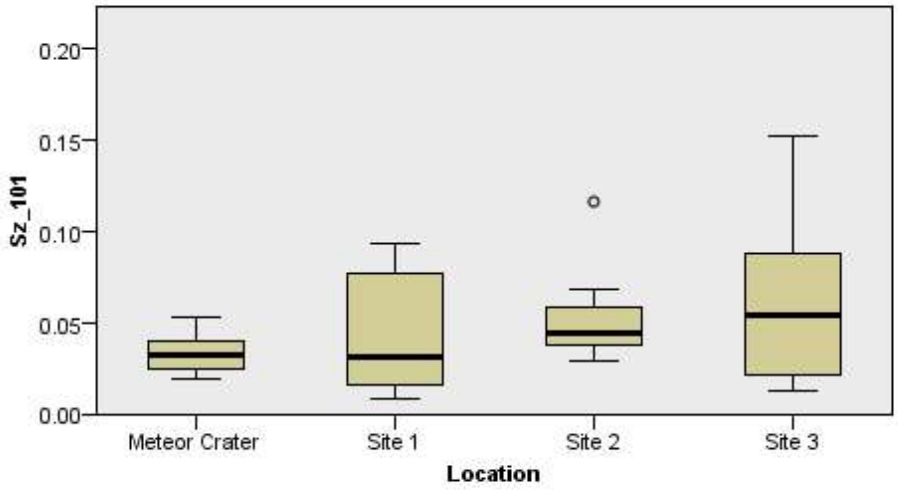
Independent-Samples Kruskal-Wallis Test



Total N	74
Test Statistic	5.725
Degrees of Freedom	3
Asymptotic Sig. (2-sided test)	.126

1. The test statistic is adjusted for ties.
2. Multiple comparisons are not performed because the overall test does not show significant differences across samples.

Independent-Samples Kruskal-Wallis Test



Total N	74
Test Statistic	7.757
Degrees of Freedom	3
Asymptotic Sig. (2-sided test)	.051

1. The test statistic is adjusted for ties.
2. Multiple comparisons are not performed because the overall test does not show significant differences across samples.

A.5.3.4. Vector Ruggedness Measure (VRM)

Table A.5.21. VRM parameter for Site 1.

Outcrop	VRM (3×3)	VRM (11×11)	VRM (21×21)	VRM (31×31)	VRM (41×41)	VRM (51×51)	VRM (101×101)
S1.2-M1	0.00	0.01	0.01	0.01	0.01	0.01	0.02
S1.2-M2	0.01	0.03	0.03	0.03	0.03	0.04	0.04
S1.2-M3	0.01	0.02	0.02	0.02	0.02	0.02	0.03
S1.2-M4	0.01	0.02	0.02	0.02	0.03	0.03	0.03
S1-M2	0.00	0.01	0.01	0.01	0.01	0.02	0.02
S1-M4_1	0.03	0.07	0.10	0.11	0.12	0.12	0.13
S1-M4_2	0.02	0.06	0.09	0.10	0.10	0.11	0.11
S1-M8_1	0.03	0.08	0.09	0.10	0.10	0.10	0.10
S1-M8_2	0.01	0.03	0.03	0.04	0.04	0.04	0.05
S1-M10	0.02	0.05	0.06	0.07	0.07	0.07	0.08
S1-M13_1	0.02	0.05	0.05	0.05	0.06	0.06	0.06
S1-M13_2	0.03	0.06	0.07	0.07	0.08	0.08	0.09
S1-M13_3	0.04	0.09	0.10	0.11	0.11	0.12	0.13

Table A.5.22. VRM parameter for Site 2.

Outcrop	**VRM (3×3)**	**VRM (11×11)**	**VRM (21×21)**	**VRM (31×31)**	**VRM (41×41)**	**VRM (51×51)**	**VRM (101×101)**
S2-M1	0.01	0.03	0.04	0.05	0.06	0.06	0.08
S2-M2	0.00	0.01	0.02	0.02	0.02	0.03	0.03
S2-M3	0.01	0.02	0.03	0.04	0.04	0.05	0.06
S2-M4	0.00	0.01	0.02	0.03	0.03	0.03	0.04
S2-M5	0.01	0.03	0.04	0.06	0.07	0.07	0.09
S2-M6	0.00	0.01	0.02	0.03	0.03	0.04	0.04
S2-M7	0.00	0.01	0.01	0.01	0.01	0.02	0.02
S2-M12	0.00	0.02	0.03	0.04	0.04	0.04	0.05
S2-M13	0.00	0.01	0.02	0.02	0.02	0.03	0.03
S2-M16	0.01	0.02	0.03	0.03	0.04	0.04	0.04
S2-M17	0.01	0.05	0.07	0.09	0.10	0.10	0.11
S2-M18	0.01	0.02	0.04	0.05	0.05	0.06	0.07
S2-M19	0.01	0.02	0.04	0.05	0.06	0.06	0.08
S2-M20	0.01	0.02	0.03	0.03	0.04	0.04	0.05
S2-M22_1	0.01	0.02	0.03	0.04	0.05	0.05	0.06
S2-M22_2	0.01	0.02	0.03	0.03	0.04	0.04	0.04

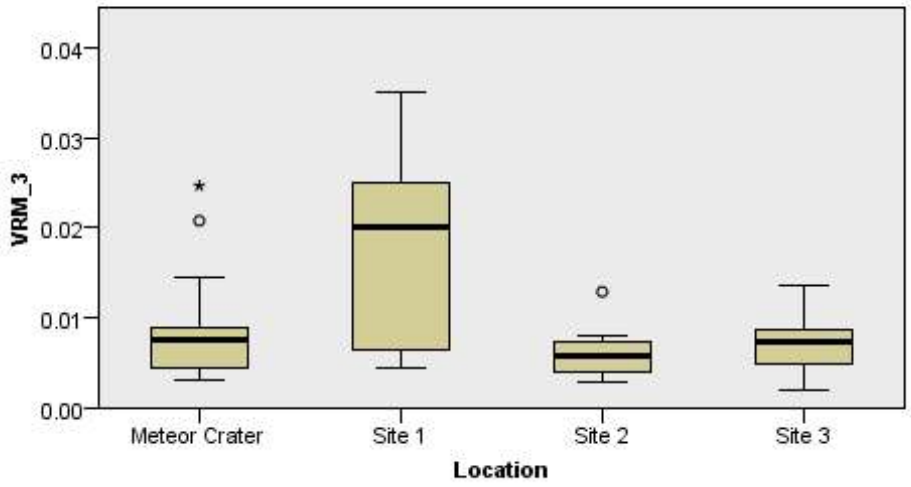
Table A.5.23. VRM parameter for Site 3.

Outcrop	VRM (3×3)	VRM (11×11)	VRM (21×21)	VRM (31×31)	VRM (41×41)	VRM (51×51)	VRM (101×101)
S3-M1_1	0.01	0.03	0.04	0.05	0.05	0.06	0.06
S3-M1_2	0.01	0.03	0.05	0.07	0.08	0.08	0.09
S3-M1_3	0.01	0.03	0.04	0.04	0.05	0.05	0.06
S3-M6	0.01	0.04	0.06	0.07	0.07	0.08	0.10
S2-M7	0.01	0.02	0.03	0.03	0.03	0.03	0.04
S3-M8	0.01	0.02	0.02	0.02	0.03	0.03	0.03
S3-M9	0.01	0.03	0.05	0.05	0.06	0.06	0.07
S3-M10	0.01	0.01	0.02	0.02	0.02	0.02	0.03
S3-M14	0.01	0.02	0.02	0.02	0.03	0.03	0.03
S3-M18	0.00	0.01	0.02	0.02	0.02	0.02	0.03
S3-M20	0.01	0.02	0.03	0.03	0.03	0.04	0.04
S3-M21	0.01	0.02	0.04	0.05	0.06	0.06	0.08
S3-M22	0.01	0.04	0.05	0.06	0.07	0.07	0.08
S3-M23	0.00	0.02	0.03	0.03	0.04	0.04	0.05
S3-M24	0.00	0.01	0.02	0.02	0.02	0.03	0.03
S3-M25	0.01	0.02	0.04	0.05	0.05	0.05	0.06
S3-M27	0.01	0.01	0.02	0.02	0.02	0.02	0.02
S3-M28	0.00	0.01	0.01	0.01	0.01	0.02	0.02
S3-M29	0.01	0.02	0.03	0.03	0.03	0.03	0.04
S3-M31	0.00	0.00	0.01	0.01	0.01	0.01	0.01
S3-M32	0.01	0.03	0.03	0.03	0.04	0.04	0.04
S3-M33	0.00	0.01	0.02	0.02	0.02	0.02	0.02
S3-M35	0.01	0.02	0.03	0.03	0.03	0.04	0.04

Table A.5.24. VRM parameter for Meteor Crater.

Outcrop	**VRM (3×3)**	**VRM (11×11)**	**VRM (21×21)**	**VRM (31×31)**	**VRM (41×41)**	**VRM (51×51)**	**VRM (101×101)**
M13-01	0.01	0.05	0.08	0.10	0.10	0.11	0.11
M13-02	0.01	0.02	0.03	0.03	0.03	0.03	0.04
M13-03	0.01	0.02	0.03	0.03	0.03	0.03	0.04
M13-04	0.02	0.08	0.11	0.12	0.13	0.14	0.14
M13-05	0.01	0.02	0.03	0.03	0.03	0.03	0.04
M13-06	0.00	0.01	0.02	0.02	0.02	0.02	0.03
M13-07	0.01	0.03	0.04	0.05	0.05	0.05	0.06
M13-08	0.01	0.02	0.03	0.03	0.04	0.04	0.04
M13-09	0.00	0.01	0.02	0.03	0.03	0.03	0.04
M13-10	0.02	0.05	0.07	0.07	0.07	0.08	0.08
M14-11	0.00	0.01	0.02	0.02	0.02	0.02	0.02
M14-12	0.00	0.01	0.02	0.02	0.03	0.03	0.03
M14-13	0.01	0.02	0.03	0.03	0.03	0.03	0.04
M14-14	0.00	0.01	0.01	0.01	0.02	0.02	0.02
M14-15	0.01	0.02	0.02	0.02	0.03	0.03	0.03
M14-16	0.01	0.03	0.04	0.05	0.05	0.05	0.06
M14-17	0.01	0.02	0.03	0.04	0.04	0.04	0.05
M14-18	0.01	0.02	0.03	0.04	0.04	0.05	0.06
M14-19	0.01	0.02	0.03	0.04	0.05	0.05	0.07
M14-20	0.01	0.04	0.05	0.06	0.06	0.07	0.07
M14-21	0.01	0.02	0.02	0.03	0.03	0.03	0.04
MC-M1-01	0.00	0.01	0.02	0.02	0.02	0.02	0.02

Independent-Samples Kruskal-Wallis Test



Total N	74
Test Statistic	12.986
Degrees of Freedom	3
Asymptotic Sig. (2-sided test)	.005

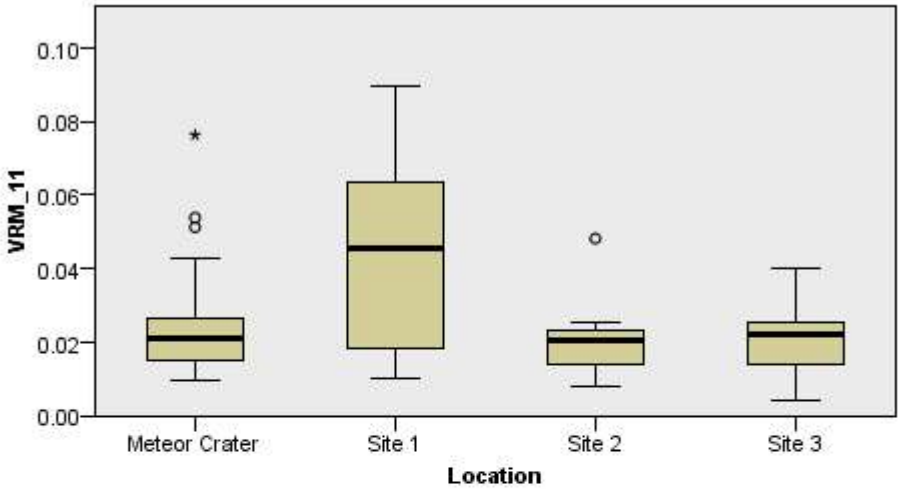
1. The test statistic is adjusted for ties.

Each node shows the sample average rank of Location.

Sample1-Sample2	Test Statistic	Std. Error	Std. Test Statistic	Sig.	Adj.Sig.
Site 2-Site 3	-9.826	7.001	-1.404	.160	.963
Site 2-Meteor Crater	11.477	7.066	1.624	.104	.626
Site 2-Site 1	28.654	8.030	3.568	.000	.002
Site 3-Meteor Crater	1.651	6.413	.257	.797	1.000
Site 3-Site 1	18.828	7.462	2.523	.012	.070
Meteor Crater-Site 1	-17.177	7.523	-2.283	.022	.135

Each row tests the null hypothesis that the Sample 1 and Sample 2 distributions are the same.
Asymptotic significances (2-sided tests) are displayed. The significance level is .05.
Significance values have been adjusted by the Bonferroni correction for multiple tests.

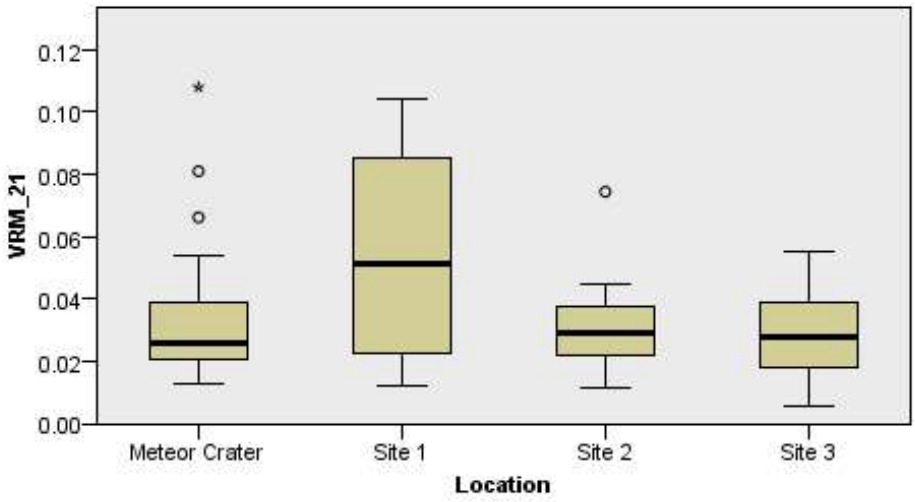
Independent-Samples Kruskal-Wallis Test



Total N	74
Test Statistic	6.229
Degrees of Freedom	3
Asymptotic Sig. (2-sided test)	.101

1. The test statistic is adjusted for ties.
2. Multiple comparisons are not performed because the overall test does not show significant differences across samples.

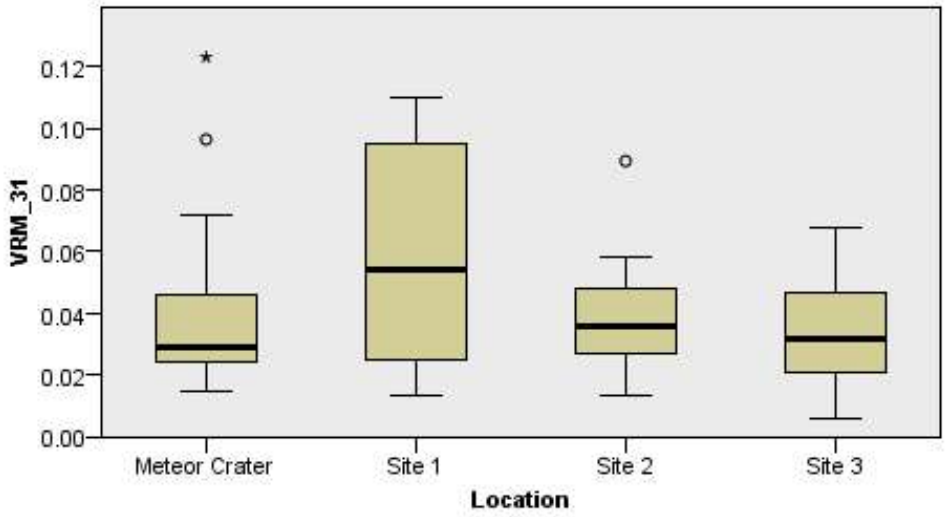
Independent-Samples Kruskal-Wallis Test



Total N	74
Test Statistic	3.703
Degrees of Freedom	3
Asymptotic Sig. (2-sided test)	.295

1. The test statistic is adjusted for ties.
2. Multiple comparisons are not performed because the overall test does not show significant differences across samples.

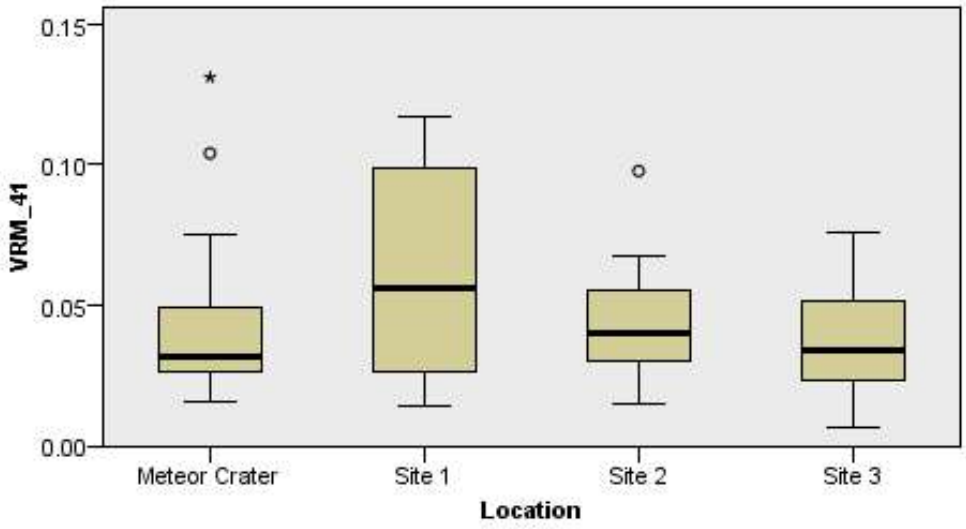
Independent-Samples Kruskal-Wallis Test



Total N	74
Test Statistic	3.358
Degrees of Freedom	3
Asymptotic Sig. (2-sided test)	.340

1. The test statistic is adjusted for ties.
2. Multiple comparisons are not performed because the overall test does not show significant differences across samples.

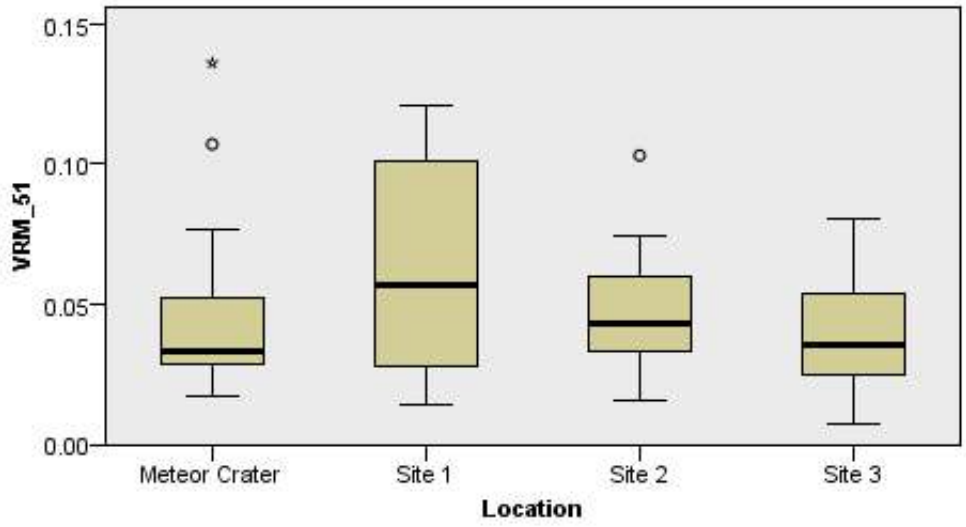
Independent-Samples Kruskal-Wallis Test



Total N	74
Test Statistic	2.973
Degrees of Freedom	3
Asymptotic Sig. (2-sided test)	.396

1. The test statistic is adjusted for ties.
2. Multiple comparisons are not performed because the overall test does not show significant differences across samples.

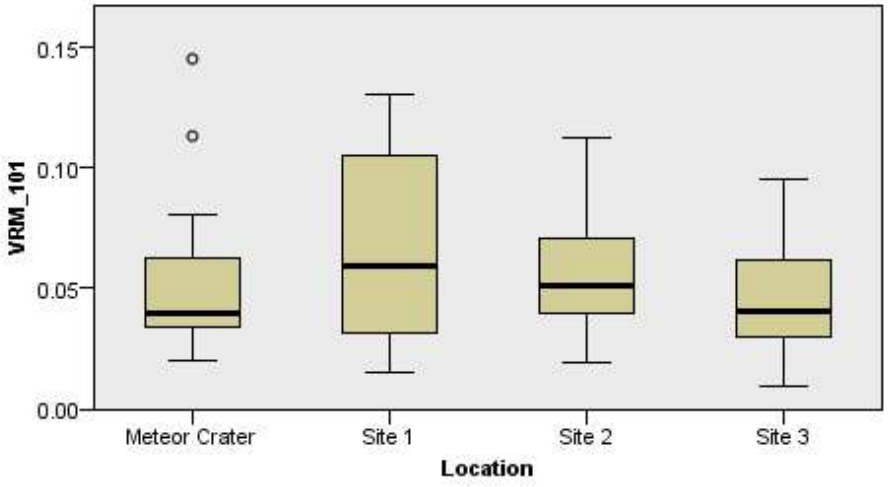
Independent-Samples Kruskal-Wallis Test



Total N	74
Test Statistic	2.850
Degrees of Freedom	3
Asymptotic Sig. (2-sided test)	.415

1. The test statistic is adjusted for ties.
2. Multiple comparisons are not performed because the overall test does not show significant differences across samples.

Independent-Samples Kruskal-Wallis Test



Total N	74
Test Statistic	2.644
Degrees of Freedom	3
Asymptotic Sig. (2-sided test)	.450

1. The test statistic is adjusted for ties.
2. Multiple comparisons are not performed because the overall test does not show significant differences across samples.

A.5.4. Morphometric feature Classification

A.5.4.1. Pit

Table A.5.25. Pit data for Site 1.

Feature	Pit						
Rock	**(3*3)**	**(11*11)**	**(21*21)**	**(31*31)**	**(41*41)**	**(51*51)**	**(101*101)**
S1.2-M1	3.18%	3.82%	3.65%	3.54%	24.16%	3.17%	2.64%
S1.2-M2	4.44%	2.56%	2.35%	2.05%	1.97%	1.91%	1.88%
S1.2-M3	2.11%	2.06%	1.85%	1.88%	1.98%	2.04%	2.59%
S1-M2	0.63%	0.38%	0.33%	0.27%	0.23%	0.22%	0.61%
S1-M4_1	0.53%	0.76%	0.97%	1.24%	1.58%	1.86%	2.65%
S1-M4_2	0.66%	1.02%	1.35%	1.67%	2.05%	2.49%	3.82%
S1-M8_1	0.55%	0.64%	0.72%	0.75%	0.77%	0.74%	0.66%
S1-M8_2	1.12%	1.62%	1.87%	2.00%	2.09%	2.13%	2.19%
S1-M10	0.41%	0.43%	0.46%	0.46%	0.46%	0.46%	0.30%
S1-M13_1	0.43%	0.53%	0.48%	0.44%	0.40%	0.34%	0.16%
S1-M13_2	0.44%	0.71%	0.76%	0.75%	0.74%	0.70%	0.72%
S1-M13_3	0.29%	0.50%	0.69%	0.72%	0.77%	0.75%	0.64%

Table A.5.26. Pit data for Site 2.

Feature	Pit						
Rock	**(3*3)**	**(11*11)**	**(21*21)**	**(31*31)**	**(41*41)**	**(51*51)**	**(101*101)**
S2-M1	0.45%	0.56%	0.70%	0.78%	0.88%	0.94%	1.35%
S2-M2	0.46%	0.49%	0.54%	0.53%	0.54%	0.53%	0.36%
S2-M3	0.21%	0.24%	0.26%	0.26%	0.26%	0.24%	0.28%
S2-M4	0.35%	0.39%	0.39%	0.42%	0.44%	0.45%	0.49%
S2-M5	0.17%	0.19%	0.20%	0.19%	0.18%	0.18%	0.24%
S2-M6	1.05%	1.17%	1.49%	1.70%	1.93%	1.91%	2.62%
S2-M7	1.51%	1.38%	1.19%	1.12%	1.18%	1.11%	1.17%
S2-M12	0.16%	0.18%	0.18%	0.15%	0.15%	0.13%	0.05%
S2-M13	0.49%	0.57%	0.59%	0.59%	0.64%	0.62%	0.58%
S2-M16	0.97%	1.05%	1.12%	1.18%	1.35%	1.30%	1.47%
S2-M17	0.41%	0.52%	0.61%	0.66%	0.73%	0.81%	1.18%
S2-M18	0.63%	0.78%	0.93%	1.00%	1.10%	1.11%	1.33%
S2-M19	0.15%	0.21%	0.22%	0.19%	0.15%	0.12%	0.04%
S2-M20	0.97%	1.03%	1.11%	1.16%	1.34%	1.30%	1.52%
S2-M22	0.86%	0.92%	1.10%	1.22%	1.34%	1.32%	1.44%

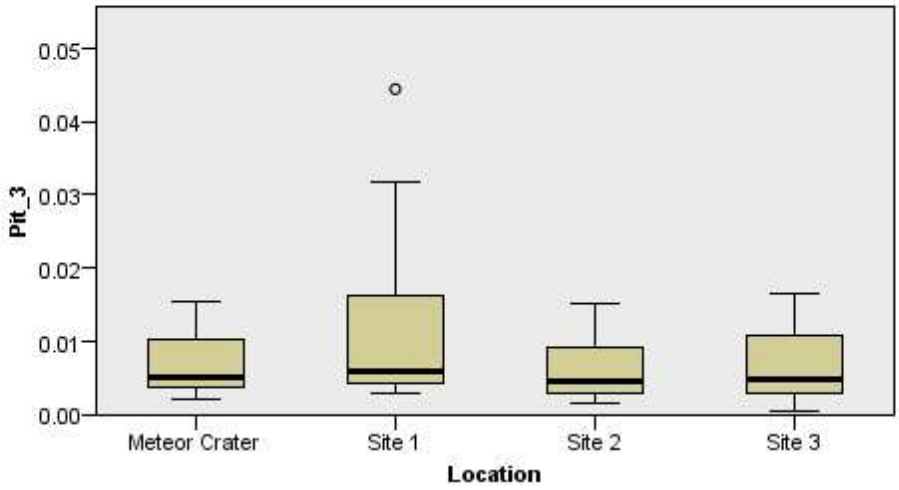
Table A.5.27. Pit data for Site 3.

Feature	Pit						
Rock	**(3*3)**	**(11*11)**	**(21*21)**	**(31*31)**	**(41*41)**	**(51*51)**	**(101*101)**
S3-M1_1	0.21%	0.19%	0.20%	0.18%	0.16%	0.17%	0.02%
S3-M1_2	0.40%	0.52%	0.65%	0.80%	1.04%	1.15%	1.28%
S3-M1_3	0.56%	0.69%	0.85%	0.94%	1.01%	1.00%	1.06%
S3-M6	0.43%	0.44%	0.49%	0.49%	0.48%	0.45%	0.49%
S3-M7	0.47%	0.44%	0.42%	0.39%	0.41%	0.38%	0.45%
S3-M8	0.24%	0.19%	0.19%	0.19%	0.20%	0.17%	0.18%
S3-M9	0.42%	0.56%	0.65%	0.74%	0.86%	0.88%	1.01%
S3-M10	0.46%	0.47%	0.47%	0.45%	0.48%	0.43%	0.36%
S3-M14	1.30%	1.57%	1.78%	1.83%	1.99%	1.94%	2.15%
S3-M18	1.64%	1.68%	1.92%	2.00%	2.28%	2.05%	2.08%
S3-M20	1.44%	1.67%	2.15%	2.41%	2.65%	2.58%	2.36%
S3-M21	0.24%	0.28%	0.31%	0.32%	0.32%	0.30%	0.16%
S3-M22	0.27%	0.35%	0.42%	0.46%	0.50%	0.51%	0.56%
S3-M23	0.29%	0.33%	0.38%	0.39%	0.41%	0.39%	0.34%
S3-M24	0.60%	0.67%	0.76%	0.80%	0.88%	0.87%	1.07%
S3-M25	1.04%	1.33%	1.62%	1.71%	1.87%	1.83%	1.49%
S3-M28	1.11%	1.37%	1.26%	1.34%	1.62%	1.63%	2.23%
S3-M29	0.05%	0.03%	0.02%	0.02%	0.02%	0.02%	0.02%
S3-M33	1.26%	1.49%	1.37%	1.30%	1.50%	1.44%	1.83%
S3-M35	0.72%	1.11%	1.22%	1.22%	1.30%	1.17%	1.23%

Table A.5.28. Pit data for Meteor Crater.

Feature	Pit						
Rock	**(3*3)**	**(11*11)**	**(21*21)**	**(31*31)**	**(41*41)**	**(51*51)**	**(101*101)**
M13-01	0.35%	0.40%	0.50%	0.63%	0.79%	0.98%	1.40%
M13-02	1.02%	0.83%	0.88%	0.87%	0.84%	0.89%	0.98%
M13-03	1.31%	1.09%	1.26%	1.41%	1.50%	1.63%	1.96%
M13-04	0.36%	0.38%	0.47%	0.55%	0.58%	0.62%	0.72%
M13-05	0.43%	0.39%	0.42%	0.43%	0.42%	0.43%	0.35%
M13-06	0.45%	0.36%	0.37%	0.36%	0.34%	0.34%	0.28%
M13-07	0.20%	0.25%	0.28%	0.30%	0.31%	0.32%	0.29%
M13-08	0.37%	0.36%	0.40%	0.42%	0.41%	0.42%	0.49%
M13-09	0.46%	0.49%	0.52%	0.46%	0.40%	0.36%	0.40%
M13-10	0.57%	0.61%	0.64%	0.66%	0.66%	0.65%	0.64%
M14-11	0.41%	0.60%	0.66%	0.68%	0.73%	0.74%	0.74%
M14-12	0.95%	1.36%	1.51%	1.51%	1.52%	1.56%	1.81%
M14-13	1.05%	1.06%	1.24%	1.35%	1.43%	1.46%	1.65%
M14-14	0.85%	0.78%	0.83%	0.85%	0.85%	0.86%	1.02%
M14-15	1.54%	1.93%	2.25%	2.43%	2.44%	2.34%	2.00%
M14-16	1.05%	0.99%	0.96%	0.87%	0.74%	0.63%	0.29%
M14-17	0.89%	0.99%	1.09%	1.13%	1.12%	1.15%	1.17%
M14-18	0.31%	0.38%	0.40%	0.42%	0.44%	0.45%	0.41%
M14-19	0.36%	0.39%	0.37%	0.37%	0.35%	0.35%	0.36%
M14-20	1.00%	1.13%	1.31%	1.40%	1.47%	1.53%	1.71%
M14-21	0.39%	0.42%	0.46%	0.46%	0.48%	0.51%	0.46%
MC-M1-01	1.03%	1.06%	1.01%	0.90%	0.82%	0.64%	0.53%

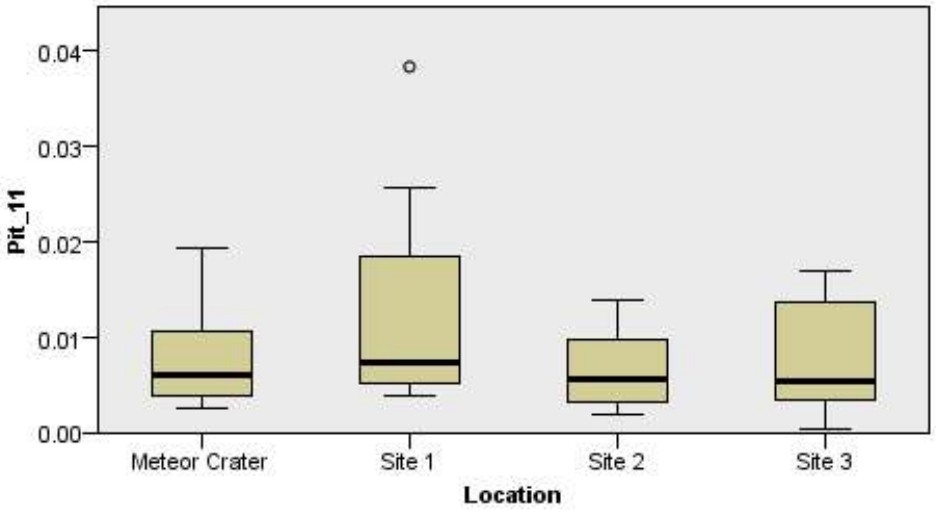
Independent-Samples Kruskal-Wallis Test



Total N	69
Test Statistic	2.557
Degrees of Freedom	3
Asymptotic Sig. (2-sided test)	.465

1. The test statistic is adjusted for ties.
2. Multiple comparisons are not performed because the overall test does not show significant differences across samples.

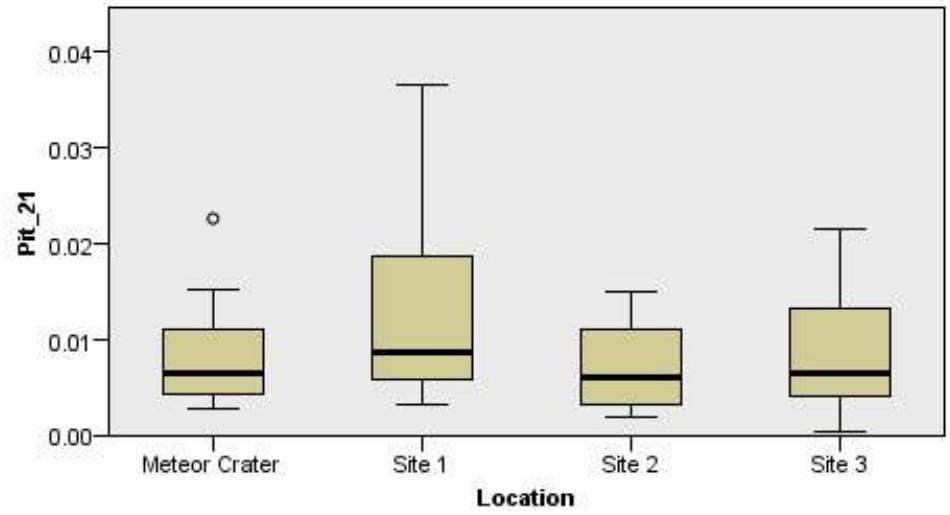
Independent-Samples Kruskal-Wallis Test



Total N	69
Test Statistic	3.290
Degrees of Freedom	3
Asymptotic Sig. (2-sided test)	.349

1. The test statistic is adjusted for ties.
2. Multiple comparisons are not performed because the overall test does not show significant differences across samples.

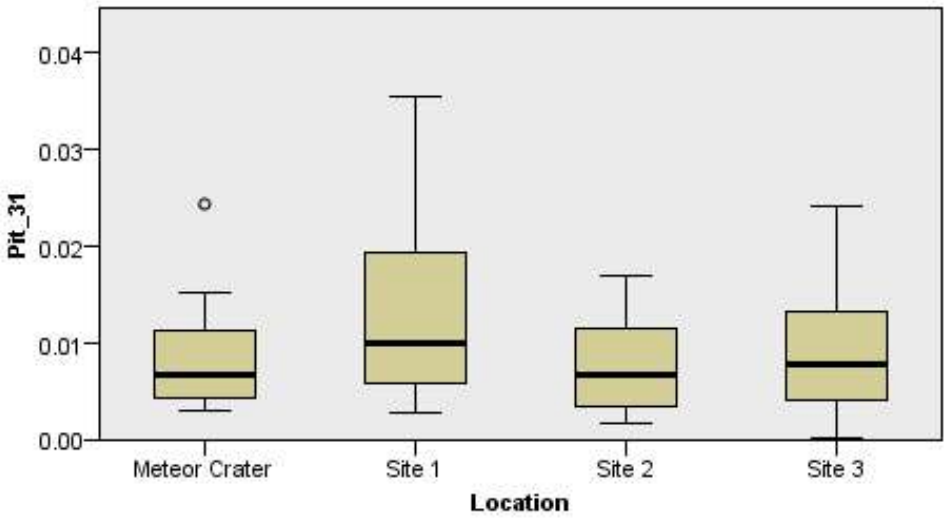
Independent-Samples Kruskal-Wallis Test



Total N	69
Test Statistic	3.378
Degrees of Freedom	3
Asymptotic Sig. (2-sided test)	.337

1. The test statistic is adjusted for ties.
2. Multiple comparisons are not performed because the overall test does not show significant differences across samples.

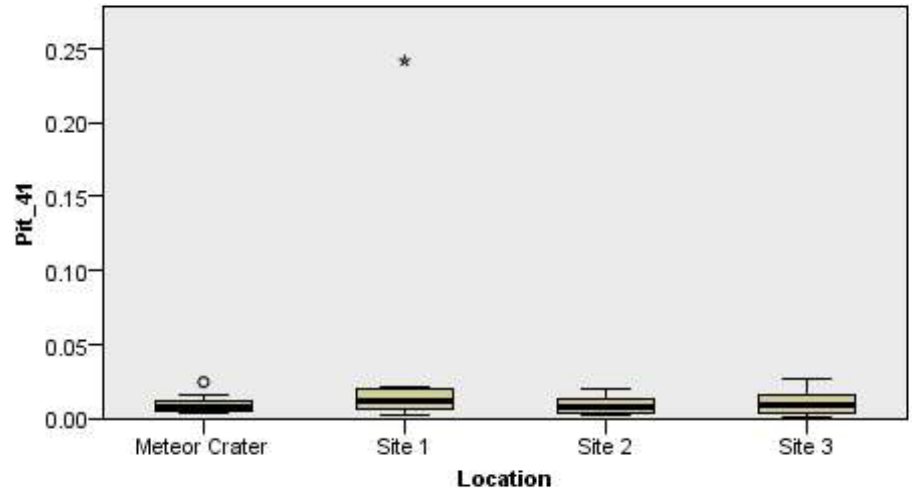
Independent-Samples Kruskal-Wallis Test



Total N	69
Test Statistic	3.181
Degrees of Freedom	3
Asymptotic Sig. (2-sided test)	.365

1. The test statistic is adjusted for ties.
2. Multiple comparisons are not performed because the overall test does not show significant differences across samples.

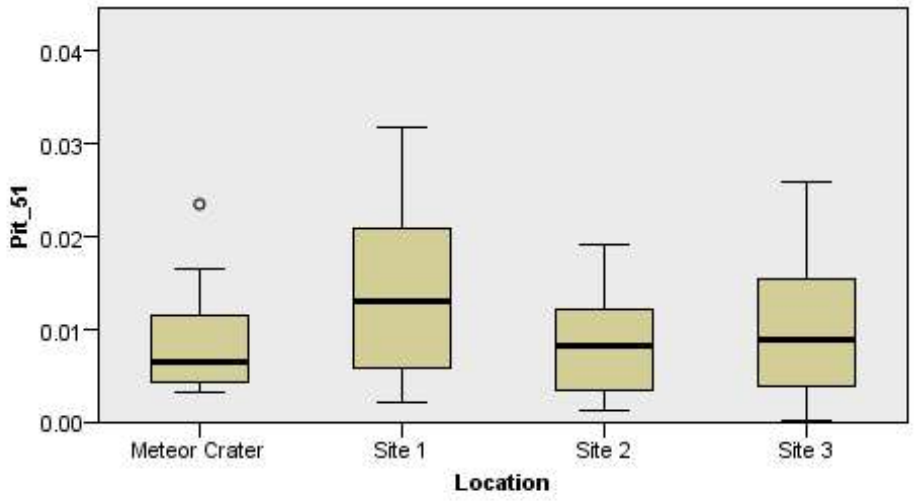
Independent-Samples Kruskal-Wallis Test



Total N	69
Test Statistic	2.987
Degrees of Freedom	3
Asymptotic Sig. (2-sided test)	.394

1. The test statistic is adjusted for ties.
2. Multiple comparisons are not performed because the overall test does not show significant differences across samples.

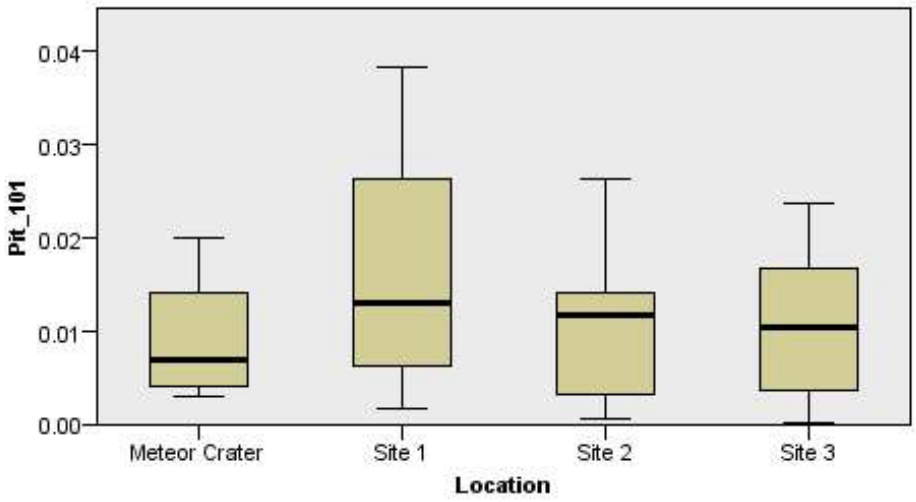
Independent-Samples Kruskal-Wallis Test



Total N	69
Test Statistic	2.953
Degrees of Freedom	3
Asymptotic Sig. (2-sided test)	.399

1. The test statistic is adjusted for ties.
2. Multiple comparisons are not performed because the overall test does not show significant differences across samples.

Independent-Samples Kruskal-Wallis Test



Total N	69
Test Statistic	3.085
Degrees of Freedom	3
Asymptotic Sig. (2-sided test)	.379

1. The test statistic is adjusted for ties.
2. Multiple comparisons are not performed because the overall test does not show significant differences across samples.

A.5.4.2. Channel

Table A.5.29. Channel data for Site 1.

Feature	Channel						
Rock	**(3*3)**	**(11*11)**	**(21*21)**	**(31*31)**	**(41*41)**	**(51*51)**	**(101*101)**
S1.2-M1	29.31%	24.83%	23.96%	23.65%	24.16%	23.73%	23.67%
S1.2-M2	34.80%	28.36%	23.02%	21.10%	20.46%	19.69%	19.03%
S1.2-M3	31.04%	25.65%	23.38%	23.13%	23.51%	23.57%	24.56%
S1-M2	30.81%	22.31%	19.67%	20.59%	22.27%	23.23%	25.01%
S1-M4_1	39.16%	41.03%	41.48%	40.56%	39.08%	37.60%	30.63%
S1-M4_2	37.75%	38.32%	38.64%	37.82%	36.49%	34.88%	28.47%
S1-M8_1	38.70%	39.10%	39.64%	39.45%	39.28%	38.44%	35.72%
S1-M8_2	30.83%	31.24%	31.51%	31.61%	31.73%	31.12%	29.77%
S1-M10	39.11%	37.08%	36.97%	36.47%	36.11%	35.08%	31.42%
S1-M13_1	39.93%	36.10%	33.36%	32.06%	31.41%	30.08%	26.30%
S1-M13_2	41.60%	37.71%	34.25%	33.17%	33.11%	32.39%	30.25%
S1-M13_3	34.14%	36.43%	36.07%	35.58%	35.19%	34.60%	32.28%

Table A.5.30. Channel data for Site 2

Feature	Channel						
Rock	**(3*3)**	**(11*11)**	**(21*21)**	**(31*31)**	**(41*41)**	**(51*51)**	**(101*101)**
S2-M1	34.04%	33.44%	35.36%	36.02%	36.83%	36.18%	33.84%
S2-M2	32.58%	28.03%	28.46%	28.15%	27.85%	26.26%	21.38%
S2-M3	35.75%	34.25%	36.22%	36.60%	37.18%	36.38%	34.44%
S2-M4	34.63%	31.53%	31.53%	31.78%	30.78%	29.01%	23.55%
S2-M5	37.27%	41.09%	44.04%	44.02%	43.71%	42.80%	39.28%
S2-M6	29.14%	28.40%	30.27%	30.52%	30.49%	29.36%	26.37%
S2-M7	29.07%	23.99%	23.41%	22.86%	23.14%	22.02%	20.61%
S2-M12	36.60%	35.35%	36.66%	36.26%	35.89%	34.60%	30.55%
S2-M13	34.09%	26.65%	26.44%	26.47%	27.06%	25.95%	24.36%
S2-M16	32.73%	30.55%	30.41%	30.64%	32.07%	30.95%	29.94%
S2-M17	37.91%	39.97%	41.44%	41.29%	41.20%	40.02%	36.19%
S2-M18	34.70%	36.11%	38.16%	38.27%	38.50%	37.27%	33.28%
S2-M19	36.80%	38.36%	41.24%	41.73%	41.44%	40.31%	37.85%
S2-M20	31.57%	29.80%	30.07%	30.24%	31.42%	30.31%	28.95%
S2-M22	33.24%	32.07%	34.28%	34.94%	35.38%	34.80%	32.05%

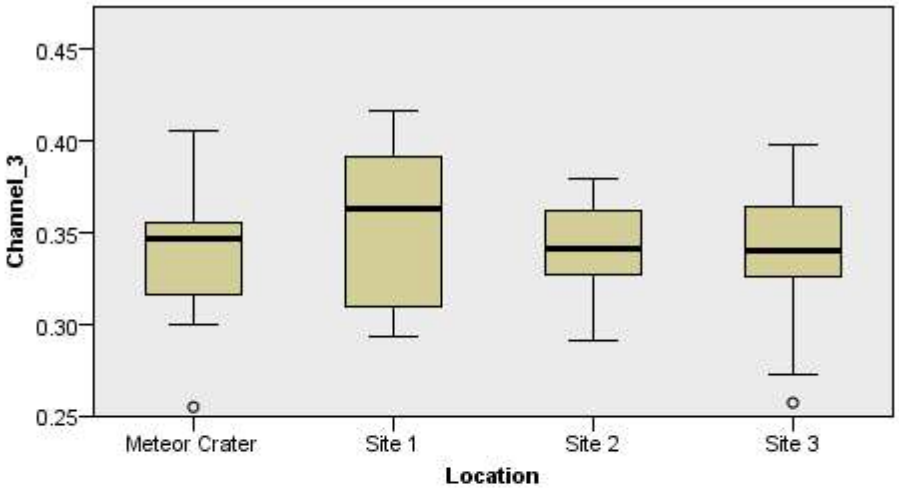
Table A.5.31. Channel data for Site 3.

Feature	Channel						
Rock	**(3*3)**	**(11*11)**	**(21*21)**	**(31*31)**	**(41*41)**	**(51*51)**	**(101*101)**
S3-M1_1	38.43%	37.41%	39.02%	39.16%	39.03%	37.67%	31.32%
S3-M1_2	37.54%	38.94%	40.09%	39.47%	38.53%	37.62%	32.41%
S3-M1_3	34.31%	33.25%	35.60%	36.27%	36.93%	36.41%	34.87%
S3-M6	37.42%	37.33%	39.36%	39.98%	40.31%	40.36%	38.26%
S3-M7	35.09%	30.52%	28.83%	28.15%	28.64%	27.71%	27.95%
S3-M8	35.80%	28.70%	28.38%	28.37%	28.77%	27.77%	25.35%
S3-M9	36.12%	36.05%	38.13%	38.54%	39.07%	38.06%	35.11%
S3-M10	33.74%	27.45%	27.56%	27.91%	28.96%	28.05%	26.10%
S3-M14	28.08%	25.60%	25.70%	25.50%	26.02%	25.26%	25.03%
S3-M18	28.97%	26.57%	26.52%	26.25%	27.40%	25.95%	24.30%
S3-M20	33.42%	32.43%	32.30%	31.46%	31.43%	29.71%	27.12%
S3-M21	36.66%	37.29%	39.00%	39.20%	39.50%	38.84%	37.10%
S3-M22	33.32%	35.74%	38.11%	38.94%	39.76%	39.16%	37.27%
S3-M23	35.83%	34.49%	37.48%	38.21%	38.58%	37.65%	33.57%
S3-M24	32.98%	30.95%	32.27%	32.44%	32.85%	31.77%	29.54%
S3-M25	33.08%	34.57%	35.78%	35.18%	34.66%	33.29%	28.92%
S3-M28	25.70%	21.90%	20.44%	20.40%	21.58%	21.27%	22.78%
S3-M29	39.81%	34.01%	33.52%	33.08%	33.07%	32.00%	30.03%
S3-M33	27.24%	24.68%	21.73%	20.35%	21.18%	20.56%	22.85%
S3-M35	32.23%	31.65%	30.38%	29.47%	30.13%	28.67%	27.66%

Table A.5.32. Channel data for Meteor Crater.

Feature	Channel						
Rock	**(3*3)**	**(11*11)**	**(21*21)**	**(31*31)**	**(41*41)**	**(51*51)**	**(101*101)**
M13-01	39.42%	43.38%	44.91%	43.85%	41.97%	40.04%	30.56%
M13-02	34.96%	27.70%	26.03%	25.66%	25.08%	24.53%	23.81%
M13-03	31.99%	25.80%	25.76%	26.04%	26.12%	26.30%	25.67%
M13-04	40.54%	41.92%	42.37%	41.56%	40.79%	40.26%	37.33%
M13-05	35.09%	29.16%	30.46%	30.84%	30.60%	30.53%	29.40%
M13-06	35.37%	27.31%	27.71%	27.98%	27.62%	27.54%	25.79%
M13-07	34.60%	30.20%	32.56%	32.95%	32.86%	32.42%	29.66%
M13-08	34.76%	29.43%	30.96%	31.23%	30.89%	30.68%	28.24%
M13-09	31.60%	28.23%	30.08%	30.27%	29.84%	29.51%	27.50%
M13-10	35.50%	33.34%	33.67%	33.46%	33.06%	32.52%	28.75%
M14-11	25.47%	28.35%	29.07%	28.83%	28.62%	27.99%	25.66%
M14-12	31.01%	31.54%	31.47%	30.72%	29.89%	29.25%	27.98%
M14-13	35.73%	30.27%	29.72%	29.28%	28.86%	28.26%	26.03%
M14-14	29.94%	24.91%	24.64%	24.34%	24.04%	23.58%	21.92%
M14-15	31.28%	29.11%	28.94%	29.00%	29.25%	29.51%	29.01%
M14-16	37.01%	31.35%	29.35%	28.63%	28.09%	27.78%	27.06%
M14-17	31.13%	31.09%	31.84%	31.65%	31.11%	31.09%	30.09%
M14-18	35.52%	33.88%	33.30%	32.74%	32.39%	31.91%	31.30%
M14-19	35.15%	34.31%	33.71%	32.98%	32.36%	31.95%	31.40%
M14-20	34.23%	32.83%	32.12%	31.43%	30.82%	30.35%	28.63%
M14-21	33.17%	27.77%	27.48%	27.53%	27.37%	27.40%	27.32%
MC-M1-01	32.24%	28.90%	27.76%	26.43%	25.11%	23.81%	17.33%

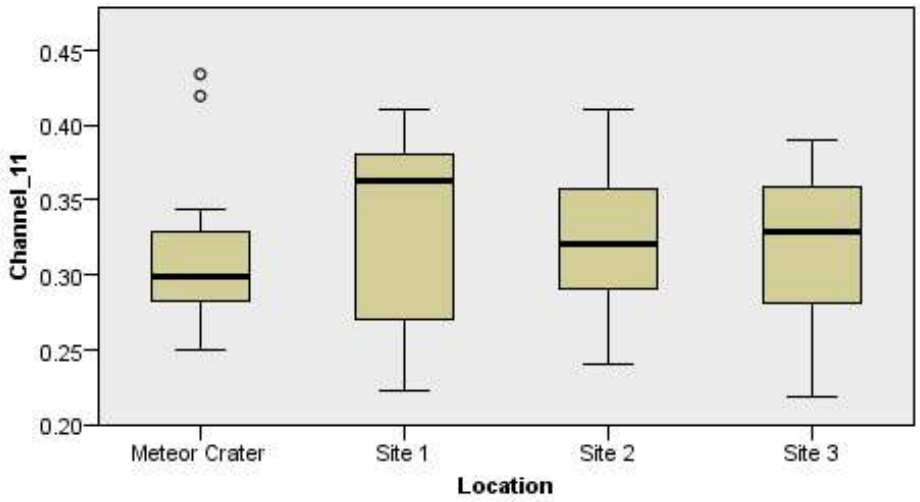
Independent-Samples Kruskal-Wallis Test



Total N	69
Test Statistic	1.510
Degrees of Freedom	3
Asymptotic Sig. (2-sided test)	.680

1. The test statistic is adjusted for ties.
2. Multiple comparisons are not performed because the overall test does not show significant differences across samples.

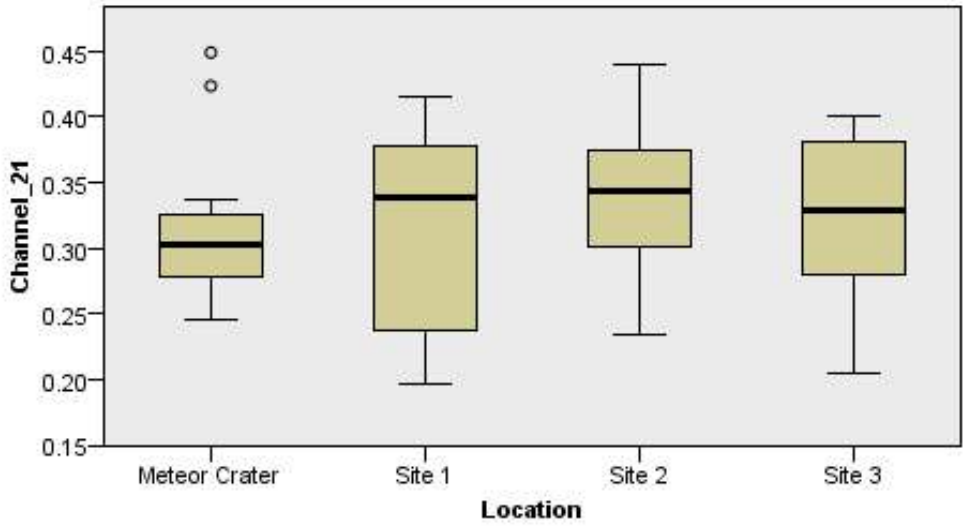
Independent-Samples Kruskal-Wallis Test



Total N	69
Test Statistic	2.675
Degrees of Freedom	3
Asymptotic Sig. (2-sided test)	.445

1. The test statistic is adjusted for ties.
2. Multiple comparisons are not performed because the overall test does not show significant differences across samples.

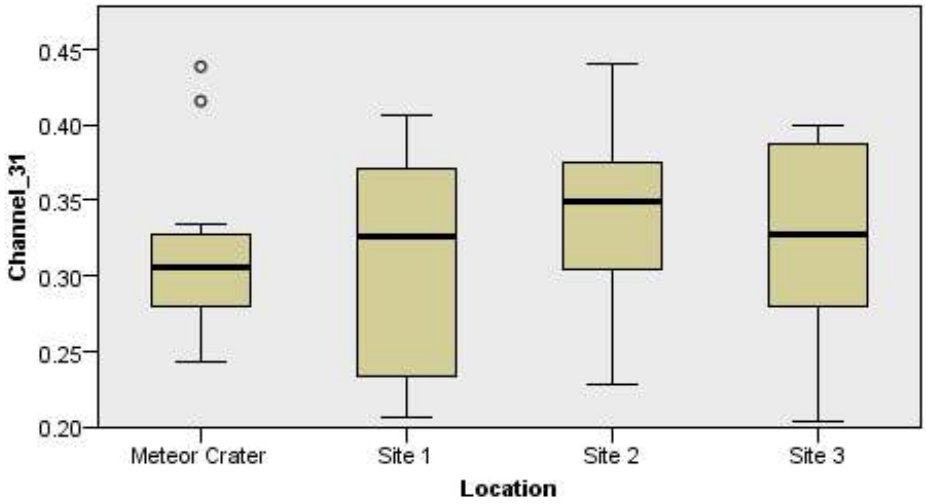
Independent-Samples Kruskal-Wallis Test



Total N	69
Test Statistic	2.516
Degrees of Freedom	3
Asymptotic Sig. (2-sided test)	.472

1. The test statistic is adjusted for ties.
2. Multiple comparisons are not performed because the overall test does not show significant differences across samples.

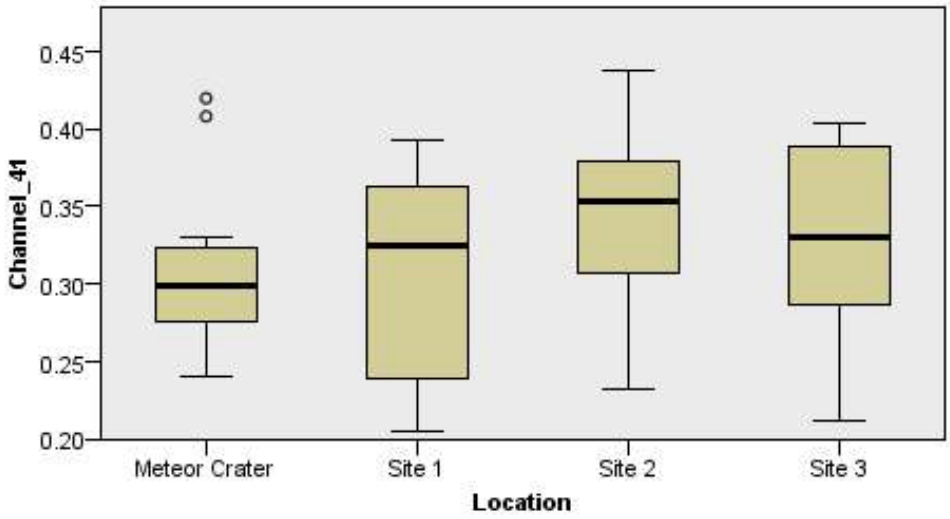
Independent-Samples Kruskal-Wallis Test



Total N	69
Test Statistic	2.878
Degrees of Freedom	3
Asymptotic Sig. (2-sided test)	.411

1. The test statistic is adjusted for ties.
2. Multiple comparisons are not performed because the overall test does not show significant differences across samples.

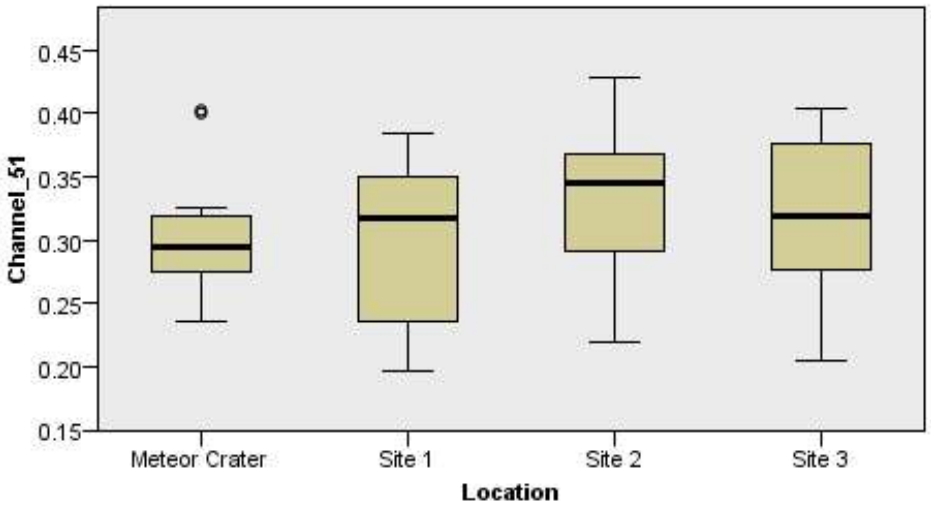
Independent-Samples Kruskal-Wallis Test



Total N	69
Test Statistic	4.612
Degrees of Freedom	3
Asymptotic Sig. (2-sided test)	.203

1. The test statistic is adjusted for ties.
2. Multiple comparisons are not performed because the overall test does not show significant differences across samples.

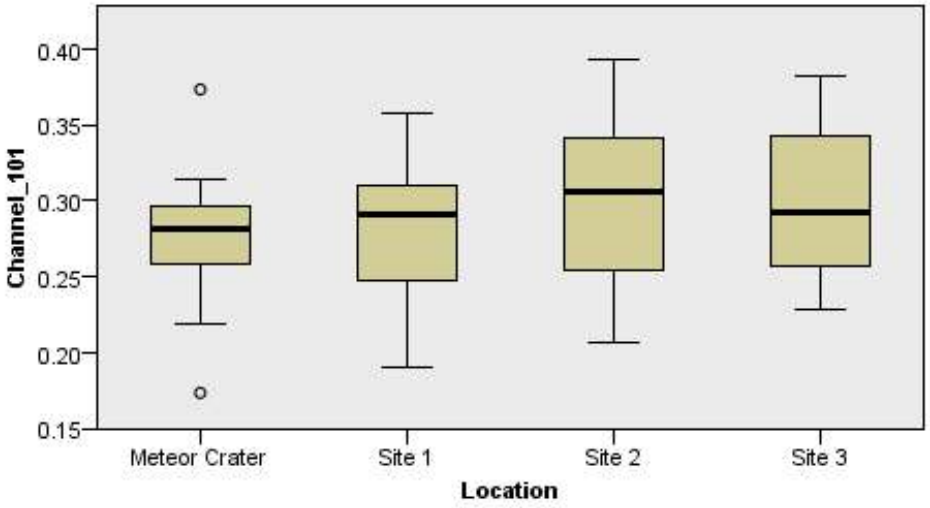
Independent-Samples Kruskal-Wallis Test



Total N	69
Test Statistic	2.891
Degrees of Freedom	3
Asymptotic Sig. (2-sided test)	.409

1. The test statistic is adjusted for ties.
2. Multiple comparisons are not performed because the overall test does not show significant differences across samples.

Independent-Samples Kruskal-Wallis Test



Total N	69
Test Statistic	2.621
Degrees of Freedom	3
Asymptotic Sig. (2-sided test)	.454

1. The test statistic is adjusted for ties.
2. Multiple comparisons are not performed because the overall test does not show significant differences across samples.

A.5.4.3. Pass

Table A.5.33. Pass data for Site 1.

Feature	Pass						
Rock	**(3*3)**	**(11*11)**	**(21*21)**	**(31*31)**	**(41*41)**	**(51*51)**	**(101*101)**
S1.2-M1	11.08%	13.15%	12.04%	11.64%	11.32%	10.87%	9.45%
S1.2-M2	5.38%	9.18%	8.38%	7.27%	6.74%	6.59%	6.36%
S1.2-M3	7.38%	7.17%	6.25%	6.21%	6.54%	6.93%	8.82%
S1-M2	2.24%	1.23%	1.02%	0.92%	0.84%	0.83%	1.25%
S1-M4_1	1.80%	2.28%	2.88%	3.87%	5.09%	6.22%	9.39%
S1-M4_2	2.28%	3.17%	4.14%	5.42%	7.09%	8.83%	14.28%
S1-M8_1	1.84%	2.03%	2.16%	2.34%	2.42%	2.50%	2.62%
S1-M8_2	3.73%	5.06%	5.93%	6.45%	6.78%	7.07%	7.98%
S1-M10	1.39%	1.38%	1.45%	1.46%	1.49%	1.49%	1.45%
S1-M13_1	1.45%	1.84%	1.72%	1.60%	1.48%	1.39%	1.10%
S1-M13_2	1.44%	2.41%	2.61%	2.60%	2.39%	2.21%	2.18%
S1-M13_3	1.05%	1.69%	2.28%	2.48%	2.52%	2.48%	1.95%

Table A.5.34. Pass data for Site 2

Feature	Pass						
Rock	**(3*3)**	**(11*11)**	**(21*21)**	**(31*31)**	**(41*41)**	**(51*51)**	**(101*101)**
S2-M1	1.59%	1.61%	1.86%	2.07%	2.31%	2.62%	4.44%
S2-M2	1.64%	1.58%	1.74%	1.76%	1.78%	1.77%	1.77%
S2-M3	0.74%	0.69%	0.74%	0.76%	0.76%	0.78%	0.93%
S2-M4	1.20%	1.20%	1.20%	1.53%	1.58%	1.65%	2.11%
S2-M5	0.56%	0.50%	0.53%	0.53%	0.53%	0.55%	0.67%
S2-M6	3.82%	4.23%	5.54%	6.43%	7.18%	7.79%	9.72%
S2-M7	5.35%	4.57%	3.83%	3.59%	3.51%	3.41%	3.39%
S2-M12	0.58%	0.53%	0.54%	0.54%	0.52%	0.53%	0.73%
S2-M13	1.75%	1.84%	1.84%	1.81%	1.84%	1.88%	2.18%
S2-M16	3.64%	3.54%	3.73%	3.92%	4.12%	4.27%	4.72%
S2-M17	1.41%	1.43%	1.65%	1.99%	2.43%	2.86%	4.08%
S2-M18	2.21%	2.15%	2.43%	2.72%	3.01%	3.26%	4.26%
S2-M19	0.49%	0.45%	0.45%	0.43%	0.41%	0.32%	0.22%
S2-M20	3.51%	3.32%	3.49%	3.68%	3.96%	4.16%	4.88%
S2-M22	2.99%	2.90%	3.29%	3.67%	3.98%	4.21%	4.68%

Table A.5.35. Pass data for Site 3.

Feature	Pass						
Rock	**(3*3)**	**(11*11)**	**(21*21)**	**(31*31)**	**(41*41)**	**(51*51)**	**(101*101)**
S3-M1_1	0.69%	0.59%	0.60%	0.58%	0.55%	0.55%	0.23%
S3-M1_2	1.31%	1.42%	1.90%	2.63%	3.53%	4.33%	5.06%
S3-M1_3	1.89%	2.01%	2.38%	2.72%	2.99%	3.20%	3.50%
S3-M6	1.44%	1.29%	1.37%	1.44%	1.44%	1.43%	1.93%
S3-M7	1.67%	1.45%	1.36%	1.29%	1.29%	1.30%	1.37%
S3-M8	0.84%	0.67%	0.67%	0.64%	0.66%	0.66%	0.80%
S3-M9	1.66%	1.81%	2.01%	2.18%	2.39%	2.61%	3.44%
S3-M10	1.60%	1.54%	1.61%	1.58%	1.57%	1.56%	1.41%
S3-M14	4.55%	4.84%	5.37%	5.71%	5.98%	6.18%	6.57%
S3-M18	6.07%	5.17%	5.73%	6.24%	6.62%	6.74%	7.00%
S3-M20	4.98%	5.19%	6.63%	7.82%	8.74%	9.34%	9.66%
S3-M21	0.89%	0.86%	0.95%	0.98%	0.98%	1.00%	0.86%
S3-M22	1.25%	1.46%	1.59%	1.67%	1.73%	1.79%	1.92%
S3-M23	0.96%	0.86%	0.99%	1.09%	1.15%	1.18%	1.42%
S3-M24	2.09%	2.15%	2.44%	2.61%	2.72%	2.82%	3.50%
S3-M25	3.51%	3.57%	4.55%	5.44%	6.17%	6.54%	6.93%
S3-M28	4.51%	4.77%	4.41%	4.70%	5.14%	5.57%	7.47%
S3-M29	0.20%	0.14%	0.13%	0.11%	0.09%	0.09%	0.08%
S3-M33	4.57%	5.19%	4.83%	4.56%	4.57%	4.61%	5.35%
S3-M35	3.12%	3.78%	4.22%	4.34%	4.28%	4.08%	3.44%

Table A.5.36. Pass data Meteor Crater.

Feature	Pass						
Rock	**(3*3)**	**(11*11)**	**(21*21)**	**(31*31)**	**(41*41)**	**(51*51)**	**(101*101)**
M13-01	1.28%	1.24%	1.53%	2.10%	2.83%	3.59%	5.68%
M13-02	3.25%	2.96%	2.97%	3.04%	3.16%	3.25%	3.21%
M13-03	4.46%	3.81%	4.18%	4.57%	4.94%	5.32%	6.74%
M13-04	1.29%	1.20%	1.45%	1.83%	2.11%	2.23%	2.53%
M13-05	1.50%	1.29%	1.37%	1.44%	1.50%	1.58%	1.64%
M13-06	1.56%	1.20%	1.20%	1.20%	1.21%	1.23%	1.20%
M13-07	0.69%	0.70%	0.75%	0.79%	0.83%	0.86%	0.94%
M13-08	1.26%	1.13%	1.28%	1.37%	1.43%	1.49%	1.80%
M13-09	1.60%	1.57%	1.57%	1.45%	1.33%	1.31%	1.32%
M13-10	2.02%	2.06%	2.20%	2.28%	2.28%	2.30%	2.36%
M14-11	1.34%	1.88%	2.09%	2.14%	2.17%	2.20%	2.18%
M14-12	3.25%	4.24%	4.95%	5.22%	5.52%	5.75%	6.12%
M14-13	3.60%	3.67%	4.13%	4.46%	4.70%	4.91%	5.93%
M14-14	2.96%	2.56%	2.71%	2.75%	2.76%	2.76%	2.97%
M14-15	5.41%	6.78%	8.03%	8.69%	8.88%	8.74%	7.74%
M14-16	3.75%	3.57%	3.35%	3.19%	2.98%	2.71%	1.85%
M14-17	3.14%	3.35%	3.65%	3.79%	3.80%	3.80%	3.78%
M14-18	1.11%	1.27%	1.35%	1.41%	1.45%	1.41%	1.07%
M14-19	1.34%	1.36%	1.37%	1.43%	1.42%	1.37%	1.56%
M14-20	3.38%	3.68%	4.22%	4.59%	4.80%	5.04%	5.82%
M14-21	1.35%	1.32%	1.38%	1.46%	1.55%	1.64%	1.89%
MC-M1-01	3.62%	3.55%	3.56%	3.36%	3.06%	2.71%	2.67%

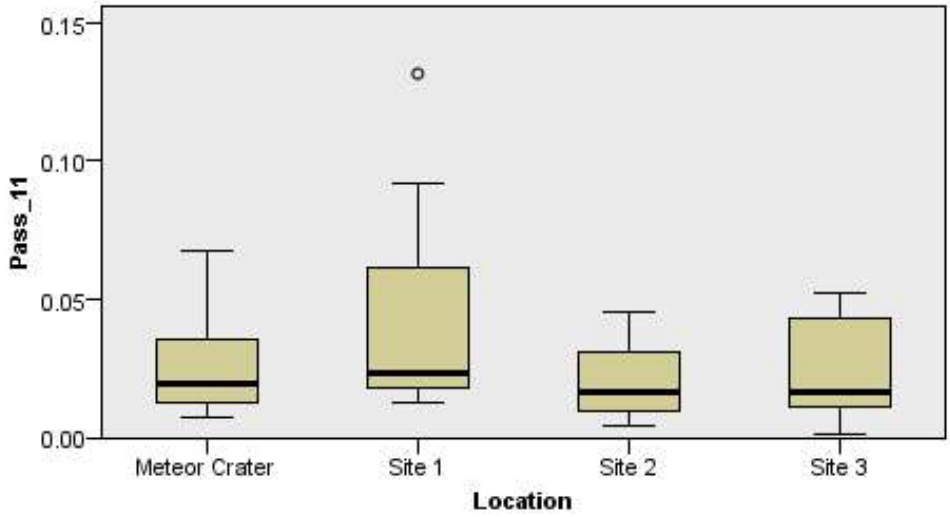
Independent-Samples Kruskal-Wallis Test



Total N	69
Test Statistic	2.014
Degrees of Freedom	3
Asymptotic Sig. (2-sided test)	.570

1. The test statistic is adjusted for ties.
2. Multiple comparisons are not performed because the overall test does not show significant differences across samples.

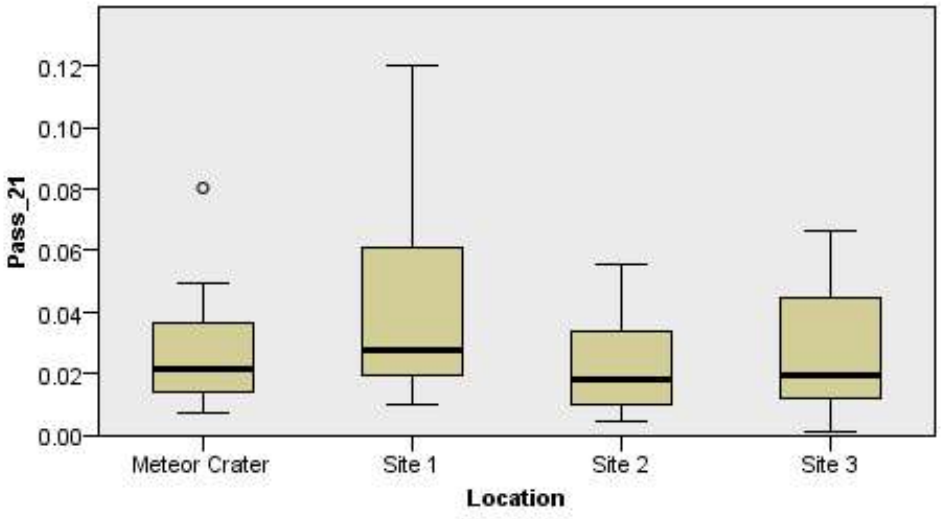
Independent-Samples Kruskal-Wallis Test



Total N	69
Test Statistic	3.953
Degrees of Freedom	3
Asymptotic Sig. (2-sided test)	.267

1. The test statistic is adjusted for ties.
2. Multiple comparisons are not performed because the overall test does not show significant differences across samples.

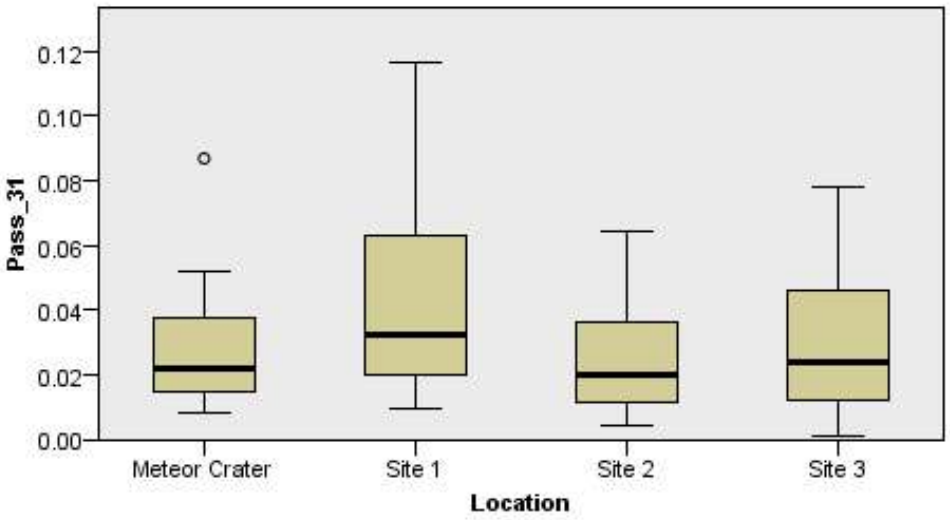
Independent-Samples Kruskal-Wallis Test



Total N	69
Test Statistic	4.006
Degrees of Freedom	3
Asymptotic Sig. (2-sided test)	.261

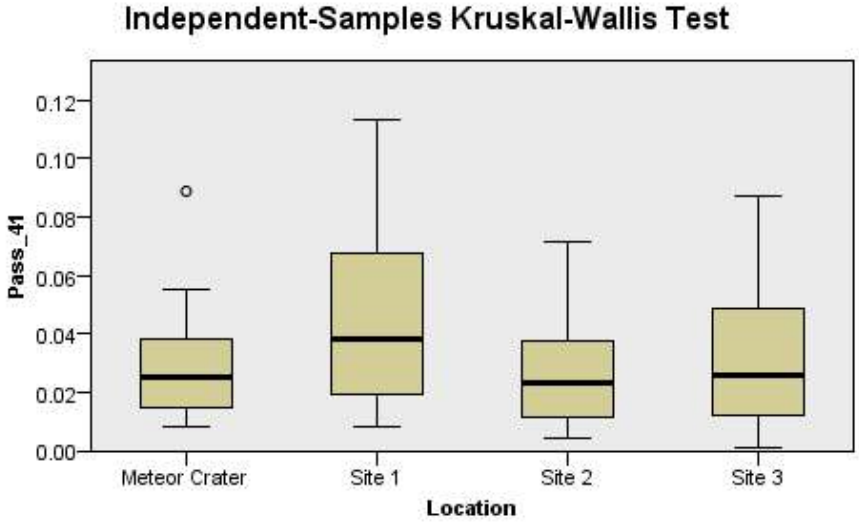
1. The test statistic is adjusted for ties.
2. Multiple comparisons are not performed because the overall test does not show significant differences across samples.

Independent-Samples Kruskal-Wallis Test



Total N	69
Test Statistic	3.692
Degrees of Freedom	3
Asymptotic Sig. (2-sided test)	.297

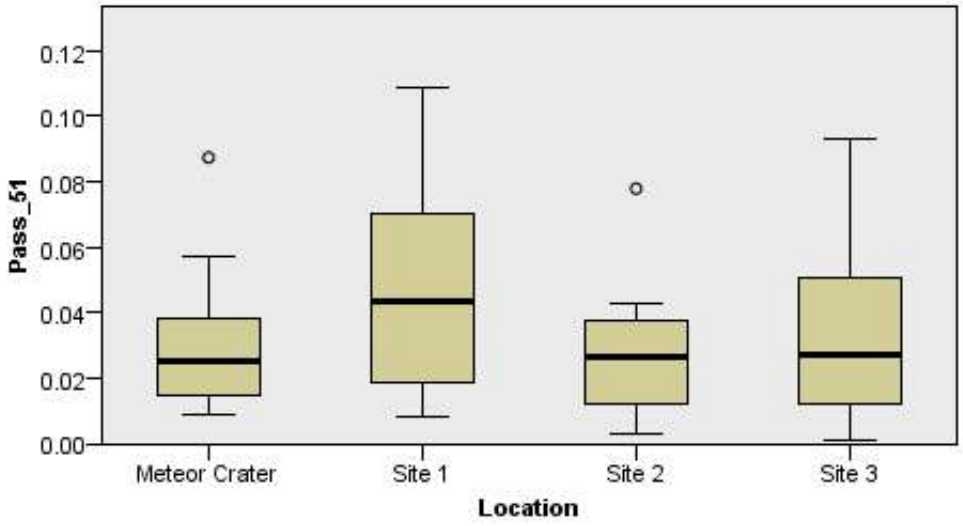
1. The test statistic is adjusted for ties.
2. Multiple comparisons are not performed because the overall test does not show significant differences across samples.



Total N	69
Test Statistic	3.245
Degrees of Freedom	3
Asymptotic Sig. (2-sided test)	.355

1. The test statistic is adjusted for ties.
2. Multiple comparisons are not performed because the overall test does not show significant differences across samples.

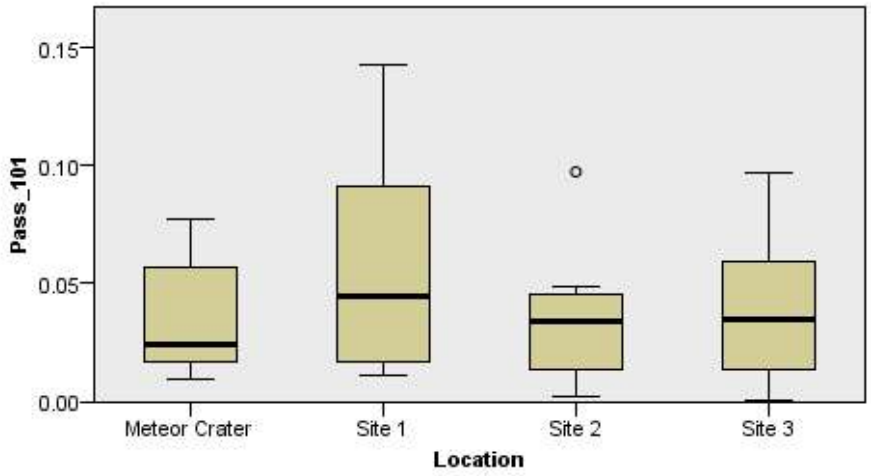
Independent-Samples Kruskal-Wallis Test



Total N	69
Test Statistic	2.747
Degrees of Freedom	3
Asymptotic Sig. (2-sided test)	.432

1. The test statistic is adjusted for ties.
2. Multiple comparisons are not performed because the overall test does not show significant differences across samples.

Independent-Samples Kruskal-Wallis Test



Total N	69
Test Statistic	2.337
Degrees of Freedom	3
Asymptotic Sig. (2-sided test)	.505

1. The test statistic is adjusted for ties.
2. Multiple comparisons are not performed because the overall test does not show significant differences across samples.

A 5.4.4. Ridge

Table A.5.37. Ridge data for Site 1.

Feature	Ridge						
Rock	**(3*3)**	**(11*11)**	**(21*21)**	**(31*31)**	**(41*41)**	**(51*51)**	**(101*101)**
S1.2-M1	29.39%	23.60%	23.23%	23.37%	23.01%	23.59%	23.75%
S1.2-M2	34.90%	27.89%	22.89%	21.18%	20.21%	20.09%	20.83%
S1.2-M3	31.23%	25.15%	22.63%	22.59%	22.90%	23.61%	26.16%
S1-M2	30.59%	21.36%	18.00%	18.44%	18.94%	19.80%	21.23%
S1-M4_1	39.35%	38.97%	38.99%	38.83%	37.91%	36.75%	32.20%
S1-M4_2	38.29%	38.02%	37.66%	36.99%	35.63%	34.01%	28.61%
S1-M8_1	38.03%	35.03%	34.88%	35.31%	35.38%	35.65%	36.02%
S1-M8_2	31.46%	31.35%	31.50%	31.63%	31.41%	31.36%	30.63%
S1-M10	39.32%	37.35%	38.25%	39.41%	40.07%	41.18%	43.54%
S1-M13_1	40.18%	35.49%	33.11%	32.49%	31.47%	31.70%	32.02%
S1-M13_2	42.05%	38.11%	35.58%	35.14%	34.72%	34.95%	35.97%
S1-M13_3	34.24%	36.52%	36.23%	35.96%	35.47%	35.22%	35.10%

Table A.5.38. Ridge data for Site 2

Feature	Ridge						
Rock	**(3*3)**	**(11*11)**	**(21*21)**	**(31*31)**	**(41*41)**	**(51*51)**	**(101*101)**
S2-M1	35.43%	33.06%	35.14%	36.58%	36.70%	37.59%	37.53%
S2-M2	33.85%	29.35%	31.41%	32.58%	33.02%	34.48%	38.70%
S2-M3	37.01%	33.36%	36.13%	37.95%	38.44%	39.70%	42.15%
S2-M4	35.44%	31.85%	31.85%	35.23%	35.30%	36.13%	41.19%
S2-M5	37.56%	35.60%	39.04%	41.21%	42.27%	43.40%	44.31%
S2-M6	29.94%	27.93%	30.31%	31.27%	31.00%	31.53%	31.80%
S2-M7	29.37%	23.31%	23.39%	23.63%	22.83%	23.31%	24.04%
S2-M12	36.95%	33.66%	36.49%	38.05%	38.70%	39.88%	43.09%
S2-M13	34.85%	25.64%	26.66%	27.93%	28.05%	29.40%	32.02%
S2-M16	33.75%	29.20%	29.32%	30.12%	29.36%	30.59%	29.83%
S2-M17	38.88%	37.16%	39.04%	39.79%	39.27%	39.29%	37.31%
S2-M18	35.28%	32.43%	34.65%	36.13%	36.26%	37.01%	36.44%
S2-M19	37.29%	33.79%	37.02%	39.20%	40.71%	42.54%	45.57%
S2-M20	32.13%	26.95%	27.73%	28.78%	28.42%	29.72%	30.12%
S2-M22	34.29%	31.47%	33.65%	35.06%	35.37%	36.14%	36.27%

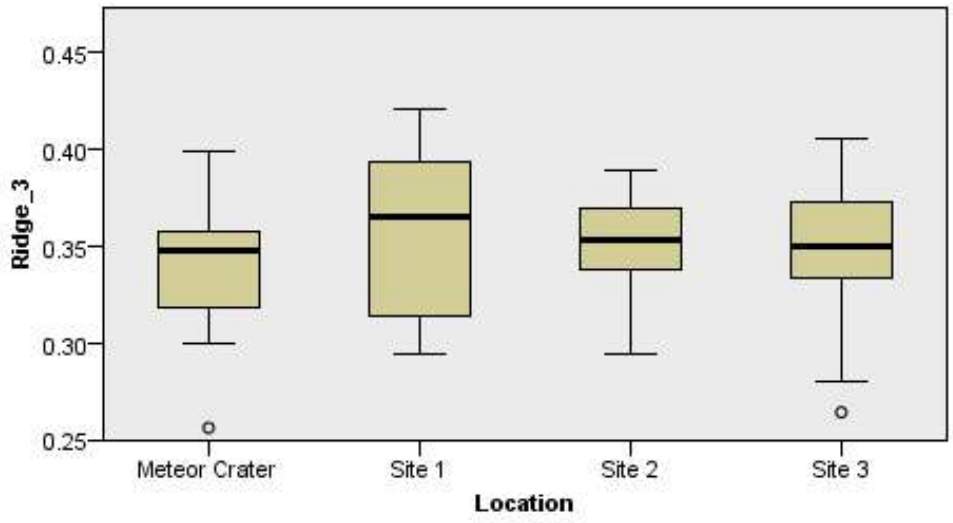
Table A.5.39. Ridge data for Site 3.

Feature	Ridge						
Rock	**(3*3)**	**(11*11)**	**(21*21)**	**(31*31)**	**(41*41)**	**(51*51)**	**(101*101)**
S3-M1_1	39.44%	36.97%	39.09%	40.75%	41.23%	41.62%	43.62%
S3-M1_2	38.21%	38.49%	40.68%	41.31%	40.54%	39.73%	37.16%
S3-M1_3	34.88%	30.09%	31.38%	32.20%	32.18%	32.71%	33.22%
S3-M6	37.41%	35.36%	36.76%	37.89%	38.55%	38.87%	40.49%
S3-M7	36.20%	30.50%	29.46%	29.64%	29.22%	30.52%	34.33%
S3-M8	37.15%	29.85%	31.24%	32.83%	33.26%	34.85%	38.70%
S3-M9	37.02%	34.10%	36.36%	37.58%	37.40%	38.11%	38.13%
S3-M10	35.10%	27.61%	28.80%	29.69%	29.12%	30.38%	33.05%
S3-M14	28.60%	24.13%	25.01%	25.50%	24.95%	25.64%	25.87%
S3-M18	29.66%	24.22%	25.05%	25.73%	24.63%	25.76%	24.93%
S3-M20	34.29%	30.18%	29.60%	29.22%	27.68%	27.60%	25.23%
S3-M21	37.36%	35.80%	38.32%	40.01%	40.76%	42.01%	44.58%
S3-M22	34.04%	33.96%	36.72%	38.61%	38.95%	39.94%	40.00%
S3-M23	36.47%	31.54%	34.57%	36.43%	37.00%	38.21%	39.52%
S3-M24	33.60%	30.49%	32.05%	32.76%	32.29%	32.94%	33.48%
S3-M25	33.75%	31.80%	33.68%	33.80%	32.62%	32.14%	28.29%
S3-M28	26.41%	21.71%	21.06%	21.64%	21.38%	22.61%	23.97%
S3-M29	40.53%	34.60%	35.42%	36.43%	36.62%	37.87%	43.27%
S3-M33	28.02%	24.39%	22.02%	21.03%	19.75%	20.70%	21.64%
S3-M35	33.13%	30.26%	28.96%	28.32%	26.69%	27.46%	28.29%

Table A.5.40. Ridge data for Meteor Crater.

Feature	Ridge						
Rock	**(3*3)**	**(11*11)**	**(21*21)**	**(31*31)**	**(41*41)**	**(51*51)**	**(101*101)**
M13-01	37.39%	36.98%	39.20%	39.95%	39.90%	39.20%	34.27%
M13-02	34.92%	28.61%	27.64%	27.48%	27.49%	27.72%	29.86%
M13-03	31.98%	26.29%	26.33%	26.76%	27.29%	27.53%	28.90%
M13-04	39.91%	39.42%	40.74%	41.10%	40.92%	40.31%	38.35%
M13-05	35.21%	29.87%	31.32%	32.30%	33.13%	33.54%	36.30%
M13-06	35.08%	28.17%	29.27%	30.15%	31.16%	31.53%	34.88%
M13-07	34.80%	29.16%	31.28%	32.56%	33.34%	34.10%	37.62%
M13-08	34.62%	30.24%	32.33%	33.36%	34.23%	34.59%	37.20%
M13-09	31.84%	29.43%	31.36%	32.28%	33.00%	33.37%	36.44%
M13-10	35.45%	33.20%	34.22%	34.52%	34.47%	34.24%	32.90%
M14-11	25.61%	28.00%	28.97%	29.12%	28.92%	29.15%	30.41%
M14-12	31.12%	31.97%	32.15%	31.53%	30.66%	29.83%	29.03%
M14-13	35.84%	30.60%	30.52%	30.63%	30.59%	30.87%	32.58%
M14-14	29.96%	25.09%	25.54%	25.72%	25.84%	26.10%	27.35%
M14-15	31.37%	29.30%	29.16%	29.13%	29.22%	29.67%	30.83%
M14-16	37.17%	32.43%	31.01%	30.66%	30.50%	30.31%	30.16%
M14-17	30.85%	32.01%	32.67%	32.57%	32.45%	31.78%	30.77%
M14-18	36.14%	35.95%	36.01%	36.23%	36.41%	36.77%	38.92%
M14-19	35.75%	36.51%	36.76%	36.84%	37.17%	37.38%	39.54%
M14-20	34.40%	33.39%	32.93%	32.71%	32.72%	32.81%	32.83%
M14-21	33.34%	29.05%	29.45%	30.26%	31.16%	31.72%	35.16%
MC-M1-01	32.66%	31.02%	30.37%	29.77%	29.18%	28.58%	27.63%

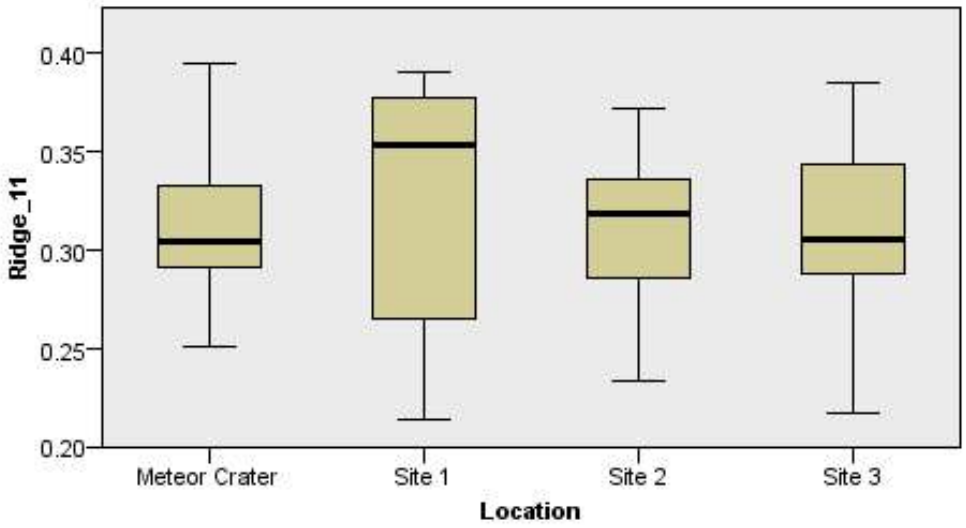
Independent-Samples Kruskal-Wallis Test



Total N	69
Test Statistic	1.980
Degrees of Freedom	3
Asymptotic Sig. (2-sided test)	.576

1. The test statistic is adjusted for ties.
2. Multiple comparisons are not performed because the overall test does not show significant differences across samples.

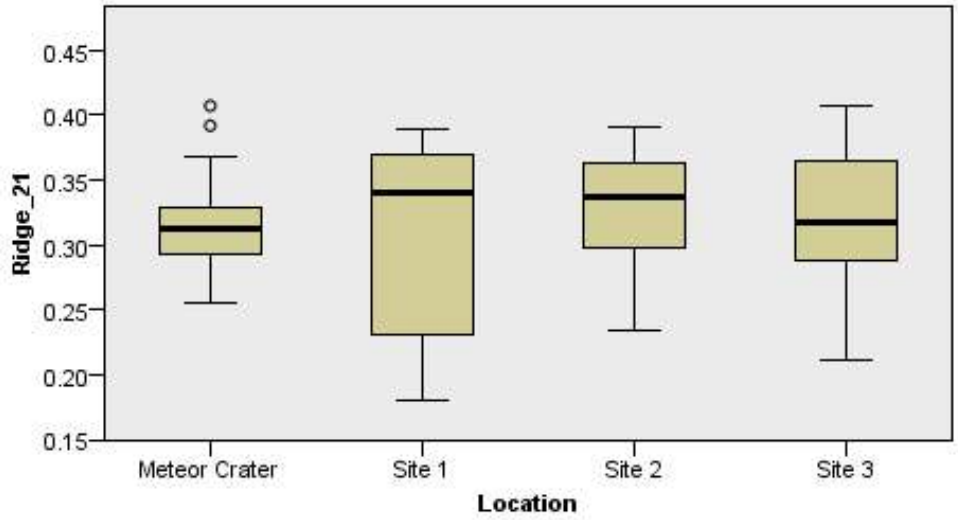
Independent-Samples Kruskal-Wallis Test



Total N	69
Test Statistic	1.373
Degrees of Freedom	3
Asymptotic Sig. (2-sided test)	.712

1. The test statistic is adjusted for ties.
2. Multiple comparisons are not performed because the overall test does not show significant differences across samples.

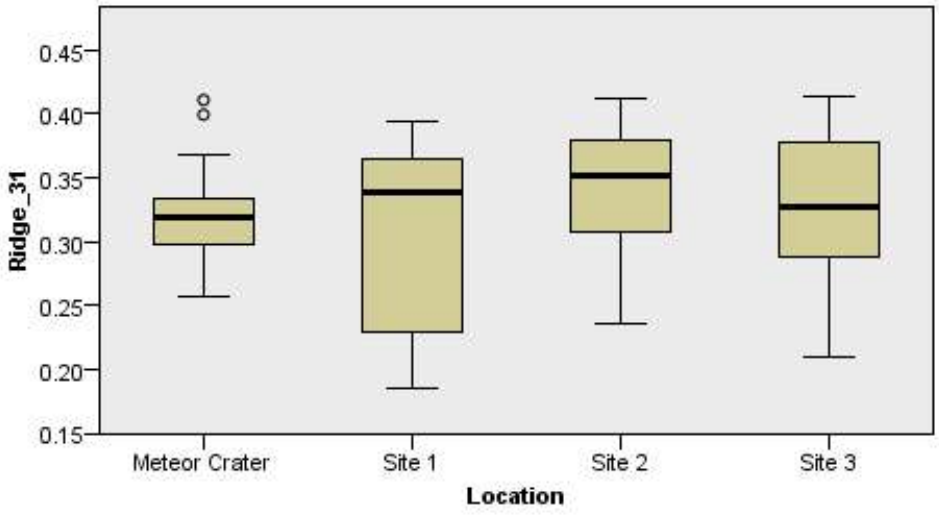
Independent-Samples Kruskal-Wallis Test



Total N	69
Test Statistic	.723
Degrees of Freedom	3
Asymptotic Sig. (2-sided test)	.868

1. The test statistic is adjusted for ties.
2. Multiple comparisons are not performed because the overall test does not show significant differences across samples.

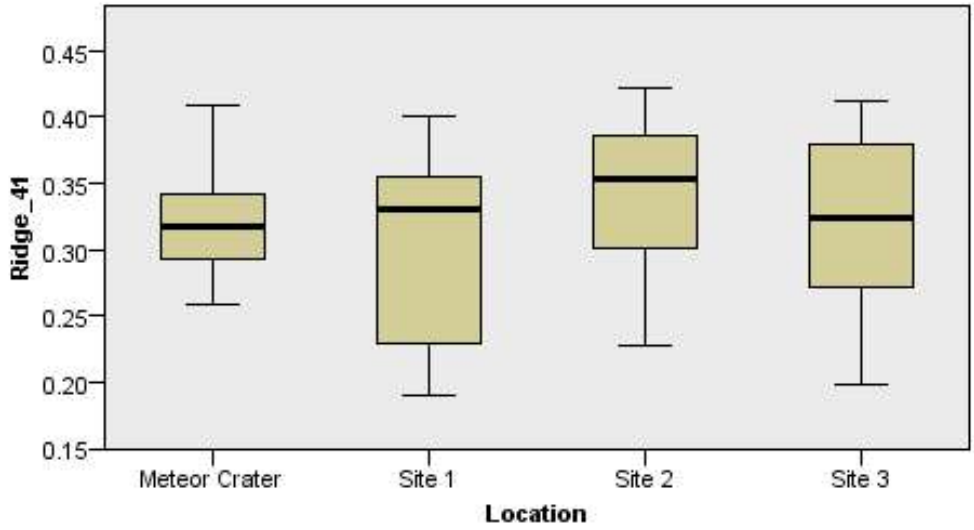
Independent-Samples Kruskal-Wallis Test



Total N	69
Test Statistic	2.171
Degrees of Freedom	3
Asymptotic Sig. (2-sided test)	.538

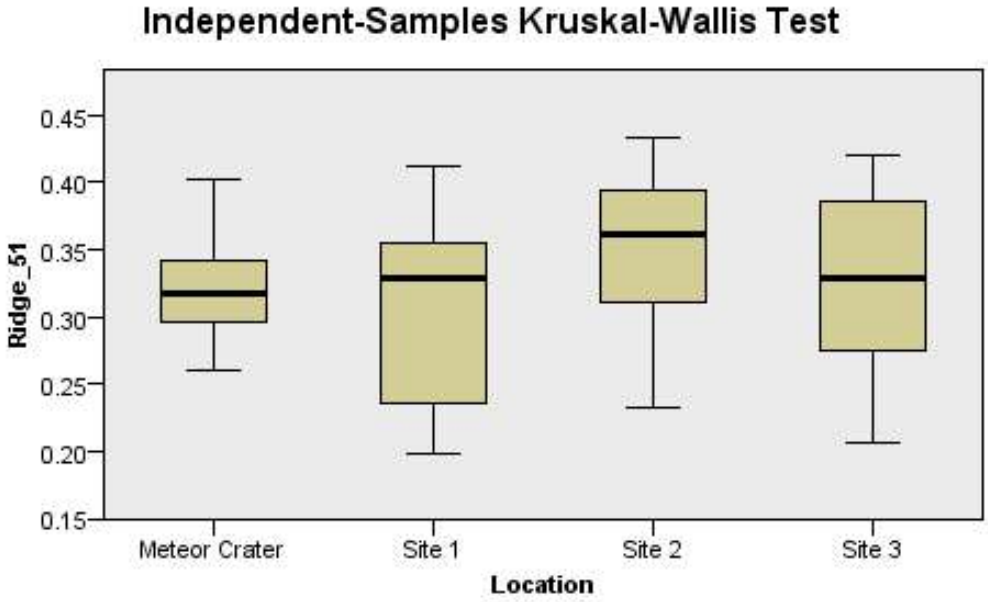
1. The test statistic is adjusted for ties.
2. Multiple comparisons are not performed because the overall test does not show significant differences across samples.

Independent-Samples Kruskal-Wallis Test



Total N	69
Test Statistic	2.225
Degrees of Freedom	3
Asymptotic Sig. (2-sided test)	.527

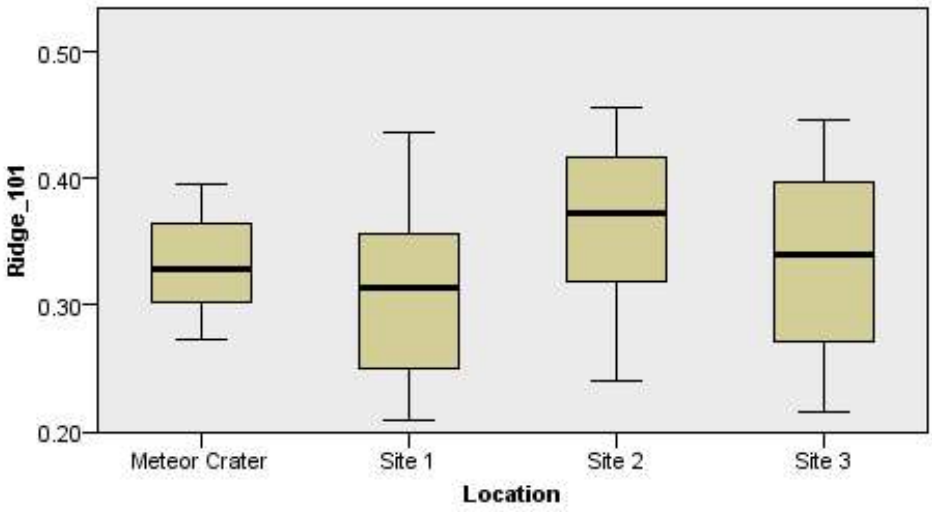
1. The test statistic is adjusted for ties.
2. Multiple comparisons are not performed because the overall test does not show significant differences across samples.



Total N	69
Test Statistic	4.158
Degrees of Freedom	3
Asymptotic Sig. (2-sided test)	.245

1. The test statistic is adjusted for ties.
2. Multiple comparisons are not performed because the overall test does not show significant differences across samples.

Independent-Samples Kruskal-Wallis Test



Total N	69
Test Statistic	6.449
Degrees of Freedom	3
Asymptotic Sig. (2-sided test)	.092

1. The test statistic is adjusted for ties.
2. Multiple comparisons are not performed because the overall test does not show significant differences across samples.

A.5.4.5. Peak

Table A.5.42. Peak data for Site 1.

Feature	Peak						
Rock	**(3*3)**	**(11*11)**	**(21*21)**	**(31*31)**	**(41*41)**	**(51*51)**	**(101*101)**
S1.2-M1	3.21%	3.57%	3.17%	3.05%	2.83%	2.83%	2.53%
S1.2-M2	1.58%	2.56%	2.25%	1.98%	1.82%	1.83%	1.80%
S1.2-M3	2.11%	2.01%	1.78%	1.78%	1.81%	1.95%	2.53%
S1-M2	0.63%	0.35%	0.28%	0.24%	0.24%	0.26%	0.49%
S1-M4_1	0.53%	0.66%	0.87%	1.17%	1.52%	1.88%	2.80%
S1-M4_2	0.66%	0.87%	1.22%	1.70%	2.24%	2.73%	3.97%
S1-M8_1	0.55%	0.53%	0.56%	0.64%	0.67%	0.71%	0.77%
S1-M8_2	1.13%	1.45%	1.70%	1.88%	1.97%	2.13%	2.50%
S1-M10	0.43%	0.44%	0.50%	0.51%	0.53%	0.50%	0.52%
S1-M13_1	0.45%	0.54%	0.52%	0.52%	0.48%	0.46%	0.50%
S1-M13_2	0.45%	0.71%	0.76%	0.77%	0.70%	0.67%	0.60%
S1-M13_3	0.28%	0.47%	0.63%	0.68%	0.69%	0.68%	0.51%

Table A.5.43. Peak data for Site 2.

Feature	Peak						
Rock	**(3*3)**	**(11*11)**	**(21*21)**	**(31*31)**	**(41*41)**	**(51*51)**	**(101*101)**
S2-M1	0.46%	0.44%	0.50%	0.56%	0.63%	0.74%	1.28%
S2-M2	0.50%	0.48%	0.53%	0.54%	0.52%	0.55%	0.59%
S2-M3	0.22%	0.19%	0.20%	0.21%	0.21%	0.21%	0.30%
S2-M4	0.34%	0.37%	0.37%	0.49%	0.51%	0.55%	0.69%
S2-M5	0.16%	0.13%	0.15%	0.16%	0.17%	0.19%	0.23%
S2-M6	1.17%	1.34%	1.74%	2.04%	2.16%	2.45%	3.03%
S2-M7	1.59%	1.25%	1.06%	1.02%	0.93%	1.00%	1.06%
S2-M12	0.17%	0.16%	0.18%	0.17%	0.15%	0.16%	0.28%
S2-M13	0.51%	0.52%	0.51%	0.50%	0.48%	0.54%	0.67%
S2-M16	1.07%	0.98%	1.07%	1.13%	1.06%	1.19%	1.33%
S2-M17	0.41%	0.40%	0.52%	0.64%	0.75%	0.90%	1.13%
S2-M18	0.66%	0.57%	0.65%	0.73%	0.79%	0.92%	1.23%
S2-M19	0.14%	0.11%	0.11%	0.11%	0.11%	0.10%	0.06%
S2-M20	1.08%	0.96%	1.04%	1.11%	1.06%	1.22%	1.35%
S2-M22	0.88%	0.82%	1.00%	1.16%	1.24%	1.34%	1.44%

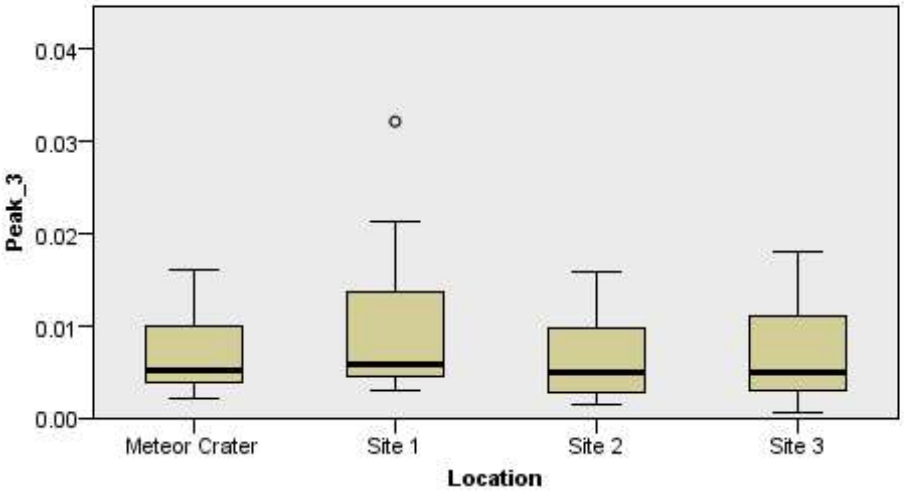
Table A.5.44. Peak data for Site 3.

Feature	Peak						
Rock	**(3*3)**	**(11*11)**	**(21*21)**	**(31*31)**	**(41*41)**	**(51*51)**	**(101*101)**
S3-M1_1	0.20%	0.19%	0.21%	0.20%	0.20%	0.19%	0.13%
S3-M1_2	0.38%	0.43%	0.65%	0.90%	1.15%	1.39%	1.76%
S3-M1_3	0.56%	0.56%	0.68%	0.78%	0.83%	0.90%	1.07%
S3-M6	0.42%	0.37%	0.41%	0.45%	0.53%	0.56%	0.66%
S3-M7	0.52%	0.41%	0.39%	0.35%	0.32%	0.34%	0.46%
S3-M8	0.26%	0.21%	0.24%	0.24%	0.25%	0.28%	0.34%
S3-M9	0.45%	0.47%	0.56%	0.65%	0.69%	0.77%	1.01%
S3-M10	0.48%	0.44%	0.49%	0.49%	0.48%	0.51%	0.55%
S3-M14	1.36%	1.35%	1.49%	1.59%	1.55%	1.65%	1.79%
S3-M18	1.79%	1.41%	1.68%	1.87%	1.73%	1.95%	2.16%
S3-M20	1.51%	1.46%	1.97%	2.38%	2.50%	2.77%	2.87%
S3-M21	0.26%	0.27%	0.31%	0.35%	0.37%	0.41%	0.46%
S3-M22	0.30%	0.33%	0.38%	0.42%	0.43%	0.48%	0.58%
S3-M23	0.28%	0.24%	0.29%	0.33%	0.34%	0.38%	0.50%
S3-M24	0.63%	0.65%	0.75%	0.77%	0.77%	0.82%	1.16%
S3-M25	1.00%	0.95%	1.36%	1.68%	1.84%	2.01%	2.24%
S3-M28	1.18%	1.33%	1.30%	1.42%	1.44%	1.69%	2.25%
S3-M29	0.06%	0.05%	0.06%	0.06%	0.06%	0.07%	0.08%
S3-M33	1.35%	1.45%	1.38%	1.35%	1.24%	1.38%	1.67%
S3-M35	0.80%	1.06%	1.19%	1.22%	1.07%	1.12%	0.92%

Table A.5.45. Peak data for Meteor Crater.

Feature	Peak						
Rock	**(3*3)**	**(11*11)**	**(21*21)**	**(31*31)**	**(41*41)**	**(51*51)**	**(101*101)**
M13-01	0.39%	0.51%	0.63%	0.78%	0.97%	1.13%	1.77%
M13-02	0.93%	0.87%	0.94%	0.94%	0.98%	1.02%	0.99%
M13-03	1.29%	1.12%	1.27%	1.41%	1.57%	1.70%	2.12%
M13-04	0.39%	0.47%	0.55%	0.65%	0.70%	0.74%	0.85%
M13-05	0.41%	0.39%	0.43%	0.47%	0.51%	0.53%	0.61%
M13-06	0.40%	0.36%	0.36%	0.35%	0.36%	0.38%	0.45%
M13-07	0.20%	0.21%	0.22%	0.23%	0.22%	0.22%	0.32%
M13-08	0.35%	0.36%	0.39%	0.41%	0.44%	0.45%	0.57%
M13-09	0.45%	0.50%	0.54%	0.53%	0.52%	0.56%	0.64%
M13-10	0.56%	0.61%	0.67%	0.69%	0.68%	0.70%	0.73%
M14-11	0.42%	0.56%	0.64%	0.63%	0.60%	0.63%	0.70%
M14-12	0.95%	1.34%	1.52%	1.64%	1.77%	1.87%	2.02%
M14-13	1.04%	1.08%	1.23%	1.33%	1.40%	1.48%	1.87%
M14-14	0.84%	0.73%	0.77%	0.80%	0.79%	0.82%	1.10%
M14-15	1.59%	2.13%	2.44%	2.60%	2.66%	2.69%	2.56%
M14-16	1.08%	1.10%	0.99%	0.94%	0.89%	0.82%	0.63%
M14-17	0.89%	1.06%	1.12%	1.13%	1.13%	1.13%	1.16%
M14-18	0.33%	0.41%	0.43%	0.42%	0.41%	0.40%	0.32%
M14-19	0.38%	0.45%	0.46%	0.50%	0.54%	0.55%	0.59%
M14-20	0.99%	1.12%	1.27%	1.35%	1.40%	1.44%	1.80%
M14-21	0.39%	0.40%	0.41%	0.44%	0.48%	0.51%	0.62%
MC-M1-01	1.07%	1.17%	1.20%	1.16%	1.11%	1.06%	0.91%

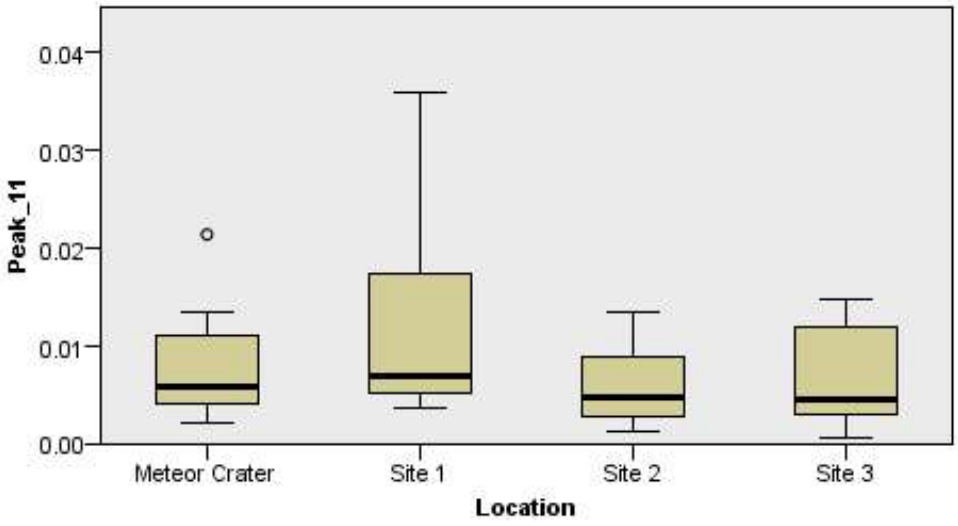
Independent-Samples Kruskal-Wallis Test



Total N	69
Test Statistic	2.137
Degrees of Freedom	3
Asymptotic Sig. (2-sided test)	.544

1. The test statistic is adjusted for ties.
2. Multiple comparisons are not performed because the overall test does not show significant differences across samples.

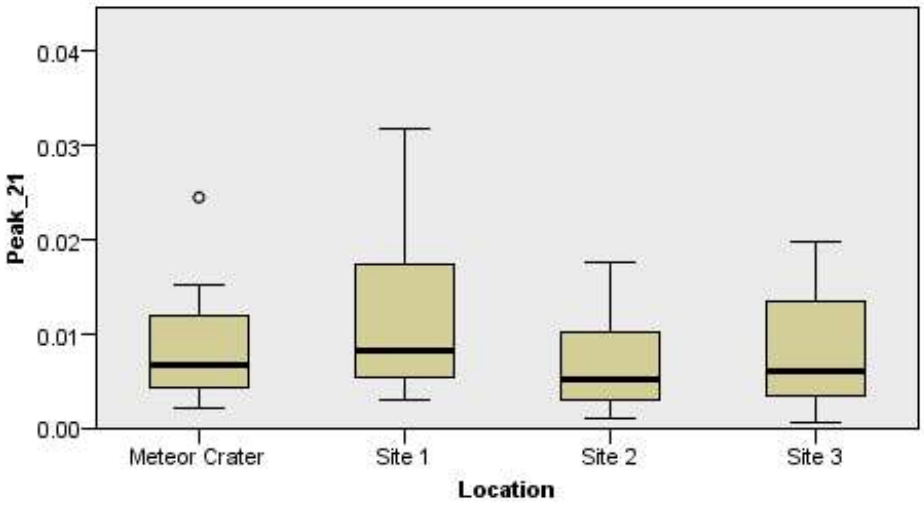
Independent-Samples Kruskal-Wallis Test



Total N	69
Test Statistic	4.709
Degrees of Freedom	3
Asymptotic Sig. (2-sided test)	.194

1. The test statistic is adjusted for ties.
2. Multiple comparisons are not performed because the overall test does not show significant differences across samples.

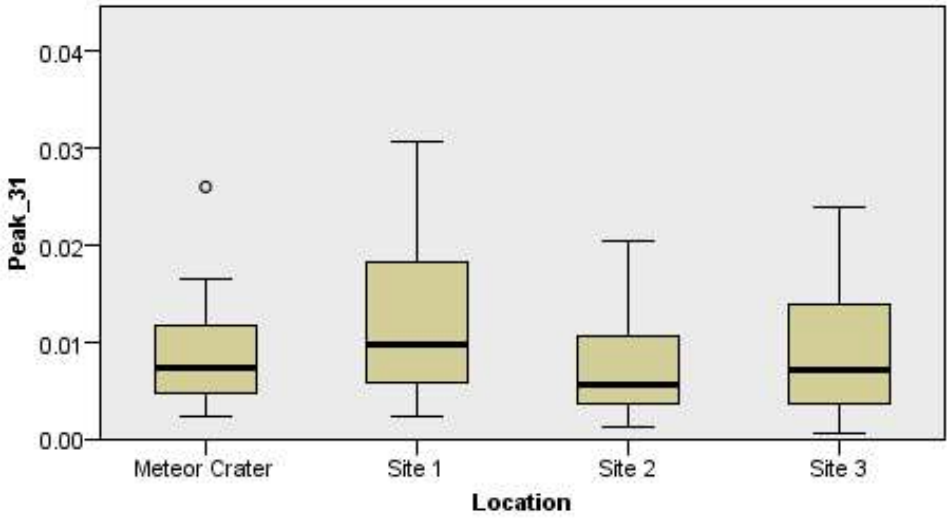
Independent-Samples Kruskal-Wallis Test



Total N	69
Test Statistic	4.488
Degrees of Freedom	3
Asymptotic Sig. (2-sided test)	.213

1. The test statistic is adjusted for ties.
2. Multiple comparisons are not performed because the overall test does not show significant differences across samples.

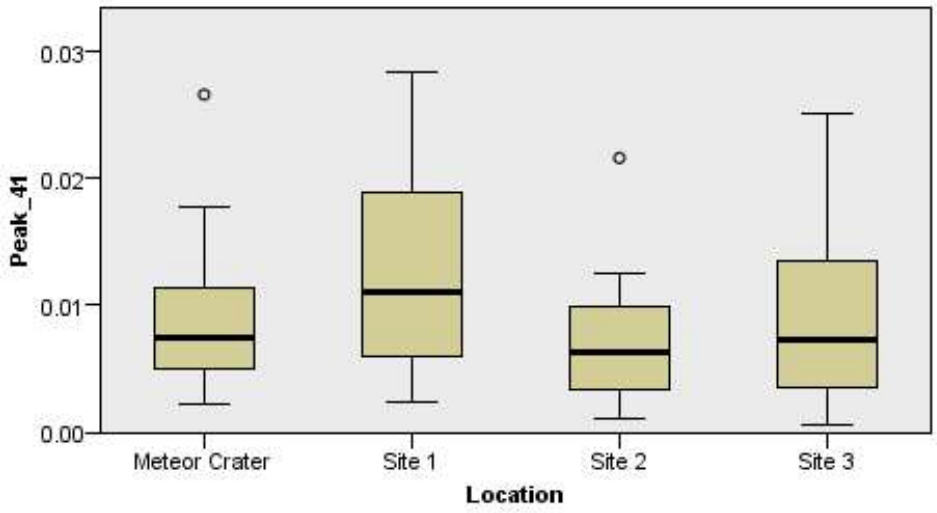
Independent-Samples Kruskal-Wallis Test



Total N	69
Test Statistic	4.034
Degrees of Freedom	3
Asymptotic Sig. (2-sided test)	.258

1. The test statistic is adjusted for ties.
2. Multiple comparisons are not performed because the overall test does not show significant differences across samples.

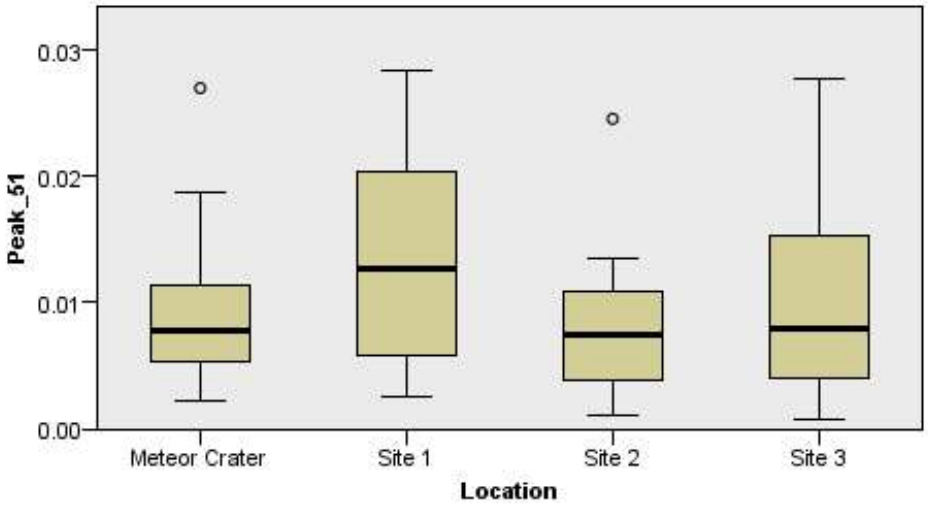
Independent-Samples Kruskal-Wallis Test



Total N	69
Test Statistic	4.016
Degrees of Freedom	3
Asymptotic Sig. (2-sided test)	.260

1. The test statistic is adjusted for ties.
2. Multiple comparisons are not performed because the overall test does not show significant differences across samples.

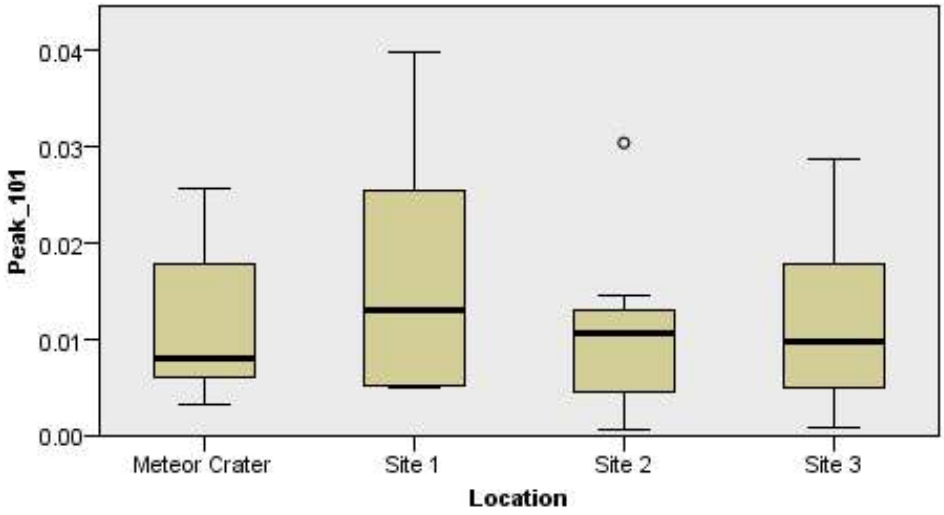
Independent-Samples Kruskal-Wallis Test



Total N	69
Test Statistic	2.703
Degrees of Freedom	3
Asymptotic Sig. (2-sided test)	.440

1. The test statistic is adjusted for ties.
2. Multiple comparisons are not performed because the overall test does not show significant differences across samples.

Independent-Samples Kruskal-Wallis Test



Total N	69
Test Statistic	1.608
Degrees of Freedom	3
Asymptotic Sig. (2-sided test)	.657

1. The test statistic is adjusted for ties.
2. Multiple comparisons are not performed because the overall test does not show significant differences across samples.

A.5.4.6. Planar

Table A.5.46. Planar data for Site 1.

Feature	Planar						
Rock	**(3*3)**	**(11*11)**	**(21*21)**	**(31*31)**	**(41*41)**	**(51*51)**	**(101*101)**
S1.2-M1	23.83%	31.02%	33.95%	34.75%	35.18%	35.83%	37.97%
S1.2-M2	21.80%	29.44%	41.12%	46.43%	48.80%	49.90%	50.10%
S1.2-M3	26.12%	37.96%	44.11%	44.41%	43.26%	41.91%	35.34%
S1-M2	35.11%	54.37%	60.69%	59.55%	57.49%	55.67%	51.41%
S1-M4_1	18.63%	16.30%	14.80%	14.34%	14.82%	15.70%	22.32%
S1-M4_2	20.36%	18.60%	16.99%	16.39%	16.50%	17.06%	20.86%
S1-M8_1	20.33%	22.67%	22.04%	21.52%	21.47%	21.96%	24.21%
S1-M8_2	31.73%	29.27%	27.50%	26.43%	26.02%	26.20%	26.93%
S1-M10	19.34%	23.33%	22.37%	21.69%	21.34%	21.29%	22.76%
S1-M13_1	17.57%	25.50%	30.81%	32.89%	34.75%	36.03%	39.92%
S1-M13_2	14.02%	20.35%	26.05%	27.57%	28.34%	29.09%	30.27%
S1-M13_3	29.99%	24.39%	24.10%	24.57%	25.37%	26.27%	29.53%

Table A.5.47. Planar data for Site 2.

Feature	Planar						
Rock	**(3*3)**	**(11*11)**	**(21*21)**	**(31*31)**	**(41*41)**	**(51*51)**	**(101*101)**
S2-M1	28.02%	30.88%	26.45%	23.98%	22.66%	21.92%	21.57%
S2-M2	30.97%	40.07%	37.32%	36.45%	36.29%	36.42%	37.19%
S2-M3	26.08%	31.27%	26.44%	24.22%	23.15%	22.69%	21.90%
S2-M4	28.04%	34.66%	34.66%	30.55%	31.39%	32.21%	31.96%
S2-M5	24.28%	22.48%	16.04%	13.88%	13.13%	12.89%	15.26%
S2-M6	34.88%	36.92%	30.65%	28.05%	27.24%	26.95%	26.45%
S2-M7	33.11%	45.50%	47.12%	47.79%	48.42%	49.16%	49.73%
S2-M12	25.53%	30.13%	25.95%	24.83%	24.59%	24.70%	25.30%
S2-M13	28.31%	44.79%	43.96%	42.70%	41.93%	41.60%	40.17%
S2-M16	27.85%	34.67%	34.35%	33.01%	32.03%	31.70%	32.71%
S2-M17	20.99%	20.52%	16.74%	15.62%	15.62%	16.12%	20.10%
S2-M18	26.52%	27.97%	23.18%	21.14%	20.34%	20.43%	23.46%
S2-M19	25.13%	27.08%	20.95%	18.33%	17.19%	16.61%	16.25%
S2-M20	30.75%	37.94%	36.56%	35.03%	33.80%	33.30%	33.17%
S2-M22	27.74%	31.82%	26.69%	23.95%	22.68%	22.18%	24.12%

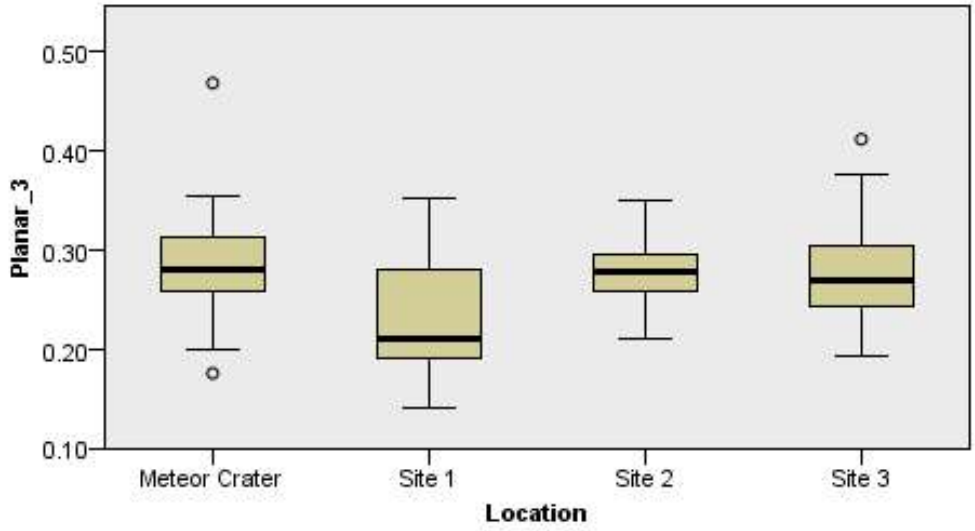
Table A.5.48. Planar data for Site 3.

Feature	Planar						
Rock	**(3*3)**	**(11*11)**	**(21*21)**	**(31*31)**	**(41*41)**	**(51*51)**	**(101*101)**
S3-M1_1	21.02%	24.65%	20.89%	19.14%	18.82%	19.81%	24.69%
S3-M1_2	22.16%	20.20%	16.04%	14.89%	15.21%	15.78%	22.34%
S3-M1_3	27.80%	33.39%	29.11%	27.09%	26.05%	25.77%	26.28%
S3-M6	22.87%	25.21%	21.62%	19.75%	18.70%	18.32%	18.17%
S3-M7	26.05%	36.68%	39.54%	40.17%	40.12%	39.74%	35.45%
S3-M8	25.71%	40.38%	39.29%	37.73%	36.86%	36.27%	34.62%
S3-M9	24.32%	27.01%	22.28%	20.32%	19.60%	19.56%	21.31%
S3-M10	28.62%	42.48%	41.07%	39.88%	39.39%	39.06%	38.53%
S3-M14	36.11%	42.49%	40.65%	39.87%	39.50%	39.33%	38.59%
S3-M18	31.88%	40.95%	39.11%	37.91%	37.35%	37.55%	39.53%
S3-M20	24.36%	29.07%	27.35%	26.72%	27.00%	28.00%	32.75%
S3-M21	24.58%	25.50%	21.11%	19.14%	18.07%	17.43%	16.84%
S3-M22	30.82%	28.16%	22.78%	19.91%	18.63%	18.13%	19.66%
S3-M23	26.17%	32.55%	26.28%	23.55%	22.52%	22.20%	24.63%
S3-M24	30.10%	35.10%	31.73%	30.61%	30.49%	30.77%	31.25%
S3-M25	27.61%	27.76%	23.01%	22.18%	22.83%	24.20%	32.14%
S3-M28	41.09%	48.91%	51.53%	50.50%	48.85%	47.23%	41.29%
S3-M29	19.36%	31.17%	30.85%	30.30%	30.14%	29.95%	26.52%
S3-M33	37.56%	42.80%	48.66%	51.41%	51.75%	51.31%	46.66%
S3-M35	30.00%	32.14%	34.03%	35.43%	36.53%	37.49%	38.45%

Table A.5.49. Planar data for Meteor Crater.

Feature	Planar						
Rock	**(3*3)**	**(11*11)**	**(21*21)**	**(31*31)**	**(41*41)**	**(51*51)**	**(101*101)**
M13-01	21.16%	17.49%	13.24%	12.70%	13.54%	15.06%	26.32%
M13-02	24.92%	39.02%	41.54%	42.01%	42.45%	42.59%	41.14%
M13-03	28.97%	41.88%	41.20%	39.82%	38.57%	37.51%	34.61%
M13-04	17.52%	16.61%	14.42%	14.32%	14.90%	15.84%	20.21%
M13-05	27.36%	38.90%	36.00%	34.52%	33.83%	33.39%	31.70%
M13-06	27.14%	42.59%	41.10%	39.96%	39.31%	38.97%	37.40%
M13-07	29.50%	39.49%	34.92%	33.17%	32.43%	32.08%	31.17%
M13-08	28.64%	38.47%	34.64%	33.22%	32.61%	32.37%	31.71%
M13-09	34.05%	39.77%	35.93%	35.01%	34.91%	34.90%	33.70%
M13-10	25.90%	30.17%	28.59%	28.39%	28.84%	29.59%	34.62%
M14-11	46.75%	40.62%	38.57%	38.60%	38.95%	39.29%	40.31%
M14-12	32.71%	29.54%	28.40%	29.37%	30.64%	31.73%	33.03%
M14-13	22.74%	33.32%	33.15%	32.95%	33.02%	33.02%	31.95%
M14-14	35.46%	45.93%	45.51%	45.55%	45.73%	45.89%	45.65%
M14-15	28.81%	30.75%	29.17%	28.16%	27.54%	27.05%	27.87%
M14-16	19.94%	30.56%	34.34%	35.71%	36.80%	37.75%	40.01%
M14-17	33.10%	31.49%	29.63%	29.72%	30.38%	31.05%	33.03%
M14-18	26.57%	28.12%	28.50%	28.78%	28.90%	29.06%	27.98%
M14-19	27.02%	26.98%	27.32%	27.87%	28.15%	28.40%	26.54%
M14-20	26.00%	27.84%	28.14%	28.52%	28.79%	28.84%	29.21%
M14-21	31.35%	41.03%	40.82%	39.84%	38.96%	38.22%	34.55%
MC-M1-01	29.38%	34.30%	36.10%	38.38%	40.73%	43.20%	50.93%

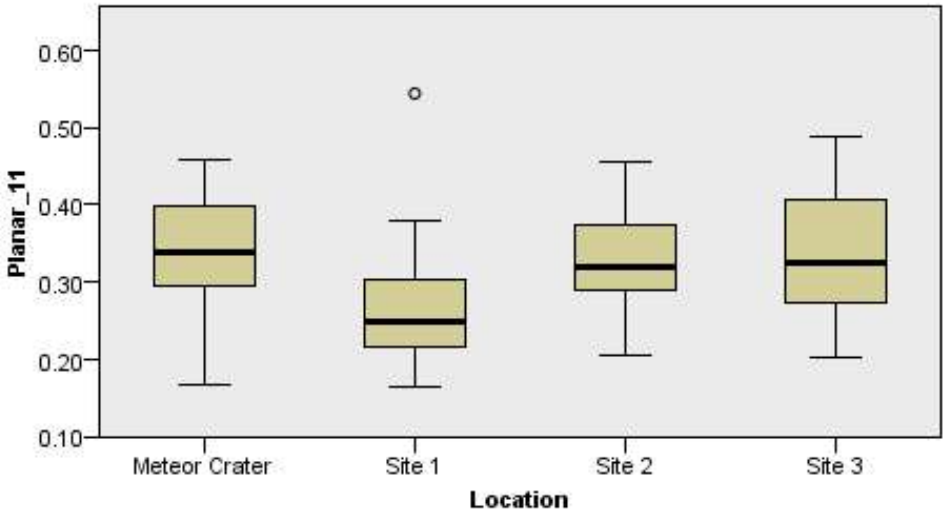
Independent-Samples Kruskal-Wallis Test



Total N	69
Test Statistic	6.507
Degrees of Freedom	3
Asymptotic Sig. (2-sided test)	.089

1. The test statistic is adjusted for ties.
2. Multiple comparisons are not performed because the overall test does not show significant differences across samples.

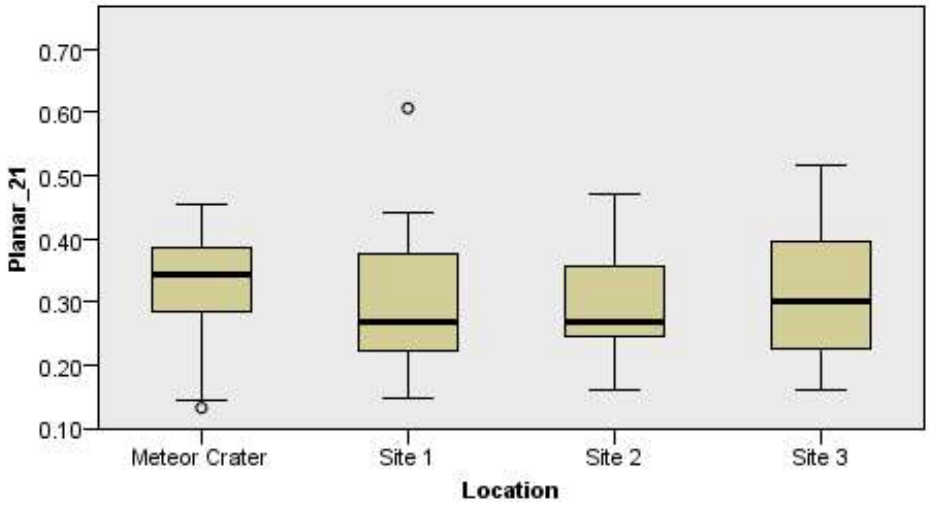
Independent-Samples Kruskal-Wallis Test



Total N	69
Test Statistic	6.837
Degrees of Freedom	3
Asymptotic Sig. (2-sided test)	.077

1. The test statistic is adjusted for ties.
2. Multiple comparisons are not performed because the overall test does not show significant differences across samples.

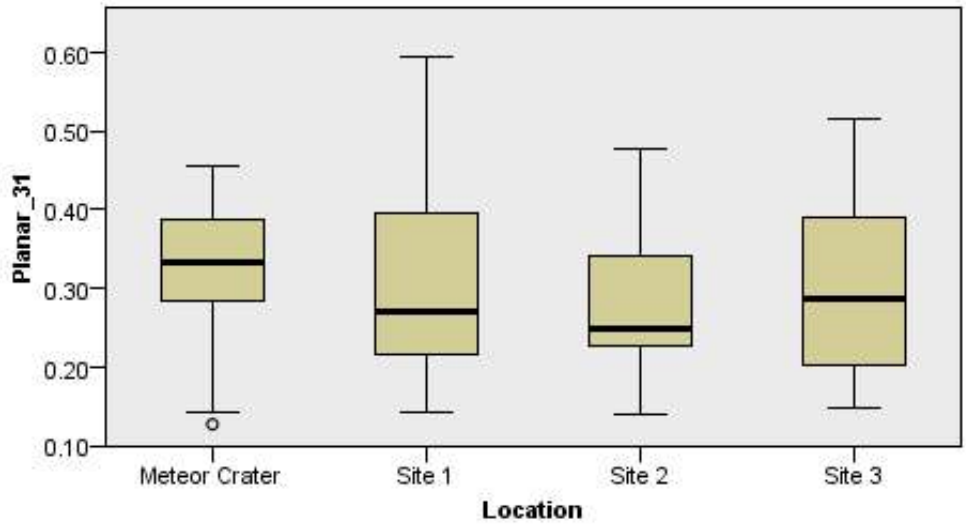
Independent-Samples Kruskal-Wallis Test



Total N	69
Test Statistic	2.387
Degrees of Freedom	3
Asymptotic Sig. (2-sided test)	.496

1. The test statistic is adjusted for ties.
2. Multiple comparisons are not performed because the overall test does not show significant differences across samples.

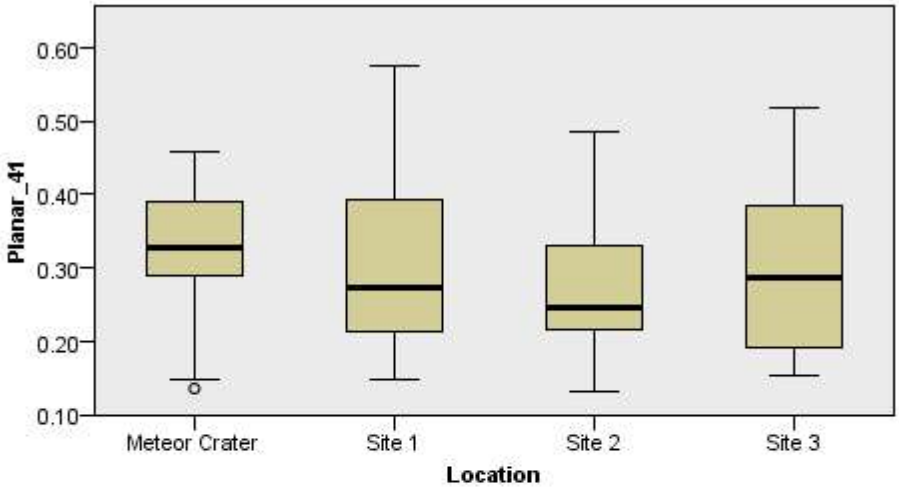
Independent-Samples Kruskal-Wallis Test



Total N	69
Test Statistic	2.933
Degrees of Freedom	3
Asymptotic Sig. (2-sided test)	.402

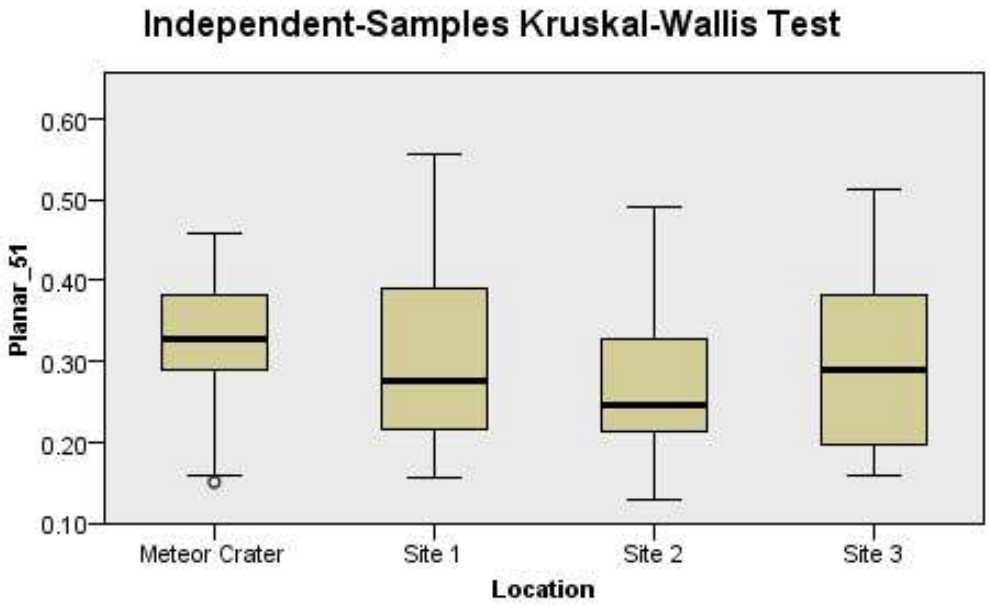
1. The test statistic is adjusted for ties.
2. Multiple comparisons are not performed because the overall test does not show significant differences across samples.

Independent-Samples Kruskal-Wallis Test



Total N	69
Test Statistic	3.430
Degrees of Freedom	3
Asymptotic Sig. (2-sided test)	.330

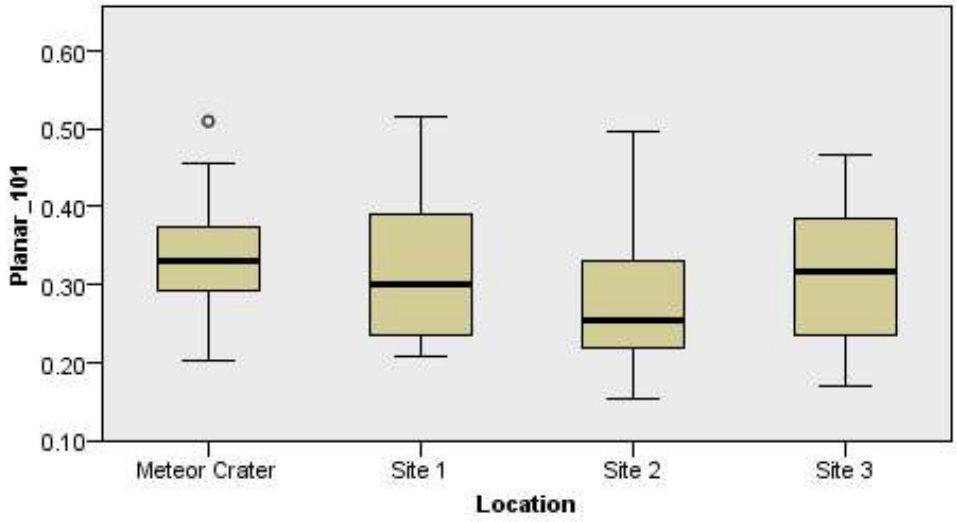
1. The test statistic is adjusted for ties.
2. Multiple comparisons are not performed because the overall test does not show significant differences across samples.



Total N	69
Test Statistic	3.679
Degrees of Freedom	3
Asymptotic Sig. (2-sided test)	.298

1. The test statistic is adjusted for ties.
2. Multiple comparisons are not performed because the overall test does not show significant differences across samples.

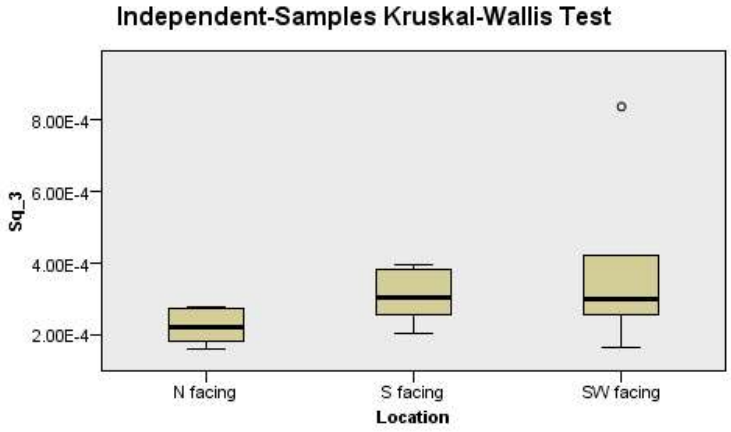
Independent-Samples Kruskal-Wallis Test



Total N	69
Test Statistic	4.795
Degrees of Freedom	3
Asymptotic Sig. (2-sided test)	.187

1. The test statistic is adjusted for ties.
2. Multiple comparisons are not performed because the overall test does not show significant differences across samples.

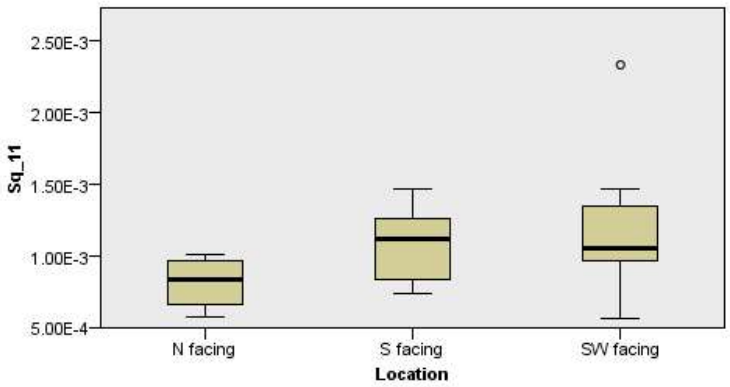
A.5.5. Schmidt hammer rebound data, areal surface roughness (Sq, Sdq, Sz, and VRM), and morphometric features (pit, channel, ridge, peak, pass, planar) comparison between North facing, South facing, and South West facing outcrops at Meteor Crater.



Total N	21
Test Statistic	4.277
Degrees of Freedom	2
Asymptotic Sig. (2-sided test)	.118

1. The test statistic is adjusted for ties.
2. Multiple comparisons are not performed because the overall test does not show significant differences across samples.

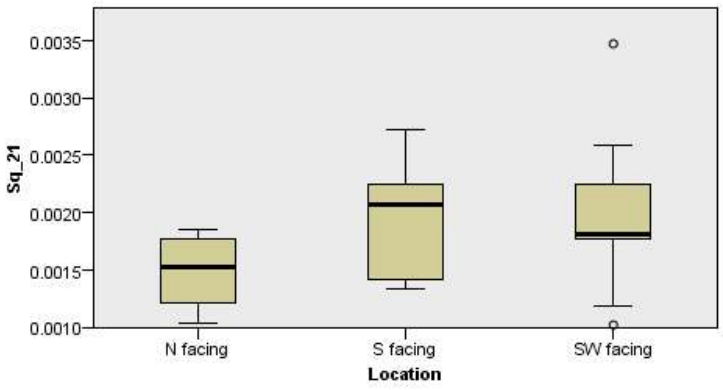
Independent-Samples Kruskal-Wallis Test



Total N	21
Test Statistic	3.820
Degrees of Freedom	2
Asymptotic Sig. (2-sided test)	.148

1. The test statistic is adjusted for ties.
2. Multiple comparisons are not performed because the overall test does not show significant differences across samples.

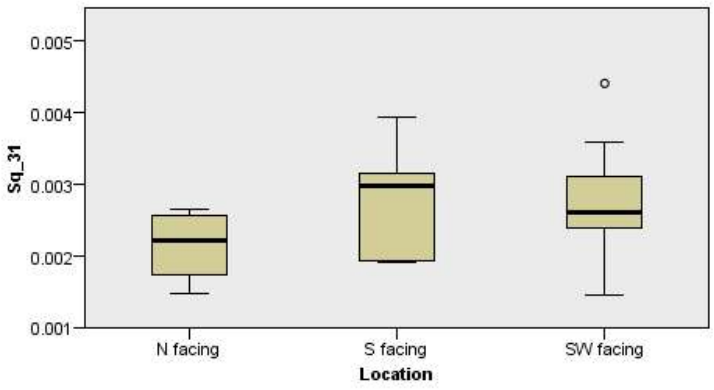
Independent-Samples Kruskal-Wallis Test



Total N	21
Test Statistic	3.030
Degrees of Freedom	2
Asymptotic Sig. (2-sided test)	.220

1. The test statistic is adjusted for ties.
2. Multiple comparisons are not performed because the overall test does not show significant differences across samples.

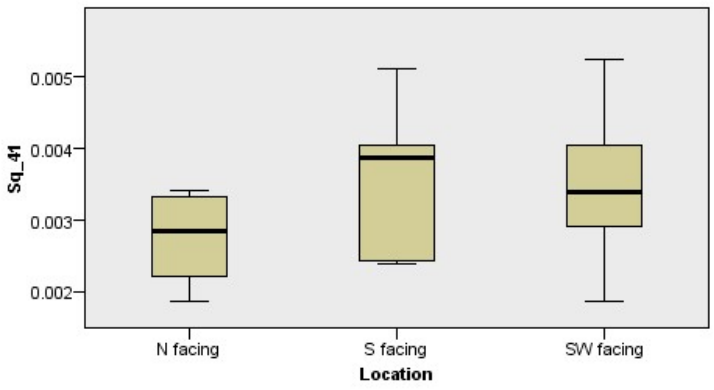
Independent-Samples Kruskal-Wallis Test



Total N	21
Test Statistic	2.789
Degrees of Freedom	2
Asymptotic Sig. (2-sided test)	.248

1. The test statistic is adjusted for ties.
2. Multiple comparisons are not performed because the overall test does not show significant differences across samples.

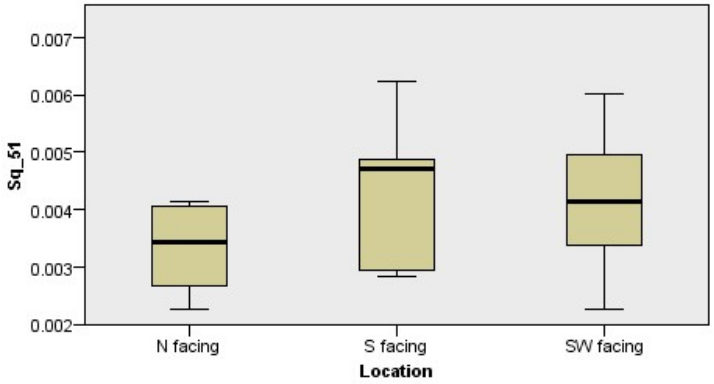
Independent-Samples Kruskal-Wallis Test



Total N	21
Test Statistic	3.063
Degrees of Freedom	2
Asymptotic Sig. (2-sided test)	.216

1. The test statistic is adjusted for ties.
2. Multiple comparisons are not performed because the overall test does not show significant differences across samples.

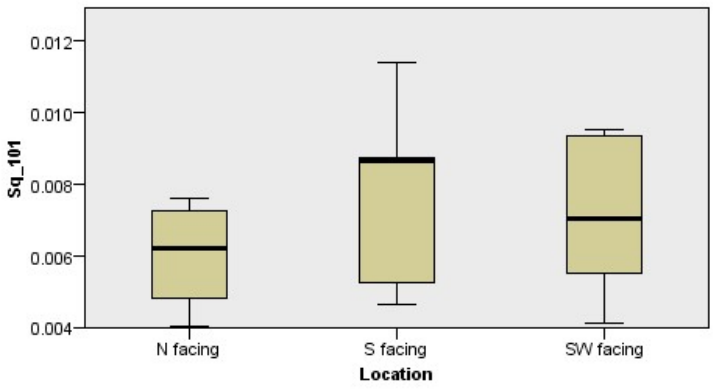
Independent-Samples Kruskal-Wallis Test



Total N	21
Test Statistic	3.020
Degrees of Freedom	2
Asymptotic Sig. (2-sided test)	.221

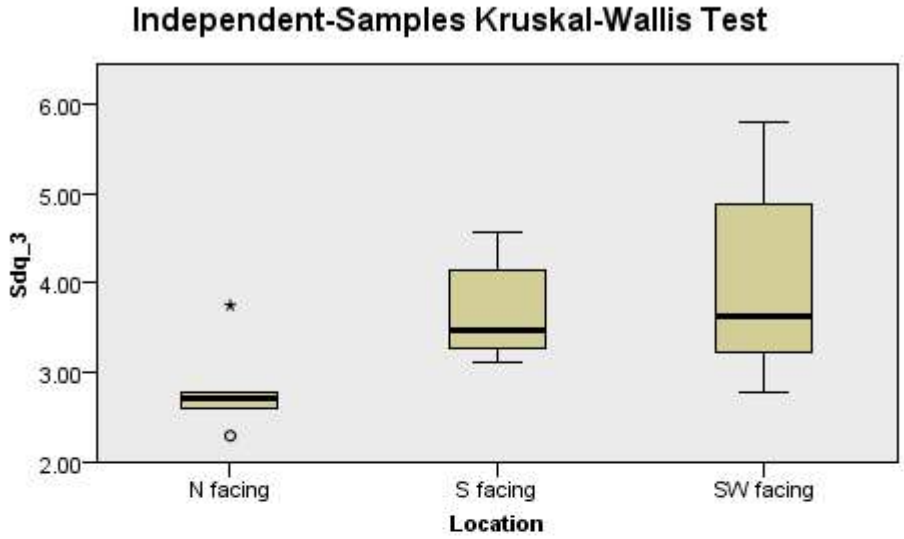
1. The test statistic is adjusted for ties.
2. Multiple comparisons are not performed because the overall test does not show significant differences across samples.

Independent-Samples Kruskal-Wallis Test



Total N	21
Test Statistic	2.190
Degrees of Freedom	2
Asymptotic Sig. (2-sided test)	.335

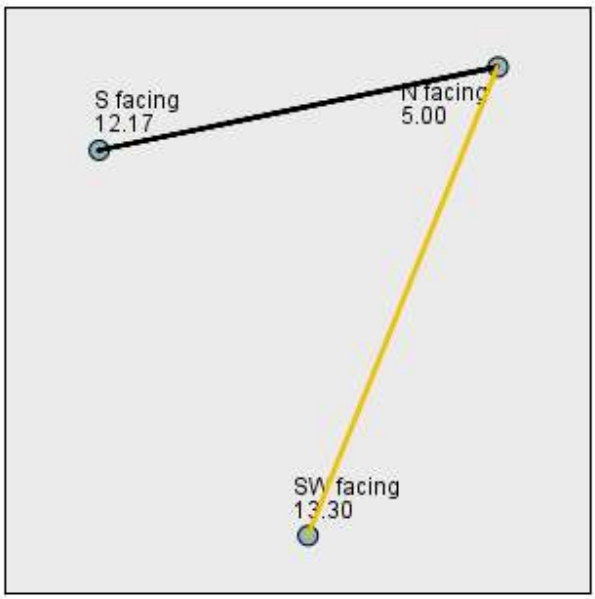
1. The test statistic is adjusted for ties.
2. Multiple comparisons are not performed because the overall test does not show significant differences across samples.



Total N	21
Test Statistic	6.261
Degrees of Freedom	2
Asymptotic Sig. (2-sided test)	.044

1. The test statistic is adjusted for ties.

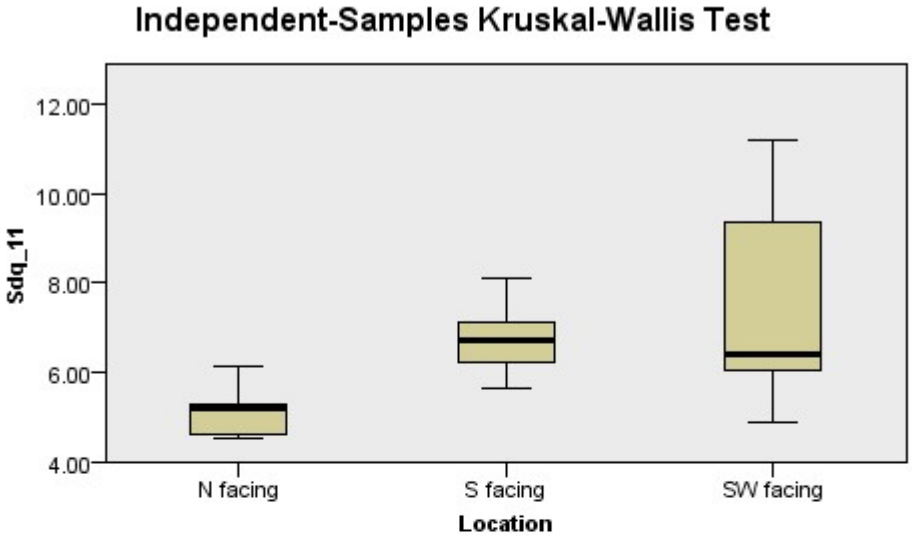
Pairwise Comparisons of Location



Each node shows the sample average rank of Location.

Sample1-Sample2	Test Statistic	Std. Error	Std. Test Statistic	Sig.	Adj.Sig.
N facing-S facing	-7.167	3.757	-1.907	.056	.169
N facing-SW facing	-8.300	3.399	-2.442	.015	.044
S facing-SW facing	-1.133	3.204	-.354	.724	1.000

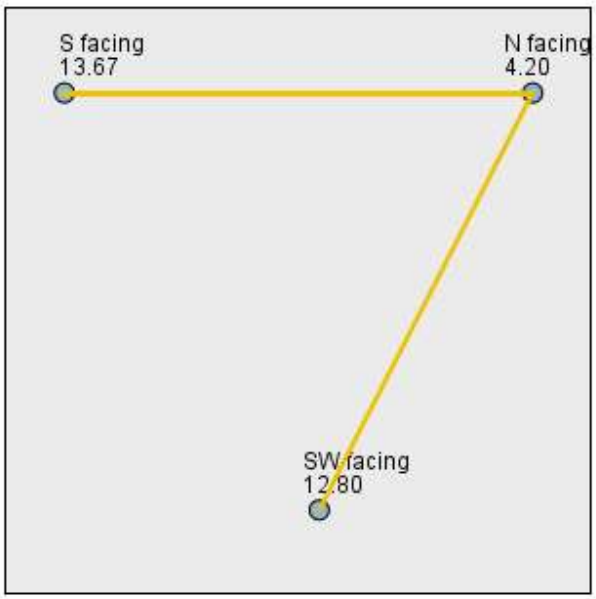
Each row tests the null hypothesis that the Sample 1 and Sample 2 distributions are the same.
Asymptotic significances (2-sided tests) are displayed. The significance level is .05.
Significance values have been adjusted by the Bonferroni correction for multiple tests.



Total N	21
Test Statistic	7.955
Degrees of Freedom	2
Asymptotic Sig. (2-sided test)	.019

1. The test statistic is adjusted for ties.

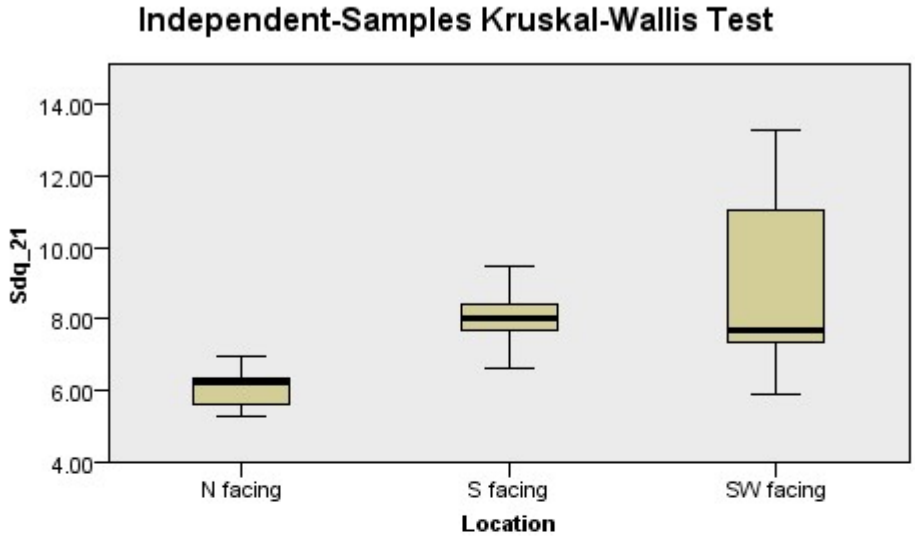
Pairwise Comparisons of Location



Each node shows the sample average rank of Location.

Sample1-Sample2	Test Statistic	Std. Error	Std. Test Statistic	Sig.	Adj.Sig.
N facing-SW facing	-8.600	3.399	-2.531	.011	.034
N facing-S facing	-9.467	3.757	-2.520	.012	.035
SW facing-S facing	.867	3.204	.270	.787	1.000

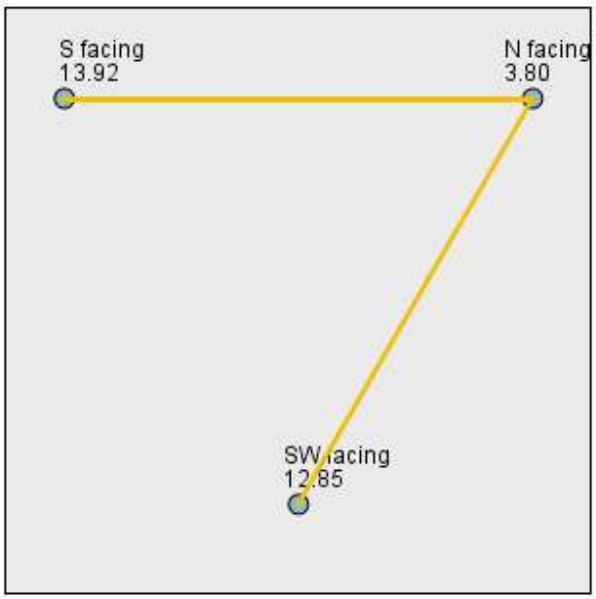
Each row tests the null hypothesis that the Sample 1 and Sample 2 distributions are the same.
Asymptotic significances (2-sided tests) are displayed. The significance level is .05.
Significance values have been adjusted by the Bonferroni correction for multiple tests.



Total N	21
Test Statistic	8.953
Degrees of Freedom	2
Asymptotic Sig. (2-sided test)	.011

1. The test statistic is adjusted for ties.

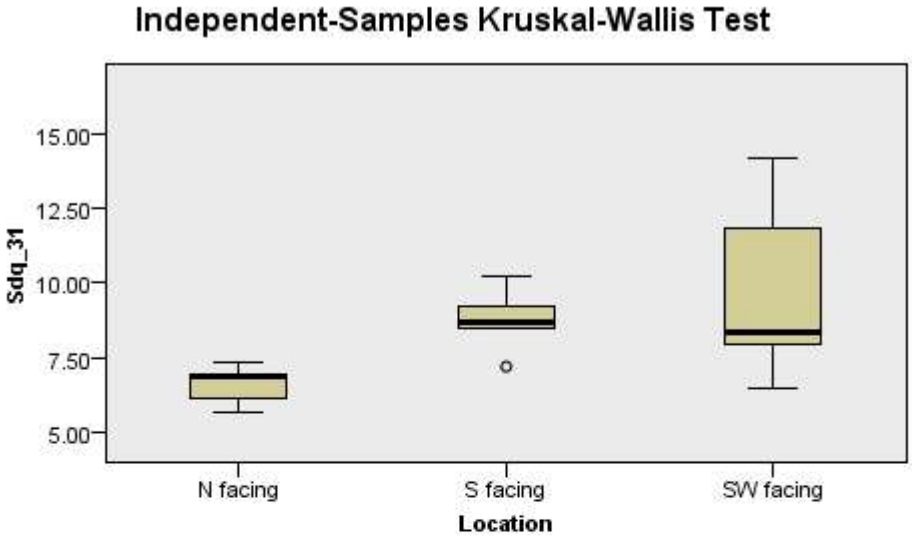
Pairwise Comparisons of Location



Each node shows the sample average rank of Location.

Sample1-Sample2	Test Statistic	Std. Error	Std. Test Statistic	Sig.	Adj.Sig.
N facing-SW facing	-9.050	3.397	-2.664	.008	.023
N facing-S facing	-10.117	3.756	-2.693	.007	.021
SW facing-S facing	1.067	3.203	.333	.739	1.000

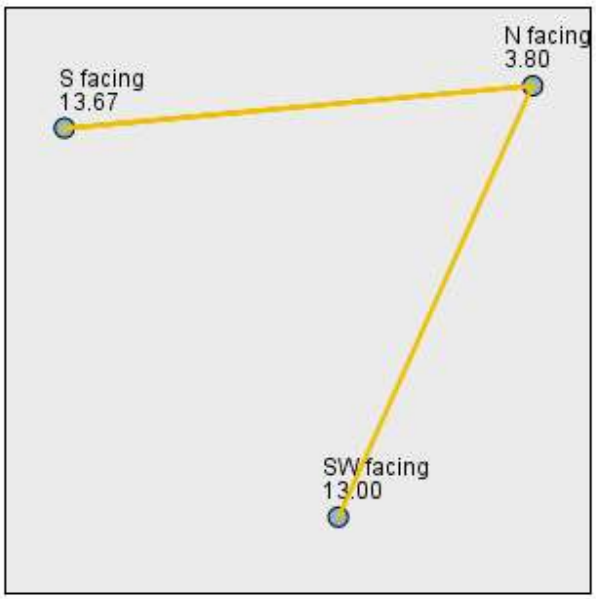
Each row tests the null hypothesis that the Sample 1 and Sample 2 distributions are the same.
Asymptotic significances (2-sided tests) are displayed. The significance level is .05.
Significance values have been adjusted by the Bonferroni correction for multiple tests.



Total N	21
Test Statistic	8.880
Degrees of Freedom	2
Asymptotic Sig. (2-sided test)	.012

1. The test statistic is adjusted for ties.

Pairwise Comparisons of Location

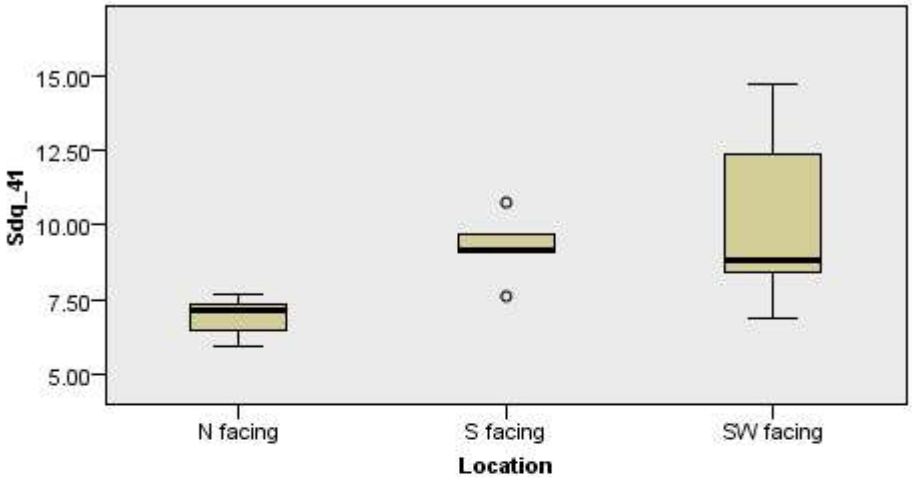


Each node shows the sample average rank of Location.

Sample1-Sample2	Test Statistic	Std. Error	Std. Test Statistic	Sig.	Adj.Sig.
N facing-SW facing	-9.200	3.399	-2.707	.007	.020
N facing-S facing	-9.867	3.757	-2.626	.009	.026
SW facing-S facing	.667	3.204	.208	.835	1.000

Each row tests the null hypothesis that the Sample 1 and Sample 2 distributions are the same.
Asymptotic significances (2-sided tests) are displayed. The significance level is .05.
Significance values have been adjusted by the Bonferroni correction for multiple tests.

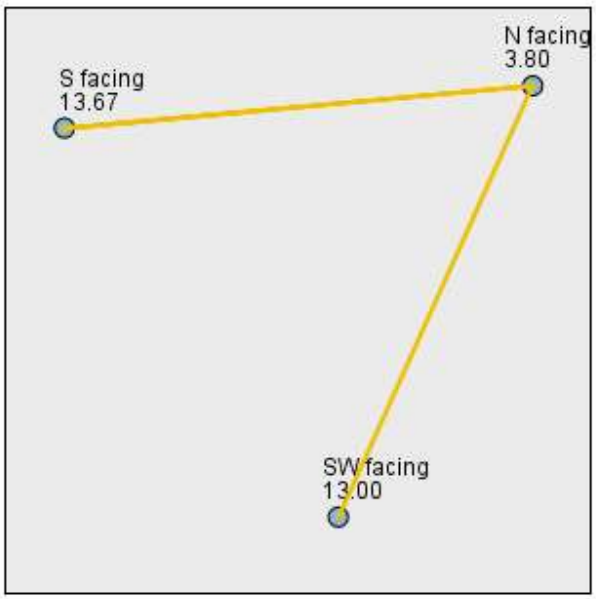
Independent-Samples Kruskal-Wallis Test



Total N	21
Test Statistic	8.880
Degrees of Freedom	2
Asymptotic Sig. (2-sided test)	.012

1. The test statistic is adjusted for ties.

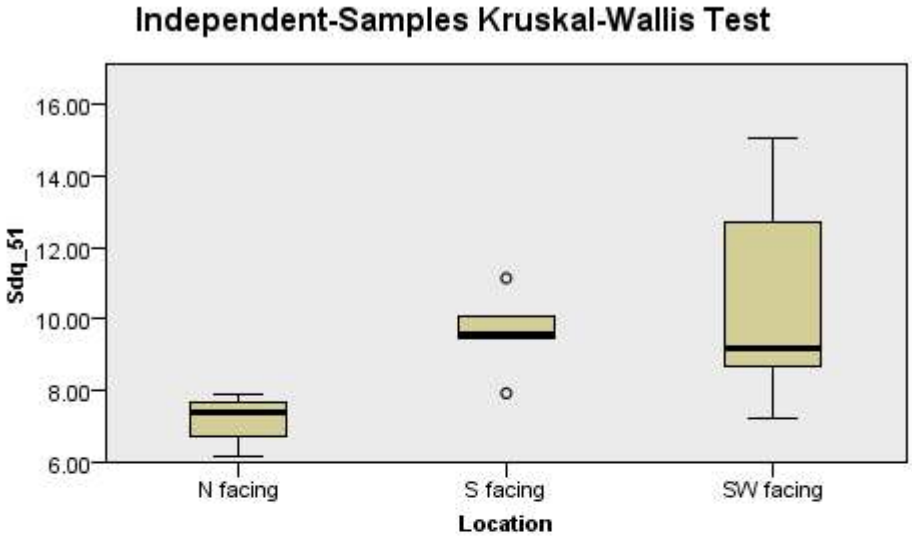
Pairwise Comparisons of Location



Each node shows the sample average rank of Location.

Sample1-Sample2	Test Statistic	Std. Error	Std. Test Statistic	Sig.	Adj.Sig.
N facing-SW facing	-9.200	3.399	-2.707	.007	.020
N facing-S facing	-9.867	3.757	-2.626	.009	.026
SW facing-S facing	.667	3.204	.208	.835	1.000

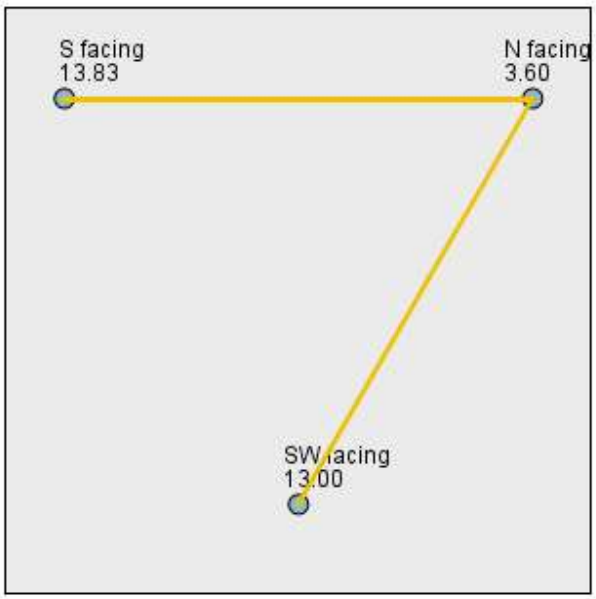
Each row tests the null hypothesis that the Sample 1 and Sample 2 distributions are the same.
Asymptotic significances (2-sided tests) are displayed. The significance level is .05.
Significance values have been adjusted by the Bonferroni correction for multiple tests.



Total N	21
Test Statistic	9.402
Degrees of Freedom	2
Asymptotic Sig. (2-sided test)	.009

1. The test statistic is adjusted for ties.

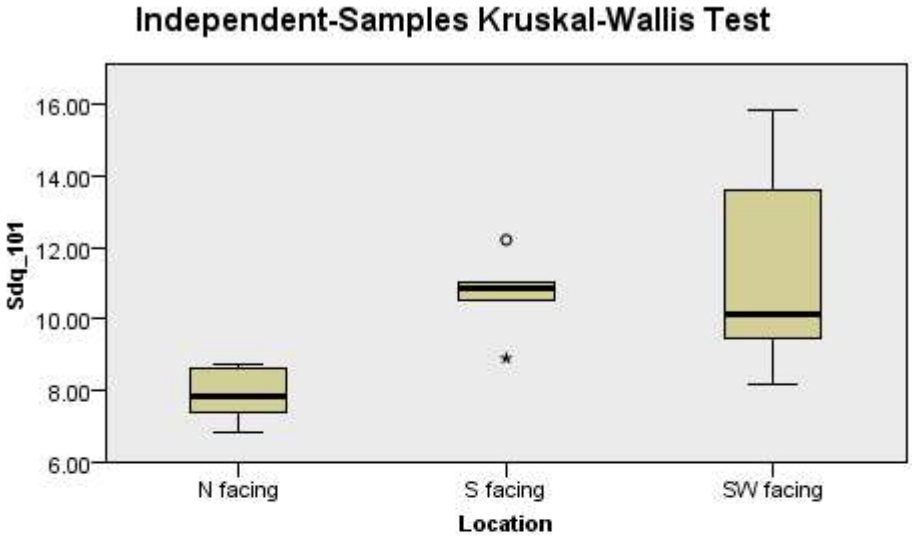
Pairwise Comparisons of Location



Each node shows the sample average rank of Location.

Sample1-Sample2	Test Statistic	Std. Error	Std. Test Statistic	Sig.	Adj.Sig.
N facing-SW facing	-9.400	3.399	-2.766	.006	.017
N facing-S facing	-10.233	3.757	-2.724	.006	.019
SW facing-S facing	.833	3.204	.260	.795	1.000

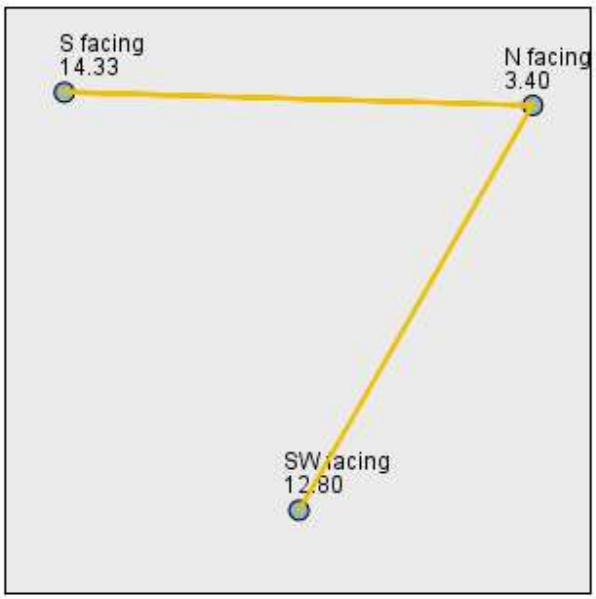
Each row tests the null hypothesis that the Sample 1 and Sample 2 distributions are the same.
Asymptotic significances (2-sided tests) are displayed. The significance level is .05.
Significance values have been adjusted by the Bonferroni correction for multiple tests.



Total N	21
Test Statistic	10.074
Degrees of Freedom	2
Asymptotic Sig. (2-sided test)	.006

1. The test statistic is adjusted for ties.

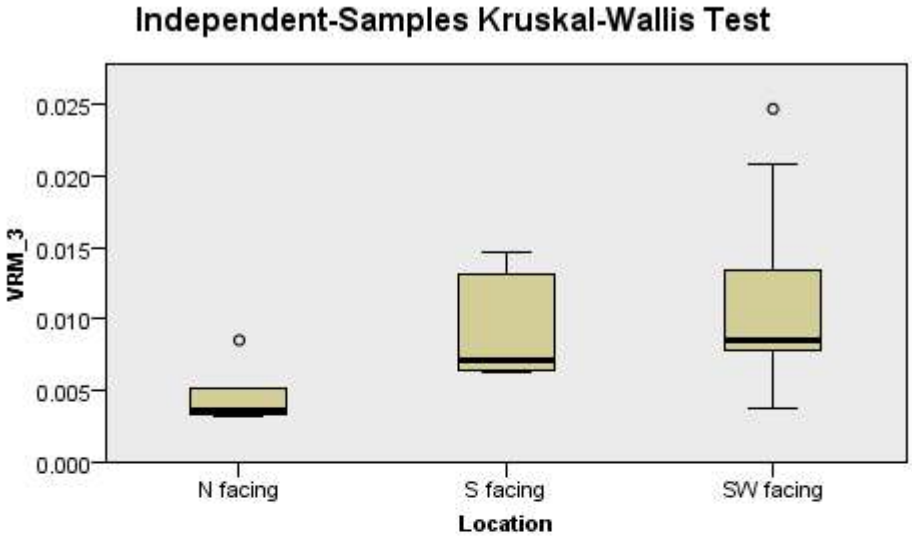
Pairwise Comparisons of Location



Each node shows the sample average rank of Location.

Sample1-Sample2	Test Statistic	Std. Error	Std. Test Statistic	Sig.	Adj.Sig.
N facing-SW facing	-9.400	3.399	-2.766	.006	.017
N facing-S facing	-10.933	3.757	-2.910	.004	.011
SW facing-S facing	1.533	3.204	.479	.632	1.000

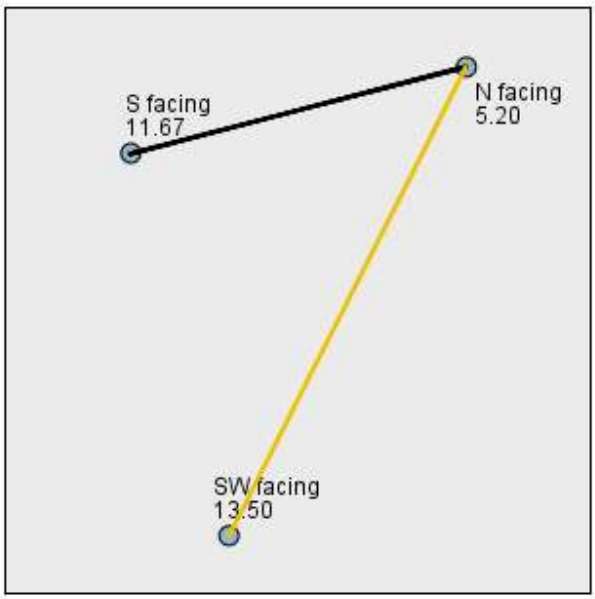
Each row tests the null hypothesis that the Sample 1 and Sample 2 distributions are the same.
Asymptotic significances (2-sided tests) are displayed. The significance level is .05.
Significance values have been adjusted by the Bonferroni correction for multiple tests.



Total N	21
Test Statistic	6.061
Degrees of Freedom	2
Asymptotic Sig. (2-sided test)	.048

1. The test statistic is adjusted for ties.

Pairwise Comparisons of Location

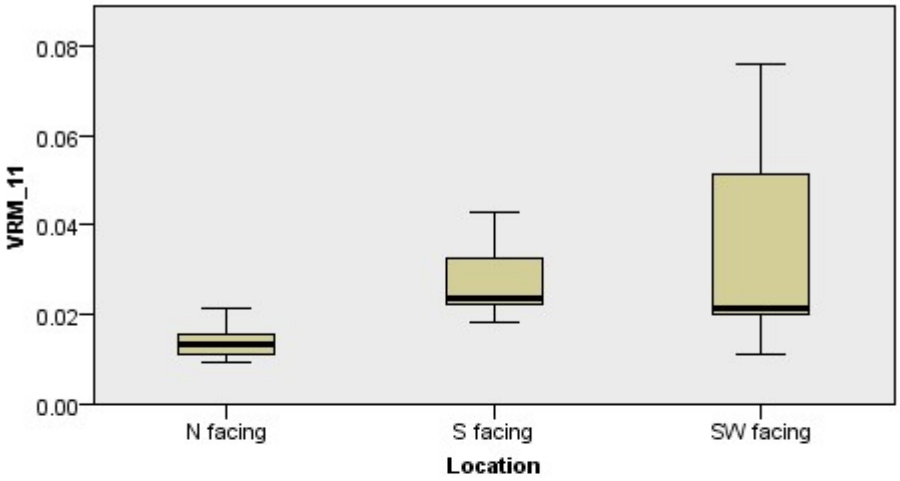


Each node shows the sample average rank of Location.

Sample1-Sample2	Test Statistic	Std. Error	Std. Test Statistic	Sig.	Adj.Sig.
N facing-S facing	-6.467	3.757	-1.721	.085	.256
N facing-SW facing	-8.300	3.399	-2.442	.015	.044
S facing-SW facing	-1.833	3.204	-.572	.567	1.000

Each row tests the null hypothesis that the Sample 1 and Sample 2 distributions are the same.
Asymptotic significances (2-sided tests) are displayed. The significance level is .05.
Significance values have been adjusted by the Bonferroni correction for multiple tests.

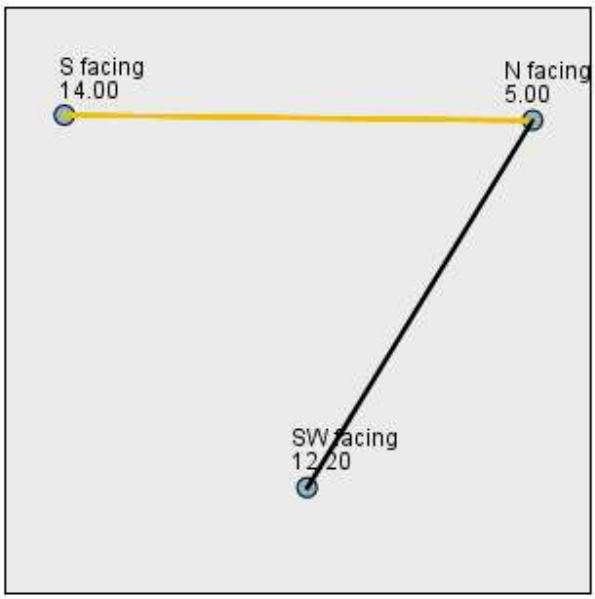
Independent-Samples Kruskal-Wallis Test



Total N	21
Test Statistic	6.452
Degrees of Freedom	2
Asymptotic Sig. (2-sided test)	.040

1. The test statistic is adjusted for ties.

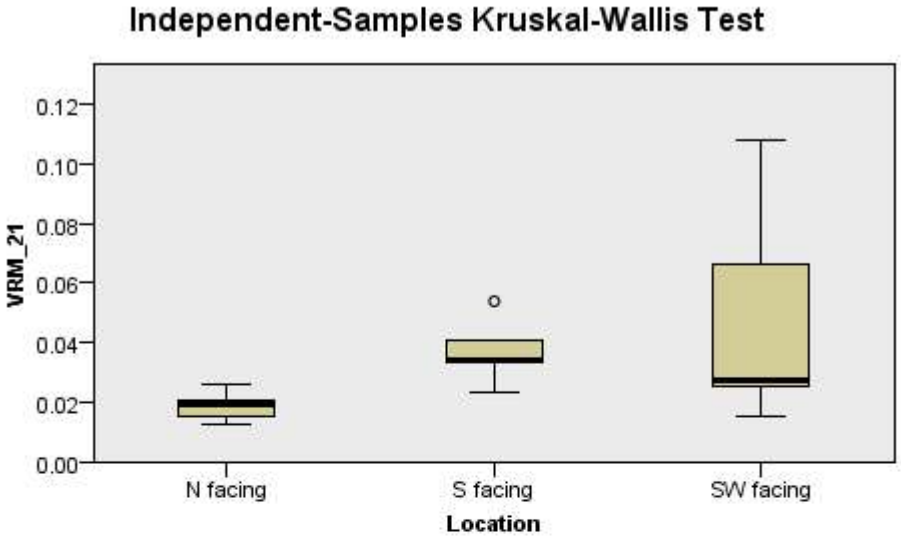
Pairwise Comparisons of Location



Each node shows the sample average rank of Location.

Sample1-Sample2	Test Statistic	Std. Error	Std. Test Statistic	Sig.	Adj.Sig.
N facing-SW facing	-7.200	3.399	-2.119	.034	.102
N facing-S facing	-9.000	3.757	-2.395	.017	.050
SW facing-S facing	1.800	3.204	.562	.574	1.000

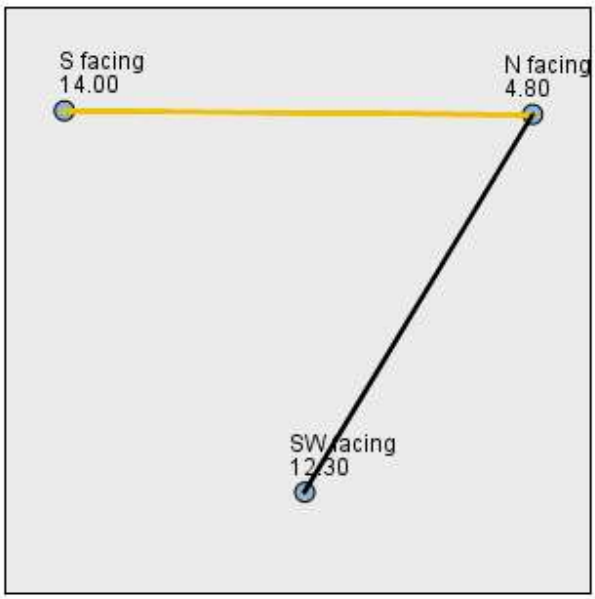
Each row tests the null hypothesis that the Sample 1 and Sample 2 distributions are the same.
Asymptotic significances (2-sided tests) are displayed. The significance level is .05.
Significance values have been adjusted by the Bonferroni correction for multiple tests.



Total N	21
Test Statistic	6.838
Degrees of Freedom	2
Asymptotic Sig. (2-sided test)	.033

1. The test statistic is adjusted for ties.

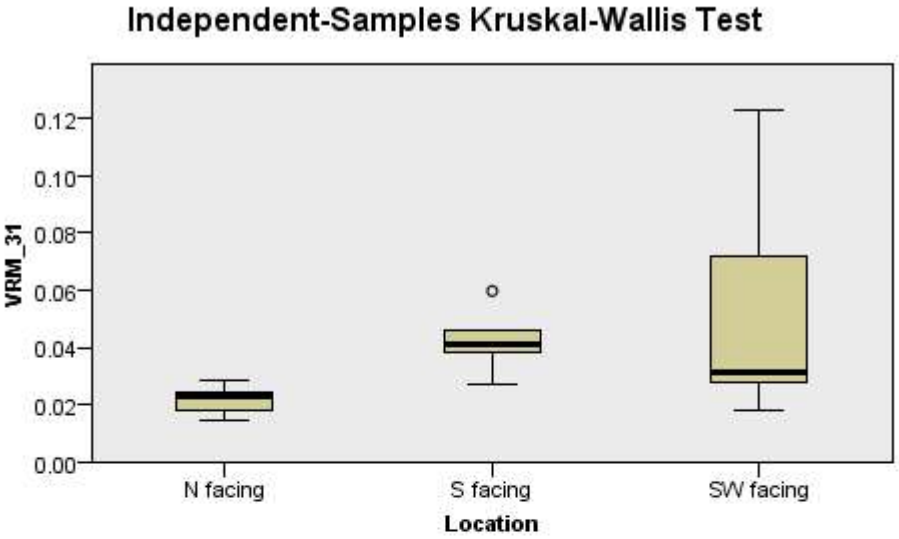
Pairwise Comparisons of Location



Each node shows the sample average rank of Location.

Sample1-Sample2	Test Statistic	Std. Error	Std. Test Statistic	Sig.	Adj.Sig.
N facing-SW facing	-7.500	3.397	-2.208	.027	.082
N facing-S facing	-9.200	3.756	-2.449	.014	.043
SW facing-S facing	1.700	3.203	.531	.596	1.000

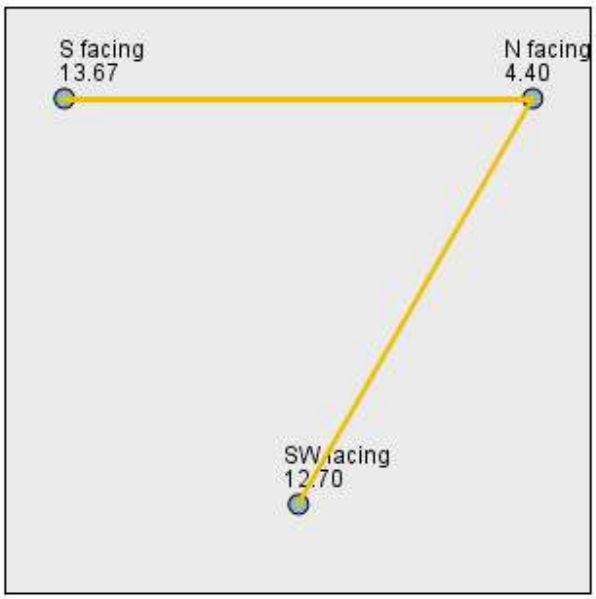
Each row tests the null hypothesis that the Sample 1 and Sample 2 distributions are the same.
Asymptotic significances (2-sided tests) are displayed. The significance level is .05.
Significance values have been adjusted by the Bonferroni correction for multiple tests.



Total N	21
Test Statistic	7.516
Degrees of Freedom	2
Asymptotic Sig. (2-sided test)	.023

1. The test statistic is adjusted for ties.

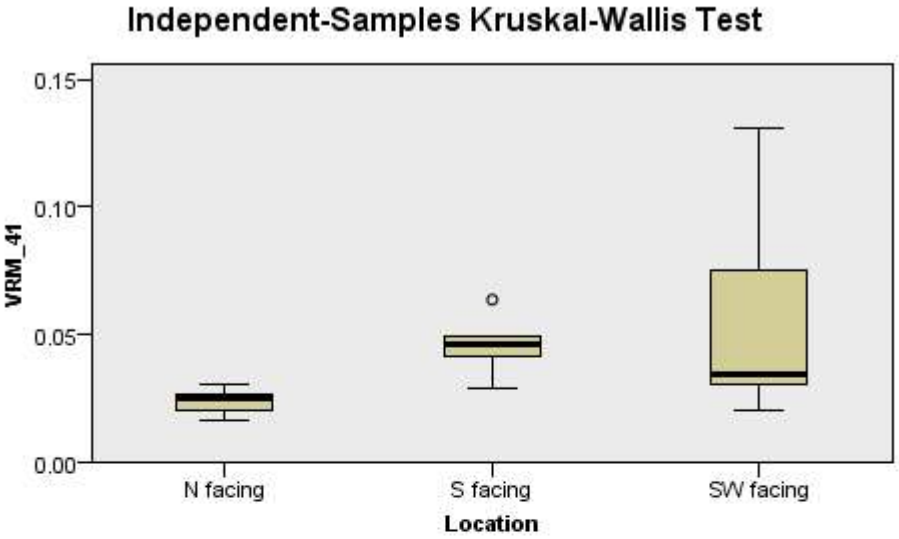
Pairwise Comparisons of Location



Each node shows the sample average rank of Location.

Sample1-Sample2	Test Statistic	Std. Error	Std. Test Statistic	Sig.	Adj.Sig.
N facing-SW facing	-8.300	3.399	-2.442	.015	.044
N facing-S facing	-9.267	3.757	-2.466	.014	.041
SW facing-S facing	.967	3.204	.302	.763	1.000

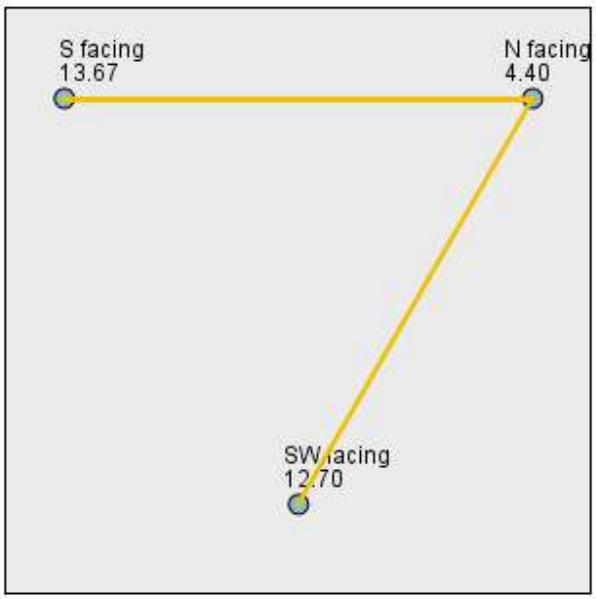
Each row tests the null hypothesis that the Sample 1 and Sample 2 distributions are the same.
Asymptotic significances (2-sided tests) are displayed. The significance level is .05.
Significance values have been adjusted by the Bonferroni correction for multiple tests.



Total N	21
Test Statistic	7.516
Degrees of Freedom	2
Asymptotic Sig. (2-sided test)	.023

1. The test statistic is adjusted for ties.

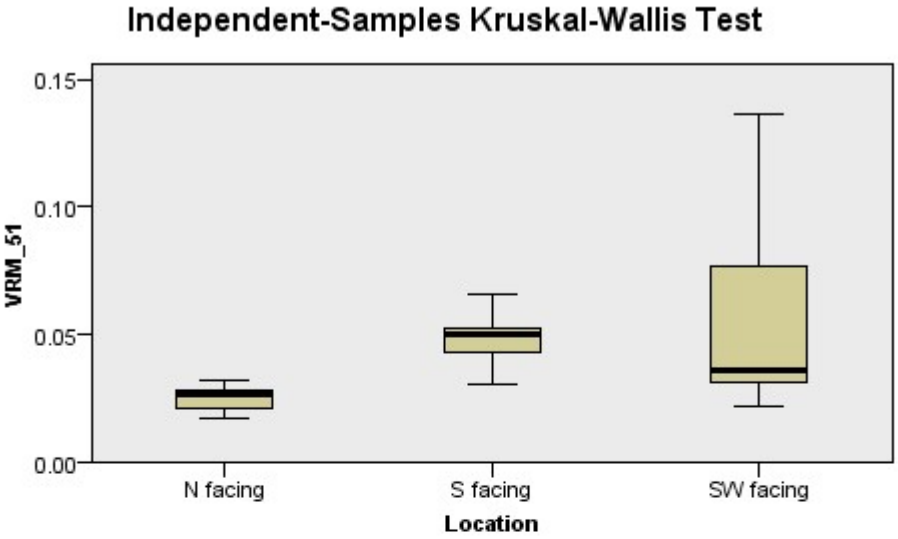
Pairwise Comparisons of Location



Each node shows the sample average rank of Location.

Sample1-Sample2	Test Statistic	Std. Error	Std. Test Statistic	Sig.	Adj.Sig.
N facing-SW facing	-8.300	3.399	-2.442	.015	.044
N facing-S facing	-9.267	3.757	-2.466	.014	.041
SW facing-S facing	.967	3.204	.302	.763	1.000

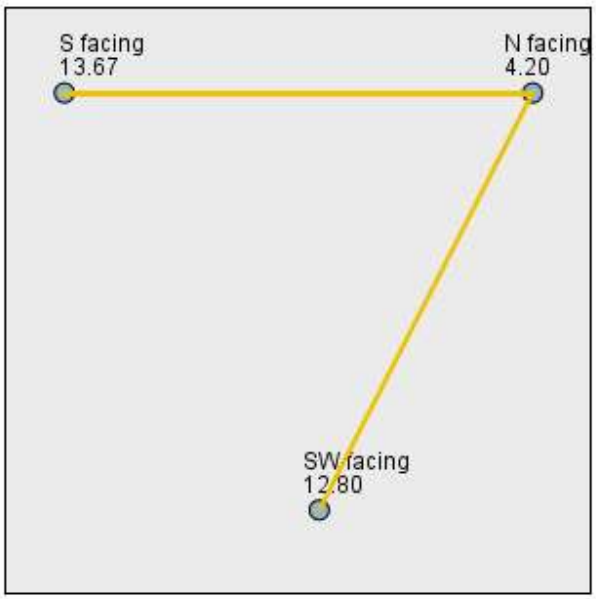
Each row tests the null hypothesis that the Sample 1 and Sample 2 distributions are the same.
Asymptotic significances (2-sided tests) are displayed. The significance level is .05.
Significance values have been adjusted by the Bonferroni correction for multiple tests.



Total N	21
Test Statistic	7.955
Degrees of Freedom	2
Asymptotic Sig. (2-sided test)	.019

1. The test statistic is adjusted for ties.

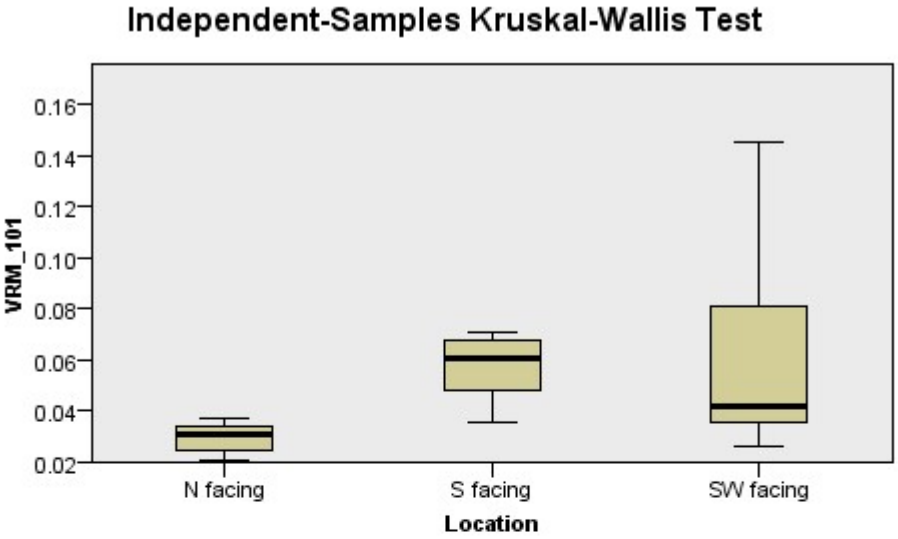
Pairwise Comparisons of Location



Each node shows the sample average rank of Location.

Sample1-Sample2	Test Statistic	Std. Error	Std. Test Statistic	Sig.	Adj.Sig.
N facing-SW facing	-8.600	3.399	-2.531	.011	.034
N facing-S facing	-9.467	3.757	-2.520	.012	.035
SW facing-S facing	.867	3.204	.270	.787	1.000

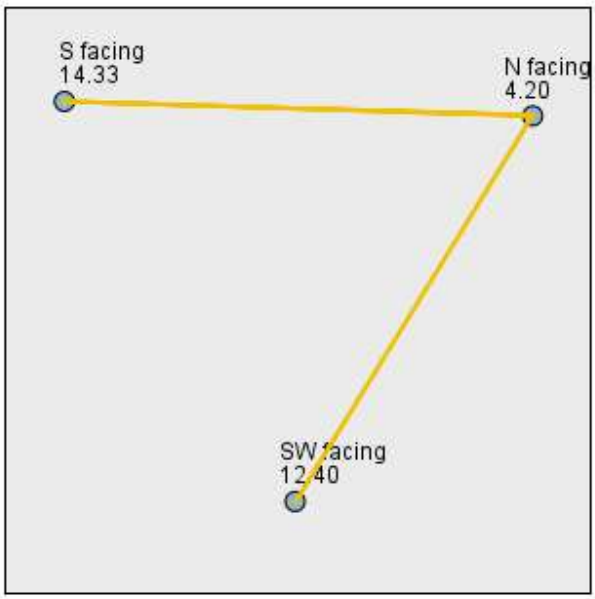
Each row tests the null hypothesis that the Sample 1 and Sample 2 distributions are the same.
Asymptotic significances (2-sided tests) are displayed. The significance level is .05.
Significance values have been adjusted by the Bonferroni correction for multiple tests.



Total N	21
Test Statistic	8.246
Degrees of Freedom	2
Asymptotic Sig. (2-sided test)	.016

1. The test statistic is adjusted for ties.

Pairwise Comparisons of Location

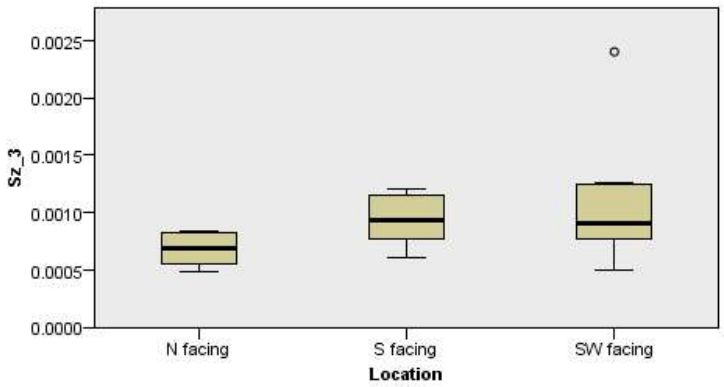


Each node shows the sample average rank of Location.

Sample1-Sample2	Test Statistic	Std. Error	Std. Test Statistic	Sig.	Adj.Sig.
N facing-SW facing	-8.200	3.399	-2.413	.016	.047
N facing-S facing	-10.133	3.757	-2.697	.007	.021
SW facing-S facing	1.933	3.204	.603	.546	1.000

Each row tests the null hypothesis that the Sample 1 and Sample 2 distributions are the same.
Asymptotic significances (2-sided tests) are displayed. The significance level is .05.
Significance values have been adjusted by the Bonferroni correction for multiple tests.

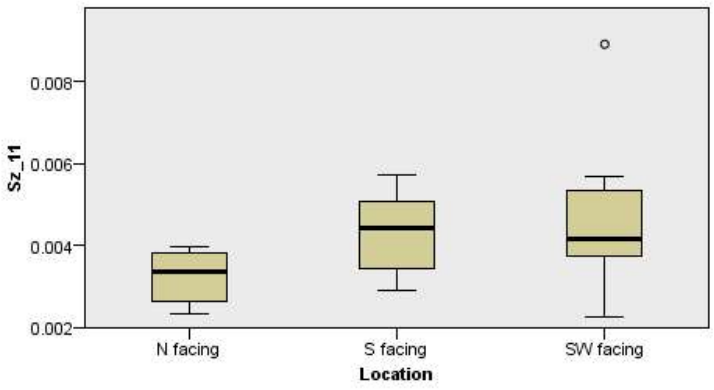
Independent-Samples Kruskal-Wallis Test



Total N	21
Test Statistic	4.274
Degrees of Freedom	2
Asymptotic Sig. (2-sided test)	.118

1. The test statistic is adjusted for ties.
2. Multiple comparisons are not performed because the overall test does not show significant differences across samples.

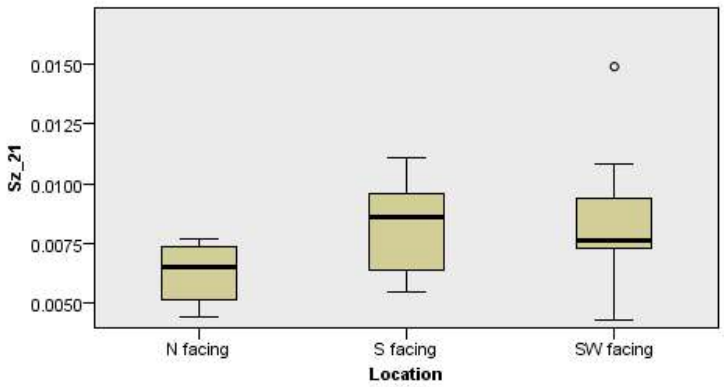
Independent-Samples Kruskal-Wallis Test



Total N	21
Test Statistic	3.686
Degrees of Freedom	2
Asymptotic Sig. (2-sided test)	.158

1. The test statistic is adjusted for ties.
2. Multiple comparisons are not performed because the overall test does not show significant differences across samples.

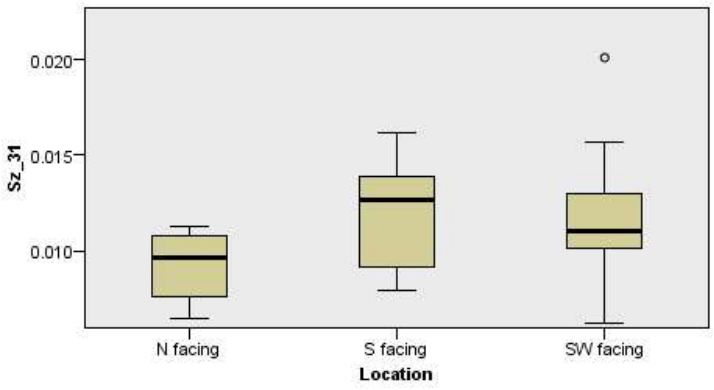
Independent-Samples Kruskal-Wallis Test



Total N	21
Test Statistic	2.818
Degrees of Freedom	2
Asymptotic Sig. (2-sided test)	.244

1. The test statistic is adjusted for ties.
2. Multiple comparisons are not performed because the overall test does not show significant differences across samples.

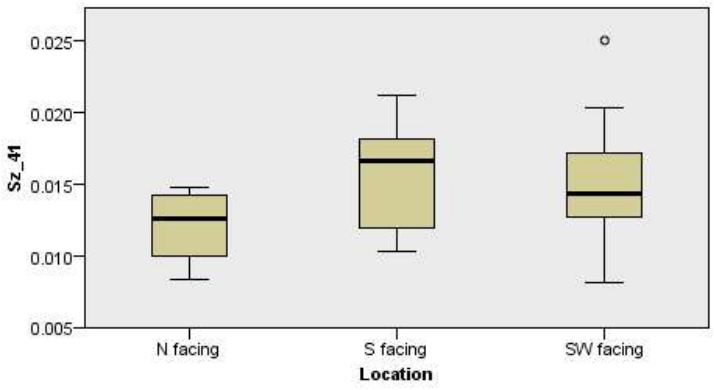
Independent-Samples Kruskal-Wallis Test



Total N	21
Test Statistic	2.681
Degrees of Freedom	2
Asymptotic Sig. (2-sided test)	.262

1. The test statistic is adjusted for ties.
2. Multiple comparisons are not performed because the overall test does not show significant differences across samples.

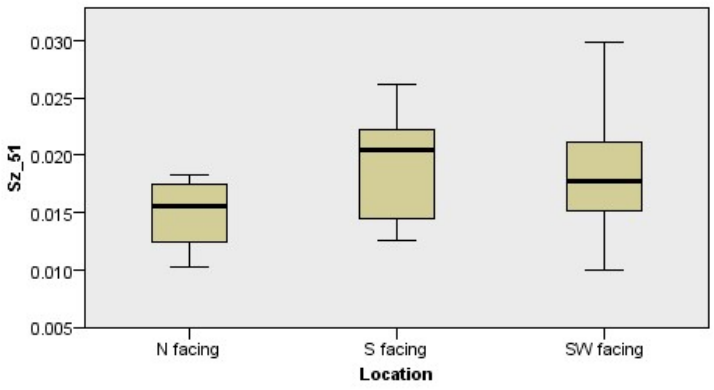
Independent-Samples Kruskal-Wallis Test



Total N	21
Test Statistic	2.573
Degrees of Freedom	2
Asymptotic Sig. (2-sided test)	.276

1. The test statistic is adjusted for ties.
2. Multiple comparisons are not performed because the overall test does not show significant differences across samples.

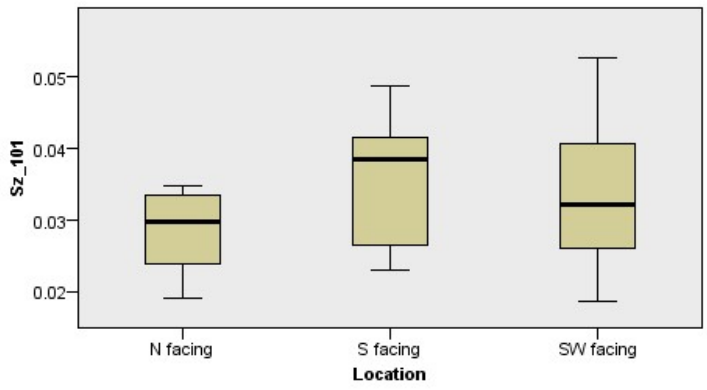
Independent-Samples Kruskal-Wallis Test



Total N	21
Test Statistic	2.486
Degrees of Freedom	2
Asymptotic Sig. (2-sided test)	.289

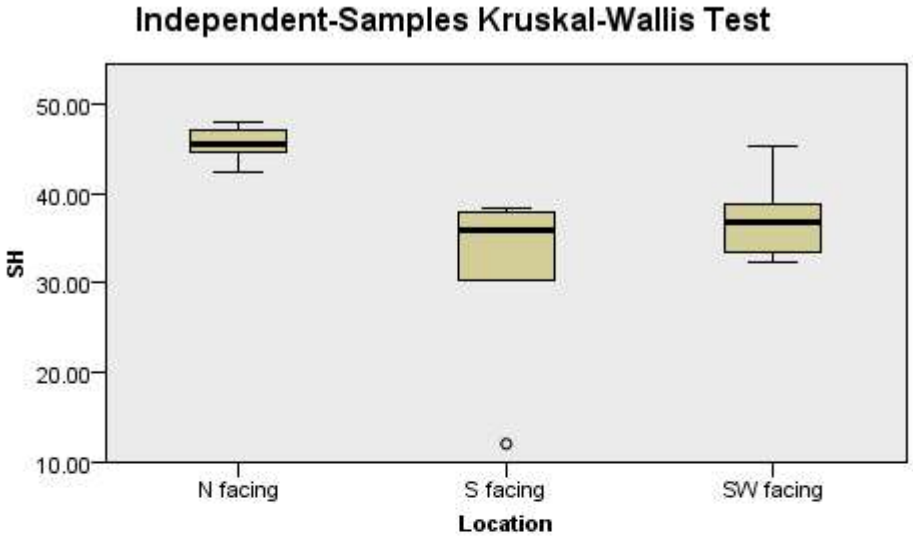
1. The test statistic is adjusted for ties.
2. Multiple comparisons are not performed because the overall test does not show significant differences across samples.

Independent-Samples Kruskal-Wallis Test



Total N	21
Test Statistic	1.867
Degrees of Freedom	2
Asymptotic Sig. (2-sided test)	.393

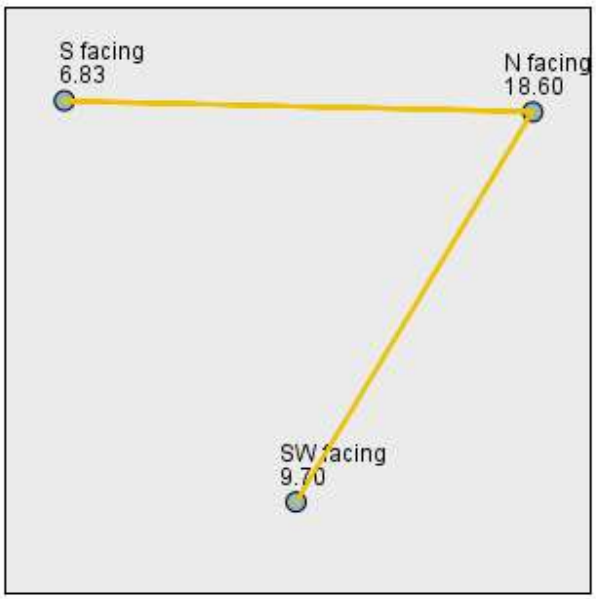
1. The test statistic is adjusted for ties.
2. Multiple comparisons are not performed because the overall test does not show significant differences across samples.



Total N	21
Test Statistic	10.646
Degrees of Freedom	2
Asymptotic Sig. (2-sided test)	.005

1. The test statistic is adjusted for ties.

Pairwise Comparisons of Location

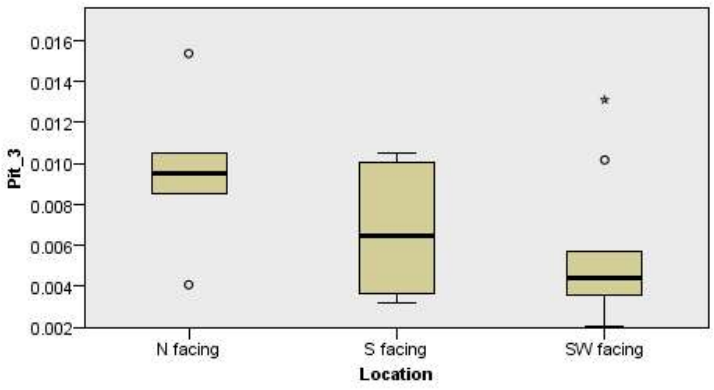


Each node shows the sample average rank of Location.

Sample1-Sample2	Test Statistic	Std. Error	Std. Test Statistic	Sig.	Adj.Sig.
S facing-SW facing	-2.867	3.204	-.895	.371	1.000
S facing-N facing	11.767	3.757	3.132	.002	.005
SW facing-N facing	8.900	3.399	2.619	.009	.026

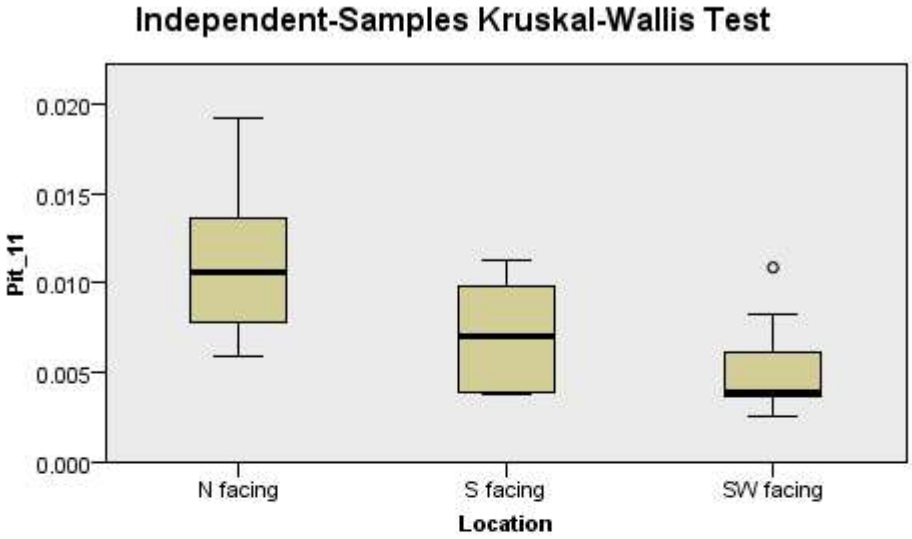
Each row tests the null hypothesis that the Sample 1 and Sample 2 distributions are the same.
Asymptotic significances (2-sided tests) are displayed. The significance level is .05.
Significance values have been adjusted by the Bonferroni correction for multiple tests.

Independent-Samples Kruskal-Wallis Test



Total N	21
Test Statistic	3.111
Degrees of Freedom	2
Asymptotic Sig. (2-sided test)	.211

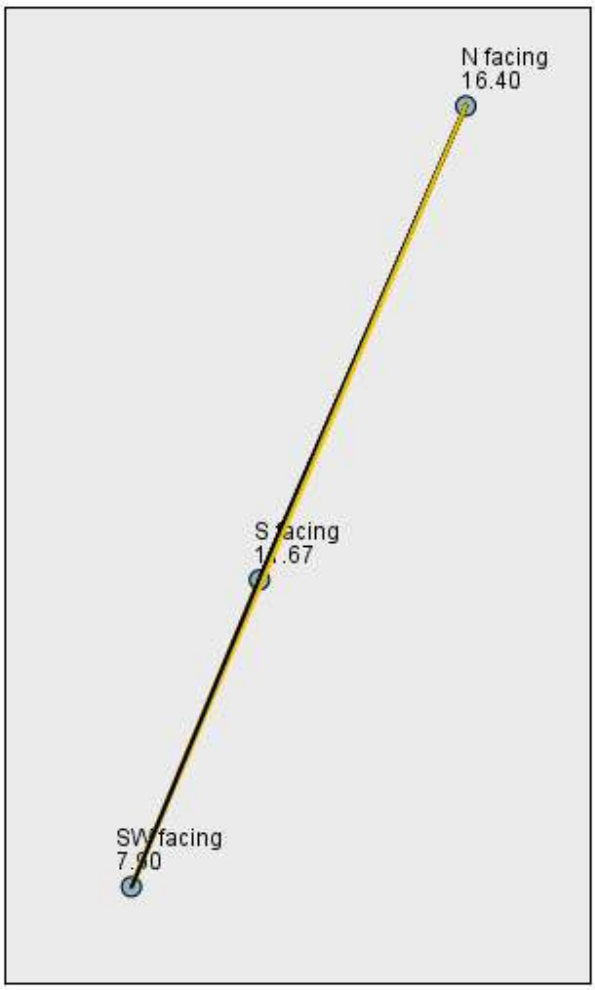
1. The test statistic is adjusted for ties.
2. Multiple comparisons are not performed because the overall test does not show significant differences across samples.



Total N	21
Test Statistic	6.352
Degrees of Freedom	2
Asymptotic Sig. (2-sided test)	.042

1. The test statistic is adjusted for ties.

Pairwise Comparisons of Location

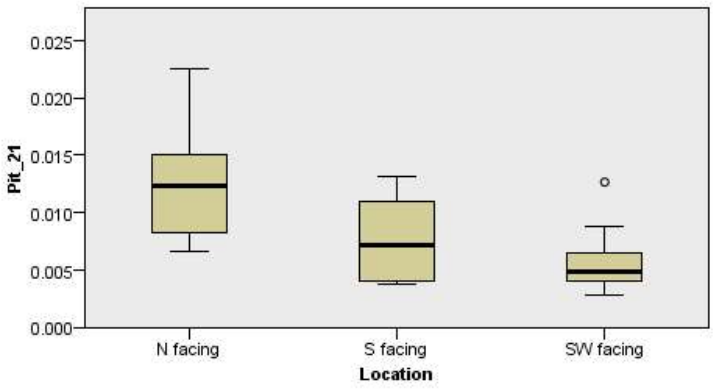


Each node shows the sample average rank of Location.

Sample1-Sample2	Test Statistic	Std. Error	Std. Test Statistic	Sig.	Adj.Sig.
SW facing-S facing	3.767	3.204	1.176	.240	.719
SW facing-N facing	8.500	3.399	2.501	.012	.037
S facing-N facing	4.733	3.757	1.260	.208	.623

Each row tests the null hypothesis that the Sample 1 and Sample 2 distributions are the same.
Asymptotic significances (2-sided tests) are displayed. The significance level is .05.
Significance values have been adjusted by the Bonferroni correction for multiple tests.

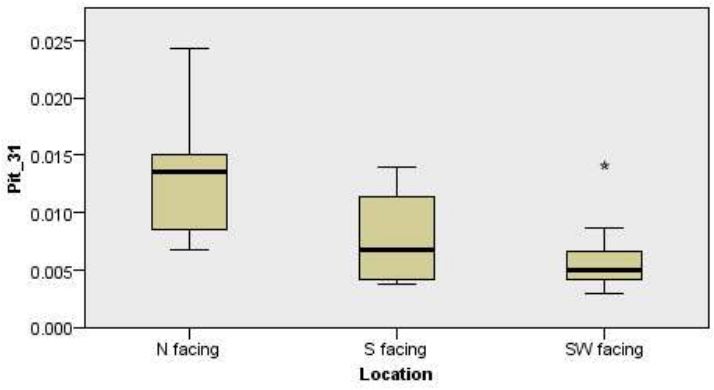
Independent-Samples Kruskal-Wallis Test



Total N	21
Test Statistic	5.735
Degrees of Freedom	2
Asymptotic Sig. (2-sided test)	.057

1. The test statistic is adjusted for ties.
2. Multiple comparisons are not performed because the overall test does not show significant differences across samples.

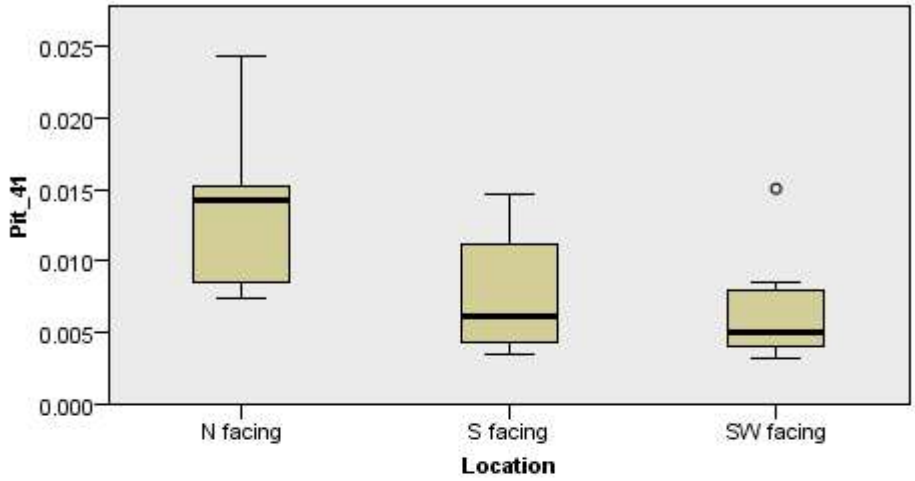
Independent-Samples Kruskal-Wallis Test



Total N	21
Test Statistic	5.971
Degrees of Freedom	2
Asymptotic Sig. (2-sided test)	.051

1. The test statistic is adjusted for ties.
2. Multiple comparisons are not performed because the overall test does not show significant differences across samples.

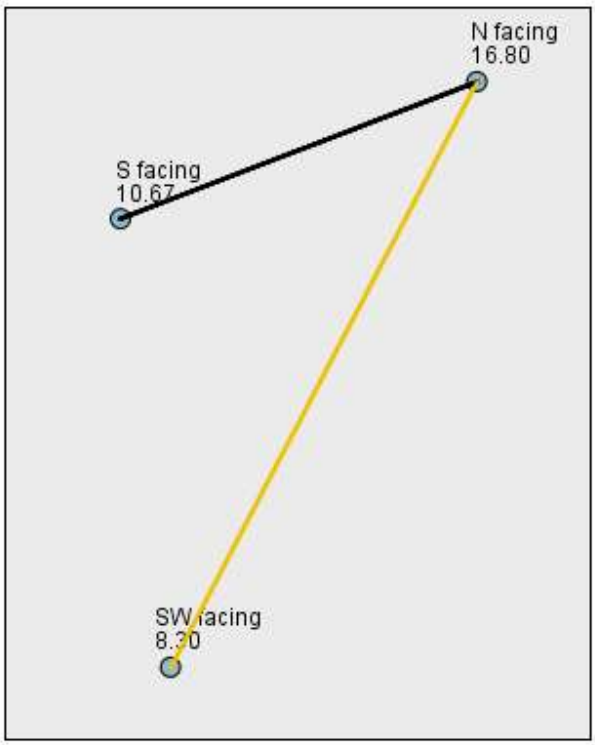
Independent-Samples Kruskal-Wallis Test



Total N	21
Test Statistic	6.280
Degrees of Freedom	2
Asymptotic Sig. (2-sided test)	.043

1. The test statistic is adjusted for ties.

Pairwise Comparisons of Location

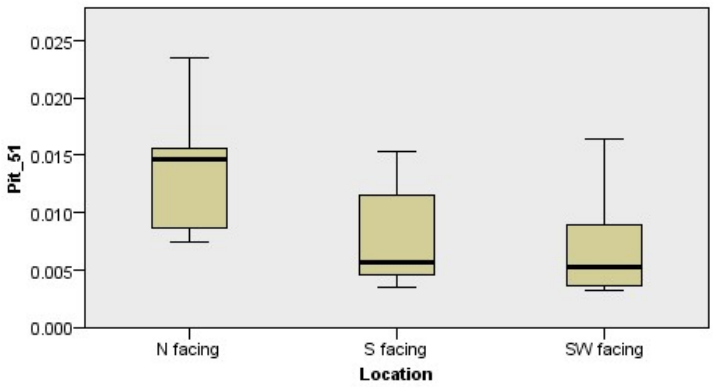


Each node shows the sample average rank of Location.

Sample1-Sample2	Test Statistic	Std. Error	Std. Test Statistic	Sig.	Adj.Sig.
SW facing-S facing	2.367	3.204	.739	.460	1.000
SW facing-N facing	8.500	3.399	2.501	.012	.037
S facing-N facing	6.133	3.757	1.632	.103	.308

Each row tests the null hypothesis that the Sample 1 and Sample 2 distributions are the same.
Asymptotic significances (2-sided tests) are displayed. The significance level is .05.
Significance values have been adjusted by the Bonferroni correction for multiple tests.

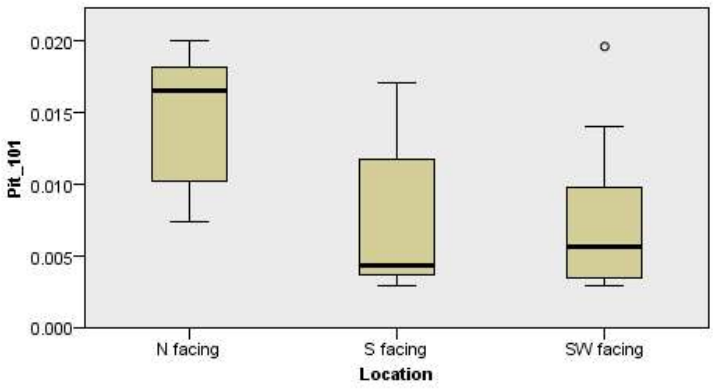
Independent-Samples Kruskal-Wallis Test



Total N	21
Test Statistic	5.230
Degrees of Freedom	2
Asymptotic Sig. (2-sided test)	.073

1. The test statistic is adjusted for ties.
2. Multiple comparisons are not performed because the overall test does not show significant differences across samples.

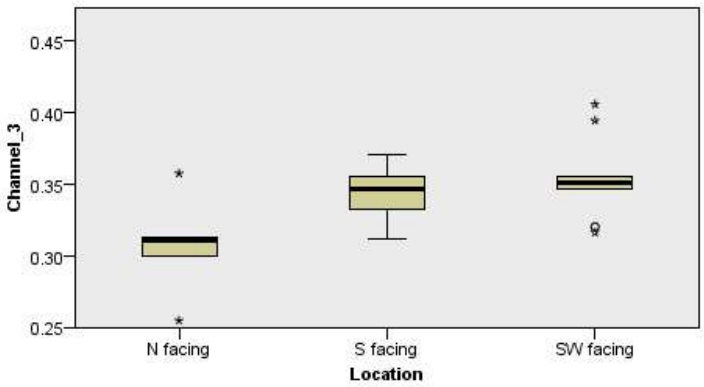
Independent-Samples Kruskal-Wallis Test



Total N	21
Test Statistic	5.347
Degrees of Freedom	2
Asymptotic Sig. (2-sided test)	.069

1. The test statistic is adjusted for ties.
2. Multiple comparisons are not performed because the overall test does not show significant differences across samples.

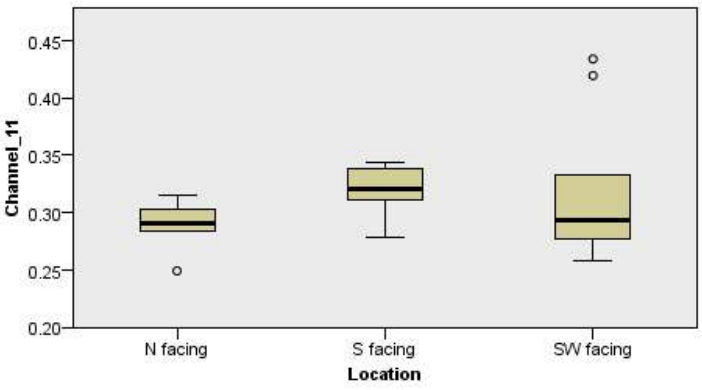
Independent-Samples Kruskal-Wallis Test



Total N	21
Test Statistic	4.765
Degrees of Freedom	2
Asymptotic Sig. (2-sided test)	.092

1. The test statistic is adjusted for ties.
2. Multiple comparisons are not performed because the overall test does not show significant differences across samples.

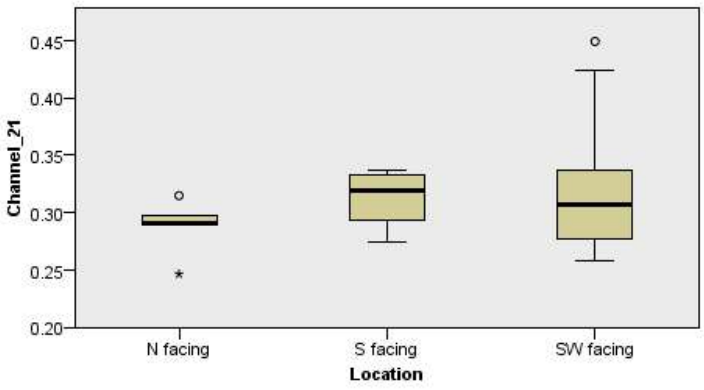
Independent-Samples Kruskal-Wallis Test



Total N	21
Test Statistic	2.438
Degrees of Freedom	2
Asymptotic Sig. (2-sided test)	.296

1. The test statistic is adjusted for ties.
2. Multiple comparisons are not performed because the overall test does not show significant differences across samples.

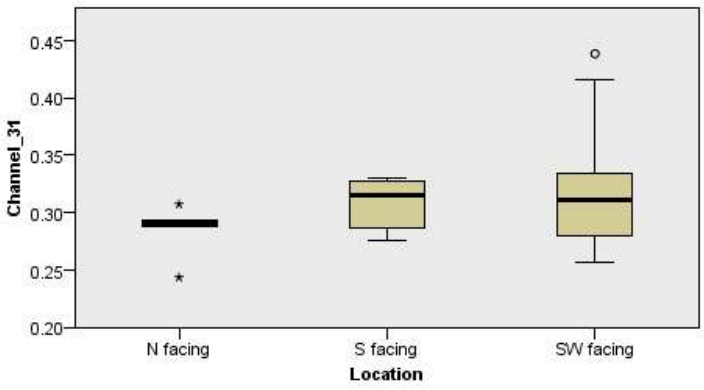
Independent-Samples Kruskal-Wallis Test



Total N	21
Test Statistic	2.565
Degrees of Freedom	2
Asymptotic Sig. (2-sided test)	.277

1. The test statistic is adjusted for ties.
2. Multiple comparisons are not performed because the overall test does not show significant differences across samples.

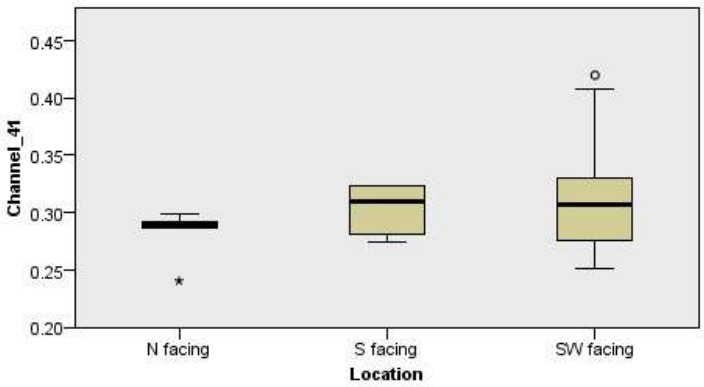
Independent-Samples Kruskal-Wallis Test



Total N	21
Test Statistic	2.461
Degrees of Freedom	2
Asymptotic Sig. (2-sided test)	.292

1. The test statistic is adjusted for ties.
2. Multiple comparisons are not performed because the overall test does not show significant differences across samples.

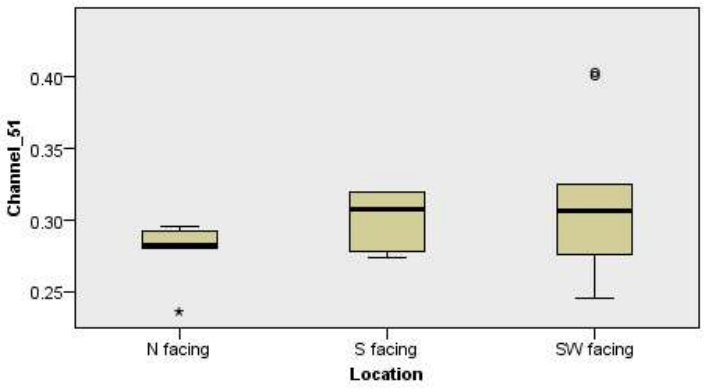
Independent-Samples Kruskal-Wallis Test



Total N	21
Test Statistic	2.493
Degrees of Freedom	2
Asymptotic Sig. (2-sided test)	.288

1. The test statistic is adjusted for ties.
2. Multiple comparisons are not performed because the overall test does not show significant differences across samples.

Independent-Samples Kruskal-Wallis Test



Total N	21
Test Statistic	2.529
Degrees of Freedom	2
Asymptotic Sig. (2-sided test)	.282

1. The test statistic is adjusted for ties.
2. Multiple comparisons are not performed because the overall test does not show significant differences across samples.

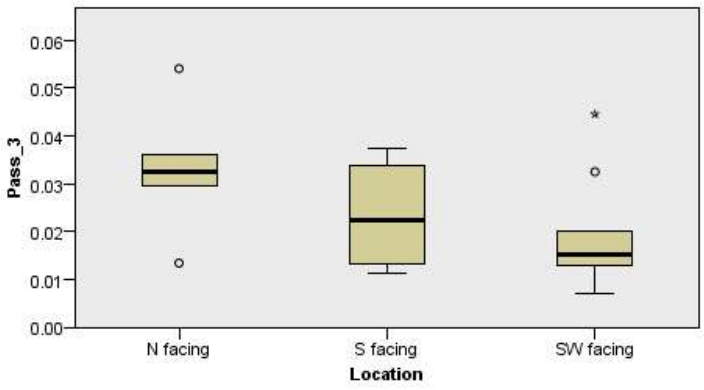
Independent-Samples Kruskal-Wallis Test



Total N	21
Test Statistic	3.584
Degrees of Freedom	2
Asymptotic Sig. (2-sided test)	.167

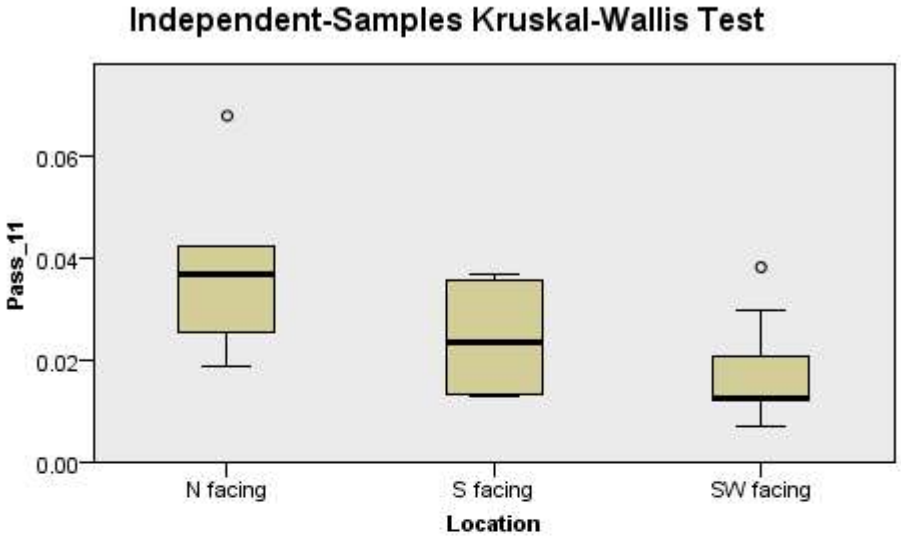
1. The test statistic is adjusted for ties.
2. Multiple comparisons are not performed because the overall test does not show significant differences across samples.

Independent-Samples Kruskal-Wallis Test



Total N	21
Test Statistic	3.117
Degrees of Freedom	2
Asymptotic Sig. (2-sided test)	.210

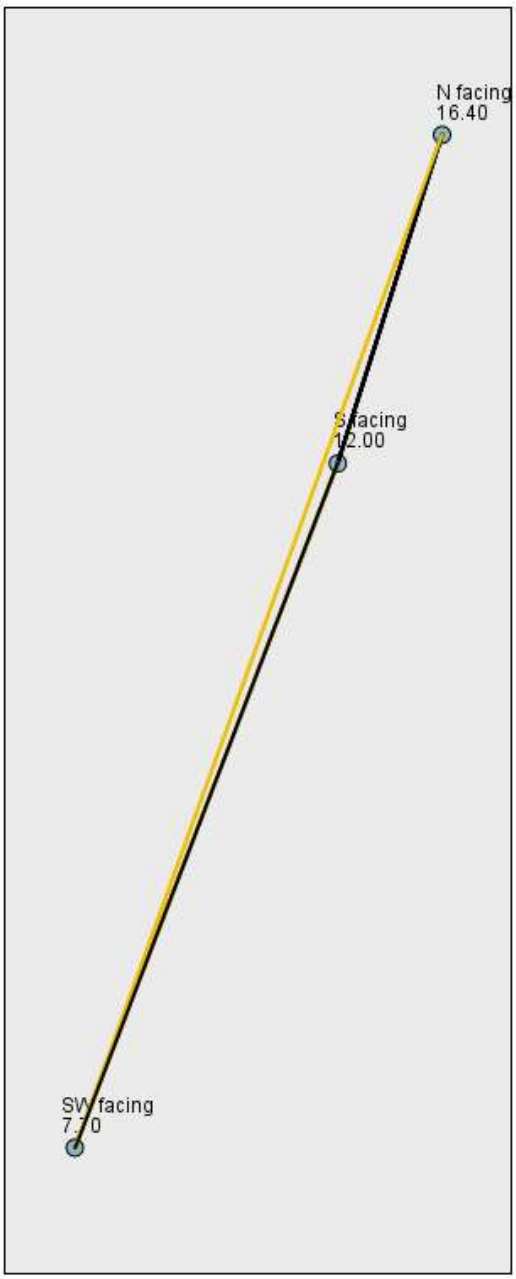
1. The test statistic is adjusted for ties.
2. Multiple comparisons are not performed because the overall test does not show significant differences across samples.



Total N	21
Test Statistic	6.771
Degrees of Freedom	2
Asymptotic Sig. (2-sided test)	.034

1. The test statistic is adjusted for ties.

Pairwise Comparisons of Location

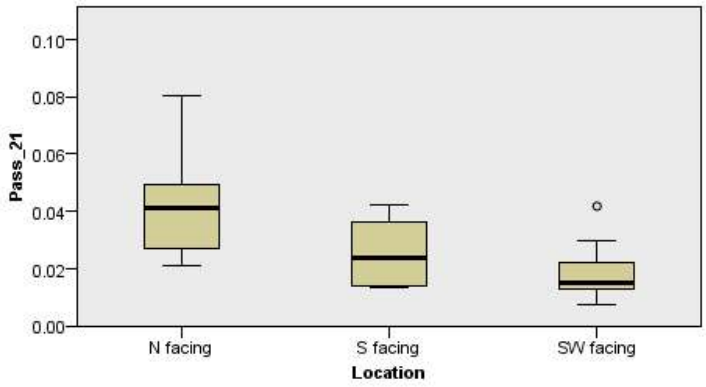


Each node shows the sample average rank of Location.

Sample1-Sample2	Test Statistic	Std. Error	Std. Test Statistic	Sig.	Adj.Sig.
SW facing-S facing	4.300	3.204	1.342	.180	.539
SW facing-N facing	8.700	3.399	2.560	.010	.031
S facing-N facing	4.400	3.757	1.171	.242	.725

Each row tests the null hypothesis that the Sample 1 and Sample 2 distributions are the same.
Asymptotic significances (2-sided tests) are displayed. The significance level is .05.
Significance values have been adjusted by the Bonferroni correction for multiple tests.

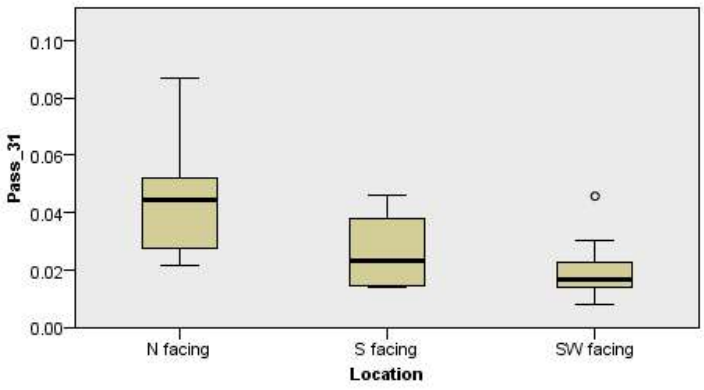
Independent-Samples Kruskal-Wallis Test



Total N	21
Test Statistic	5.828
Degrees of Freedom	2
Asymptotic Sig. (2-sided test)	.054

1. The test statistic is adjusted for ties.
2. Multiple comparisons are not performed because the overall test does not show significant differences across samples.

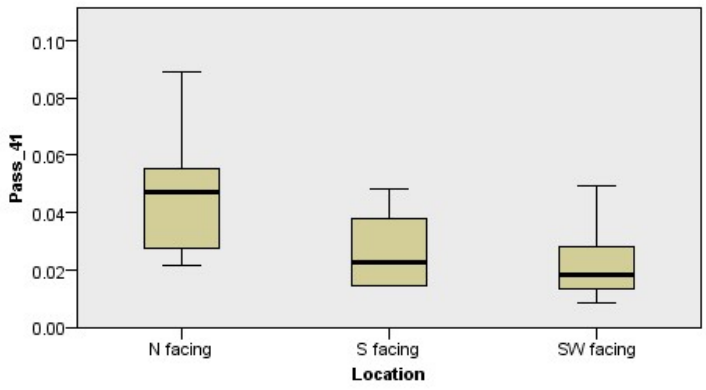
Independent-Samples Kruskal-Wallis Test



Total N	21
Test Statistic	5.828
Degrees of Freedom	2
Asymptotic Sig. (2-sided test)	.054

1. The test statistic is adjusted for ties.
2. Multiple comparisons are not performed because the overall test does not show significant differences across samples.

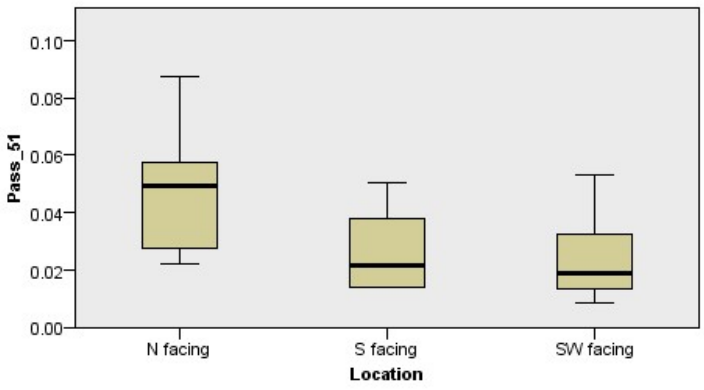
Independent-Samples Kruskal-Wallis Test



Total N	21
Test Statistic	4.870
Degrees of Freedom	2
Asymptotic Sig. (2-sided test)	.088

1. The test statistic is adjusted for ties.
2. Multiple comparisons are not performed because the overall test does not show significant differences across samples.

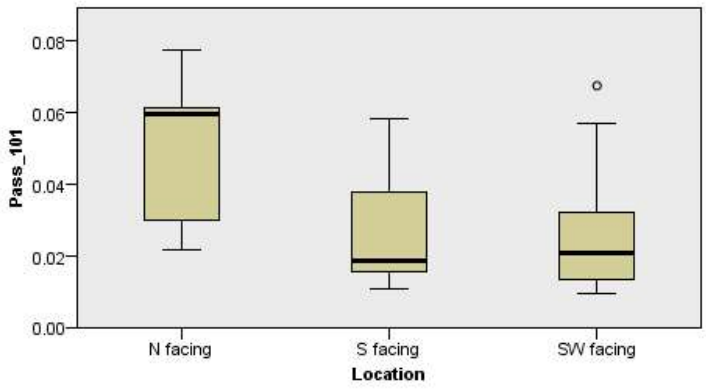
Independent-Samples Kruskal-Wallis Test



Total N	21
Test Statistic	4.543
Degrees of Freedom	2
Asymptotic Sig. (2-sided test)	.103

1. The test statistic is adjusted for ties.
2. Multiple comparisons are not performed because the overall test does not show significant differences across samples.

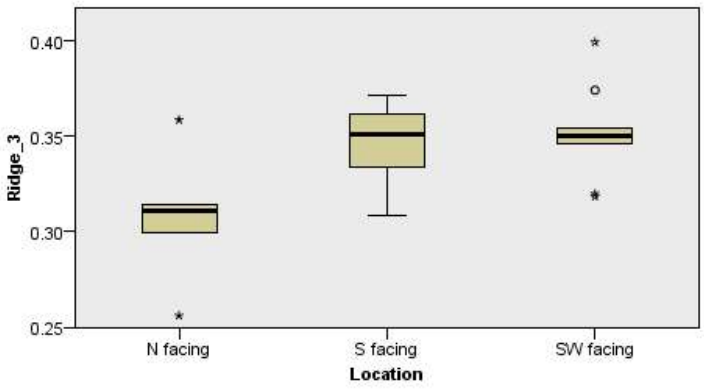
Independent-Samples Kruskal-Wallis Test



Total N	21
Test Statistic	4.610
Degrees of Freedom	2
Asymptotic Sig. (2-sided test)	.100

1. The test statistic is adjusted for ties.
2. Multiple comparisons are not performed because the overall test does not show significant differences across samples.

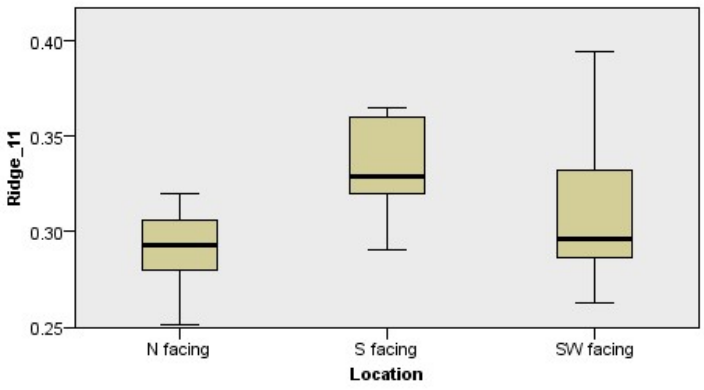
Independent-Samples Kruskal-Wallis Test



Total N	21
Test Statistic	4.661
Degrees of Freedom	2
Asymptotic Sig. (2-sided test)	.097

1. The test statistic is adjusted for ties.
2. Multiple comparisons are not performed because the overall test does not show significant differences across samples.

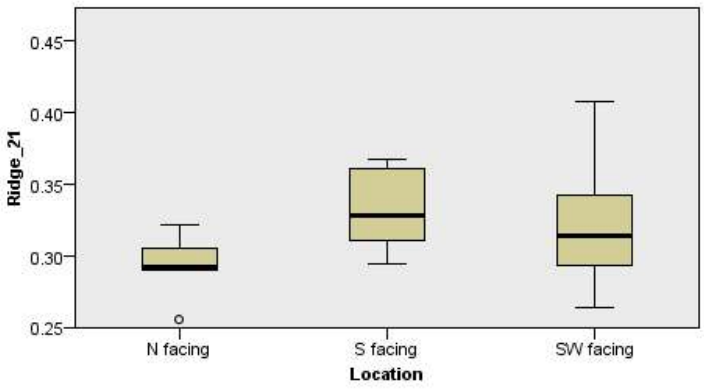
Independent-Samples Kruskal-Wallis Test



Total N	21
Test Statistic	4.038
Degrees of Freedom	2
Asymptotic Sig. (2-sided test)	.133

1. The test statistic is adjusted for ties.
2. Multiple comparisons are not performed because the overall test does not show significant differences across samples.

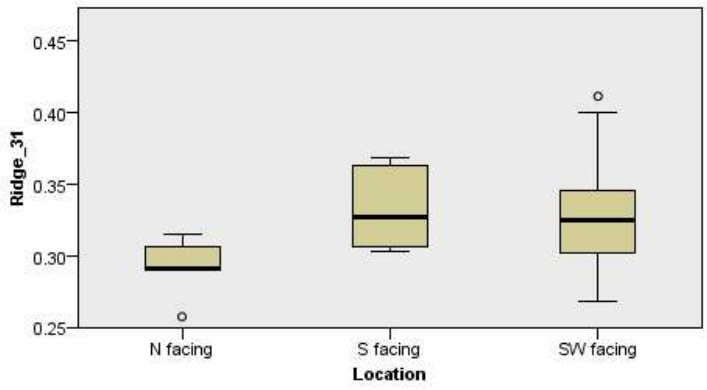
Independent-Samples Kruskal-Wallis Test



Total N	21
Test Statistic	4.488
Degrees of Freedom	2
Asymptotic Sig. (2-sided test)	.106

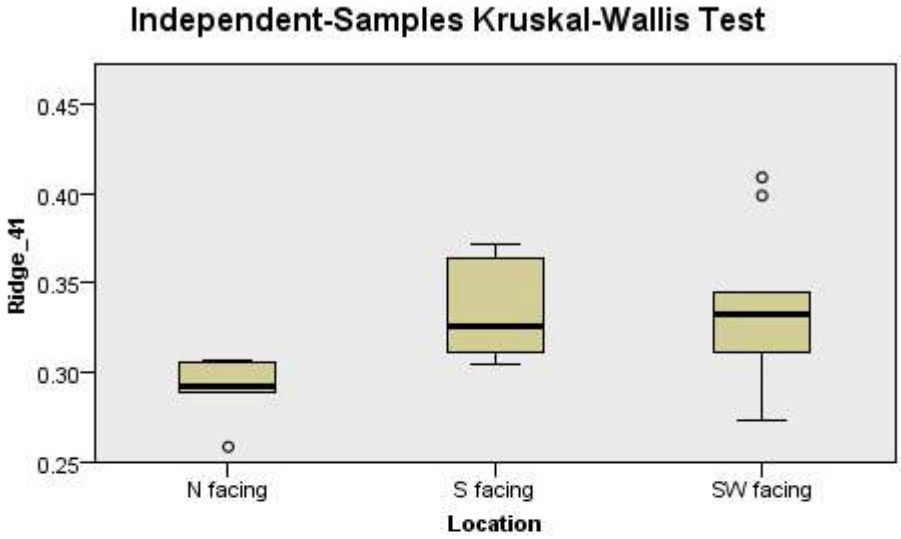
1. The test statistic is adjusted for ties.
2. Multiple comparisons are not performed because the overall test does not show significant differences across samples.

Independent-Samples Kruskal-Wallis Test



Total N	21
Test Statistic	5.210
Degrees of Freedom	2
Asymptotic Sig. (2-sided test)	.074

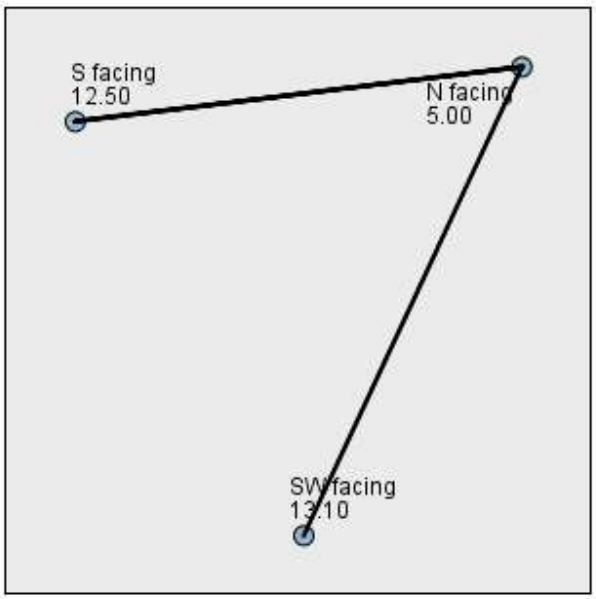
1. The test statistic is adjusted for ties.
2. Multiple comparisons are not performed because the overall test does not show significant differences across samples.



Total N	21
Test Statistic	6.171
Degrees of Freedom	2
Asymptotic Sig. (2-sided test)	.046

1. The test statistic is adjusted for ties.

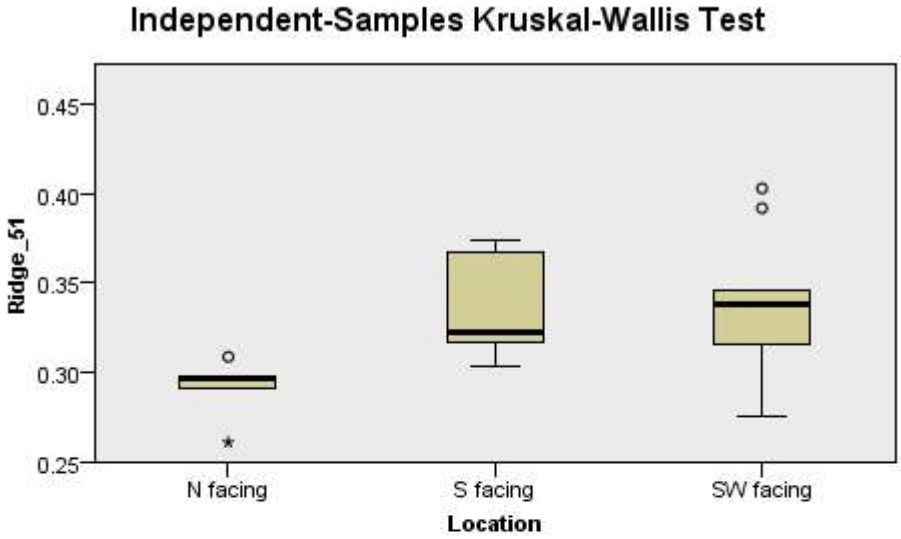
Pairwise Comparisons of Location



Each node shows the sample average rank of Location.

Sample1-Sample2	Test Statistic	Std. Error	Std. Test Statistic	Sig.	Adj.Sig.
N facing-S facing	-7.500	3.757	-1.996	.046	.138
N facing-SW facing	-8.100	3.399	-2.383	.017	.051
S facing-SW facing	-.600	3.204	-.187	.851	1.000

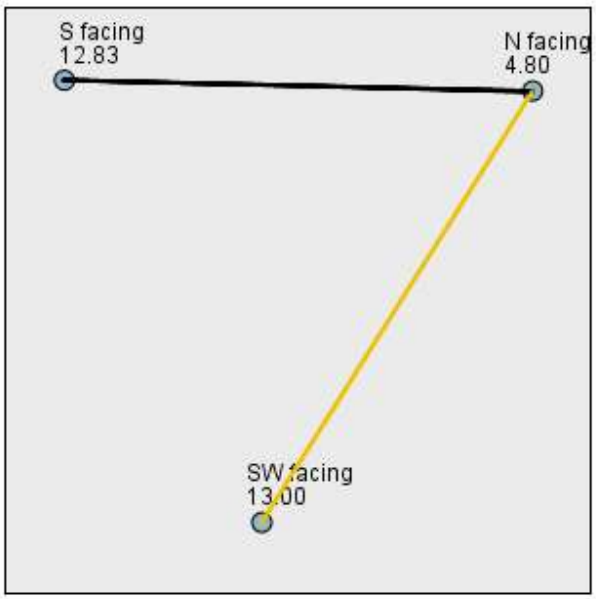
Each row tests the null hypothesis that the Sample 1 and Sample 2 distributions are the same.
Asymptotic significances (2-sided tests) are displayed. The significance level is .05.
Significance values have been adjusted by the Bonferroni correction for multiple tests.



Total N	21
Test Statistic	6.555
Degrees of Freedom	2
Asymptotic Sig. (2-sided test)	.038

1. The test statistic is adjusted for ties.

Pairwise Comparisons of Location



Each node shows the sample average rank of Location.

Sample1-Sample2	Test Statistic	Std. Error	Std. Test Statistic	Sig.	Adj.Sig.
N facing-S facing	-8.033	3.757	-2.138	.033	.098
N facing-SW facing	-8.200	3.399	-2.413	.016	.047
S facing-SW facing	-.167	3.204	-.052	.959	1.000

Each row tests the null hypothesis that the Sample 1 and Sample 2 distributions are the same.
Asymptotic significances (2-sided tests) are displayed. The significance level is .05.
Significance values have been adjusted by the Bonferroni correction for multiple tests.

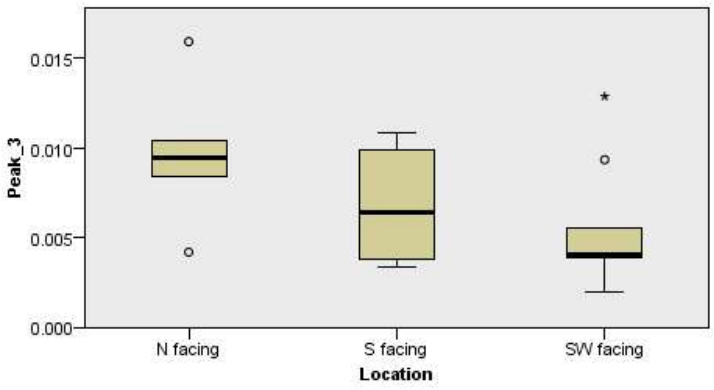
Independent-Samples Kruskal-Wallis Test



Total N	21
Test Statistic	5.347
Degrees of Freedom	2
Asymptotic Sig. (2-sided test)	.069

1. The test statistic is adjusted for ties.
2. Multiple comparisons are not performed because the overall test does not show significant differences across samples.

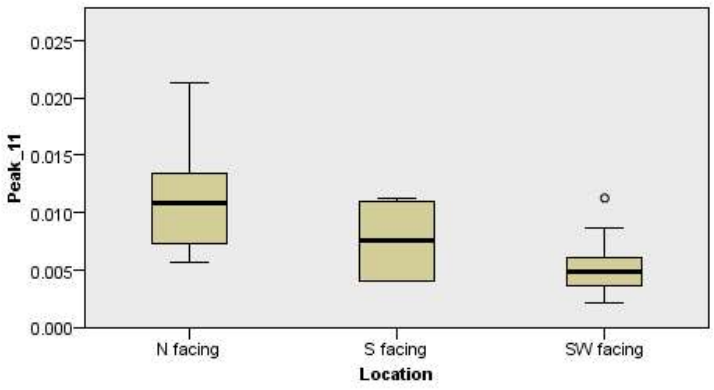
Independent-Samples Kruskal-Wallis Test



Total N	21
Test Statistic	3.698
Degrees of Freedom	2
Asymptotic Sig. (2-sided test)	.157

1. The test statistic is adjusted for ties.
2. Multiple comparisons are not performed because the overall test does not show significant differences across samples.

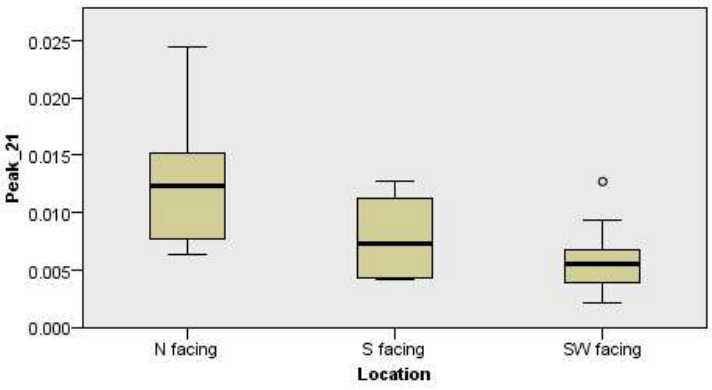
Independent-Samples Kruskal-Wallis Test



Total N	21
Test Statistic	5.565
Degrees of Freedom	2
Asymptotic Sig. (2-sided test)	.062

1. The test statistic is adjusted for ties.
2. Multiple comparisons are not performed because the overall test does not show significant differences across samples.

Independent-Samples Kruskal-Wallis Test



Total N	21
Test Statistic	5.681
Degrees of Freedom	2
Asymptotic Sig. (2-sided test)	.058

1. The test statistic is adjusted for ties.
2. Multiple comparisons are not performed because the overall test does not show significant differences across samples.

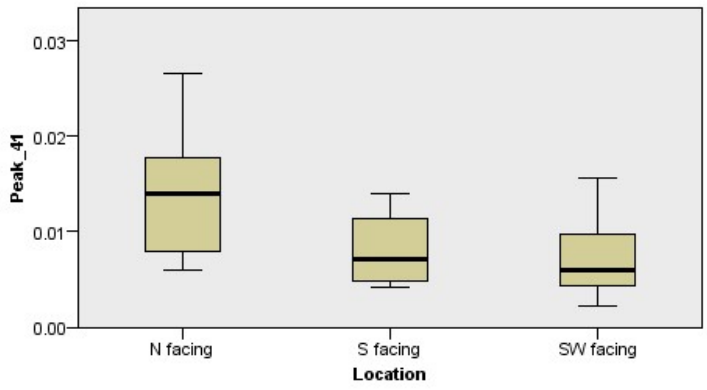
Independent-Samples Kruskal-Wallis Test



Total N	21
Test Statistic	4.638
Degrees of Freedom	2
Asymptotic Sig. (2-sided test)	.098

1. The test statistic is adjusted for ties.
2. Multiple comparisons are not performed because the overall test does not show significant differences across samples.

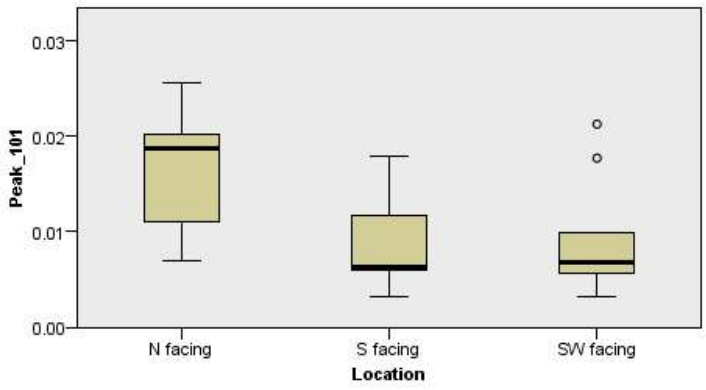
Independent-Samples Kruskal-Wallis Test



Total N	21
Test Statistic	4.461
Degrees of Freedom	2
Asymptotic Sig. (2-sided test)	.107

1. The test statistic is adjusted for ties.
2. Multiple comparisons are not performed because the overall test does not show significant differences across samples.

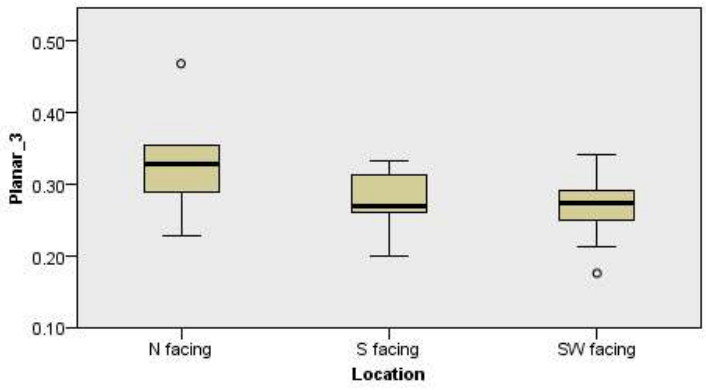
Independent-Samples Kruskal-Wallis Test



Total N	21
Test Statistic	4.995
Degrees of Freedom	2
Asymptotic Sig. (2-sided test)	.082

1. The test statistic is adjusted for ties.
2. Multiple comparisons are not performed because the overall test does not show significant differences across samples.

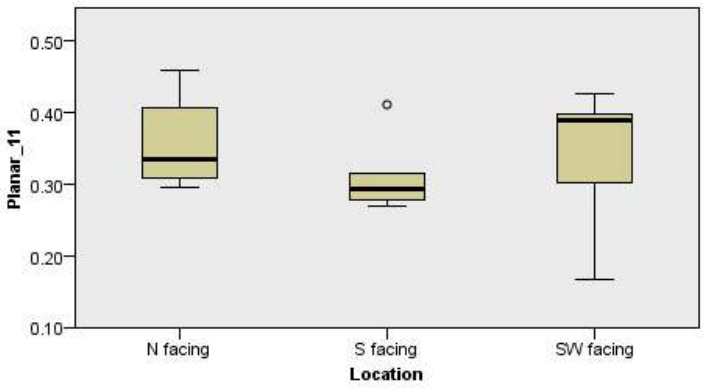
Independent-Samples Kruskal-Wallis Test



Total N	21
Test Statistic	2.743
Degrees of Freedom	2
Asymptotic Sig. (2-sided test)	.254

1. The test statistic is adjusted for ties.
2. Multiple comparisons are not performed because the overall test does not show significant differences across samples.

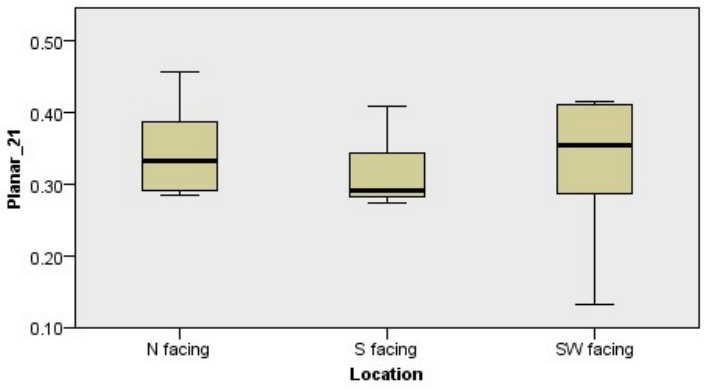
Independent-Samples Kruskal-Wallis Test



Total N	21
Test Statistic	2.034
Degrees of Freedom	2
Asymptotic Sig. (2-sided test)	.362

1. The test statistic is adjusted for ties.
2. Multiple comparisons are not performed because the overall test does not show significant differences across samples.

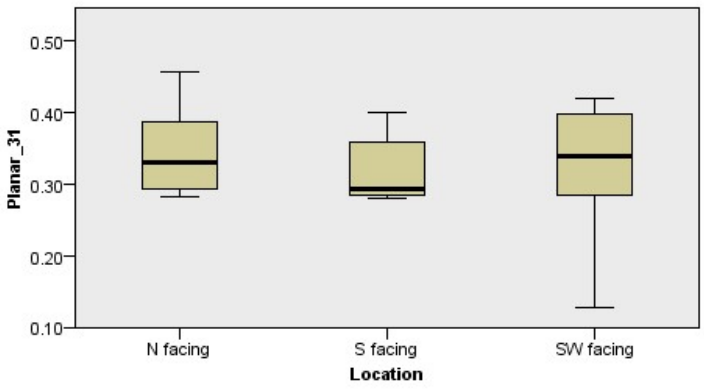
Independent-Samples Kruskal-Wallis Test



Total N	21
Test Statistic	1.552
Degrees of Freedom	2
Asymptotic Sig. (2-sided test)	.460

1. The test statistic is adjusted for ties.
2. Multiple comparisons are not performed because the overall test does not show significant differences across samples.

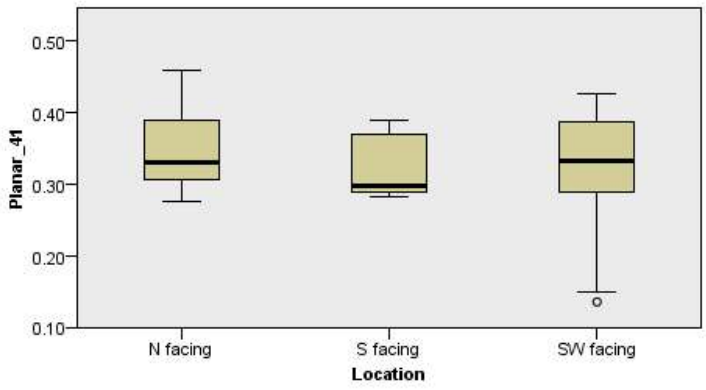
Independent-Samples Kruskal-Wallis Test



Total N	21
Test Statistic	.402
Degrees of Freedom	2
Asymptotic Sig. (2-sided test)	.818

1. The test statistic is adjusted for ties.
2. Multiple comparisons are not performed because the overall test does not show significant differences across samples.

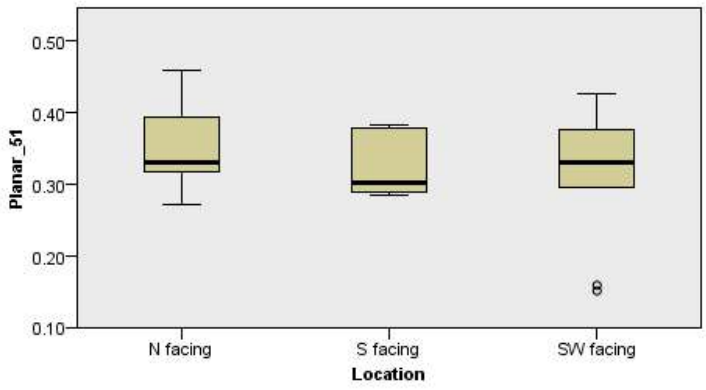
Independent-Samples Kruskal-Wallis Test



Total N	21
Test Statistic	.616
Degrees of Freedom	2
Asymptotic Sig. (2-sided test)	.735

1. The test statistic is adjusted for ties.
2. Multiple comparisons are not performed because the overall test does not show significant differences across samples.

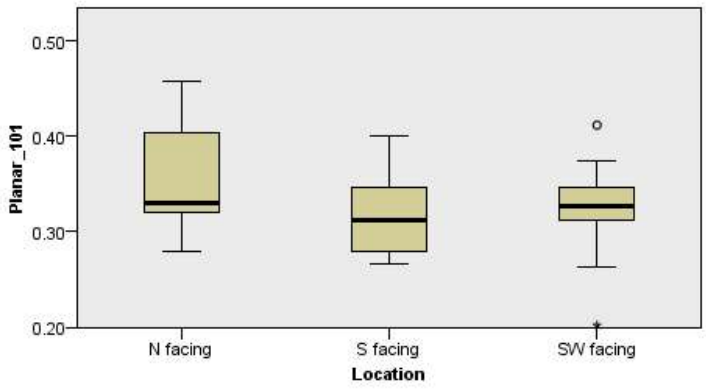
Independent-Samples Kruskal-Wallis Test



Total N	21
Test Statistic	.856
Degrees of Freedom	2
Asymptotic Sig. (2-sided test)	.652

1. The test statistic is adjusted for ties.
2. Multiple comparisons are not performed because the overall test does not show significant differences across samples.

Independent-Samples Kruskal-Wallis Test



Total N	21
Test Statistic	.807
Degrees of Freedom	2
Asymptotic Sig. (2-sided test)	.668

1. The test statistic is adjusted for ties.
2. Multiple comparisons are not performed because the overall test does not show significant differences across samples.